



University  
of Glasgow

Lafta, Abbas Jassim Attia (2013) *New materials for photocatalysis and photovoltaics*. PhD thesis.

<http://theses.gla.ac.uk/4105/>

Copyright and moral rights for this thesis are retained by the author

A copy can be downloaded for personal non-commercial research or study

This thesis cannot be reproduced or quoted extensively from without first obtaining permission in writing from the Author

The content must not be changed in any way or sold commercially in any format or medium without the formal permission of the Author

When referring to this work, full bibliographic details including the author, title, awarding institution and date of the thesis must be given



University  
of Glasgow | School of  
Chemistry

## New Materials for Photocatalysis and Photovoltaics

Abbas Jassim Attia Lafta  
BSc, MSc

Submitted in Fulfilment of the Requirements for the  
Degree of Doctor of Philosophy

School of Chemistry  
College of Science and Engineering  
University of Glasgow

March 2013

## Abstract

Photocatalytic processes are of widespread interest. Among different types of photocatalytic material  $\text{TiO}_2$  is the generally considered amongst the best due to its favourable physical and chemical properties. In recent decades, photovoltaic devices have been widely studied to provide alternative routes to energy and reduce dependency upon fossil fuel. Solar photovoltaic are cells capable of harvesting of sunlight into electrical power. This technology is one of the most promising routes in the search for sustainable and renewable sources of energy. The study presented in this thesis relates to the preparation and characterization of a range of different materials which can be applied in photocatalytic processes and for photovoltaic devices.

The photocatalysis work has been focused mainly upon modification of the various phases of titanium dioxide. This has been undertaken via doping with nitrogen by treatment with ammonia at different temperatures. In addition, samples containing Al, Co and Cu dopants, as well as their N doped counterparts, have been prepared, characterized and tested. The photocatalytic activity was screened by following photocatalytic decomposition of an aqueous solution of methylene blue using a light source containing various components in the UV and visible regions. For selected samples, the photocatalytic activity for polymerization of methyl methacrylate and styrene has been determined with the aim of producing composites.

In terms of potential photovoltaic materials, the synthesis of novel viologen compounds and polymerization via electrochemical and chemical means has been undertaken. Different viologen monomers have been synthesized with various moieties in conjugation to a phenanthroline core to afford novel push-pull systems. These compounds have incorporated both TCNE and TCNQ moieties as strong electron acceptors and hence yield chromophore with large dipole moments. In addition, novel ruthenium complexes were prepared featuring bipyridine and phenanthroline ligands. The optical and redox properties of these materials have been investigated. DSSCs have been fabricated from some of these systems and their properties have been compared to dye 719.

## Acknowledgements:

First of all, I would like to thank my supervisors Dr. Justin Hargreaves and Prof. Graeme Cooke for their assistance and advice to me during my studies. They always supported me with ideas and scientific knowledge and suggestions of providing continuous encouragement for me, displaying patience with me towards development of my English. Also I would like to acknowledge my gratitude to all members of the Hargreaves research group and the all members of the Cooke research group. I would like to thank Dr. Deliang Long for his contribution in doing X-ray crystallography. I am very grateful to Prof. Peter Skabara and his research group, especially a PhD student Saadeldeen Elmasely, at Strathclyde University for their contribution in the electropolymerization reactions. I would like also to thank Dr. Neil Robertson and his group and, especially a PhD student Nina Chadwick, at Edinburgh University for their assistance with some initial photovoltaic studies. There are a number of other people from the School of Chemistry I wish to thank for their assistance during my work over the last three years. A special thanks should go to Mr Jim Tweedy for his help acquiring mass spectra, Mr Jim Gallagher for his assistance with the SEM studies, Mrs Kim Wilson for doing microelemental analysis, Mr Michael Beglan for his assistance with the atomic absorption analysis and Mr Andrew Monaghan for doing TGA analysis and BET measurements.

Also, I would like to thank my family for their patience with me during my study. Finally, I would like to express my extreme gratitude to Ministry of Higher Education in Iraq, Babylon University and the Iraqi Cultural Attaché in London for their contribution and funding of my scholarship.

## Contents

Content	Page
Abstract	ii
Acknowledgements	iii
Contents	iv
List of abbreviations	xi
Declaration	xv
<b>Chapter one: Introduction</b>	1
1- Photochemistry	1
1- 2 The nature of light	2
1-3 Absorption and emission of radiation	4
1-4 Molecular electronic excitation	5
1-4-1 Molecular spectroscopy and photochemistry	5
1-4-2 Molecular excitation and de-excitation events	8
1-4-3 Intramolecular energy transfer	9
1-5 Chemical change	11
1-5-1 Types of chemical change	11
1-5-2 Optical photodissociation	11
1-6 Photochemistry in nature	14
1-6-1 Atmospheric photochemistry	14
1-6-2 Photosynthesis	17
1-7 Solar energy storage	18
1-8 Photochemistry in synthesis	20
1-9 Photopolymerization	21
1-9-1 Photochemical initiation of polymerization	23
1-9-2 Organic photoinitiators	23
1-9-3 Inorganic photoinitiators	24
1-10 Kinetic of free radical polymerization	25
1-11 Photocatalytic polymerization	26
1-12 Aims of Thesis	29
1-13 References	30
<b>Chapter two: Modification of the photocatalytic activity of titanium dioxide by doping with nitrogen</b>	32
2-1 General introduction	32
2-2 General properties of titanium dioxide	33

2-2-1 Morphology of titanium dioxide	33
2-2-2 Crystal forms of titania	34
2-2-3 Electronic and Conductance properties of TiO <sub>2</sub>	35
2-2-4 Electronic excitation of semiconductors	37
2-3 Surface modification	40
2- 3-1 Non-metal doping	41
2-3-2 Identification of doped nitrogen species	42
2-3-3 Mechanism of photoresponse for doped TiO <sub>2</sub> in visible light	42
2-3-4 Methods of doping	43
2-4 Adsorption on the TiO <sub>2</sub> surface	43
2- 5 Results and Discussion	44
2-5 -1 Parent and nitrogen doped titanium dioxide	44
2-5-1-1 Elemental analysis	45
2-5-1-2 BET Surface area measurements	46
2-5-1-3 UV- visible Spectra for nitrogen doped titania	47
2-5-1-4 XRD patterns for parent and doped TiO <sub>2</sub> samples	50
2-6 Determination of point zero charge for nitrogen doped titania (PZC)	51
2-7 Photocatalytic activity for neat and doped titania	56
2-7-1 Photocatalytic decomposition of methylene blue over parent and nitrogen doped TiO <sub>2</sub>	56
2-7-2 MB decomposition over rutile	57
2-7-3 MB decomposition over nitrogen doped P25	60
2-7-4 MB decomposition over nitrogen doped anatase	62
2-7-5 Proposed mechanism for the photocatalytic decomposition of MB over titanic	65
2-8 Photocatalytic polymerization over neat anatase	66
2-8-1 Characterisation of the polymer	66
2-8-2 Optimization of the weight of the TiO <sub>2</sub> used	72
2-8-3 Effect of exposure time	73
2-8-4 Effect of the amount of the used monomer	74
2-8-5 Effect of temperature on the reaction	75
2-8-6 Activation energy for photocatalytic polymerization over titania	76
2-8-7 Effect of atmosphere on the polymerization reaction	77
2-8-8 Effect of the monomer type on the photocatalytic polymerization over anatase	78
2-8-9 Effect using Et <sub>3</sub> N on the photocatalytic polymerization	79

2-8-10 Effect of exposure time on grafting	80
2-8-11 Proposed mechanism for photocatalytic polymerization	81
2-8-12-Effect of the amount anatase on grafting	82
2-8-13 Photocatalytic decomposition of MB over PMMA grafted anatase	78
2-9 Photocatalytic polymerization over nitrogen doped titania	84
2-9 -1 Photocatalytic polymerization over N/ TiO <sub>2</sub>	84
2-9 -2 Characterisation of the polymer	80
2-9-3 Photocatalytic polymerization over nitrogen doped anatase	88
2-10 Photopolymerization	91
2-10-1 Photopolymerization of styrene and methyl methacrylate	91
2-10-1-1 Characterization of the polymer	91
2-10-1-2 <sup>1</sup> H NMR spectroscopy	91
2-10-1-3 FTIR spectroscopy	93
2-10-1-4 Kinetics of polymerization	94
2-10-1-5 The effect of the amount of the used monomer	95
2-10-1-6 Effect of inert atmosphere on the rate of reaction	96
2-10-1-7 Effect of the reaction temperature on the photopolymerization	98
2-10-2 Thermal polymerization of ST and MMA	99
2-11 Proposed mechanism for the photocatalytic polymerization	100
2-12 Proposed mechanism for the photopolymerization	101
2-13 Conclusions	103
2-14 References	104
<b>Chapter three: Modification of the photocatalytic activity of titanium dioxide by metal doping</b>	109
3-1 Introduction	109
3-2 Band structure of semiconductors	111
3-3 Deposition of metals on titanic	112
3- 3-1 Bandgap modification by metal doping	113
3- 3-2 Mechanism of photoactivity of neat and doped titania	114
3-3-3 The aim of the project	116
3-4 Results and discussion	116
3-4-1 Doping titania with metals	116
3-4-1-1 XRD patterns for metal doped titania	116
3-4-1-2 UV-visible spectra for doped titanic with Al, Co and Cu	118
3-4-1-3 Specific surface area (BET)	120

3-5 Point of zero charge of the metal doped titania	121
3- 6 Photocatalytic activity for neat and metal doped titania	124
3-6-1 Photocatalytic decomposition of MB over metal doped titania	124
3-6-2 Photocatalytic polymerization of methyl methacrylate over metal doped anatase	128
3-6-3 Characterisation of the polymer	128
3-6-4 Photocatalytic polymerization over metal doped anatase	134
3-6-4-1 Proposed mechanism for polymerization over metal doped titania	135
3-7 Modification of metal doped anatase by doping nitrogen	136
3-7-1 Characterisation of the modified samples	136
3-7-1-1 Microelemental analysis	137
3-7-1-2 Specific surface area (BET) measurements	137
3-7-1-3 XRD patterns for the samples	138
3- 8 The PZC of co-doped anatase	143
3-9 Photocatalytic activity of the co-doped anatase	145
3-9-1 Photocatalytic polymerization of methyl methacrylate over co-doped anatase	14
3-9-2 Characterization of the polymer	149
3-9- 3 Photocatalytic polymerization of methyl methacrylate over co-doped anatase	158
3-10 Conclusions	162
3-11 References	163
<b>Chapter four: Towards synthesis of novel viologen acceptors for photovoltaic devices</b>	167
4- 1 Introduction	167
4-1-1 Bipyridinium dication (Bipm <sup>2+</sup> )	168
4-1-2 Bipyridinium radical cation (Bipm <sup>+</sup> )	168
4-2 Adsorption of viologen compounds	170
4-3 Electron transfer reaction in viologens	170
4-4 Organic conducting polymers	171
4-4-1 Conjugated polymer for organic solar cells	172
4-4- 2 Conducting polymers comprising viologen	176
4-5 Electrochemical polymerization	178
4-5-1 Doping conjugated polymer and bandgap energy	179
4-5-2 Viologen and solar energy conversion	182
4-5-3 General aim of the project	183
4-6 Results and Discussion	183

4-6-1 Synthesis of target compound (1)	184
4-6-1-1 Analysis of compound (1)	185
4-6-1-2 Polymerization of compound (1)	185
4-6-2 Syntheses of targeted compound (2)	187
4-6-2-1 Analysis of target compound (2)	189
4-6-2-2 Polymerization of compound (2)	189
4-6-3 Synthesis of target compound(3)	191
4-6-3-1 Analysis of compound (3)	192
4-6-3-2 Polymerization of compound (3)	193
4-6-4 Synthesis of target compound (4)	197
4-6-4-1 Analysis of compound (17)	198
4-6-4-2 Electrochemical growth of poly(17)	201
4-6-4-3 The voltammogram of poly(17)	202
4-6-4-4 Analysis of compound (4)	205
4-6-5 Synthesis of compound (5) and (6)	207
4-6-5-1 Analysis of compound (5)	209
4-6-5-2 The voltammogram of compound (5)	209
4-6-5-3 Polymer growth of poly(5)	211
4-6-5-4 Spectroelectrochemistry of poly (5)	218
4-6-6 Analysis of compound (6)	220
4-6-6-1 UV- visible and CV of compound (6)	220
4-6-6-2 The voltammogram of compound (6)	221
4-6-6-3 Electrochemical polymerization of compound (6)	223
4-6-6-4 Spectroelectrochemistry of poly(6)	228
4-7 Conclusions	229
4-8 Acknowledgements	229
4-9 References	230
<b>Chapter five: Towards synthesis of some novel push-pull systems for potential applications as nonlinear optical materials</b>	234
5-1 Introduction	234
5-2 Push-pull systems and nonlinear optics	237
5-3 TCNE and TCNQ incorporating push- pull system	239
5-3-1 Symmetrical push- pull system with phenanthroline core	240
5-4 General aim	240
5-5 Results and Discussion	241

5-5-1 Synthesis of target compound (20)	241
5-5-2 Analysis of compound (20)	242
5-6 Synthesis of target compounds (21) and (22)	244
5-6-1 Proposed mechanism for [2+2] cycloaddition	245
5-6-2 Analysis of compound (21)	246
5-7 Synthesis of target compounds (23 and 24)	248
5-7-1 The electronic spectrum of compound (23)	249
5-7-2 The electrochemistry of compound (23)	250
5-8 Synthesis of target compound (25)	252
5-8-1 Analysis of compound (25)	252
5-8-2 The voltammogram of compound (25)	253
5-9 Conclusions	255
5-10 References	256
<b>Chapter six: Synthesis of some novel ruthenium (II) complexes as luminescence materials and dye sensitized solar cells.</b>	258
6-1 Introduction	258
6-2 Ruthenium chelating compounds	259
6-3 Conducting polymer of Ru(II) complexes	261
6-4 Dye sensitized solar cells	263
6-4-1 Operation principle of the Grätzel dye sensitized nanocrystalline solar cell	264
6-4-2 General design of dyes for DSSCs	266
6-4-3 Methods of attaching dye to semiconductor in DSSCs	263
6-5 Ruthenium complexes for dye sensitized solar cells	267
6-6 The general aim	268
6-7 Results and Discussion	268
6-7-1 Synthesis of compound (32)	269
6-7-1-2 Analysis of compound (32)	270
6-7-1-3 UV- visible spectroscopy and CV of compound (32)	271
6-7-1-4 The voltammogram of compound (32)	272
6-7-1-5 Electropolymerization of compound (32)	274
6-7-2 Synthesis of target compound (33)	274
6-7-2-1 Analysis of compound (33)	275
6-7-2-2 Electropolymerization of compound (33)	277
6-7-2-3 Spectroelectrochemistry of poly(33)	282
6-7-3 Synthesis of target compounds (40) and (34)	283

6-7-3-1 Analysis of compound (40)	284
6-7-3-2 Analysis of compound (34)	285
6-8 Synthesis of dyes sensitized solar cells (DSSCs)	286
6-8-1 Analysis of compound (35)	288
6-8-2 The voltammogram of dye (35)	289
6-8 -3 Analysis of compound (36)	289
6-8-4 the voltammogram of dye (36)	290
6-9 Dyes loading over TiO <sub>2</sub>	291
6-10 Current density- voltage for photovoltaic devices	292
6-11 Conclusions	294
6-12 Acknowledgements	295
6-13 References	296
<b>Chapter seven: Suggestions and future work</b>	300
<b>Chapter eight: Experimental</b>	303
8-1 Doping of titanium dioxide with nitrogen	303
8-2 Doping reactor	303
8-3 Doping TiO <sub>2</sub> with nitrogen	304
8-3-1 Samples characterization	304
8-3-1-1 Elemental analysis	304
8-3-1-2 BET Surface area measurements	304
8-3-1-3 UV- visible spectra for nitrogen doped titania	304
8-3-1-4 XRD patterns for parent and doped TiO <sub>2</sub> Samples	304
8-4 Photochemical reactor	305
8-5 Photocatalytic activity for nitrogen doped titania	306
8-5-1 Photocatalytic decomposition of MB over parent and nitrogen doped TiO <sub>2</sub>	306
8-5-2 Photocatalytic polymerization	307
8-6 Photopolymerization	310
8-7 Modification titania by doping metals	312
8-8 Experimental of organic materials	313
8-8-1 General notes	313
8-8-2 Synthetic experimental	314
8-8-3 Fabrication of DSSCs devices	338
8-9 References	339
8-10 Appendix	340

## Abbreviations

Abbreviations	Definition
AA	Atomic absorption
Abs	Absorbance
A	Acceptor
a. u.	Arbitrary unit
Å	Angstrom
$\beta$	Hyperpolarizability factor
BET	Brunauer, Emmett and Teller
BHJ	Bulk heterojunction
Bpy	2,2'- Bipyridine
Bipm	Bipyridinium
°C	Degree Celsius
CT	Intramolecular charge transfer complex
CB	Conduction band
Conv%	Conversion percentage
CV	Cyclic voltammetry
CHN	CHN elemental analysis
CP	Conjugated polymer
D	Donor
d	Doublet
Dec	Decomposed
DCM	Dichloromethane
DMF	Dimethylformamide
DMSO	Dimethylsulfoxide
DMPU	1,3-Dimethyl-3,4,5,6-tetrahydro-2(1H)-pyrimidinone
DSSCs	Dye sensitized solar cells
E <sub>a</sub>	Activation energy
E <sub>1/2</sub>	Half wave potential
e <sup>-</sup> <sub>CB</sub>	Conduction band electron
ECD	Electrochromic display device
EDG	Electron donating group
EDOT	3,4- Ethylenedioxythiophene
EWG	Electron withdrawing group

E <sub>g</sub>	Bandgap energy
eV	Electron volt
ESR	Electron spin resonance
Et	Ethyl
e <sup>-</sup> <sub>tr</sub>	Trapped electron
EtOAc	Ethyl acetate
Et <sub>3</sub> N	Triethylamine
FAB	Fast atomic bombardment
Fc	Ferrocene
FF	Fill factor
FL	Fermi level
G	Gram
G%	Grafting percentage
GPC	Gel permeation chromatography
Δ	Heat
h	Planck constant
h <sup>+</sup>	Positive hole
h <sup>+</sup> <sub>VB</sub>	Valence band hole
h <sup>+</sup> <sub>tr</sub>	Trapped hole
hν	Electromagnetic radiation
HOMO	Highest occupied molecular orbital
HRS	Hyper Rayleigh scattering
I	Initiator
IC	Internal conversion
IR	Infra red
IPCE	Incident photon to current efficiency
ITO	Indium tin oxide
IT	Immersion technique
J <sub>sc</sub>	Photocurrent density
ISC	Intersystem crossing
K	Kelvin temperature
k	Rate constant
LUMO	Lowest unoccupied molecular orbital
LMB	Leuco form of methylene blue

MB	Methylene blue
m	Multy
M	Mole per liter
MeCN	Acetonitrile
MeOH	Methanol
Me	Methyl
MLCT	Metal-to ligand charge transfer
MMA	Methyl methacrylate
mV	Millivolt
mL	Milliliter
MLCT	Metal- to- ligand charge transfer transitions
$M_n$	Number average molecular weight
MT	Mass titration technique
$M_w$	Weight average molecular weight
NBS	N- bromosuccinimide
$NiCl_2(dppp)$	Dichloro(1,3-bis(diphenylphosphino)propane) nickel
nm	Nanometer
N3	Cis-dithiocyanato-bis(4,4'-dicarboxy-2,2'-bipyridine)Ru(II)
N719	Doubly deprotonated N3
NLO	Nonlinear optics
NMR	Nuclear magnetic resonance
PA	Polyacetylene
PCBM	Phenyl-C61-butyric acid methyl ester
PDI	Poly dispersion index
PEC	Photoelectrochemical cell
$PF_6$	Hexafluorophosphate
PLEDs	Polymer light emitting diodes
PT	Potentiometric titration
ppm	Parts per million
PV	Photovoltaic
PZC	Point of zero charge
q	Quartet
R%	Reflectance percentage

RT	Room temperature
s	Singlet
S	Excited singlet state
SHG	Second harmonic generation
SHE	Standard hydrogen electrode
SEM	Scanning electron microscopy
ST	Styrene
$\delta$	Chemical shift
T	Triplet excited state
TBAPF <sub>6</sub>	Tetrabutylammonium hexafluorophosphate
TCNE	Tetracyanoethylene
TCNQ	Tetracyanoquinone
T%	Transmittance percentage
TGA	Thermal gravimetric analysis
THF	Tetrahydrofuran
TLC	Thin layer chromatography
t	Triplet
TPF	Two-photon fluorescence
UV	Ultraviolet
UV-vis	Electronic spectrum
VB	Valence band
$\nu$	Frequency
V <sub>oc</sub>	Open circuit voltage
Vis	Visible
$\lambda$	Wavelength
XAFS	X-ray absorption fine structure
XPS	X-ray photoelectron spectroscopy
XRD	X-ray diffraction

## Declaration

I hereby declare that the substance of this thesis has not been submitted, nor is currently submitted for any other degree. Also, I declare that the projects presented in this thesis are the result of my own investigations and where the work of other investigations has been used, this has been fully acknowledged in the text.

Abbas Jassim Attia Lafta  
March 2013

## **Chapter- one: Introduction**

### **1 Photochemistry**

#### **1-1 The nature of photochemistry**

It is well known that the life of human being on the earth is dependent completely on solar energy<sup>(1)</sup>. Radiation energy from the sun is a crucial factor for the existence of life on our planet, some deep sea ecosystems based entirely on geothermal energy. Green plants can utilize this energy in the production of carbohydrates and oxygen by photosynthesis. The main subject of photochemistry is the study of interaction of light with matter. In some cases, this interaction can result in chemical changes in the absorbing species<sup>(1)</sup>. However, in other cases light may be released from photoexcited species without any chemical change. Photochemical processes encompass both those that occur via absorption light and the chemical processes that produce light.

Generally, some processes involve absorption or emission of light without overall chemical change such as fluorescence and phosphorescence and in these processes light is emitted from the chemical species, which absorbed it initially without any chemical change.

However, when a molecule or an atom absorbs a photon of light with a suitable energy, its electronic structure changes and produces an electronically excited state. This then reacts in different ways with other species, and under these circumstances, the energy that is initially absorbed from light can result in photochemical change. In some cases, this process leads to photochemical change in species other than initial absorbing species as in photosensitization processes. In addition, energy of the excited species can be released as thermal energy (heat) or as a lower energy light which results in return the excited state to its ground state. Each type of chemical species has a different affinity toward these mechanistic routes. For example, some species are more prone to fluorescence rather than chemical change<sup>(1)</sup>.

The first law of photochemistry, the Grotthuss- Drapper law states that light must be absorbed for photochemistry to occur. According to this law, light must be absorbed by a desired species for a chemical change to occur. However, this process requires absorption of light of a particular wavelength otherwise, no photochemistry occurs.

The second law of photochemistry, the Stark- Einstein law states that for each photon of light absorbed by a chemical system, only one molecule is activated for each photon. So that, each molecule absorbs one photon, and hence each photon can activate only one molecule for a photochemical reaction to occur. This law is valid only for systems of normal light intensity. For higher light intensities such as in lasers, two photons absorption can occur by absorbing molecule, which results in a higher energy state in comparison with the first case as follows:



According to the Bunsen-Roscoe law of the reciprocity states that, the overall photochemical effect is directly proportional to the total amount of energy absorbed by the system, irrespective of the time which is required to gain this amount of energy<sup>(2)</sup>.

### 1-2 The nature of light

Light is a type of energy which possesses both wave and particle properties<sup>(3)</sup>. It is composed of electric and magnetic component fields, which propagated in space at right angles to one other<sup>(1)</sup>. Both the electrical and magnetic fields are shown in the following figure:

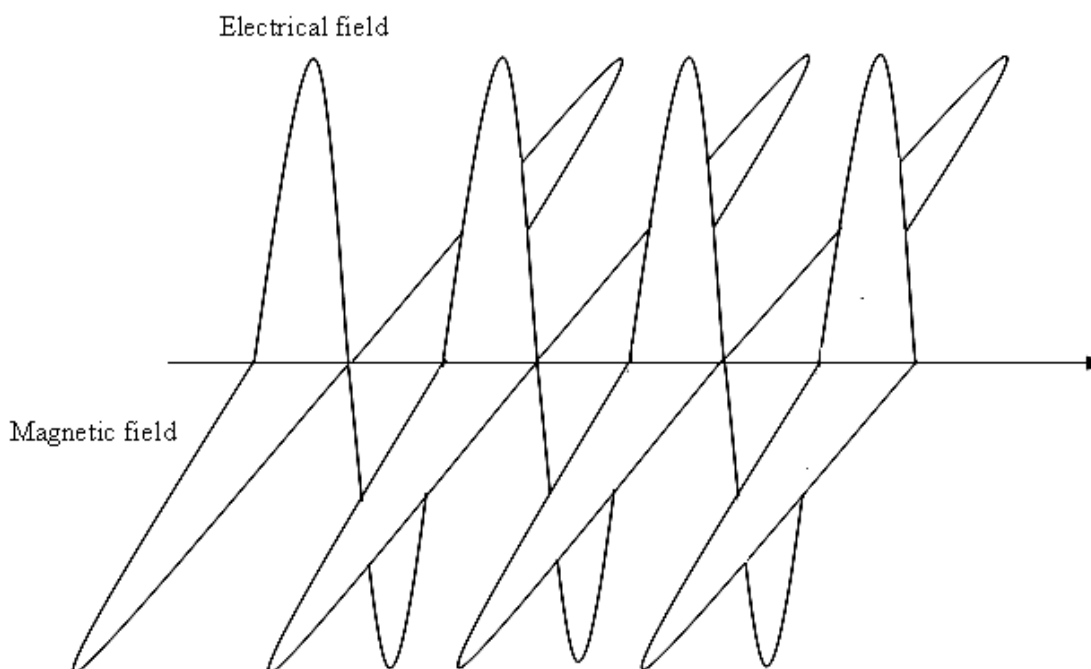


**Figure 1-1:** Schematic description of waves of electromagnetic radiation<sup>(3)</sup>.

The electromagnetic spectrum propagates in a straight line in space with a speed in vacuum of around  $3 \times 10^8 \text{ m s}^{-1}$ . This spectrum comprises of different wavelengths of light with different photon energies as shown in the following figure:

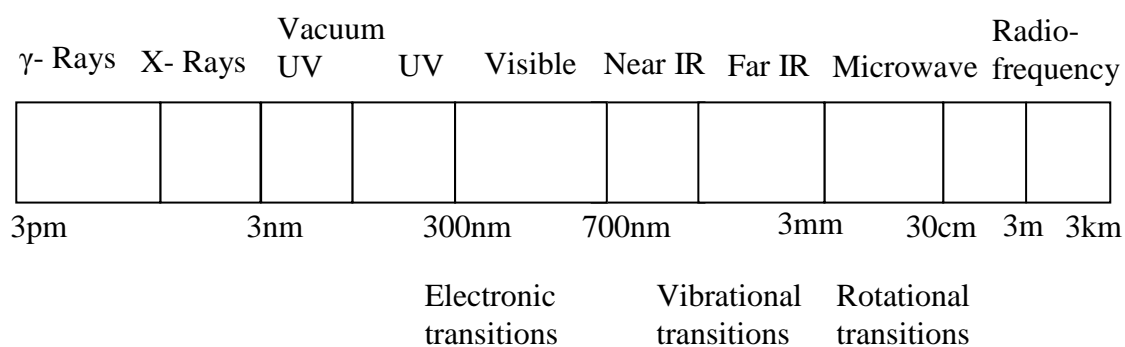
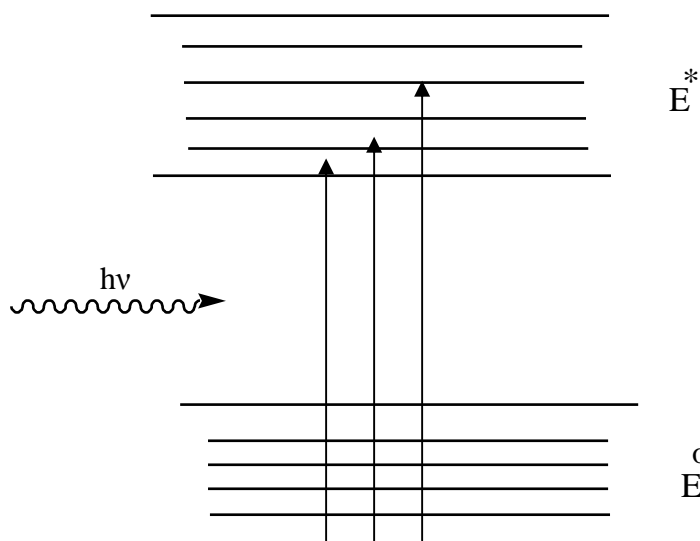


**Figure 1-2:** The spectral regions of electromagnetic spectrum<sup>(3)</sup>.

James Clerk Maxwell<sup>(1)</sup> showed that light is a type of electromagnetic radiation and its wave properties result from the transverse oscillation of both electric and magnetic fields as illustrated in Figure 1-1. These fields are presented in planes that are perpendicular with each other and with respect to the direction of propagation of light in space. Many of the intrinsic properties of light can be explained according to wave theory such as reflection, refraction, polarization and interference. On the other hand, light has some other properties that can't be explained according to the above theory, such as black body radiation and the photoelectric effect. According to these properties, light has both wave properties and particle properties. Einstein's investigation of the photoelectric effect proved that radiation can be considered as a stream of particles or photons with an energy which is dependent on the frequency of radiation<sup>(1)</sup>. The interaction between photons of a particular energy and matter can be visualised by assuming that the radiation can be considered as a stream of particles with quantized energy<sup>(1)</sup>. Upon interaction between radiation and matter, photon of light can interact with one atom or molecule in the absorbing system, so that the energy which would be available for the reacting species is the energy of that photon ( $E = h\nu$ , where  $h$  is a Planck's constant and  $\nu$  is the frequency of the radiation). The intensity of light is related to the number of the incident photons per unit time. Generally, each photon has a fixed amount of energy, increasing intensity of incident light increases the number of excited species with same excitation energy<sup>(1)</sup>. Over the wide range of electromagnetic radiation, the regions of interest for photochemistry are the visible and ultraviolet regions. These regions can cause electronic transitions in the absorbing species, while longer wavelength regions such as infrared light cause vibrational excitation. Higher energy radiation (shorter wavelengths) such as X- rays may result in the ionization of the absorbing species<sup>(2)</sup>.

### 1-3 Absorption and emission of radiation

Generally, each chemical species has particular quantized energy levels, meaning that each species can exist only in discrete energy states. Accordingly, a molecule can only transfer energy between any of these two separated energy states. Due to the quantization of energy levels, for each individual species only a particular energy with a characteristic wavelength ( $h\nu$ ) can be absorbed or emitted by the chemical species. Absorption of radiation of photons with a sufficient energy, normally in the UV-visible region can lead to transitions between the ground state of the absorbing species ( $E_0$ ) into the excited state ( $E^*$ ) as illustrated in the following scheme:



**Scheme 1-3:** Excitation of a molecule by absorbing light with a particular energy ( $h\nu$ ).

Beside electronic transitions, chemical species can possess other types of quantized energy such as rotational and vibrational. However, these types of transitions occur only for absorption of radiation of longer wavelength in the microwave and infrared regions respectively<sup>(1)</sup>. In contrast to absorption, in emission processes excited chemical species relax from excited state (higher energy state) into the ground state (lower energy state). Generally, there are two types of emission process, stimulated emission that results when excited species interact with radiation and spontaneous emission. The emission of radiation from excited chemical species occurs via fluorescence, phosphorescence and chemiluminescence<sup>(1)</sup>. In these processes, excitation energy is lost from excited species without any net chemical change. However, according to the selection rules electronic transitions between same atomic orbitals are not allowed.

## 1-4 Molecular electronic excitation

### 1-4-1 Molecular spectroscopy and photochemistry

As stated previously, matter absorbs or emits radiation in discrete quanta and upon absorption excitation occurs. Rotational transitions require absorption radiation in the microwave region or absorbing lower energies in the far infrared radiation. Changes in the vibrational energy levels of the molecules requires higher energy than that which is sufficient for the rotational transitions (about 10-100 more) and this occurs by absorption of radiation in the infrared region <sup>(4)</sup>.

Electronic transitions require higher energy and this energy is about 1000 times than that required for rotational energy transitions. However, absorption radiation of energy in the wavelength range 290 -800 nm can promote electrons in the absorbing species into high energy levels and in some cases, this may result in ionization or even reach bond dissociation energies. The energy of one mole of photons of a wavelength of 250 nm can be calculated by applying the Planck relationship and is around 480 kJ mol<sup>-1</sup> <sup>(5)</sup> as follows:

$$E=Nh\nu = NhC/\lambda = 6.02 \times 10^{23} \times 6.62 \times 10^{-34} \times 3 \times 10^8 / 250 \times 10^{-9} = 480 \text{ kJ mol}^{-1}$$

By comparing this energy with that required for carbon- carbon bond dissociation which is approximately around 347 kJ mol<sup>-1</sup>, it can be envisaged that irradiation with UV light in this range can in principle lead to breakage of C-C bonds. However, not all absorbed radiation can lead to chemical changes as some of the excitation energy may be lost by other photophysical processes such as thermal loss, fluorescence and phosphorescence processes and molecular collisions. According to the Grotthuss-Draper law, only radiation that absorbed by a molecule can result in chemical changes. These processes can be summarized according to the Jablonski diagram as shown below <sup>(5)</sup>:

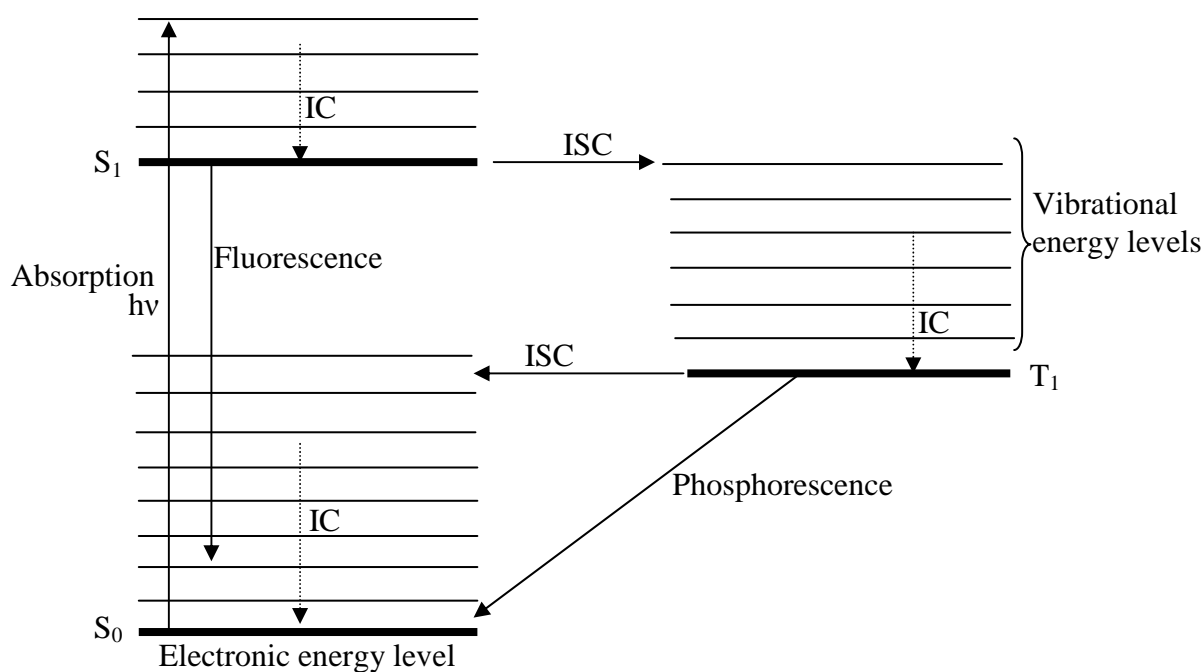
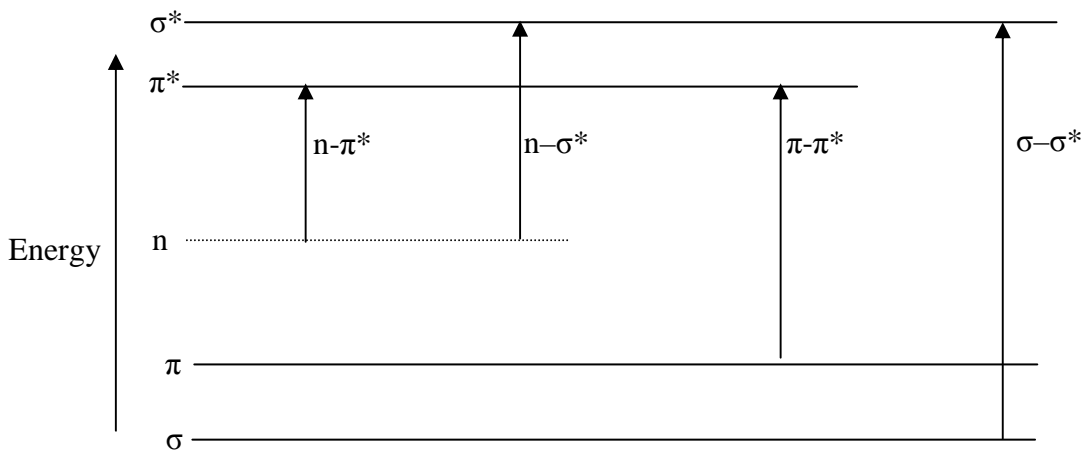


**Figure 1-4:** Jablonski diagram summarizing electronic and vibrational energy levels<sup>(5)</sup>.  $S_0$  is ground electronic state,  $S_1$  is first singlet excited state,  $T_1$  is first triplet excited state, IC is internal conversion and ISC is intersystem crossing.

The above diagram illustrates the main routes that can lead to loss of excitation energy from excited molecules. Generally, radiative processes involve initially absorption of light to give electronically excited state of absorbing molecule. The excited molecule can follow two routes to lose its energy, these involve radiative and non-radiative processes. The radiative processes involve loss of excitation energy from the excited molecule as light. This type of relaxation involves fluorescence and phosphorescence. In fluorescence, the excited molecule loses excitation energy as a radiation by transition between two states of the same spin multiplicity, while in phosphorescence, dissipation of the excitation energy as light occurs by transition between states of different spin multiplicity. On the other hand, non-radiative processes occur by loss of the excitation energy to the surroundings as heat. If this process occurs by transition between states of the same multiplicity, this process is known internal conversion (IC). When the transition occurs between states of different multiplicity, this leads to loss excitation energy as heat and the process is known as an intersystem crossing (ISC)<sup>(5)</sup>.

Generally, electronic transitions can be described according to the type of the orbitals involved. Molecular orbitals based upon linear combination of atomic orbitals can be considered to give corresponding bonding and anti-bonding molecular orbitals ( $\sigma$ ,  $\sigma^*$  and  $\pi$ ,  $\pi^*$ ). The possible electronic transitions are summarized in the following scheme:



**Scheme 1-5:** General diagram of the energy levels of molecular orbitals<sup>(5)</sup>.

Upon electronic excitation, one electron in the molecule can be promoted into a higher energy level. From above figure it can be seen that the transfer electrons from  $\sigma$  to  $\sigma^*$  requires higher energy in comparison with  $\pi$  to  $\pi^*$  transitions. The transitions of most interest are  $\pi$  to  $\pi^*$  and  $n$  to  $\pi^*$ ,  $n$  to  $\sigma^*$ , electronic transitions can lead to two different electron arrangements in the excited state defining the spin multiplicity. When the spins are paired, this gives a singlet excited state (S) and when the spins are unpaired (parallel) this state gives the triplet excited state (T). The excited multiplicity can be calculated according to the following relationship:

$M = 2\Sigma s + 1$ , where,  $M$  is the spin multiplicity,  $s$  is the spin quantum number, either  $+\frac{1}{2}$  or  $-\frac{1}{2}$ . Generally, singlet excited states have a higher energy than triplet states and triplet states have longer lifetimes than singlet states due to spin inversion. However, electronic transitions occur much faster (about  $10^{-15}$  sec) than molecular vibrations (about  $10^{-13}$  sec).

According to the Franck-Condon Principle, when electronic transitions occur the relative nuclear positions are unchanged. The properties of the excited molecule can be seen from potential energy diagrams (Franck-Condon diagrams)<sup>(5)</sup>. The diagram below shows the potential energy curve for the electronic ground state ( $S_0$ ) and the first electronic excited state ( $S_1$ ) of a diatomic molecule as a function of nuclear configuration. These curves sometimes are called potential wells, the horizontal lines of each curve refer to the vibrational levels of each electronic state. Electronic transitions between electronic levels according to Franck-Condon principles are shown in the following figure:

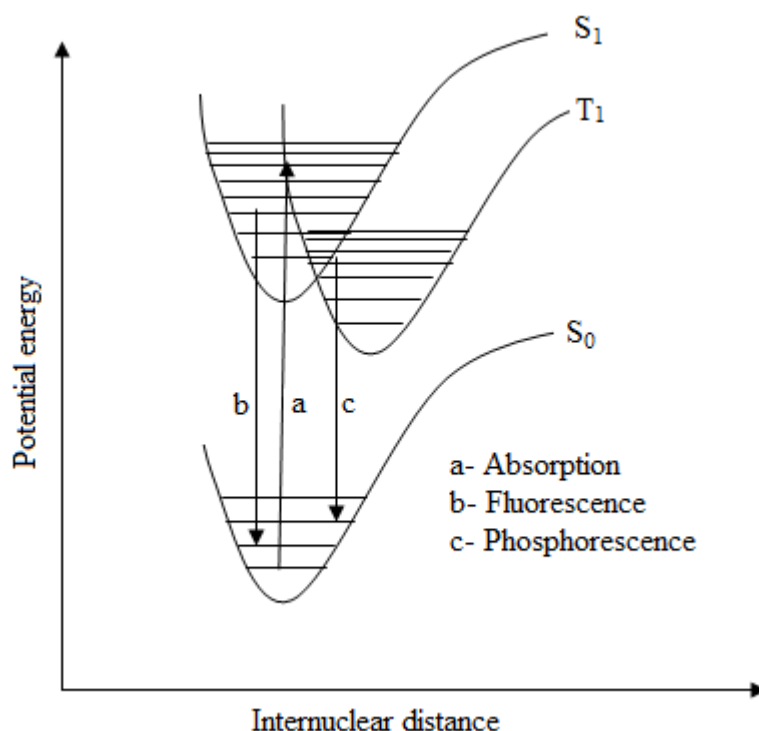


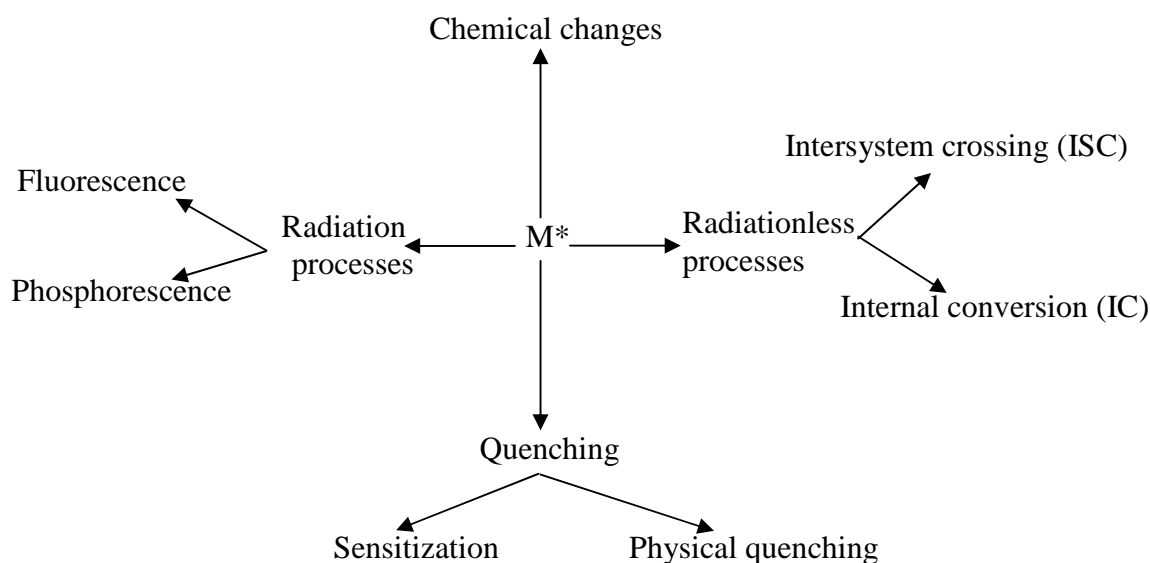
**Figure 1-6:** Relative nuclear positions at various electronic states according to the Franck- Condon principle<sup>(5)</sup>.  $S_0$  is electronic ground state,  $S_1$  is singlet excited state and  $T_1$  is triplet excited state.

Electronic excitation raises the vibration energy level of the excited molecule for a short time ( $10^{-9}$  sec). Electronic transitions can be classified into various categories which are either allowed in case of transitions between different orbitals or forbidden for transitions between same orbitals. Following the principles of quantum mechanics, transitions which involve conservation of spin are favourable. Transitions, which involve a change in the spin multiplicity for excited molecule from singlet into triplet ( $S_0$  to  $T_1$ ), are strictly forbidden. In addition transitions between states that have the same symmetry are allowed such as  $\pi$  to  $\pi^*$  and  $\sigma$  to  $\sigma^*$ , while transitions between states of different symmetry are forbidden.

#### 1-4-2 Molecular excitation and de-excitation events

After excitation, molecules in their excited state possess properties that differ from those in the ground state. For example, singlet spin excited states have diamagnetic properties while those in the triplet states exhibit paramagnetic properties. Generally, excited molecules can lose excitation energy by chemical reactions to yield a new product reaction, by radiative and/or non- radiative energy loss in which there is no net chemical change occurs in the

absorbing molecule. The following scheme shows the main routes that can be followed by excited molecules to lose excitation energy<sup>(5)</sup>:



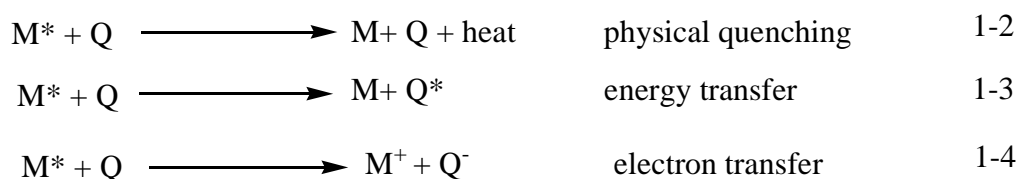
**Scheme 1-7:** The possible routes for energy loss from excited molecule ( $M^*$ )<sup>(5)</sup>.

As can be seen in this diagram one route to loss of excitation energy is through chemical reaction. Additionally, excitation energy can be lost by dissipation between two excited states of same spin multiplicity ( $S_1$  to  $S_0$ ) by radiative energy loss results in emission of excitation energy as light (fluorescence). On the other hand, radiative loss between two states of different spin multiplicity ( $T_1$  to  $S_0$ ) results in phosphorescence, this process has longer lifetime in comparison with fluorescence with a lower energy. Also due to involve spin change in this process its probability is lower than fluorescence<sup>(5)</sup>. In addition to these two routes, excitation energy can be lost by transferring between  $S_1$  to  $T_1$  or  $T_1$  to  $S_0$  by non-radiative processes (thermal process), this is called intersystem crossing (ISC). However, according to this route excited molecules can dissipate excitation energy as heat and return to the ground state by internal conversion (IC). The rate of each of these loss processes depends on the concentration of the excited singlet state ( $^1M^*$ ) state and the rate constant for each process where M is a molecule excited by absorption<sup>(5)</sup>.

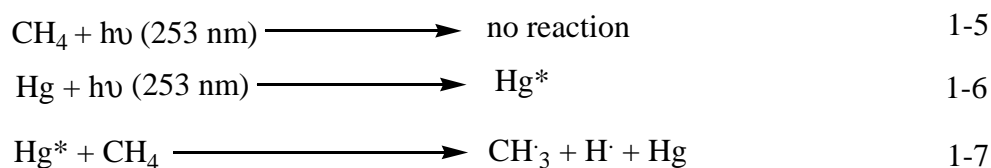
### 1-4-3 Intramolecular energy transfer

When a photoexcited molecule interacts with other molecules in their ground state, loss of excitation energy by various routes can occur. For example, collisions can induce loss of excitation energy as heat, and this process is called physical quenching<sup>(6)</sup>. Energy may also be transferred into the ground state of another molecule through electron transfer or by

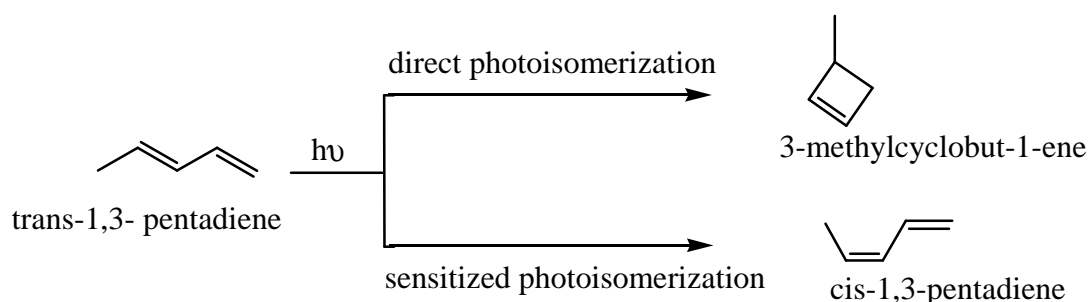
another means (energy transfer). The transfer of energy between the excited molecule ( $M^*$ ) and the quencher (Q) can be represented by the following equations<sup>(2)</sup>:



Sensitization route plays a significant role in the photochemistry of different organic and inorganic species. For example, in the organic photochemistry of olefins, it isn't possible to form triplet excited states by direct absorption as these compounds don't absorb light effectively. In this case, energy transfer from the excited states of other molecules into the ground state of olefin molecules can use alternative methods. In this case, the excited molecules behave as photosensitizers, while the olefins molecules are quenchers. In another example, methane does not absorb light at wavelengths more than 170 nm. However, methane can be excited by sensitization route using mercury vapour under irradiation with light ( $\lambda = 253$  nm). The transfer of excitation energy to methane can lead to dissociation of methane as follows<sup>(1)</sup>:



In some cases result of reaction under sensitization is different from that under direct absorption. For example, direct absorption by trans-1,3-pentadiene results in a photoisomerization product which differs from that under sensitized photoisomerization as shown in the following scheme<sup>(1)</sup>:



**Scheme 1-8:** Schematic description for isomerization of trans-1,3-pentadiene<sup>(1)</sup>.

In sensitization processes, energy transfer is adiabatic, meaning that spin is conserved in the interaction between the sensitizer and the quencher molecules. Generally, there are different types of compounds that can be used as photosensitizers and important examples

of organic photosensitizers are ketone compounds. For this reason in photochemistry, ketone compounds can be used to transfer energy for many others, accepted compounds that can't produce triplet excited state by direct irradiation and have triplet energies lower than those of carbonyl triplets<sup>(1)</sup>. This is an important phenomenon in photochemistry as the producing triplet state for some compounds by direct absorption is impossible. For example, olefin compounds don't produce this type of excited state by direct irradiation.

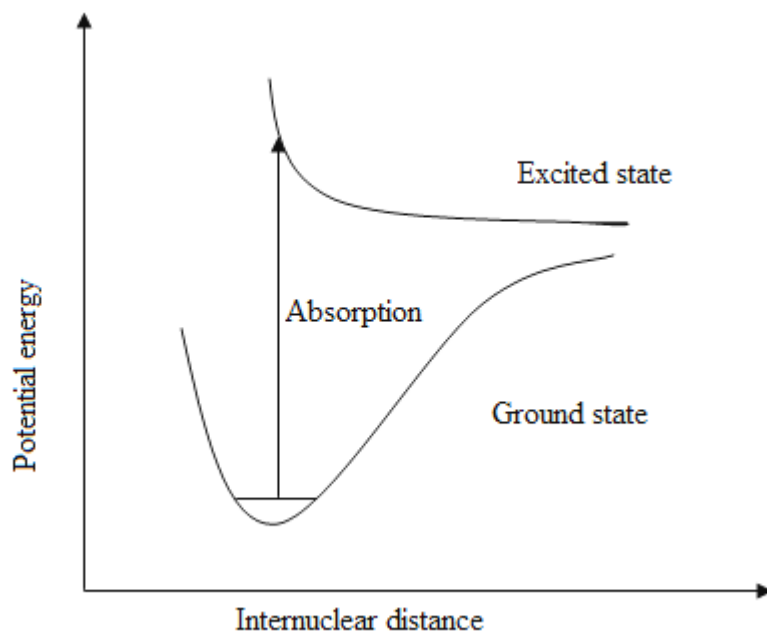
## **1-5 Chemical change**

### **1-5 1 Types of chemical reaction**

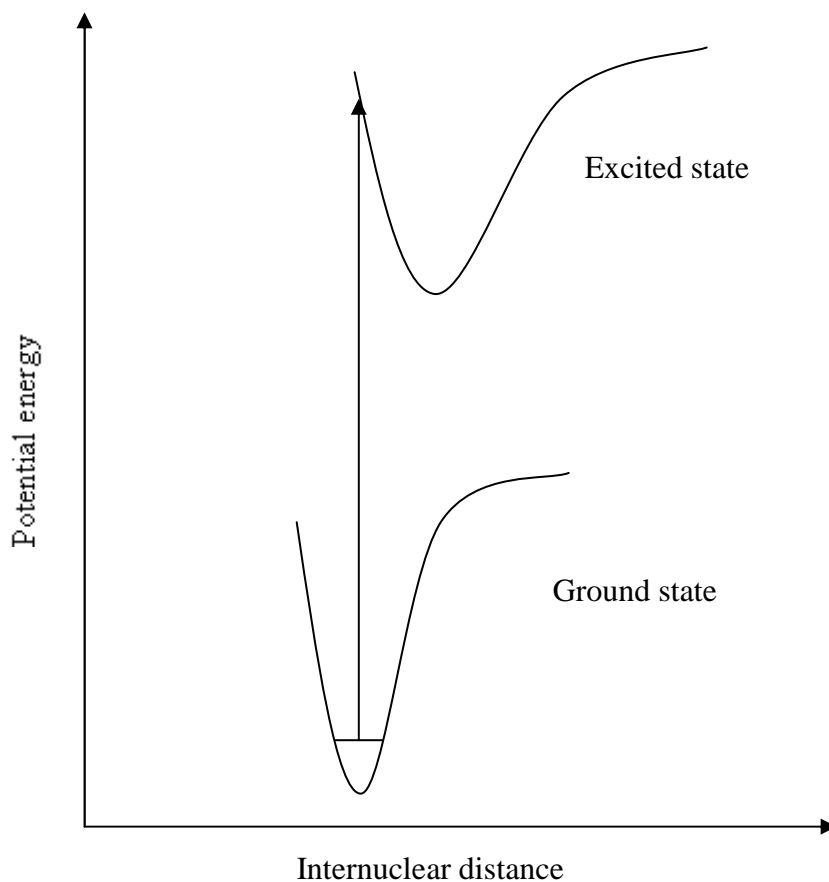
After excitation processes, excited species can follow the pathways mentioned earlier. Chemical reaction is one of these possible routes. Generally, photodissociation is the most interesting type of chemical change, and it can occur upon absorption of radiation with a sufficient energy to break the absorbed species into different fragments. Different fragments can be produced by photodissociation of the excited species. In some cases and upon absorption with high energy radiation such as far UV and X-ray radiation, ionization of the absorbing species occurs which is known as photoionization<sup>(1)</sup>. Beside that absorption light by photocatalytic semiconductors can lead to excite these materials producing active species (electrons and holes). These species can then participate in other reactions, such as photocatalytic decomposition reactions and photocatalytic polymerization reactions.

### **1-5-2 Optical photodissociation**

Optical photodissociation of photoexcited molecules can be explained by the following potential energy diagram Figure 1-9 for the excited specie. Generally, this diagram is predominately applied for diatomic molecules. Application this phenomenon for more complex molecules is more complex. However, for diatomic molecules, this can be explained by following the relationship between potential energy and internuclear distance for a diatomic molecule. According to this mechanism, dissociation can occur when the excited species gain energy that is greater than that of their own dissociation energies. Additionally, dissociation may occur when absorption occurs to the unbound repulsive state of the absorbing molecules. Optical dissociation according to these two possibilities is shown in the following schemes:



**Scheme 1-9:** Absorption to an energy state at greater than that of dissociation energy leading to dissociation<sup>(1)</sup>.

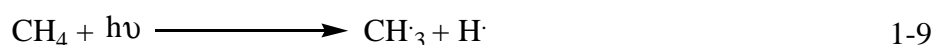


**Scheme 1-10:** Absorption to an energy state at energy greater than that of dissociation energy<sup>(1)</sup>.

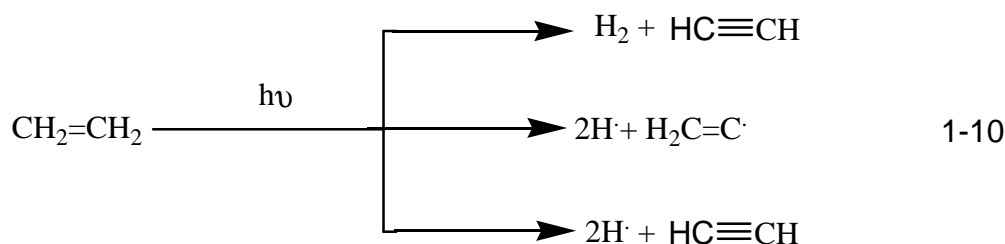
The potential energy curve for excited state relates with the excited state products that relates with the excited product (A+B)\* that corresponding to S<sub>0</sub> to S<sub>1</sub>. If this excited state doesn't possess a sufficient, then (A+B)\* product can break up to form ground state (A+B). In this case, excitation energy is lost as heat either IC or ISC radiationless loss and this process is known as a predissociation. On the other hand when (A+B)\* possesses an energy that is greater than the dissociation energy or if excitation occurs to a repulsive state. This process can lead direct dissociation, and bond breaking then occurs within very short time (10<sup>-13</sup>-10<sup>-14</sup> sec)<sup>(1)</sup>. In this case, vibrational energy levels become close to each other. After the dissociation point, any excess energy may be transferred into the resultant fragments as translational energy. As this energy is not quantized, so that the spectrum of these fragments beyond the dissociation point becomes continuous. If the excitation energy is sufficient this can lead to removal of electrons completely from the excited molecule which results in ionization as shown below:



This type of photodissociation occurs in the upper atmosphere under far UV radiation, resulting in removal of electrons from the available chemical species. An important example of photoionization is the ionization of nitric oxide in the upper atmosphere by UV light from the sun<sup>(1)</sup>. However, despite the fact that the discussion of photodissociation mainly focuses on diatomic molecules, it can also be applied to some extent to polyatomic molecules, but in this case, it is expected to yield different fragments of products<sup>(1)</sup>. Important examples of this type of dissociation are hydrocarbons and carbonyl compounds. For example, methane absorbs at around ( $\lambda = 144$  nm) resulting in  $\sigma$  to  $\sigma^*$  transitions. However, the expected result of photodissociation of methane is hydrogen removal as follows:



In case of irradiation of methane at shorter wavelengths ( $\lambda < 96.7$  nm) this can result in photoionization. For unsaturated hydrocarbons, lower energy transitions ( $\pi$  to  $\pi^*$ ) occur at higher wavelengths. However, in this case different fragments can be formed as a result of photodissociation as shown below for ethylene<sup>(1)</sup>:

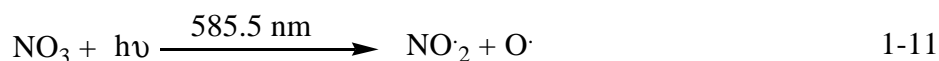


Aromatic hydrocarbons absorb light in the near UV region with high efficiency, absorption in this region results in emission of radiation from the excited species, and the result of the photodissociation of benzene in the gas phase are polymeric species, carbon and traces of some volatile products<sup>(1)</sup>. Generally, irradiation with photons of high energy (in far UV region) can result in ionization or fragmentation of the absorbing species. For this reason, this spectral region of solar spectrum is not suitable in photocatalytic reactions, and normally this type of reaction carried out in UV-visible region of the spectrum.

## 1-6 Photochemistry in nature

### 1-6-1 Atmospheric photochemistry

Atmospheric chemistry is a branch of atmospheric science which focuses on the study of the Earth's atmosphere. Studying both the composition and the chemistry of the atmosphere is important due to the mutual interaction between living organisms on the Earth and the atmosphere. Generally, the composition of the atmosphere changes continuously, arising from natural processes such as volcanoes, lightning and activities due to humankind. However, some of these changes may be harmful to human health and that of other living organisms<sup>(1)</sup>. Important examples of these effects that are related to some photochemical changes in the composition of the atmosphere. These changes occur due to reaction between different components of the atmosphere after initiation by absorption of solar spectrum. The result of some of these reactions can be seen in acid rains, ozone depletion, photochemical smog, and global warming. Many changes in composition of atmosphere may occur due to photochemical reactions that are initiated by absorption of light from solar radiation in the atmospheric layers. Upon absorption, light in visible region of the spectrum NO<sub>3</sub> species can decompose by two routes depending on the wavelength of the absorbed light, as shown below<sup>(7)</sup>:



NO species play a catalytic role in the destruction of ozone in the atmosphere and they can also be produced by photolysis of NO<sub>2</sub> in the atmosphere. NO<sub>2</sub> is one of the most important species in atmosphere, it can absorb radiation and dissociate as follows<sup>(7)</sup>:



Generally, there are many other photochemical reactions can affect the composition of atmosphere as these reactions produce atoms or free radicals and these species are more reactive in comparison with the parent molecular species. According to the above reaction,

photodissociation of nitrogen oxide produces atomic oxygen. This can react with the oxygen in the air producing ozone as shown below:



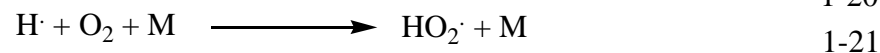
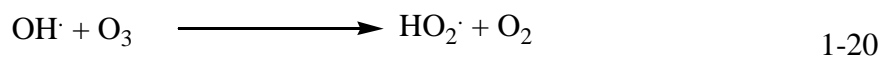
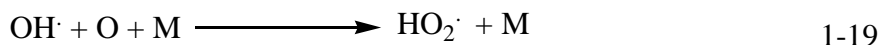
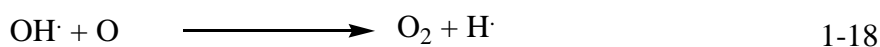
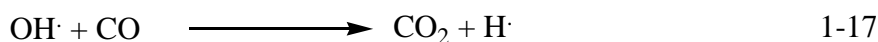
According to this equation M is a third body which may be molecular nitrogen, ozone is an important constituent of some regions of the stratosphere which is known as the ozone layer. Generally, ozone is a strong oxidizing agent and it can react with other chemical compounds to form some toxic oxides. Also the ozone produced may dissociate upon absorption of light as follows<sup>(5)</sup>:



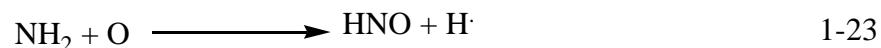
At a higher altitude levels, there is a high level of UV radiation with low O<sub>2</sub> concentration. High concentrations of O<sub>3</sub> can be found at high atmosphere levels. Absorption light of wavelength less than 315 nm can produce oxygen atoms in their triplet excited state, whereas oxygen in the ground state is produced upon absorption of light with longer wavelength. The ground state oxygen may recombine with a molecular oxygen forming ozone again. The excited oxygen atom may lose excitation energy and return to its ground state by radiative processes. On the other hand, it can react with available water molecules producing hydroxyl radicals as follows<sup>(1)</sup>:



Hydroxyl radicals (OH<sup>·</sup>) produced by reaction of excited oxygen atoms initially formed by photodecomposition of ozone also can react with CO in atmosphere. This process results in the production of hydrogen atoms and hydroperoxy radicals as follows<sup>(1)</sup>:



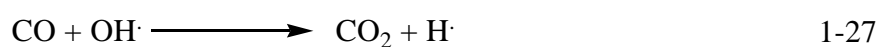
Generally, these reactive species play important role in the reactions that occur between different gases in the atmosphere. As these species are so reactive, they are only found in trace concentration in the Earth 's atmosphere. Ammonia can also react with these radicals and this route is responsible for NH<sub>3</sub> removal from atmosphere. The resulting species can participate in other subsequent reactions as follows:



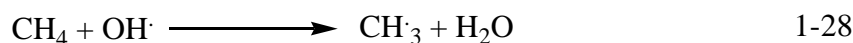
The produced NO according to this route can be oxidized to NO<sub>2</sub>, this can react with OH radicals to produce nitric acid. The produced nitric acid can be removed from the atmosphere by dissolution in rainwater to produce acid rain as follows:



In addition hydroxyl radicals can react with carbon monoxide in the atmosphere to produce carbon dioxide and hydrogen radicals<sup>(8)</sup>.



Methane is one of the important species which is released into atmosphere from many human activities especially the oil industry. Methane in the Earth's atmosphere is an important greenhouse with global warming. Excess amounts of this gas from landfill and other natural products of CH<sub>4</sub> are burned producing carbon dioxide to the atmosphere. This can participate in the global warming. Also, in the atmosphere, methane can be oxidized by OH radicals producing methyl radicals and water as follows:



The resultant CH<sub>3</sub>· species can participate in the methane cycle in the atmosphere to form CH<sub>3</sub>O<sub>2</sub>· as shown below:



CH<sub>3</sub>O<sub>2</sub>· reacts with hydroperoxy radical in the following manner:



In the presence of some suitable molecular species (M), hydroxyl radicals may react with each other to form hydrogen peroxide:



Hydroperoxy radical may be a more efficient route for the formation of hydrogen peroxide:



$\text{H}_2\text{O}_2$  is a highly water-soluble and a strong oxidizing agent so it probably plays an important role in oxidation processes within water droplets in the atmosphere. This can lead to produce hydroxyl radicals, reaction of these radicals with  $\text{NO}_2$  can lead to formation of acid rains as mentioned earlier.

### 1-6-2 Photosynthesis

Photosynthesis is one of the most important photochemical processes in nature. In this process green plants, algae and photosynthetic bacteria synthesise carbohydrates from sunlight,  $\text{CO}_2$  and  $\text{H}_2\text{O}$  as follows <sup>(1)</sup>:



In this process, sunlight provides photochemical energy that is used in the reduction of  $\text{CO}_2$  and in splitting of water, resulting in evolution of oxygen. However, some intermediate compounds with high potential energy are formed and these play an important role in the driving synthetic sequence. The reaction requires a large amount of light energy. The standard energy that is required to reduce  $\text{CO}_2$  into glucose is about + 478 kJ mol<sup>-1</sup>, and in this case photosynthesis can be represented as follows <sup>(1)</sup>:



Formally, conversion of  $\text{CO}_2$  into carbohydrates is a reduction process, which involves rearrangement of covalent bonds between carbon, hydrogen and oxygen. The above reaction is impossible thermodynamically without light, as formation of one mole of oxygen requires the transfer four moles of electrons, and additionally another four moles of electrons must be supplied to reduce one mole of  $\text{CO}_2$  as follows:



Photosynthetic processes in all green plants and other living organisms, which involve reduction of  $\text{CO}_2$  into carbohydrate with removal of electrons from, water and evolution of oxygen is known as oxygenic photosynthesis. According to this process, water is oxidized by a multisubunit protein which is found in the photosynthetic membrane (the photosystem II reaction centre)<sup>(9)</sup>. The other type of photosynthesis is known as an-oxygenic which is used by other organisms, in which light energy is used to extract electrons from molecules other than water. However, only small portions of sunlight reach the earth, which can be

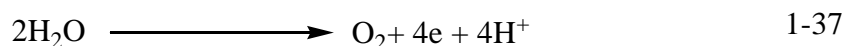
absorbed by green plants and other synthetic organisms. These species then convert light energy into chemical free energy in a stable form, which can be stored or used in different ways to release this energy for different applications.

Generally, photosynthetic process in green plants occurs in small organelles (chloroplasts). This process involves two stages, "the light reaction and the dark reaction". The light reaction involves electrons and proton transfer reactions, which occur in a complex membrane system, which is called the photosynthetic membrane. This membrane has a complex structure of protein complexes, electron carriers, and lipid molecules. It is surrounded by water, which can pass through to participate in photosynthesis. Dark reactions involve the biosynthesis of carbohydrate from CO<sub>2</sub>. The first step in the light reaction is the conversion of a photon to an excited electronic state of an antenna pigment molecule that is present in the antenna system. The antenna system contains many types of pigment molecule (chlorophyll) connected to proteins forming the reaction centre. The electronic excited state of these pigments is trapped by the reaction centre protein. Excitons that were trapped by reaction centre protein provide the energy, which is necessary to initiate the primary photochemical reaction of photosynthesis and the transfer of electrons between donor and acceptor molecules in the synthetic system. The overall result of these reactions is the transfer of electrons from water which leads to the reduction of NADP<sup>+</sup> into the NADPH which then participate in the reduction of CO<sub>2</sub>. Generally, the net effect of light in this series of reactions is the conversion of light into the redox free energy as NADPH and the phosphate group, which transfer energy into the form of ATP. In this context, photosynthesis process is a direct essential application of photochemistry. In addition to this process, photochemistry can be applied in many other fields in both research field and industrial processes.

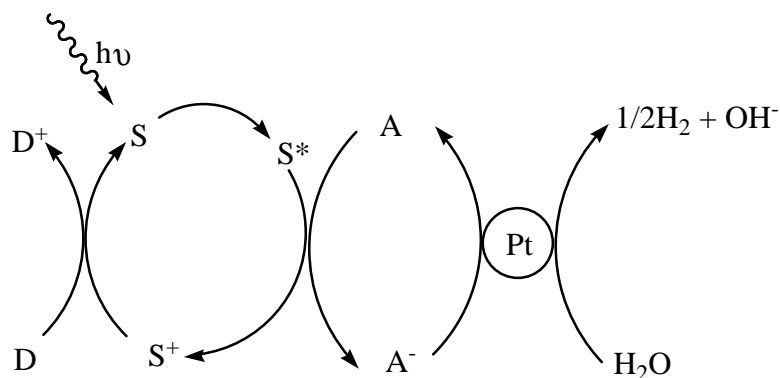
### **1-7 Solar energy storage**

Photosynthesis produces around  $2 \times 10^{14}$  kg of solid carbon in various forms annually and accordingly solar energy is the main source of the fossil fuels. It contains mainly coal, petroleum and natural gases. This huge amount of carbon has been decomposed and transformed over long geological time scales to other forms of energies such as oil, coal and natural gas. Concern about potential depletion of energy sources in the future has led to interest in the use of solar light in the production of fuel that is know clean fuel such as hydrogen and methane. Photoelectrochemical processes use sunlight to drive chemical reactions that can lead to produce this type of fuel by utilization from water and carbon dioxide to produce hydrogen, methanol and methane<sup>(10)</sup>. The photochemical processes

involve formation of electronically excited states, which are used in the production of the final compounds. The final products are energy rich compounds in comparison with their starting materials. Chemical reactions that are induced by solar energy can be classified as thermochemical and photochemical types. Different types of fuel can be produced using artificial photosynthesis, for example, multielectron catalytic reactions can be used in the formation of carbon based fuels such as in the production of methanol by reduction of CO<sub>2</sub>. In addition, hydrogen can be produced from protons using water as a source of electrons as shown in the following equations <sup>(1)</sup>:



Production of hydrogen is a promising area in solar chemical research. Photosplitting of water under solar energy is not possible as water doesn't absorb visible light. Additionally, photosplitting of water into H<sup>•</sup> and OH<sup>•</sup> is not easy as this process requires absorption of high energy radiation ( $\lambda = 240 \text{ nm}$ ). Generally, the relative intensity of this wavelength in AM 1.5 solar spectrum is very low and it is not sufficient to initiate this reaction. On the other hand, the ionic redox mechanism requires transfer of four electrons that corresponds to energy of photons of wavelength around 1000 nm. As this range of wavelength can be obtained effectively from solar radiation, multiphoton redox fission of water seems to be a good approach towards photosplitting of water. It is not easy to run both oxidation and reduction process with the same redox pair. For this system, using an external electron source as a sacrificial electron donor would be effective to regenerate ground state of used sensitizer. At the same time, a suitable electron acceptor must be used with photooxidation process to harvest the electrons from the system. A general description for this system is shown in the following scheme <sup>(1)</sup>:



**Scheme 1-11:** Photosplitting of water using sacrificial species with a photosensitizer.

For this system, colloidal platinum can be used as an electron trap for electron-reduced species. In this system S is a photosensitizer, A is an electron acceptor which works as an electron relay between the Pt/ H<sub>2</sub>O reactant and the photosensitizer, D is an electron donor and Pt refers to platinum particles which trap electrons from one electron- reduced species<sup>(1)</sup>. In this process, sunlight can play a key role in production of new fuels in the future to replace expected depletion of classical fuel. In addition to above, system water splitting can occur on titania electrode by using photoelectrochemical cell (PEC) under irradiation with UV light to produce hydrogen at the anode of this cell. Doping titania can absorb light in visible region and hence instead of using artificial UV light in operation of PEC in case of electrode of neat titania. Probably it will be possible to run this cell under normal solar spectrum by using an electrode of doped titania.

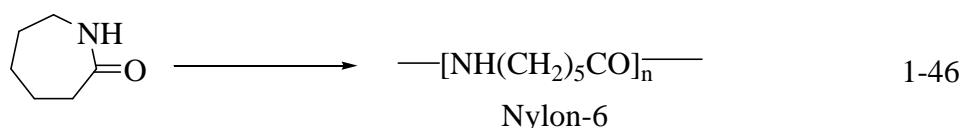
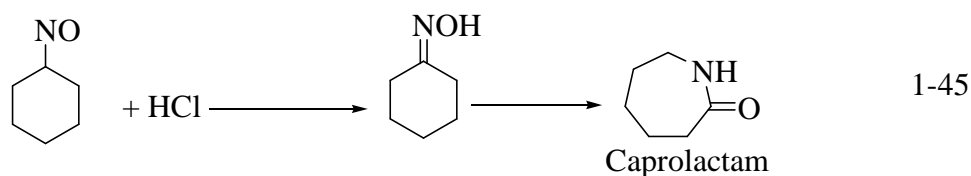
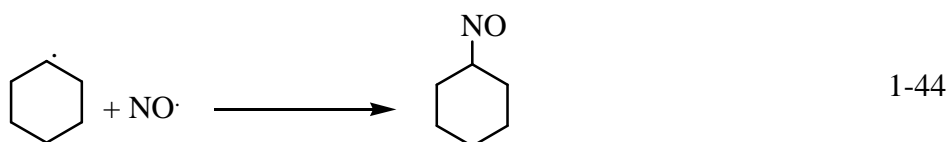
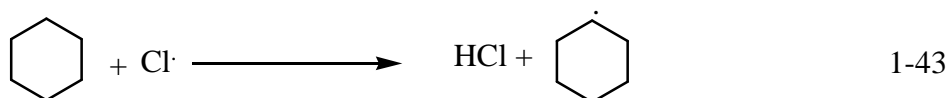
### **1-8 Photochemistry in synthesis**

The first step in photochemical synthesis is the absorption of photons by the reactant species to form excited state this then undergoes chemical change to give final product<sup>(5)</sup>. Photons can be absorbed directly by reacting species or by photosensitizer, which absorbs photons and then transfers the energy to the reactants. Photochemical reactions can be used in the synthesis of organic and materials. This type of alternative synthesis route has important applications in the synthesis in chemical industry. Generally, it can be viewed as a green alternative to thermal processes<sup>(11)</sup>. The main source of activation energy in this type of reaction is the photon that is completely different from other activating agents or catalysts.

A major advantage of this approach is that highly specific reactions can be carried out using light, so that a desired product can be obtained which is not produced by normal thermal reactions<sup>(12,13)</sup>. However, in this route two important factors should be considered environmental effects and economical cost<sup>(13)</sup>. Currently, photochemical methods are used in the synthesis of four- membered rings, inter and intramolecular cycloaddition reactions, halogenation reactions, photochemical addition reactions, photoisomerization reactions and crosslinking reactions of polymers. In addition, photochemical methods offer routes for the reaction of compounds thermodynamically unsuitable for thermal methods. The most important application of photochemistry is its application in industrial synthesis such as chlorination of hydrocarbons and toluene. Photochemical processes always yield products with high yield and purity. Photochemical processes can be initiated by a chain mechanism (radical chain carriers). For example, chain reactions are applied on an industrial scale in the chlorination of hydrocarbons as shown in the following equations<sup>(1)</sup>:



Another example of a photochemical reaction is the photooxidation of cyclohexane to produce caprolactam that is a starting material in the production of nylon-6<sup>(1)</sup>. The last product is an important material that is used in many industrial applications. Formation of caprolactam is shown in the following equations <sup>(1)</sup>:

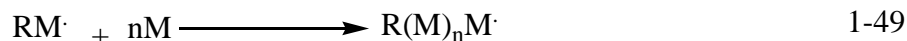


Irradiation of the reaction system with visible light results in the cleavage of NOCl producing reactive radical species, which react with the cyclohexane ring producing oxime, which then converts into caprolactam. This reaction is used in an industrial scale to produce a widely used material polycaprolactam (nylon-6)<sup>(1)</sup>. This polymer used in wide range of products that required materials of high strength.

### 1-9 Photopolymerization

Polymerization reactions are an important type of chemical reactions that used in the synthesis of different types of polymers. Among different types of these reactions are chemical polymerization, electrochemical polymerization and photopolymerization. Photopolymerization is defined as a process whereby light is used to induce the conversion of monomer to polymer. According to this process, an organic photosensitizer absorbs light

and then splits to produce imitating radicals. The process can be summarized as follows (14):



Where, I is the initiator molecule, R $\cdot$  is the free radical and M is the monomer molecule. The active centres (RM $\cdot$ ), must have the ability to grow quickly. The nature of the primary active centres depends upon the nature of both initiator and monomer. Photoinitiation processes can be classified as two general types: (i) chain reaction polymerization of the monomer molecules is carried out by photoinitiator as described above and (ii) photografting and photocrosslinking processes. In the second type, photoinitiation is carried out by pre-existing polymer in the presence of the monomer, which could be photoactive to formation active free radicals upon absorption light with sufficient energy (15). Generally, the photoinitiators that are used in photopolymerization are compounds capable of generating active free radicals that bond to the monomer molecules to form active centres (16). The free radicals can be produced photochemically or thermally and there are a wide variety of photoinitiators that can be classified into different types: organic such as (carbonyl compounds and azo compounds), inorganic such as ( peroxide and metal oxide) and organometallic compounds such as transition metal carbonyls and transition metal chelates (16). Free radical polymerization was initially demonstrated by Taylor and Johnes (17) in 1930. They studied polymerization (17) of ethylene in the gas phase by the thermal decomposition of diethyl mercury organometallic compounds Hg(Et)<sub>2</sub>. Taylor and Bates (18) suggested a free radical mechanism for the polymerization of ethylene in the vapor phase. Free radical polymerization by photoinitiated process has played an important role in developing of polymer chemistry. Free radical polymerization has some important advantages over other types of polymerization as this type of polymerization can take place in the liquid, the solid, and in the gaseous phases. Additionally, it takes place in different conditions such as bulk, solution, emulsion, and in suspension solutions (19). However, free radical polymerization initiated by light has some disadvantages such as low yield of polymer (low conversion percentage), and is also requires a relatively expensive photolysis system. On the other hand, photoinitiators have two advantages in comparison with thermal initiators, it can be achieved at ambient temperatures without need to heat reaction mixture. In addition it is possible to control concentration of active radicals by adjusting intensity of radiation (19).

### 1-9-1 Photochemical initiation of polymerization

The initiators that are used in polymerization are compounds that are capable of producing active free radicals which interact with monomer molecules to form active centres.

Photoinitiators have two main advantages over thermal initiators. The first is the ability to control radical concentrations by adjusting light intensity. The second is that the initiation of polymerization may be carried out at ambient temperature <sup>(16)</sup>.

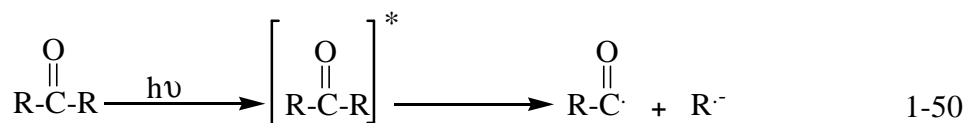
There are several groups of organic photoinitiators which can be applied such as organic carbonyl compounds; organic peroxides, azo compounds and halogen containing organic compounds. Inorganic photoinitiators include ion pair complexes, transition metal halides, inorganic solid salts and oxides, as well as hydrogen peroxide.

### 1-9- 2 Organic photoinitiators

As stated there are several groups of organic photoinitiators:

#### A- Organic carbonyl compounds

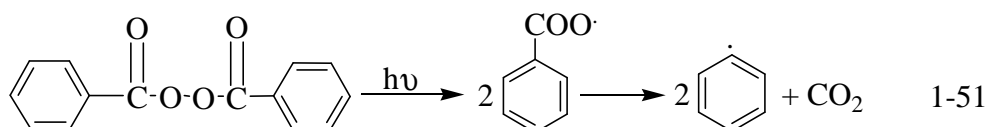
The carbonyl group is capable of absorbing UV light results in the cleavage of the adjacent C-C bond to produce radicals that as follows:



Generally, there are many types of carbonyl compounds that have been used as photoinitiators such as acetone, benzophenone and cyclohexanone<sup>(20)</sup>.

#### B- Organic peroxides

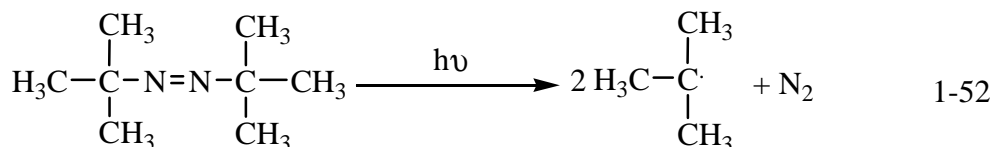
The organic peroxides decompose under light (or heat) to yield free radicals due to cleavage of the relatively weak O-O bond <sup>(21)</sup> as follows:



Important example of this type of photoinitiators is tert-butyl peroxide. This type of photoinitiators used in vinyl polymerization of vinyl acetate and tert-butyl acrylate<sup>(21)</sup>.

### C- Azo compounds

This type of compound decomposes photochemically (or thermally) to produce free radicals and nitrogen gas. An important example of this type of compound is  $\alpha,\alpha$ -azobisisobutyronitrile (AIBN) which absorbs light at 365 nm, photodecomposing to produce cyano isopropyl radical by cleavage of two relatively weak C-N bonds as follows <sup>(22)</sup>:



### D- Halogen containing organic compounds

Halogen containing organic compounds is light sensitive. Photolysis of these compounds produces halogen atoms and alkyl radicals that initiate polymerization as follows <sup>(23)</sup>:



#### 1-9-3 Inorganic photoinitiators

Inorganic photoinitiators involve the following types:

##### A- Inorganic solid salts and oxides

There several inorganic solid salts and oxides which are used as photoinitiators such as HgBr, AgX, ZnO, CdS and TiO<sub>2</sub> <sup>(23-27)</sup>. These compounds can be used to initiate polymerization reactions by generation of active species by absorbing radiation with a sufficient energy. These species participate in reaction with monomer molecules to form propagation active radicals with monomer molecules which results in formation of the final polymer. Titanium dioxide used as a photoinitiator for photopolymerization. This process is initiated by absorption radiation with suitable energy to produce electron/ hole pair in titania. These species then participate in reaction with monomer molecules to yield a polymer.

##### B- Hydrogen peroxide

Hydrogen peroxide absorbs light and decomposes as follows to produce hydroxyl radicals which could initiate polymerization <sup>(28)</sup>:



## 1-10 Kinetics of free radical polymerization

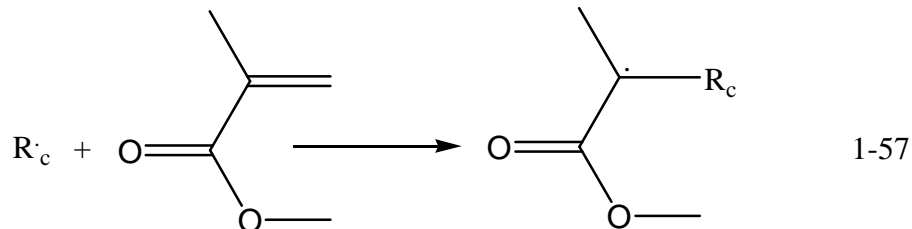
The conversion of monomer to polymer according to this mechanism involves three main steps<sup>(19)</sup>. The first step is the initiation which involves decomposition of the initiator either thermally or by light to generate a primary free radical. Generally, this step is slow and it can be carried out by either irradiative initiation or by thermal initiation. The initiation step is followed by a rapid propagation reaction between free radicals and monomer molecules. This stage continues until the termination steps occur. The final step is the termination step which involves either combination between two polymer radicals to produce one polymer molecule or by disproportionation of the two polymer radicals to yield two polymer molecules.

### A: Initiation step

This step involves decomposition of initiator molecules to produce active radicals, which then react with monomer molecules to produce primary radicals as follows<sup>(19)</sup>:



where, I is the initiator molecule,  $R_c \cdot$  is the primary free radical produced from I, this then reacts with monomer molecule such as methyl methacrylate and  $R_c M \cdot$  is the radical of initiator and monomer produced from initiation step as follows:



### B: Propagation step

The propagation step is the continuation of the last reaction, in which  $R_1 \cdot (R_c M \cdot)$  that is produced from the first step reacts with another monomer molecule to generate  $R_2 \cdot$  and so on. The monomer molecule is added in one step:

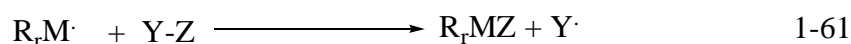


Generally, the propagation step can be represented as follows:



Where,  $R_r \cdot$  represents a polymer radical containing (r) monomer molecules<sup>(19)</sup>. The polymer growth chain may contribute to the chain transfer reaction. In this reaction

unimolecular atoms can be transferred from any available molecule in the reaction system such as the solvent, the initiator, the monomer, the polymer or the chain transfer agent to the propagated radical to produce a polymer molecule such as alkyl halide (C<sub>2</sub>H<sub>5</sub>Cl). This process can be represented by equation:



### C: Termination step

This process involves reaction of two growing polymer chains. In this step termination can proceed by two mechanisms depending on the polymer type and other reaction conditions. Termination mechanisms involve combination and disproportionation. Termination by combination occurs by coupling of two active chain ends producing one long chain of polymer. This process can be represented as follows:



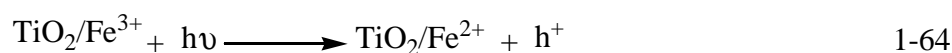
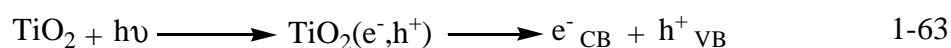
Termination by disproportionation occurs when an atom transfers from one chain end to another chain. This process producing a polymer with a terminal unsaturated group and a polymer with a terminal saturated group. In most common cases hydrogen or halogen atom is abstracted from one chain to another and this process is controlled by steric effects<sup>(19)</sup>.

### 1-11 Photocatalytic polymerization

In photocatalytic polymerization, both composites of polymers and inorganic nanoparticles can be obtained. This type of polymer can be synthesized via mixing and *in-situ* polymerization. In the *in-situ* polymerization, the monomers are polymerized using organic initiators<sup>(29)</sup>. In photocatalytic polymerization, polymer formation is initiated by the excited nanoparticles by absorption radiation with sufficient energy ( $h\nu \geq E_g$ ). When TiO<sub>2</sub> is irradiated with radiation of energy that is equal to or greater than bandgap, produced conduction band electrons and valence band holes. These species then interact with monomer molecules producing polymer on the surface of the catalyst. Photocatalytic polymerization, not only offers a new application of semiconductor photocatalysis, but also provides a strategy to fabricate composites of polymers and inorganic nanoparticles<sup>(30)</sup>. Since the nanoparticles are retained during photocatalytic polymerization, polymers and the composites can be obtained simultaneously<sup>(31)</sup>. Photocatalytic polymerization offers a simplified process to prepare polymer/inorganic nanocomposites. This method has a promising future in fabricating photo-cured films, heterojunction composites, and protective coatings on semiconductors<sup>(31)</sup>. Considering that many modified bandgap semiconductor nanoparticles are able to perform photocatalysis under UV and visible light

irradiation such as TiO<sub>2</sub>, ZnO and CdS, one can take advantage of solar energy to produce the nanocomposites<sup>(32)</sup>. Generally, these nanoparticle photocatalysts such can initiate photopolymerization. According to band theory, semiconductors have a completely filled valence band and empty conduction band at absolute zero. Irradiation particles of the photocatalyst produce conduction band electrons (e<sup>-</sup><sub>CB</sub>) and valence band holes (h<sup>+</sup><sub>VB</sub>). These species can diffuse through the solid followed by their trapping or recombination. A photocatalytic reaction is only efficient if electrons and holes are present on the surface in order to react with adsorbed species. Charge transfer from the bulk to the surface is possible only if it is thermodynamically allowed and has a sufficient lifetime<sup>(33)</sup>. The photogenerated electrons and holes upon irradiation of the photocatalyst can initiate polymerization, when reacting with adsorbed monomer molecules on the surface. This is distinguished from normal photopolymerization in which organic or inorganic photosensitizers are activated due to absorption of light with a sufficient energy to produce initiating free radicals<sup>(34,35)</sup>. In the last few years, composite materials have attracted considerable attention due to their interesting properties. Titanium dioxide has frequently been employed to prepare composites with these types of polymers. For instance, Wang and co-workers studied polymerization of MMA over titania under irradiation with UV light from mercury lamp. They reported formation two types of polymers, extracted and grafted polymer with titanic surface<sup>(36)</sup>. In another study Hong and co-workers studied polymerization of MMA over ZnO. They reported formation a composite material of PMMA/ZnO<sup>(37)</sup>. Damm and co-workers studied photocatalytic polymerization of MMA over titania that was prepared by different methods. They found that activity of polymerization was affected by particle size and phase of titania<sup>(38)</sup>. In further study Damm and co-workers studied the photocatalytic polymerization of acrylate using iron doped TiO<sub>2</sub>. For this type of reaction, the photocatalytic initiation occurs upon irradiation with UV light and the following mechanism was suggested<sup>(39)</sup>:

A- Initiation step



B- Photocatalytic formation of initiating radicals:



In above equations, M is a monomer molecule and A is an electron acceptor

A- Chain growth:



According to this mechanism irradiation of Fe/TiO<sub>2</sub> with light of a sufficient energy promotes electrons from the valence band of titania to the conduction band. Fe<sup>3+</sup> doped TiO<sub>2</sub> can form interband below conduction band of titanic. This can lead to the generation of additional holes (h<sup>+</sup>) as shown in equation (1-64). On the other hand, Fe<sup>3+</sup> may act as an electron trap as shown in equation (1-65). Positive holes in the valence band can oxidize monomer molecules as in equation (1-66), which results in formation of a radical cation. The radical cations can donate protons to the hydroxyl group on the surface, leading to production of a monomer radical as shown in equation (1-66). Transferring electrons from the conduction band to the electron acceptor produces radical anions as shown in equation (1-67). This radical anion can accept protons to give a radical as shown in equation (1-68). The radicals of both monomer and electron acceptors can initiate chain growth as shown in equation (1-69). Termination may occur by direct radical combination or by disproportionation<sup>(39)</sup>. Generally, it is possible to initiate polymerization over titania under irradiation with suitable light of suitable energy. Normally this process is achieved under irradiation with UV light. The important challenge in this manner is to initiate this type of polymerization under visible light or solar spectrum. However, photoresponse of titania towards visible light can be performed by surface modification by doping with metals and non-metals.

## **1-12 Aims of Thesis**

The present work reports an investigation of the synthesis of new materials that can be used in photocatalysis, electrochromic materials, nonlinear optics materials, catalytic materials, and photovoltaic devices. In terms of photocatalysis processes, attention have been directed towards using neat and doped titanium dioxide. Doping was undertaken with nitrogen and some metal ions such as  $\text{Al}^{3+}$ ,  $\text{Co}^{2+}$  and  $\text{Cu}^{2+}$ . Doping titania samples with nitrogen species was achieved at three different temperatures 400 °C, 500 °C and 600 °C. Doping titania with metal ions was performed using impregnation method in which a required amount of titania powder is suspended in aqueous solution of metal salt. Photocatalytic activity of neat and doped samples was investigated by following photocatalytic degradation of methylene blue in aqueous solution. In addition, photocatalytic polymerization of methyl methacrylate (MMA) over neat, nitrogen doped titania and co- doped titania. In addition, photopolymerization of MMA and styrene (ST) has been investigated under irradiation with UV light at different conditions. In terms of photovoltaic materials, some of novel viologen monomers have been synthesized. These were targeted to synthesize due to some potential applications such as electrochromic devices and redox active materials. Attention was directed towards study polymerization of these compounds. These compounds and/ or their polymeric forms can be used in some potential applications in terms of photovoltaic applications. In addition, some novel push-pull compounds have been synthesized. These compounds have some potential applications. Additionally, some novel ruthenium complexes were targeted to synthesize as these compounds have different potential applications as photovoltaic materials.

## 1-13 References

1. C. Wayne, R. Wayne, Hand Book, *Photochemistry*, Oxford University Press, 1996.
2. B. Wardle, Hand Book, *Principles and Applications of Photochemistry*, John Wiley and Sons, Ltd, 2009.
3. P. Monk, Hand Book, *Physical chemistry*, John Wiley and Sons, 2004.
4. M. Fox, M. Dulay, *Chem. Rev.*, 1993, **93**, 341.
5. J. Sugden, *Biotechnic and Histochemistry*, 2004, **79**, 71.
6. T. Miyashita, T. Murakata, Y. Yamaguchi, M. Mastuda, *J. Phys. Chem.*, 1985, **89**, 497.
7. M. Grubb, M. Warter, K. Johnson, S. North, *J. Phys. Chem.*, 2011, **115**, 3218.
8. M. Grubb, M. Warter, A. Suits, S. North, *J. Phys. Chem. Lett.*, 2010, **1**, 2455.
9. N. Nelson, A. Shem, *BioEssays.*, 2005, **27**, 914.
10. J. Fendler, *J. Photochem.*, 1981, **17**, 303.
11. A. Albin, M. Fagnoni, *Green Chem.*, 2004, **6**, 1.
12. A. Albin, M. Fagnoni, M. Mella, *Pure Appl. Chem.*, 2001, **72**, 1321.
13. S. Protti, D. Dondi, M. Fagnoni, A. Albin, *Pure Appl. Chem.*, 2007, **79**, 1929.
14. J. Fouassier, F. Molert, J. Lalevee, X. Allonas, C. Ley, *Materials*, 2010, **3**, 5130.
15. J. Kabate, M. Gruszewska, B. Jedrzejewska, J. Paczkowski, *Polym. Bull.*, 2007, **58**, 691.
16. H. Chen, J. Yang, D. Guo, L. Wang, J. Nei, *J. Photochem. Photobiol. A: Chem.*, 2012, **232**, 57.
17. H. Taylor, W. Johnes, *J. Am. Chem. Soc.*, 1930, **52**, 1111.
18. H. Taylor, J. Bates, *J. Am. Chem. Soc.*, 1927, **49**, 2438.
19. L. Sperling, Hand Book, *Introduction to Physical Polymer Science*, 2006, John Wiley and Sons, Inc.
20. K. Nguyen, J. West, *Biomaterials*, 2002, **23**, 4307.
21. K. Tokumar, *Res. Chem. Intermed.*, 1996, **22**, 255.
22. O. Novikova, V. Syromyatnikov, L. Avramenko, N. Kandratenko, T. Kolisnichenko, M. Abadie, *Mater. Sci.*, 2002, **20**, 19.
23. D. Eaton, A. Horgan, J. Horgan, *Photochem. Photobiol. A: Chem.*, 1991, **58**, 373.
24. J. Kuriacose, M. Markham, *J. Phys. Chem.*, 1961, **65**, 2232.
25. M. Markham, K. Laidler, *Trans. Farad. Soc.*, 1946, **42**, 526.
26. A. Hoffman, G. Mills, H. Yee, *J. Phys. Chem.*, 1992, **96**, 5540.
27. B. Kraeutler, H. Reiche, A. Bard, *J. Polym. Sci. Lett.*, 1979, **17**, 535.
28. F. Dainton, *J. Am. Chem. Soc.*, 1956, **78**, 1278.
29. C. Bamford, A. Ferrar, *J. Chem. Soc. Faraday Trans. I*, 1972, **68**, 1243.

30. W. Caseri, *Mater. Sci. Technol.*, 2006, **22**, 807.
31. G. Grubert, M. Stockenhuber, O. Tkachenko, M. Wark, *Chem. Mater.*, 2002, **14**, 2458.
32. C. Dong, Y. Ni, *J. Macromol. Sci. Pure. A*, 2004, **41**, 547.
33. X. Ni, J. Ye, C. Dong, *J. Photochem. Photobiol A: Chem.*, 2006, **41**, 547.
34. J. Wang, X. Ni, *J. Appl. Poly. Sci.*, 2008, **108**, 3552.
35. X. Zhang, P. Liue, Z. Su, *Polym. Degrad. Stabil.*, 2006, **91**, 2213.
36. G. Steiner, C. Zimmerer, R. Salzer, *Langmuir*, 2006, **22**, 4125.
37. R. Hong, J. Qian, J. Cao, *Powder Technol.*, 2006, **163**, 160.
38. C. Damm, D. Voltzke, H. Abicht, G. Israel, *J. Photochem. Photobiol. A: Chem.*, 2005, **174**, 171.
39. C. Damm, *J. Photochem. Photobiol. A: Chem.*, 2006, **181**, 279.

## **Chapter-two: Modification of the photocatalytic activity of titanium dioxide by doping with nitrogen**

### **2-1 General introduction**

Semiconductors are considered an important type of catalyst used in modern industry, due to their physical and chemical properties, which enable them to catalyze many reactions<sup>(1)</sup>. About forty years ago, a new field of application of heterogeneous photocatalytic systems was initiated when Fujishima and Honda<sup>(1)</sup> discovered photocatalytic splitting of water over TiO<sub>2</sub>. Environmental clean up has been one of the most important applications for these systems. Photocatalysts are an important type of catalyst as they can be used in advanced physicochemical processes<sup>(2-4)</sup> and can be applied to the destruction of hazardous chemical wastes. Photocatalysis potentially allows the use of sunlight for the destruction of many environmental pollutants. Systems have been applied for the total destruction of organic compounds in polluted air, soil and wastewater and generally pollutants are decomposed into water, carbon dioxide and other volatile inorganic species. In addition to this, photocatalytic systems can be used for selective synthetically useful redox transformations of specific organic compounds, for production of clean fuel (hydrogen), and for the conversion of sunlight to electrical power<sup>(5, 6)</sup>.

Among the different types of semiconductors which are used as photocatalysts, titanium dioxide is the most important due to its excellent physical and chemical properties. These include photoactivity, high thermal and chemical stability, low cost, non-toxicity and high reproducibility. Consequently, it has been used to catalyze a wide spectrum of chemical reactions such as oxidation / reduction reactions, condensation reactions and polymerization reactions<sup>(7)</sup>.

However, the interest in these types of system started early, with the use of titanium dioxide in a photocatalytic reaction being first reported in 1921<sup>(8)</sup>. Most investigations have been focused on the use of pure n-type semiconducting oxides as photocatalysts as these semiconductors have strong reduction power which enable them to catalyze many reactions<sup>(9)</sup>. The main problem with titania, it has high bandgap (3.20 eV), this means that it can be excited only in UV region of the spectrum. This makes titania inactive photocatalyst in visible region. So that, it is necessary to extend photoresponse of titania towards visible region to enhance photocatalytic activity in visible region. This process can be achieved by modification titania surface. Generally, in recent years many efforts were directed towards the modification of the catalytic properties of titanium dioxide by metal and non-metal doping<sup>(10-15)</sup>. Generally, photocatalysis on both pure and modified titanium dioxide is initiated by absorption of light with an energy that is equal to, or greater than the bandgap (E<sub>g</sub>). This process leads to generation of conduction band

electrons, and valence band holes, since electrons are promoted from the valence band (VB) to the conduction band (CB). When an electron is photoexcited from the VB to the CB it can diffuse into the surface and then undergo charge transfer with an adsorbate or can become trapped by electron traps within the bandgap<sup>(16)</sup>. When these processes don't occur, deactivation of the electron-hole pair occurs with the release of energy as heat or photons. The probability of recombination reaction between electron-hole pairs is directly influenced by charge separation and the mobility of the electrons and the holes<sup>(16)</sup>.

Doped metals or non-metals assist in the separation of photoelectrons and photoholes, which may otherwise recombine within the semiconductor particles<sup>(4)</sup>. Among possible supported metals and non-metals dopants are those involving iron ( $\text{Fe}^{2+}$ ), silver ( $\text{Ag}^+$ ), copper ( $\text{Cu}^{2+}$ ), nickel ( $\text{Ni}^{2+}$ ), nitrogen, carbon and sulphur which result in higher photocatalytic activity for titanium dioxide<sup>(17-20)</sup>. In the last few decades, photocatalytic reactions have played an increasingly significant role in the search for new types of energy.

In the presence of catalysts, photoreactions can be used for the development of new systems that can be used in the production of hydrogen and in photoelectrochemical cells for storage and conversion of solar energy<sup>(21-24)</sup>.

## **2-2 General properties of titanium dioxide**

### **2-2-1 Morphology of titanium dioxide**

Titanium was discovered in England in 1791 by William Gregor, while titanium dioxide ( $\text{TiO}_2$ ) discovered in Germany in 1795 by Klaproth<sup>(25)</sup>. Titanium dioxide, also called titania is formed naturally and it's a main source for titanium. It can be used as a pigment that is called titanium white<sup>(26)</sup>. Generally, titanium dioxide is found as an ore on earth, forming about 0.6% of the earth's crust. The main ores related to titania are ilmenite ( $\text{FeTiO}_3$ ) and rutile which is one of the three crystalline forms of titania. As the metal titanium ( $^{22}\text{Ti}$ ), is the second element in the d-block and has four electrons in its valence shell and its electronic configuration is  $[\text{Ar}] 4s^2 3d^2$ . Ti (IV) is the most stable oxidation state. The amount of energy that is required to remove electrons from the 3d and the 4s orbitals is 6.1 and 5.6 eV respectively.  $\text{Ti}^{\text{IV}}$  compounds are generally covalent<sup>(27)</sup>. There are three main forms of titania: rutile, anatase and brookite. Rutile has a density of  $4.25 \text{ g cm}^{-3}$  and melts at  $2130 \text{ K}$ <sup>(28)</sup>. Anatase has a density of  $3.84 \text{ g cm}^{-3}$  and melts at  $2108 \text{ K}$ . Brookite has a density of  $4.17 \text{ g cm}^{-3}$  and it melts at  $2098 \text{ K}$ . The rutile form is more stable than anatase, which transforms irreversibly and exothermally to rutile in the temperature range of  $880\text{-}1000 \text{ K}$ <sup>(29)</sup>. Generally, titania is insoluble in water and dilute acids, but it dissolves slowly in HF and concentrated  $\text{H}_2\text{SO}_4$ <sup>(30)</sup>.

### 2-2-2 Crystal forms of titania

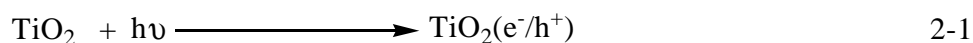
As mentioned above, titanium dioxide has three main crystal structures: anatase, rutile and brookite. Anatase is found to be more stable at low temperatures and converts into rutile above 850 K. Both anatase and rutile have a tetragonal structure while brookite has an orthorhombic structure. Among these polymorphs, the anatase form is used in photocatalytic processes more than the other two forms due to its excellent catalytic properties<sup>(31-34)</sup>. The two main catalytic forms of titania, anatase and rutile have some structural and functional differences and both have large bandgap. Development of titania materials for use as a paint pigment has led to the use of mixed phase titania preparations such as Degussa P25 which is comprised of 25 % anatase and 75 % rutile<sup>(35)</sup>. These mixed phase materials have used widely as pigments, and they can show higher photocatalytic activity in comparison with pure phases alone<sup>(36)</sup>.

Generally, the structure of both rutile and anatase can be described in terms of chains of  $\text{TiO}_6$  octahedra in which oxygen ions are in a distorted arrangement. The difference in the structure of anatase and rutile arises from the way in which octahedra are linked together. In anatase, each octahedron shares four of its edges with other octahedra, whereas in rutile each one shares two of its edges with other octahedra. Rutile, anatase and brookite have six coordinated titanium. According to this structure, each  $\text{Ti}^{\text{IV}}$  species is surrounded by six  $\text{O}^{2-}$  species, whereas each  $\text{O}^{2-}$  is surrounded by three  $\text{Ti}^{\text{IV}}$  species. Therefore, titania has a coordination of (3:6) with the presence of  $\text{Ti}^{\text{IV}}$  in the centre of the cell<sup>(37)</sup>. It is found that the length of the Ti- Ti distances in anatase are greater than those for rutile (3.70-3.04 Å vs 2.57- 2.96 Å respectively), while the Ti- O bond distances for anatase are shorter than those for rutile (1.934-1.980 Å and 1.949-1.980 Å respectively). Also in rutile, each octahedron is in contact with ten neighbouring octahedra, whereas in anatase each octahedron is in contact with eight neighbouring ones. There is a considerable difference in dimensions of the unit cell of the three forms of titania: for anatase a is 3.785 Å and c is 9.510 Å, for rutile they are 4.593 Å, and 2.961 Å respectively while for brookite a is 5.456 Å, b is 9.182 Å, and c is 5.143 Å<sup>(38)</sup>. Czanderna and co- workers applied X- ray diffraction (XRD) to follow the conversion of anatase into rutile. They found that the conversion was slow at temperatures less than 833 K, and they suggested that this conversion depends on time as well as the temperature<sup>(39)</sup>. Bard and co-workers prepared impure anatase containing rutile by heating anatase for eight hours at 1373 K, and they found that the preparation of pure rutile to require heating of anatase for 26 hours at 1373 K<sup>(40)</sup>. Promet and co-workers studied conversion of anatase to rutile under a vacuum atmosphere. They reported that heating anatase from 573 to 673 K under this atmosphere results in the dehydration of surface hydroxyl groups. They found that about half the OH

groups were left behind as identified by their IR absorption at 3675 and 3715  $\text{cm}^{-1}$  <sup>(41)</sup>. Titanium dioxide with a high purity was prepared by Czanderna and co-workers by dissolving titanium metal powder in a solution of 90%  $\text{H}_2\text{O}_2$  at pHs more than 11. According to the XRD pattern, the resultant oxide was ranged between  $\text{TiO}_{1.98}$  to  $\text{TiO}_{2.01}$  in stoichiometry. Non-stoichiometry commonly occurs as a result of crystal defects which are responsible for some of the physical and chemical properties <sup>(42)</sup>. Straumains and co-workers showed that reduced  $\text{TiO}_2$  can be produced by losing about 0.034 of oxygen ions for each unit cell and to reduce charge deficiency, an equivalent quantity of  $\text{Ti}^{\text{IV}}$  reduced to  $\text{Ti}^{\text{III}}$  <sup>(43)</sup>. The surface of rutile has been studied by using infrared spectroscopy (IR) and it was found that the outer surface of rutile crystal contains molecules of water as ligands, which are coordinated with  $\text{Ti}^{\text{IV}}$  species in addition to hydroxyl groups <sup>(44)</sup>.

### 2-2-3 Electronic and conductance properties of $\text{TiO}_2$

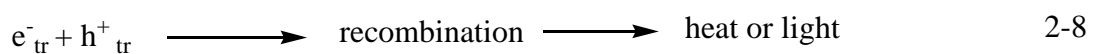
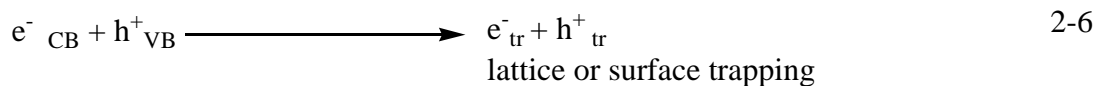
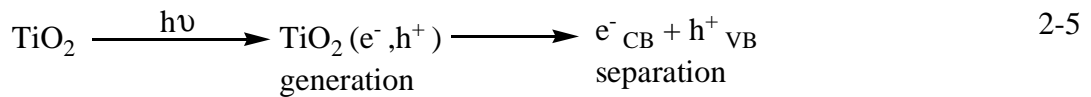
Both the photoconductivity and the semiconductivity of titania can be explained by using band theory. According to this theory, semiconductors can be defined as a type of material with electronic conductivity lying between that of conductors and insulators. Intrinsic semiconductors at 0 K are characterized by a filled valence band and an empty conduction band. Generally, semiconductors have a band structure characterized as a series energetically closely spaced energy levels associated with covalent bonding among atoms composing the crystallite (valence band) along with a second series of spatially diffuse energetically similar levels lying at higher energy associated with conduction (conduction band). The magnitude of the fixed energy gap between valence and conduction bands is known as the bandgap ( $E_g$ ), which can be viewed as the wavelength sensitivity of the semiconductor toward irradiation <sup>(45)</sup>. Titanium dioxide absorbs light in the ultraviolet region. Irradiation with light of  $\lambda < 400\text{nm}$  promotes electrons from valence band to the conduction band. This process produces positive holes ( $h^+_{\text{VB}}$ ) in the valence band and electrons ( $e^-_{\text{CB}}$ ) in the conduction band as follows <sup>(45)</sup>:



The photogenerated electrons in the conduction band are rapidly trapped through equilibrium localization at traps, followed by recombination with photogenerated holes at the surface of  $\text{TiO}_2$ . Titanium dioxide has a continuum of interband states which assist in the recombination of these species. When these species are separated from each other and transferred across interfaces, they can contribute to the oxidation or reduction of adsorbate substrates <sup>(46)</sup>:



When  $h^+_{VB}$  reach the  $TiO_2$  surface they can react with adsorbates by interfacial electron transfer if these adsorbates have a redox potential appropriate for a thermodynamically allowed reaction. Thus adsorbed electron donors (D) can be oxidized by transferring electrons to the hole, while adsorbed electron acceptors (A) can be reduced by accepting electrons from the surface of  $TiO_2$ . It is evident that the recombination reaction which commonly occurs between conduction band electrons and valence band holes, determines the efficiency of the semiconductor as a photocatalyst <sup>(47)</sup>. It has been found that modification of semiconductor surfaces by doping with transition metals, non-metal elements and combination with other semiconductors can lead to reduced recombination rates and enhanced the activity of the photocatalytic reaction in visible region of the spectrum <sup>(48)</sup>. Generally, valence electrons in semiconductors are localized in the bands and the Fermi level (FL) is half the distance between the two bands in the pure intrinsically semiconducting crystal. The relationship between the Fermi level and the bandgap is therefore given by the relationship ( $E_f = 1/2 E_g$ ) <sup>(49)</sup>. For defective crystals, the position of the FL changes according to the type of the semiconductor. For p-type semiconductors, it lies at the half distance between valence band and the acceptor level. For n-type it lies at the half distance between conduction band and the donor level. When these two types of the semiconductors have direct contact, a double charge layer is generated <sup>(50)</sup>. The process of the capture of electrons and holes in the suspensions of neat titania occurs within 30 picoseconds as in the following equation <sup>(51)</sup>:



Where  $e^-_{tr}$  are the trapped electrons as  $Ti^{III}$ , and  $h^+_{tr}$  are the holes trapped as  $OH^\cdot$  radicals. Generally, electron traps are oxygen vacancies in the lattice of  $TiO_2$  or  $Ti^{IV}$

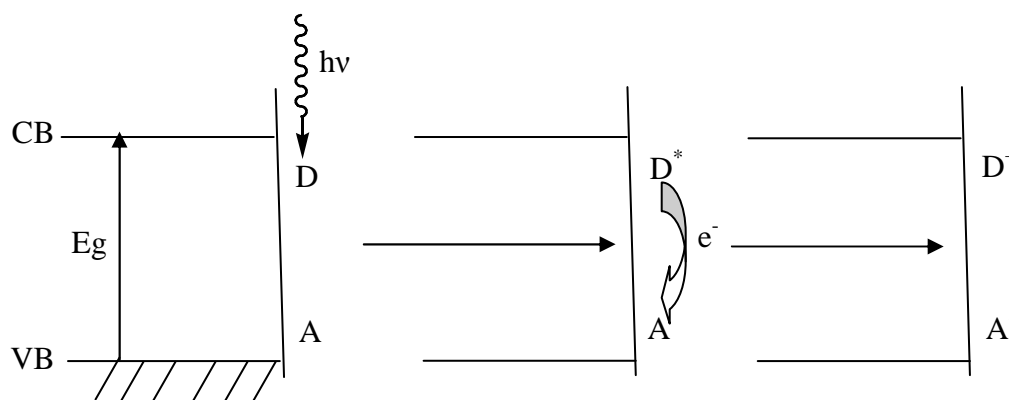
species<sup>(52)</sup>. All the forms of titania absorb the light in the near ultraviolet region of the solar spectrum. Anatase, rutile and brookite absorb at 3.23, 3.01 and 3.26 eV respectively. The presence of oxygen on the surface plays an important role in electron capture. The ability to capture electrons is negatively affected when reducing titania surface by thermal treatment at 973 K for 15 mins or by the irradiation of light for 10 hours and reacting with CO to produce CO<sub>2</sub><sup>(53)</sup>. This probably arises from losing some oxygen ions from the surface due to thermal treatment that affects negatively on capturing of electrons. The active sites on the surface of titania have been studied using electron spin resonance spectroscopy (ESR) and Ti<sup>III</sup> species were shown to be the electron donating centres<sup>(54)</sup>.

#### 2-2-4 Electronic excitation of semiconductors

In heterogeneous photocatalytic systems, photoinduced molecular reactions occur at the surface of the catalyst. Photocatalysis can be divided into two types, in the first type, initial photoexcitation occurs in adsorbate molecules which then interact with a ground state catalyst substrate and this type is referred to as a catalyzed photoreaction. For the second type, the initial excitation occurs in the catalyst substrate, which then transfers electrons or energy into the ground state adsorbed molecules. These types of reactions are referred to as photocatalytic reactions<sup>(55)</sup>. These processes can be explained in the following figure:

#### I: Initial excitation of adsorbate molecules

##### a- Insulators



Eg is bandgap of the photocatalyst, VB is valence band, CB is conduction band, D is a an electron donor, A is an acceptor, D\* is an excited state of the donor, D<sup>+</sup> oxidized state of donor, A<sup>-</sup> is reduced state of electron acceptor

According to above figure, the incident photons are absorbed by the reactant species that pre-adsorbed on the catalyst. Then the excited state of adsorbed species donate electrons to the adsorbed acceptor species on the surface.

**b- Semiconductors**

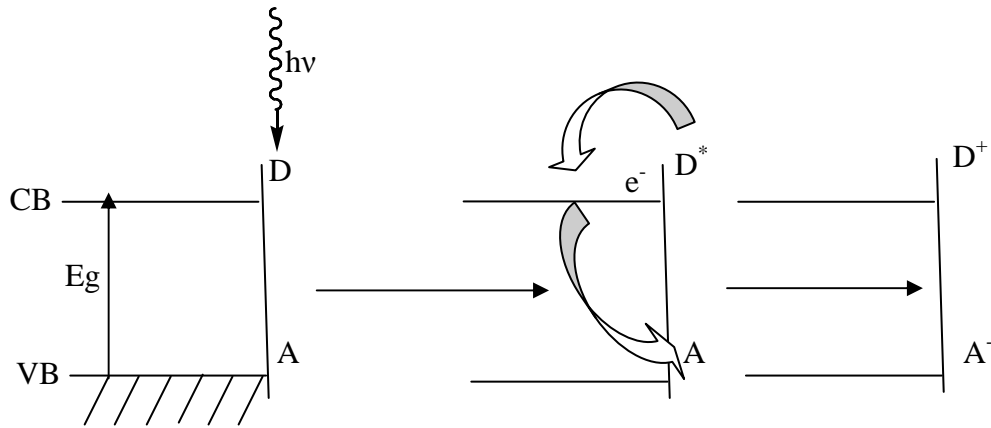
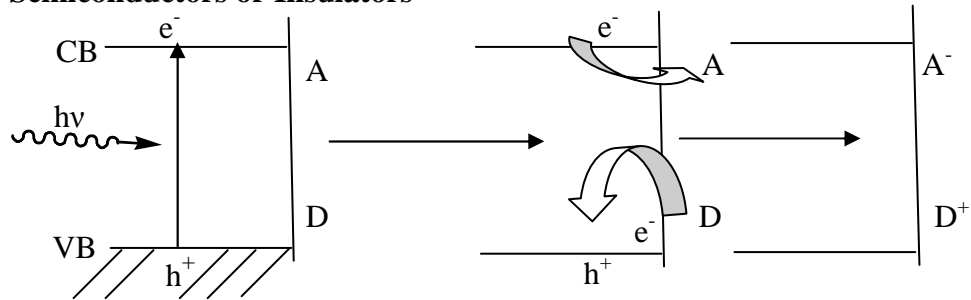


**Figure 2-1:** a,b Photoexcitation initial excitation of adsorbate molecules. In this case, energy level of D is higher than CB of the catalyst, and energy level of A is higher than that of VB of catalyst.

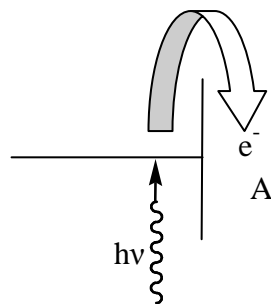
**II: Photoreaction initial excitation of the solid photocatalyst**

**a- Semiconductors or Insulators**



In this case, photoexcitation occurs in photocatalyst to generate (e-,h+) pair , the electron is captured by adsorbed acceptor (A), while positive hole accepts an electron from adsorbed donor (D).

**b- Metals**



In case of metal, energy level depends on the oxidation potential of the metal.

**Figure 2-2:** a,b Photoreaction initial excitation of the solid<sup>(55)</sup>.

When excitation occurs in the bandgap, there is a sufficient lifetime (which is about  $10^{-9}$  -  $10^{-7}$  s) for the production of ( $e^-_{CB}$ ,  $h^+_{VB}$ ) pairs, which are then transferred to adsorbed species on the surface of the catalyst<sup>(56)</sup>. The following figure shows excitation of a photoelectron from the valence band to the conduction band initiated by absorption of light of energy that is equal to or greater than the bandgap energy of titania, which is 3.23 eV for anatase and 3.01 eV for rutile. Photoexcitation in the titanium dioxide particles followed by deexcitation events is shown in the following figure:

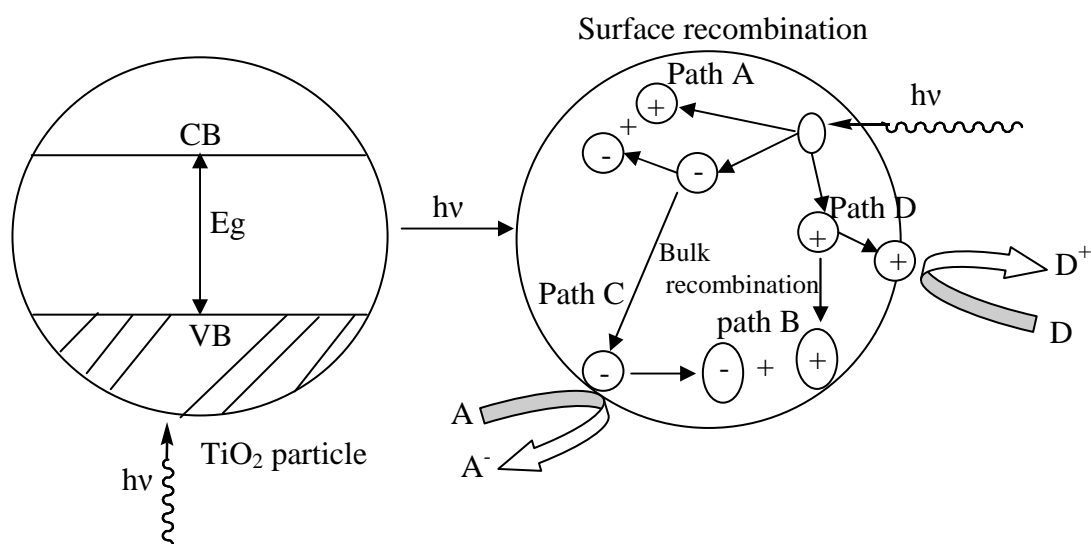
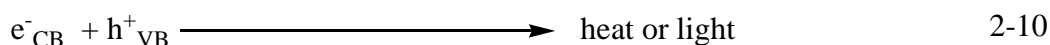


**Figure 2-3:** Photoexcitation in solid TiO<sub>2</sub> followed by deexcitation events. D is an electron donor and A is an electron acceptor<sup>(57)</sup>.

The fate of ( $e^-_{CB}$ /  $h^+_{VB}$ ) separation can follow several pathways. Recombination can occur at the surface, which gives surface recombination (path A), or recombination of electrons and holes occurs in the bulk of semiconductor that gives bulk recombination (path B). Electron transfer is more efficient if the species are pre adsorbed on the surface of the catalyst (path C). The surface of titania can donate electrons to reduce electron acceptors e.g. oxygen aerated solutions. Holes can migrate to the surface where electrons from a donor can combine with them resulting in oxidized surface donor species (path D)<sup>(57)</sup>. Titanium dioxide is a reducible oxide, so that the valence of Ti ion can change from stable tetravalent Ti<sup>IV</sup> species to the trivalent state Ti<sup>III</sup> species that has (3d<sup>1</sup>) electronic configuration as has been detected by ESR. TiO<sub>2</sub> exhibits evidence of Ti<sup>III</sup> with ESR even when treated under oxidized conditions. Irradiation TiO<sub>2</sub> with light ( $h\nu \geq E_g$ ) can produce conduction band electrons and valence band holes. If these species are not consumed rapidly redox reactions, energy of excitation would deexcitate as a heat and/or light as follows<sup>(58)</sup>:



In order to reduce the rate of recombination reactions which commonly occur in neat titania and to enhance photocatalytic activity, it is helpful to modify its surface. Generally, surface modification can be performed by different methods such as surface sensitization, the use of composite semiconductors and also by metal and non-metal doping<sup>(59)</sup>.

### 2-3 Surface modification

For high photocatalytic activity, recombination of ( $e^-_{\text{CB}}/h^+_{\text{VB}}$ ) pairs must be reduced by using a suitable charge carrier trap to prevent the recombination reaction and increase the lifetime of the separated  $e^-_{\text{CB}}$  and  $h^+_{\text{VB}}$  species to  $> 10^{-9}$  s. About 90% of excitation energy is lost by this route which commonly occurs in neat photocatalyst<sup>(60)</sup>. Generally, electron states are charge carrier traps. These electron states are surface defect sites, which depend on the chemical methods used in the preparation of the photocatalyst surface<sup>(60)</sup>. There are several methods used to modify the surface. The main purpose of this modification is the reduction of back electron transfer, enhanced selectivity to desired products, enhanced stability of the photocatalyst under illumination conditions and increasing the absorption in the visible region of the spectrum<sup>(61)</sup>. For example, CdS has a small band gap and it can be photoexcited with visible light, but it is unstable towards light and is photodegraded after a period of irradiation as follows<sup>(62)</sup>



Titanium dioxide is a quite stable photocatalyst, but it has high bandgap (3.2 eV), which means that it can be excited in UV region of the spectrum and it is inactive in visible region of the spectrum. Consequently, much effort has been focused towards increasing its photoresponse in to visible light and accordingly various modification processes have been undertaken. Many benefits of surface modification have been reported such as<sup>(62)</sup>:

1. Inhibition of the rate of recombination reaction by increasing charge separation, which leads to increased efficiency of photocatalytic processes,
2. Increasing the range of the wavelength photoresponse into the visible region of the spectrum,
3. Changing selectivity for desired products,
4. Enhancement of surface properties such as increasing surface area, photoactivity, and photoconductivity, and
5. Increasing the stability of the semiconductor under irradiation conditions.

Generally, surface modification can be performed by using different methods such as<sup>(46)</sup>:

1. Surface sensitization,
2. Application of composite semiconductors,
3. Metal deposition and
4. Non-metal doping.

From these methods, in our plan to modify titania surface by doping nitrogen as a non-metal dopant. Also to dope titania with some metal ions and then co-doped with nitrogen. The resulted modified titania samples will test in terms of photoactivity in comparison with neat titania.

### **2- 3-1 Non-metal doping**

The term doping can be defined as an intentional introduction of impurities into the catalyst<sup>(63)</sup>. In photocatalysis the ideal dopant must increase valence band edge position, which leads to reduction of the bandgap of catalyst without lowering the conduction band. One of the most effective methods that have been used to improve the photoactivity of TiO<sub>2</sub> is doping with species such as N, C, S, P, and I. The improved behavior of nitrogen doped TiO<sub>2</sub> was reported by Sato in 1985<sup>(63)</sup>. After calcining commercial Ti(OH)<sub>4</sub>, the resultant TiO<sub>2</sub> exhibited improved photocatalytic activity in the visible region. When the original sample was subjected to analysis, it was found to contain NH<sub>4</sub>Cl, which was an impurity resulting from the hydrolysis of TiCl<sub>4</sub> with NH<sub>4</sub>Cl. It was found that preparation of Ti(OH)<sub>4</sub> in the absence of NH<sub>4</sub>Cl led to TiO<sub>2</sub> which after calcination did not exhibit any absorption bands in the visible range unlike the N containing sample. From this observation Sato concluded that the existence of nitrogen species originating from NH<sub>4</sub>Cl enhanced visible light activity<sup>(63)</sup>. Sato found that high calcination temperatures of doped TiO<sub>2</sub> reduced visible light absorption. It was suggested that loss of the photoactivity in visible region resulted because the dopant was volatile at high temperature and long calcination time. Sato was not the first to work with N/TiO<sub>2</sub>.

About fifteen years earlier, Che and Naccache observed a paramagnetic species which was detected by electron paramagnetic resonance (EPR) spectroscopy for TiO<sub>2</sub> samples which were prepared by treating titanium samples with aqueous ammonia prior to calcination at 300 to 450 °C<sup>(64)</sup>. They attributed EPR signals in these samples to the existence of NO<sub>2</sub><sup>2-</sup> radical species adsorbed only on the surface and not within the lattice of titania. They based on their identification of these radicals on the magnetic parameters of NO<sub>2</sub><sup>2-</sup> when it was adsorbed on the surface of other metal oxides. It has been reported that similar parameters were observed for adsorption and oxidation of NO<sub>2</sub><sup>2-</sup> on the surfaces of MgO and ZnO. In 2001 Asahi and co-workers proposed a new method for the modification of

TiO<sub>2</sub>, which depends on the introduction of nitrogen into the TiO<sub>2</sub> matrix, leading to increased photocatalytic activity. It was found that doping nitrogen into TiO<sub>2</sub> reduces its bandgap, which leads to a considerable shift in its absorption spectrum from the ultraviolet into the visible region by about 3%<sup>(65)</sup>. The main theories suggest that, nitrogen species exist interstitially, substitutionally or a combination of both. Nitrogen can be found as interstitial NO<sub>x</sub> and other species such as N and NH<sub>x</sub> can also be involved. There are many approaches which have been used to identify the nitrogen species such X-ray photoelectron spectroscopy (XPS), which is used to measure the nature of the N (1s) binding energy, which corresponds to its chemical environment<sup>(65)</sup>.

### 2-3-2 Identification of doped nitrogen species

Until now the location and the type of the doped nitrogen species in the titania lattice is still contentious. There are many theories, but the main theories suggest that doped nitrogen species are present as interstitial or substitutional species or in other cases, as a combination of these two states. In one study, Sato suggested the presence of NO<sub>x</sub> as interstitial species within the lattice of TiO<sub>2</sub><sup>(20)</sup>. In addition, there were shown to be other species such as NH<sub>x</sub> which can exist as substitutional species<sup>(66)</sup>. In order to identify nitrogen species, several methods have been employed. XPS has been used to measure the N(1s) binding energy, which gives an indication of its chemical environment. N(1s) binding energies at 402, 399 and 396.7 eV were observed and the attribution of these three energies is also still contentious<sup>(67)</sup>. Samples of titania prepared by hydrolysing Ti(SO<sub>3</sub>)<sub>2</sub> with aqueous ammonia solution exhibited strong N-H IR bands at 3145 and 1400 cm<sup>-1</sup>, even after sample calcination at 320 °C. When further increasing the calcination temperature to 450°C, these bands disappeared and new bands appeared at 1529, 1398, 1265 and 1171 cm<sup>-1</sup>, assigned to NO<sub>2</sub>, NO and NH<sub>3</sub> species. In addition, EPR spectroscopy was applied, and it showed two distinct paramagnetic nitrogen species, attributed to neutral NO and NO<sub>2</sub><sup>2-</sup> radical species<sup>(68)</sup>.

### 2-3-3 Mechanism of photoresponse for doped TiO<sub>2</sub> in visible light

In terms of photoresponse for nitrogen doped titania, there are two theories in this field; the first one is the mixing of 2p states of the doped nitrogen species with the O 2p states of the host oxide, and the second one, is the existence of an isolated N 2p narrow band lying above the O 2p valence band. The evidence for this orbital mixing is obtained from XPS data<sup>(65)</sup>. Asahi and co-workers calculated electron densities for N doped TiO<sub>2</sub> (both substitutional and interstitial positions), in an eight TiO<sub>2</sub> unit cell of the anatase phase. They reported that the substitutional N doped TiO<sub>2</sub> (N 2p) band overlapped with the (O 2s)

state and they concluded that the bands were mixed together<sup>(67)</sup>. Hashimoto suggested that nitrogen doping resulted in a unique band above the valence band of neat TiO<sub>2</sub>. In the mineralization of isopropyl alcohol, when reaction was carried out by UV- light irradiated doped TiO<sub>2</sub>, the quantum yield was higher than when the doped TiO<sub>2</sub> was exposed to visible light. Hashimoto argued the existence of two distinct bands, so that illumination with UV light caused excitation from both bands, while visible light caused excitation only from the higher lying band. He proposed that this effect would not occur if the N 2p band overlapped with the valence band of TiO<sub>2</sub> and thus doped nitrogen forms a single higher lying band<sup>(69)</sup>. Despite contention about nature of nitrogen doped titania, but the existence of red shift in absorption of nitrogen doped titania gives an indication to the presence of isolated N2p states located above O2p states. This can lead to reduce bandgap of titania and enhance the absorption in visible region of the spectrum<sup>(69)</sup>.

### **2-3-4 Methods of doping**

There many different methods are reported in the literature for introducing nitrogen species into TiO<sub>2</sub>. Generally, they can be divided into two categories: chemical and physical methods. Chemical methods involve sol- gel synthesis, hydrolytic synthesis methods, annealing titania powder under high temperatures in the presence of NH<sub>3</sub> gas, direct alkylation of ammonium salts and oxidation of titanium nitride<sup>(70)</sup>. Physical methods for doping nitrogen into titania, include ion implantation<sup>(71)</sup>, magnetron sputtering, plasma enhanced vapor deposition and pulsed laser deposition. Doping titania by this method in most cases results in anatase titania films with nitrogen doping in the range of 2.0 - 4.4 wt %<sup>(72)</sup>.

### **2-4 Adsorption on the TiO<sub>2</sub> surface**

For heterogeneous photocatalytic systems, the catalyst is present in a different phase (solid) from the rest of the reaction medium. Many types of reactions occur on the surface of the photocatalyst, so that surface area, particle size and chemical composition of the surface play a major role in its efficacy as a catalyst. Catalytic activity occurs when reactant species are adsorbed on the active sites on the surface. This activity plays a major role in the formation of intermediate species that dissociate to give the final product. These intermediates are formed as a result of interaction between adsorbed species and defect sites on the surface<sup>(73)</sup>. Generally, heterogeneous photocatalytic reactions can be defined as reactions in which at least one of the following steps is isothermally enhanced by the absorption of light with suitable energy by the photocatalyst. These steps are<sup>(74)</sup>:

1. Adsorption of the reaction species,
2. Reaction of the adsorbed species and
3. Desorption of the products.

Adsorption on the surface may be physical or chemical in nature and it depends on the temperature, pressure and pretreatment of the surface of the catalyst. Also it depends on the interaction between active groups in the adsorbents and that of the surface. The later interaction determines nature of the adsorption.

## **2- 5 Results and Discussion.**

### **2-5 -1 Parent and nitrogen doped titanium dioxide**

Titania samples treated in a flow of  $\text{NH}_3$  at 400 °C, 500 °C and 600 °C are denoted as titaniaN400, titaniaN500 and titaniaN600 respectively. The nitrogen and hydrogen contents of the parent and nitrogen doped samples were determined by elemental analysis and the data are presented in Table 2- 1. From this data, it can be seen that ammonia is effective for the introduction of nitrogen into the samples, as expected from the yellow colouration of the samples that was observed to develop upon  $\text{NH}_3$  treatment.

Furthermore, the level of nitrogen dopant increases and is substantial after treatment at 600°C. In addition, hydrogen is observed to be present in nearly all samples. BET surface areas have been measured for the three sets of samples and the results are presented in Table 2-2, where it can be seen that the surface area of the anatase materials is roughly constant upon  $\text{NH}_3$  treatment for the 400 and 500 °C samples, although a significant decrease upon reaction at 600°C is apparent. A smaller decrease is also observed for rutile. However, in case of the P25 samples, it appears that the surface area is slightly enhanced upon  $\text{NH}_3$  treatment. In all cases, powder XRD indicates the retention of the original crystal phase upon reaction. The UV-visible diffuse reflection spectra of doped and undoped samples are shown in Figures 2-4 to 2-6. For all doped samples, there are considerable shifts of the absorption shoulders into the visible light region. The absorption shoulder in the range 400- 550 nm is related with the presence of doped nitrogen with these samples and it increased with increasing in nitrogen content. Additionally, these samples after they have been doped, were pale- yellow in colour<sup>(75,76)</sup> and the colour deepened gradually with elevation in doping temperature.

It has been reported that the colour of the N doping samples partially results from bulk reduction. This probably arises from existence of mixed  $\text{N}2p$  states with  $\text{O}2p$  states or isolated  $\text{N}2p$  states lying above valence band<sup>(77,78)</sup>. The presence of the visible absorption band in the electronic spectra for the doped samples provides a possible indication that

nitrogen may have changed the electronic structure of titania effectively<sup>(79)</sup>. Normal absorption in titania is due to an electronic transition from the valence band to the conduction band which commonly occurs in the ultraviolet region of the spectrum<sup>(80,81)</sup>.

### 2-5-1-1 Elemental analysis

The results of nitrogen and hydrogen contents for neat and doped TiO<sub>2</sub> samples are shown in the following table:

**Table 2-1:** Elemental analysis for doped TiO<sub>2</sub> measured by CHN microelemental analysis.

Catalyst	H wt% ± 0.03%	N wt% ± 0.02%	N/H atomic ratio
anatase parent	0.31	0.00	-----
anataseN400	0.28	0.35	0.09
anataseN500	0.24	0.48	0.14
anataseN600	0.21	1.80	0.61
rutile parent	0.88	0.00	-----
rutileN400	0.50	0.22	0.03
rutileN500	0.38	0.36	0.07
rutileN600	0.35	1.46	0.30
P25 parent	0.31	0.00	-----
P25N400	0.18	0.32	0.13
P25N500	0.00	0.48	0.00
P25N600	0.00	1.52	0.00

These results showed that the ratio of nitrogen content for the nitrogen doped titania samples was increased with increase in the doping temperatures. Additionally, from the stoichiometric values for atomic ratio of H/N for the doped nitrogen species, it can be seen that the expected doping species don't correspond simply to NH<sub>3</sub> and NH<sub>2</sub> residues.

### 2-5-1-2 BET Surface area measurements

BET surface area results for neat and doped samples are shown in the following table:

**Table 2-2:** BET measurements for parent and dopedTiO<sub>2</sub>, particle size was measured using Scherrer equation.

Catalyst name	BET surface area (m <sup>2</sup> /g) ± 1	Particle size(nm) from XRD
anatase parent	112	16.5
anataseN400	113	16.1
anatase N 500	116	15.6
anataseN600	89	17.1
rutile parent	148	12.5
rutileN400	158	12.2
rutileN 500	160	11.8
rutileN 600	142	13.2
P25 parent	50	18.5
P25N400	52	17.8
P25N500	58	17.4
P25N600	65	17.3

Specific surface areas have been measured for the three sets of samples and the results are presented in Table 2-2, where it can be seen that the surface area of the anatase materials is relatively unchanged upon NH<sub>3</sub> treatment for the samples doped at 400 °C and 500 °C, although a significant decrease upon reaction at 600 °C is apparent. In all cases, powder XRD indicates the maintenance of the original crystal phase upon reaction. Generally, specific surface area is mainly independent of the amount of doped nitrogen. The XRD patterns for the doped and undoped samples are similar, and their patterns did not differ significantly except for slight variation in the intensity and broadening of their peaks. Generally, samples that doped at 400 and 500 °C were relatively broader than that doped at 600 °C. The Scherrer equation<sup>(82)</sup> was used in the estimation of the particle size for neat and doped samples. When the size of crystallites is less than 100 nm, appreciable broadening of the x-ray diffraction reflections occurs. This may be related to the actual size of the crystallites, in this case the observed line broadening can be used in the estimation of the average particle size. For application for this equation, the following assumptions must be made: negligible broadening caused by the instrument, negligible broadening due to

strain disorder and when working from a single reflection coherent diffraction domain size is isotropic. In the simplest case where the particles are free from strain, the size of the particle can be estimated from a single diffraction peak.

### 2-5-1-3 UV-visible spectra for nitrogen doped titania

The UV-visible diffuse reflectance spectroscopy for parent and modified TiO<sub>2</sub>, rutile, anatase and P25 are shown in the following figures:

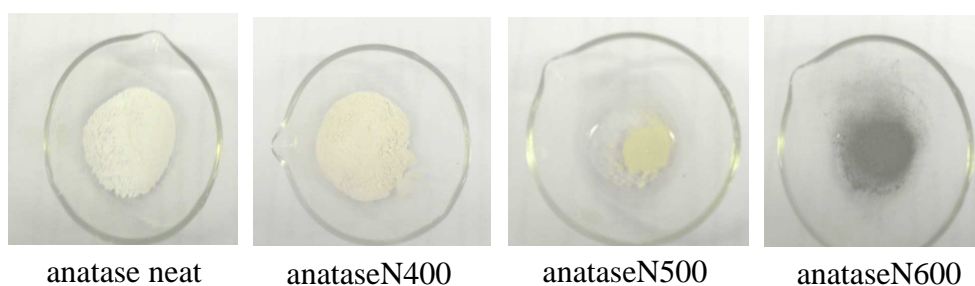
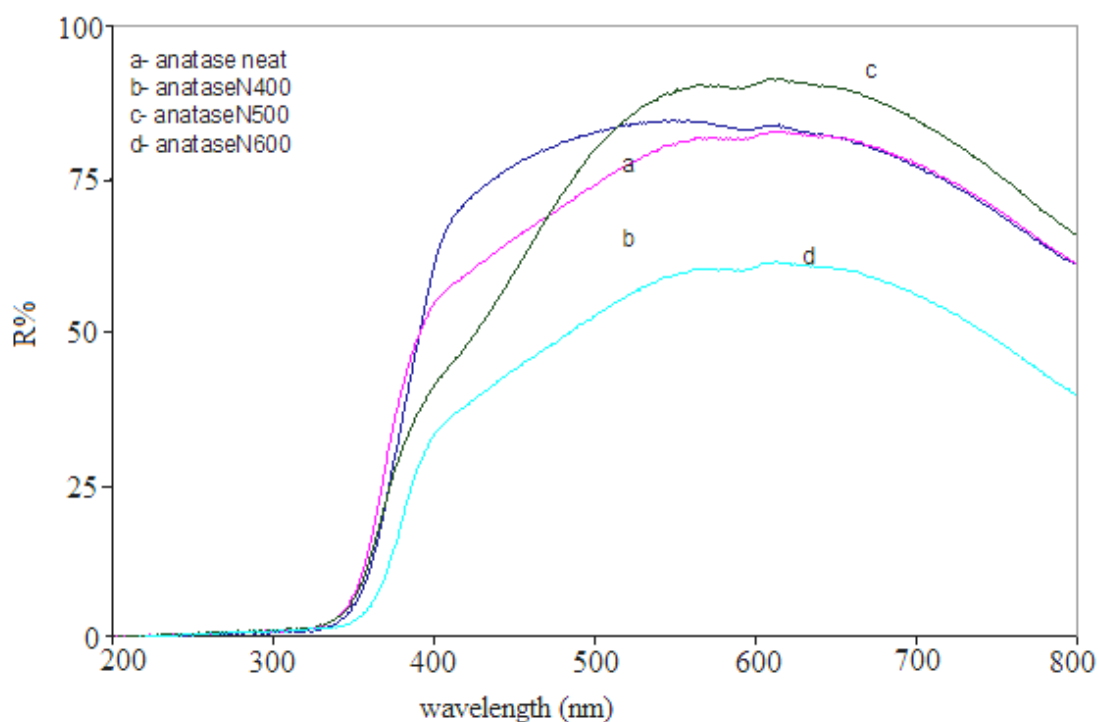


**Figure 2-4:** UV-visible diffuse reflection spectra for neat and N doped anatase, change in colour for N doped samples is shown from left to right.

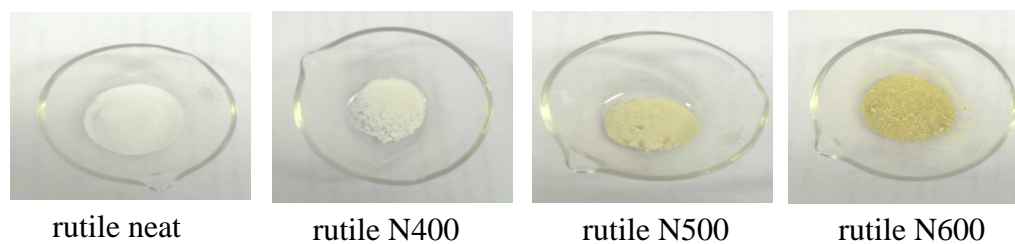
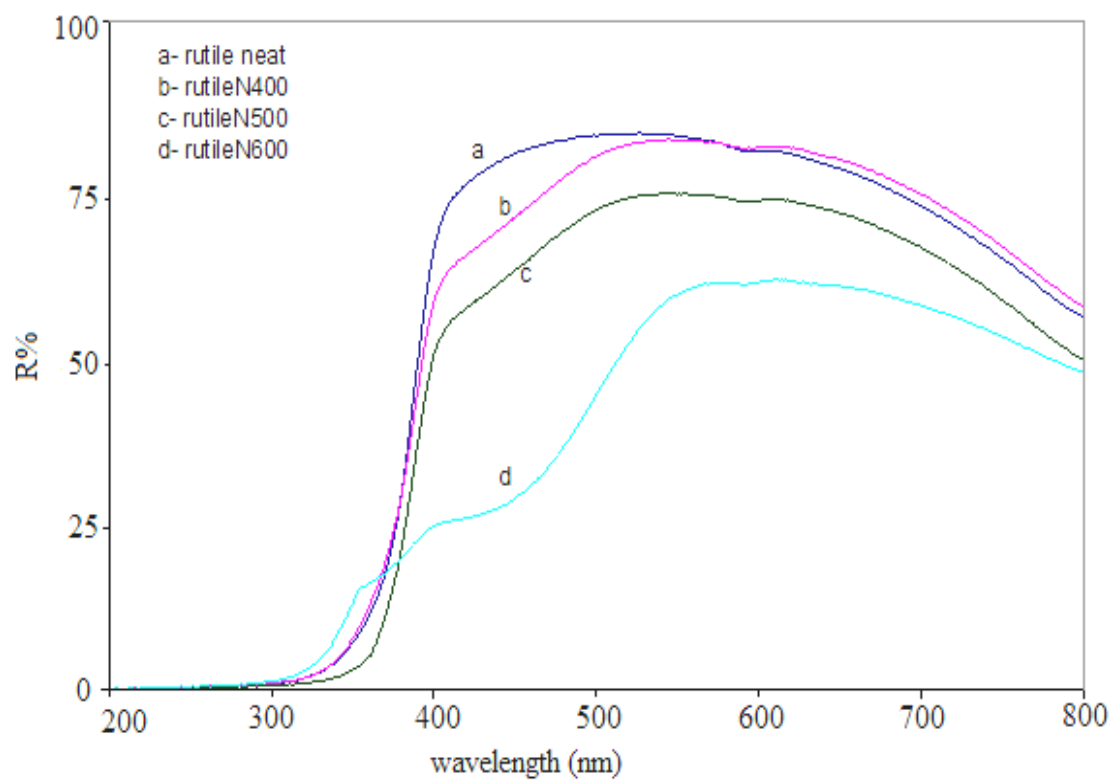


**Figure 2-5:** UV- visible diffuse reflection spectra for neat and N doped rutile, change in colour is shown for N doped samples.

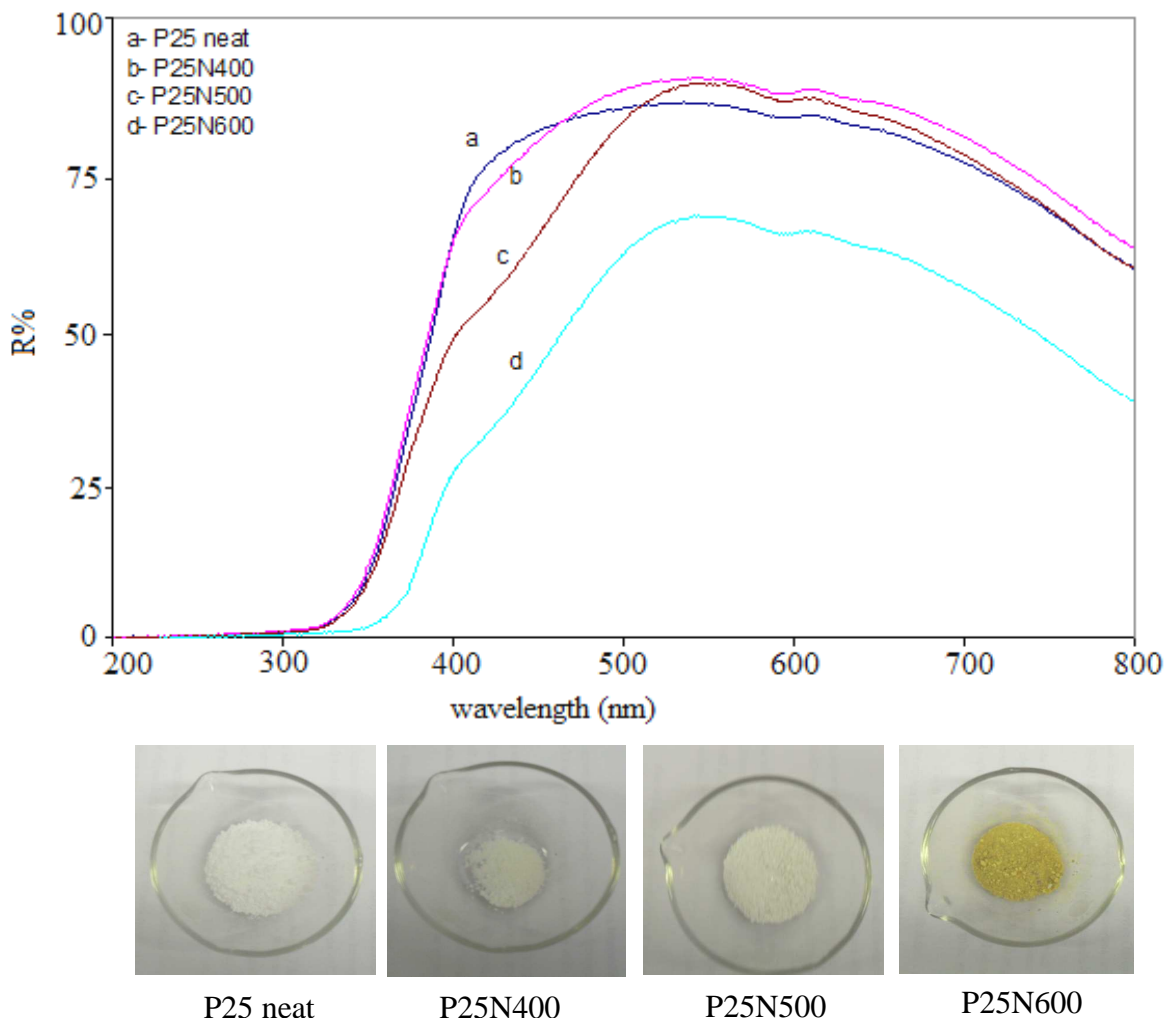


**Figure 2-6:** UV- visible diffuse reflection spectra for neat and N doped P25, change in colour is shown for N doped samples.

The UV-visible diffuse reflection spectra were measured for parent and doped forms of  $\text{TiO}_2$ . These spectra are shown in the Figures 2.4- 2.6. From these results, it was observed that, there is red shift in the band edge absorption of the doped samples ( $\text{TiO}_{2-x}\text{N}_x$ ). This means that, the photoresponse of these samples was shifted towards the visible region of the spectrum. It was reported that nitrogen could be loaded in the lattice of titania. Generally, the extension of the absorption spectrum from UV light to the visible range arises from contribution of both doped nitrogen atoms and oxygen vacancies in the lattice of  $\text{TiO}_2$ . That is because the interstitial nitrogen atoms would induce the local states near the valence band edge and the oxygen vacancies generate local states below the conduction edge<sup>(83)</sup>. Generally, doped nitrogen atoms induce local states close to the valence band, while oxygen vacancies induce local states below the conduction band. These local states can enhance light harvesting for the catalyst in both the near UV and visible region of the spectrum. Oxygen vacancies induced by doping  $\text{TiO}_2$  can act as colour centres. The electrons that leave oxygen vacancies may interact with the adjacent  $\text{Ti}^{\text{IV}}$  species to

generate  $Ti^{III}$  species as colour centres. The presence of these colour centres in titania can increase the absorption of visible light for the N doped titania <sup>(84)</sup>.

#### 2-5-1-4 XRD patterns for parent and doped $TiO_2$ Samples

XRD patterns for parent and doped  $TiO_2$  with nitrogen are shown in the following figures:

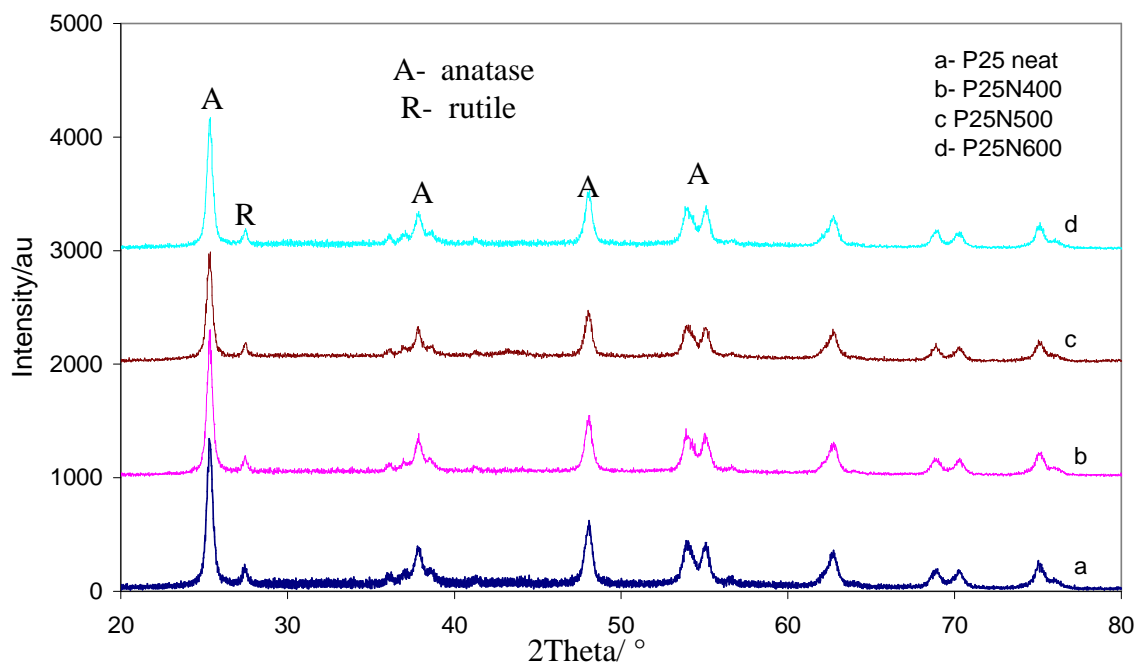


**Figure 2-7:** XRD patterns for neat and nitrogen doped P25.

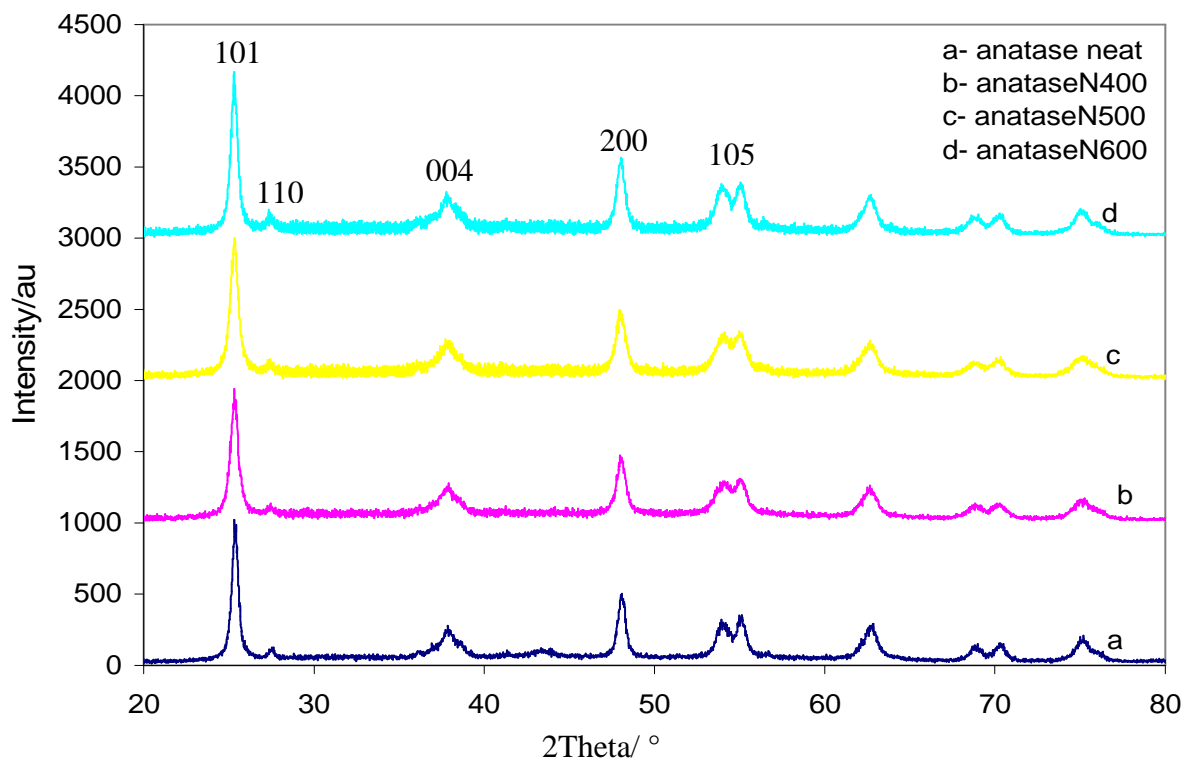


**Figure 2-8:** XRD patterns for neat and nitrogen doped anatase.

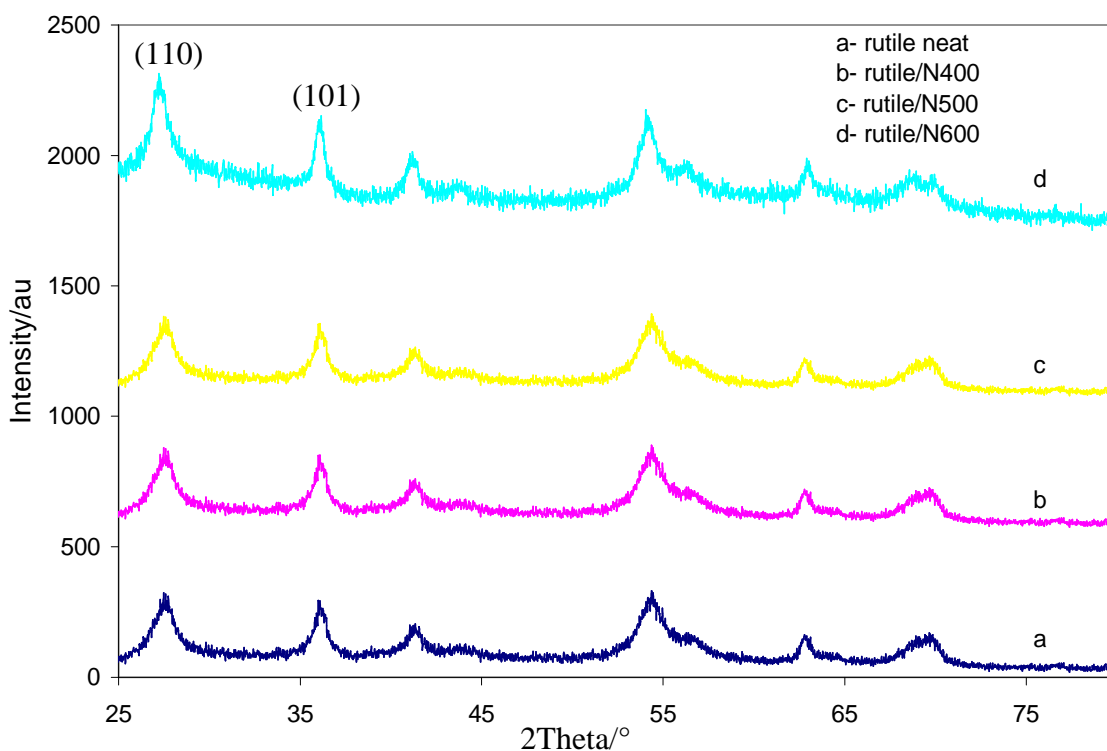


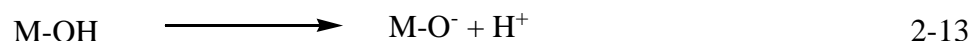
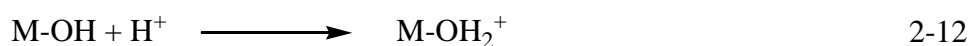
**Figure 2-9:** XRD patterns for neat and nitrogen doped rutile.

The XRD patterns for neat and doped samples of each of P25, anatase and rutile are shown in the above figures. These samples possess similar diffraction peaks without significant changes in the positions of these peaks occurring after doping<sup>(63)</sup>. In addition, doping of both anatase and rutile at 600 °C gives slightly higher intensity with sharper peaks, which indicates that well crystallized materials with a relatively large particle size can be produced at 600 °C by nitrogen doping. For the doped samples, there is not evidence for the occurrence of any phase transformation. For neat anatase and that doped with nitrogen, there is a residual peak around ( $2\theta = 27$ ) which arises probably for rutile phase. It has been reported that, when replacing  $O^{2-}$  in titania by nitrogen species by doping minimal structure change occurs, although the radius of the nitrogen ion (0.171nm) is larger than that for the oxygen ion (0.132nm)<sup>(85)</sup>. Hence, the expected change in the structure due to doping nitrogen in this range of concentrations would be relatively minor<sup>(86)</sup>.

### 2-6 Determination of the point zero charge for nitrogen doped titania (PZC)

The PZC is an important parameter for the catalysts as it can be correlated with the acid - base behaviour of solid materials and their ability to interact with species for surface adsorption. The point of zero charge of metal oxide ( $pH_{PZC}$ ) can be defined as the pH at which the net surface charge is zero<sup>(87-89)</sup>. The PZC is important for many applications of oxides, for example if the oxide is used as a support in the preparation of supported catalysts. Several methods can be used to determine the PZC for an oxide. Potentiometric

titration (PT), the mass titration technique (MT) and the immersion technique (IT) have all been reported<sup>(87-89)</sup>. Among these methods, PT is more suitable than the other methods, because IT is low accuracy and MT requires a large amount of oxide suspension consequently, PT is the method of choice. However, the reliability of this method may be affected by ionic strength, which can affect the solubility of different acidic/ basic groups on surface of the oxide<sup>(89,90)</sup>. The pH of solution has to some extent a role in the rate of reaction metal hydroxides have amphoteric behaviour in their solutions as follows<sup>(90,91)</sup>:



As a result of this amphoteric behaviour, metal oxide surfaces are net positively charged below the PZC, and negatively charged above the PZC. These considerations have obvious implications in adsorption of species.

### 2-6-1 Evaluation of PZC for titania doped with nitrogen

Generally, the PZC for catalyst can be evaluated by potentiometric titration as stated above<sup>(87-89)</sup>. Results of the titration are plotted as a volume of the added acid against pH of the mixture, and the PZC is taken as the point of intersection with the blank pH curve as shown in the following figures:

**Table 2- 3:** PZC values for neat and doped titania.

Catalyst	rutile (pH) ± 0.10	anatase (pH) ± 0.10	P25 (pH) ± 0.10
neat titania	5.50	6.20	6.00
titaniaN400	6.20	6.65	6.40
titaniaN500	6.90	7.35	7.10
titaniaN600	7.80	8.35	8.10

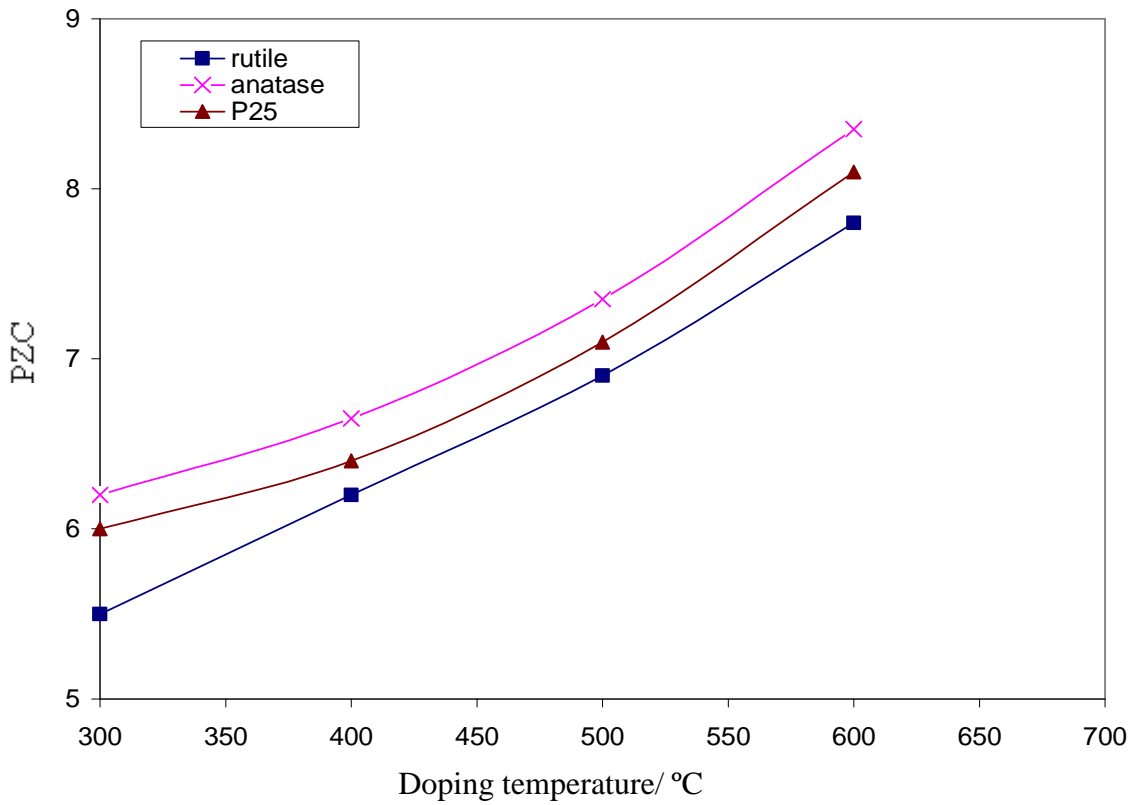


**Figure 2-10:** PZC values for neat and nitrogen doped titanic, the average error bar was  $\pm 0.1$ .

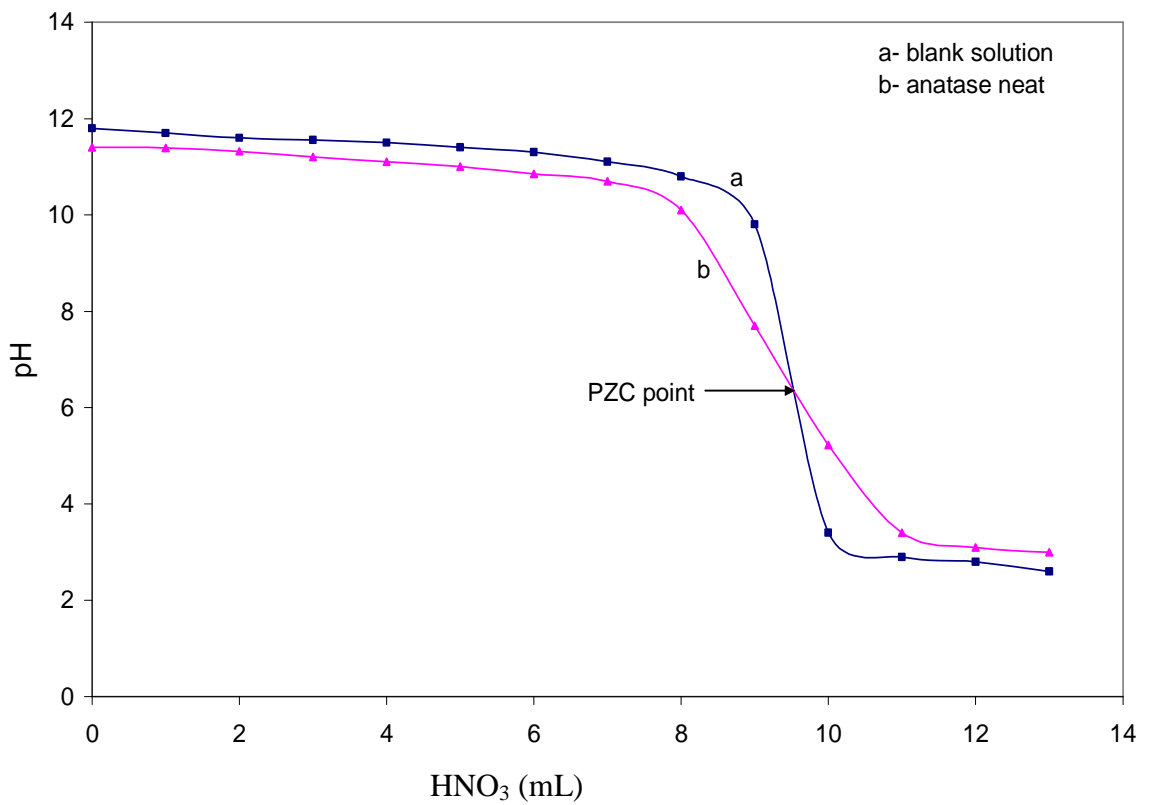


**Figure 2-11:** Potentiometric titration for neat anatase, the average error bar  $\pm 0.1$ .

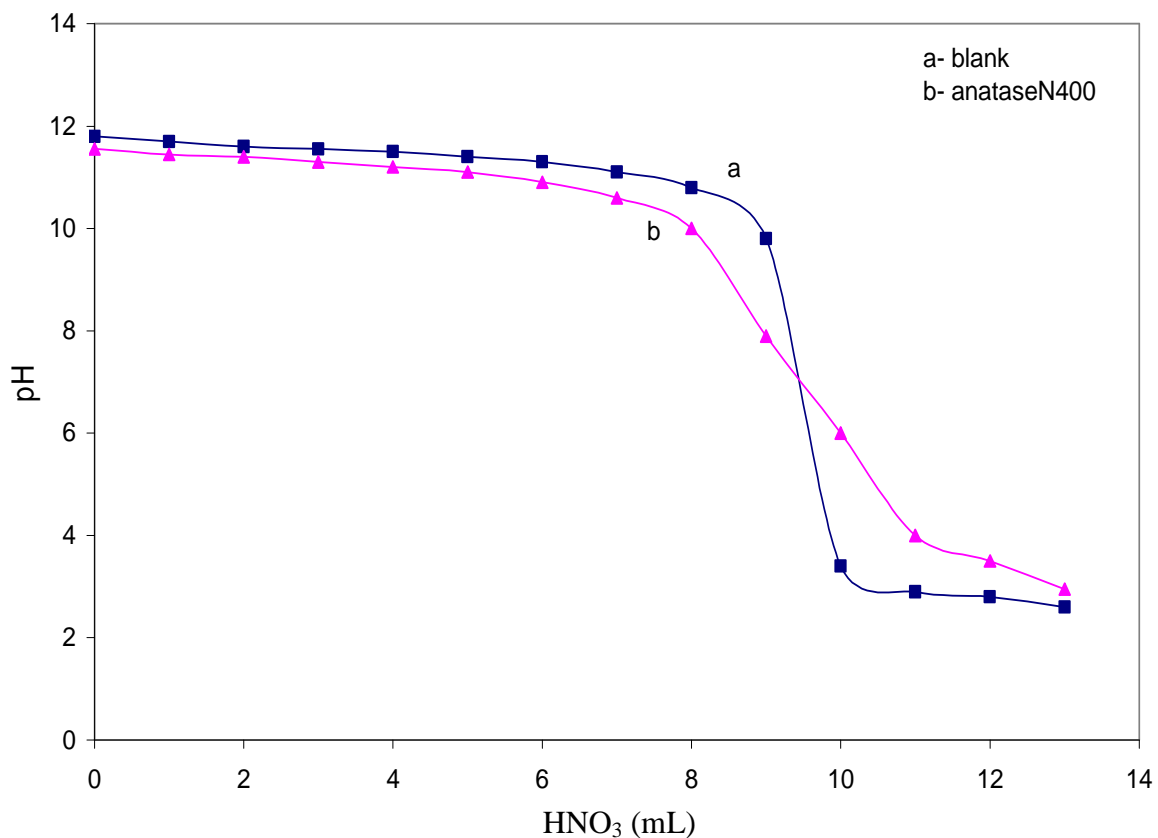


**Figure 2-12:** Potentiometric titration for anataseN400, the average error bar  $\pm 0.10$ .

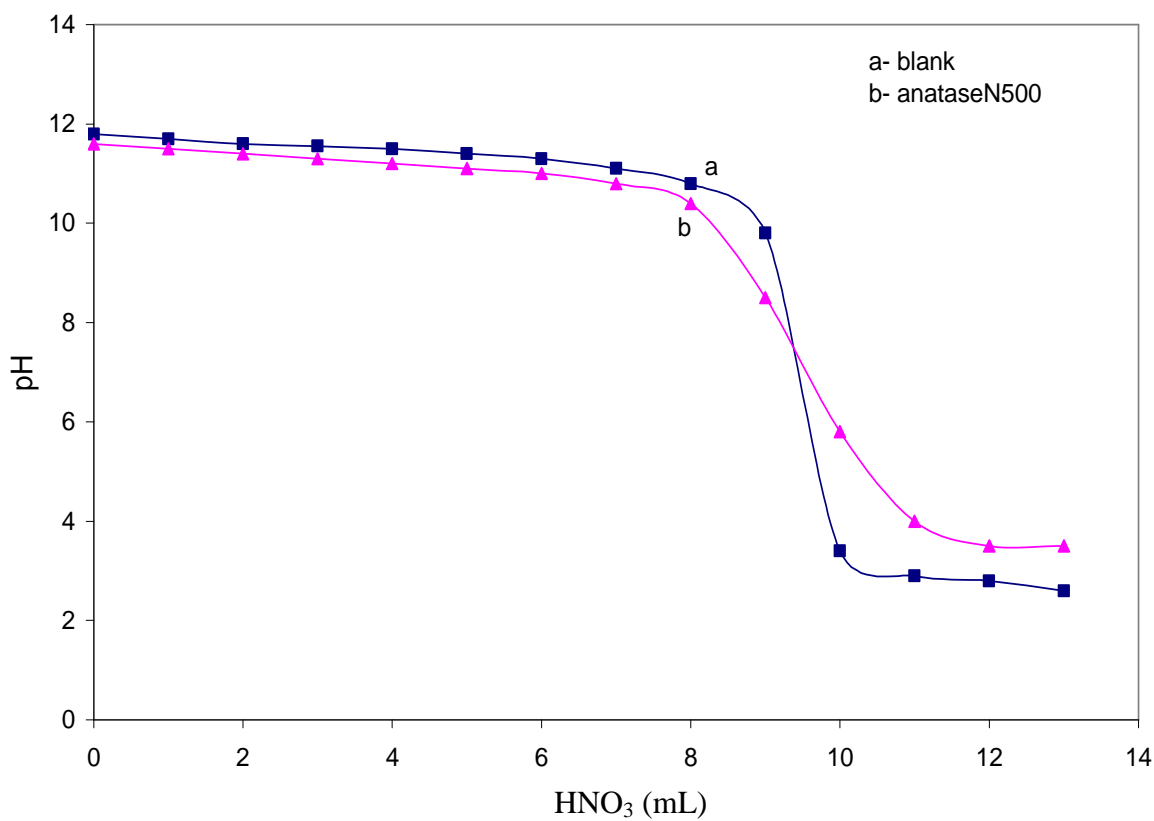


**Figure 2-13:** Potentiometric titration for anataseN500, the average error bar  $\pm 0.10$ .

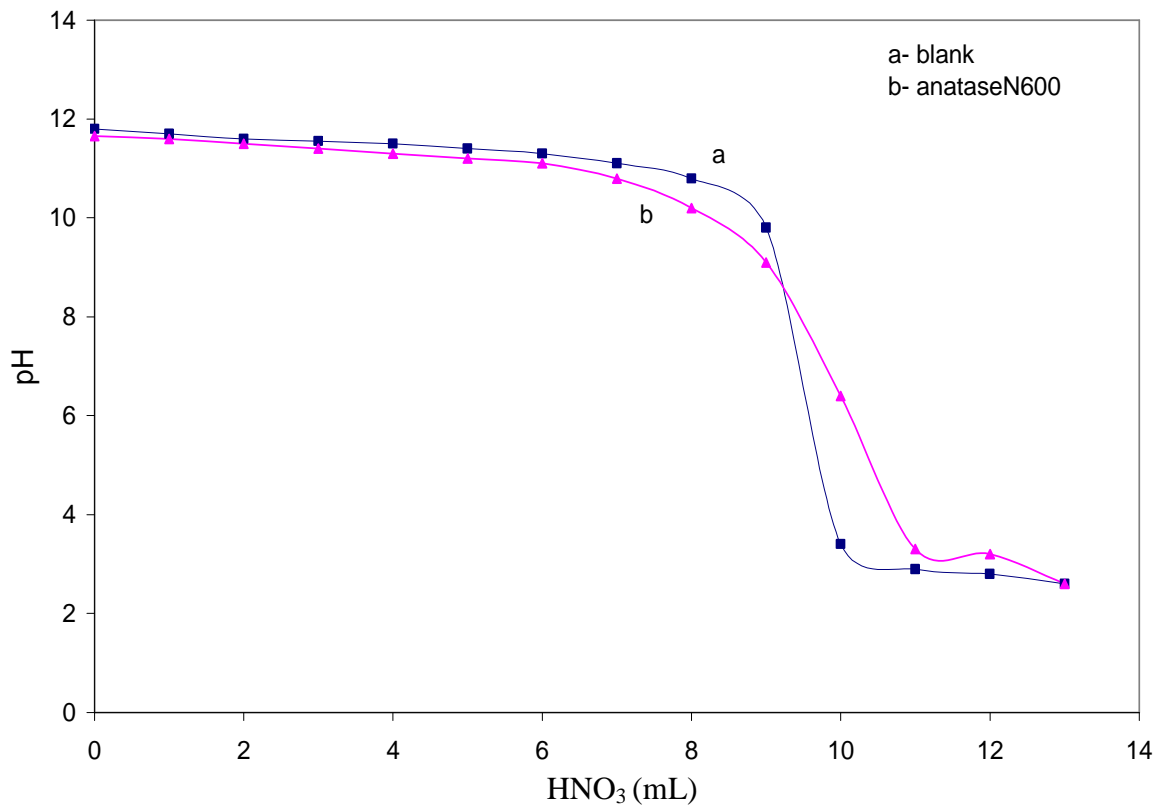


**Figure 2-14:** Potentiometric titration for anataseN600, the average error bar  $\pm 0.10$ .

The values of PZC for neat and doped titania are given in Table 2-3, and are plotted in Figure 2-10. Initially the pH of the all samples is fractionally increased by the presence of  $\text{TiO}_2$ , which could be related to the adsorption of  $\text{H}^+$  from the solution on the surface of titania, that leads to protonated basic sites on the surface. When equilibrium is reached in the titania suspension, adding the base gives pH of solution lower than that for the blank solution ( $\text{KNO}_3$ ). In this case, the added hydroxyl groups would neutralize hydrogen ions in the solution and remove hydrogen ions from the sites on the surface creating basic sites on the surface of titania. In the titration with  $\text{HNO}_3$  at pH higher than the PZC, hydrogen ions added to the suspension are consumed to neutralize hydroxyl ions in the solution and neutralize the basic sites on the surface of titania<sup>(87-89)</sup>. So that, titration curves for blank and suspension of titania approach each other and intersect at a certain pH value (the PZC). After this point, the pH of suspension is higher than that for the blank solution that gives evidence to the PZC point. At values of pH lower than the PZC, adding further acid would lead to the creation of acidic surface groups, which leads to consumption of a portion of the hydrogen ions added by titration with  $\text{HNO}_3$ .

From these results, it was observed that the values of the PZC for the doped titania were higher than that for neat titania and the values of the PZC were increased with increase in the concentration of nitrogen in the doped samples. This is probably due to the contribution of the adsorbed ammonia and the other nitrogen species on the surface.

Increasing percentage of doping would increase the basicity of the surface with the increase in the amount of doped nitrogen species. Consequently, this causes increasing in the basic behaviour of the surface, which leads accordingly to increase in the PZC values.

## **2-7 Photocatalytic activity for neat and doped titania**

### **2-7-1 Photocatalytic decoloration of methylene blue over parent and nitrogen doped TiO<sub>2</sub>**

Photocatalytic activity of the parent and doped titanium dioxide forms was investigated by photocatalytic decomposition of methylene blue (MB). Photocatalytic activity was determined by measuring change in the absorbance of a  $2.5 \times 10^{-5} \text{ mol dm}^{-3}$  aqueous solution of MB<sup>(92)</sup>. Reactions were performed by stirring a suspension of 0.01 g of material in 100 mL of MB solution at 20 °C in air. TiO<sub>2</sub> samples were stirred in the dye solution for 10 minutes prior to starting reaction by irradiation with UV light from middle pressure mercury lamp (125 watt), with continuous stirring for one hour in air. In the photocatalytic reactions, catalytic activity occurs when reactant species are adsorbed on the active sites on the surface, when all these active sites are saturated with the adsorbed molecules, equilibrium is achieved. In order to remove the contribution of adsorption on the photocatalytic degradation of MB, TiO<sub>2</sub> samples were suspended in MB solution with continuous stirring without irradiation for ten minutes. The initial pH of the reaction mixture was kept at 7 by adding NaOH solution to reference all the measurements to neutral pH as MB solution is slightly acidic. Subsequently, the reaction vessel was illuminated and periodic sampling was performed to determine the degradation of MB (measured as the change in absorbance at 655 nm). Photocatalytic decomposition of MB was investigated in a suspension of titania and in absence of titania with irradiation with UV light under same conditions. The results of MB decompositions are shown in the following figure:

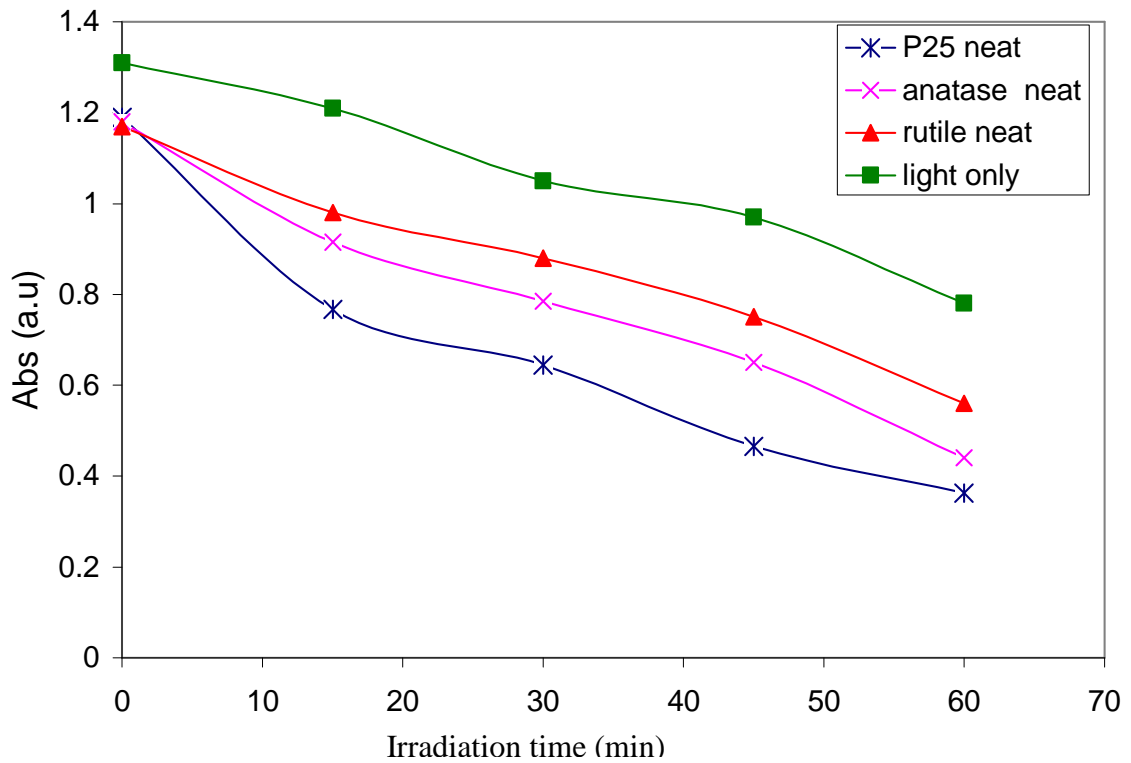


**Figure 2-15:** MB decoloration over a suspension of titania, and without titania under UV irradiation.

### 2-7-2 MB decoloration over nitrogen doped rutile

The photocatalytic decomposition of MB over neat and nitrogen doped titania was followed by measuring the absorbance of the dye. The decomposition curve is shown in Figure 2-16. Generally, there is enhancement in the decomposition over doped rutile at 400°C and 500 °C. Photocatalytic activity for this case has been observed in the following order (rutileN500> rutileN400> rutile neat > rutileN600). Hence, photocatalytic activity for N doped rutile generally increased with N content. However, for the rutile samples doped at 600 ° C with a higher nitrogen content gave a lower activity in comparison with that doped at 400 °C and 500°C as shown in the following figure:

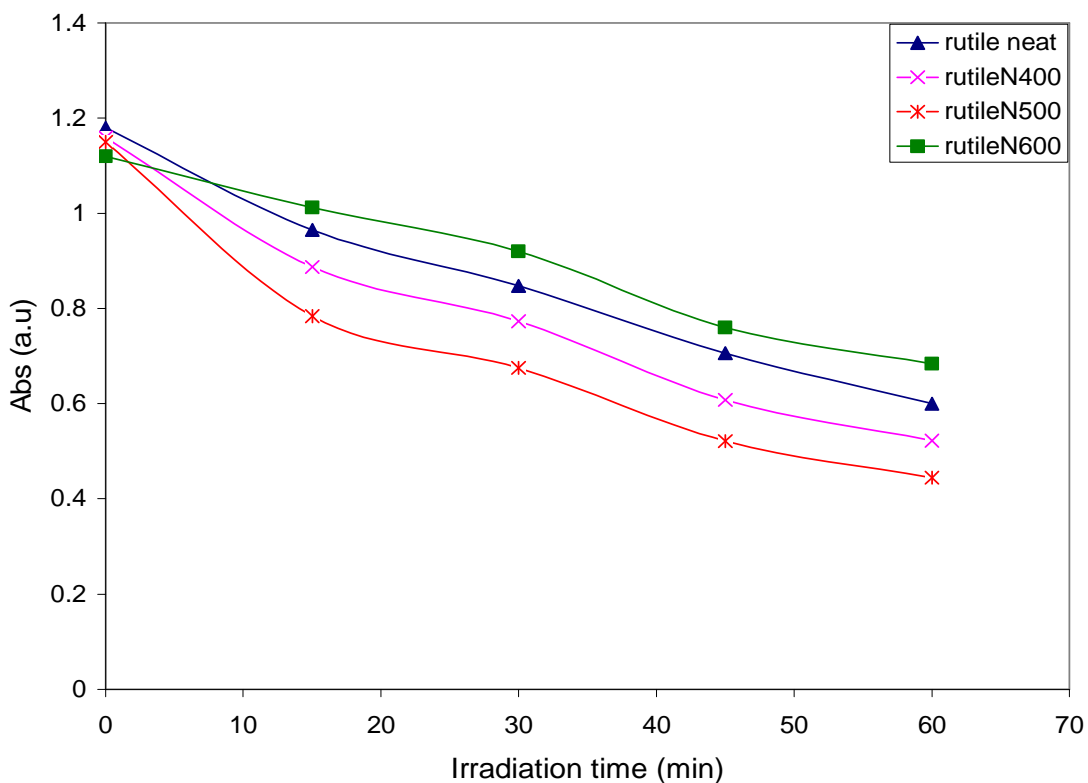


**Figure 2-16:** MB decoloration over nitrogen doped rutile.

The rate of the photocatalytic decoloration of MB over doped rutile was calculated by assuming photocatalytic decomposition of MB over titania is first order kinetics<sup>(92-94)</sup>.

Plotting  $\log(\text{Abs})$  at 655 nm against irradiation time the slope gives the rate constant ( $k$ ,  $\text{min}^{-1}$ ). The rate of decomposition of MB over titania was calculated as follows:

Rate of reaction = Rate constant  $\times$  Initial concentration of MB.

Rates of decoloration of MB over doped rutile are shown in the following figure:

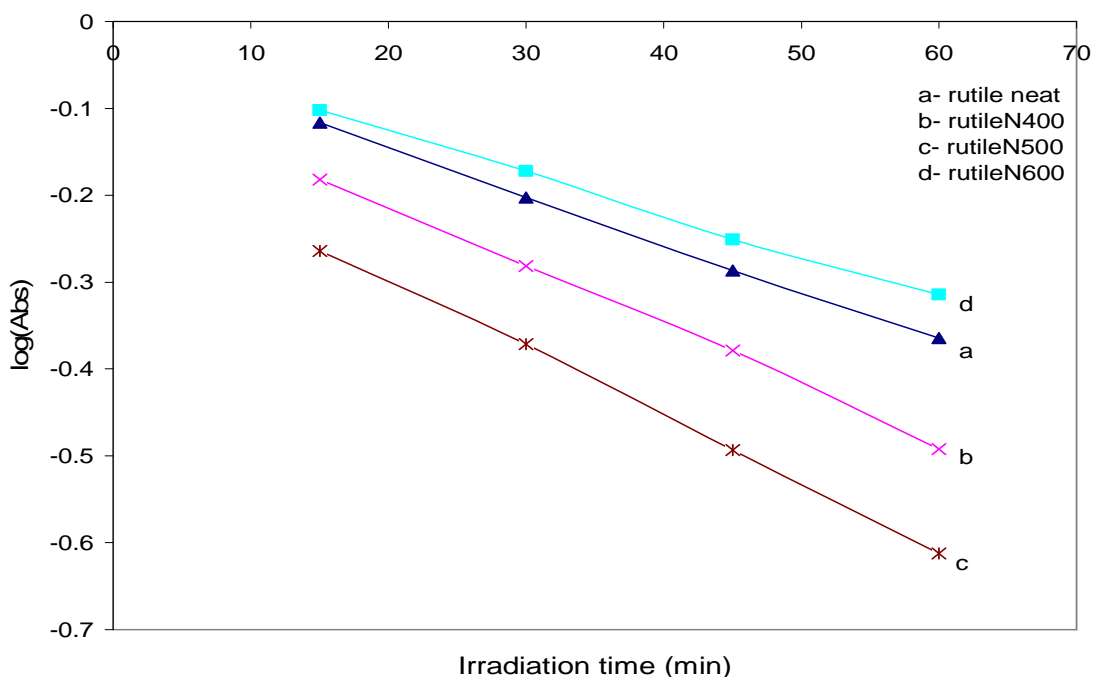


**Figure 2-17:** Rate of MB decoloration over nitrogen doped rutile.

Rates of MB decoloration over doped rutile are summarized in the following table:

**Table 2- 4:** Rates of the photocatalytic decoloration of MB over doped rutile.

Catalyst	Rate of decoloration $\times 10^{-8} \pm 0.12 \text{ mol. l}^{-1} \cdot \text{s}^{-1}$
rutile neat	0.91
rutileN400	1.17
rutileN500	1.34
rutileN600	0.75
light only	0.53

The relation between photocatalytic decoloration of MB and the PZC values for doped rutile is shown in the following figure:

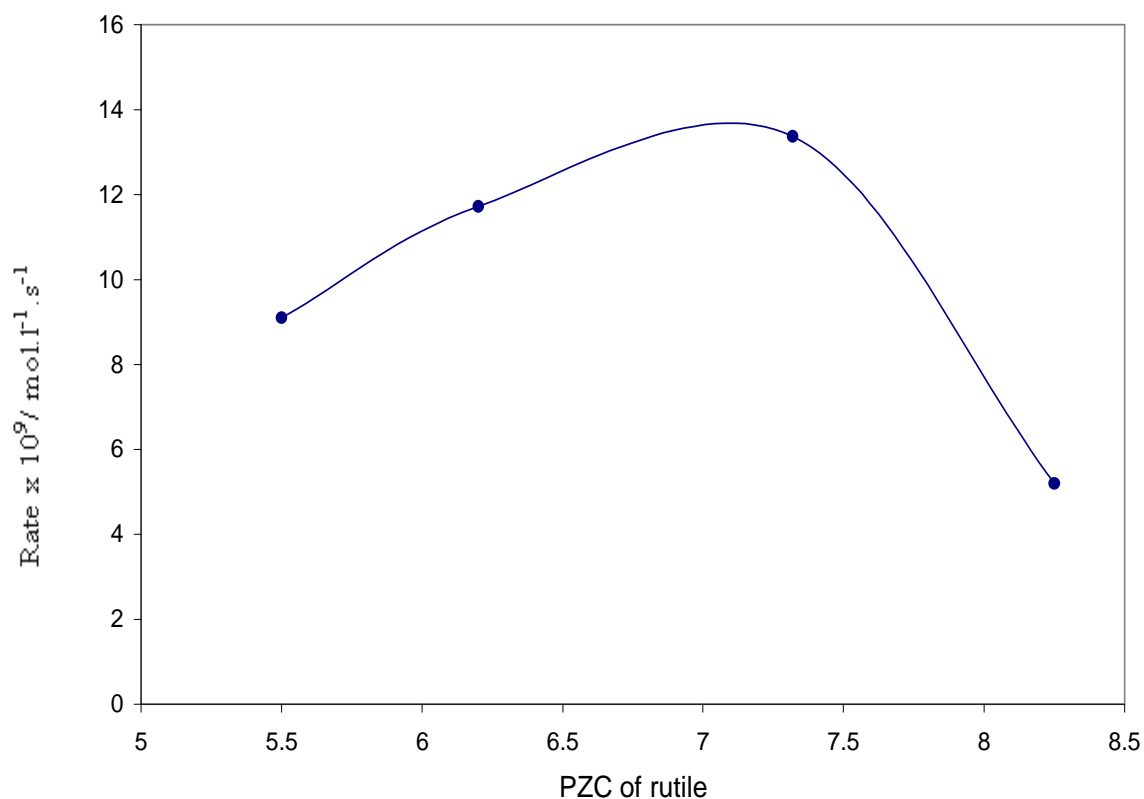


**Figure 2-18:** The relation between PZC and rate of decoloration of MB over neat and doped rutile.

As mentioned previously, the surface of metal oxide is predominantly has a net positive charge below the  $\text{pH}_{\text{PZC}}$  and negatively charged above that. In this study, rate of decomposition increased with increasing the PZC values and a maximum rate occurred around PZC 7.5. Rate of decomposition decreased at PZC higher than this value. The value of the PZC affects on the net charge of the surface that affects on the adsorption of MB

molecules on the titania surface. This adsorption can be considered as electrostatic interaction where positively charged species MB<sup>(95)</sup> are more likely to be adsorbed at the negative sites on the titania surface. It is well known that adsorption of reacting species is an essential step in photocatalytic reaction. As the PZC value becomes high for doped titania rutileN600, the surface has a net positive charge at high pH values. That may affect negatively in adsorption of MB on the surface, which may give a low rate of reaction. The surface area normalized the rates for neat and doped rutile is given in the following table:

**Table 2-5:** Normalized rates for photocatalytic decoloration of MB over doped rutile.

Catalyst	BET (m <sup>2</sup> /g)	Surface area normalized rate x 10 <sup>-8</sup> mol. l <sup>-1</sup> . s <sup>-1</sup> . m <sup>-2</sup>
rutile neat	148	0.61
rutileN400	158	0.74
rutileN500	160	0.84
rutileN600	142	0.53

From these results, it was found that, while there was increase in the rate of the reaction with the increase of surface area of the catalyst. Surface area normalisation showed that the effect was not solely dependent upon this parameter. Increasing the surface area of the catalyst in heterogeneous photocatalytic reactions can improve the activity of the catalyzed reaction that is probably due to increase the available adsorption sites on the surface<sup>(96)</sup>.

### 2-7-3 MB decoloration over nitrogen doped P 25

MB decoloration over neat P25 and that doped with nitrogen at 400 °C, 500 °C and 600 °C was investigated by using the same procedure that was used with rutile. The results for the photocatalytic decoloration of MB over P25/N are shown in the following figure:

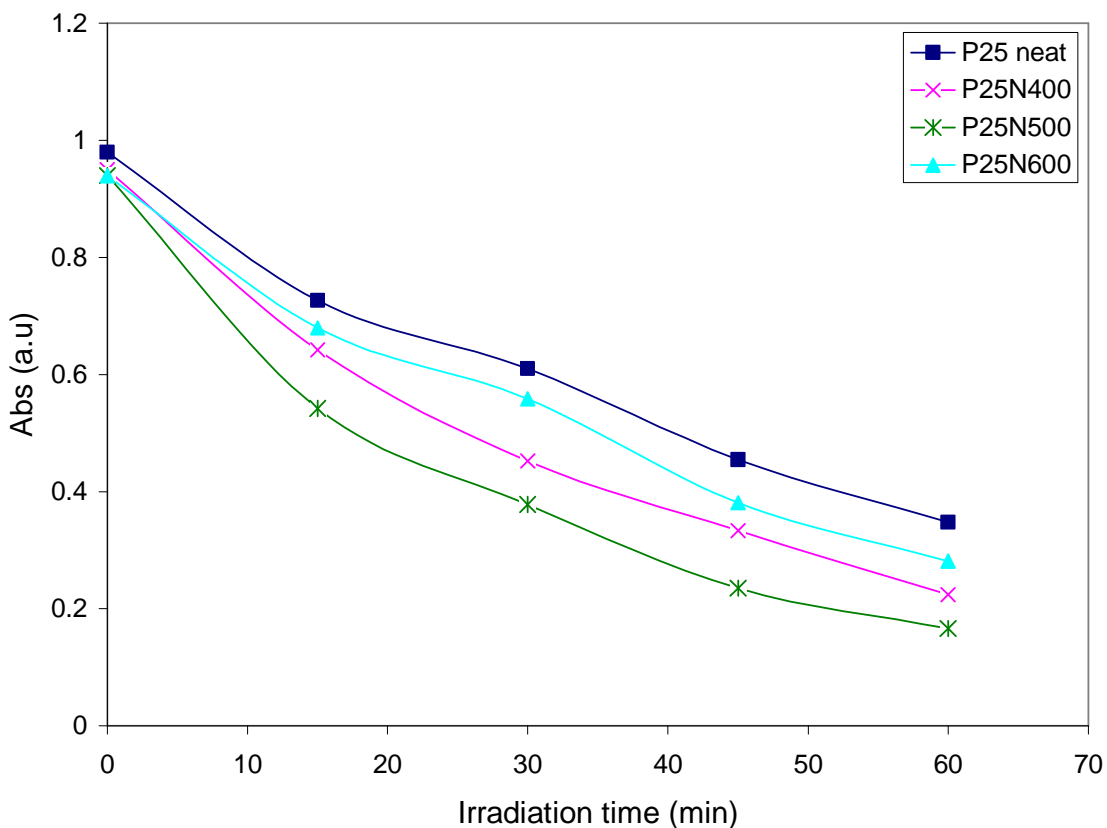


**Figure 2-19:** MB decoloration over nitrogen doped P25.

The rate of the photocatalytic decoloration of MB over neat and doped P25 is shown in the following table:

**Table 2-6:** Rates of photocatalytic decoloration of MB over P25N.

Catalyst	Rate of decoloration $\times 10^{-8} \pm 0.10 \text{ mol} \cdot \text{l}^{-1} \cdot \text{s}^{-1}$
P25 neat	1.42
P25N400	1.73
P25N500	1.92
P25N600	1.61
light only	0.53

From these results, the activity of the photocatalytic decomposition over neat and doped P25 was as follows: P25N500 > P25N400 > P25N600 > P25 neat. The surface area normalized the rates for neat and doped P25 are given in the following table:

**Table 2-7:** Normalized rates for photocatalytic decoloration of MB over P25N.

Catalyst	BET (m <sup>2</sup> /g)	Surface area normalized rate x 10 <sup>-8</sup> mol. l <sup>-1</sup> . s <sup>-1</sup> . m <sup>-2</sup>
P25 neat	50	2.84
P25N400	52	3.33
P25N500	58	3.31
P25N600	65	2.48

#### 2-7-4 MB decoloration over nitrogen doped anatase

MB decoloration over neat anatase and that doped with nitrogen at 400 °C, 500 °C and 600 °C was investigated by following the same procedure that was used with rutile and P25.

The photocatalytic decoloration profiles of MB over anatase/N are shown in the following figure:

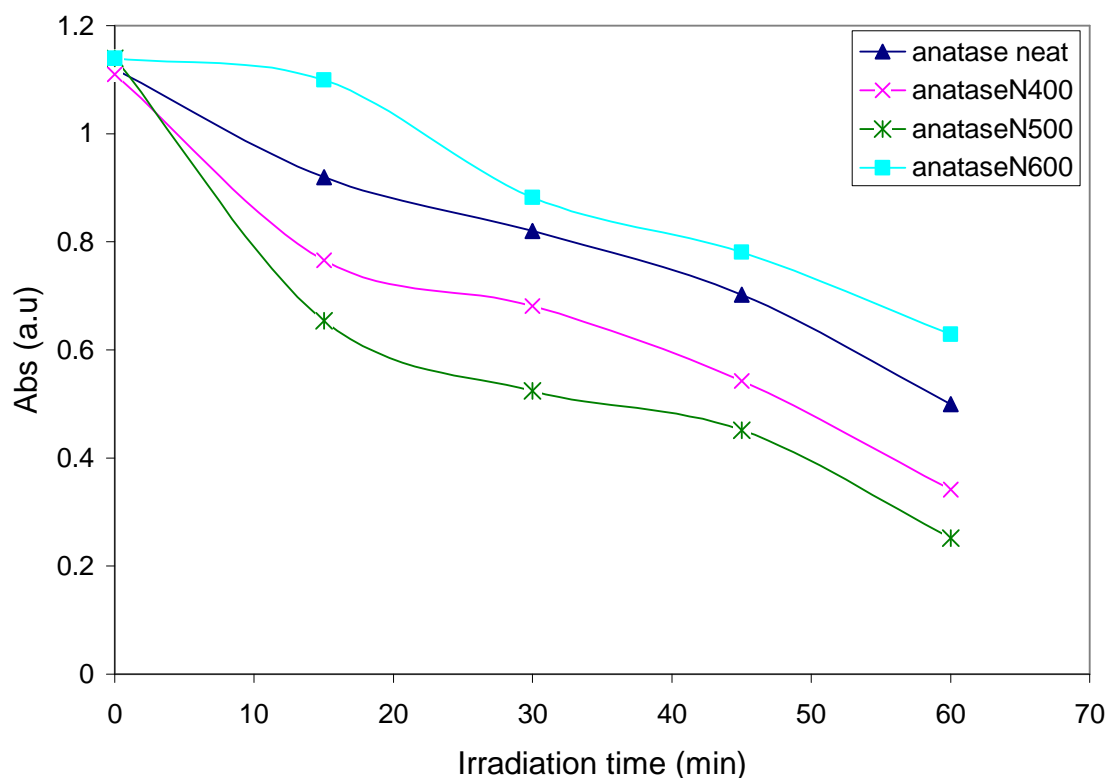


**Figure 2-20:** MB decoloration over nitrogen doped anatase

The rate of the photocatalytic decoloration of MB over neat and doped anatase is shown in the following table:

**Table 2-8:** Rate of photocatalytic decoloration of MB over doped anatase.

Catalyst	BET (m <sup>2</sup> /g)	Surface area normalized rate x 10 <sup>-8</sup> mol. l <sup>-1</sup> . s <sup>-1</sup> .m <sup>-2</sup>
anatase neat	112	0.98
anataseN400	113	1.35
anataseN500	116	1.53
anataseN600	89	0.94

From these results, the activity of the photocatalytic decomposition over neat and doped anatase was as follows: anataseN500 > anataseN400 > anatase neat > anataseN600. The surface area normalized rates for neat and doped anatase is given in the following table:

**Table 2-9:** Normalized rates for photocatalytic decoloration of MB over doped anatase.

Catalyst	Rate of decoloration x 10 <sup>-8</sup> ± 0.11 mol. l <sup>-1</sup> . s <sup>-1</sup>
anatase neat	1.10
anataseN400	1.52
anataseN500	1.77
anataseN600	0.84
Light only	0.53

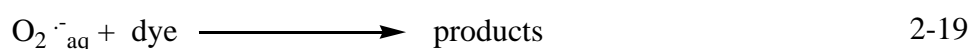
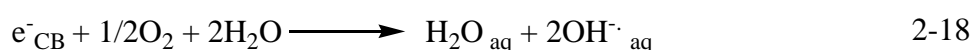
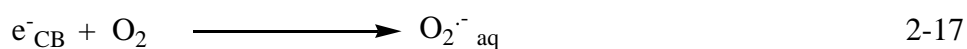
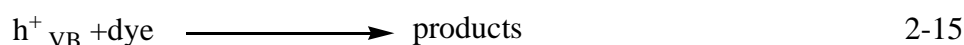
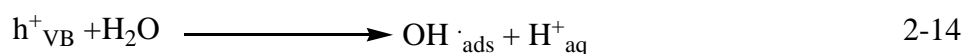
The photobleaching of MB sensitized by TiO<sub>2</sub> in aqueous solutions was studied by many researchers<sup>(92-94)</sup>. The vast majority of these studies which involve MB as a reactant with the presence of titania as a sensitized photocatalyst fall mainly into two categories<sup>(78,79)</sup>. In the first category, for reactions performed under anaerobic conditions, MB is reduced to colourless form of MB, which is called the leuco form (LMB). This reaction is a reversible process and upon addition of oxygen into the anaerobic system, LMB is oxidized back to MB. The second category involves mineralization of MB into inorganic species and this reaction occurs in aerobic conditions and it is irreversible<sup>(96-98)</sup>.

From the above results of the photocatalytic decomposition of MB over neat and doped

anatase, rutile and P25, it can be seen that there was a notable enhancement in the photocatalytic activity for the doped samples at 400 °C and 500 °C. Generally, the activity for the photocatalytic reaction for anatase and rutile fall in the order: titaniaN500> titaniaN400> titania neat> titaniaN600, while for P25, the activity falls in the order: P25N500> P25N400> P25N600> P25 neat. The improvement in photocatalytic activity for these samples probably arises from the increase in the absorption intensity in the near UV region and in the visible region with the increase in nitrogen content. Additionally, these samples have a higher surface area with smaller particle size, producing a higher photocatalytic activity<sup>(83)</sup>. Generally, doped nitrogen atoms induce local states close to the valence band (N 2p), while oxygen vacancies induce local states below the conduction band. These local states can enhance light harvesting for the catalyst in both the near UV and visible region of the spectrum. As mentioned earlier, oxygen vacancies induced by doping TiO<sub>2</sub> can act as colour centres. The electrons that leave oxygen vacancies may interact with the adjacent Ti<sup>IV</sup> to generate Ti<sup>III</sup> as colour centres. The presence of these colour centres in lattice of titania can increase the absorption of the visible light for the N doped titania. However, improvement in the photocatalytic activity for samples that were doped at 400 °C and 500 °C may be due to excitation that occurs from N2p local states above the valence band of the doped titania<sup>(99)</sup>. In addition to this, doping samples using NH<sub>3</sub> gas may lead to decomposition into H<sub>2</sub> and N<sub>2</sub> gas, with the possibility of causing reduction of Ti<sup>IV</sup> to Ti<sup>III</sup>. Ti<sup>III</sup> may contribute in the enhancement of the photocatalytic activity for these samples<sup>(100)</sup>. In contrast to the above results, anataseN600 and rutileN600 samples showed a lower activity in comparison with undoped parent. These samples with higher nitrogen content have a greyish green colour and the high nitrogen content in this case may assist in formation of recombination centres close to the valence band of the catalyst. These recombination centres can increase rate of the recombination reaction, which leads to reduction of photocatalytic activity of the material<sup>(84)</sup>. Additionally, these samples have a relatively smaller specific surface area with relatively larger particle size in comparison with their undoped parents. These two factors also have a negative effect on the photocatalytic activity of the photocatalyst. For the neat samples of titania, the best photocatalytic activity was observed with P25, while rutile showed a lower activity. This probably due to higher photocatalytic activity that arises from mixed phases titania (P25) in comparison with the pure phase.

### 2-7-5 Proposed mechanism for the photocatalytic decomposition of MB over titania

Dyes are a source of environmental pollution<sup>(99)</sup>. These compounds are used widely in modern industry as dyeing materials or as reagents in many chemical industries, especially in the textile industry. The problem with dyes is that most of them to some extent are toxic<sup>(99, 100)</sup>. MB is considered as a good model as test reaction for the modification of the photocatalysts. Upon excitation conduction, band electrons and valence band holes are produced. As a result of the presence of oxygen in the reaction solution, electrons can be trapped by O<sub>2</sub>, while the holes can oxidize the adsorbed dye MB on the surface. In addition, electrons and holes may react with H<sub>2</sub>O and oxygen in the solution, producing some active species such as OH<sup>·</sup> and O<sub>2</sub><sup>·-</sup>. These species can also participate in decomposition of dye molecules as follows<sup>(101,102)</sup>:



The expected products of decomposition of MB are carbon dioxide, ammonium ions and nitrate ions, which are not serious environmental pollutants. In this manner, photocatalysis can be used in environmental clean-up. It has been reported that<sup>(97, 98)</sup>, if photocatalytic decomposition of MB was carried out in anaerobic conditions colourless leuco form (LMB) is produced. This can be reoxidized in the presence of oxygen to MB in a reversible process. Complete mineralization to inorganic species can occur in aerobic conditions in an irreversible process<sup>(97, 98)</sup>. However, in our work, decomposition of MB was undertaken in air atmosphere and the blue colouration was not re-established upon standing. Hence, it is suggested MB decomposition proceeded according to the second mechanism as was confirmed by subjecting the resultant reaction mixture in air overnight. Generally, from the results that obtained for photocatalytic decoloration of MB over neat and doped titania, samples doped at 400 and 500 °C showed enhancement in photoactivity of doped titania. In opposite to that samples that doped at 600°C showed a negative photoactivity in comparison with neat titania samples. The next study involves investigation photoactivity of nitrogen doped titanic in terms of photocatalytic polymerization of MMA in comparison with use neat titanic samples.

## 2-8 Photocatalytic polymerization over neat anatase

Excitation of titania particles by absorption of light of a suitable energy ( $h\nu \geq E_g$ ) leads to production of conduction band electrons and valence band holes, which can be used for photocatalytic polymerization when reactions with monomer molecules occur<sup>(103)</sup>. Radical species due to reaction of monomer molecules with  $h^+_{VB}$  yields primary radicals which participate in polymerization reactions<sup>(104)</sup>. To investigate photocatalytic polymerization over neat anatase a series of experiments were undertaken at different reaction conditions using methyl methacrylate (MMA) and styrene (ST) as monomers in an aqueous suspension of titania under irradiation with UV light from a middle pressure mercury lamp (125 Watt). Different parameters were investigated.

### 2-8-1 Characterisation of the polymer

Polymer formation was characterized by using FTIR spectroscopy, NMR spectroscopy, GPC, SEM and TGA analysis for the bound and extracted polymer.

#### 2-8-1-1 FTIR spectra

The FTIR spectra for PMMA extracted and PMMA grafted anatase are shown in the following figures:

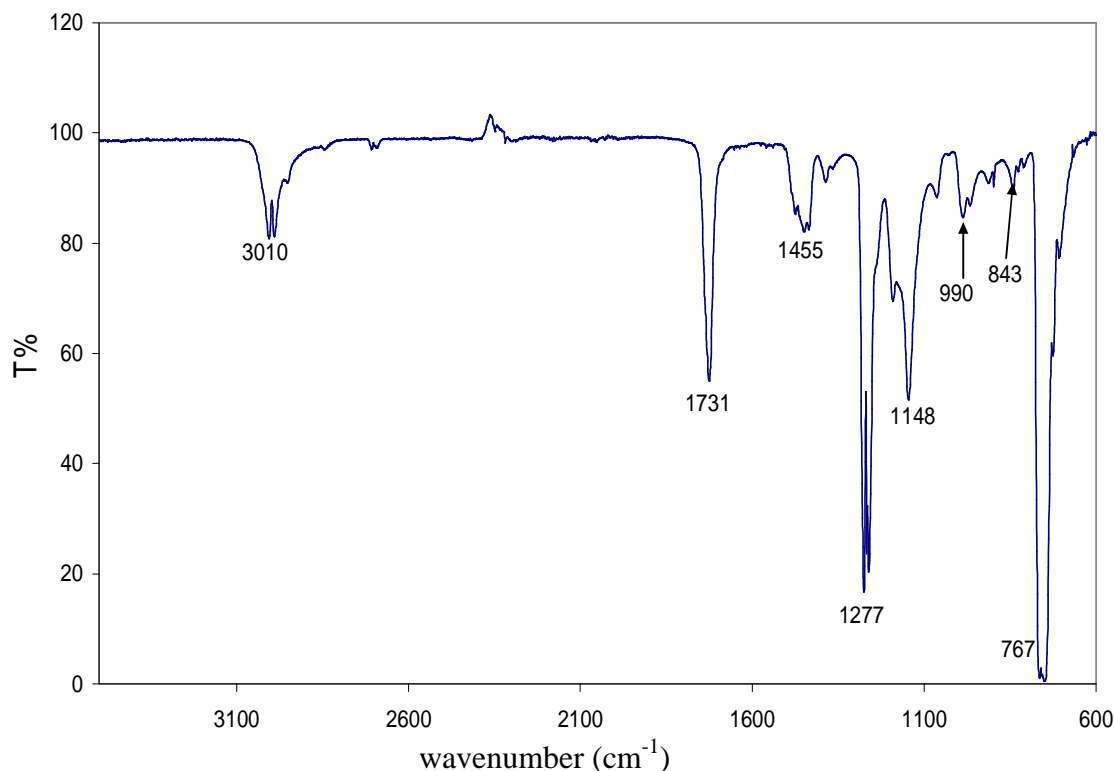


**Figure 2-21:** FTIR spectrum for the extracted PMMA.

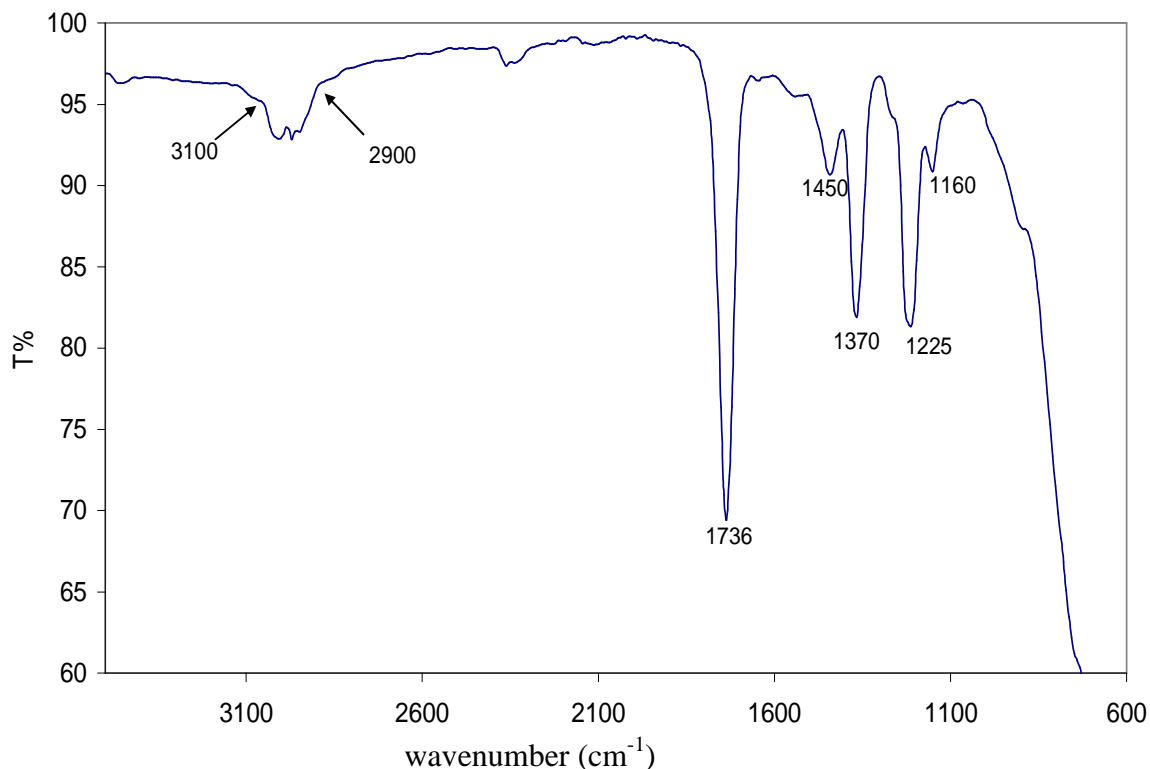


**Figure 2-22:** FTIR for composite PMMA grafted anatase.

Both extracted and grafted PMMA on the anatase show a characteristic sharp band at 1730-1736  $\text{cm}^{-1}$ . This sharp peak indicates the presence of the grafted PMMA on the anatase and the formation of the PMMA/anatase composite. For the extracted PMMA, the broad band around 3010  $\text{cm}^{-1}$  is related to free  $\text{CH}_3$  vibrations in the PMMA. The band at 1000-1460  $\text{cm}^{-1}$  can be assigned to the C-O-C stretching mode of ester bond in PMMA. The other bands at 750-950  $\text{cm}^{-1}$  are due to the bending of C-H bonds<sup>(104)</sup>. For PMMA grafted anatase, the broad band at 2900-3100  $\text{cm}^{-1}$  is due to the stretching vibrations of –OH groups on the titania surface. In addition, the FTIR spectrum of PMMA grafted anatase shows another characteristic peaks at 1450, 1370, 1225 and 1160  $\text{cm}^{-1}$ . These are assigned to the C–H,  $-\text{CH}_2$  and C-O-C band of PMMA. It seems that the  $\text{CH}_3$  vibration mode for PMMA grafted anatase at 3000-3100  $\text{cm}^{-1}$  overlaps with the stretching vibration of OH group<sup>(101)</sup>. Generally, this type of polymerization requires adsorption of monomer molecules on the surface of solid catalyst and then the solid particles are excited by absorption radiation energy.

### 2-8-1-2 $^1\text{H}$ NMR spectroscopy

Further investigation for the extracted polymer from composite materials of PMMA/anatase was undertaken by measuring  $^1\text{H}$  NMR spectra for MMA and extracted PMMA as shown in the following figures:

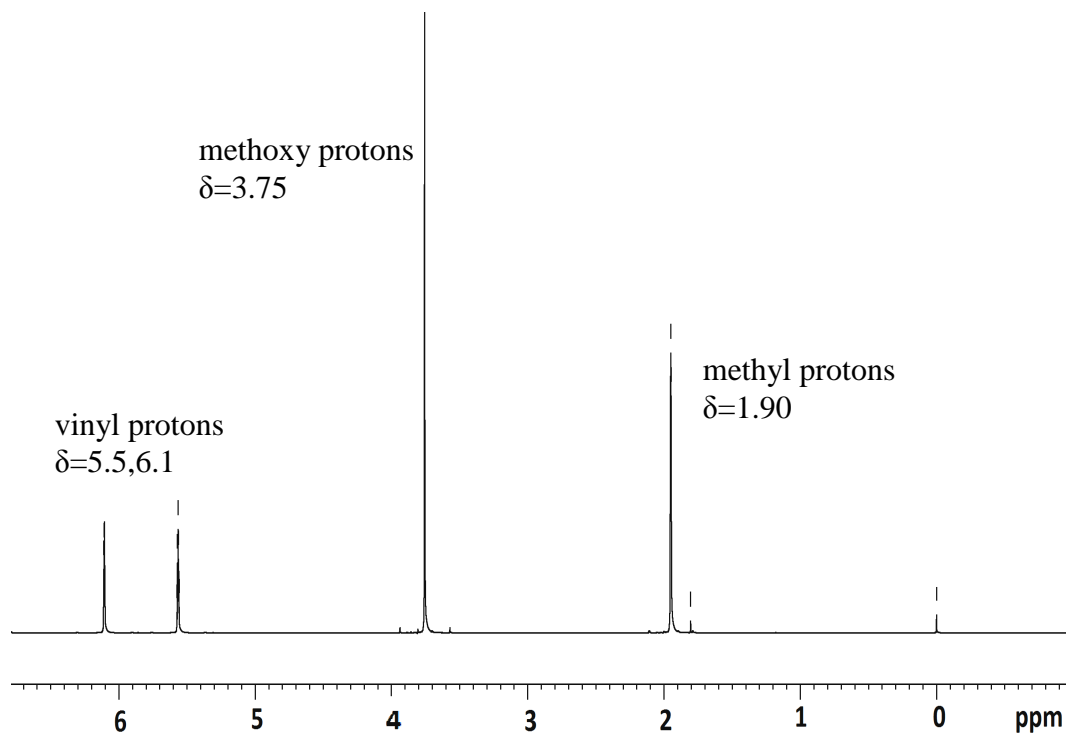


**Figure 2-23:**  $^1\text{H}$  NMR spectrum for MMA in  $\text{CDCl}_3$ .

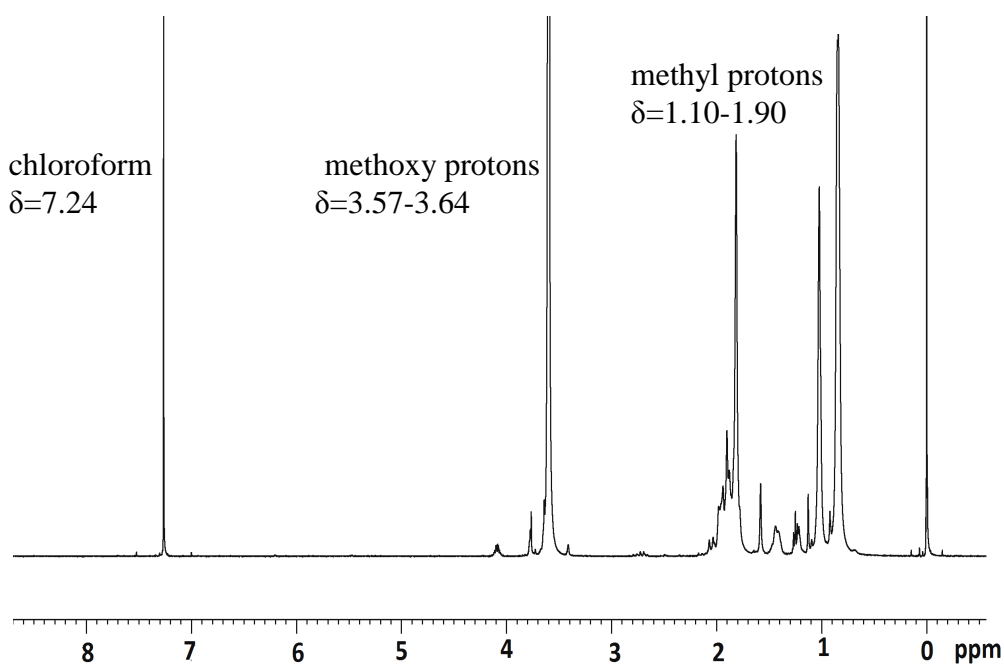


**Figure 2-24:**  $^1\text{H}$  NMR spectrum for the extracted PMMA in  $\text{CDCl}_3$ . This type of polymer was extracted from titania using THF, and then it was precipitated with excess of methanol

The most interesting thing in these spectra is that the peaks at  $\delta = 5.5$ , and  $6.0$  which are assigned to the  $(\text{H}_2\text{C}=\text{C}-\text{CH}_3)-$  in MMA (Figure 2-23) are completely absent in extracted PMMA as shown in Figure 2-24. The main features of  $^1\text{H}$  NMR spectrum for the extracted PMMA, is the presence of a peak which corresponds to the methoxy protons at

$\delta = 3.57\text{-}3.64$  <sup>(105)</sup>. It is observed that, the extracted PMMA was similar to PMMA that is synthesized by normal chemical polymerization.

### 2-8-1-3 Scanning electron microscopy (SEM)

Morphological studies for each of neat anatase, grafted with PMMA, extracted PMMA have been undertaken using Scanning Electron Microscopy (SEM), and the resultant micrographs are shown in the following figure:

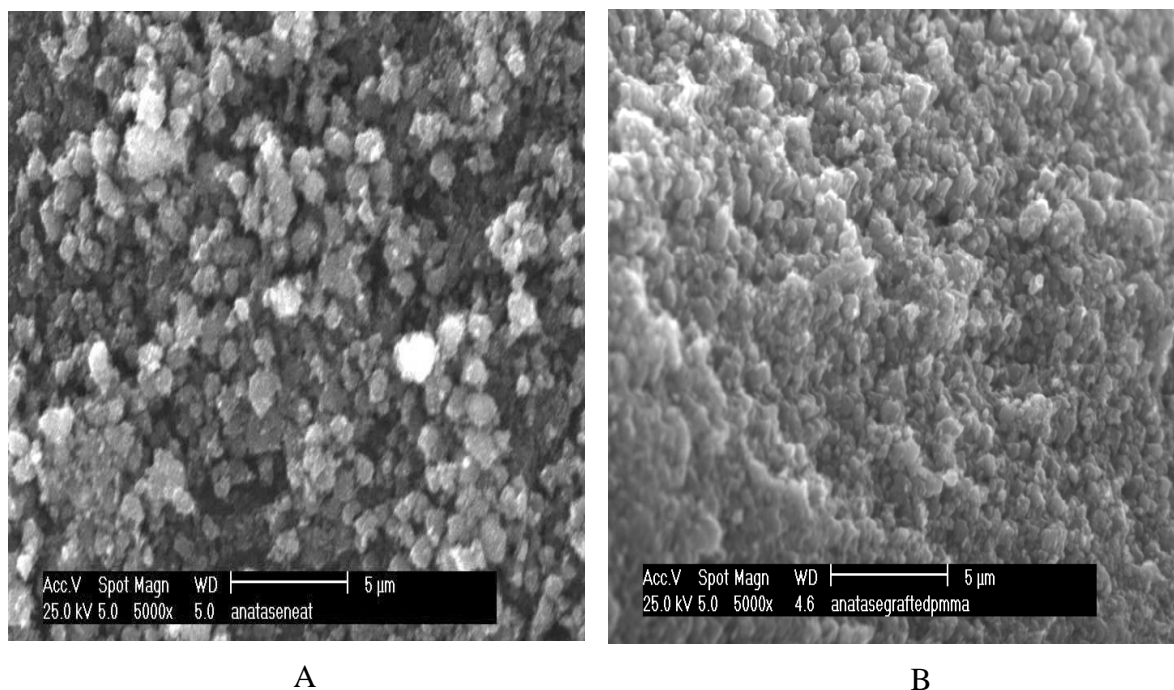


**Figure 2-25:** SEM images for (A) neat anatase and (B) grafted anatase with PMMA.

From these figures, the change in the morphology of the surface after grafting with the polymer can be seen. PMMA grafted anatase exhibited high dispersion on the surface and anatase nanoparticles are aggregated severely after grafting with PMMA. That may result from a high surface energy when PMMA was grafted on the surface <sup>(102)</sup>.

### 2-8-1-4 Thermal gravimetric analysis (TGA)

The grafted polymer was further investigated by thermal gravimetric analysis TGA that was performed under both air and nitrogen atmospheres and the identical data was obtained for the different atmospheres. From this data, there is an evidence for the formation of the grafted polymer on anatase due to the characteristic mass loss about 12% in the 300- 500 °C temperature range. The most important point here is that polymer-grafted anatase begins to decompose at different temperature than that for the traditional

PMMA (extracted polymer). This is interpreted as resulting from the interaction between polymer chains and anatase nanoparticles<sup>(106)</sup>. This interaction occurs between  $Ti^{4+}$  and TiOH surface species with electron donating atoms in PMMA (oxygen atoms). TGA for the composite anatase/PMMA in air is shown in the following figure:

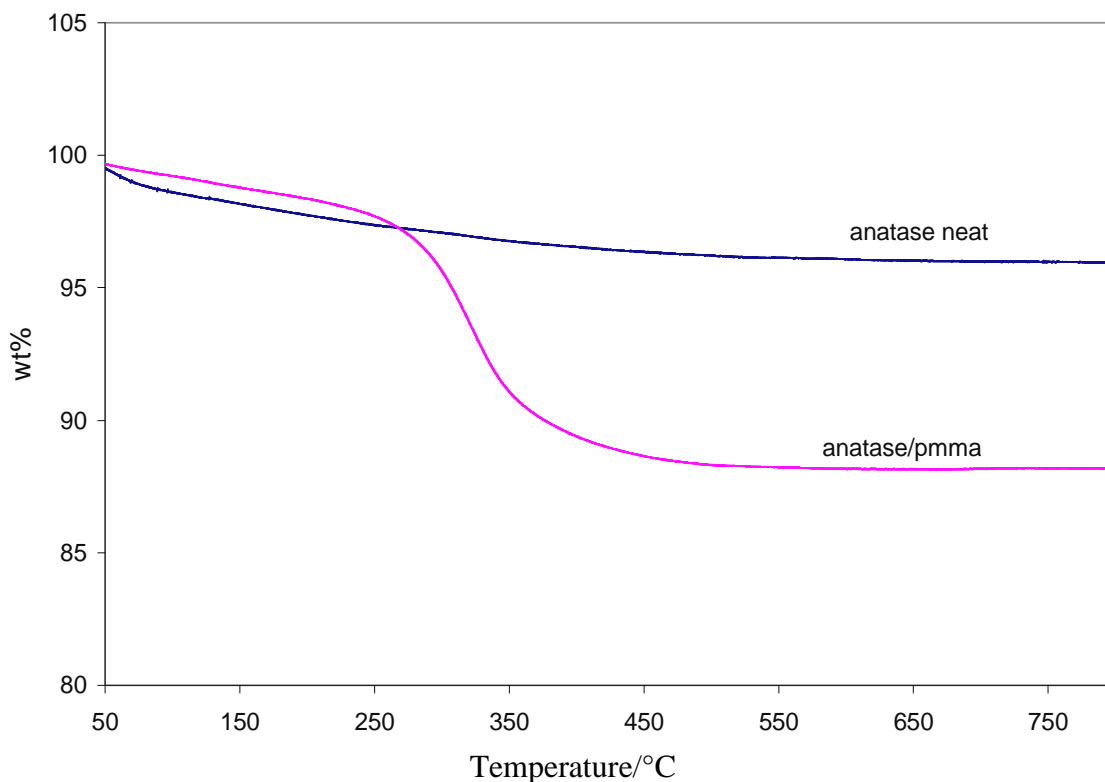


**Figure 2-26:** TGA for neat and grafted anatase with PMMA in air. From TGA result, the conversion percentage of grafting 13.6%.

#### 2-8-1-5 X-ray diffraction patterns (XRD)

In order to investigate the effect of grafting of the polymer on the crystalline structure of anatase, X-ray powder diffraction studies of anatase before and after grafting was carried out and the results are presented in the following figures:

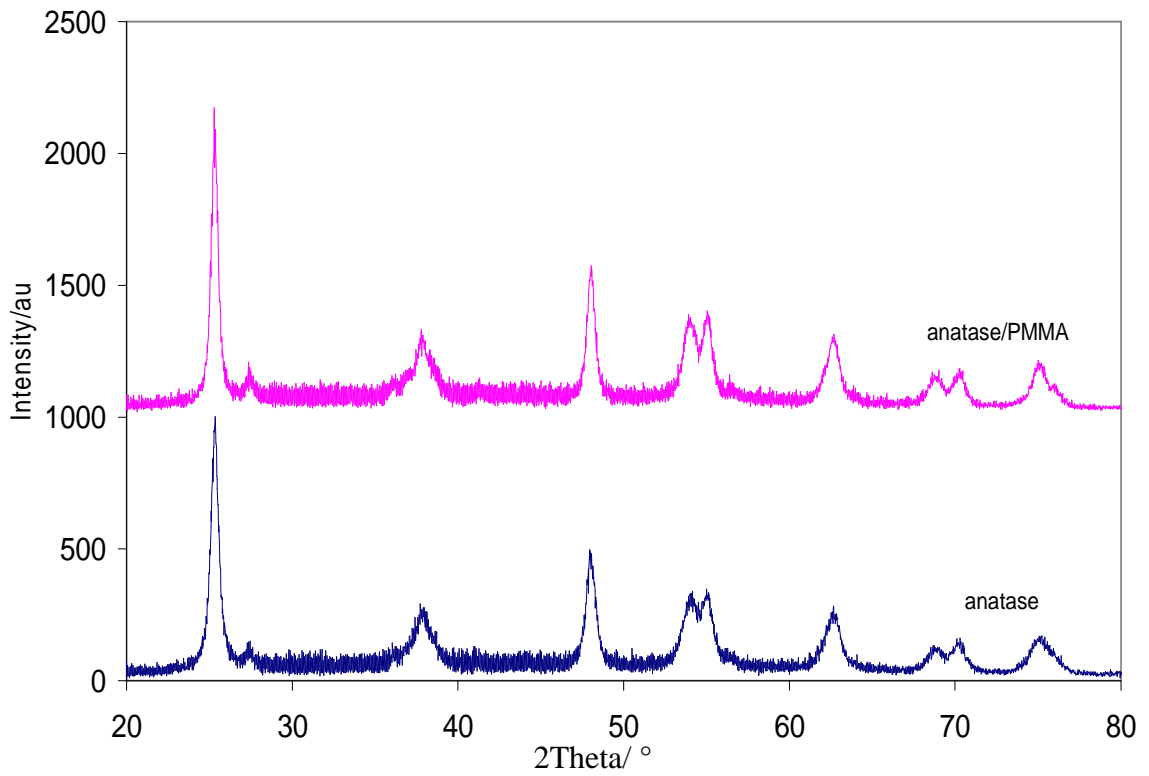


**Figure 2-27:** XRD patterns for neat and grafted anatase with PMMA.

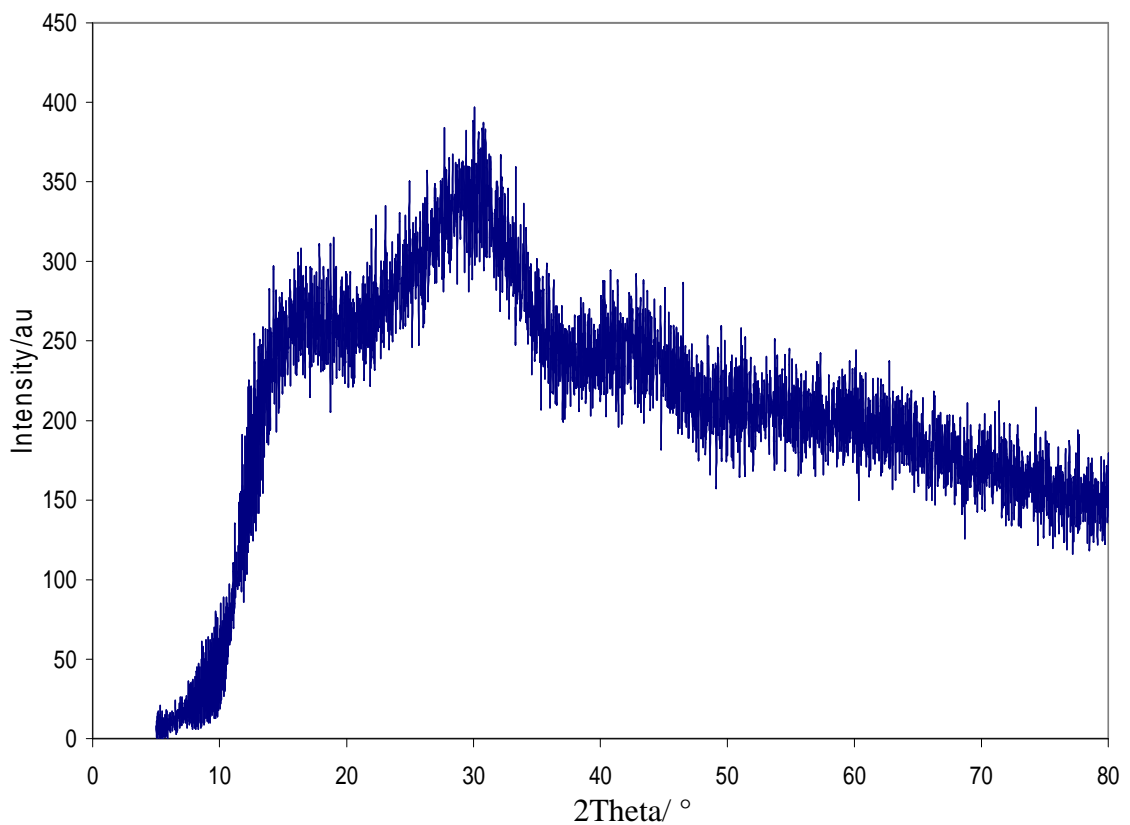


**Figure 2-28:** XRD pattern for the extracted PMMA.

From these patterns, it can be seen that the characteristic diffraction signals of the PMMA grafted anatase samples were almost the same as those of the neat anatase samples. This indicates that the grafting doesn't affect the crystalline structure of TiO<sub>2</sub> nanoparticles.

XRD patterns for the extracted PMMA shows diffuse features at lower values of  $2\theta$ . These patterns are typical of amorphous materials<sup>(107)</sup>. This probably arises from high steric effect of methoxy groups in PMMA. Methoxy groups in PMMA are not aligned sufficiently around the backbone of the polymer, which results in an amorphous structure for this material<sup>(107)</sup>.

### 2-8-2 Optimization weight of the TiO<sub>2</sub> used

In order to find the optimal weight of anatase photocatalyst, a series of experiments was performed using different masses of the catalyst with the reaction mixture containing 2 mL of purified MMA. Experiments were carried out at 20 °C in air with irradiation for two hours. These results were repeated three times in the range of 0.001 to 0.300 g, and the average of the results are plotted in Figure 2-29, the average error bar for the results was  $\pm 0.25\%$ . From these results, it was found that 0.15 g of TiO<sub>2</sub> is the optimum weight for this system.

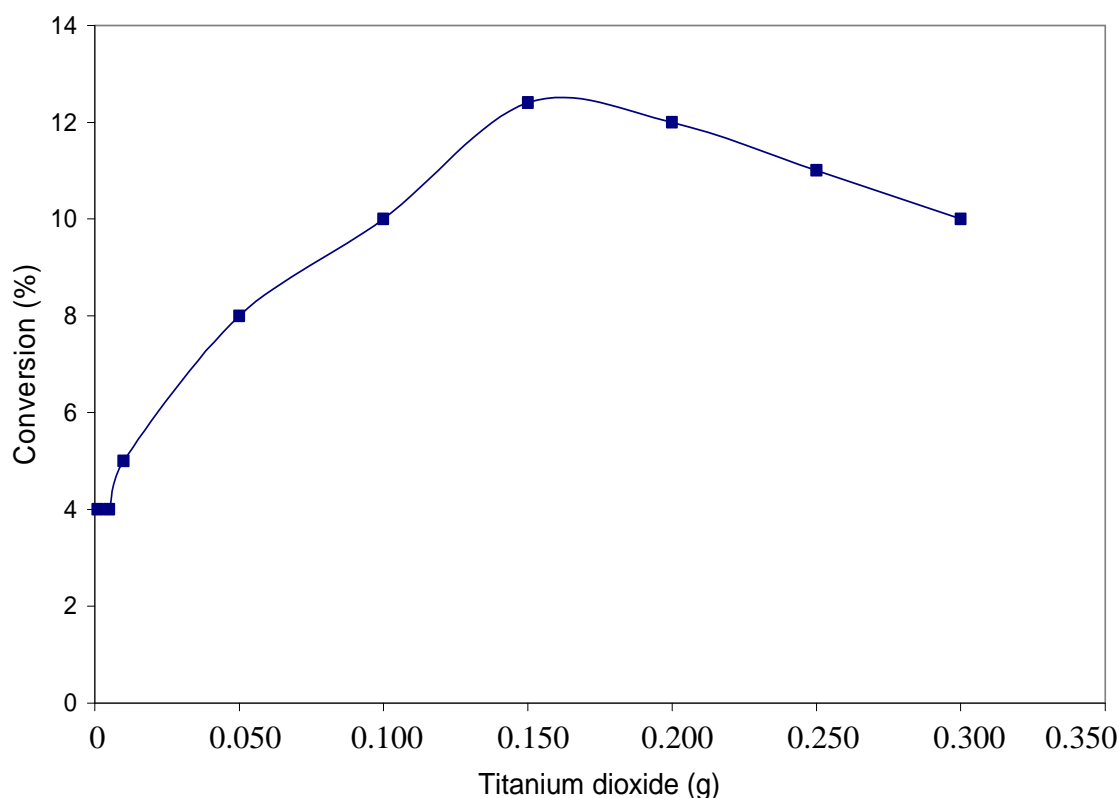


**Figure 2-29:** Optimization weight for the photocatalytic polymerization over TiO<sub>2</sub>, the average error bar for these results  $\pm 0.25\%$

The experiments of using different loading of titania have shown a considerable variation in product formation. Initially there was increase in conversion percentage with increase of used titania weight. After this weight, any increase in titania amount doesn't increase reaction rate significantly. After this step, using higher weight of titania results in

reduction rate of reaction. According to these results, there is an optimal weight of anatase, which should be used to give the best photocatalytic activity. In this system, the optimal weight is 150 mg/100 mL. Lower weights than this give a direct proportionality between weight and photocatalytic activity. Using higher weights leads to negative results in comparison with the optimum weight of titania. The explanation for this is that when using a low mass suspension of anatase the number of titania particles are few in comparison with the number of the incident photons that reach into the reaction mixture<sup>(108)</sup>. According to the second law of photochemistry, each atom or molecule absorbs one photon. So that, the absorbed photons will be few, this gives a direct proportionality between the used weight and photocatalytic activity. For more dense suspensions of anatase (more than 150 mg), the particles form an inner filter which absorbs a high proportion of the incident photons and scatters the other part of the light, leading to a reduced number of active photons for the reaction. Therefore, it is necessary to find a determined weight of titania which absorbs a high portion of the incident photons<sup>(108)</sup>.

### 2-8-3 Effect of exposure time

The effect of radiation exposure time was studied using 0.150 g of anatase suspended in 100 mL of distilled water containing 2 mL of purified MMA under air for various durations at 20 °C. The results were repeated twice for a period from 30 to 210 minutes. The average error bar was  $\pm 0.30\%$ , and the average results are shown in the following figure:

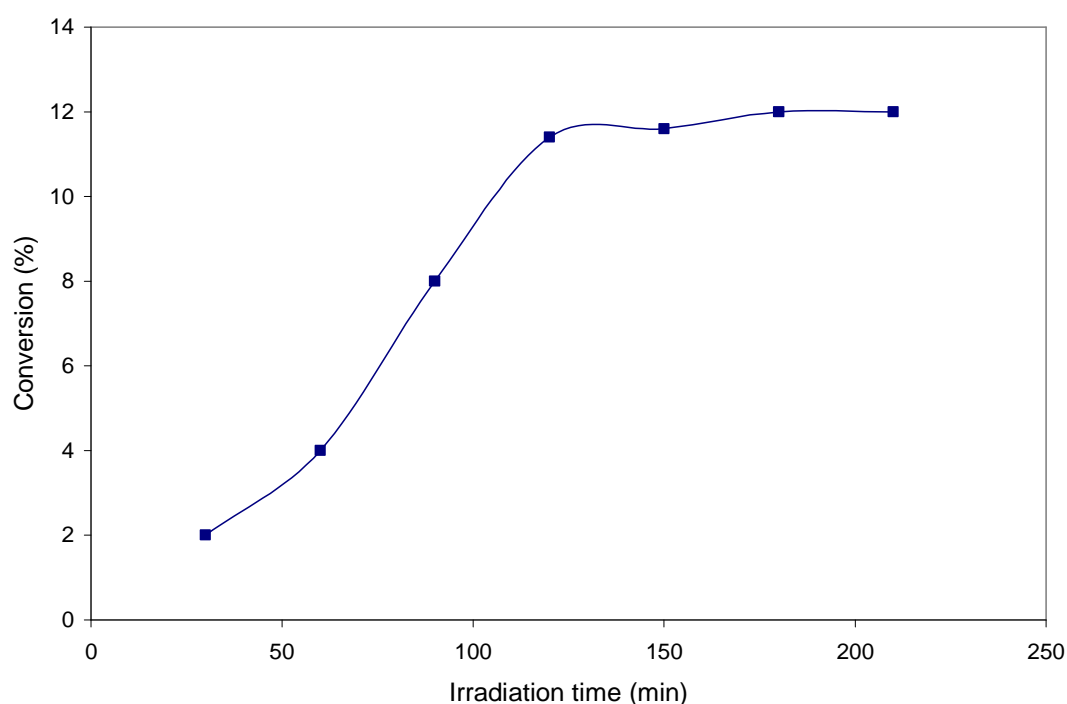


**Figure 2-30:** Effect of time exposure on the photocatalytic polymerization of MMA over TiO<sub>2</sub>.

From this study, it can be seen that there is progressive increase in conversion of monomer into polymer with the time of reaction and keeping other reaction conditions constant. The conversion percentage was increased from initial stage of polymerization until up to two hours of exposure. After this point, there was no significant increase in the conversion percentage. Initial increase in conversion with exposure time is probably due to formation more radicals that contribute to polymer formation. After higher exposure time (more than two hours), there was no significant increase in conversion with the time. That is may be due to termination of growing grafted chains with the newly formed primary radicals on the surface of titania.

#### 2-8-4 Effect of the amount of the used monomer

To investigate effect of the amount of the used monomer for this system, different amounts of MMA from 0.25 to 3.00 mL were used with 0.15 g of anatase in 100 mL of distilled water and irradiation under air for two hours at 20 °C. The average error bar was  $\pm 0.21\%$ , the results are shown in the following figure:

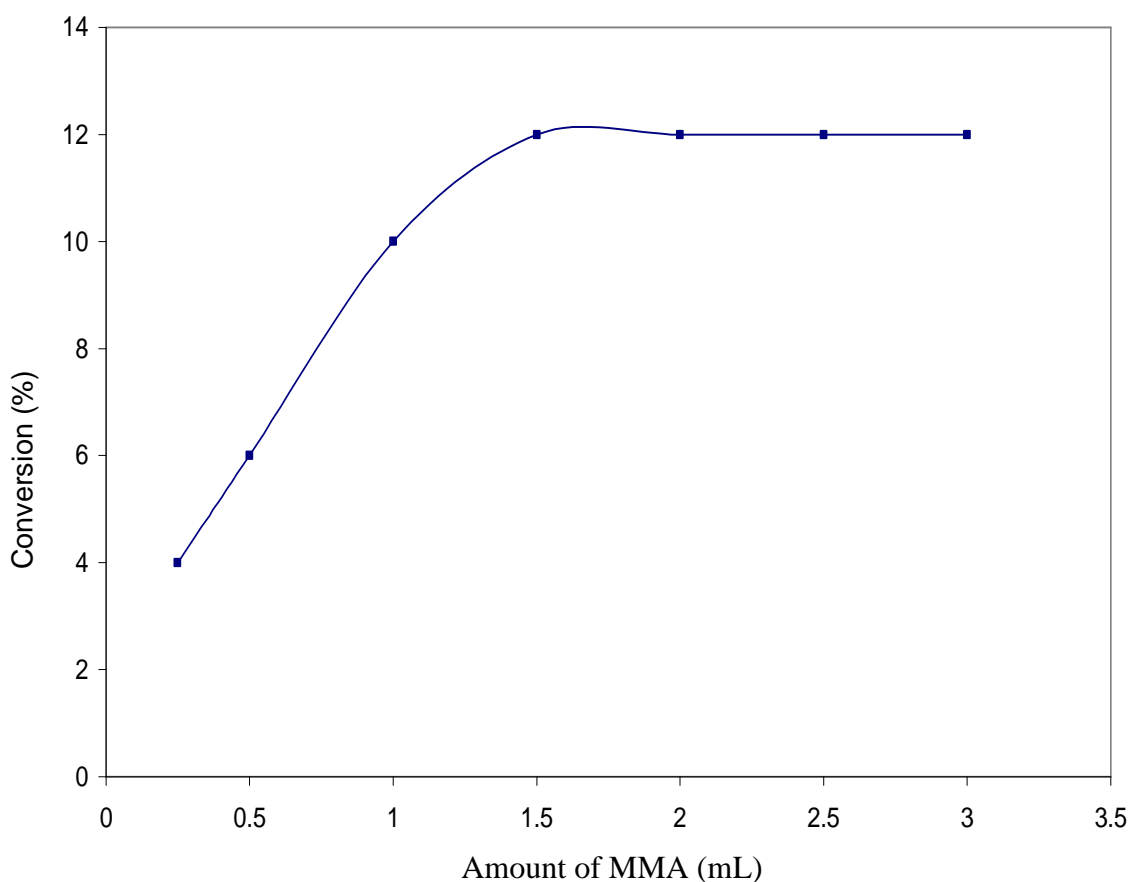


**Figure 2-31:** Effect of the amount of MMA on photocatalytic polymerization over TiO<sub>2</sub>.

When using small amounts of the used monomer initially, it is clear that the rate of reaction was progressively increased but beyond a certain point, conversion was constant. In this type of reaction, the rate of reaction doesn't depend mainly on the concentration of the reactants, but it depends on the surface of the catalyst. Initially, the small amount of MMA would adsorb on the surface and participate in the reaction progressively with the increase for MMA until a certain point. Beyond this point, any further increase amount of MMA becomes ineffective on the rate of reaction.

### 2-8-5 Effect of temperature on the reaction

The effect of the temperature on the photocatalytic polymerization was carried out by following the conversion of MMA into PMMA at different temperatures with all of the other parameters of the reaction being fixed at 2 mL MMA, 0.15 g of anatase with 100 mL of distilled water and irradiation for two hours in air. The results showed enhancement in the rate of reaction with increasing temperature. The error bar was  $\pm 0.42\%$ , These results are shown in the following figure:

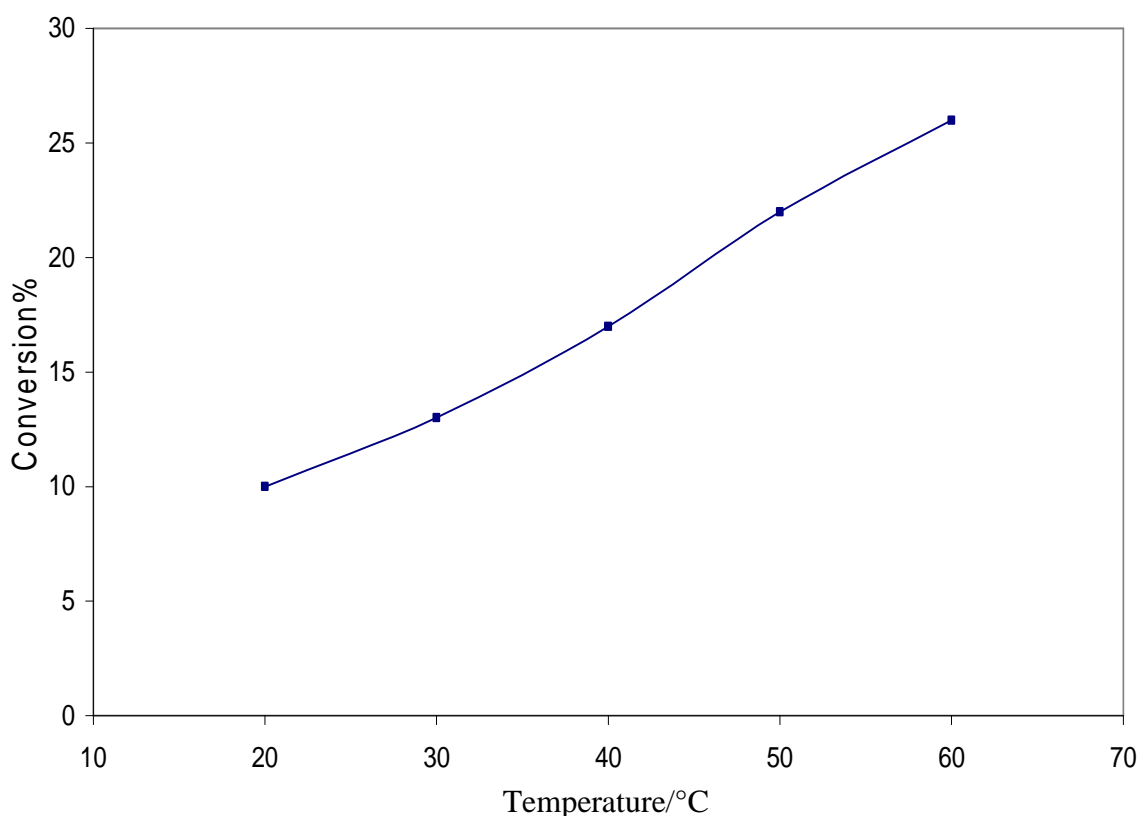


**Figure 2-32:** Effect of temperature on the photocatalytic polymerization.

From these results, it can be seen that, increase temperature of reaction in this range results in an increase of rate of reaction. This probably arises from effect of temperature on the adsorption and desorption processes on the surface. However, photoreactions are not very

sensitive toward minor changes in the temperature<sup>(109)</sup>. However, some reaction steps are potentially dependent on temperature such as adsorption and desorption. Generally, an increase in the rate of reaction with an increase of the temperature may be attributed to the effect of temperature on these steps on the TiO<sub>2</sub> surface<sup>(110)</sup>. These steps involve adsorption of monomer molecules on the surface of titania, then producing active radicals due to reaction of monomer molecules with electron/hole pair.

### 2-8-6 Activation energy for photocatalytic polymerization over titania

The activation energy for the photocatalytic polymerization reaction can be determined by applying the Arrhenius equation after measuring rate of the reaction at least three temperatures, and rate constant can then be calculated from the relation between rate of the reaction and initial concentration of MMA. Then by plotting 1/T on the x-axis and ln(k) on the y-axis, the gradient can be used to find the activation energy as shown in the following figure<sup>(111)</sup>:

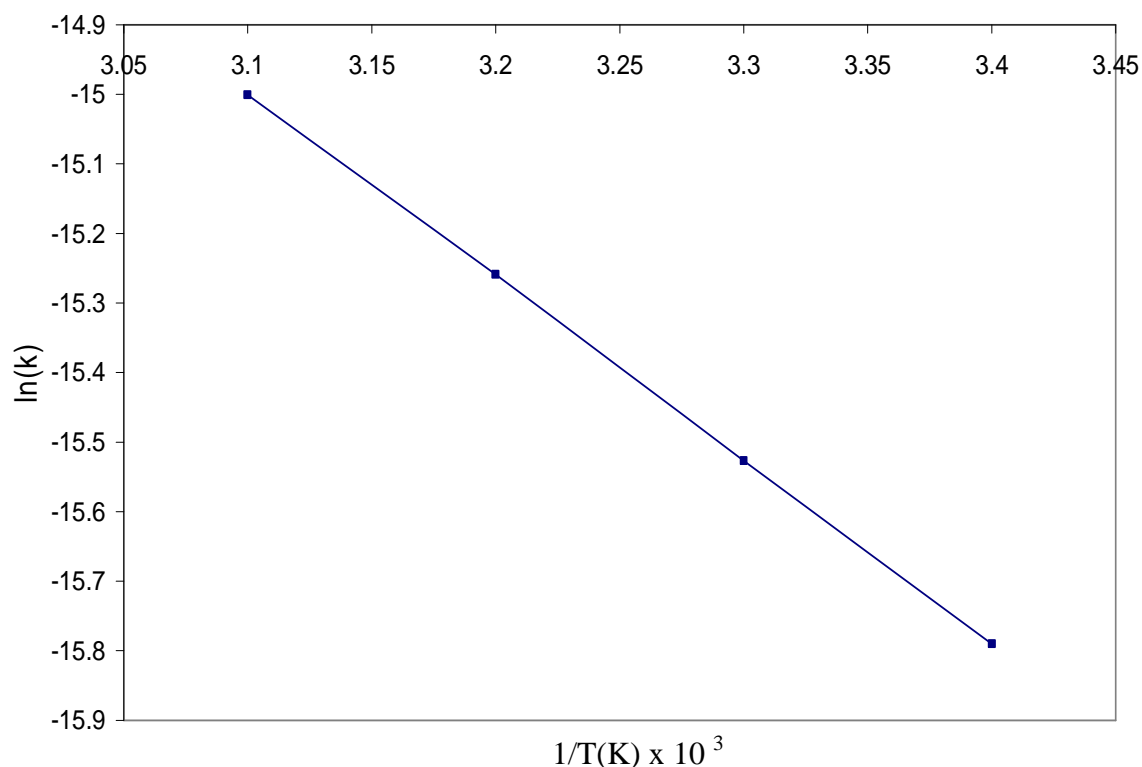


**Figure 2-33:** Arrhenius plot for the photocatalytic polymerization over anatase.

From plot, gradient = -2630 K<sup>-1</sup>

-E = gradient x R = -2630 x 8.31 = 21865.82 J mol<sup>-1</sup>

E = 21.87 kJ mol<sup>-1</sup>

Generally, photoreactions are not too sensitive towards minor variation in temperature. The steps that are potentially dependent on reaction temperature such as adsorption and

desorption are not the rate determining steps in this type of reaction. However, this value of activation energy is similar to that found in the other photocatalytic reactions over titania such as photocatalytic oxidation of alcohols over  $\text{TiO}_2$  <sup>(112,113)</sup>. However, this amount of activation energy is higher than that required to transfer electron from valence band to the conduction band (3.20 eV). This amount of activation energy is probably related to adsorption/desorption processes on the surface.

### 2-8-7 Effect of atmosphere on the polymerization reaction

The effect of air and inert atmosphere was studied by performing a series of experiments under a flow of nitrogen in comparison with air. In each experiment, 150 mg of anatase was suspended in 2 mL of purified MMA in 100 mL of distilled water. The mixture was stirred for 10 minutes prior to starting the reaction by irradiation with UV light at 20 °C with stirring for 150 minutes. The results of the polymerization under nitrogen showed a higher activity in comparison to the air. The average error bar was  $\pm 0.55\%$ . These results are shown in the following figure:

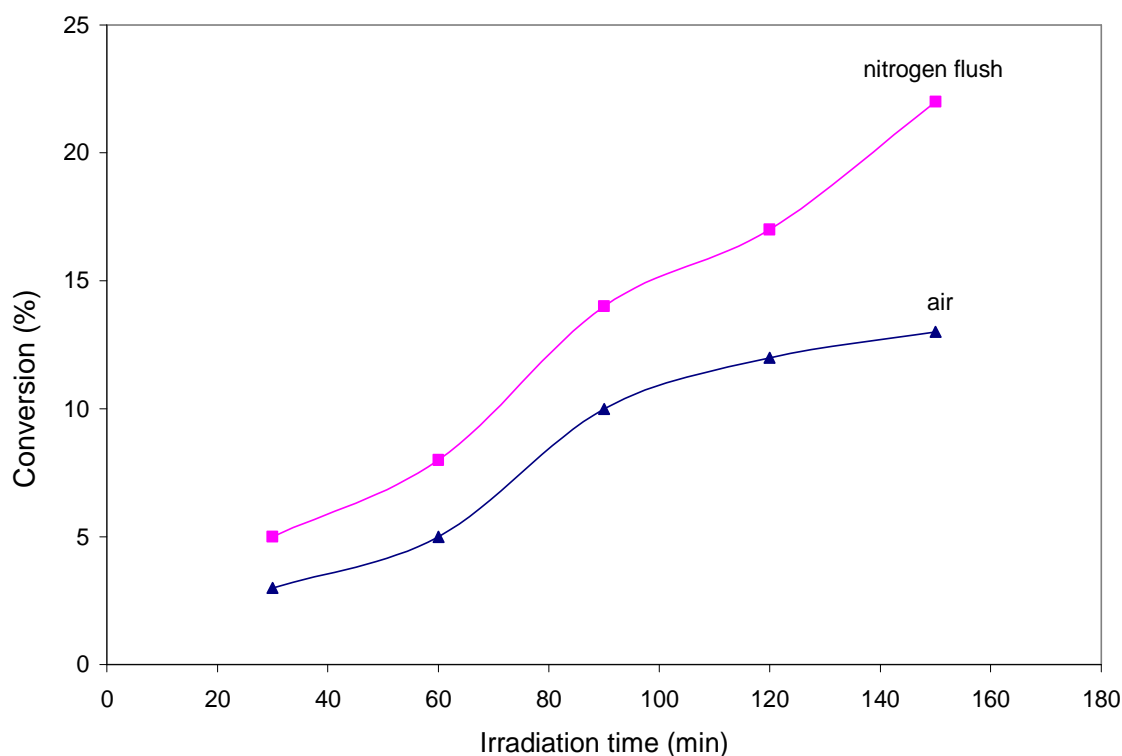
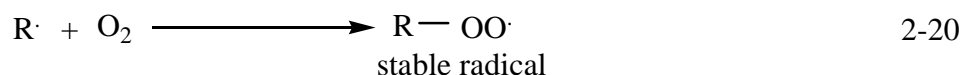


**Figure 2-34:** Effect of atmosphere on photocatalytic polymerization of MMA over anatase.

From these results, the rate of reaction under nitrogen can be seen to be higher than that under normal atmosphere, probably due to reaction of oxygen with the propagating radicals, this reaction may result in reduction the rate of propagating radicals <sup>(114)</sup>. In addition to that, this observation exhibits an important difference between this type of

polymerization and other types of chemical polymerization, which require inert atmosphere and are completely inhibited by normal atmosphere. Generally, oxygen inhibits free radical polymerization due to oxidation of the propagating radicals by oxygen, which leads to the production of more stable radicals such as peroxides. These species have a lower reactivity toward monomer molecules as follows <sup>(115-117)</sup>:



### 2-8-8 Effect of the monomer type on the photocatalytic polymerization over anatase

The effect of the monomer used on the rate of photocatalytic reaction was investigated by comparing MMA and ST as two monomers. The polymerization of both was carried out under the same conditions at 20 °C. In each experiment, 2 mL of each monomer was suspended with 150 mg of anatase in 100 mL of distilled water. The mixture was then stirred under air for 150 minute. The average of the error bar was  $\pm 0.32\%$ , the results are shown in the following figure:

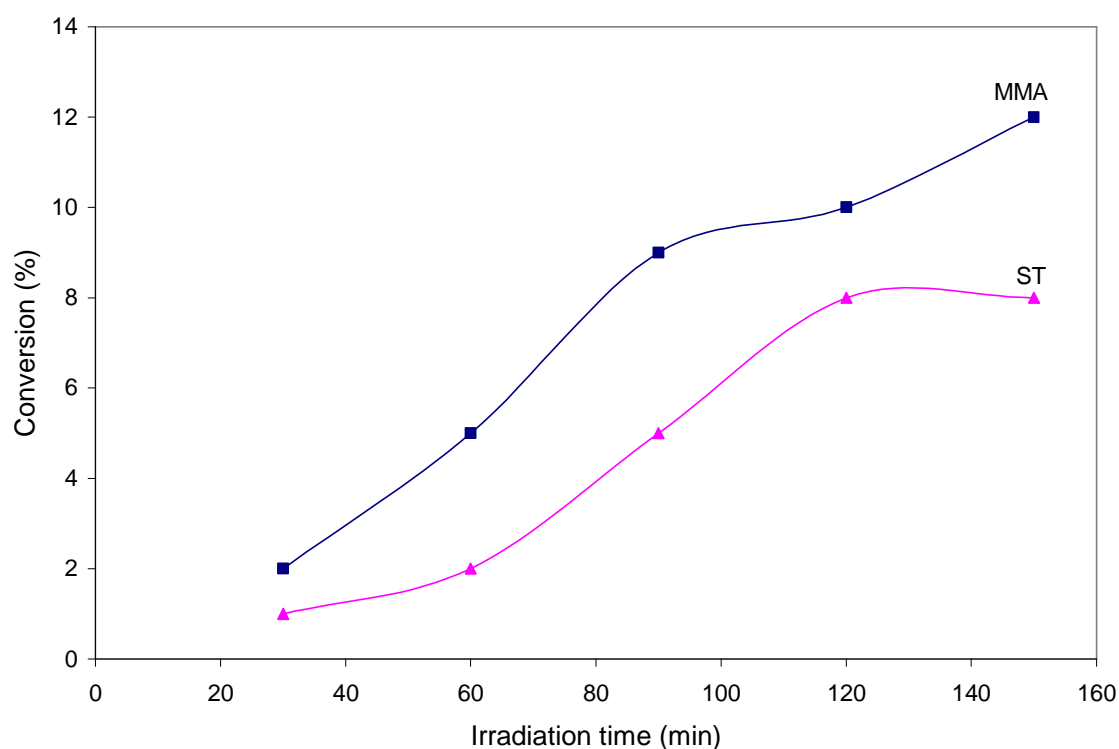


**Figure 2-35:** Photocatalytic polymerization of MMA and ST over anatase.

From these results, the rate of polymerization when using MMA is a little higher than that for ST under the same conditions of the reaction. This type of polymerization is free radical polymerization. Radical species which are produced during the initiation and propagation steps in case of ST monomer are more stable than those for MMA<sup>(118)</sup>. That is

probably due relative stability of propagating radicals in case of styrene as these radicals are relatively stabilized by resonance <sup>(118)</sup>, while in case of MMA the radical is more active.

### 2-8-9 Effect using Et<sub>3</sub>N on the photocatalytic polymerization

To investigate effect of addition of an electron donor on the photocatalytic polymerization of MMA, 2mL of MMA was suspended with 0.15 g of anatase with mixing and irradiation for two hours at 20 °C under normal atmosphere with using various amounts of triethylamine additive (Et<sub>3</sub>N). The average error bar was ± 0.34%, and these results are shown in the following figure:

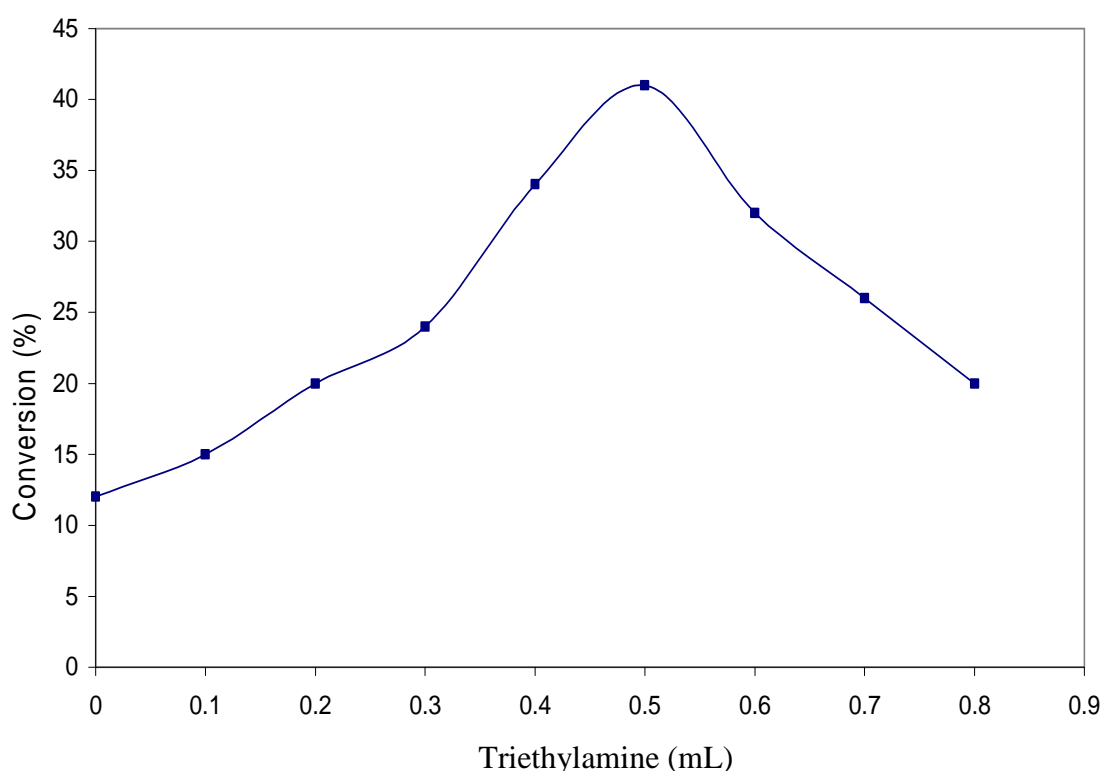


**Figure 2-36:** Effect of using Et<sub>3</sub>N on the photocatalytic polymerization.

From these results, a maximum conversion of around 41% was obtained using 0.5 mL of Et<sub>3</sub>N. This result is probably due to facile formation of the radicals on the surface of anatase with the presence of Et<sub>3</sub>N. Beyond this volume of Et<sub>3</sub>N the conversion was reduced. That is expected as polymerization in this case becomes controlled by initiation with Et<sub>3</sub>N mainly. Initiation with Et<sub>3</sub>N would be expected to be less effective in photocatalytic polymerization <sup>(119)</sup>.

The number averaged molecular weights ( $M_n$ ) for the extracted PMMA when use anatase and anatase/ Et<sub>3</sub>N were 62,000 and 35,000 respectively. From these results, using anatase alone affords a higher molecular weight, while using anatase/ Et<sub>3</sub>N gives lower molecular

weight and higher conversion percentage. These observations are probably due to the relation between rate of polymerization and the viscosity of polymerization mixture <sup>(120)</sup>. High viscosity would give low rate of polymerization (low conversion percentage), while low viscosity would give high rate of polymerization (high conversion percentage). At high viscosities, the chain growth propagation reactions and chain termination reactions become diffusion controlled <sup>(120)</sup>.

### 2-8-10 Effect of exposure time on grafting

Progressive increase in reaction time can lead to increase the rate of polymerization reaction on the surface. This increases the rate of propagating chains, which yield a high percentage of grafted polymer with the time. The effect of exposure radiation time on the grafting can be calculated by the equation:

$$\text{Grafting (\%)} = \frac{\text{weight of grafted catalyst} - \text{weight of original catalyst}}{\text{weight of original catalyst}} \times 100\%$$

For each case, 0.15 g of anatase was suspended in 100 mL of distilled water with 2 mL of the monomer in air at 20 °C. The mixture was stirred for ten minutes prior to start reaction by irradiation with UV light for different reaction periods. The average error bar was  $\pm 0.26\%$ , the results are shown in the following figure:

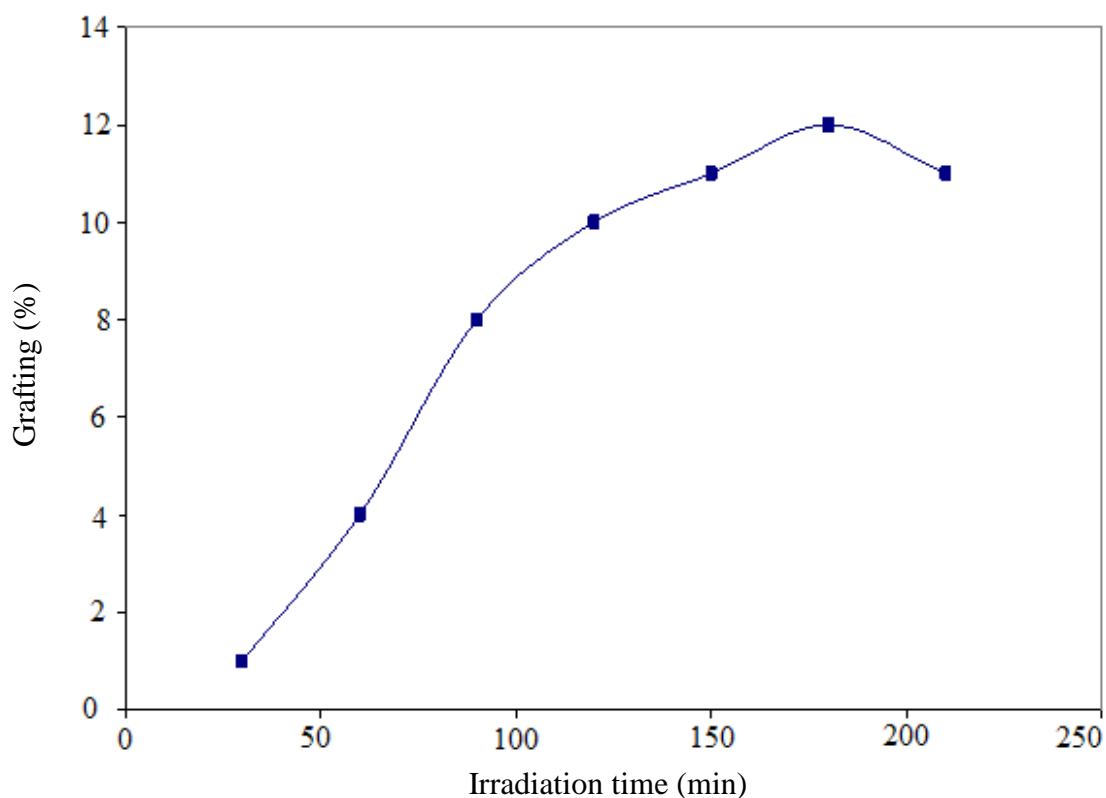


**Figure 2-37:** Effect of exposure time on the grafting PMMA over anatase.

From the above results, it can be seen that there is an increase in grafting with reaction time up to a certain level time. This is probably due to formation of more active propagating radicals on the surface of anatase. These active radicals then contribute in formation of grafted polymer on the surface. The limitation of grafting at a certain limit is due to increase termination process at high concentration of these radicals and then termination of growing grafted chains by excess primary radicals that are formed in the reaction mixture with increase in the reaction time <sup>(121)</sup>.

### 2-8-11-Effect of the amount anatase on grafting

To study the effect of the amount of the used titania on the grafting percentage, different amount of anatase were used under the same reaction conditions. For each case, the grafting percentage was calculated. In each experiment, a required amount of anatase was suspended with 2 mL of purified MMA in 100 mL of distilled water. The mixture was stirred for ten minutes prior to initiating the reaction by irradiation from the lamp. The reaction mixture then was stirred at 20 °C under air for two hours. The average error bar was  $\pm 0.22\%$ , the results are shown in the following figure:

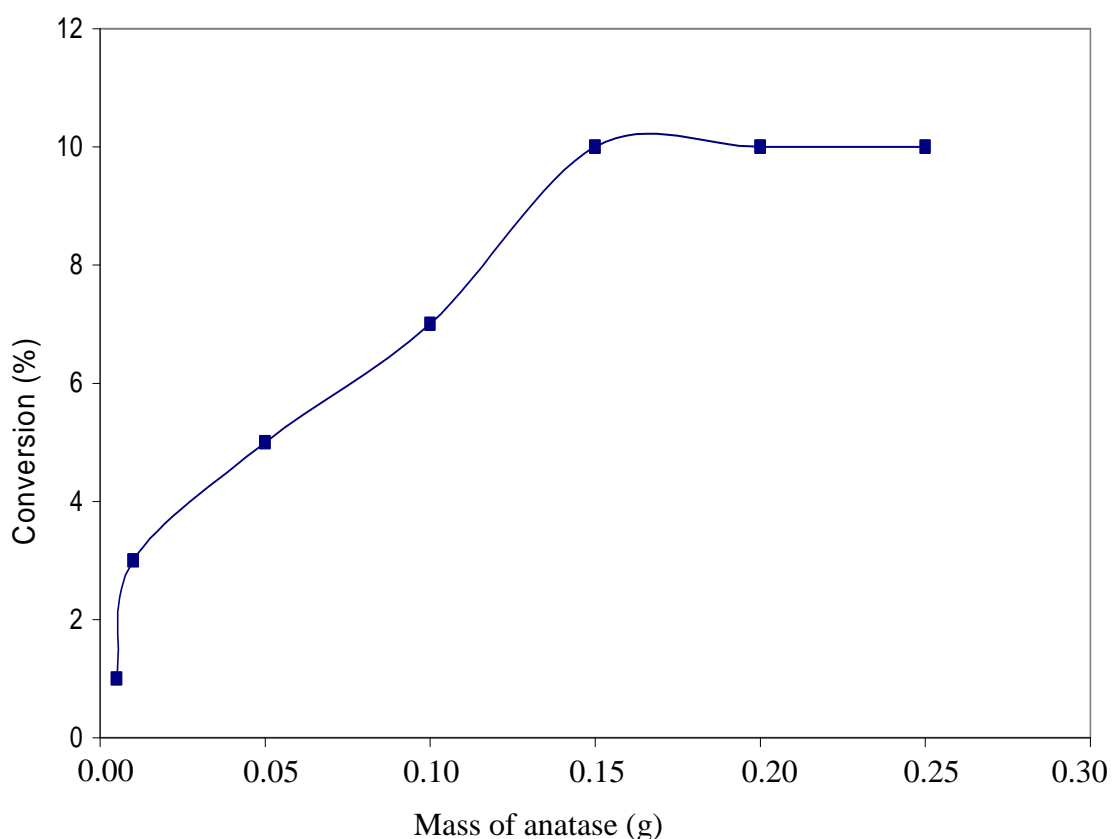


**Figure 2-38:** Effect of the amount of anatase on the grafting PMMA.

From the above results, it can be seen that, initially there was an increase in conversion percentage of monomer to polymer with increasing amount of the anatase used. This proportionality continues until a certain concentration of the used catalyst of about 150 mg. After this no further increase in conversion percentage occurred, probably due to formation inner filter in dense solution. This filter absorbs high portion of incident photons and prevents the other photons to reach other anatase particles. This produces a negative effect for the reaction at high concentrations of the catalyst used. On the other hand, applying high concentrations of catalyst could produce a high concentration of radicals that could terminate growing grafted chains <sup>(108)</sup>.

### 2-8-12 Photocatalytic decoloration of MB over PMMA grafted anatase

The photocatalytic activity of the parent and PMMA grafted anatase was investigated photocatalytic decoloration of methylene blue. Photocatalytic activity was determined by measuring the loss of absorbance of a  $2.5 \times 10^{-5} \text{ mol dm}^{-3}$  aqueous solution of methylene blue. Reactions were performed by stirring a suspension of 0.01 g of material in 100 mL of MB solution and the samples were stirred in the dye solution at 20 °C for 10 minutes prior to the start of irradiation. Then reaction vessel was illuminated and periodic sampling was performed to determine the conversion of methylene blue (measured as the change in absorbance at 655 nm). These results are shown in the following figure:

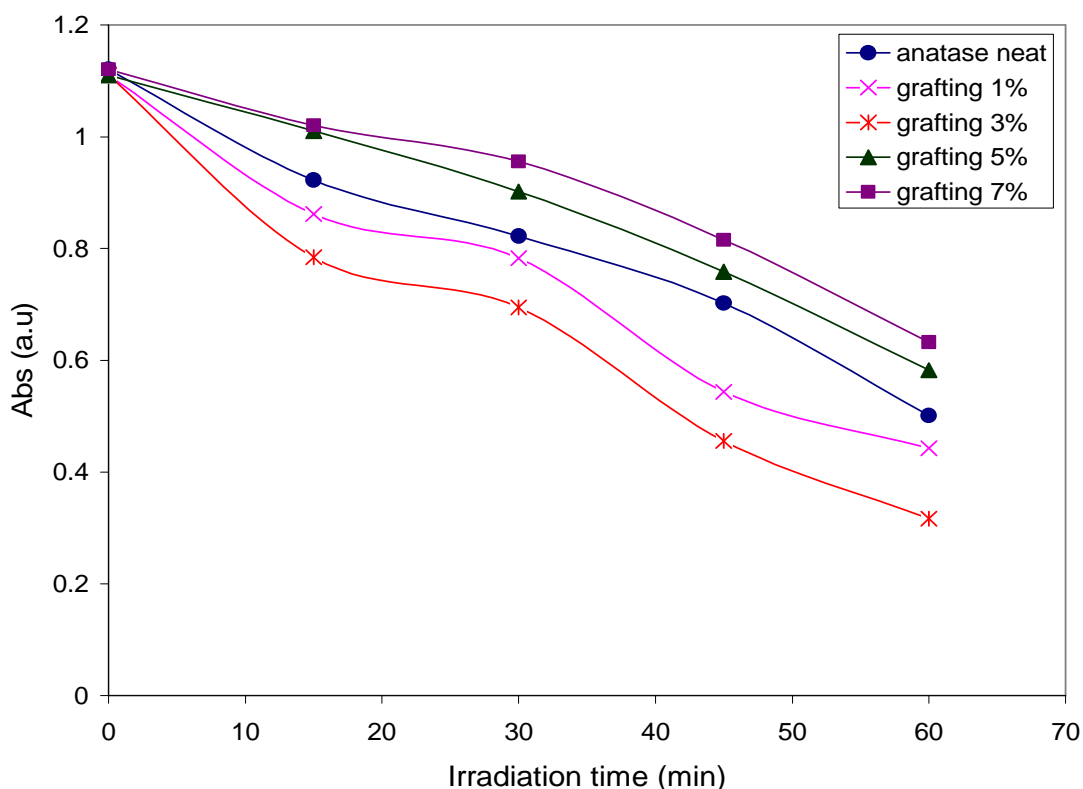


**Figure 2-39:** MB decoloration over PMMA grafted anatase.

**Table 2-10:** Rate of decoloration of MB over PMMA grafted anatase.

Catalyst	Rate of reaction $\times 10^{-8} \pm 0.10 \text{ mol. l}^{-1} \cdot \text{s}^{-1}$
anatase neat	1.12
anatase G1%	1.31
anatase G3%	1.46
anatase G5%	0.96
anatase G7%	0.83

The photocatalytic decoloration of MB dyes using neat and PMMA grafted titania was followed by measuring the absorbance at 655nm. From the above results, it can be observed an enhancement in the decomposition over grafted titania with low grafting percentage (1%G and 3%G) in comparison with neat anatase. For samples, with higher grafting percentage ( $G\% \geq 5\%$ ), there is a negative effect on the photocatalytic decoloration of MB<sup>(122)</sup>. Relative enhancement in the activity of reaction for the samples with low grafting is probably due to enhancement the activity of titania by doping with PMMA, which could possibly act as a photosensitizer<sup>(123)</sup>. High grafting percentages of PMMA, can lead to an increase in the rate of recombination between conduction band electrons and valence band holes. This can affect negatively the efficiency of the photocatalytic reaction.

## **2-9 Photocatalytic polymerizations over N doped titania**

### **2-9 -1 Photocatalytic polymerization over N/ TiO<sub>2</sub>**

In order to investigate effect of doping nitrogen on the activity of anatase in the photocatalytic polymerization of MMA a series of experiments have been undertaken using neat anatase as a reference in comparison to anatase modified by N doping at 400 °C, 500 °C and 600 °C. The previous procedure was followed in the modification of the catalysts, and the same characterization was applied. In addition, the same technique was used in the photocatalytic polymerisation for TiO<sub>2-x</sub>N<sub>x</sub> samples.

### **2-9-2 Characterisation of the polymer**

Polymer formation was characterized by using FTIR spectroscopy, NMR spectroscopy, SEM and TGA analysis for the two types of polymer (grafted and extracted).

### 2-9-2-1 FTIR spectroscopy

The FTIR spectra for PMMA extracted and PMMA grafted with nitrogen doped anatase are shown in the following figures:

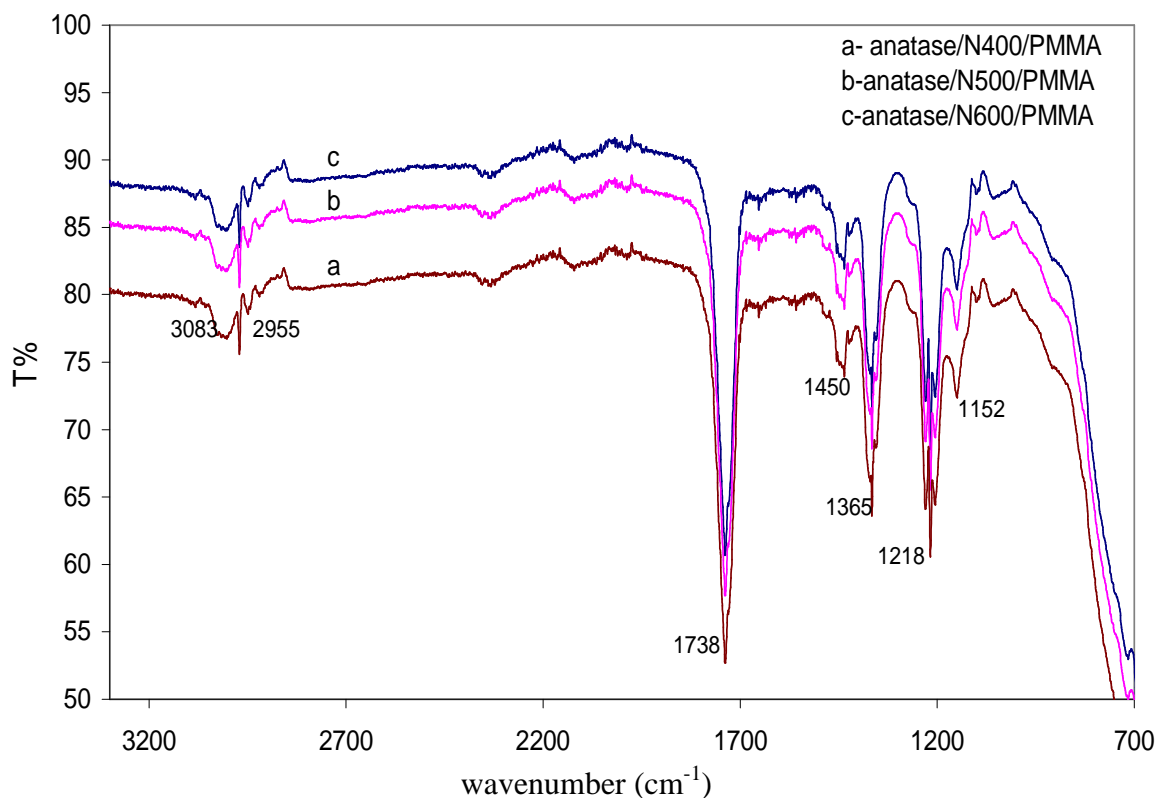


**Figure 2-40:** FTIR spectra for composite PMMA/anatase.

FTIR spectra for PMMA grafted nitrogen doped anatase, show a characteristic sharp band at around  $1738\text{cm}^{-1}$  which is assigned to the C=O vibration mode, this sharp peak indicates the presence of the grafted PMMA on the anatase/N and the formation of PMMA/anatase/N composite material. The broad band around  $3000\text{cm}^{-1}$  is due to the stretching vibrations of –OH groups on the titania surface<sup>(101)</sup>.

FTIR spectra of PMMA grafted anatase shows another characteristic peaks at 1450, 1365, 1218 and  $1152\text{cm}^{-1}$ . These are assigned to the C–H, –CH<sub>2</sub> and C–O–C bands of PMMA. The band at  $2955\text{cm}^{-1}$  is assigned to the CH<sub>3</sub> stretching vibration mode for PMMA grafted anatase. The sharp peak around  $700\text{cm}^{-1}$  is related to the grafted anatase with PMMA and it confirms the presence of grafted PMMA/anatase.

### 2-9-2-2 <sup>1</sup>H NMR spectroscopy

Further investigation for the extracted polymer was performed by <sup>1</sup>H NMR spectroscopy for extracted PMMA as shown in the following figure:

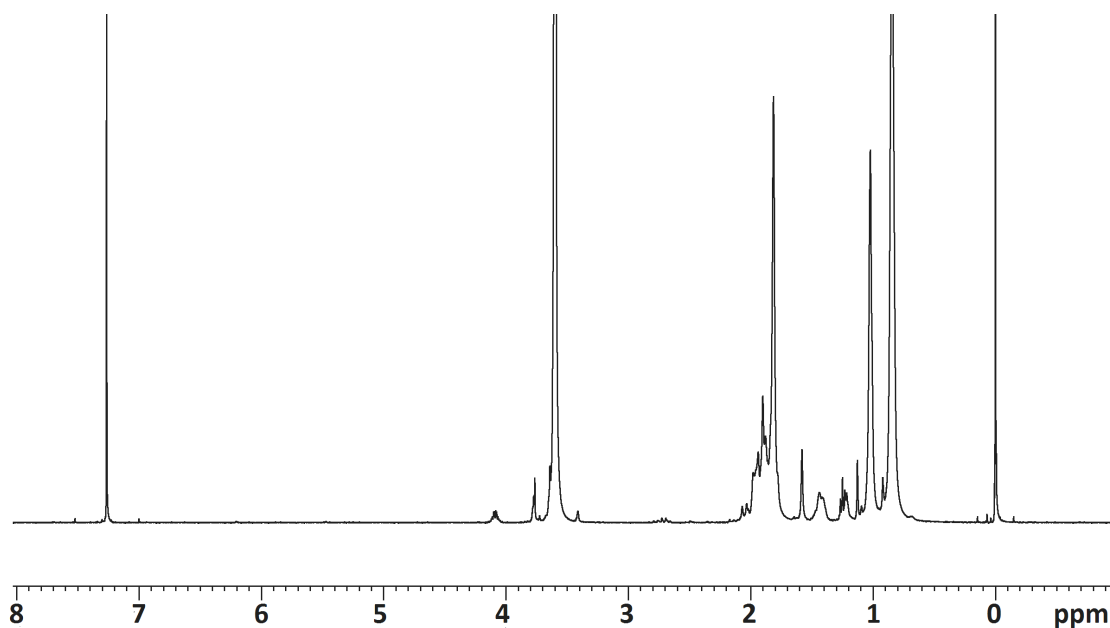
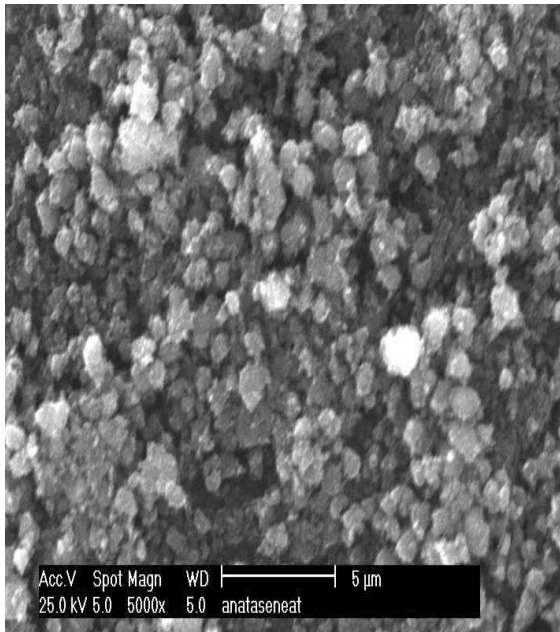


**Figure 2-41:**  $^1\text{H}$  NMR spectrum for the extracted PMMA in  $\text{CDCl}_3$ .

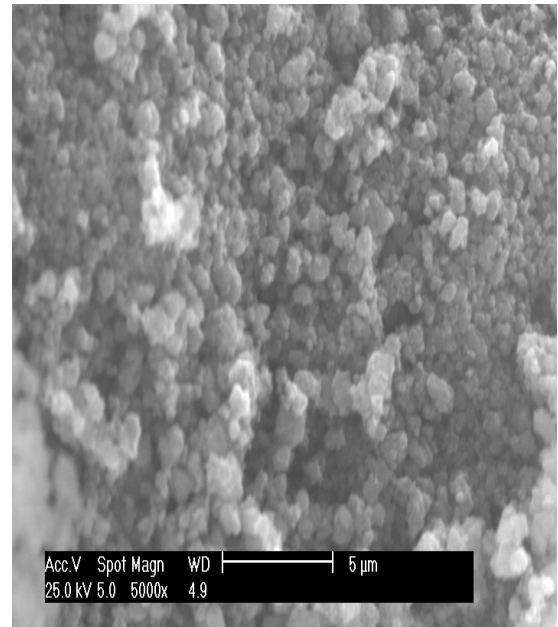
The most interesting thing in the above spectrum is that the peaks at  $\delta = 5.50$ , and  $6.05$  which are assigned to the  $\text{H}_2\text{C}=\text{C}-$  in MMA as it was seen in Figure 2-24, were completely absent in PMMA as shown in Figure 2-41. In addition to that the peak at  $\delta = 3.57-3.64$  which arises to  $-\text{OCH}_3$  confirms formation of PMMA. However, this spectrum is similar to that of PMMA that is synthesized by common chemical methods<sup>(103,105)</sup>.

### 2-9-2-3 Scanning electron microscopy

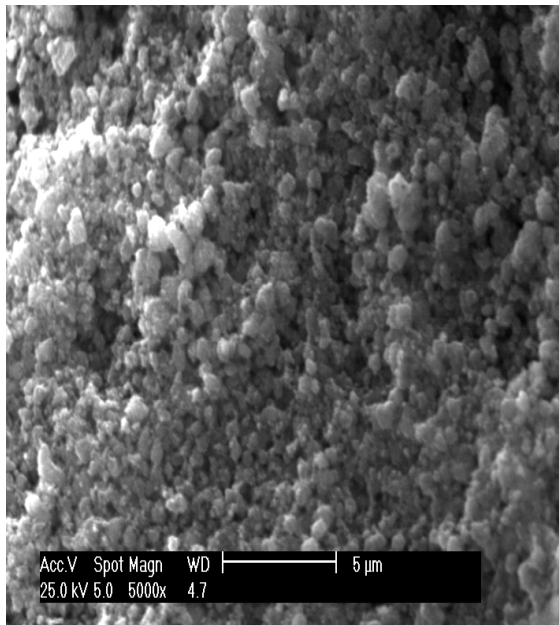
Morphological studies for PMMA grafted doped anatase have been undertaken using SEM and the results are shown in the following figure:



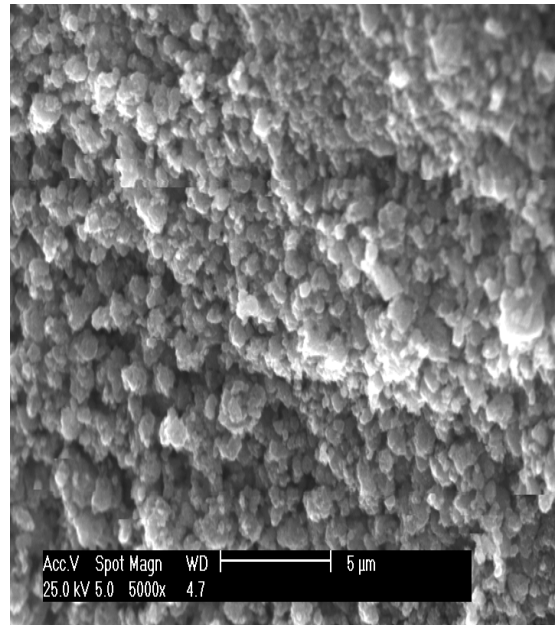
A



B



C



D

**Figure 2-42:** SEM images for neat anatase neat (A), anataseN400 (B), anataseN500 (C) and anataseN600 grafted with PMMA (D).

From these results, it can be seen that there is some change in the morphology of the surface upon grafting with the polymer. Anatase nanoparticles after grafting are aggregated with the polymer. The apparent roughness of surface for PMMA grafted  $\text{TiO}_2$  is relatively increased. In addition, when PMMA was grafted on the surface it can lead to a relatively compact interfacial structure<sup>(102)</sup>.

#### 2-9-2-4 Thermal gravimetric analysis

The bound polymer was further investigated using TGA analysis for PMMA grafted anatase doped with nitrogen. The results are shown in the following figure:

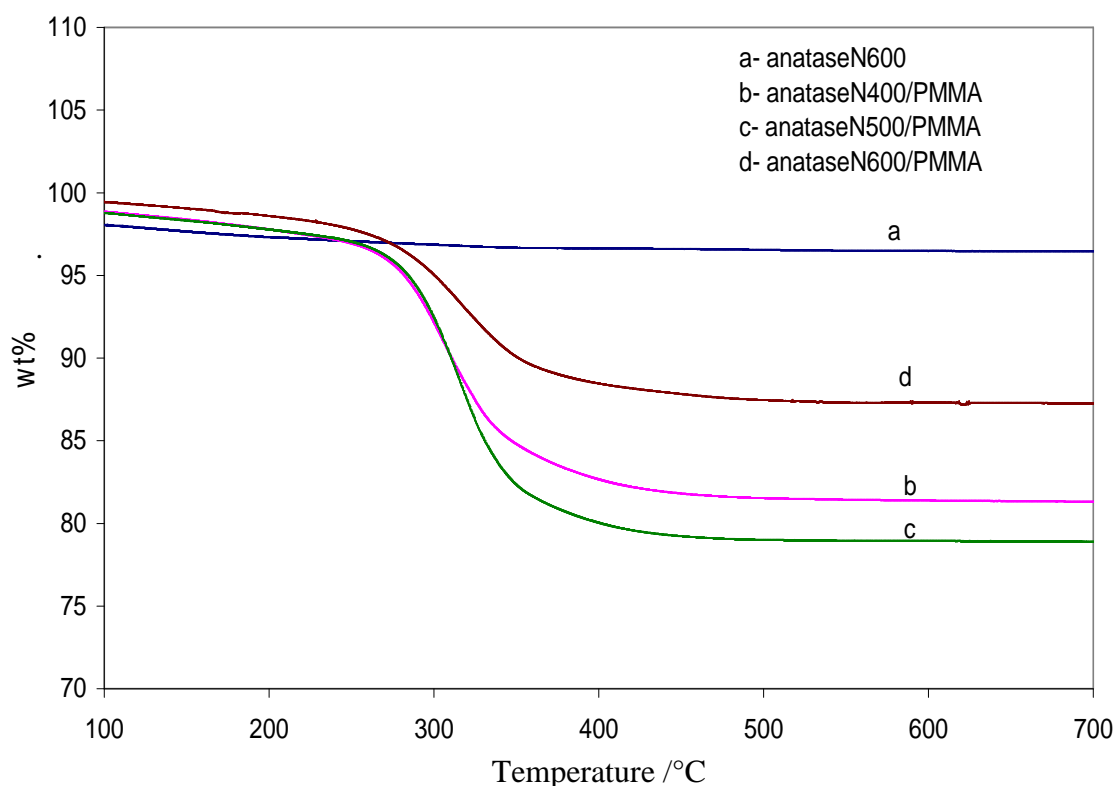


**Figure 2-43:** TGA for PMMA grafted nitrogen doped anatase.

From the above results, there is an evidence for the formation of the grafted polymer over anatase due to a characteristic mass loss about 12- 23% of the weight in the temperature range of 300- 500 ° C. In addition to that, and as was mentioned earlier, the polymer grafted titania (PMMA/anatase) begins to decompose at different temperature than that for the traditional PMMA (extracted polymer). This is probably due to interaction between polymer chains and the surface of anatase nanoparticles<sup>(106)</sup>. In addition to that, the higher percentage mass loss can be seen with anataseN500, while the lowest percentage loss occurs with anataseN600. So that the grafting percentage follows the order: anataseN500> anataseN400> anataseN600, and the grafting percentage for these samples were 25%, 22% and 12% respectively.

### 2-9-2- 5 X-ray diffraction (XRD)

In order to investigate the effect of grafting polymer on the crystalline structure of the doped anatase, XRD of doped anatase after grafting were carried out. These patterns are shown in the following figure:

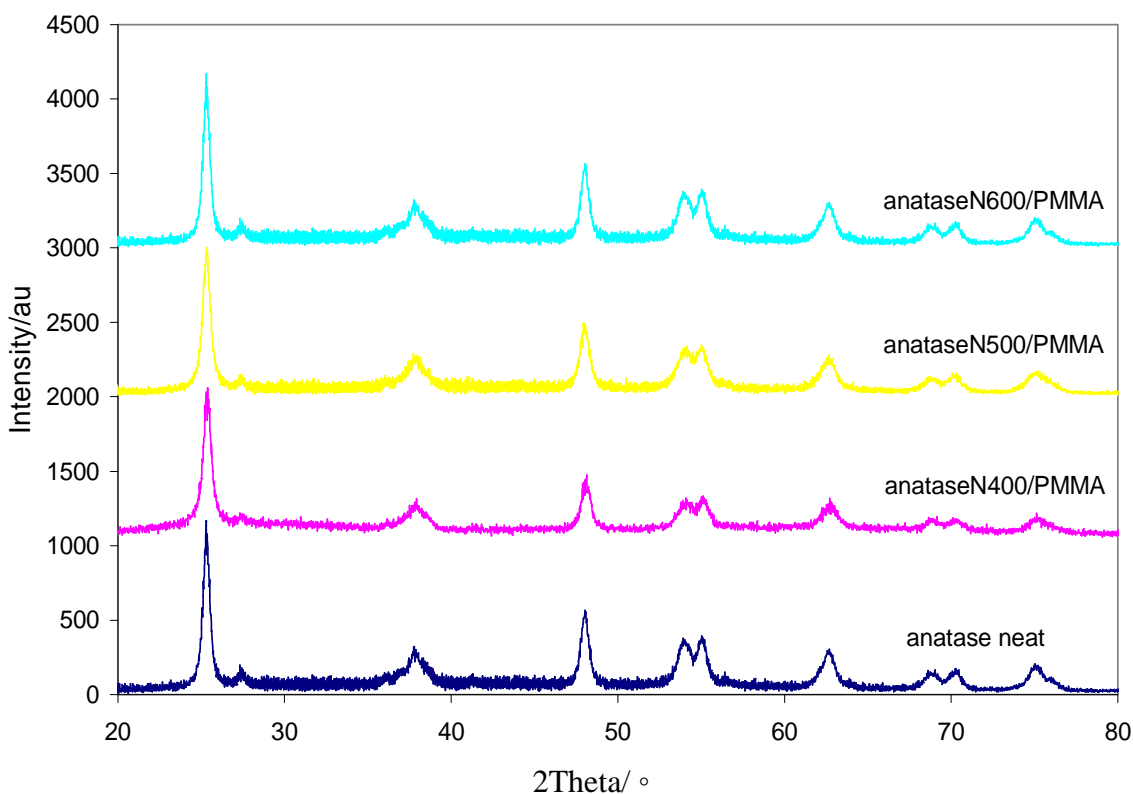


**Figure 2-44:** XRD patterns for PMMA grafted anatase doped with nitrogen.

From the above patterns, it can be seen that the characteristic reflections of the PMMA grafted doped anatase were almost the same as those of the neat anatase. The patterns for the samples after grafting are almost having the same peak positions in comparison with samples before grafting. This indicates that grafting doesn't affect the crystalline structure of the TiO<sub>2</sub>.

### 2-9-3 Photocatalytic polymerization over nitrogen doped anatase

To investigate the effect of doped nitrogen in photocatalytic polymerisation of MMA, a series of experiments were undertaken. In each one, 0.150 g of doped anatase suspended in 100 mL of distilled water with 2 mL of MMA under air for a durations of two hours at 20 ° C. The average error bar was  $\pm 0.28\%$ , the results are shown in the following figure:

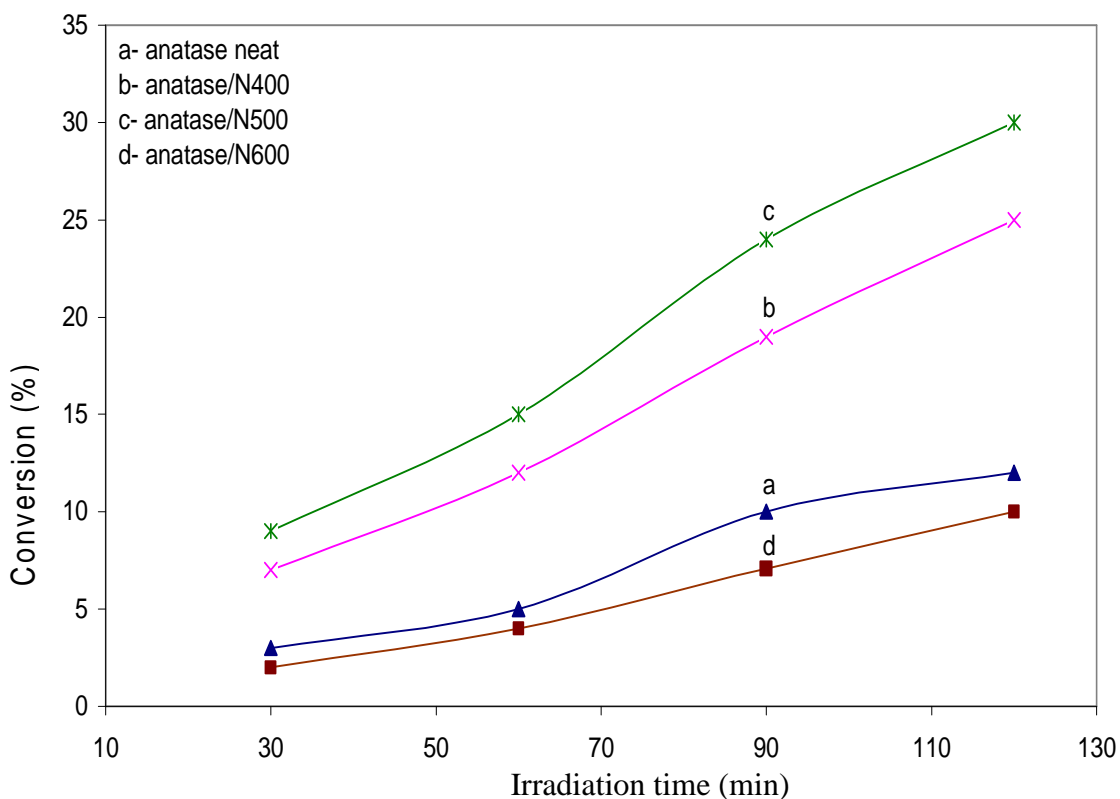


**Figure 2-45:** Photocatalytic polymerization over anatase doped with nitrogen.

From these results, it can be seen that there is enhancement in the photocatalytic activity for the doped samples, anataseN500 and anataseN400 that gives relatively higher conversion percentage for the formation of PMMA over these catalyst in comparison with the neat anatase under the same conditions. Generally, the activity for the photocatalytic polymerization for these catalysts fall in the order: anataseN500 > anataseN400 > anatase neat > anataseN600. The improvement in photocatalytic activity for these samples, as mentioned previously, probably arises from the increase in the absorption intensity in the near UV region with the increase in nitrogen content. Additionally, these samples have a relatively higher surface area with smaller particle size and the decrease in particle size with the increase in surface area produces a higher photocatalytic activity<sup>(83)</sup>. In contrast, anataseN600 exhibits a lower photocatalytic activity in comparison with neat anatase. In this sample, that has higher nitrogen content and a greyish green colour, the high nitrogen content may assist in formation of recombination centres close to the valence band of the catalyst. These recombination centres can increase rate of recombination leading to reduction photocatalytic activity<sup>(111)</sup>. The number averaged molecular weights ( $M_n$ ) for the extracted PMMA for anatase neat, anataseN400, anataseN500, and anataseN600 were 62,000, 55,000, 52,000, and 63,000 respectively. From these results, the highest molecular weight was obtained with a lower conversion percentage, while a lower molecular weight

was obtained with a higher conversion percentage. This may be as a consequence of the relation between rate of the polymerization reaction and the viscosity of the polymerization mixture<sup>(110)</sup>. High viscosity would result in a low rate of polymerization (low conversion percentage), while low viscosity would result in a high rate of polymerization (high conversion percentage). At high viscosities, the chain growth propagation reactions and chain termination reactions become diffusion controlled<sup>(120)</sup>.

### 2-9-3-1 Effect of temperature on the reaction

The effect of temperature on the photocatalytic polymerization was investigated by following the conversion of MMA into PMMA at different temperatures with the other parameters of the reaction being fixed, 2 mL MMA and 0.150 g of anatase doped with nitrogen and 100 mL of distilled water with irradiation for two hours in air. The results showed enhancement in the rate of reaction with increasing temperature. The average error bar was  $\pm 0.32\%$  and these results are shown in the following figure:

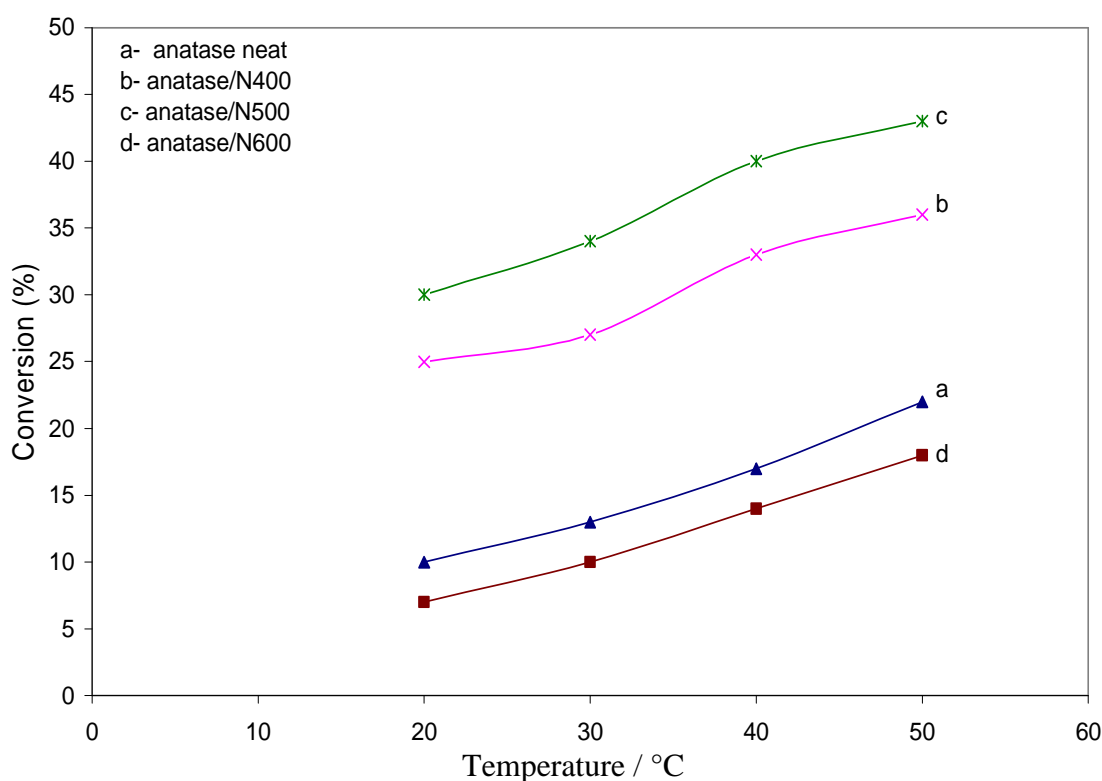


**Figure 2-46:** Effect of temperature on the photocatalytic polymerization over anatase doped with nitrogen.

From these results, it can be seen that, there is a direct proportionality between rate of polymerization and temperature. As was mentioned previously, photoreactions are not very sensitive toward minor changes in the temperature<sup>(109)</sup>. However, some reaction steps are potentially dependent on the temperature such as adsorption and desorption. These

processes are not rate determining steps for this type of reactions. The rate determining step is electron transfer from valence band of titanic to the conduction band<sup>(110)</sup>. Generally, an increase in the rate of reaction with an increase of the temperature may be attributed to the effect of temperature on the above steps on the TiO<sub>2</sub> surface.

## **2-10 Non-photocatalytic photopolymerization**

### **2-10-1 Photopolymerization of styrene and methyl methacrylate**

Photopolymerization of styrene and methyl methacrylate and was performed by using 2,2'-azo-bis(isobutyronitrile) (AIBN) as a photoinitiator under inert atmosphere. Reaction was carried out at 20 °C for two hours under irradiation with UV light. A required amount of purified monomer was degassed to exclude oxygen, and to this a required quantity of AIBN was added. The reaction materials were mixed together with the solvent (toluene).. Then the reaction was started by irradiation the mixture with UV light from the middle pressure mercury lamp (125 watt) with continuous stirring and nitrogen flushing. At the end of reaction, the produced polymer was precipitated by adding methanol. The results are presented as the conversion percentage against irradiation time.

#### **2-10-1-1 Characterization of the polymer**

The polymer formed was characterized by FTIR, NMR spectroscopy and GPC and the yield of the polymerization reaction was calculated as the percentage of conversion of the monomer into the corresponding polymer.

#### **2-10-1-2 <sup>1</sup>H NMR spectroscopy**

The characterization of the formed PST and PMMA was performed by <sup>1</sup>H NMR spectroscopy as shown in the following figures:

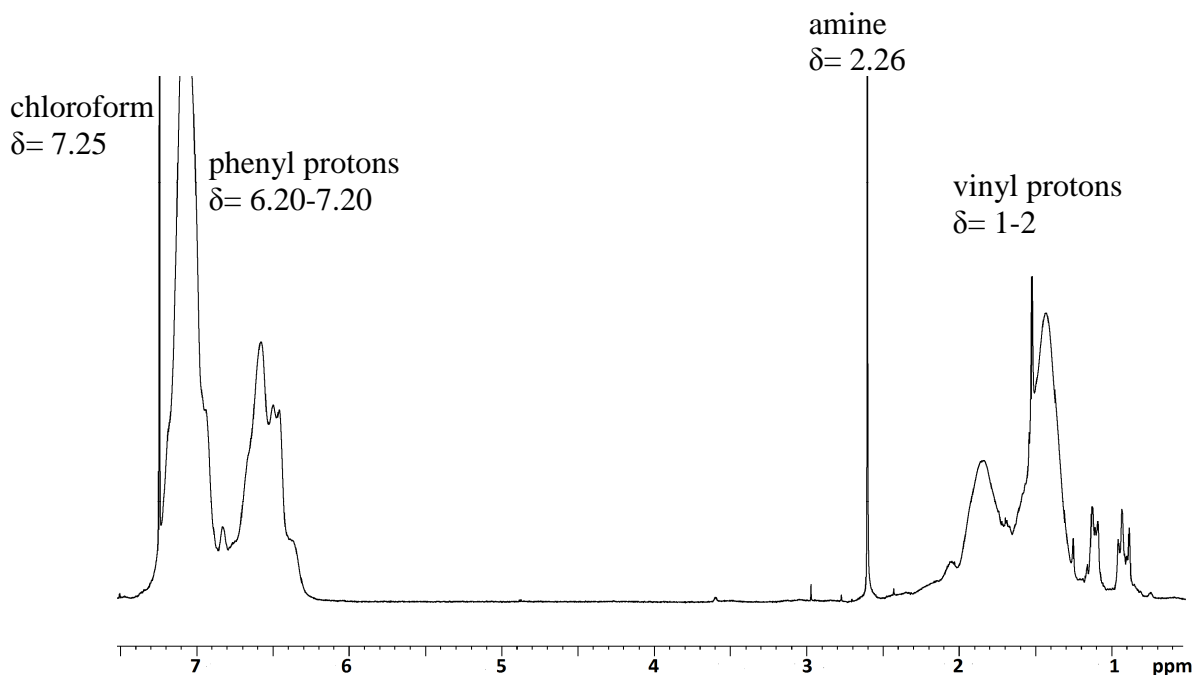


**Figure 2-47:** <sup>1</sup>H NMR spectrum of polystyrene produced by photopolymerization using AIBN as a photoinitiator under irradiation with UV light in N<sub>2</sub> atmosphere.

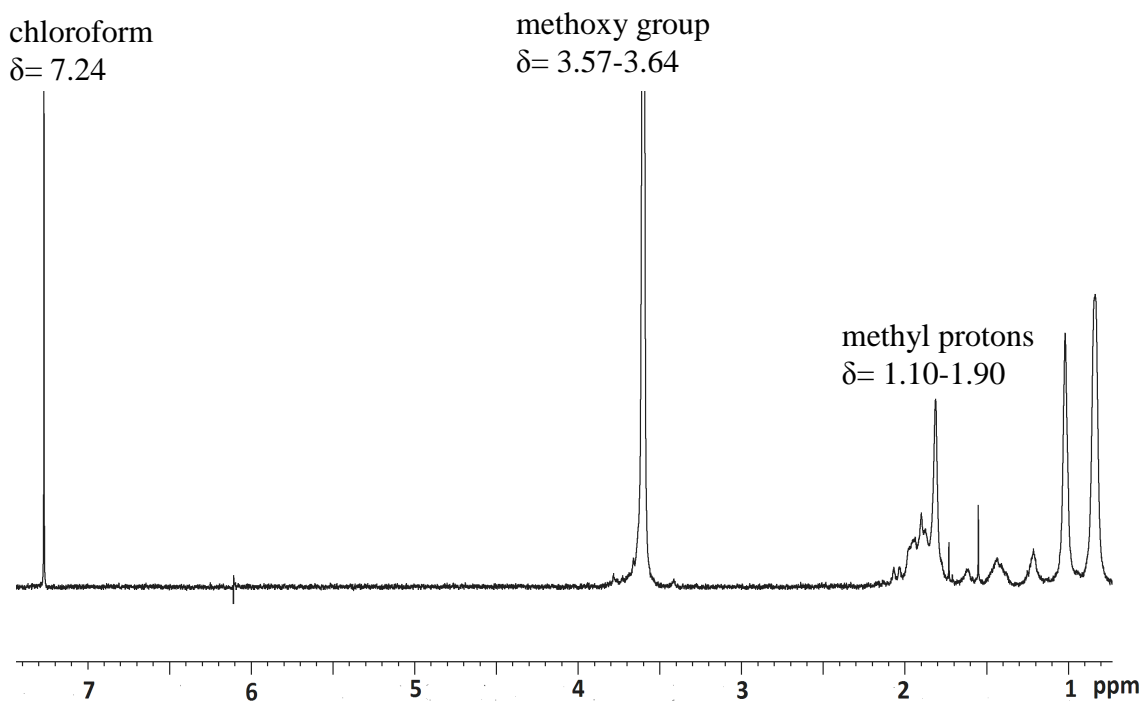


**Figure 2-48:** <sup>1</sup>H NMR spectrum of PMMA produced by photopolymerization using AIBN as a photoinitiator under irradiation with UV light in N<sub>2</sub> atmosphere.

From Figure 2-48 the peak at  $\delta = 3.57$ -  $3.64$  which arises to  $-\text{OCH}_3$  confirms formation of PMMA. However, this spectrum is similar to that of PMMA that is synthesized by common chemical methods<sup>(105)</sup>. The <sup>1</sup>H NMR spectrum of PST is shown in Figure 2-47.

This spectrum shows four bands which are corresponding to the protons of PST. The bands at  $\delta= 1-2$  are assigned to the three vinyl protons, the other two bands at  $\delta= 6- 7.5$  are assigned to the five aromatic protons in phenyl ring<sup>(124)</sup>.

### 2-10-1-3 FTIR spectroscopy

The FTIR spectra for the formed PMMA and PST are shown in the following figures:

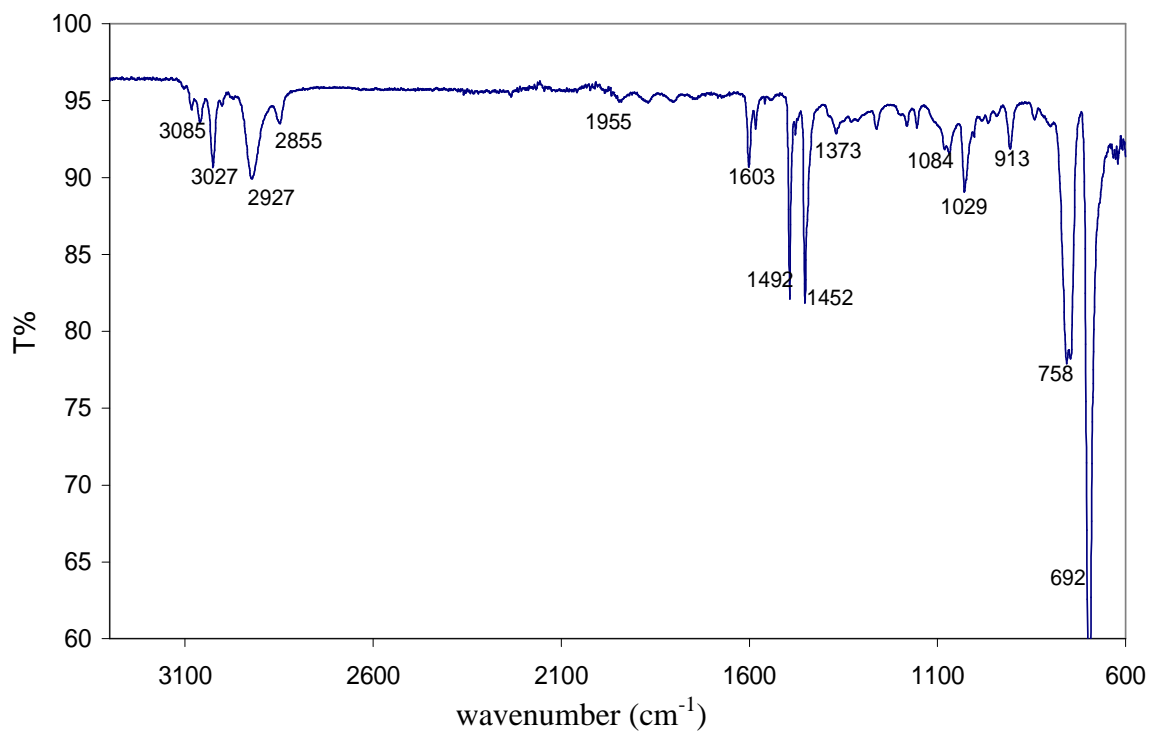


**Figure 2-49:** FTIR spectrum for PST produced by photopolymerization.

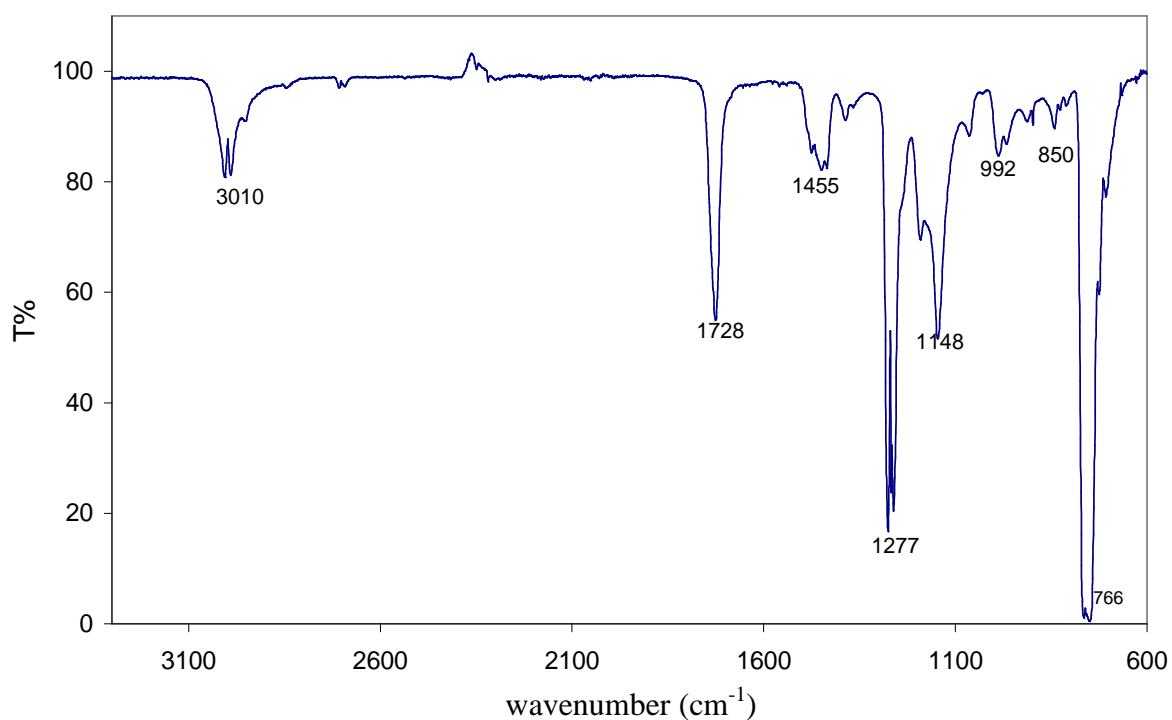


**Figure 2-50:** FTIR spectrum for PMMA produced by photopolymerization.

The FTIR spectrum for PST is shown in Figure 2-49. This spectrum shows peaks related to the PS, the peaks at 692 and 758  $\text{cm}^{-1}$  are related to the singly substituted phenyl group. The peaks at 1452, 1492, and 1603  $\text{cm}^{-1}$  are assigned to the vibration of C-C bonds in the phenyl group. In addition to that, the peaks in the range of 3000- 3090  $\text{cm}^{-1}$  and the weak peaks from 1063- 1995  $\text{cm}^{-1}$  are corresponding to C-H modes in the phenyl ring <sup>(125)</sup>. FTIR of PMMA is shown in Figure 2-50, this figure shows main peaks which are characteristic peaks for this polymer. The characteristic sharp band at 1728  $\text{cm}^{-1}$  is assigned to C=O in PMMA <sup>(101)</sup>. In addition, FTIR for PMMA, the broad band around 3010  $\text{cm}^{-1}$  is related to free CH<sub>3</sub> vibrations in the PMMA. The bands at 1000- 1455  $\text{cm}^{-1}$  can be assigned to the C-O-C stretching mode of the ester bond in PMMA. The other bands at 766- 1000  $\text{cm}^{-1}$  are due to the bending of C-H bonds.

#### **2-10-1-4 Kinetics of polymerization**

To study the effect of irradiation time on the photopolymerization, a series of experiments were undertaken. In each, 2 mL of ST and MMA used were mixed with 0.02 g of AIBN as an initiator with 100 mL of toluene at 20 °C. The mixture was flushed with nitrogen for 5 minutes prior to irradiation with the middle pressure mercury lamp (125 watt) to exclude the oxygen from the solution. The reaction was initiated by irradiation of the mixture with continuous stirring and nitrogen flushing. At the end of reaction, the produced polymer was precipitated by adding methanol with vigorous stirring, and the resultant polymer was dried overnight. The yield of polymerization was reported as the percentage of conversion. The average error bar  $\pm 0.36\%$  and the results are plotted in the following figure:

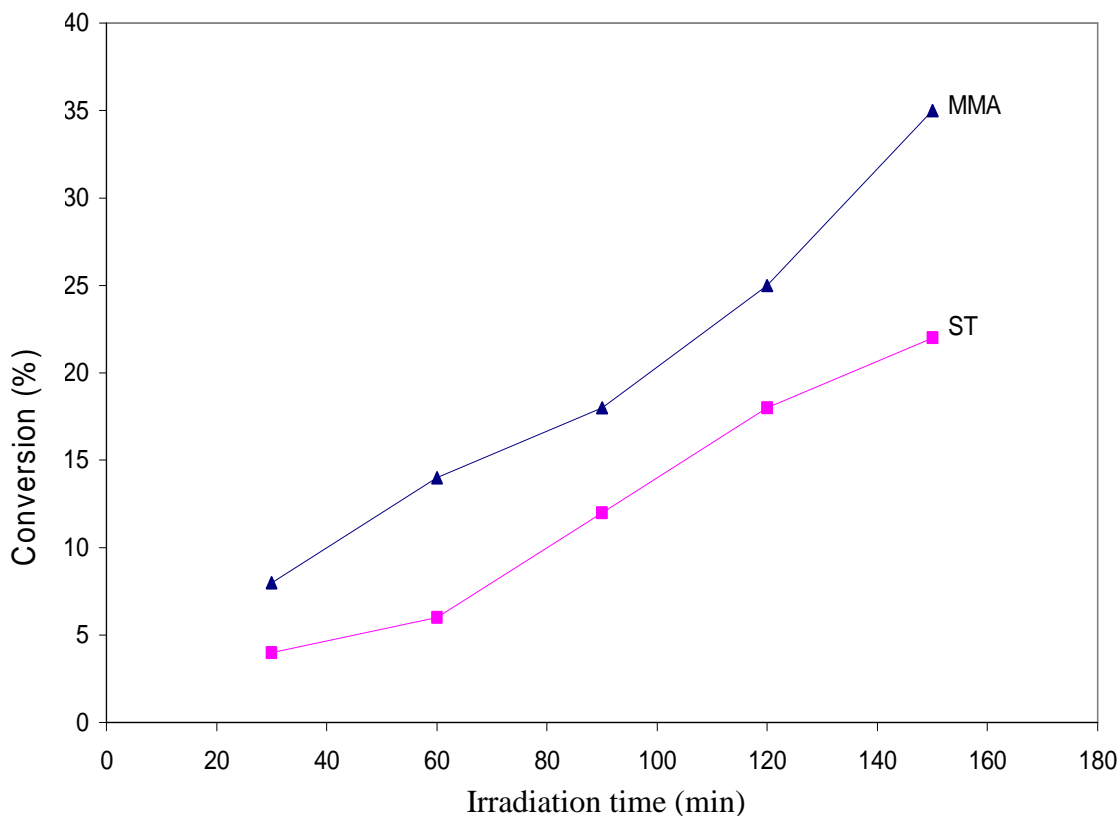


**Figure 2-51:** Effect of exposure time on the photopolymerization of MMA and ST.

From these results, it is clear that, there is increasing yield of polymerization with increasing of exposure time. This can be attributed to formation more radical species that contribute to the growth of the formed polymer. In addition, the results showed that the yield of PMMA is higher than that for PST as was mentioned previously, that could be expected as styrene radicals more stable than MMA radicals due to resonance effect in ST phenyl ring<sup>(118)</sup>. Thus, MMA can polymerize faster than PS. The results of GPC for PS and PMMA were PS ( $M_n = 56,000$ , and for PMMA ( $M_n = 52,000$ ).

#### **2-10-1-5 The effect of the amount of the monomer used**

To study the effect of using different amounts of the monomers under the same reaction conditions, a series of experiments were undertaken in which a required amount of the used monomer was mixed with 0.02 g of AIBN and 100 mL of toluene at 20 °C with flushing nitrogen over reaction mixture prior to the start of irradiation. The reaction was initiated by illumination from the middle pressure lamp for two hours. The results are presented as percentage of conversion for both MMA and ST. The average error bar was  $\pm 0.22\%$  and these results are shown in the following figure:

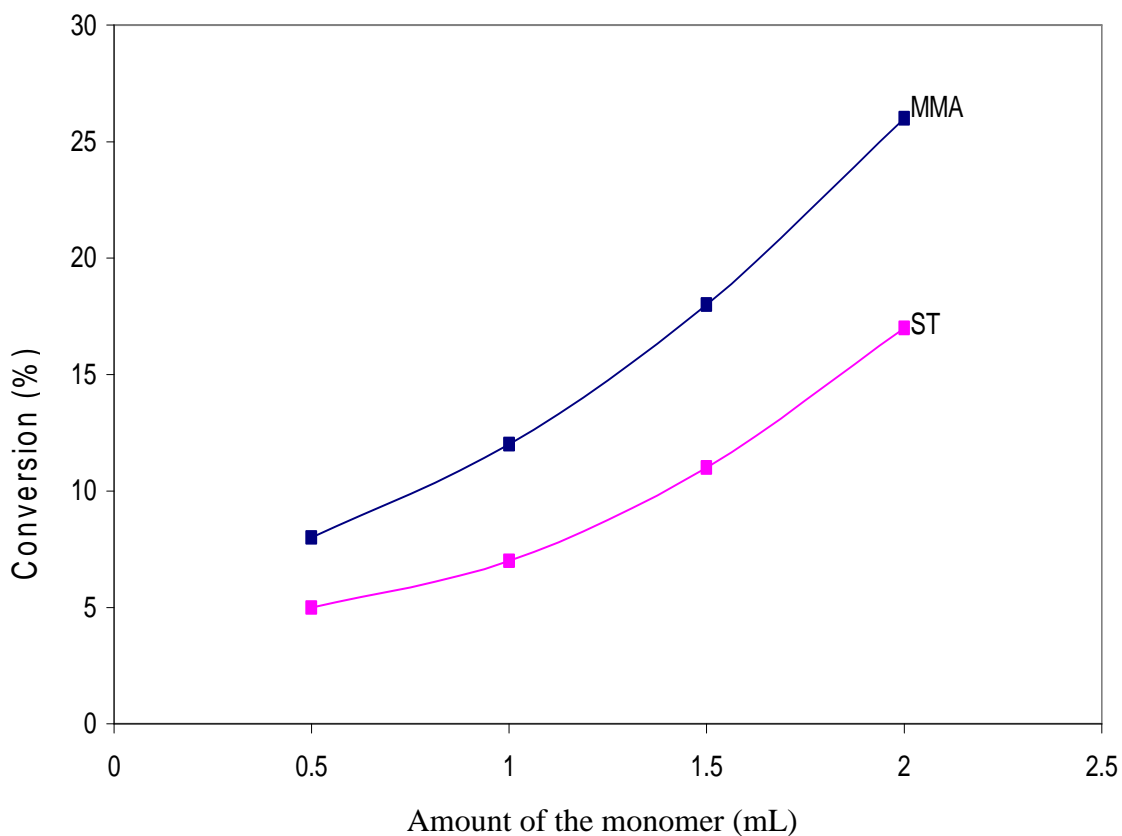


**Figure 2-52:** Effect amount of the monomer on the photopolymerization of MMA and ST.

The results showed that, there is a progressive increase in the yield of reaction with the increase amount of the used monomer under the same reaction conditions. This is probably due to the increased number of active centres with increase for monomer that can lead to high rate in the growth of polymer chains<sup>(102)</sup>. This can lead to increase the rate of polymerization reaction, which gives high conversion percentage. Also from these results, it can be seen that conversion of MMA into PMMA is higher than that for conversion ST into PST. This probably arises from relatively more stable radicals of styrene that are further stabilized by resonance structure with benzene ring in styrene.

#### **2-10-1-6 Effect of inert atmosphere on the rate of reaction**

In order to investigate the effect of the atmosphere on the photopolymerization, a series of experiments had been performed under flowing nitrogen flush and the normal atmosphere of air. In this case, 2 mL of the used monomer was mixed with 0.02 g of AIBN in 100 mL of toluene with initiation a nitrogen atmosphere at 20 °C. Reaction was initiated by irradiation with continuous stirring for two hours. The formed polymer was precipitated by adding an excess of methanol, the polymer then was separated and dried. The average error

bar was  $\pm 0.30\%$ . The results are presented in the Table 2-11 and plotted as percentage of conversion versus irradiation time for the two cases as in the following figure:

**Table 2-11:** Effect of atmosphere on the photopolymerization of ST and MMA.

Time (min)	MMA Conversion(%) $\pm 0.04\%$ N <sub>2</sub> atmosphere	ST Conversion(%) $\pm 0.04\%$ N <sub>2</sub> atmosphere	MMA Conversion (%) air atmosphere	ST Conversion(%) air atmosphere
30	8	6	Nil	Nil
60	14	10	Nil	Nil
90	18	13	Nil	Nil
120	26	18	Nil	Nil

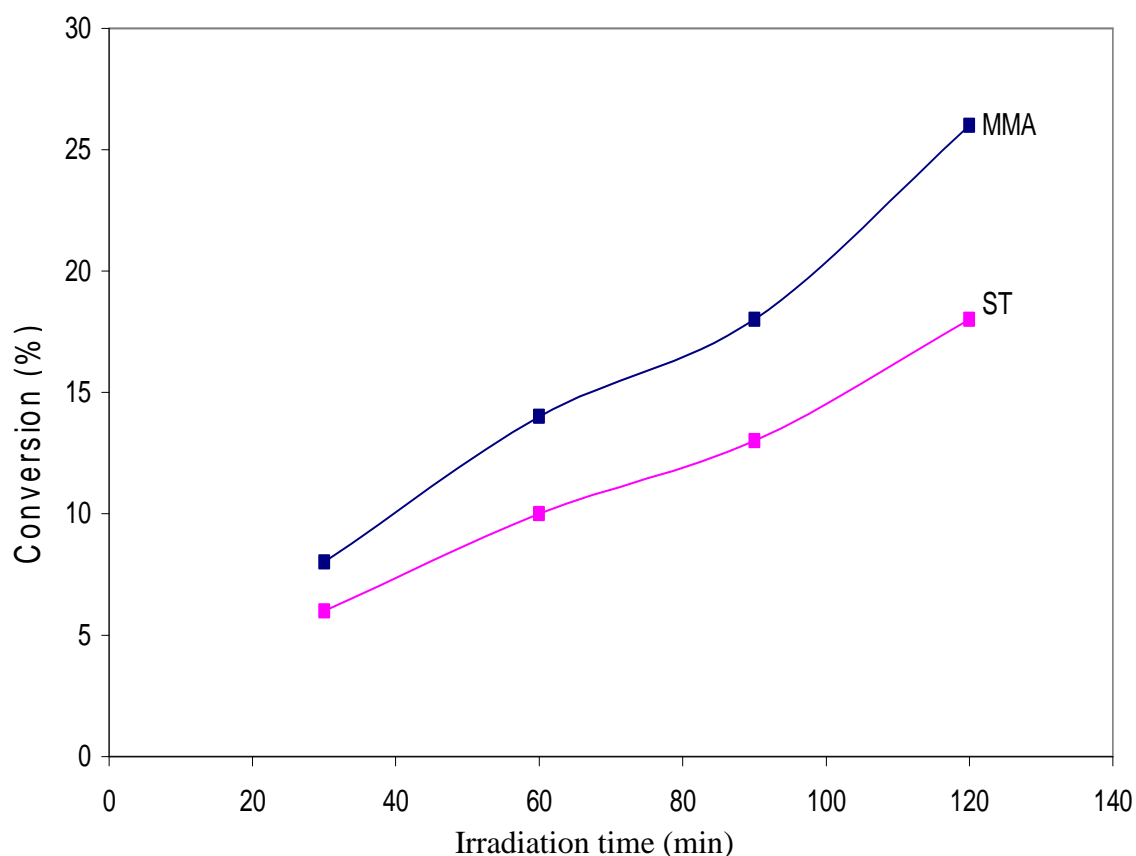


**Figure 2-53:** Effect of atmosphere on the photopolymerization of ST and MMA.

From these results, it was found that no polymer was formed under an air atmosphere. This is probably due to the termination of the polymerization reaction by oxygen, which inhibits polymer formation<sup>(125)</sup>. Molecular oxygen can combine directly with the active radicals that are formed by excitation of initiator molecules by light. The radicals which

are produced from oxygen and the radicals of initiator are mainly peroxide radicals, and this type of radical is not active in formation a polymer due to low reactivity<sup>(126, 127)</sup>.

### 2-10-1-7 Effect of the reaction temperature on the photopolymerization

In order to investigate the effect of temperature on the photopolymerization, a series of experiments was performed. In each experiment, 2 mL of the used monomer was mixed with 0.02 g of AIBN in 100 mL of toluene with nitrogen flowing over reaction mixture. Reaction was started by irradiation with UV radiation from the middle pressure mercury lamp with continuous stirring for two hours. The average error bar was  $\pm 0.40\%$ , and the results are presented in the following figure:

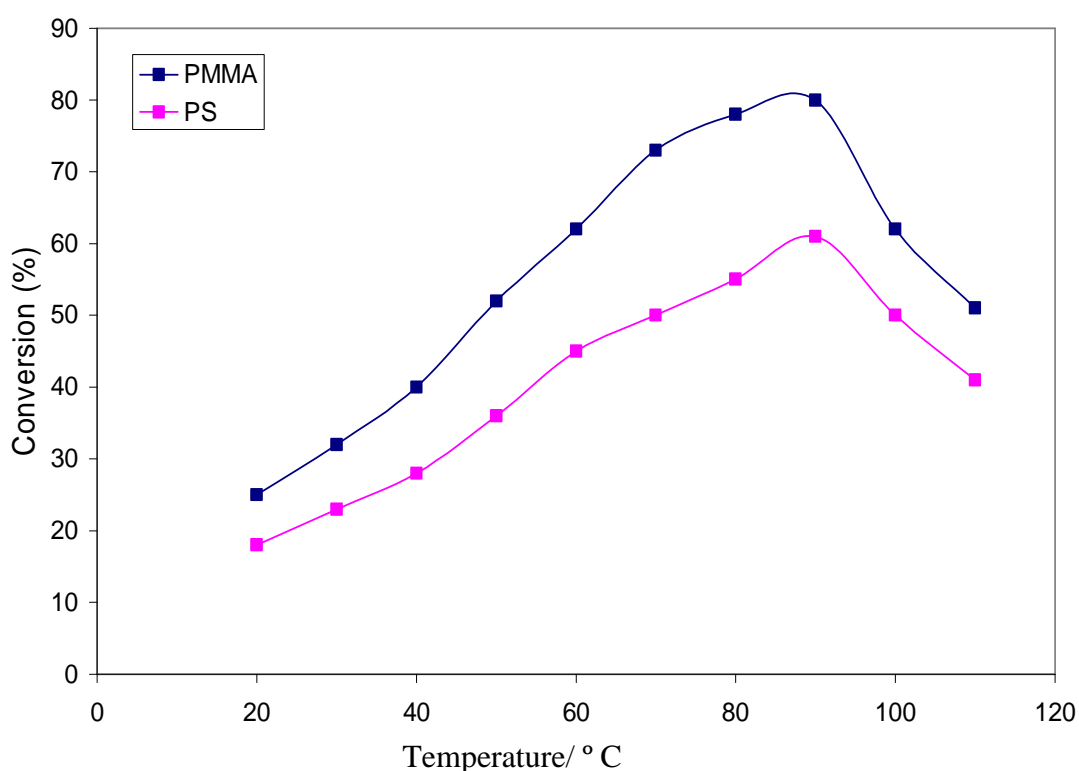


**Figure 2-54:** Effect of the reaction temperature on the photopolymerization of ST and MMA.

From these results, it is clear that there was a positive effect for temperature on the efficiency of the reaction at temperatures up to 100 °C, and at higher temperatures (>100 °C), there was a negative effect for the temperature on the rate of polymerization. At low temperatures, an increase in temperature of reaction can enhance the formation of the active radicals from the initiator molecules to give a high concentration of the radicals that enhance the formation of the polymer chains. At higher temperatures (>100 °C), it may be that the concentration of the radicals becomes too high<sup>(128,129)</sup>, which can lead to an increased termination rate of the radicals which inhibits the formation of the polymer

chains under these conditions. In addition to increased reaction rate with temperature, it may cause an increase in the viscosity of the whole mixture, which negatively can affect the mixing of reaction components leading to inhibition of the reaction at higher temperatures.

### 2-10-2 Thermal polymerization of ST and MMA

To make a comparison between thermal and photoinitiation of polymerization, a series of experiments were undertaken using 2 mL of each monomer with 0.02 g of AIBN and 100 mL of toluene under flowing nitrogen for two hours for each experiment. These experiments were performed at different temperatures, and the results are represented as a conversion percentage as a function of the reaction temperature. The average error bar was  $\pm 0.28\%$ , and these results are shown in the following figure:

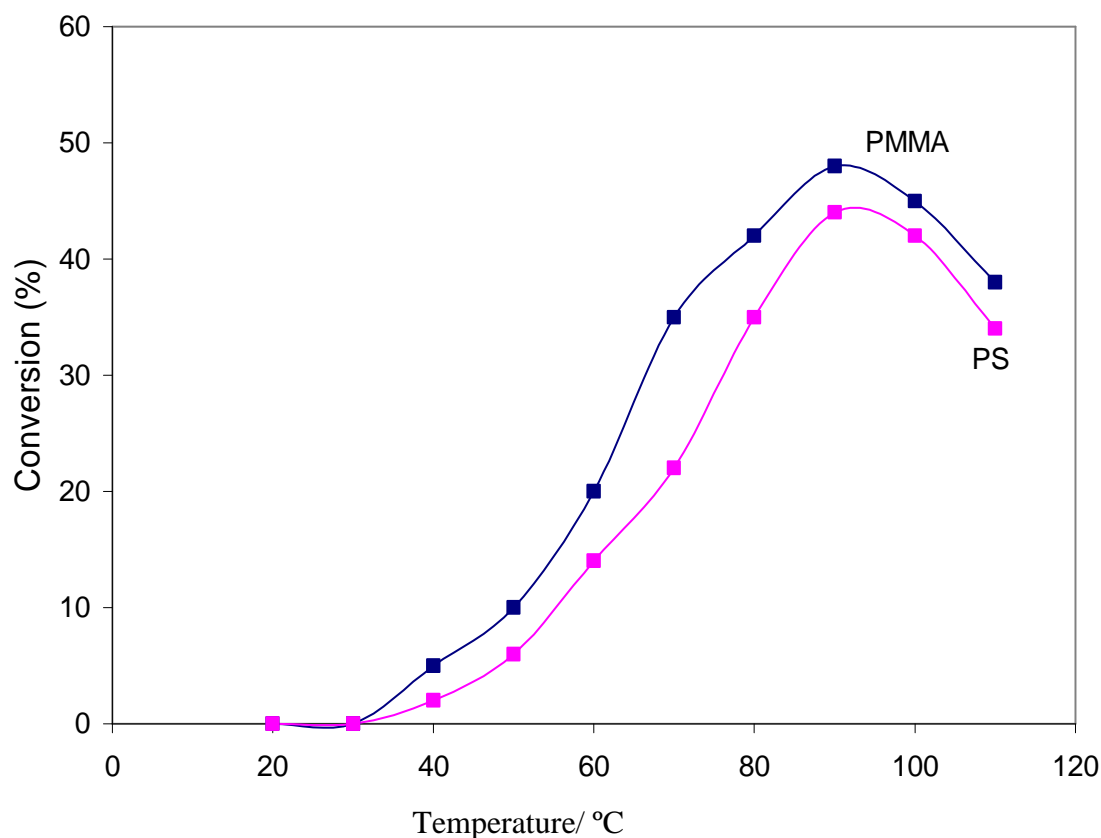


**Figure 2-55:** Thermal polymerization of MMA and ST.

From these results, it was found that, under thermal initiation of polymerization no polymer was formed at low temperature ( $< 40\text{ }^{\circ}\text{C}$ ) and that at temperatures higher than  $40\text{ }^{\circ}\text{C}$ , there was a positive effect of temperature on the rate of polymerization up to  $100\text{ }^{\circ}\text{C}$ . At temperatures higher than  $100\text{ }^{\circ}\text{C}$ , there was a negative effect on polymerization. These observations can be explained by the effect of temperature on the formation free radicals from the used initiator. With temperatures lower than  $40\text{ }^{\circ}\text{C}$  free radicals are not produced

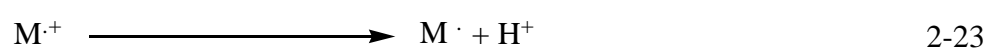
from the initiator, and at temperatures greater than 40°C, the concentration of the free radicals increases with elevation in temperature. At temperatures greater than 100 °C, the high concentration of the radicals formed may enhance termination steps, resulting in a negative effect on the polymerization reaction. By comparison of these results with those obtained under photoinitiation, it can be seen that, photoinitiation was more efficient than thermal initiation. This is due to formation of polymer at ambient temperature, while thermal initiation requires high temperatures to occur<sup>(128, 129)</sup>.

### 2-11 Proposed mechanism for the photocatalytic polymerization

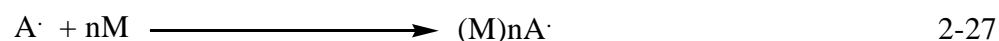
Generally, this type of polymerization involves adsorption of the monomer molecules on the surface of the photocatalyst. Then the particles of the catalyst are excited by absorbing a light with a suitable energy in order to initiate polymerization, so that it is known as in situ polymerization. The proposed mechanism for the generation of free radicals on the titania particles can be represented as follows: irradiation of titania with a light of a suitable energy can generate conduction band electrons and valence band holes<sup>(130)</sup>:



Then photocatalytic formation of initiator radicals can occur when monomer molecules (M) are oxidized by valence band holes, producing radical cations which can produce radical of the monomer by losing a proton, conduction band electrons are captured by an electron acceptor (A) as follows:



Then chain growth with monomer molecules can occur as follows:

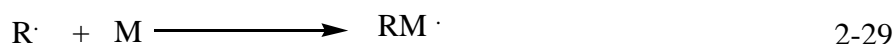


The termination of chains can occur by radical combination or by disproportionation<sup>(112)</sup>.

## 2-12 Proposed mechanism for the photopolymerization

Conversion of monomer molecules into polymer by free radical polymerization involves three main steps, initiation which involves decomposition of the initiator by absorbing light to generate primary free radicals, which is relatively slow. The initiation step is followed by rapid propagation reaction between free radicals and monomer molecules. This step continues until the termination step occurs. The final step is the termination step, which involves either combination between two polymer radicals to give one polymer molecule, or by disproportionation of two polymer radicals to give two polymer molecules<sup>(109,110)</sup>.

**A: Initiation step:** Generation of radicals by absorbing light from initiator molecules (I) reaction with monomer molecules (M) as follows:



**B: Propagation step:**

This step involves further reaction of the polymer radicals with the monomer molecules as follows:



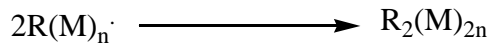
The last step represents polymer radical containing  $(M)_{n+2}$  of the monomer molecules, in this way the polymer chains are built up with a head to tail arrangements of polymer molecules. In this step, the growth polymer chains may contribute to chain transfer reaction, which involves unimolecular atom transfer from any available molecule in the system, such as solvent, monomer and initiator into the propagated radical to produce a polymer molecule and at the same time donor molecules convert into free radicals. This process can be represented as follows:



In above equation, AB is a donor molecule in the system

**C-Termination step**

This step involves reacting of two growing polymer chains and this proceeds according to the termination mechanism by coupling of two propagating chains to give the final saturated end polymer as follows<sup>(110)</sup>:

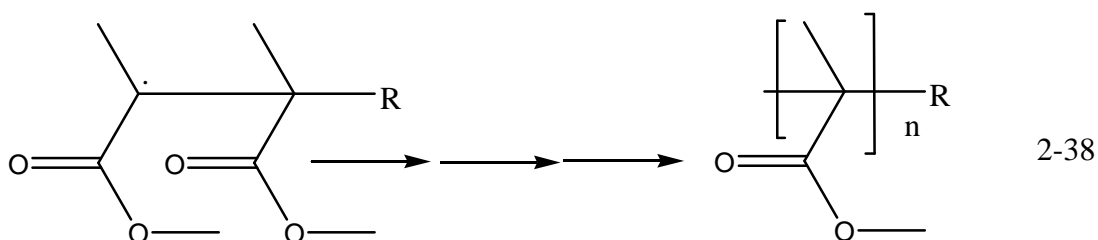
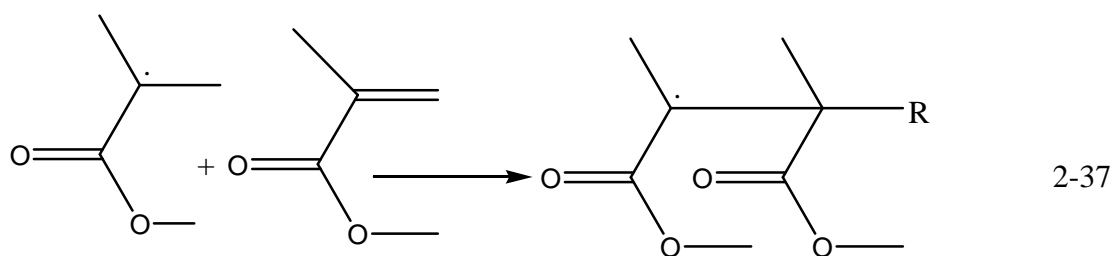
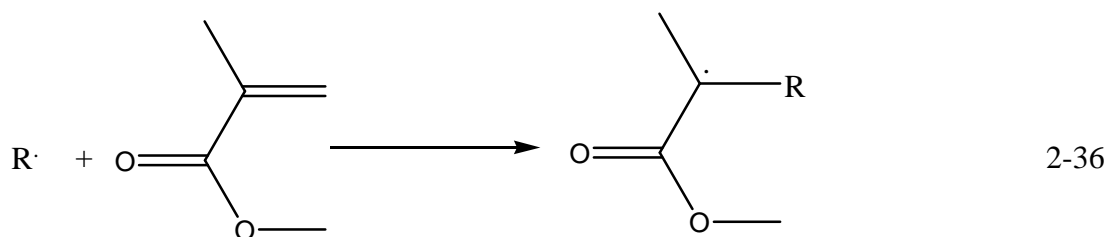


2-33

In addition, termination could occur by disproportionation mechanism, in this case hydrogen or other atoms transfer from end of one chain to another chain. This process gives two types of polymer, one with saturated end and the other with unsaturated end as follows<sup>(110)</sup>:



Generally, free radical polymerization for MMA can be represented in the scheme below. In this mechanism R is a photoinitiator that absorbs light to give initiation free radicals(R $\cdot$ ). This then coupled with the monomer e.g. MMA to give active propagating radicals from initiator molecule and the monomer. This process is continued to form propagating chains until termination occurs as mentioned above. This process is represented in the following scheme:



**Scheme 2-56:** Proposed free radical photopolymerization of MMA.

## 2-13 Conclusions

In this chapter doping titanium dioxide with nitrogen was performed at three different temperatures, 400 °C, 500 °C and 600 °C. It is believed that doped nitrogen species within titania may exist as interstitial species or substitutional species or a combination of both these states. It was found that doping titania with nitrogen doesn't alter its structure, as the XRD patterns for the doped samples were similar to those of the non-doped counterparts. In addition, doping titania with nitrogen generates a red shift in its absorption spectrum, possibly as a result of mixing of 2p states of the doped nitrogen species with the O 2p states as suggested in the literature. Doping samples at 400 °C and 500 °C results in higher BET specific surface areas. The photocatalytic activity for the various samples was investigated by measurements of the photocatalytic decomposition of MB. In addition, the photocatalytic polymerization of styrene and methyl methacrylate was undertaken for selected titania samples. It was found that, doping titania at 400 °C and 500 °C resulted a higher photocatalytic activity in comparison with parent undoped titania, while doped samples at 600 °C showed lower photocatalytic activity. The improvement in photocatalytic activity for titaniaN400 and titaniaN500 probably arises from the increase in the absorption intensity in the near UV and visible region with increase in nitrogen content. Additionally, these samples have a higher surface area with smaller particle size resulting in higher photocatalytic activity. While photocatalytic polymerization has been reported elsewhere in the literature<sup>(129-131)</sup>, the influence of the modification of titania by nitrogen doping for this process does not appear to have been investigated in detail. A limitation of the current study is the application of a non-monochromatic light source, which was middle pressure mercury lamp (125 watt). The lamp give a wide rang of radiation ranged from UV to visible region of the spectrum. This aspect should be investigated in future studies, with particular emphasis upon wavelengths in the visible region.

## 2-14 References

1. A. Fujishima, K. Honda, *Nature*, 1972, **37**, 328.
2. K. Hashimoto, H. Irie, A. Fujishima, *Jpn. J. Appl. Phys.*, 2005, **44**, 8269.
3. M. Anpo, *Bull. Chem. Soc. Jpn.*, 2004, **77**, 1427.
4. A. Kudo, H. Kato, I. Tsuji, *Chem. Lett.*, 2004, **33**, 1534.
5. T. Thompson, J. Yates, *Chem. Rev.*, 2006, **106**, 4428.
6. H. Yates, M. Nolan, D. Sheel, E. Pemble, *J. Photochem. Photobiol. A: Chem.*, 2006, **17**, 213.
7. M. Fox, C. Chen, *J. Am. Chem. Soc.*, 1981, **103**, 6757.
8. C. Renz, *Helv. Chim. Acta.*, 1921, **4**, 961.
9. A. Fujishima, X. Zhang, D. Tyrk, *Surf. Sci. Rep.*, 2008, **63**, 515.
10. M. Anpo, *Pure. Appl. Chem.*, 2000, **72**, 1787.
11. K. Takeuchi, I. Nakamura, O. Matsumoto, S. Sugihara, M. Ando, T. Ihara, *Chem. Lett.*, 2000, **29**, 1354.
12. T. Ohno, T. Mitsui, M. Matsumura, *Chem. Lett.*, 2003, **32**, 365.
13. Y. Liu, X. Chen, J. Li, C. Burda, *Chemosphere*, 2005, **61**, 11.
14. J. Wang, T. Ma, G. Zhang, *Catal. Commun.*, 2007, **8**, 607.
15. W. Zhou, Y. Zheng, G. Wu, *Appl. Surf. Sci.*, 2006, **252**, 1387.
16. M. Anpo, M. Takeuchi, *J. Catal.*, 2003, **216**, 505.
17. S. Sato, J. White, *J. Am. Chem. Soc.*, 1980, **102**, 7206.
18. S. Nishimoto, B. Ohtani, T. Yoshikawa, T. Kagiya, *J. Am. Chem. Soc.*, 1983, **105**, 7180.
19. H. Courbon, J. Herman, P. Pichat, *J. Catal.*, 1981, **72**, 129.
20. S. Sato, J. White, *J. Am. Chem. Soc.*, 1980, **102**, 7206.
21. J. Lee, S. Oh, D. Park, *Thin Solid Films*, 2004, **457**, 230.
22. H. Irie, S. Washizuka, Y. Watanabe, T. Kako, K. Hashimoto, *J. Electrochem. Soc.*, 2005, **152**, 351.
23. M. Radecka, *Thin Solid Films*, 2004, **98**, 451.
24. M. Hoffman, S. Martin, W. Choi, D. Bahnemann, *Chem. Rev.*, 1995, **95**, 69.
25. R. Higgins, *Engineering Metallurgy*, 1<sup>st</sup> Edition, English Universities Press LTD, 1973, p. 373.
26. A. Mills, G. Porter, *J. Chem. Soc. Faraday Trans. I*, 1984, **78**, 1302.
27. F. Cotton, G. Wilkinson, *Basic Inorganic Chemistry*, John Wiley and Sons, 1980.

28. K. Awazu, X.Wang, M. Fujimaki, T. Komatsubra, T. Ikeda, *J. Appl. Phys.*, 2004, **38**, 44308.
29. R. Deckok, H. Gray, *Chemical Structure and Chemical Bonding*, 1<sup>st</sup> Edition, The Benjamin, 1980, p. 600.
30. R. Weast, *Hand Book of Chemistry and Physics*, 57<sup>th</sup> Edition, Chemical Rubber Company, Cleveland, 1976. p. B. 234.
31. C. Tang, V. Chen, *Water Res.*, 2004, **38**, 2775.
32. I. Konstantinou, T. Albanis, *Appl. Catal. B: Environ.*, 2004, **49**, 1.
33. H. Shen, L. Mi, P. Xu, W. Shen, P. Wang, *Appl. Surf. Sci.*, 2007, **253**, 7024.
34. K. Mackay, R. Mackay, *Introduction to Modern Inorganic Chemistry*, 4<sup>th</sup> Edition, Blacket, 1976, p. 86.
35. G. Shang, H. Fu, S. Yang, T. Xu, *Int. J. Photoenergy*, 2011, **2012**.
36. R. Bacsá, P. Kiwi, *J. Appl. Catal.*, 1998, **16**, 19.
37. M. Rao, K. Rajeshwar, V. Pai Verneker, J. Dubow, *J. Phys. Chem.*, 1980, **84**, 1987.
38. A. Fahmi, C. Minot, B. Siliv, *Phys. Rev. B*, 1993, **47**, 1171.
39. A. Czanderna, C. Rao, J. Henig, *J. Chem. Soc. Faraday Trans. I*, 1988, **54**, 1069.
40. A. Bard, W. Dunn, B. Kraeutler, US Pat., 4264421, 1981.
41. M. Promet, P. Pichat, M. Mathieu, *J. Phys. Chem.*, 1971, **75**, 1216.
42. A. Czanderna, A. Clifford, J. Honig, *J. Am. Chem. Soc.*, 1957, **79**, 5407.
43. M. Straumanis, T. Ejima, W. James, *Acta. Cryst.*, 1961, **14**, 493.
44. P. Jones, J. Hockey, *J. Chem. Soc. Faraday Trans. I*, 1971, **67**, 2679.
45. W. Choi, A. Termin, M. Hoffmann, *J. Phys. Chem.*, 1994, **98**, 13669.
46. K. Smith, V. Hernich, *Phys. Rev. B*, 1987, **35**, 5822.
47. A. Bard, *J. Phys. Chem.*, 1979, **83**, 3146.
48. H. Gerisher, *Photocatalytic Treatment of Water and Air*, Elsevier Science Publishing: Amstrdam, 1993. p. 83
49. S. Sato, J. White, *J. Chem. Phys. Lett.*, 1980, **72**, 83.
50. R. Bickley, *Chem. Phys. Solids and their Surfaces*, 1987, **79**, 118.
51. K. Ghore, Q. Miller, *J. Chem. Soc. Faraday Trans. I*, 1984, **10**, 140.
52. N. Serpone, *EPA Newsletter*, 1977, **59**, 54.
53. M. Anpo, N. Aikawa, S. Kodama, Y. Kobokawa, *J. Phys. Chem.*, 1984, **88**, 26.
54. K. Kawai, T. Sakata, *Chem. Phys. Lett.*, 1980, **72**, 87.
55. R. Breakenridge, W. Hosler, *J. Phys. Chem.*, 1953, **1**, 793.
56. Y. Rosem, B. Thacker, C.Tang, *J. Phys. Chem.*, 1994, **98**, 2739.
57. L. Linsebiglen, T. John, *Surface Science Centre*, 1995, **95**, 753.

58. M. Ward, A. Bard, *J. Phys. Chem.*, 1982, **86**, 3599.
59. A. Bard, *J. Science*, 1980, **207**, 139.
60. S. Nakabayashi, A. Kira, *J. Phys. Chem.*, 1981, **19**, 195.
61. L. Spanhel, M. Haase, H. Weller, A. Henglein, *J. A. Chem. Soc.*, 1987, **109**, 5649.
62. G. Moser, J. Gratzel, N. Serpone, N. Sherma, *J. Am. Chem. Soc.*, 1985, **107**, 8054.
63. S. Sato, *Chem. Phys. Lett.*, 1986, **123**, 126.
64. M. Che, C. Naccache, *Chem. Phys. Lett.*, 1971, **8**, 45.
65. D. Li, N. Ohashi, S. Hishita, T. Kolodiazhnyi, H. Haneda, *J. Solid State Chem.*, 2005, **178**, 3293.
66. J. Jang, H. Kim, S. Ji, J. Jung, B. Shon, J. Lee, *J. Solid State Chem.*, 2006, **179**, 1067.
67. R. Asahi, T. Morikawa, T. Ohwaki, K. Aoki, Y. Taga, *Science*, 2001, **293**, 269.
68. Y. Lin, Y. Tseng, J. Huang, C. Chao, C. Chen, I. Wang, *Environ. Sci. Technol.*, 2006, **40**, 1616.
69. K. Hashimoto, H. Irie, Y. Watanabe, *J. Phys. Chem. B*, 2005, **107**, 5483.
70. S. Livraghi, A. Vatta, M. Giamello, *Chem. Commun.*, 2005, **4**, 98.
71. J. Gole, J. Stout, C. Burda, Y. Lou, X. Chen, *J. Phys. Chem. B*, 2004, **108**, 1230.
72. A. Ghicov, J. Macak, H. Tsuchiy, J. Kunzo, P. Schmuki, *J. Nanoscience Lett.*, 2006, **6**, 1080.
73. M. Hoffmann, S. Martin, W. Choi, D. Bahnemann, *Chem. Rev.*, 1995, **95**, 6974.
74. V. Kireev, *Physical Chemistry*, 3<sup>rd</sup> Edition, Mir Publishings, 1977, p.126.
75. A. Fujishima, T. Rao, D. Tryk, *J. Photochem. Photobiol. C*, 2000, **1**, 1.
76. D. Li, H. Haneda, S. Hishita, N. Ohashi, *Chem. Mater.*, 2005, **17**, 2588.
77. O. Diwald, T. Thompson, T. Zubkov, G. Goralski, S. Wakk, J. Yates, *J. Phys. Chem. B*, 2004, **108**, 6004.
78. Y. Nosaka, M. Matsushita, J. Nishino, Y. Nosaka, *Sci. Technol. Adv. Mater.*, 2005, **6**, 143.
80. H. Maruska, A. Gosh, *Sol. Energy. Mater.*, 1979, **91**, 237.
81. S. Zhang, L. Song, *Catal. Commun.*, 2009, **10**, 1725.
82. N. Goncalves, J. Garvalho, Z. Lima, J. Sasaki, *Mater. Lett.*, 2012, **72**, 36.
83. C. Damm, *J. Photochem. Photobiol. A: Chem.*, 2006, **181**, 279.
84. S. Livraghi, M. Chierotti, E. Giamello, G. Magnacca, M. Paganini, G. Cappelletti, C. Bianchi, *J. Phys. Chem. C*, 2008, **112**, 17244.
85. P. Awati, S. Awate, P. Shah, V. Ramaswamy, *Catal. Commun.*, 2003, **4**, 293.
86. D. Haneda, S. Hishita, N. Ohashi, *Chem. Mater.*, 2005, **17**, 2588.
87. C. Valentin, G. Pacchian, A. Selloni, *Phys. Rev. B*, 2004, **70**, 91.

88. J. Noh , J. Schwarz, *J. Colloid Interface Sci.*, 1989, **130**,157.
89. P. Tewari, A. Campbell, *J. Colloid Interface Sci.*, 1982, **55**, 531.
90. Y. Bernbe, P. De Bruyn, *J. Colloid Interface Sci.*,1968, **27**, 305.
91. H. Gerischer, *Electrochim. Acta.*, 1993, **38**, 3.
92. V. Ramaswamy, N. Jagtap, S. Vijayanand, D. Bhangе, P. Awati, *Mater. Res. Bull.*, 2008, **43**, 1145.
93. S. Lakshmi, R. Renganathan, S. Fujita, *J. Photochem. Photobiol. A: Chem.*, 1995, **88**, 163.
94. N. Xu, Z. Shi, Y. Fan, J. Dong, J. Shi, M. Hu, *Ind. Eng. Chem. Res.*, 1999, **38**, 373.
95. H. Habibi, A. Hassanzadeh, S. Mahdavi, *J. Photochem. Photobiol. A: Chem.*, 2005, **172**, 89.
96. H. Yamashita, Y. Ichihashi, M. Harada, G. Stewart, M. Fox, M. Anpo, *J. Catal.*,1996, **127**, 97.
97. A. Mills, J. Wang, *J. Photochem. Photobiol. A: Chem.*, 1999, **127**, 123.
98. N. Naskar, S. Pillay, M. Chant, *J. Photochem. Photobiol. A: Chem.*, 1998, **113**, 257.
99. H. Irie, Y. Watanabae, K.Hashimoto, *J. Phys. Chem.*, 2003, **107**, 5483.
100. C. Wu, J. Chern, *Ind. Eng. Chem. Res.*, 2006, **45**, 6450.
101. C. Damm, D. Voltzke, G. Israel, *J. Photochem. Photobiol. A: Chem.*, 2005, **174**, 171.
102. R. Hong, J. Qian, J. Cao, *Powder Technol.*, 2006, **163**, 160.
103. D. Yang, X. Ni, W. Chen, Z. Weng, *J. Photochem. Photobiol. A: Chem.*, 2008, **195**, 323.
104. C. Damm, R. Herrmann, G. Israel, F. Muller, *Dyes and Pigments*, 2007, **74**, 335.
105. A. Balamurugan, S. Kannan, V. Selvaraj, S. Rajeswari, *Artif. Organs.*, 2004, **18**, 41.
106. X. Ni, J. Ye, C. Dong, *J. Photochem. Photobiol. A: Chem.*, 2006, **19**, 181.
107. R. Hussain, D. Mohammad, *Turk. J. Chem.*, 2004, **28**, 725.
108. P. Pichat, J. Herrmann, J. Disdier, H. Courbon, M. Mozzanega, *Nouv. J. De Chim.*, 1982, **6**, 559.
109. E. Borgarello, E. Pelizzetti, *Chim. Ind.*, 1983, 65, 474.
110. R. Ojah, S. Dolui, *Sol. Energy Mater. Sol. Cell*, 2006, **90**, 1615.
111. P. Harey, R. Rudham, S. Ward, *J. Chem. Soc. Faraday Trans. I*, 1 983, **79**, 2975
112. P. Pichat, J. Herman, J. Disdier, M. Mozzanega, *Nouv. J. De Chim.*, 1981, **5**, 627.
113. M. Kawai, S. Naito, K. Tamaru, T. Kawai, *Chem. Phys. Lett.*, 1983, **98**, 377.

114. B. Faust, M. Hoffmann, D. Banemann, *J. Phys. Chem.*, 1989, **93**, 6371.
115. W. Xia, D. Cook, *Polymer*, 2003, **44**, 79.
116. P. Vallittu, *J. Oral Rehabil.*, 1999, **26**, 208.
117. M. Yatab, H. Seki, N. Shirasu, *J. Oral Rehabil.*, 2001, **28**, 180.
118. C. Hsu, L. James, *Polymer*, 1993, **34**, 4506.
119. V. Ramamuthy, K. Schanze, (Eds), *Organic Photochemistry, Vol. 1*, Marcel Dekker, New York, 1997, p. 295.
120. K. Fujimori, G. Trainaor, *Polym. Bull.*, 1983, **9**, 204.
121. R. Ojah, S. Dolui, *Bioresource Technology*, 2006, **97**, 1529.
122. K. Reddy, B. Baruwati, M. Jayalakshmi, M. Rao, S. Manorama, *J. Solid State Chem.*, 2005, **178**, 3352.
123. J. Wang, D. Tafen, J. Lewis, Z. Hong, M. Li, *J. Am. Chem. Soc.*, 2009, **131**, 12290.
124. D. Doskacilova, B. Schneider, J. Jakes, *J. Magn. Reson.*, 1978, **29**, 79.
125. R. Hang, B. Feng, G. Lui, S. Wang, H. Li, J. Ding, Y. Zheng, D. Wei, *J. Alloys and Compounds*, 2009, **476**, 612.
126. M. Goodner, C. Bowman, *Chem. Eng. Sci.*, 2002, **57**, 887.
127. A. Brien, C. Bowman, *Macromol. Theory Simul.*, 2006, **15**, 176.
128. C. Hamford, *J. Chem. Soc. Faraday Trans. I*, 1982, **78**, 855.
129. A. North, G. Reed, *J. Chem. Soc. Faraday Trans. I*, 1961, **57**, 859.
130. A. Henglein, *Chem. Rev.*, 1989, **8**, 1861.
131. X. Wang, S. Meng, X. Zhang, H. Wang, W. Zhong, Q. Du, *Chem. Phys. Lett.*, 2007, **444**, 292.
132. J. Wang, X. Ni, *J. Appl. Polym. Sci.*, 2008, **108**, 3552.
133. A. Stroyuk, I. Sorban, S. Kuchmiy, *J. Photochem. Photobiol. A: Chem.*, 2007, **192**, 98.

## Chapter-three: Modification of the photocatalytic activity of titanium dioxide by metal doping

### 3-1 Introduction

The anatase polymorph of  $\text{TiO}_2$  is the most commonly used photocatalytic material, which can be used as an anti-bacterial agent due to its high oxidation activity. One disadvantage of this material<sup>(1)</sup> is its high bandgap energy, which is 3.2 eV, meaning that the absorption edge of  $\text{TiO}_2$  occurs at about 390 nm. Consequently, the solar spectrum cannot be efficiently used in heterogeneous photocatalytic reactions with this material<sup>(2)</sup>. The nature of the surface properties of titania play a significant role in its photocatalytic activity. The activity of the doped metals depends on some factors such as oxidation state and the type of defects that can be created within the lattice of the semiconductor. Metal-doped titania has been studied widely in photochemical and photocatalytic systems, but the results of such studies are often conflicting<sup>(3)</sup>. In some cases, metal doping titania leads to a reduction in activity of the photocatalysed reaction and the type and the amount of the doped metal can play a significant role. Generally, photocatalytic processes performed using the solar spectrum would be more economical than using artificial UV light.

Importantly, in relation to this, it has been found that doping titania with trace amounts of some metals can shift its absorption to the visible region<sup>(3)</sup>. Much effort has been directed to modify the spectral properties of titania to cover a wide- range of the spectrum. One way to do this is spectral sensitization of  $\text{TiO}_2$  using dyes such as perylene derivatives, phthalocyanines, porphyrins or Ru(II)-complexes but the long-term stability of sensitized  $\text{TiO}_2$  photocatalysts may be limited by self- degradation of the sensitizing dyes on the catalyst surface<sup>(4)</sup>. Doping  $\text{TiO}_2$  with transition metal ions may be a good alternative to dye sensitisation. It was found that doping  $\text{TiO}_2$  by metal ions with a valence higher than 4+ increases the photoactivity of  $\text{TiO}_2$ <sup>(5)</sup>. Study of the photoelectric properties of the photocatalyst combined with photocatalytic activity tests is a good tool to gain an improved understanding of doping effects<sup>(5)</sup>. It has been found that doping  $\text{TiO}_2$  with  $\text{Mo}^{\text{V}}$ ,  $\text{Cr}^{3+}$  or  $\text{Fe}^{3+}$  leads to reduction of the charge carrier lifetime in the surface of the modified catalyst because the dopants occupy lattice sites and can act as recombination centres leading to inhibition the photocatalytic activity of the catalyst<sup>(5)</sup>. Generally, doping low concentrations of some metals can extend the absorption of the photocatalyst toward the visible region of the spectrum. In addition, some metals of group (VIII), such as Pd and Pt can improve the photocatalytic activity of the doped catalyst<sup>(6)</sup>. The study of

metal deposition on the surface of titania relates to the properties of metal/ metal oxide interface. This can affect the properties of both the metal and the semiconductor. For example, doping titania with small particles of gold ions can enhance the photocatalytic activity of titania, while silver gives a different activity<sup>(7,8)</sup>. Generally, reactive metals e.g Fe, Al, Mg, Cu and Zn can reduce titania and become oxidized, which facilitates their deposition in the lattice of titania. Growth of the doped metallic particles can occur in two dimensions and starts on the top of the interfacial layer that is composed of both reduced titania and oxidized metal. On the other hand, deposition of non- reactive metals such as silver, platinum, copper and gold does not result in reduction of titania and these metals can be deposited by three dimensional crystal growth<sup>(9)</sup>. It has been found that deposition of titania with chromium result in strong interaction between the metal and the substrate and gives two-dimensional growth leading to the formation of an interfacial layer with titania, composing reduced titania and oxidized Cr<sup>(10)</sup>. Deposition of titania with Cr can induce two states within the band gap region at 3eV and 1eV below the Fermi level, reflecting both partially filled Cr 3d and Ti 3d states. The character of these states was studied using resonant photoemission and it has been concluded that the state at -3 eV is a Cr 3d state and the -1 eV state is a Ti 3d state<sup>(11)</sup>. Diebold and co-workers reported a distinguishable gap state for iron doped titania, and they suggested a weaker interaction for this case in comparison with Co and Cr dopants<sup>(12)</sup>. The same result was reported by Shao and co-workers when they studied the properties of titania supported by cobalt metal and cobalt oxide, where they proposed a weak interaction between Co and titania<sup>(13)</sup>. Generally, doping titanic with some metals can improve photocatalytic activity of many reactions. In this context, photocatalytic decomposition of some pollutants in wastewater can be performed over these systems.

The photodegradation of organic and inorganic pollutants on the surfaces of the semiconductors has become a major subject of research<sup>(14-16)</sup>. For example, textile and other factories produce different types of organic dye. These are considered as an important class of aquatic pollutants and are becoming a major source of environmental contamination. For this reason, many research studies have been focused on the treatments of coloured wastewater. However, because of the complexity and variety of dyestuffs that are used in the dyeing processes, it is difficult to find a suitable treatment procedure that completely covers the effective elimination of all types of dyes. Biochemical oxidation methods particularly suffer from significant limitations because most of the dyes that are commercially available have a high resistance toward aerobic microbial degradation. Furthermore, these dyes may be converted to toxic or carcinogenic compounds<sup>(17)</sup>. On the other hand, using physical methods such as flocculation and adsorption on activated

charcoal are not effective and merely transfer the pollutant to other media, thus causing secondary pollution<sup>(17)</sup>. Due to all these potential problems, semiconductors, and especially titania are the most effective and commonly studied systems for organic dye degradation. The heterogeneous photocatalytic degradation of a large number of organic pollutants in water has been widely studied applying bare and doped titania and in almost all cases this route was found to be effective from an environmental and cost point of view. Both the surface as well as intrinsic properties of titania can play a key role in influencing the photocatalytic activity in these processes<sup>(18-21)</sup>. In addition to use titania in the treatment of pollution of air and soil, there are some other materials can be used in this process such as solid acid catalysts. For solid acid catalysis processes, doping small concentrations of transition metals can enhance the activity of semiconductors. This is dependent on some considerations that must be met. These are metal concentration, the energy level of the dopants, available oxidation states and the type of defects that can be created in the lattice of the semiconductor. Despite widespread study, there is still a degree of disagreement in the literature relating to metal doped titania<sup>(22-26)</sup>.

### **3-2 Band structure of semiconductors**

In the case of small crystallites, it can be considered that there are an infinite number of atoms within the structure of the solid so that, the overlapping of the individual atomic orbitals and electronic states can lead to the formation of a continuous electronic band structure in the solid. This can lead to the creation of a valence band and a conduction band, and the difference between energy levels of these two bands determines the photoactivity and excitation energy for semiconductors. For a semiconducting transition metal oxide such as titanium dioxide, these levels are determined by bonding and anti-bonding characteristics of the electrons in the molecular orbitals (MOs)<sup>(27)</sup>. However, the combination of these MOs produces the VB, which is filled by electrons at 0 K. At the same time, antibonding MOs combine to form the CB, which for  $d^0$  transition metal oxide such as  $\text{TiO}_2$  that comprises  $\text{Ti}^{\text{IV}}$  is empty at 0 K<sup>(28)</sup>. The energy separation between VB and CB is referred to as the bandgap. Electrons transfer from VB into the CB by absorption of photons of sufficient energy. For a semiconductor materials of transition metal oxide at 0 K, all the energy states down to the FL are fully occupied with electrons which relates to the HOMO level at the same time all energy states above Fermi level are empty which relates to the LUMO<sup>(29)</sup>. The position of Fermi level within the bandgap of the semiconductor depends on some factors such as temperature, and whether the semiconductor is intrinsic or extrinsic. For n-type semiconductors, Fermi level lies closer to the CB while in case of p-type semiconductors,

Fermi lies closer to the VB. The position of FL in intrinsic semiconductor, p-type and n-type is shown in the following figure:

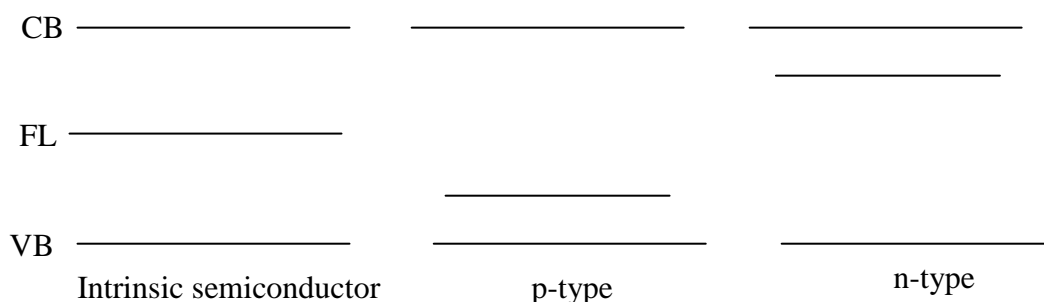


**Figure 3-1:** Fermi level position in an intrinsic, p-type and n-type semiconductor.

### 3-3 Deposition of metals on TiO<sub>2</sub>

Several methods have been used to load metals on titania, including photodeposition<sup>(30)</sup>, impregnation<sup>(31)</sup> and ion-exchange<sup>(32)</sup>. The photodeposition method involves using UV light irradiation for a suspended powder of the semiconductor in a solution containing a metal salt as well as an electron donor such as ethanoic acid or ethanal. Kraeutler and Bard first used this method in 1978 who reported preparation of Pt/ TiO<sub>2</sub> comprising highly dispersed small clusters of the metal formed by irradiation with UV light at low temperature, which minimised surface diffusion of the metal atoms<sup>(33)</sup>. Dunn and Bard studied the effect of pH on the deposition of Pt on titania and reported that the higher deposition rate was in the pH range 5-6. They showed that photodeposition of Pt can occur even in the absence of ethanoic acid, since H<sub>2</sub>O acted as an electron donor being oxidized with lower efficiency<sup>(34)</sup>. In another procedure, Grätzel and co-workers<sup>(35,36)</sup> and Mills<sup>(37)</sup> found that metal ions can be reduced by conduction band electrons that are produced upon excitation of titania by UV light, and the resultant photoholes contribute to the oxidation of methanal and methanol. In the impregnation method, powder semiconductor is impregnated with an aqueous solution of metal salt at a desired temperature, then separated and washed with water and calcined at high temperature to remove unreacted salts from the catalyst. The salts that are commonly used are the nitrate salts of the metals<sup>(38)</sup>. Dybowski and co-workers prepared titania doped with Rh by using Rh(NO<sub>3</sub>)<sub>2</sub> with a small amount of aqueous ammonia. Using aqueous ammonia can increase the pH of the mixture forming a rhodium/ammonia complex. This technique resulted in a high dispersion of the Rh on the titania<sup>(39)</sup>. In the ion-exchange method, Pt doped TiO<sub>2</sub> can be prepared by dropwise addition of hexachloroplatinic acid (H<sub>2</sub>PtCl<sub>6</sub>) to a stirred aqueous suspension of titania. Then the resultant slurry is dried and then reduced in a flow of hydrogen<sup>(40)</sup>. It has been found that ion exchange with Pt(NH<sub>3</sub>)<sub>4</sub>(OH)<sub>2</sub> can result in a doped catalyst with platinum particles more highly dispersed than those which result from the impregnation

method and ion exchange using  $\text{H}_2\text{PtCl}_6$  <sup>(40)</sup>. In 2000, Anpo reported a new preparation route towards doped titania photocatalysts which gives a good response to light absorption in the visible region. This modified titania was prepared by an advanced high voltage ion implantation method <sup>(41)</sup>. According to this technique, the electronic properties of titania were modified by bombarding them with high energy metal ions. Ions of metals such as Cr and V were injected deep into the bulk of titania by using high acceleration energy, following which samples were then calcined in air at 450 °C. The resultant doped titania was used effectively in the photocatalytic decomposition of NO to  $\text{N}_2$  and  $\text{O}_2$  under illumination with visible light <sup>(41)</sup>. The same technique has been used for doping other transition metals such as Fe, Ni and Mn, for which the resultant titania exhibited photoactivity in the visible region <sup>(42)</sup>. Titanium dioxide doped with iron has been synthesized by a hydrothermal method, in which titanium (IV) tetra-tert-butoxide and  $\text{FeCl}_3$  were mixed in octanol alcohol and heated at 230 °C for 2 hours in the presence of water. The powder formed was then rinsed, dried and calcined at 560 °C. The resultant  $\text{Fe}/\text{TiO}_2$  was photocatalytically efficient for the photodegradation of some dyes under illumination in both the UV and the visible regions <sup>(43)</sup>. In another study, a series of vanadium doped titania samples were prepared by two modified sol-gel methods, in the first one, vanadyl acetylacetonate was dissolved in butanol alcohol and then mixed with titanium butoxide by water resulting in esterification of acetic acid and butanol. The solution was then dried 150 °C and calcined at 400 °C. The second method involved the slow addition of the solutions of vanadium chloride, ethanol and titania into cooled acidic solution at 0 °C. The final product then was dried and calcined to give  $\text{V}/\text{TiO}_2$ . This modified catalysts showed activity in the visible region <sup>(44)</sup>.

### 3-3-1 Bandgap modification by metal doping

There are many methods that can be used to dope titania with metals. For example, the implantation technique is a better alternative than the chemical sol-gel technique when used for doping of transition metals ions into the  $\text{TiO}_2$  lattice. Using this method results in a significant red shift in the absorption edge of titania <sup>(45,46)</sup>. However, some metals such as Fe, V, Cr, Mn, Co, N and Cu have been doped into the bulk of titania substituting  $\text{Ti}^{\text{IV}}$  species in the lattice using the ion implantation method <sup>(47)</sup>. Doping titania with these metals causes a red shift in the absorption edge of titania, which may result from the overlap between Ti 3d levels and the d levels of these metals <sup>(45-47)</sup>. It has been reported that, Fe doping in the titania by chemical routes produces impurity states within its bandgap <sup>(48-50)</sup>. This leads to a red shift in the bandgap of titania as a result of substitution of  $\text{Ti}^{\text{IV}}$  sites by  $\text{Fe}^{3+}$ . When increasing the amount of Fe dopant, visible light absorption

was increased but higher visible light activity was achieved at lower Fe content. This effect may be related to the role of these species in the trapping and transfer of both photogenerated electrons and holes to the surface of titania. For high dopant concentrations, these ions act as recombination centres that give lower photocatalytic activity<sup>(48, 49, 51)</sup>. In another study, it was reported that V doping of titania films by a dip coating technique resulted in a higher photocatalytic activity under day light irradiation and visible light irradiation simultaneously<sup>(52)</sup>. Both these observations can be explained in terms of bandgap narrowing which is caused by doping these metals within the titania lattice, resulting in a higher activity for the doped samples in comparison with the neat titania<sup>(53, 54)</sup>. Pt can be doped into titania by the photodeposition method as metallic particles on the titania surface, and can be used in this manner to scavenge photogenerated electrons due to its suitable Fermi level energy position<sup>(55, 56)</sup>. It was reported that doping Pt on titania induced visible light activity as doped Pt can introduce intergap impurity states which assist valence band electrons absorbing visible light. These states did not act as recombination centres as indicated by improvement in both the UV and the visible light activity for Pt doped titania<sup>(57)</sup>. Other transition metals such as Zn, Ag, and lanthanides with ionic radii greater than that of  $\text{Ti}^{\text{IV}}$  cannot substitute at the Ti sites in the titania lattice<sup>(58- 60)</sup>. For example,  $\text{Zn}^{2+}$  was found to be dispersed in the form of ZnO clusters on the surface of titania forming a coupled semiconductor system<sup>(58)</sup>. It was found that the content of the surface oxygen vacancies in the titania surface was increased with increasing dopant content. This generated some energy states close to the conduction band of titania and therefore interfacial coupling between ZnO and  $\text{TiO}_2$ . These effects lead to the narrowing of the band gap of titania, which resulted in photocatalytic activity under irradiation with visible light<sup>(58)</sup>. Another study reported that doping Ag didn't modify the band gap of titania, but the resultant material was active in the photocatalytic degradation of rhodamine 6G under illumination with the visible light as a result of dye sensitization. For this system, irradiation with visible light would lead to quick scavenging of the photogenerated electrons by Ag that inhibits carrier recombination<sup>(60)</sup>.

### **3-3-2 Mechanism of photoactivity of neat and doped titania**

The mechanism for photoexcitation of the photocatalysts is initiated by absorption of light with a sufficient energy ( $h\nu \geq E_g$ ). Upon excitation a conduction band electron and valence band hole are generated on the surface of the catalyst. Photoexcitation events can be presented in the following figure:

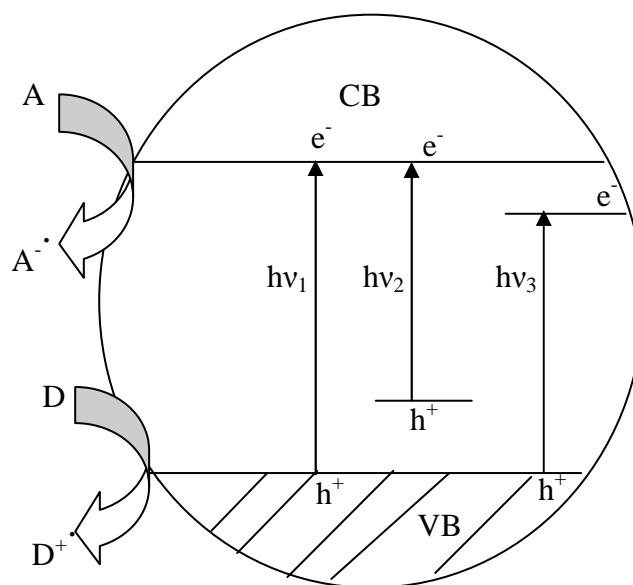


**Figure 3-2:** Photoexcitation events over neat and doped titania:  $h\nu_1$  bare titania,  $h\nu_2$  doped with non-metal, and  $h\nu_3$  doped with metal.

When pure titania is excited by absorption of a light with a suitable energy ( $h\nu \geq E_g$ ), an electron is transferred to the conduction band, leaving a positive hole in the valence band as in the path ( $h\nu_1$ ). There are several paths for the electron and hole. They may recombine again, which leads to dissipation of their energy as light and/or thermal energy. In addition, they can be trapped on surface sites or react with electron donors/ acceptors that are pre-adsorbed on the surface of the catalyst or with the surrounding charged particles that may be present in the electrical double layer. Reaction between electron donor species and holes can occur, species can be produced which possesses a high oxidizing potential. These reactive species e.g. OH radicals,  $O_2^{\cdot -}$ ,  $H_2O_2$  and  $O_2$  can play an important role in the mechanism of the photocatalytic reaction<sup>(61)</sup>. Visible light photocatalytic activity for example, metalized titania (Pt/  $TiO_2$ ) results from the new energy levels that are produced within the bandgap, so that electrons can be excited from the VB to these defect states below the CB by absorption light with suitable energy ( $h\nu_3$ ). This can lead to excitation of the photocatalyst in the visible region. In addition, the dopants can improve trapping of the excited electrons leading to reduction of the rate of the recombination reaction. These two factors can lead to enhance the photocatalytic activity of the doped titania<sup>(62- 64)</sup>.

### 3- 3-3 The aim of the project

The aim of this project is to investigate both the photoreponse and the photocatalytic activity for titania upon doping with  $\text{Al}^{3+}$ ,  $\text{Cu}^{2+}$  and  $\text{Co}^{2+}$ . The metal-doped samples were also doped with nitrogen to produce co-doped samples of titania. The photocatalytic activities of the doped samples were investigated for the photocatalytic degradation of methylene blue. In addition, the doped and co-doped samples were used in photocatalytic polymerization of methyl methacrylate.

## 3- 4 Results and Discussion

### 3-4-1 Doping titania with metal

Doping titanium dioxide (anatase, rutile and P25) with aluminium, copper and cobalt was performed by the impregnation method. The weight percentage of the dopants introduced was determined using atomic absorption. The results are shown in the following table:

**Table 3-1:** The weight percentage of the dopants metal ions doped titania samples.

Catalyst	Co wt% $\pm 0.10$	Cu wt% $\pm 0.10$	Al wt% $\pm 0.12$
anatase	1.25	1.32	1.40
rutile	1.30	1.26	1.31
P25	1.28	1.22	1.30

#### 3-4-1-1 XRD patterns for metal doped titania

XRD patterns for titania doped with Al, Co and Cu are almost similar to those of the pure  $\text{TiO}_2$  parent. For the doped anatase, the main peak of anatase remained at  $2\theta = 25.5^\circ$  and all the peaks for anatase doped with copper, cobalt and aluminium were slightly broader than that of the parent sample. For rutile, the main peaks for its doped form with Al, Cu and Co were reduced in intensity compared to the undoped form, but the position of these peaks also did not change. For P25 doped with Co, Cu and Al the reflections were lower intensity than those for the undoped one. Generally, doping titania with metal ions in this range didn't affect its crystalline structure. The coherent diffraction domain size of titania was apparently decreased upon doping and/or disorder in the lattice was increased. Characteristic reflections of the dopant metals or metal oxides were not evident in any of

these samples. If this was apparent it would have indicated that the metal ions had formed a segregated phase<sup>(65-67)</sup>. The XRD patterns for the neat and metal-doped titania samples are shown in the following figures:

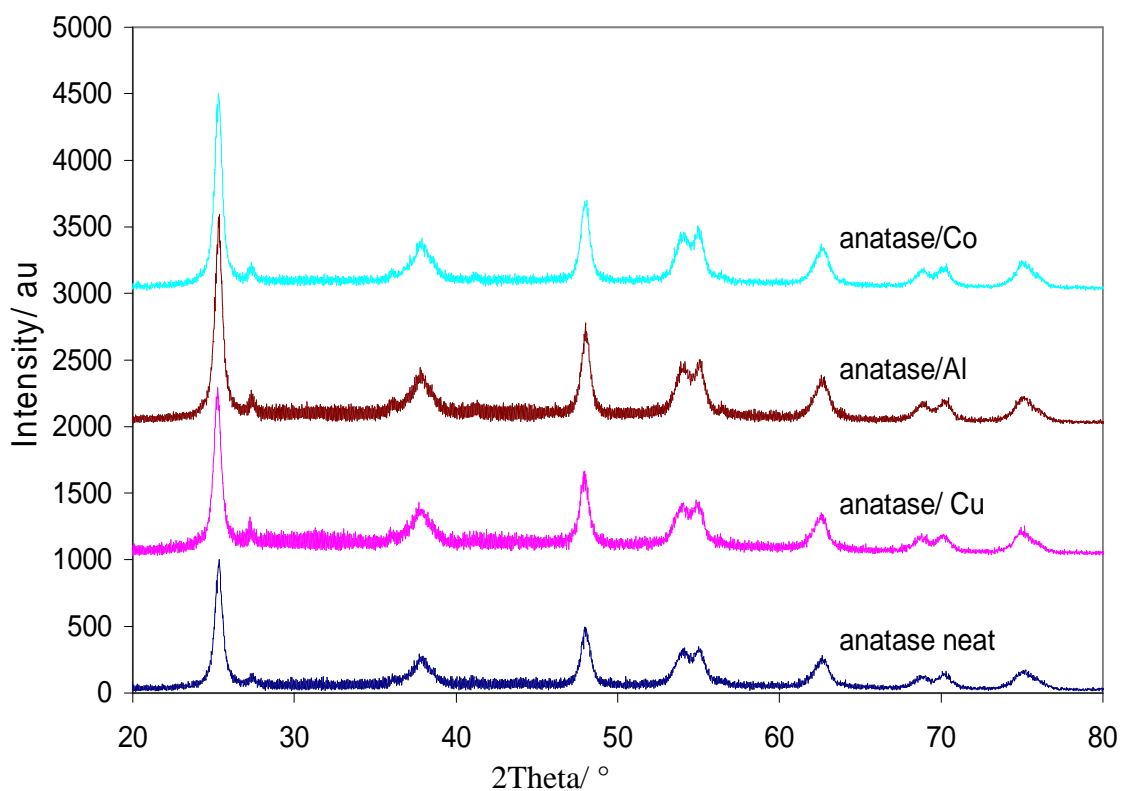


**Figure 3-3:** XRD patterns for neat and Al, Cu and Co doped anatase.

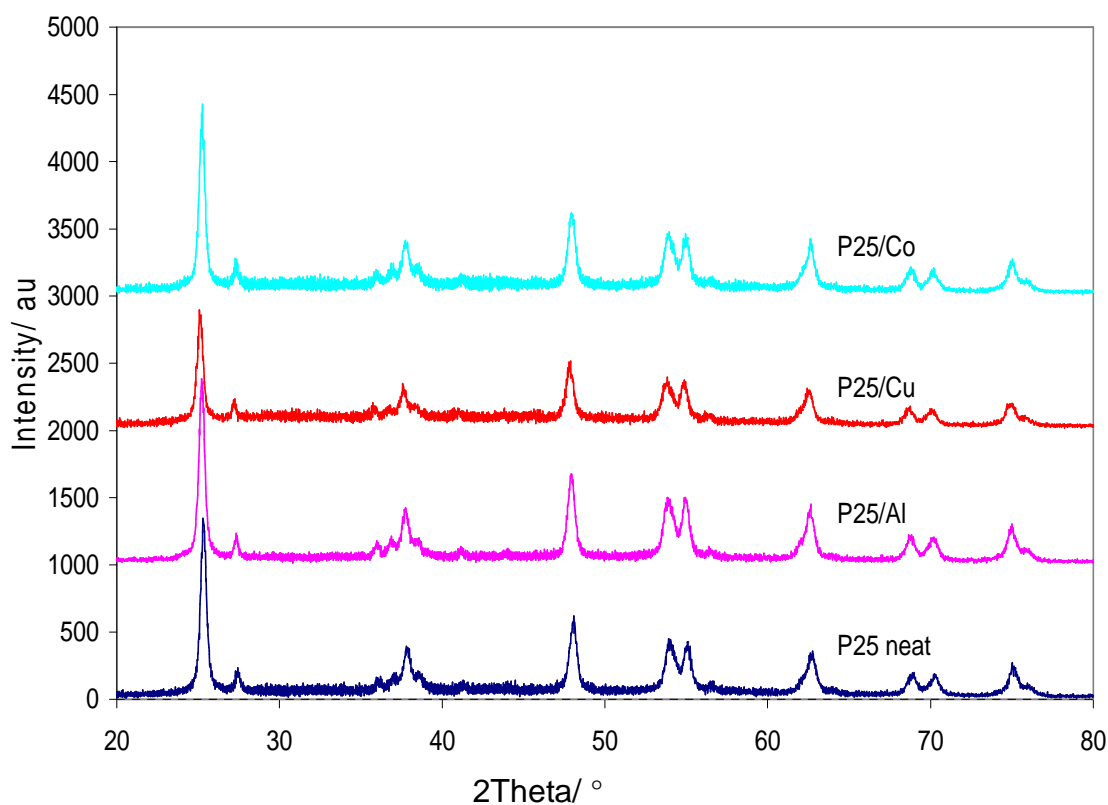


**Figure 3-4:** XRD patterns for neat and Al, Cu and Co doped P25.

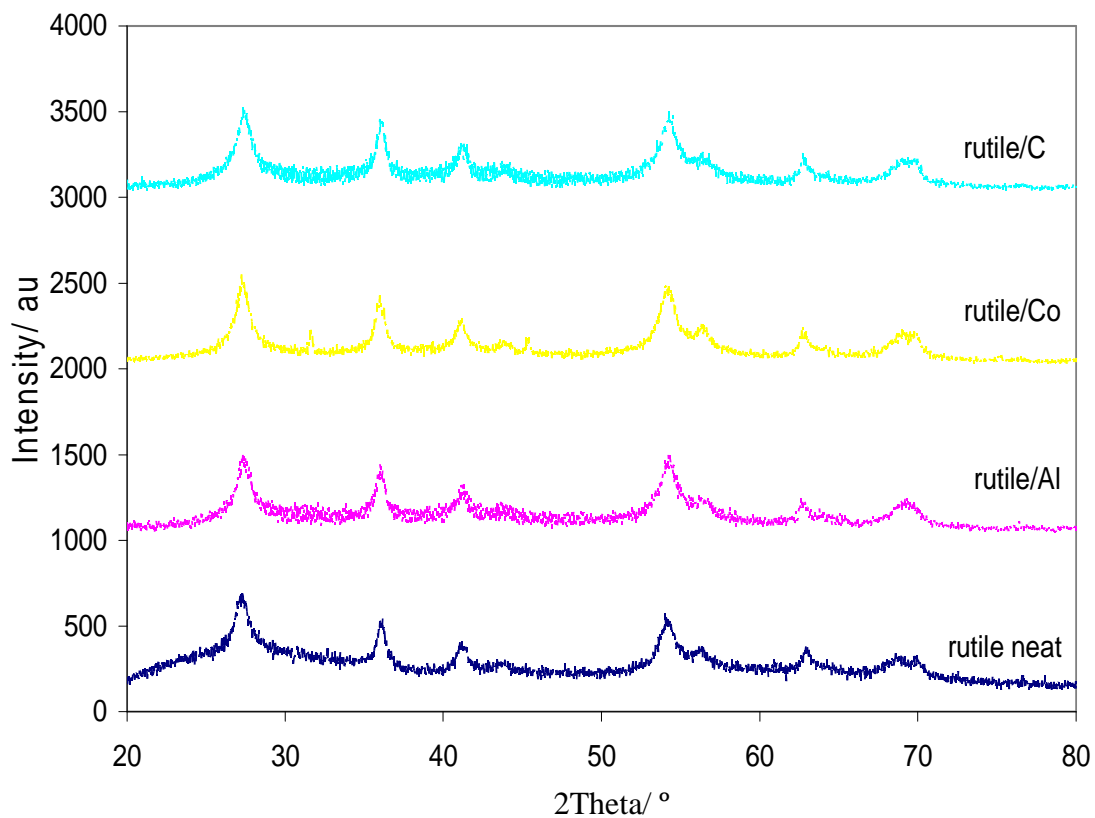


**Figure 3-5:** XRD patterns for neat and Al, Cu and Co doped rutile.

### 3-4-1-2 UV-visible spectra for doped titania with Al, Co and Cu

The UV- visible spectra for parent and metalized TiO<sub>2</sub> (rutile, anatase and P25) are shown in the following figures:

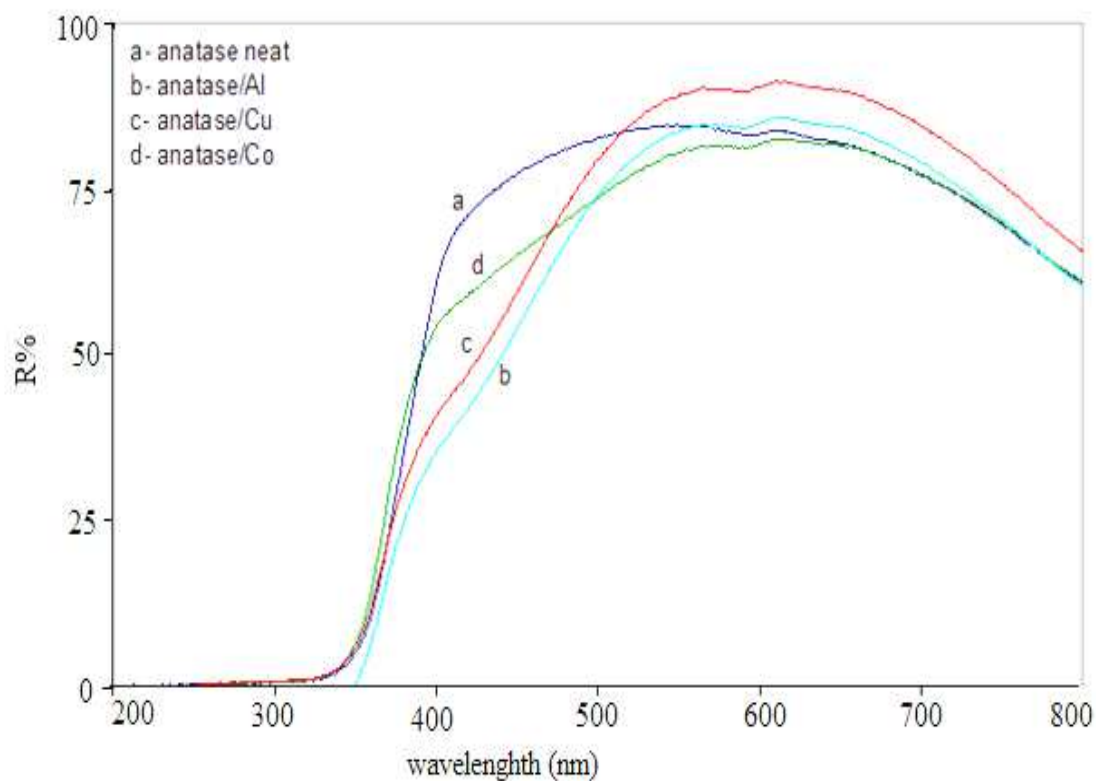


**Figure 3-6:** UV-visible diffuse reflection spectra for metal doped anatase.

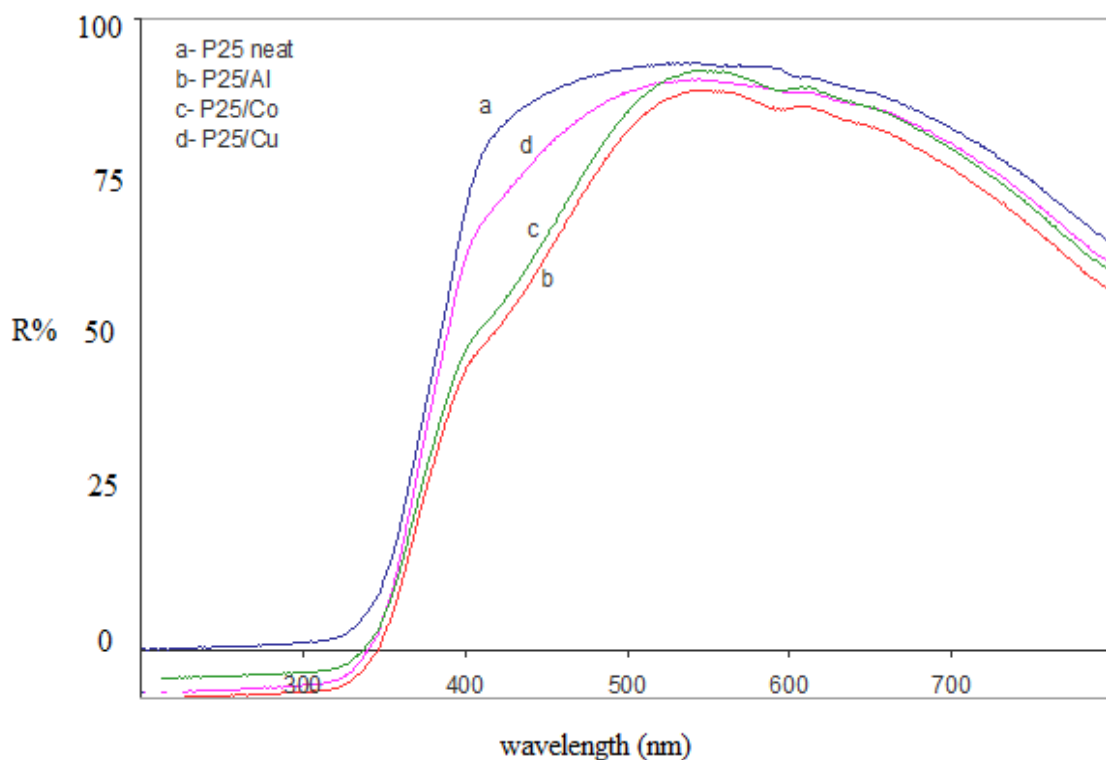


**Figure 3-7:** UV-visible diffuse reflection spectra for metal doped P25.

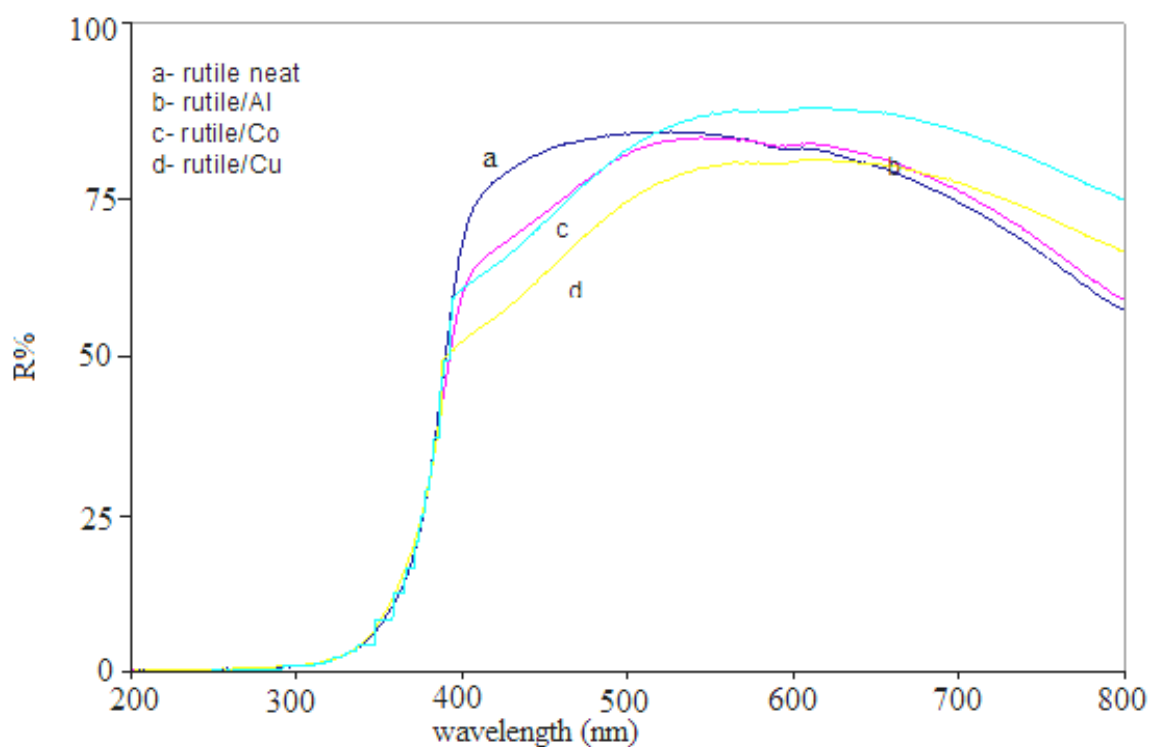


**Figure 3-8:** UV-visible diffuse reflection spectra for neat and metal-doped rutile.

From these figures, it can be seen that all the doped samples with metal have extended absorption within the visible region of the spectrum in comparison with the parent titania samples. The red shift in the absorption of metal-doped titania ( $M/TiO_2$ ) is probably due to the narrowing of the bandgap and charge transfer transition that occurs between d electrons

of the dopant metal ions and the conduction band or valence band of titania<sup>(68)</sup>. The doped metals may form dopant energy levels within the original band gap of titania below the conduction band. These impurity levels can cause a red shift in the absorption spectra of the doped samples so that, when excitation occurs by absorption of light with sufficient energy. Electronic transitions occur from the VB of titania to these dopant levels, and then from these dopant levels into the conduction band of titania<sup>(69,70)</sup>. This can lead to enhanced absorption and cause a red shift in the spectra of the doped samples. Generally, these samples showed a variation in their shift towards visible region. For anatase, Al doped anatase showed higher shift while Co doped anatase showed lower shift. For doped rutile, higher shift can be seen with anatase doping with copper while lower shift can be seen for Al doped rutile. For metal-doped P25, higher shift was found for Al doped P25 and lower shift for Cu doped P25. This variation absorption edge for these samples arises from formation of different interbands with doped titania.

#### **3-4-1-3 Specific surface area (BET)**

The specific surface areas for the metal doped samples were measured by the BET method. The particle sizes were calculated from XRD patterns for neat and doped samples using the Scherrer equation assuming that they were isotropic and that there was no contribution of lattice disorder to reflection widths. The specific surface areas for the doped samples are shown in the following table:

**Table 3-2:** BET specific surface areas for metal-doped titania. The average particle size was determined by applying Scherrer equation.

Catalyst	BET (m <sup>2</sup> /g) ± 1	Particle size by XRD (nm)
anatase neat	112	16.5
anatase/Al	120	16.4
anatase/Co	116	16.2
anatase/Cu	116	16.3
P25 neat	50	18.5
P25/Al	55	18.4
P25/Co	54	18.3
P25/Cu	52	18.2
rutile neat	148	12.5
rutile/Al	154	12.3
rutile/Co	152	12.4
rutile/Cu	152	12.3

From these results, it can be seen that the surface area for the metal-doped samples was apparently increased slightly in comparison with the parent samples although the changes may be within experimental error. The reason for this is possibly that loading these metals prevented aggregation of the powder and prevented crystal growth when calcining the metal-doped samples at 300 °C<sup>(71)</sup>.

### **3-5 Point of zero charge of the metal doped titania**

The point of zero charge (PZC) for the doped titania with metals was evaluated by potentiometric titration<sup>(72)</sup>. Results of the titration are plotted as a volume of the added acid against the pH of the mixture, and the PZC is taken as the point of intersection with the blank pH curve as shown. These results are summarised in Table 3-3, and Figures (3-9) – (3-11).

**Table 3-3:** PZC values for metal doped titania.

Catalyst	PZC (pH) ± 0.10
anatase neat	6.20
anatase/ Co	6.60
anatase/Cu	6.65
anatase/Al	6.75
P25 neat	6.00
P25/ Co	6.55
P25/ Cu	6.45
P25/Al	6.65
rutile neat	5.50
rutile/Co	6.20
rutile/Cu	6.15
rutile/ Al	6.30

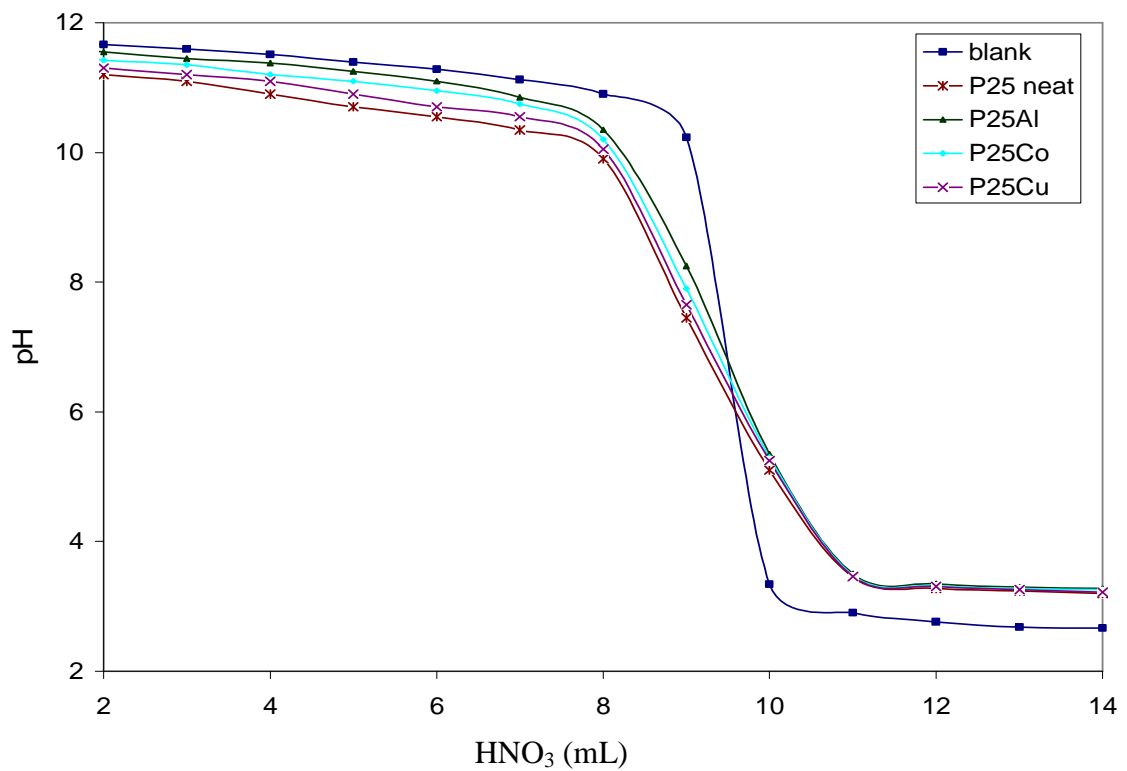


**Figure 3-9:** PZC values for neat and metal-doped P25 samples, the average error bar ± 0.1.

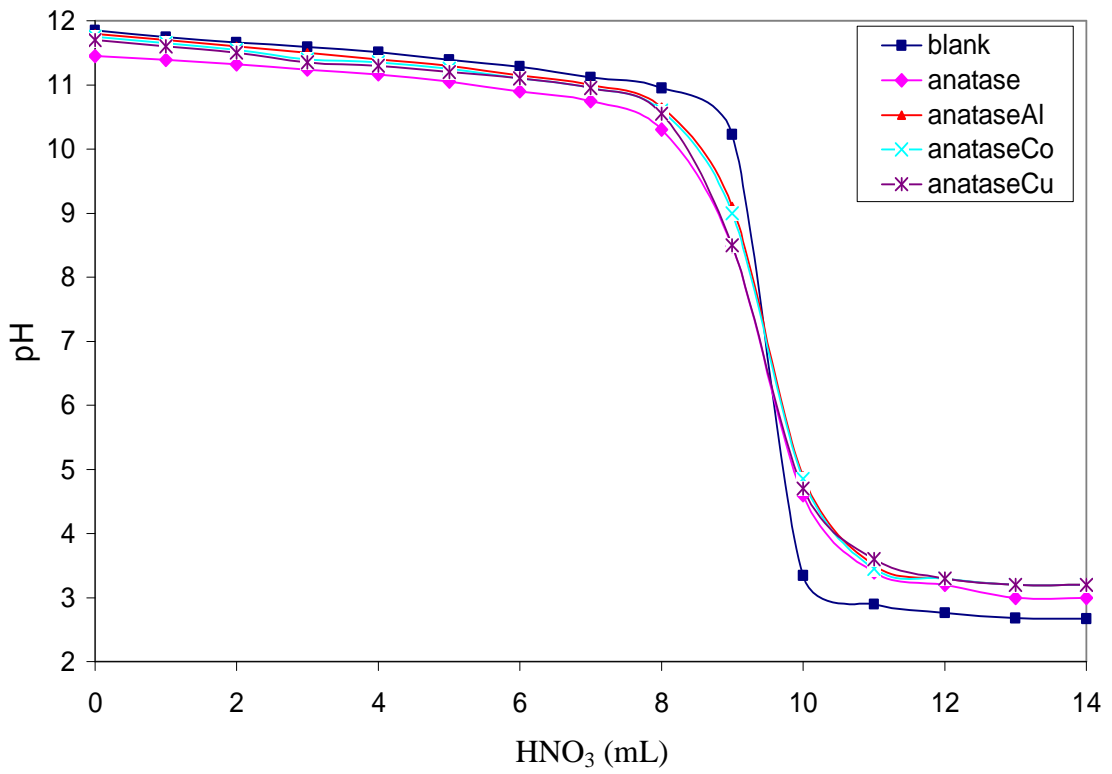


**Figure 3-10:** PZC values for neat and metal-doped anatase samples, the average error bar  $\pm 0.1$ .

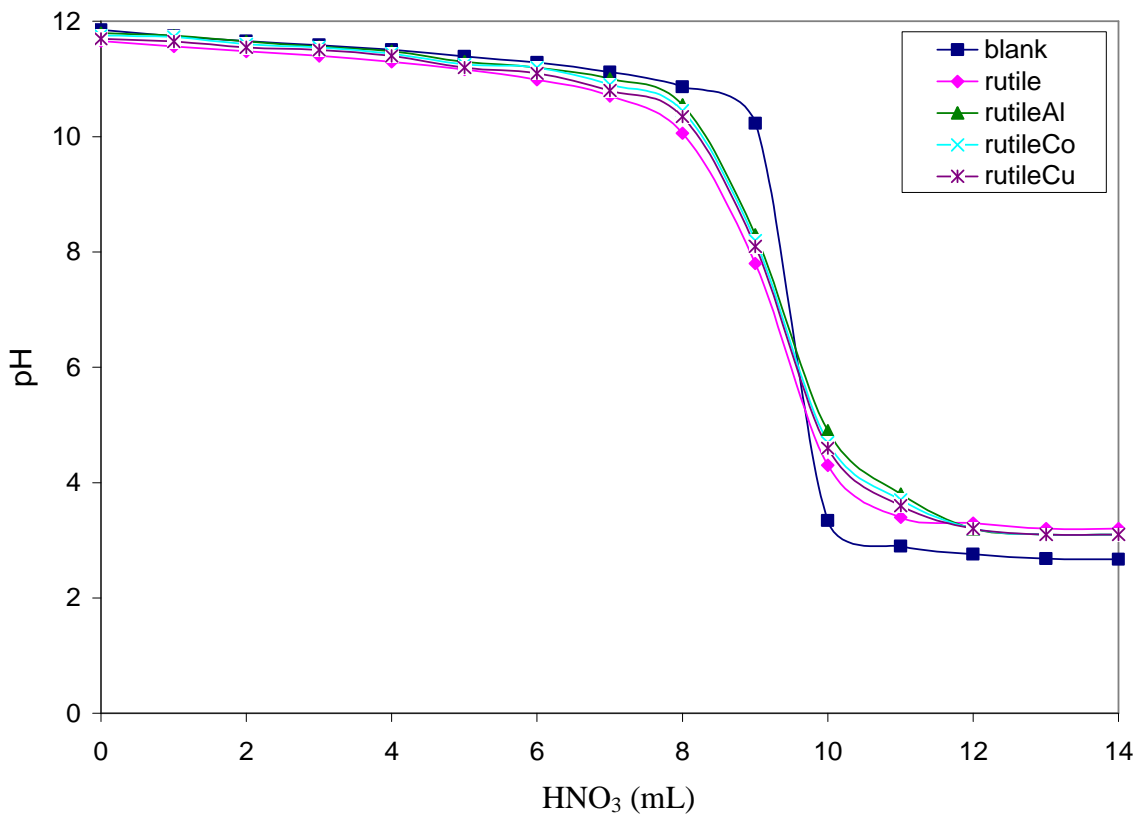


**Figure 3-11:** PZC values for neat and metal-doped rutile samples, the average error bar  $\pm 0.1$ .

The PZC values for neat and doped titania with metals are shown in the above figures. From these results it can be seen that there was a slight increase in the value of the PZC for the doped samples in comparison with parent titanic samples. Slightly increase in PZC value for metal doped samples probably arises from contribution of metal dopants in acidic-basic behaviour of the surface.

### 3- 6 Photocatalytic activity for neat and metal doped titania

#### 3-6-1 Photocatalytic decoloration of MB over metal-doped titania

To investigate the photocatalytic activity for doped and neat titania, a series of experiments was carried out to follow photocatalytic decoloration of MB as a model of a common dye. For comparison, neat titania was used under the same conditions. The decoloration of MB was followed by measuring the absorbance at 655 nm. The results are shown in the following figures:

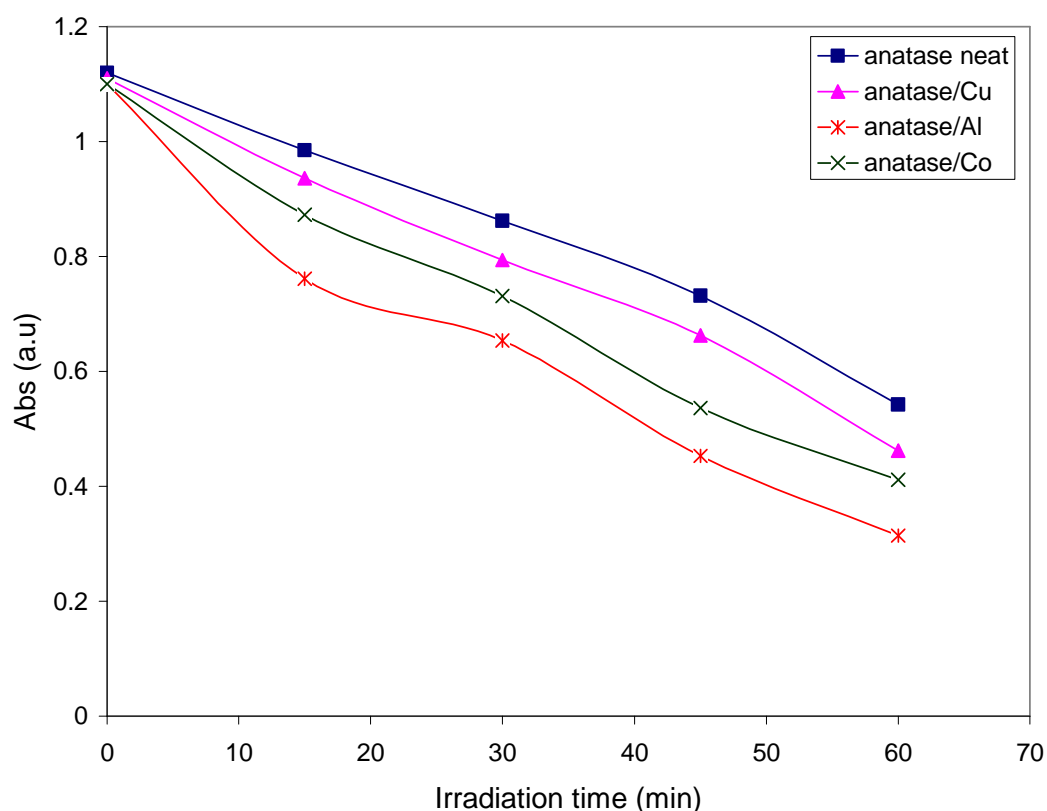


**Figure 3-12:** MB decoloration over metal-doped anatase.

From the above results, the rate of the photocatalytic decoloration of MB over metal-doped anatase for one hour is shown in the following table:

**Table 3-4:** Rates of decoloration MB over metal-doped anatase.

Catalyst	Rate of reaction $\times 10^{-8} \pm 0.14 / \text{mol. l}^{-1} \cdot \text{s}^{-1}$	Surface area normalized rate $\times 10^{-8} / \text{mol. l}^{-1} \cdot \text{s}^{-1} \cdot \text{m}^{-2}$
anatase neat	1.12	1.00
anatase/Cu	1.44	1.24
anatase/Al	1.68	1.40
anatase/Co	1.46	1.26

From the above results, the surface area normalizes activity for the photocatalytic decoloration of MB over neat and metal-doped anatase was found to be in the following order:

anatase/Al > anatase/Co > anatase/Cu > anatase neat

The results for the photocatalytic decoloration over metal-doped P25 are shown in the following figure:

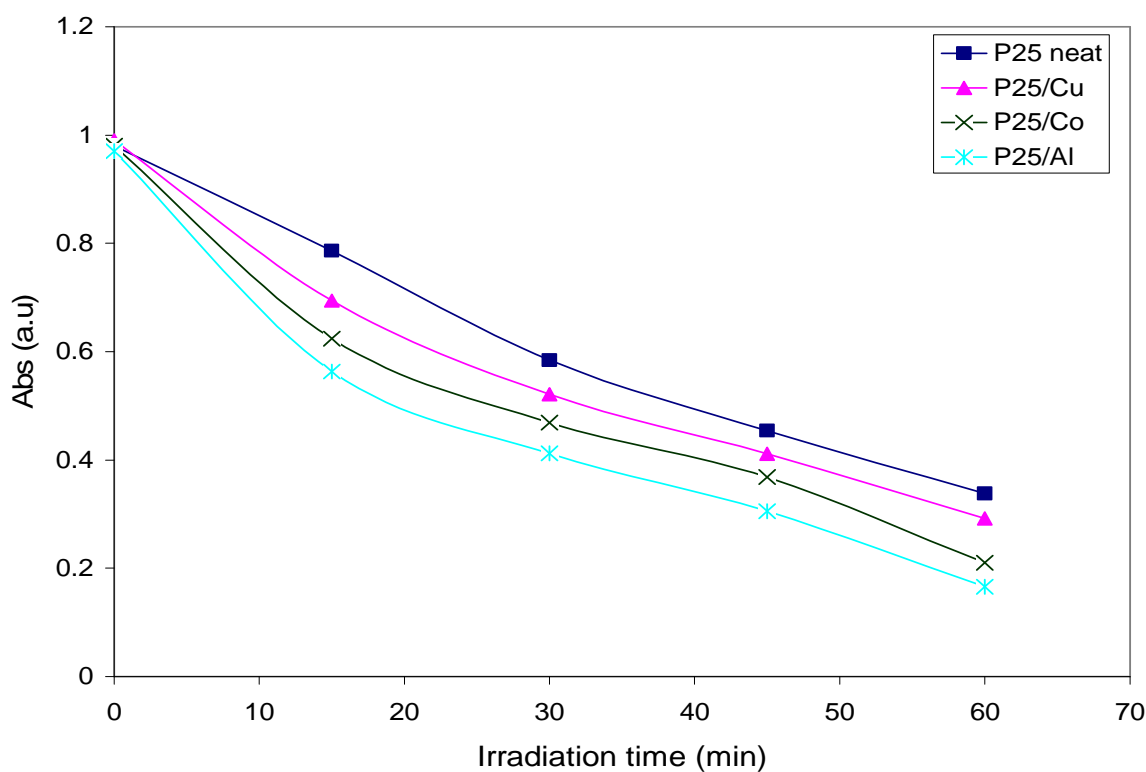


**Figure 3-13:** MB decoloration over metal-doped P25.

The rate of the photocatalytic decoloration of MB over metal-doped P25 is shown in the following table:

**Table 3-5:** Rates of MB decoloration over metal doped P25.

Catalyst	Rate of reaction $\times 10^{-8}$ $\pm 0.10/ \text{mol. l}^{-1}. \text{s}^{-1}$	Surface area normalized rate $\times 10^{-8} / \text{mol. l}^{-1}. \text{s}^{-1}. \text{m}^{-2}$
P25 neat	1.42	2.84
P25/Al	1.74	3.16
P25/Co	1.62	3.00
P25/Cu	1.58	3.04

From the above results, the activity for the photocatalytic decoloration of MB over neat and metal doped P25 fell in the order:

P25/Al > P25/Co > P25/Cu > P25 neat.

The results for the photocatalytic decoloration of MB over metal-doped rutile are shown in the following figure:

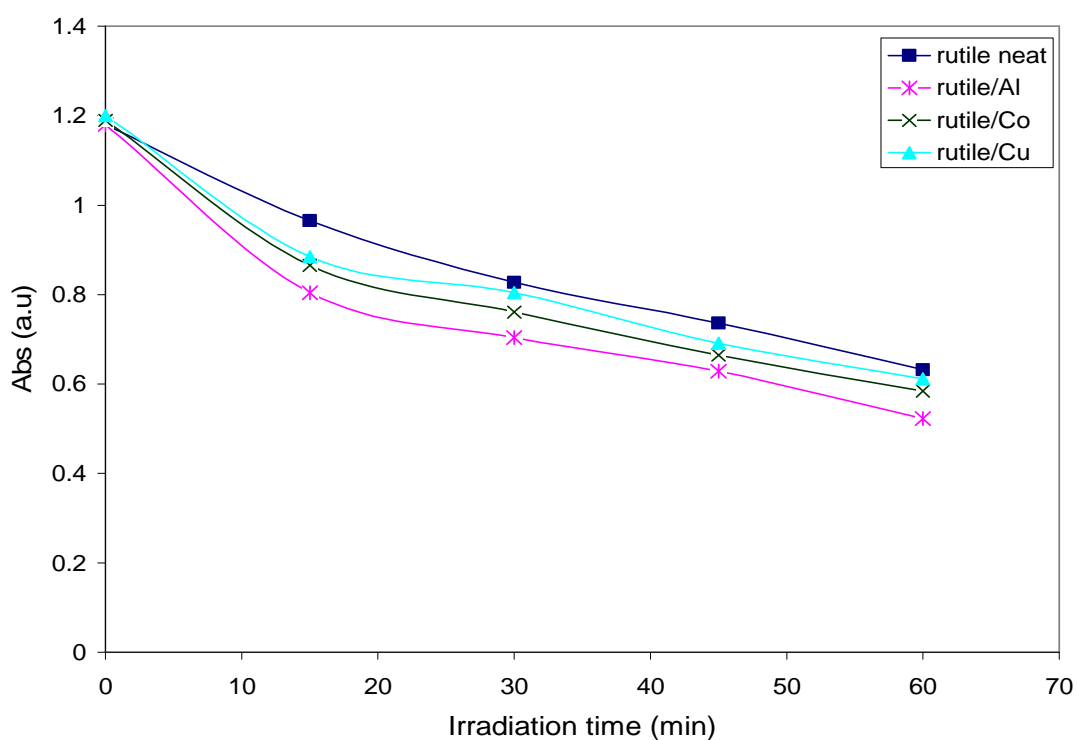


**Figure 3-14:** MB decoloration over metal-doped rutile.

The rates of the photocatalytic decoloration of MB over metal-doped rutile are shown in the following table:

**Table 3-6:** Rates of decoloration MB over metal-doped rutile.

Catalyst	Rate of reaction $\times 10^{-8} \pm 0.10/ \text{mol. l}^{-1}. \text{s}^{-1}$	Surface area normalized rate $\times 10^{-8} / \text{mol. l}^{-1}. \text{s}^{-1}. \text{m}^{-2}$
rutile neat	0.94	0.63
rutile/Al	1.55	1.01
rutile/Cu	1.28	0.84
rutile/Co	1.35	0.89

From the above results in Figures (3-12)- (3-14) and Tables (3-4)- (3-6), it can be found that the rate of photocatalytic decomposition of MB over metal doped titania, anatase, rutile and P25 was higher than that for the undoped samples. That is probably due to the enhanced surface properties of the doped catalyst. Dispersion of metal ions in the lattice of the catalyst can reduce the recombination reaction between  $e^-_{CB}$  and  $h^+_{VB}$  as these ions can act as electron traps<sup>(73-75)</sup>. In addition, the particle size for the doped samples were slightly smaller than that for the neat titania and since photocatalytic activity increases with a decrease in the particle size a higher activity may be anticipated. For the neat samples, P25 showed the highest activity while rutile showed the lowest activity in the photocatalytic decomposition of MB. This arises from higher activity for the mixed phase titania as established in often studies. However, for all the above the three sets of samples that were doped with Al, Co and Cu showed a better photocatalytic activity with respect to their parent samples. As mentioned previously, conduction band electrons and valence band holes that are produced upon irradiation of pure, titania may recombine directly in back electron transfer. This represents a main energy-wasting step as about 90% of the species recombine again and this normally occurs in the case of excitation of pure titania. On the other hand, if the charge separation is maintained holes can react with surface bound species ( $\text{H}_2\text{O}$  or  $\text{OH}^-$ ), leading to formation of active radicals on the surface ( $\text{OH}^\cdot$ ). Conduction band electrons can capture by adsorbed oxygen producing superoxide radical anion ( $\text{O}_2^-$ ) and these species play a major role in the photocatalytic reaction<sup>(76)</sup>. Generally, doping titania with metals can reduce rate of the rate of the recombination reaction, as these species are important electron traps for the CB electrons<sup>(77,78)</sup>. Enhancement in the photocatalytic activity in the decomposition of organic pollutants over metalized titania have been studied by many researchers<sup>(77,79,80)</sup>. It is believed that general improvement in the activity for  $\text{M}/\text{TiO}_2$  is probably due to the difference in the concentration of both ( $e^-_{CB}$ ,  $h^+_{VB}$ ) pairs. That is caused by direct oxidation of adsorbed electron donors by ( $h^+_{VB}$ ) and reduction of adsorbed electron acceptors by ( $e^-_{CB}$ )<sup>(81)</sup>.

However, as discussed in the previous chapter, photocatalytic decomposition of MB in aqueous suspensions of titania can follow two mechanisms. In the first mechanism, reaction can occur under anaerobic conditions and the result of this mechanism is the reduction of MB into colourless form that is known LMB. This reaction is a reversible process and LMB can be oxidized back into MB in air. In contrast to this, second mechanism involving complete mineralization of MB into inorganic species in an irreversible process. However, in the current study it believes that decomposition of MB occurs according to the second mechanism as the LMB did not oxidized back into MB in air overnight.

### **3-6-2 Photocatalytic polymerization of methyl methacrylate over metal doped anatase**

Photocatalytic polymerization of MMA over metal-doped anatase was carried out under irradiation with UV light from an immersion type middle pressure mercury lamp (125 Watt) for two hours. The product was then separated by centrifugation and the resultant solid then washed with water to remove unreacted monomer and dried in a vacuum. The crude product was then dissolved in THF with vigorous stirring and the mixture was separated by centrifugation. The solid was found to contain bonded polymer and the liquid contained extracted polymer. The extracted polymer was precipitated by adding methanol to give the final solid polymer.

### **3-6-3 Characterisation of the polymer**

The formed polymer was characterized by using FTIR spectroscopy, NMR spectroscopy, SEM and TG analysis for the both bonded and extracted polymer.

#### **3-6-3-1 FTIR spectroscopy**

The FTIR spectra for PMMA extracted and PMMA grafted metal-doped anatase are shown in the following figures:

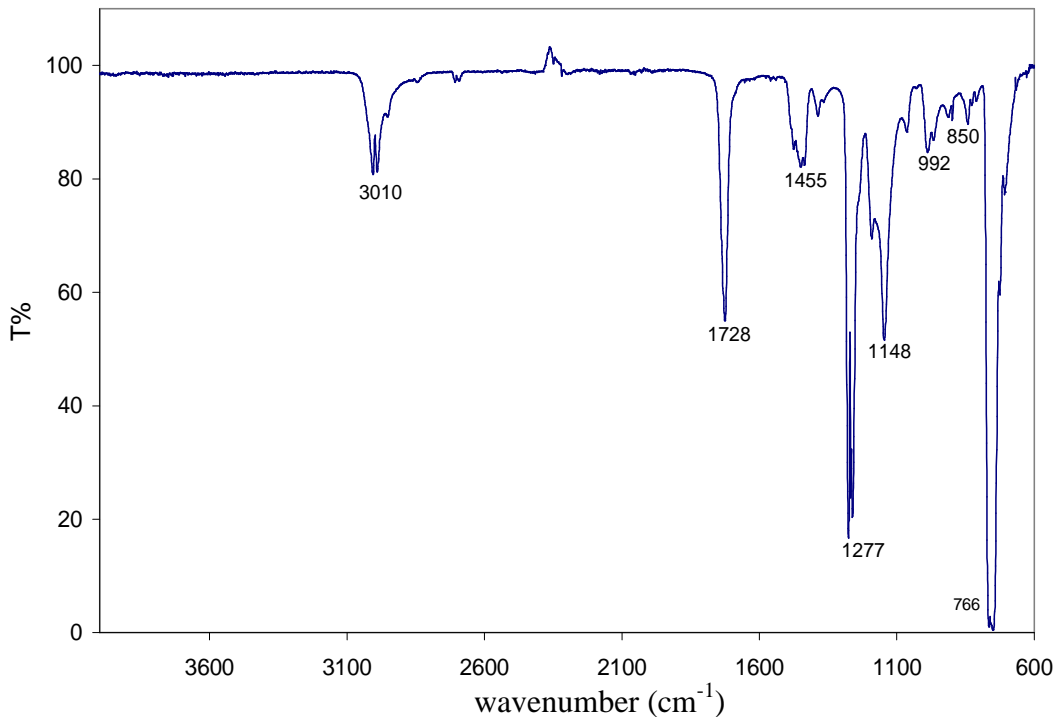


**Figure 3-16:** FTIR spectrum for the extracted PMMA.

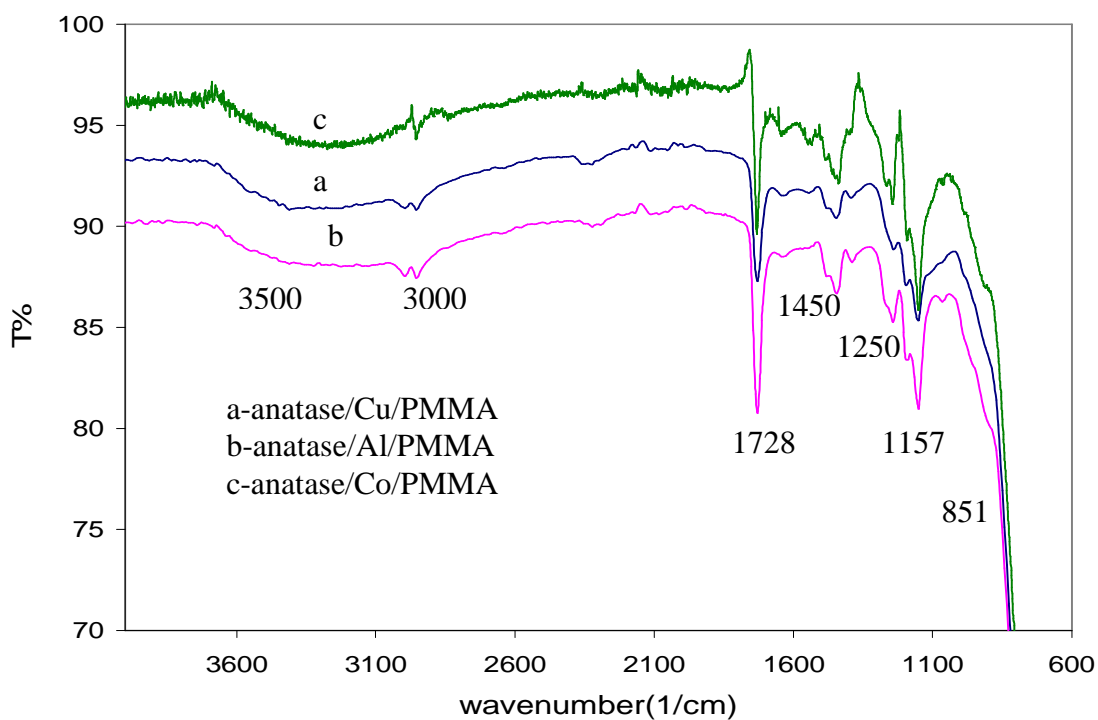


**Figure 3-17:** FTIR spectra for PMMA grafted metal-doped anatase.

Both extracted and grafted PMMA on the anatase show a characteristic band at  $1728\text{ cm}^{-1}$  that can be assigned to the stretching vibration of carbonyl group, and this sharp peak indicates the presence of the grafted PMMA on the anatase. Also the band at  $2990\text{--}3000\text{ cm}^{-1}$  is related to free  $\text{CH}_3$  vibrations and the band at  $1157\text{ cm}^{-1}$  can be assigned to the C-C-O- stretching mode, which is not present in MMA<sup>(82)</sup>. The broad peak at  $3350\text{--}3450\text{ cm}^{-1}$  belongs to the stretching vibration mode of OH groups on the surface of titania

nanoparticles. Both extracted and grafted PMMA on the anatase show a characteristic band at  $1728\text{ cm}^{-1}$  and this sharp peak indicates the presence of grafted PMMA on the anatase. In addition, the band at  $2990\text{--}3000\text{ cm}^{-1}$  is related to the free  $\text{CH}_3$  vibrations<sup>(83)</sup>.

### 3-6-3-2 $^1\text{H}$ NMR spectroscopy

Further investigation for the extracted polymer was undertaken by measuring the  $^1\text{H}$  NMR spectra for MMA and extracted PMMA as shown in the following figures:

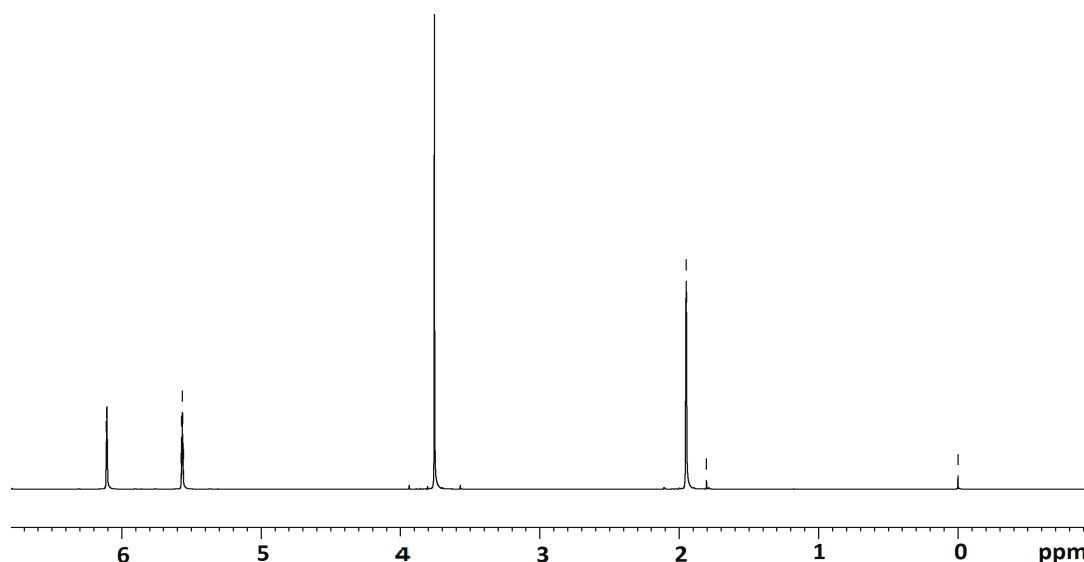


**Figure 3-18:**  $^1\text{H}$  NMR spectrum for MMA in  $\text{CDCl}_3$ .

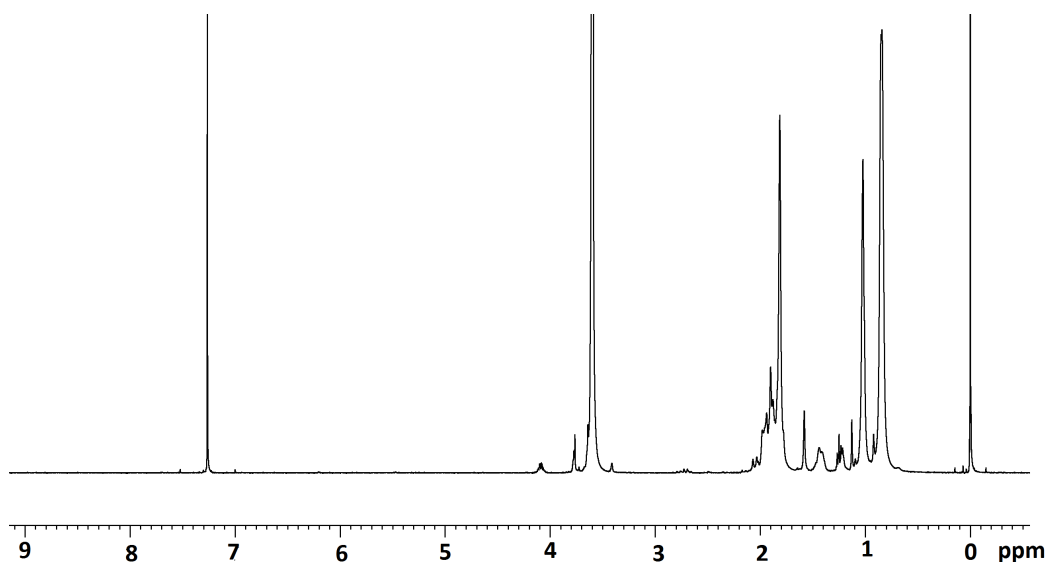


**Figure 3-19:**  $^1\text{H}$  NMR spectrum for the extracted PMMA in  $\text{CDCl}_3$ .

The most interesting aspects of these spectra are the peaks at  $\delta = 5.50$ , and  $6.05$  which are assigned to the  $\text{H}_2\text{C}=\text{C}(\text{CH}_3)-$  in MMA, Figure 3-18 are completely absent in extracted PMMA as shown in Figure 3-19. The main features of  $^1\text{H}$  NMR spectrum for the extracted

PMMA, is the presence of the peak which corresponds to the methoxy protons at  $\delta = 3.57$ - $3.64$ . It was observed that the spectrum of extracted PMMA was similar to PMMA that is synthesised by normal chemical polymerization <sup>(84)</sup>.

### 3-6-3-3 Scanning electron microscopy

Morphological studies for metal-doped anatase that grafted with PMMA were undertaken using SEM. These images are shown in the following figure:

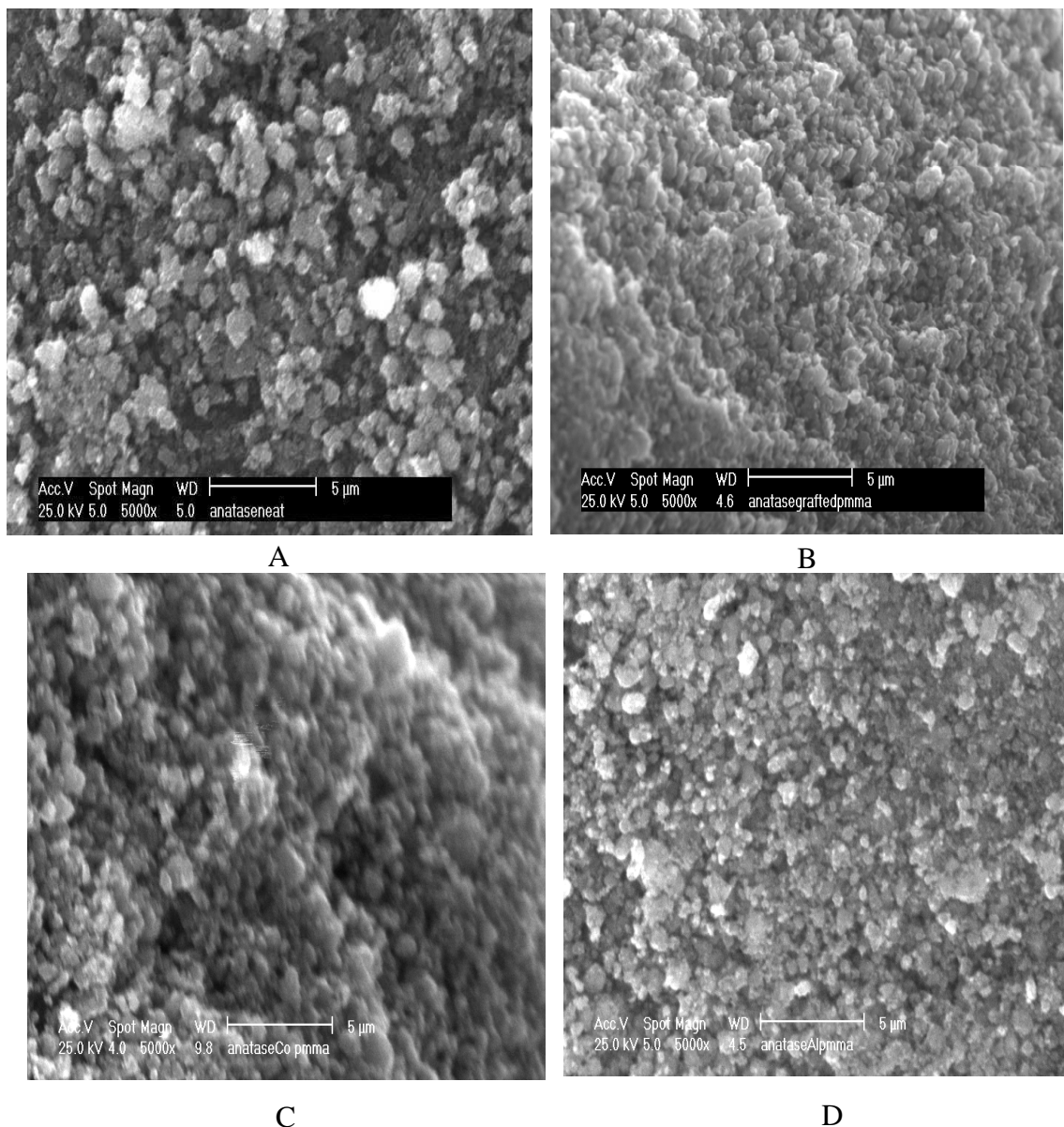


**Figure 3-20:** SEM images for (A) neat anatase, (B) anatase/CuPMMA, (C) anatase/CoPMMA and (D) anatase/AlPMMA.

From these images, it can be found that there is some change in the morphology of the surface of anatase after grafting with the polymer. It was found that anatase nanoparticles

are aggregated after grafting with the polymer<sup>(85)</sup>. When PMMA was grafted onto the surface it showed a better dispersibility.

### 3-6-3-4 TGA analysis

The grafted polymer was further investigated by thermal gravimetric analysis. This was performed under air and nitrogen atmospheres and the same results were obtained for both cases. The TGA profiles for PMMA grafted metal-doped anatase are shown in the following figure:

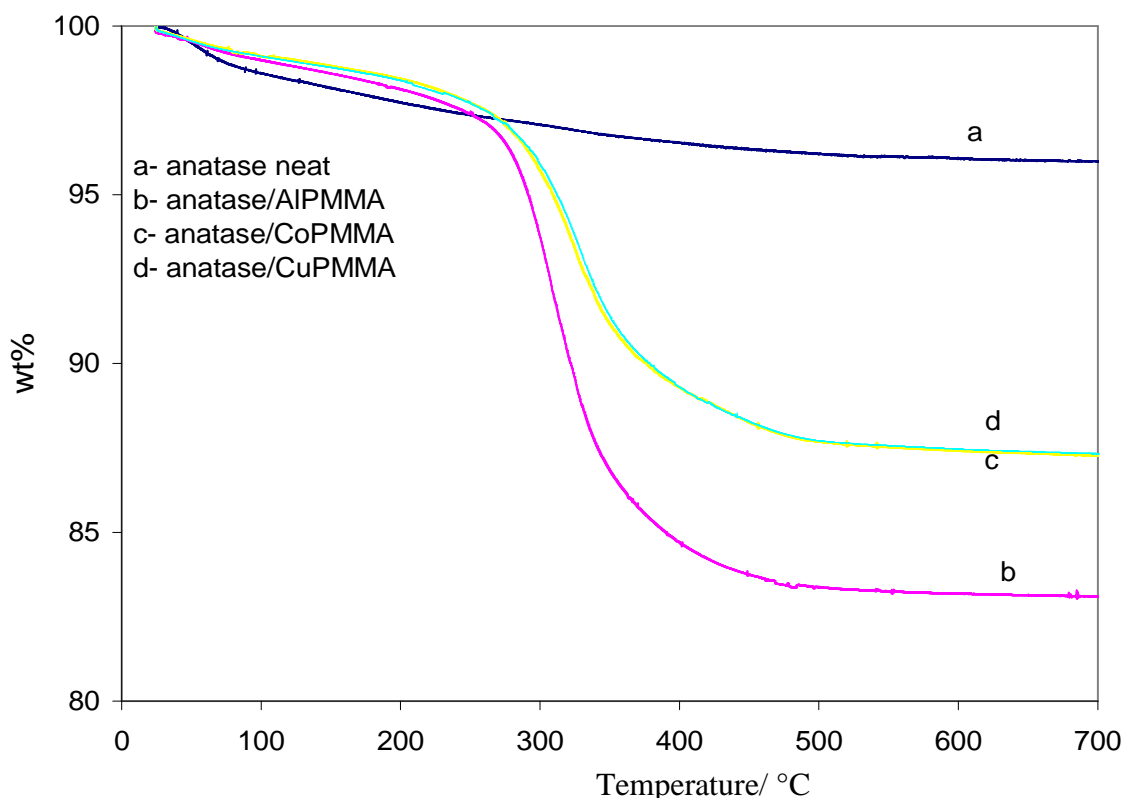


**Figure 3-21:** TGA for neat and grafted anatase with PMMA under air atmosphere.

From these results, it can be seen that, there is a clear evidence for the formation of the grafted polymer within metal-doped anatase due to the characteristic mass loss about 12-18% of the weight of composite materials. The difference in decomposition temperature for these materials (PMMA grafted metal-doped anatase) than that of traditional PMMA (extracted polymer) probably arises from the interaction between polymer chains and anatase nanoparticles<sup>(86)</sup>. Conversion percentage of grafting for anatase/Al, anatase/Co and anatase/Cu was 20.5%, 14.9%, and 14.3% respectively.

### 3-6-3-5 X-ray diffraction patterns (XRD)

In order to investigate the effect of the grafting of the polymer on the crystalline structure of the metal-doped anatase, X-ray powder diffraction studies of metal-doped anatase before and after grafting were carried out. The patterns for the extracted PMMA and that grafted with the metal-doped anatase are shown in the following figures:

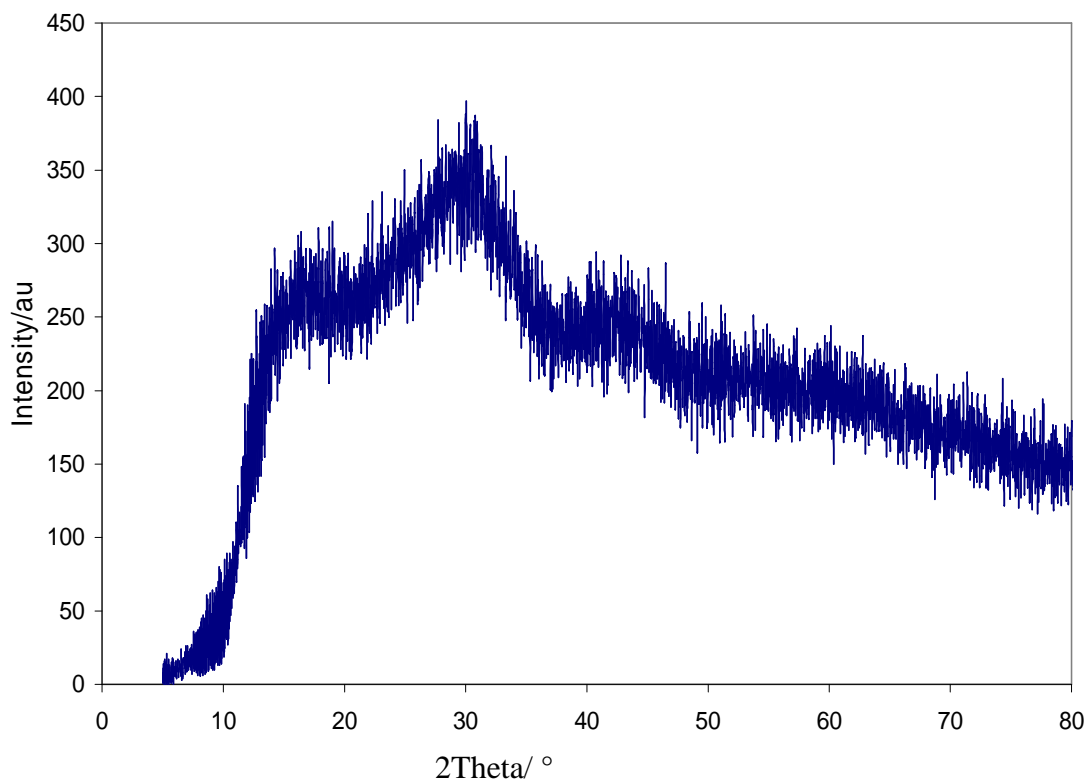


**Figure 3-22:** XRD patterns for the extracted PMMA.

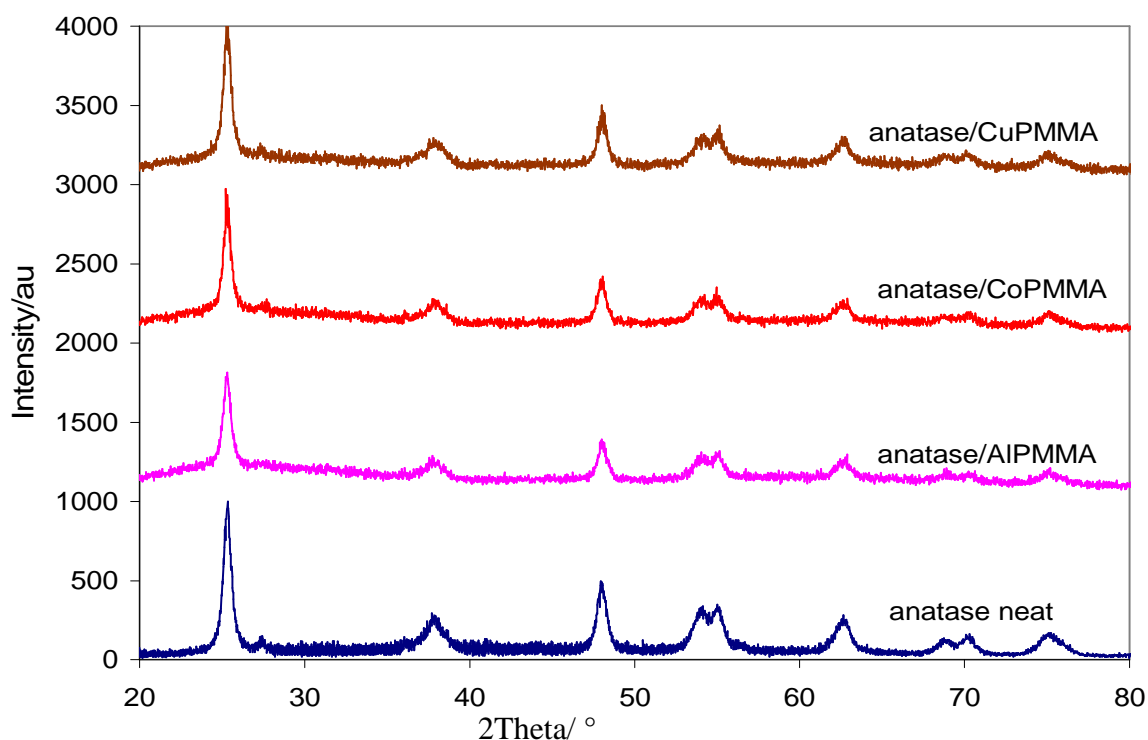


**Figure 3-23:** XRD patterns for neat and grafted PMMA over metal-doped anatase.

From the above patterns, it can be seen that the XRD patterns of extracted PMMA is the same as that of extracted PMMA produced over nitrogen doped anatase as shown earlier in Figure 2-28. In all cases, grafting polymer over anatase doesn't alter its crystallite structure as the patterns XRD for PMMA grafted anatase is almost the same as for pure anatase as shown in Figure 2-27.

### 3-6-4 Photocatalytic polymerization over metal doped anatase

Photocatalytic polymerization of MMA was performed over metal-doped anatase and for comparison photocatalytic polymerization was also performed over neat anatase. The reaction was carried out under an air atmosphere and using irradiation with UV light from an immersion type middle pressure mercury lamp. The reaction was then initiated by irradiation with light from the mercury lamp with stirring at 20 °C and the reaction was continued for two hours under irradiation with UV radiation. The extracted polymer was precipitated by adding methanol to give the final solid polymer. The yield of the reaction was calculated as a percentage of conversion of the monomer in to the polymer. The average error bar for conversion percentage of these results was  $\pm 0.24\%$ . The results are presented as irradiation time against conversion percentage as shown in the following figure:

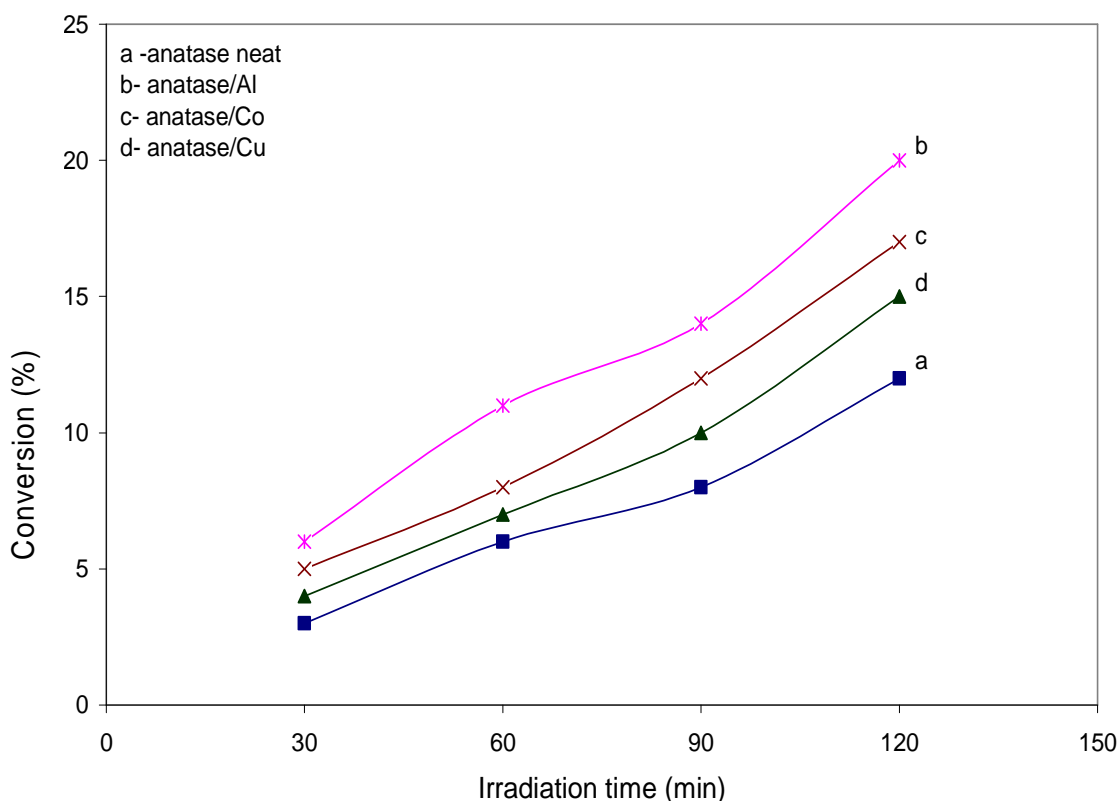


**Figure 3-24:** Photocatalytic polymerization of MMA over metal-doped anatase.

The order of activity falls in the sequence anatase/Al > anatase/Co > anatase/Cu > pure anatase. From these results, it was found that there is relative enhancement for the efficiency of photocatalytic polymerization for the metal-doped anatase in comparison with the neat sample. These observations may be attributed to an improvement in the activity of the catalyst by increasing its specific surface area and decreasing the particle size by doping metals, as the activity of the catalyst enhances with increasing surface area and reduction in the particle size <sup>(35)</sup>. In addition to that, the presence of metal species in the lattice of the catalyst may reduce the rate of back electron transfer and reduce the recombination reaction between conduction band electron and valence band hole. Generally, for all the above three sets of samples the doped samples showed better photocatalytic activity with respect to the neat sample. The number averaged molecular weights ( $M_n$ ) for the PMMA formed over parent anatase, anatase/ Al, anatase/ Co and anatase/ Cu were 60,000, 50,000, 54,000, and 56,000 respectively. From these results, it can be concluded that the highest molecular weight was obtained with a lower conversion percentage, while a lower molecular weight was obtained with a higher conversion percentage. This probably arises from the relation between rate of polymerization reaction and viscosity of the polymerization mixture. High viscosity results in a low rate of polymerization, which gives a low conversion percentage. For a mixture with a low viscosity high rate of polymerization occurs which yield a high conversion percentage <sup>(87)</sup>.

#### 3-6-4-1 Proposed mechanism for polymerization over metal doped titania

Redox reaction between excited photocatalyst particles and monomer molecules is an essential step for photocatalytic polymerization. Monomer molecules (M) donate electrons to the positive hole producing radical cations from the monomer molecule. These radical cations contribute to chain growth to give the final polymer, and the proposed general mechanism for polymerization over metal-doped titania is as follows <sup>(88)</sup>:

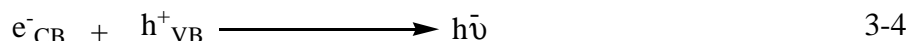
The first step is the excitation of titania by absorbing light with a sufficient energy producing ( $e^-_{CB}$ ,  $h^+_{VB}$ ) pairs as follows for undoped titania



For the doped titania with metal species (m), the following processes are suggested:



Recombination reaction between  $e^-_{CB}$  and  $h^+_{VB}$  may occur as follows:



The formation of the initiating radicals from monomer molecule (M) would occur as follows:



The chain growth can occur via reaction of a radical of the monomer or a radical of the electron acceptor (A) with the monomer, as shown:



Chain termination occurs by radical combination or by disproportionation.

### 3-7 Modification metal doped anatase by doping nitrogen

#### 3-7-1 Characterization of the modified samples

Characterization of nitrogen doping metal-doped anatase was carried out by using different methods such as XRD powder diffraction, BET measurement, UV- visible spectroscopy and microelemental analysis.

##### 3-7-1-1 Microelemental analysis

The microelemental analysis was used to follow the existence of nitrogen species in the nitrogen doped metalized samples. The results of H and N contents for neat and co-doped  $TiO_2$  are shown in the following table:

**Table 3-7:** CHN analysis for H and N contents for co-doped TiO<sub>2</sub>.

Catalyst	H / wt% ± 0.01	N / wt% ± 0.02	N/H atomic ratio
anatase/Co	0.30	0.00	----
anatase/Co/N400	0.27	0.31	0.08
anatase/Co/N500	0.25	0.43	0.12
anatase/Co/N600	0.21	1.72	0.59
anatase/Cu	0.31	0.00	---
anatase/Cu/N400	0.28	0.36	0.09
anatase/Cu/N500	0.24	0.40	0.12
anatase/Cu/N600	0.20	1.63	0.58
anatase/Al	0.30	0.00	---
anatase/Al/N400	0.26	0.22	1.06
anatase/Al/N500	0.23	0.34	0.11
anatase/Al/N600	0.22	1.58	0.51

From these results, the ratio of nitrogen content for the metal-doped anatase was increased with increase in the doping temperatures. In terms of stoichiometric values for atomic ratio of H/N for the doped nitrogen species, it can be concluded that the expected doping species don't correspond simply to NH<sub>3</sub> and NH<sub>2</sub> species.

### 3-7-1-2 Specific surface area (BET) measurements

The surface areas of the co- doped TiO<sub>2</sub> samples were determined using the BET method. Table 3-8 shows the results of surface area for parent and co- doped TiO<sub>2</sub> samples. From these results, it can be seen that there was a decrease in the surface area of the doped anatase at 600 °C, which arises from sintering which arises from annealing titania powder at this temperature. Average particle sizes for the co-doped samples were estimated using the Scherrer equation. However, the same assumptions as mentioned in Chapter 2 were applied. The results of BET are shown in the following table:

**Table 3-8:** BET surface area for nitrogen doped metalized anatase.

Catalyst	BET (m <sup>2</sup> /g) ± 1	Particle size(nm) from XRD
anatase/Co	116	16.2
anatase/Co/N400	120	16.1
anatase/Co /N500	124	15.9
anatase/Co/N600	86	16.3
anatase/Cu	116	16.1
anatase/Cu/N400	122	15.9
anatase/Cu/N500	126	15.8
anatase/Cu/N600	84	16.4
anatase/Al	120	16.0
anatase/Al/N400	122	16.0
anatase/Al/N500	128	15.8
anatase/Al/N600	88	16.2

From these results, it was found that for the samples that were doped with nitrogen at 400 °C, and 500 °C there was a slight increase in the specific surface area for all samples. In addition, in accordance with this, these samples showed a slight decrease in the apparent particle size. For the samples that were doped with nitrogen at a higher temperature (600 °C) there was a significant decrease in the surface area. This probably due to the sintering of the catalyst due to the effect of the temperature. In all cases, powder XRD indicates the maintenance of the original crystal phase upon doping under these conditions as shown next.

### 3-7-1-3 XRD patterns for the samples

XRD patterns for the co-doped anatase were investigated by using a powder X-ray diffractometer. These patterns are shown in the following figures:

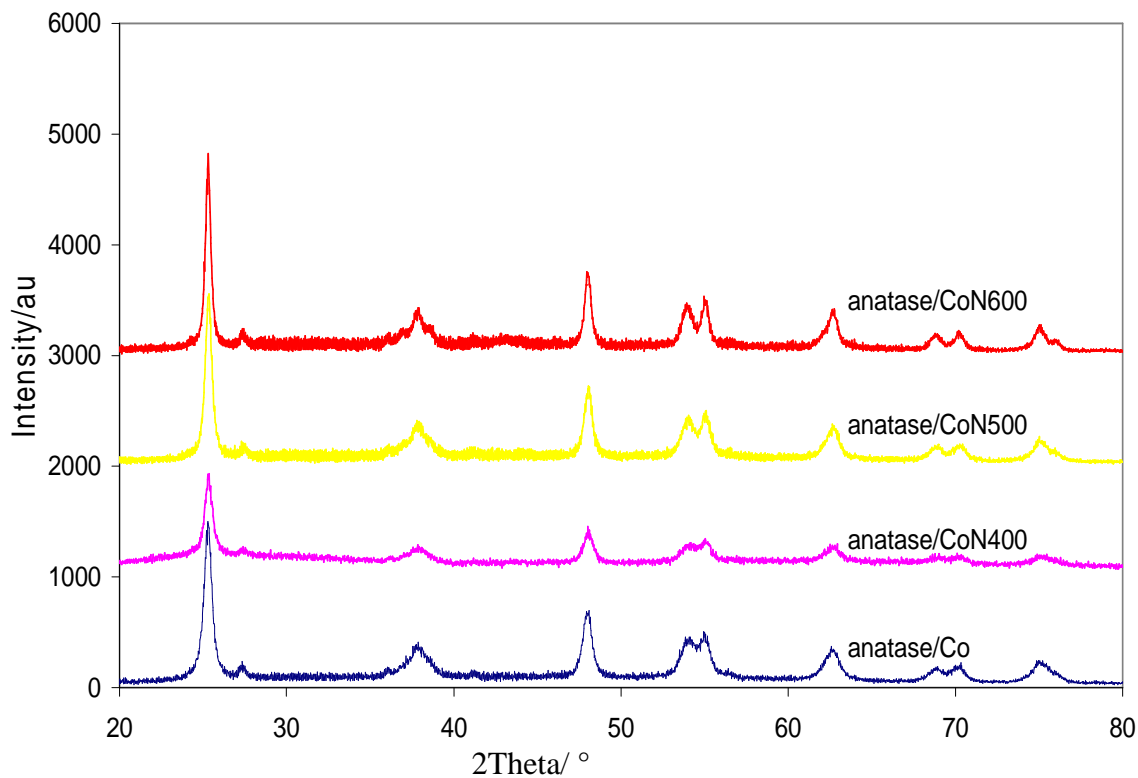


**Figure 3-25:** XRD patterns for co-doped anatase.

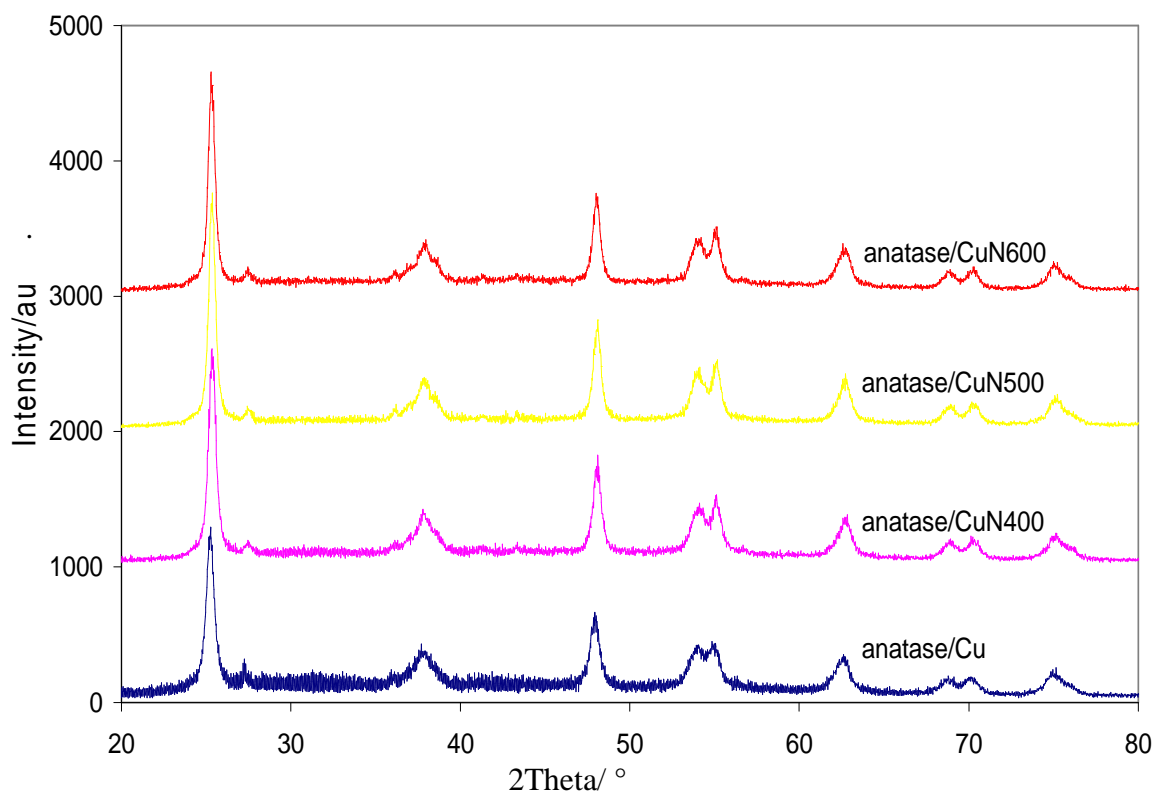


**Figure 3-26:** XRD patterns for co-doped anatase.

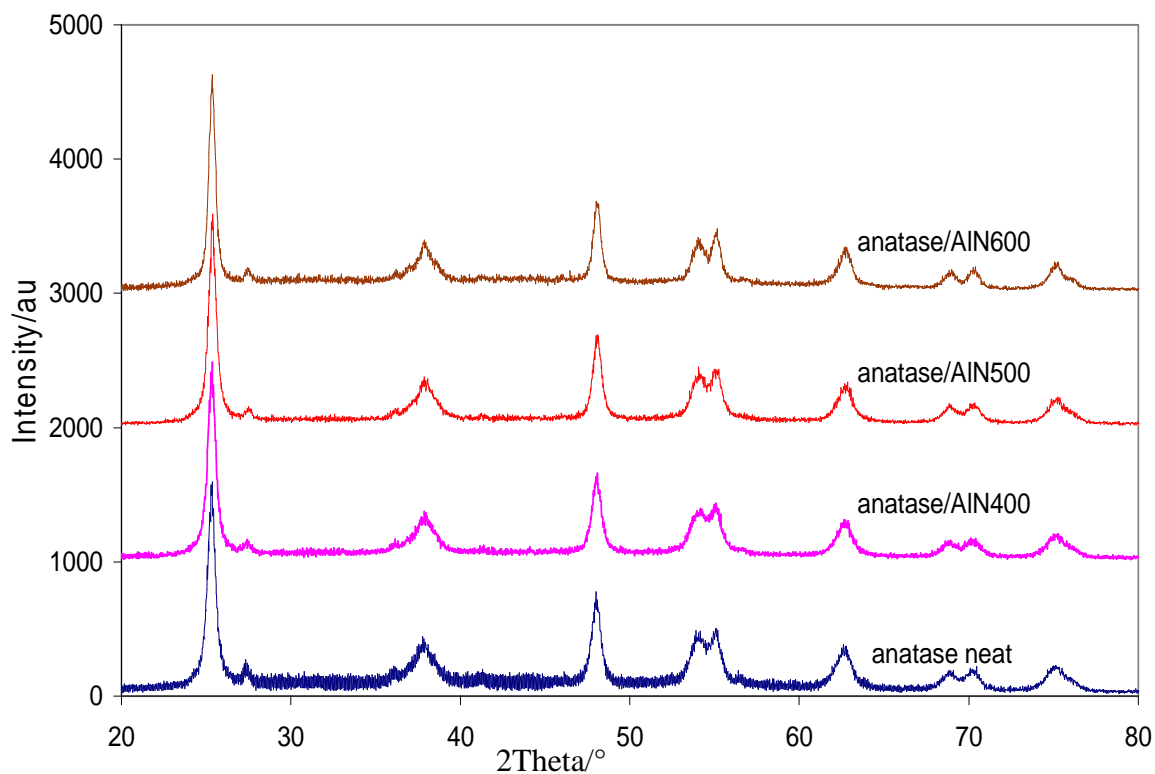


**Figure 3-27:** XRD patterns for co-doped anatase.

From these patterns, it can be observed that the patterns of the co-doped anatase are almost the same as those of the parent samples. There is no change in the main peaks upon co-doping which indicates that doping titania doesn't alter the phase composition. In addition, reflections for the samples treated at 400 °C and 500 °C are slightly broader than for the parent samples while for doping at 600 °C, the peaks are slightly sharper with relatively higher intensity. This indicates a relatively smaller particle size and/or greater degree of disorder for the co-doped samples at 400 °C and 500 °C. The apparent particle sizes for co-doped samples at 400 °C and 500 °C were relatively smaller than that for the metal-doped samples.

#### **3-7-1-4 UV-visible spectra for co-doped anatase**

The UV- visible spectra for the co-doped samples were measured and are shown in the following figures:

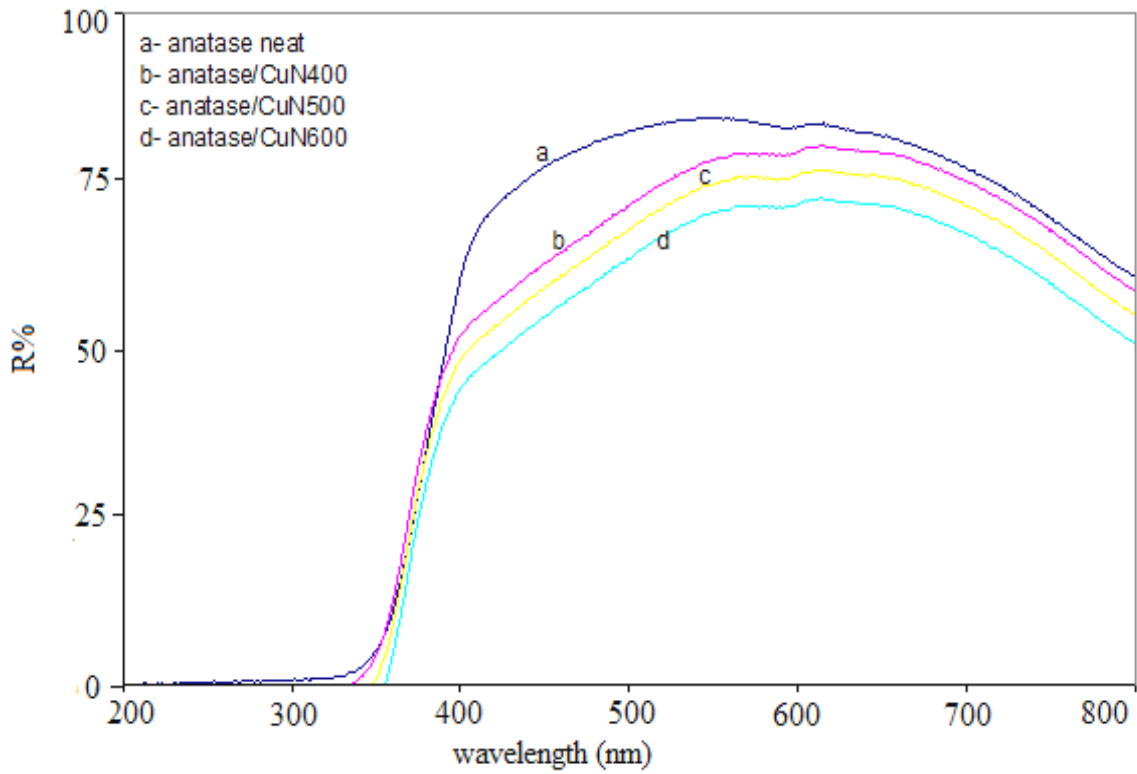


**Figure 3-28:** UV-visible diffuse reflection spectra for co-doped anatase/ Cu.

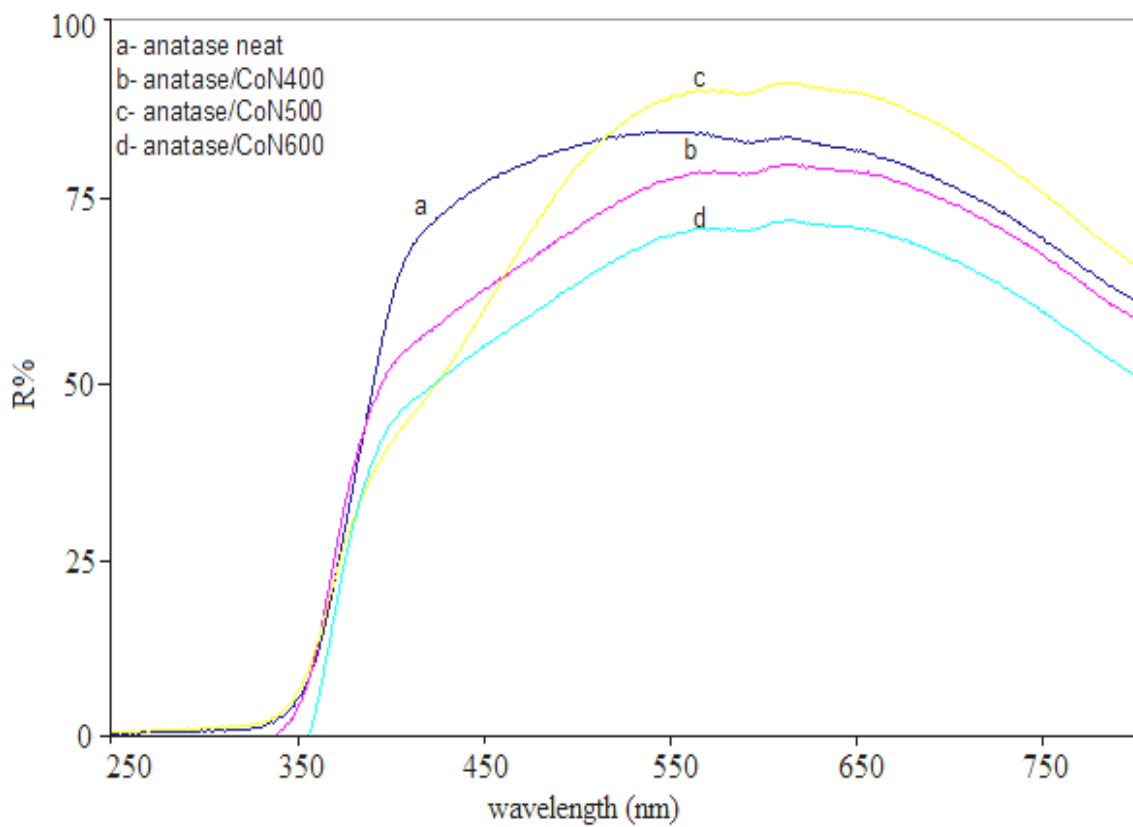


**Figure 3-29:** UV-visible diffuse reflection spectra for co-doped anatase / Co.

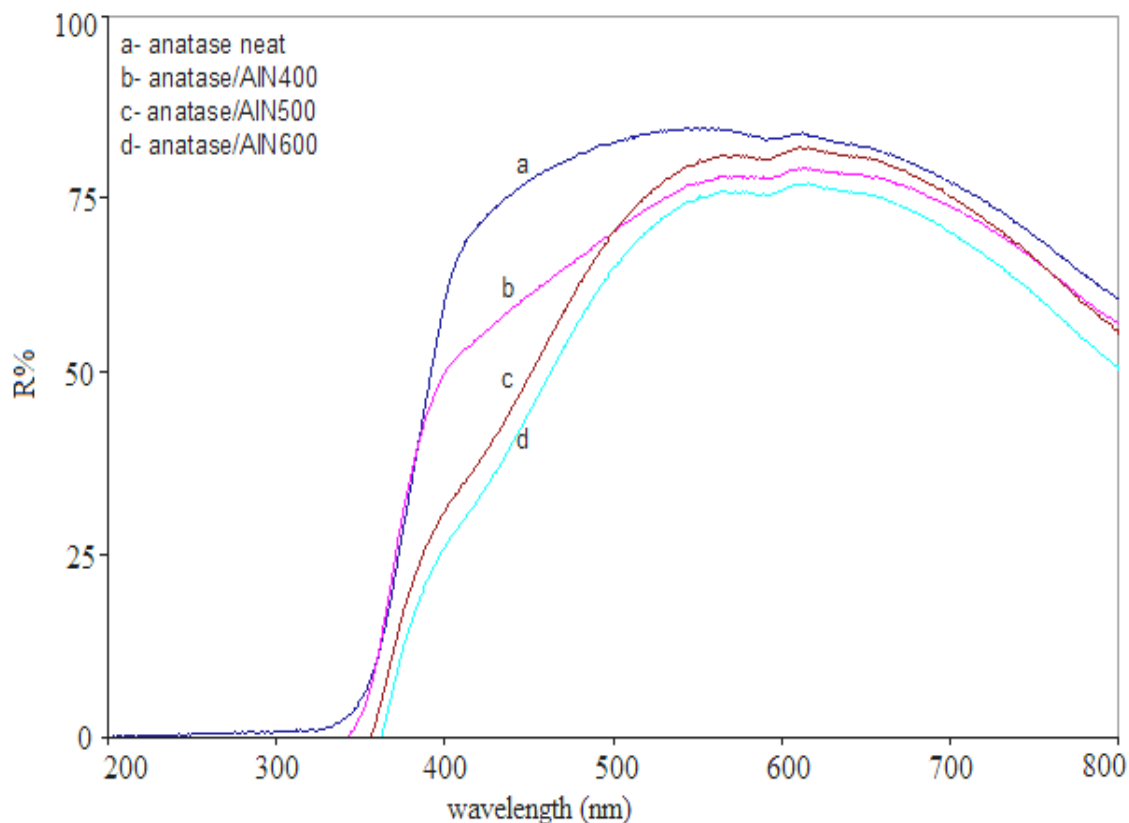


**Figure 3-30:** UV-visible diffuse reflection spectra for co-doped anatase/Al.

From these figures, it can be seen that there is an extension in absorption band edge of these samples towards the visible region. The extension in the absorption into visible region was increased by increasing the amount of nitrogen content for the doped samples. Nitrogen co-doping can narrow the bandgap of titania by mixing of N2p and O2p states because they have a similar energy<sup>(89,90)</sup>. The dopant metal ions Al<sup>3+</sup>, Cu<sup>2+</sup> and Co<sup>2+</sup> can provide a dopant energy level, which is located below the conduction band of titania. This impurity level can result in a red shift in the absorption spectra of the co-doped samples. Hence for co-doped samples the presence of two dopant levels within the bandgap energy of titania has been suggested<sup>(91-93)</sup>. Wei and co-workers<sup>(94)</sup> reported electronic transitions for co-doped samples of titania. They suggested three possibilities for electronic transitions: excitation from the nitrogen level to the metal ion levels, excitation from the VB level of titania to the metal ion impurity, and excitation from nitrogen level to the CB level of titania. The co-doped samples show a better photoresponse over wide spectral range in comparison with the parent samples, due to lowering of the band gap and the occurrence of multiple electronic transitions<sup>(95,96)</sup>.

### 3- 8 The PZC of co-doped anatase

Determination of the PZC values for co-doped anatase was achieved by using potentiometric titration<sup>(72)</sup>. According to this method, the obtained results are plotted as a volume of the added nitric acid against the pH of the resulting mixture. The PZC value is taken as the point of intersection with the blank pH titration curve as discussed previously. These results are shown in the following table and are plotted in the following figures:

**Table 3- 9:** The PZC values for co-doped anatase.

Catalyst	PZC (pH) ± 0.10
anatase/Al	6.75
anatase/Al/N400	7.20
anatase/Al/N500	7.35
anatase/Al/N600	8.20
anatase/Co	6.60
anatase/Co/N400	6.65
anatase/Co/N500	7.40
anatase/Co/N600	8.25
anatase/Cu	6.65
anatase/Cu/N400	6.90
anatase/Cu/N500	7.65
anatase/Cu/N600	8.35

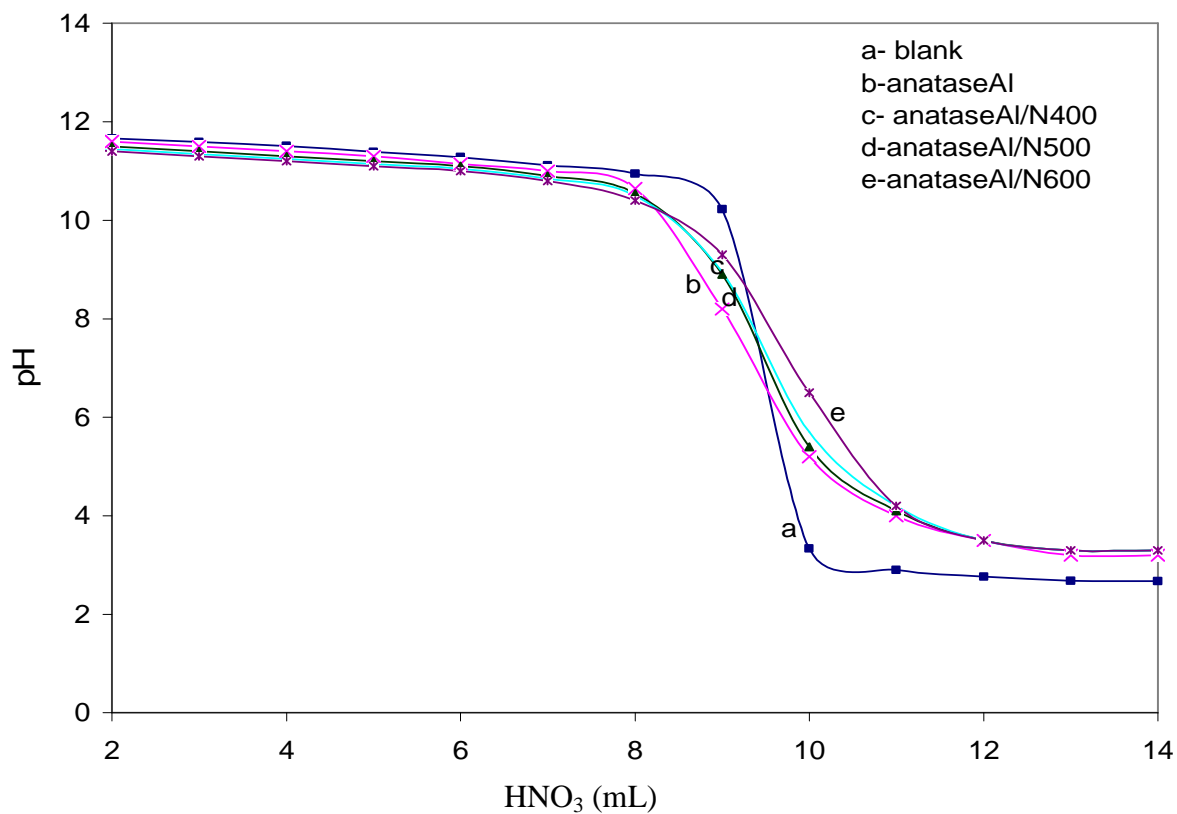


**Figure 3-31:** Titration curve for co-doped anatase/Al/N, the average error bar  $\pm 0.10$ .

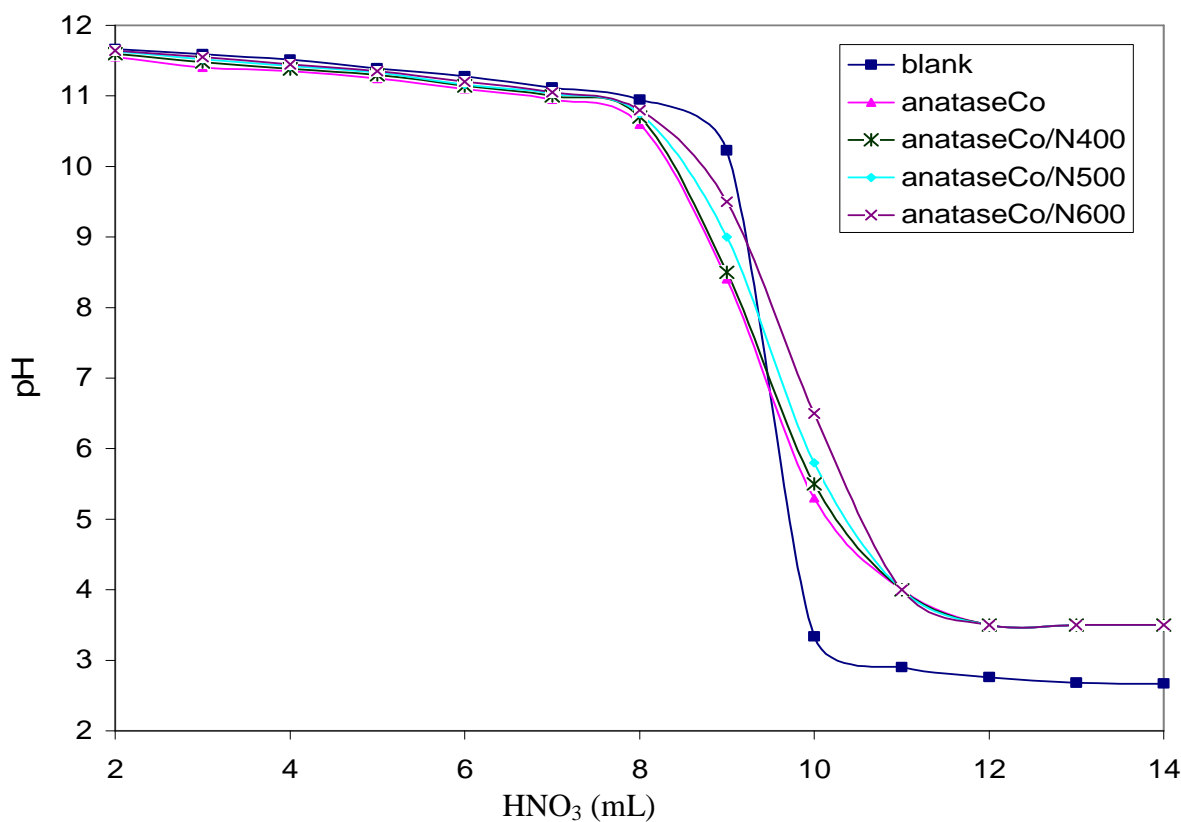


**Figure 3-32:** Titration curve for co-doped anatase/Co/N, the average error bar  $\pm 0.10$ .

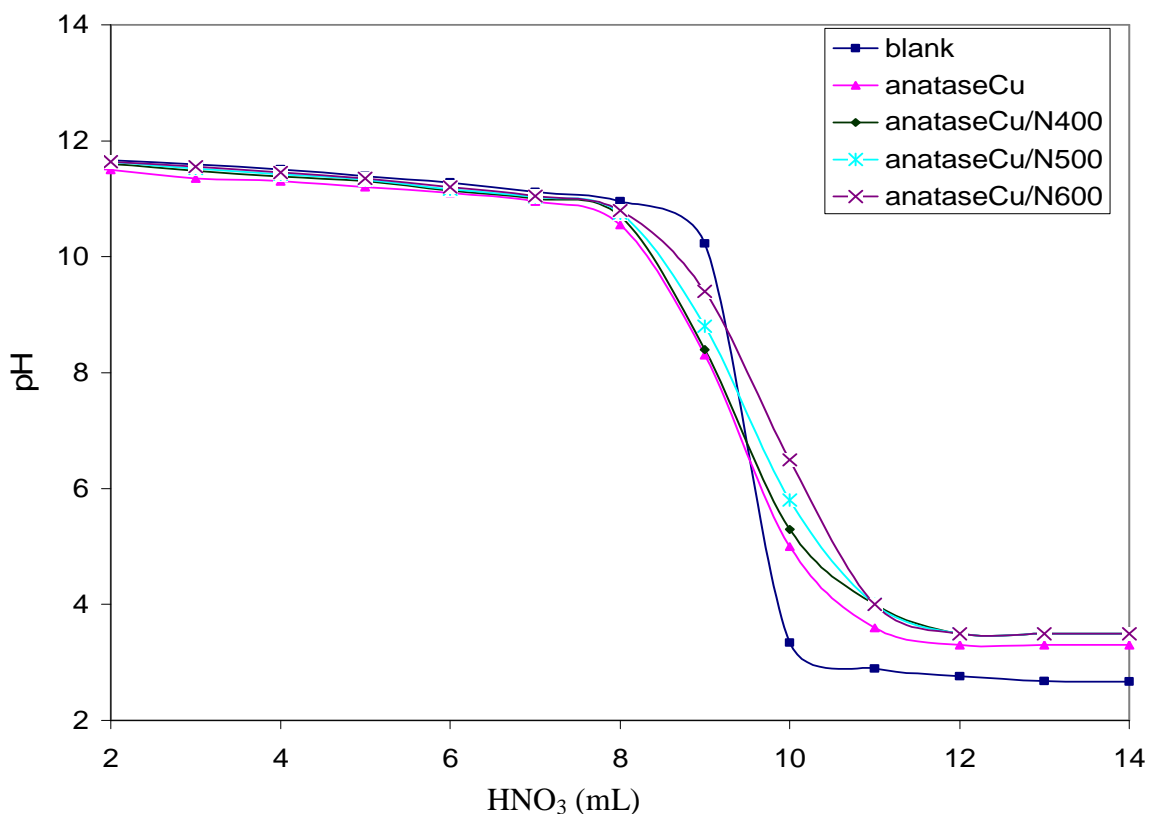


**Figure 3-33:** Titration curve for co-doped anatase/Cu/N, the average error bar  $\pm 0.10$ .

From the above results, it was observed that the values of the PZC values for the co-doped anatase were higher than that for the metal-doped anatase and the value of the PZC was increased with increase in the concentration of nitrogen in the doped samples. This could possibly be due to the presence of the adsorbed ammonia and the other nitrogen species on the surface of the doped titania. These adsorbed species could contribute to the acid- base interaction on the surface of doped titania. Hence, increasing the percentage of doping would increase the basicity of the surface with the increase in amount of the doped nitrogen species<sup>(97)</sup>. Consequently, this causes increasing in the basic behaviour of the surface, which leads accordingly to the observed increase in the PZC values. Comparison these results with that for nitrogen doped anatase showed slightly increase in the PZC values for co-doped samples. This probably arises from adsorption of ions on the surface of titania.

### 3-9 Photocatalytic activity of the co-doped anatase

To investigate the photocatalytic activity of co- doped antase (TiO<sub>2</sub>/M/N), photocatalytic decoloration of MB dye was used as a test reaction. Reaction was carried out by irradiation with UV light from the middle pressure mercury lamp at 22 °C. Decoloration of MB was followed by measuring absorbance at 655nm. These results are presented in the following figure:

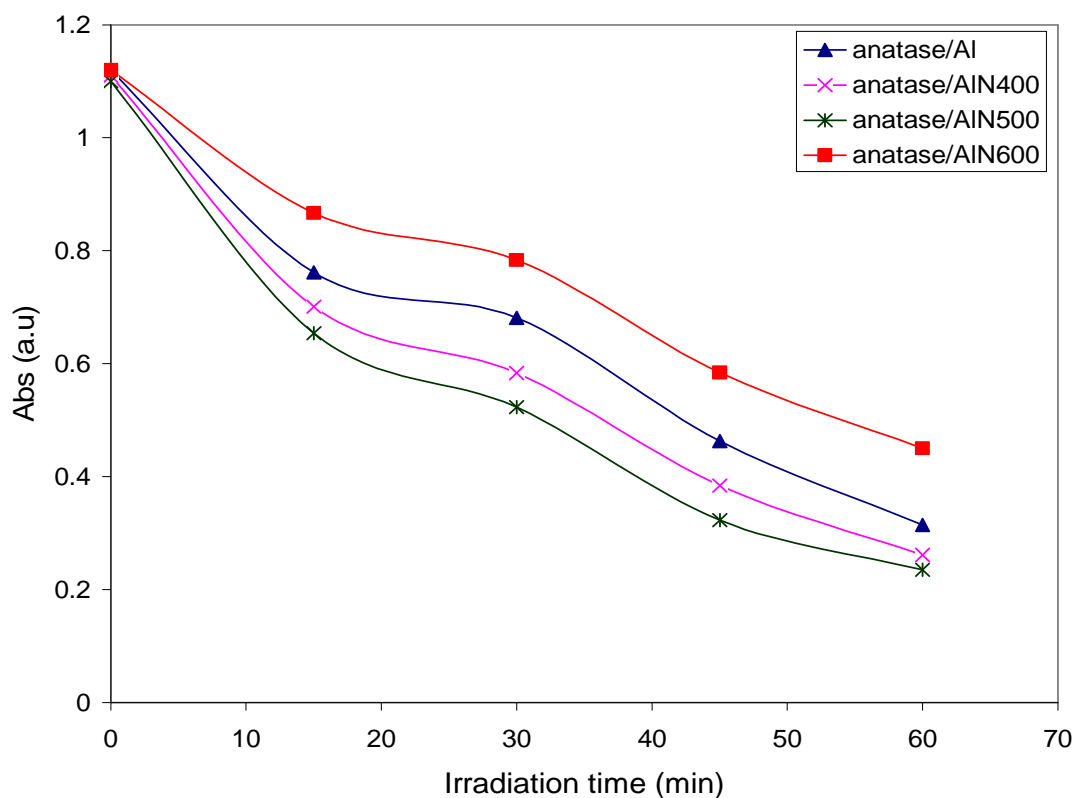


**Figure 3-34:** Photocatalytic decoloration of MB over anatase co-doped with N and Al.

The rate of the photocatalytic decoloration of MB over co-doped anatase/Al is shown in the following table:

**Table 3-9:** Rate of decoloration of MB over co-doped anatase/Al.

Catalyst	Rate of reaction $\times 10^{-8} \pm 0.10/ \text{mol. l}^{-1} \cdot \text{s}^{-1}$	Surface area normalized rate $\times 10^{-8}/ \text{mol. l}^{-1} \cdot \text{s}^{-1} \cdot \text{m}^{-2}$
anatase/Al	1.68	1.40
anatase/Al/N400	1.82	1.52
anatase/Al/N500	1.96	1.53
anatase/Al/N600	1.48	1.68

From the above results, the activity for the photocatalytic decoloration of MB over co-doped anatase/Al fall in the order:

anatase/Al/N500 > anatase/Al/N400 > anatase/Al > anatase/Al/N600.

The results for the photocatalytic decoloration of MB over co-doped anatase/Co are shown in the following figure:

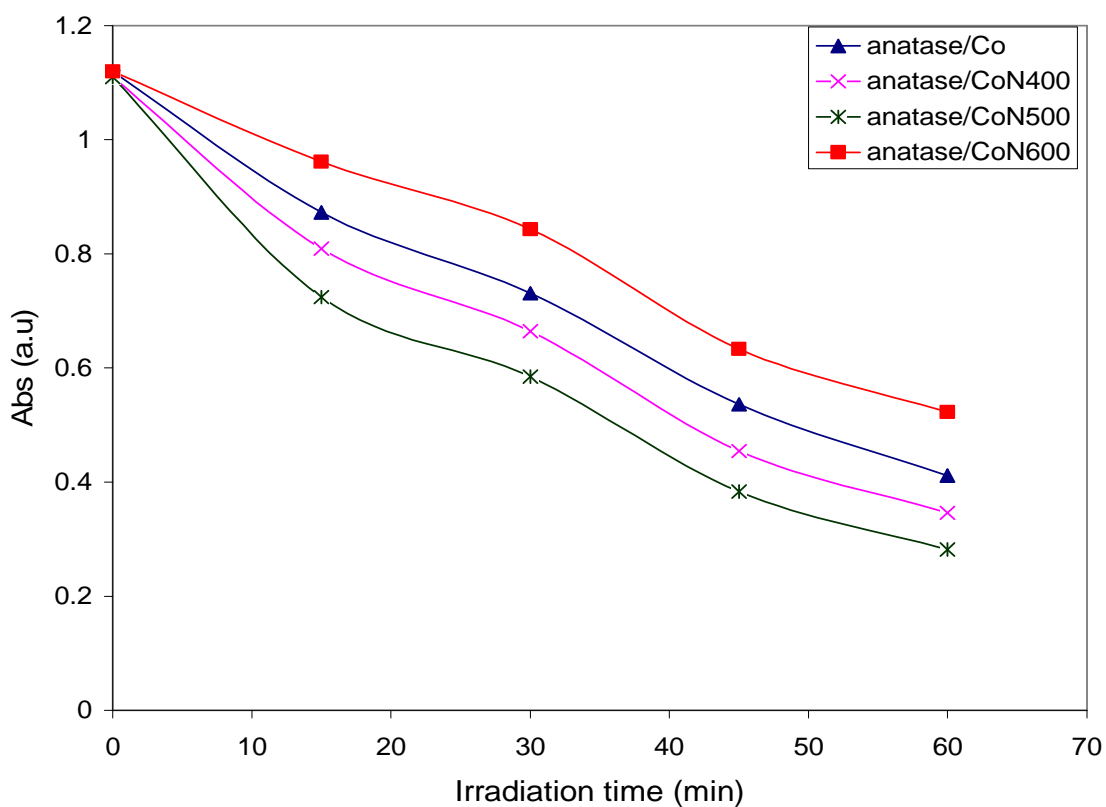


**Figure 3-35:** Photocatalytic decoloration of MB over anatase co-doped with N and Co.

The rate of the photocatalytic decoloration of MB over co-doped (N/Co/ anatase) is shown in the following table:

**Table 3-10:** Rate of decoloration of MB over co-doped anatase/Co.

Catalyst	Rate of reaction $\times 10^{-8} \pm 0.10/ \text{mol. l}^{-1}.\text{s}^{-1}$	Surface area normalized rate $\times 10^{-8}/ \text{mol. l}^{-1}.\text{s}^{-1}.\text{m}^{-2}$
anatase/Co	1.48	1.27
anatase/Co/N400	1.62	1.35
anatase/Co/N500	1.74	1.41
anatase/Co/N600	1.36	1.58

From the above results, the activity for the photocatalytic decoloration of MB over co-doped anatase/Co fell in the order:

anatase/Co/N500 > anatase/Co/N400 > anatase/Co > anatase/Co/N600.

The results for the photocatalytic decoloration of MB over co-doped anatase/Cu is shown in the following figure:

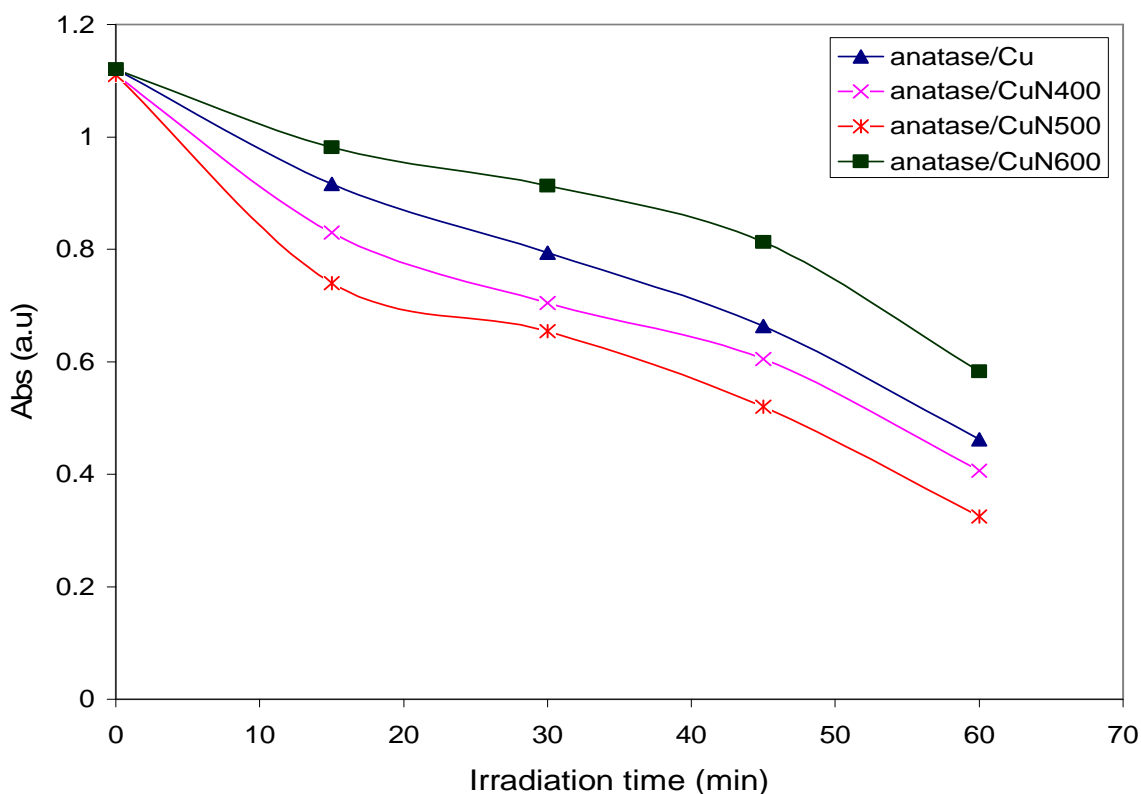


**Figure 3-36:** Photocatalytic decoloration of MB over anatase co-doped with N and Cu.

The rate of the photocatalytic decoloration of MB over co-doped anatase/Cu is shown in the following table:

**Table 3-11:** Rate of decoloration of MB over co-doped anatase/Cu.

Catalyst	Rate of reaction $\times 10^{-8}$ $\pm 0.08 / \text{mol. l}^1 \cdot \text{s}^{-1}$	Surface area normalized rate $\times 10^{-8} / \text{mol. l}^{-1} \cdot \text{s}^{-1} \cdot \text{m}^{-2}$
anatase/Cu	1.44	1.24
anatase/Cu/N400	1.58	1.30
anatase/Cu/N500	1.71	1.36
anatase/Cu/N600	1.32	1.57

From the above results, the activity for the photocatalytic decoloration of MB over co-doped anatase/Cu fell in the order:

anatase/Cu/N500 > anatase/Cu/N400 > anatase/Cu > anatase/Cu/N600.

From these above results, it was found that there was a general improvement in the photocatalytic activity for the co-doped samples of anatase that was initially doped with Al, Co and Cu and then doped with nitrogen at 400 °C and 500 °C. Photoactivity increased with an increase of nitrogen content for all the samples of the three metals, the increase activity is probably related to the presence of the metal ions which can act as electron traps for conduction band electrons improving the charge separation between ( $e^-_{CB}$ ,  $h^+_{VB}$ ) pairs. The co-doped samples which were doped with nitrogen at 600 °C and which had higher nitrogen contents showed poorer photocatalytic activity in comparison with those doped at 400 °C and 500 °C and also with the samples singly doped with metal ions. This negative effect is probably due to relatively high nitrogen concentrations with these samples. For this case nitrogen impurities may act as a recombination centres for ( $e^-_{CB}$ ,  $h^+_{VB}$ ) pairs. Generally, improvement in the photoactivity for the co-doped samples at 400 °C and 500 °C is related to the formation of a nitrogen dopant level above the valence band of titania for the substitutional nitrogen. In addition, doping metals would lower the conduction of titania, both these two factors would improve the photoactivity of the co-doped samples<sup>(89)</sup>.

### **3-9-1 Photocatalytic polymerization of methyl methacrylate over co-doped anatase**

Photocatalytic polymerization of methyl methacrylate over co-doped anatase was investigated under illumination with UV light from the middle pressure mercury lamp (125 watt, immersion type) for two hours at 20 °C.

### **3-9-2 Characterization of the polymer**

Polymer formation was characterized by using FTIR spectroscopy, NMR spectroscopy, SEM and TG analysis for both the bound and the extracted polymer.

#### **3-9-2-1 FTIR spectra**

The FTIR spectra for MMA, PMMA extracted and PMMA grafted co-doped anatase are shown in the following figures:

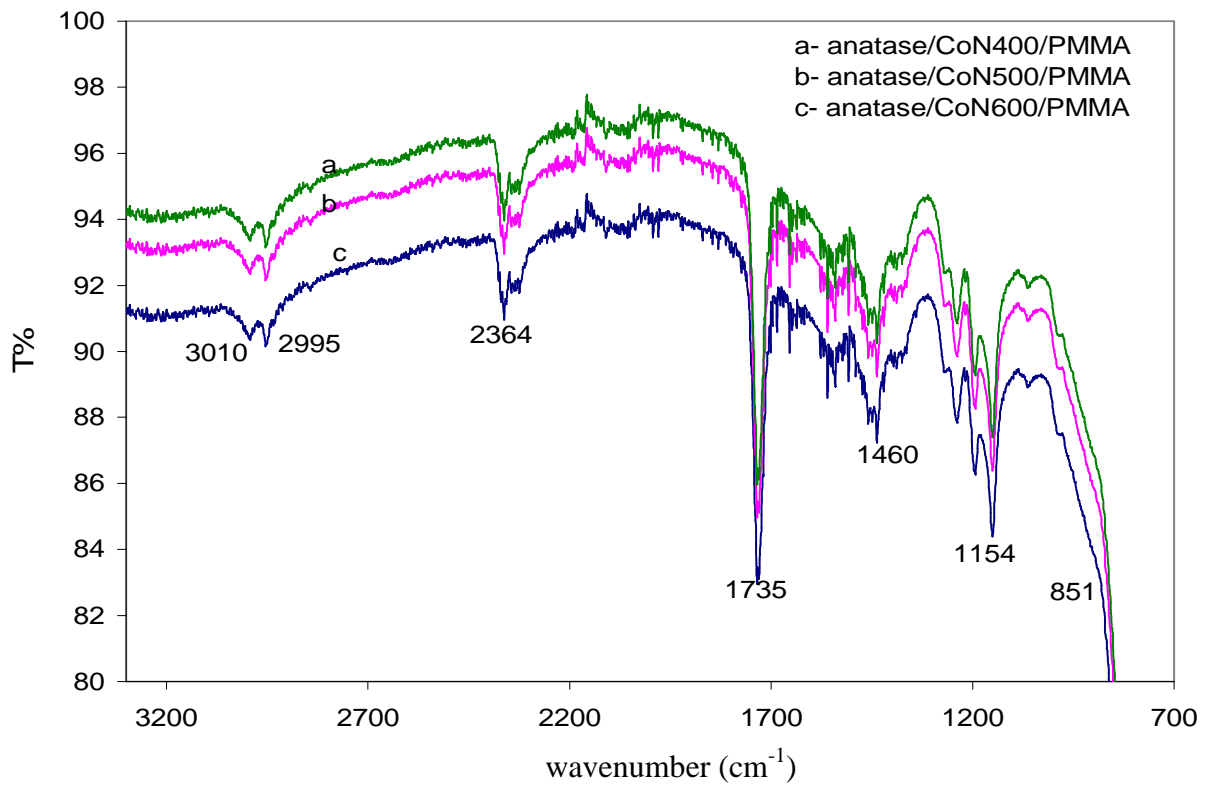


**Figure 3-37:** FTIR spectra for PMMA grafted co-doped anatase/Co/N.

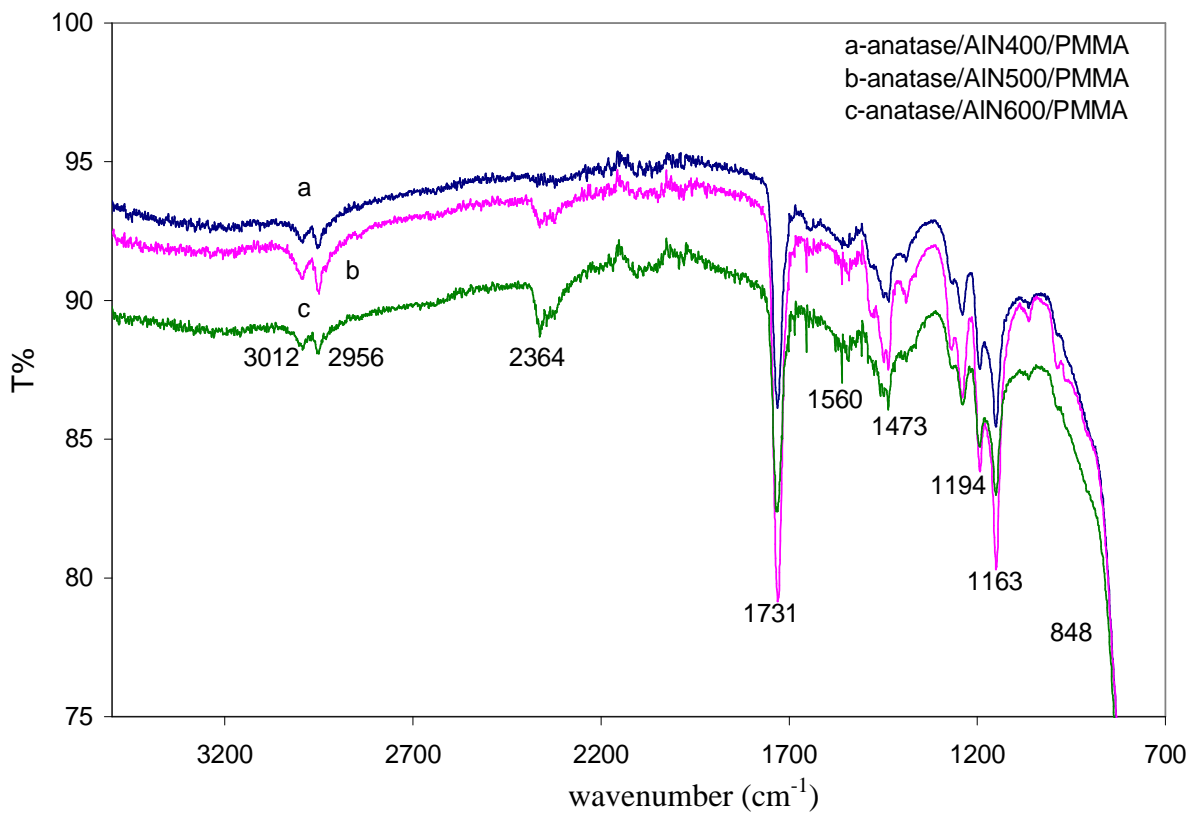


**Figure 3-38:** FTIR spectra for PMMA grafted co-doped anatase/Al/N.

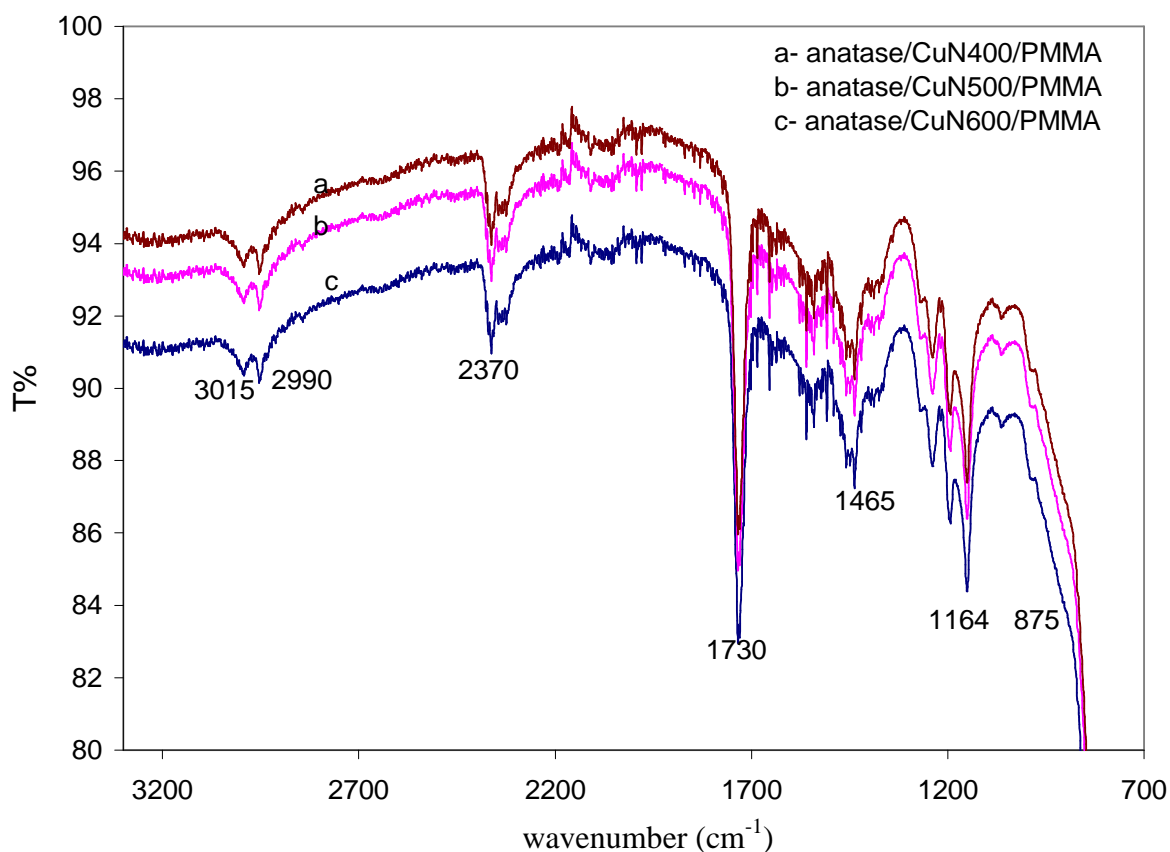


**Figure 3-39:** FTIR spectra for PMMA grafted co-doped anatase/Cu.

FTIR spectra for both extracted PMMA and grafted PMMA on the co-doped anatase show a characteristic sharp band around  $1735\text{ cm}^{-1}$ , which indicates the presence of the grafted PMMA on the anatase and the forming of a PMMA/ metal co-doped anatase composite. For the extracted PMMA, the broad band around  $3010\text{ cm}^{-1}$  is related to free  $\text{CH}_3$  vibrations in the PMMA. The band at  $1000\text{-}1460\text{ cm}^{-1}$  can be assigned to the C-O-C stretching mode of the ester bond in PMMA. The other bands at  $750\text{-}950\text{ cm}^{-1}$  are due to the bending of C-H bonds<sup>(82)</sup>. For PMMA grafted anatase, the broad band at  $2995\text{-}3010\text{ cm}^{-1}$  is due to the stretching vibrations of -OH groups on the titania surface. In addition, the FTIR spectrum of PMMA grafted anatase shows other characteristic peaks at  $1450$ ,  $1370$ ,  $1225$  and  $1154\text{ cm}^{-1}$ . These are assigned to the C-H,  $-\text{CH}_2$  and C-O-C band of PMMA. It appears that the  $\text{CH}_3$  vibrational mode for PMMA grafted anatase at  $3000\text{-}3100\text{ cm}^{-1}$  overlaps with the stretching vibration of OH<sup>(82)</sup>. These features are consistent with the presence of PMMA grafted to the surface of titania. The FTIR spectra for PMMA grafted co-doped anatase are similar to those for grafted singly doped anatase with nitrogen and metal shown earlier. Both extracted and grafted PMMA on the anatase showed a characteristic band around  $1735\text{ cm}^{-1}$ , this sharp peak indicates the presence of the grafted PMMA on the anatase. Also the band at  $2990\text{-}3000\text{ cm}^{-1}$  is related to free  $\text{CH}_3$

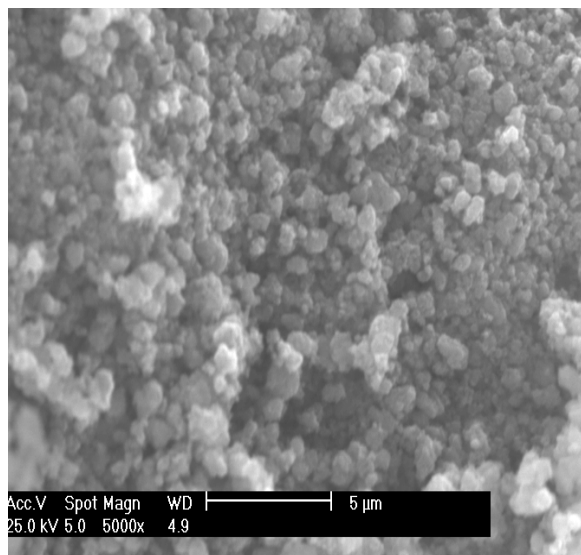
vibrations and the band at  $1135\text{ cm}^{-1}$  can be assigned to the -C-C-O- stretching mode which is not present in MMA<sup>(83)</sup>.

### **3-9-2-2 <sup>1</sup>H NMR spectroscopy**

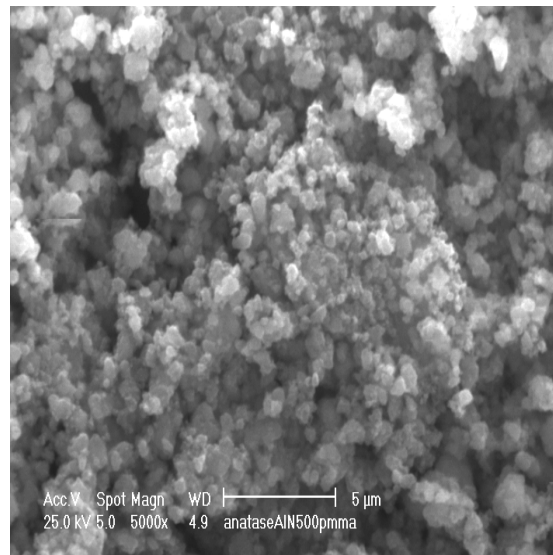
Further investigation for the extracted polymer was undertaken using <sup>1</sup>H NMR spectroscopy. The spectrum was similar to that obtained for PMMA that extracted from metal-doped anatase (Figure 3-19). The <sup>1</sup>H NMR spectrum of the extracted PMMA from co-doped anatase showed an identical spectrum for that extracted from singly doped titania with nitrogen and metal alone. This spectrum confirms the formation of the polymer. From the above figure, it can be observed that the peaks at  $\delta = 5.50$ , and  $6.05$  which are assigned to the  $(\text{H}_2\text{C}=\text{C}(\text{CH}_3)-)$  in MMA was absent in PMMA as shown in Figures (3- 18) - (3- 19). In addition the <sup>1</sup>H NMR spectrum for the extracted PMMA, showed a peak which is related to the methoxy protons at  $\delta = 3.57\text{-}3.64$ <sup>(84)</sup>.

### **3-9-2-3 Scanning electron microscopy**

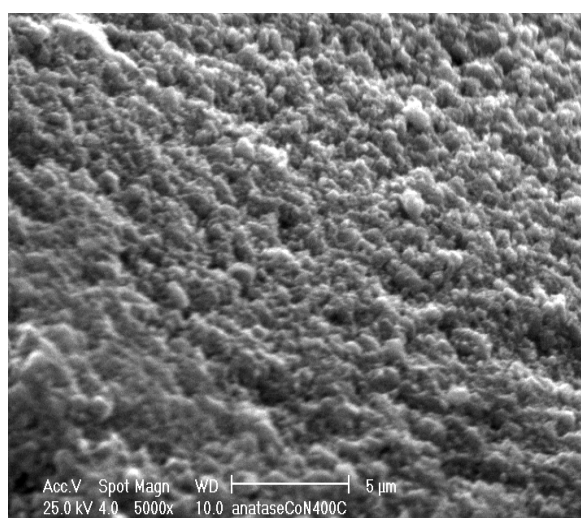
Morphological studies for co-doped anatase grafted with PMMA were undertaken using SEM, and the results are shown in the following figure:



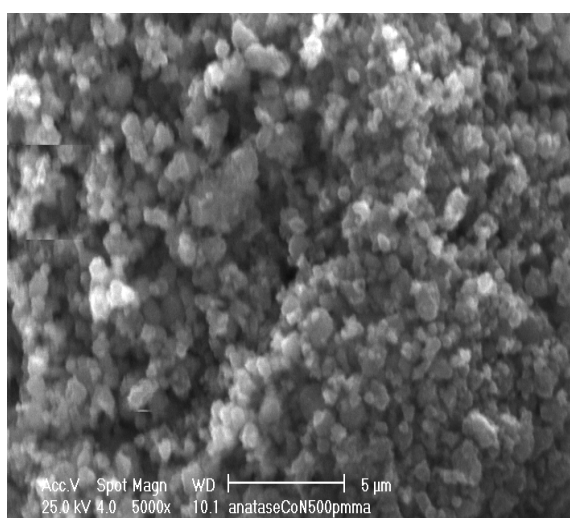
A



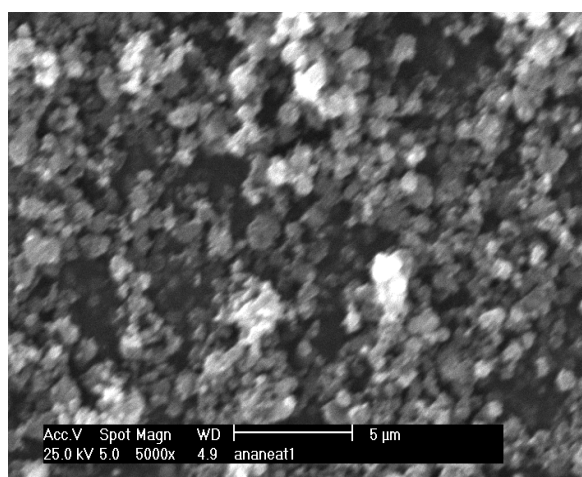
B



C



D



E

**Figure 3-40:** SEM for anatase/AlN400PMMA(A), anatase/AlN500PMMA (B), anatase/CoN400PMMA (C), anatase/CoN500PMMA (D) and neat anatase (E).

From the above images, it can be seen that the morphology of the surface after grafting with the polymer was changed<sup>(85)</sup>. Upon grafting with the polymer, nanoparticles of titania are aggregated together. When PMMA was grafted on the surface, it showed a better dispersion and the aggregation of nanoparticles was increased in this case.

### 3-9-2-4 TGA analysis

The bound polymer was further investigated by thermal gravimetric analysis and the results are shown in the following figures:

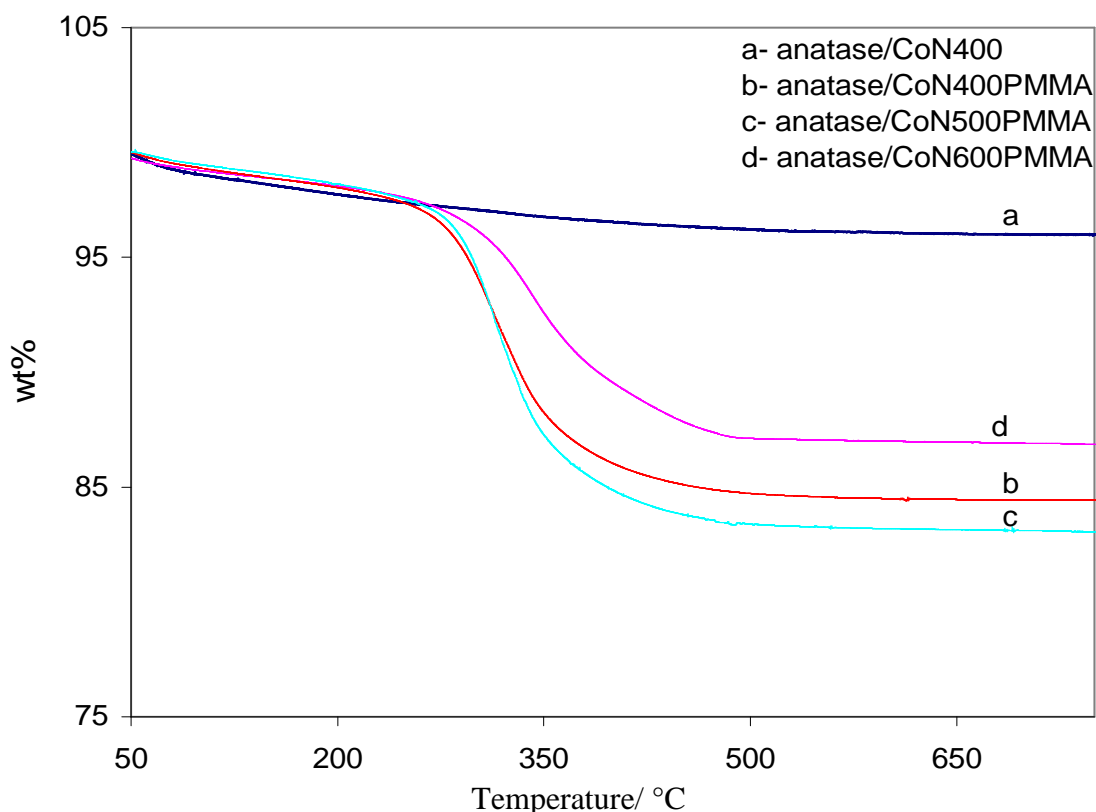


**Figure 3-41:** TGA for PMMA grafted co-doped anatase/Co in air. Conversion percentage of grafting for anataseCoN400, anataseCoN500, and anataseCoN600 were 17.%, 19.8% and 13.6% respectively.

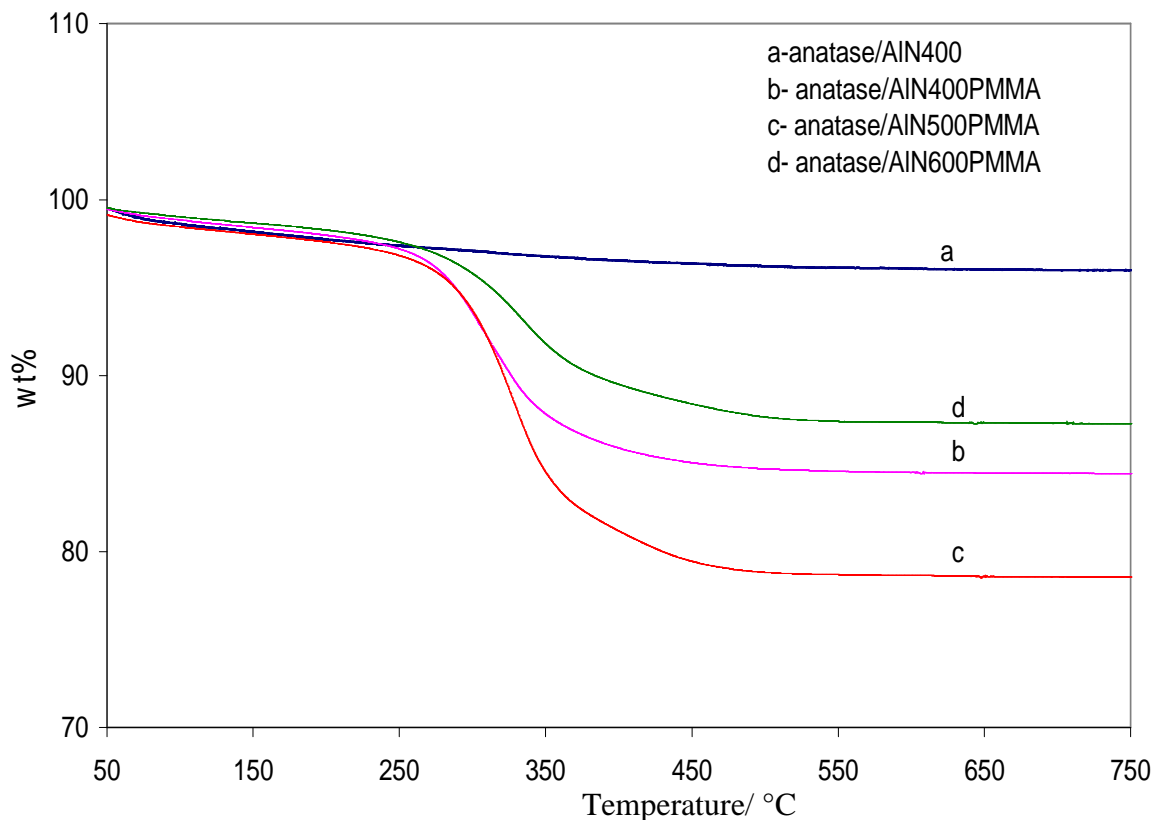


**Figure 3-42:** TGA for PMMA grafted co-doped anatase/Al in air. Conversion percentage of grafting for anataseAlN400, anataseAlN500, and anataseAlN600 were 13.6%, 24.4%, and 12.4% respectively.

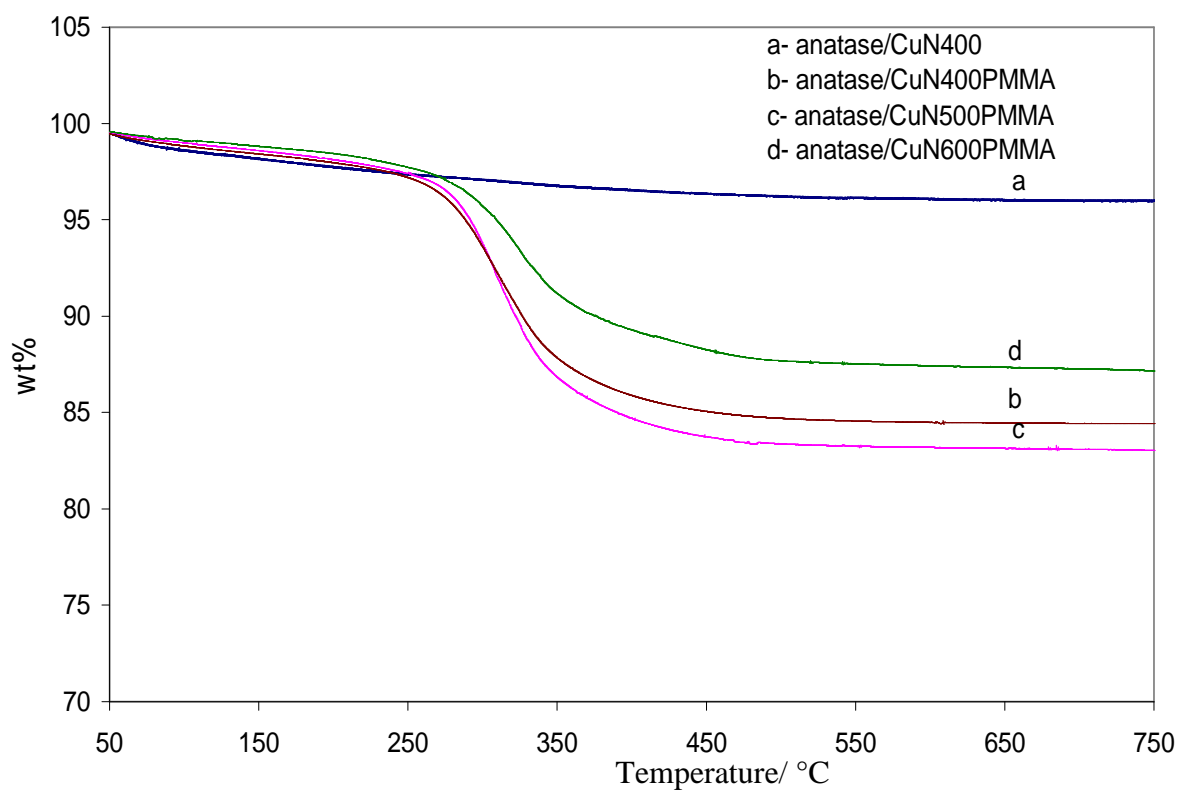


**Figure 3-43:** TGA for PMMA grafted co-doped anatase/Cu in air. Conversion percentage of grafting for anataseCuN400, anataseCuN500, and anataseCuN600 were 17.4, 20.1% and 14.3% respectively.

The above figures confirmed the formation of the polymer within the composite PMMA/ anatase due to the mass loss about 12-22% of the weight in the range 300- 450 °C.

In addition, the grafted PMMA was decomposed at different temperature than that for the traditional PMMA<sup>(86)</sup>. This arises from strong interaction between the chains of the grafted polymer and the surface of titania particles.

### 3-9-2-5 X-ray diffraction patterns

The XRD patterns for the extracted PMMA and grafted on co-doped anatase were investigated to study the effect of the grafting on the crystal structure of titania. The XRD patterns are shown in the following figures:

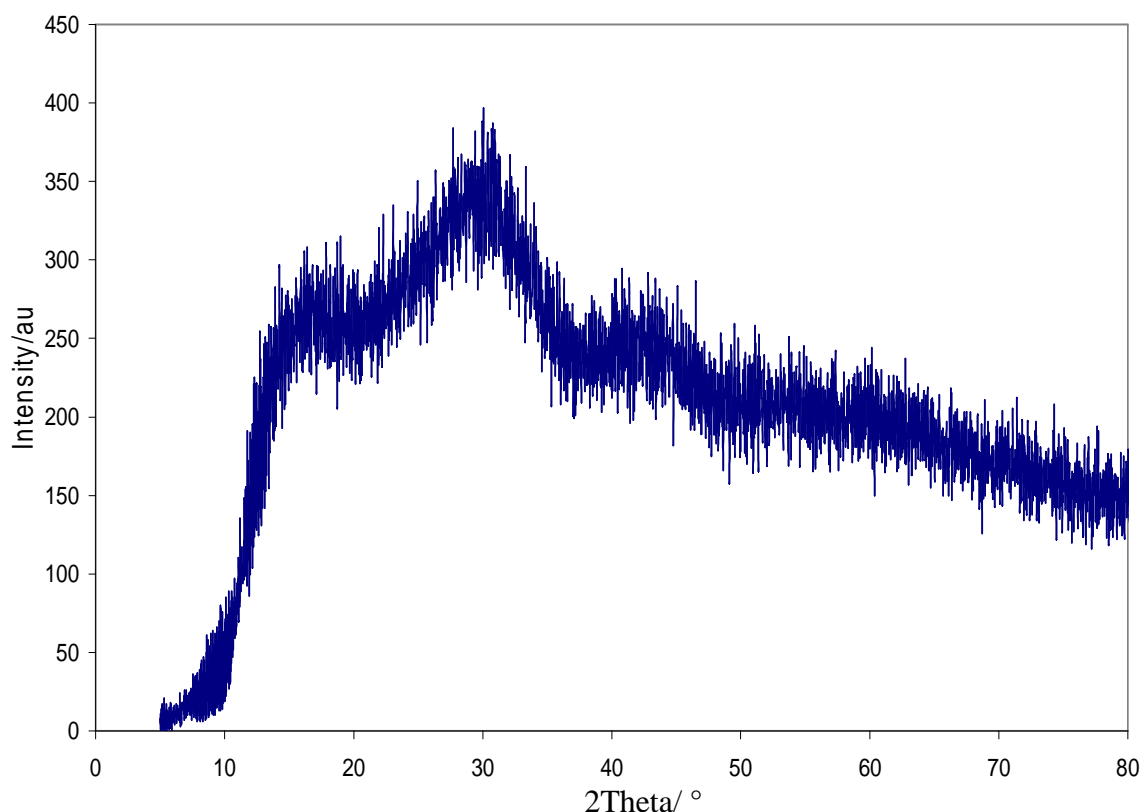


**Figure 3-44:** XRD pattern for extracted PMMA.

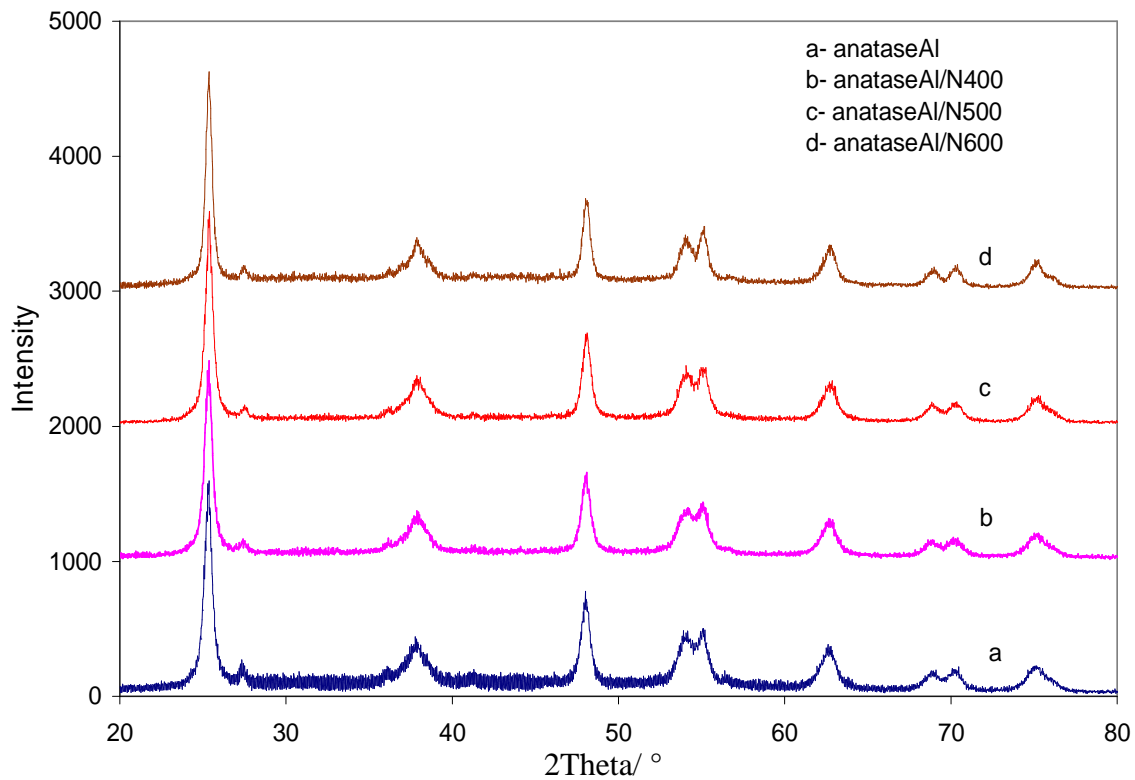


**Figure 3-45:** XRD patterns for grafted PMMA with co-doped anatase/Al/N.

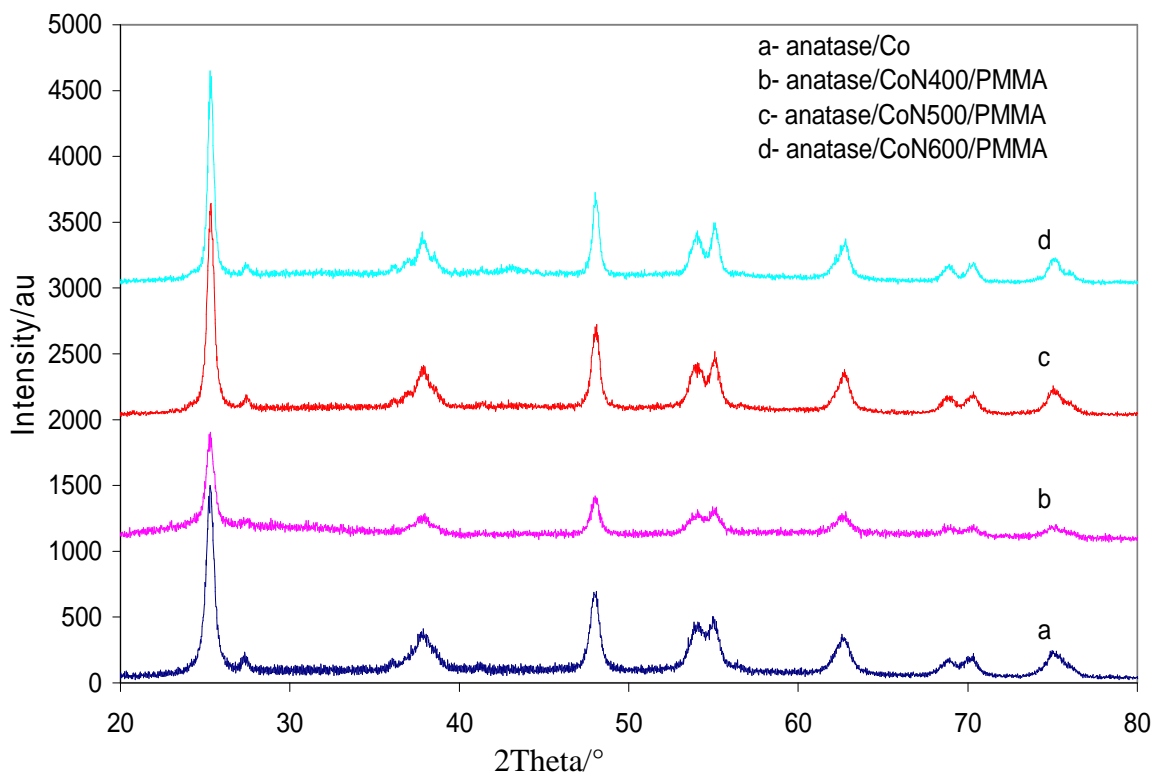


**Figure 3-46:** XRD patterns for grafted PMMA with co-doped anatase/Co/N.

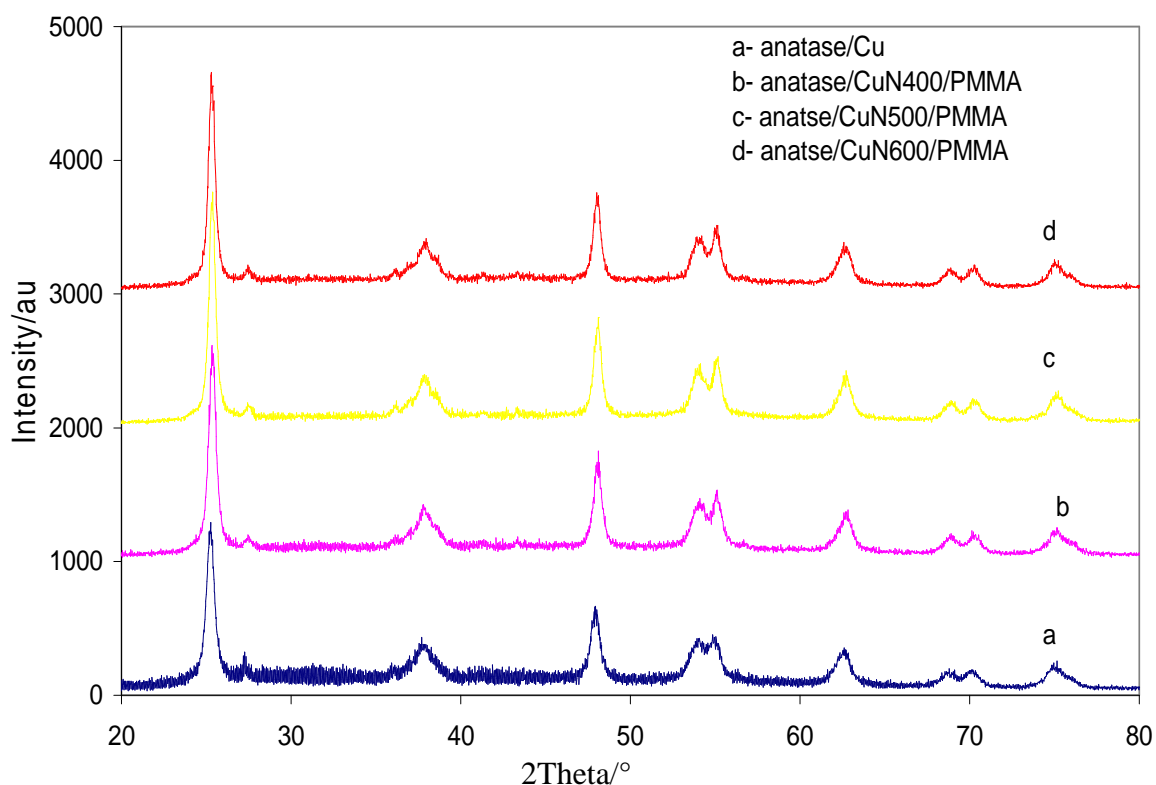


**Figure 3-47:** XRD patterns for PMMA grafted co-doped anatase/Cu/N.

From the above figures, it can be seen that the XRD pattern of the extracted PMMA was identical with that obtained via photocatalytic polymerization over nitrogen and metal doped titania. This pattern is typical of an amorphous material. Additionally, the XRD patterns for anatase grafted with PMMA are similar to that of the parent anatase. This indicates that grafting of the polymer over titania surface doesn't alter its crystalline structure.

### 3-9- 3 Photocatalytic polymerization of methyl methacrylate over co-doped anatase

Photocatalytic polymerization of MMA was undertaken over nitrogen co-doped anatase. The reaction was performed by irradiation with UV light at 22 °C for two hours for each experiment under normal atmosphere. The average error bar was  $\pm 0.30\%$ . The results are presented as a percentage of conversion against irradiation time in minutes as shown in the following figures:

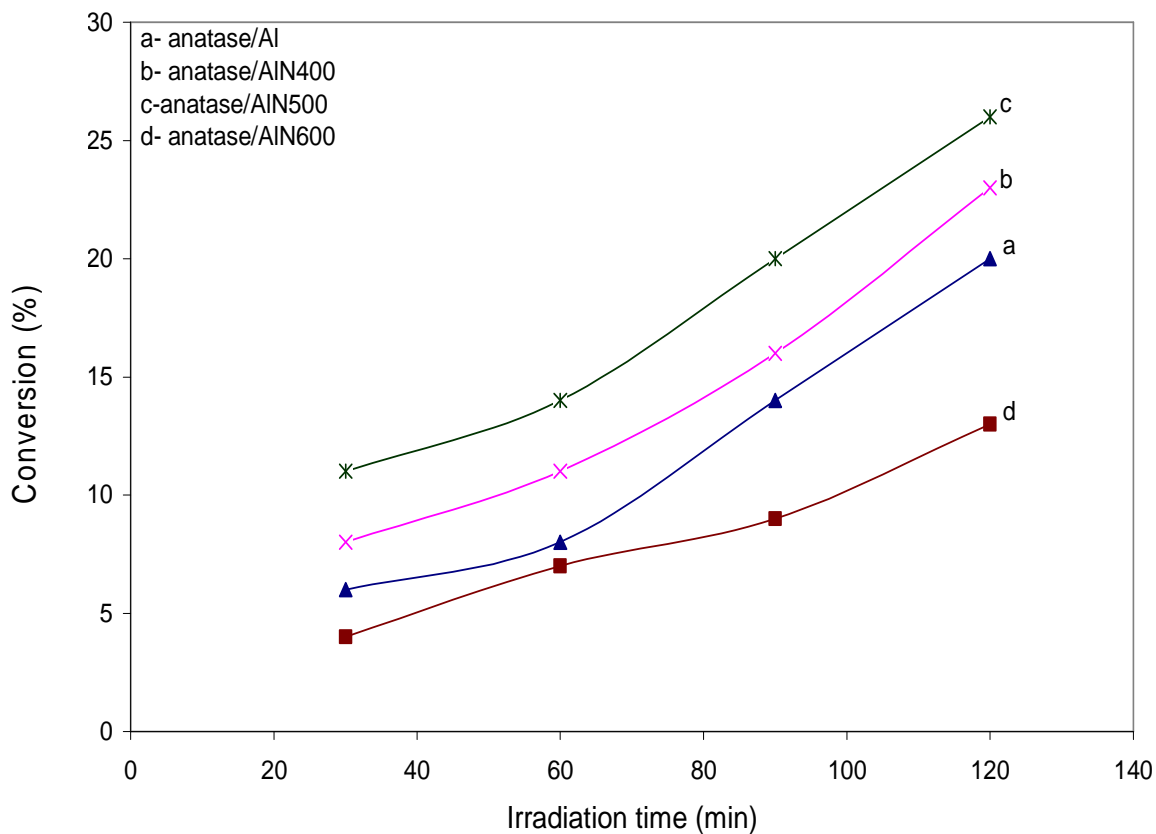


**Figure 3-48:** Photocatalytic polymerization of MMA over anatase co-doped with Al and N.

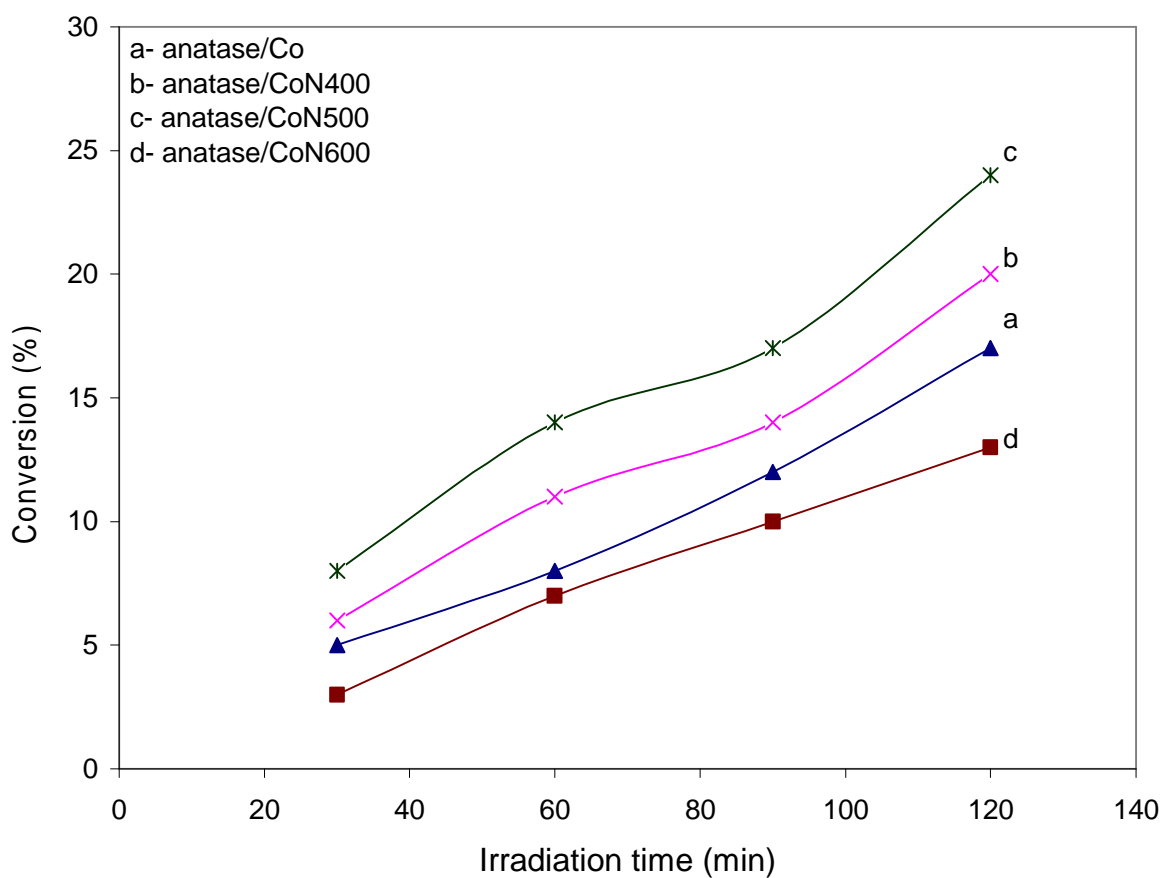


**Figure 3-49:** Photocatalytic polymerization of MMA over anatase co-doped with Co and N.

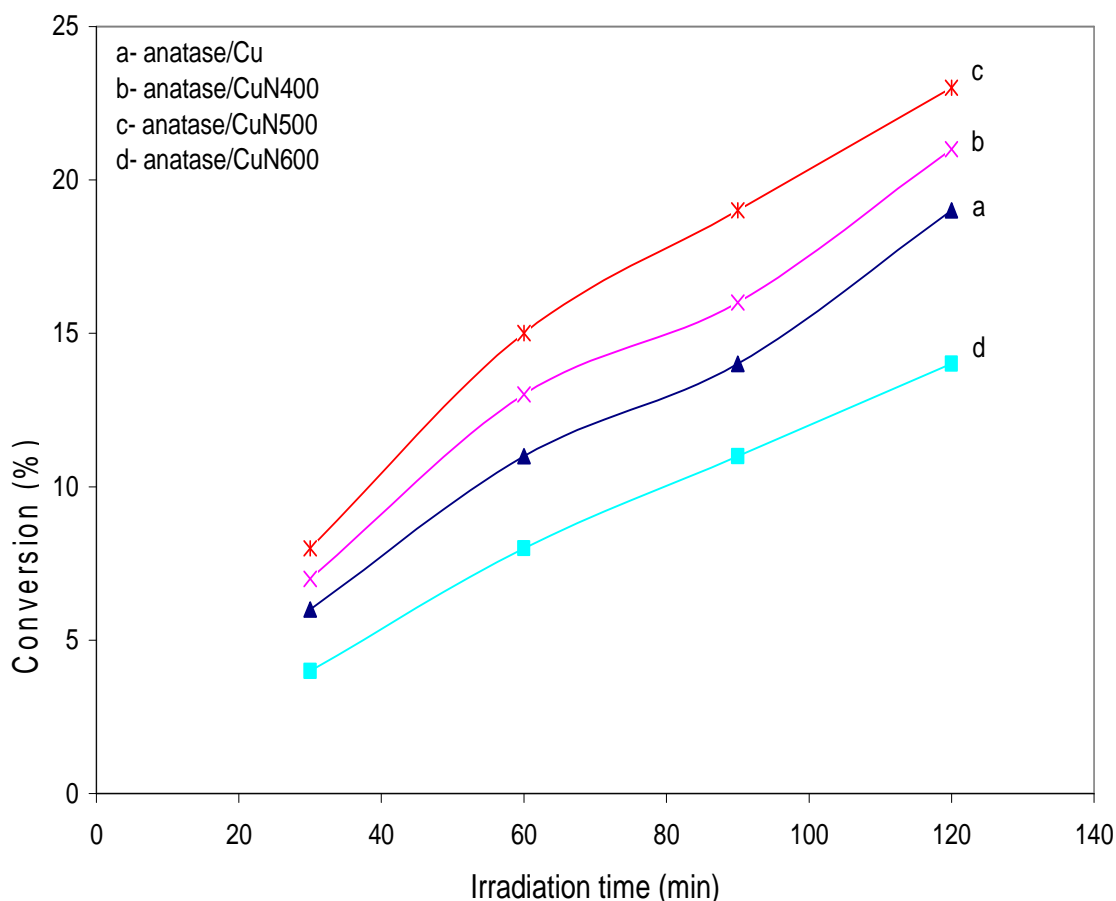


**Figure 3-50:** Photocatalytic polymerization of MMA over anatase co-doped with Cu and N.

From these results, it was found that there is a general improvement in the photocatalytic activity for the co-doped samples of anatase that were initially doped with Al, Co and Cu and then doped with nitrogen at 400 °C and 500 °C. Photoactivity was increased with an increase of nitrogen content for all samples of the three metals, the increase in the activity probably related to the presence of the metal ions which can act as electron traps for the conduction band electrons, this can improve the charge separation between ( $e^-_{CB}$ ,  $h^+_{VB}$ ) pairs<sup>(98,99)</sup>. In addition to, enhancement in the photoactivity for the co-doped anatase at 400 °C and 500 °C for the three metals doped (Al, Cu and Co) is probably due to the relative increase in the specific surface areas for the three samples when loaded with nitrogen at 400 °C and 500 °C<sup>(100,101)</sup>. There was a relative decrease in the particle size for these samples. It is well known that these two factors can improve photoactivity of the photocatalyst. That can lead to enhanced yields of polymerization in comparison with the metalized photocatalysts at the same reaction conditions. Generally, improvement in the photoactivity for the co-doped samples at 400 °C and 500 °C can be related to the formation of a nitrogen dopant level above the valence band of titania. In addition, doping metals would lower the conduction of titania. Both these factors would improve the photoactivity

of the co-doped samples<sup>(102,103)</sup>. On the other hand, co-doped samples, which were doped with nitrogen at 600 °C with a higher nitrogen contents, showed poorer photocatalytic activity in comparison with those doped at 400°C and 500 °C and with the samples singly doped with metal ions. This negative effect is probably due to a relatively high nitrogen concentration in these samples. For this case, nitrogen impurities may act as a recombination centres for ( $e^-_{CB}$ ,  $h^+_{VB}$ ) pairs, there was a significant decrease in the specific surface area with an increase in the particle size, due to the sintering effect which normally occurs when subjecting a catalyst to high temperatures<sup>(104, 105)</sup>. Generally, the activity of the catalyzed reaction decreases with the reduction in its specific surface area, beside that the amount of the doped nitrogen increases with elevation in temperatures. Furthermore, high levels of dopants also have a negative effect on the reaction because it may generate recombination centres within the lattice of the catalyst, these centres increase rate of the recombination reaction between conduction band electron and valence band hole. Recombination plays a major role in the reduction photocatalytic activity of the photocatalyst<sup>(106,107)</sup>. Generally, improvement in the photoactivity for the co-doped samples at 400 °C and 500 °C is related to the formation of a nitrogen dopant level above the valence band of titania for the substitutional nitrogen. In addition to that, doping metals would lower the conduction of titania, both these two factors would improve the photoactivity of the co-doped samples. Generally, from previous results for metal doped and co-doped titanic, it can be found that there was enhanced in the photoactivity of titanic for metal doped titania and co-doped samples at 400 and 500 °C. In opposite that samples co-doped at 600 °C showed negative activity with respect to the neat titania samples. These results seem to be similar to that were obtained in Chapter 2.

### 3-10 Conclusions

This chapter describes modification of titania by doping  $\text{Al}^{3+}$ ,  $\text{Co}^{2+}$  and  $\text{Cu}^{2+}$ . Then metal-doped samples were also co-doped with nitrogen at 400 °C, 500 °C, and 600 °C. Doping was not observed to affect the crystalline structure of the various phases investigated. Samples doped with metals and nitrogen at 400 °C and 500 °C showed slightly higher BET surface area in comparison with the parent samples. In contrast, co-doped samples at 600 °C showed a lower BET surface area. The PZC for the variously doped samples was measured by potentiometric titration. The metal-doped samples and co-doped samples showed relatively higher PZC values, and the PZC value was increased with increase of the treatment temperature. The photocatalytic activity of these samples was investigated by following the photocatalytic decomposition of methylene blue and the photocatalytic Polymerization of methyl methacrylate.

Generally, samples doped with  $\text{Al}^{3+}$ ,  $\text{Co}^{2+}$  and  $\text{Cu}^{2+}$  alone showed better photocatalytic activity in comparison with the parent samples. This possibly due to the improvement in the absorption of these samples in the visible region and reduction the rate of recombination reaction between conduction band electron and valence band hole in the parent samples. Co-doped samples at 400 °C and 500 °C showed higher photocatalytic activity. However, the co-doped samples at 600 °C showed a lower activity in comparison with the neat samples. This may be attributed to the reduction in the BET surface area of these samples. Additionally, these samples have a high nitrogen content, which may enhance recombination between ( $e^-_{\text{CB}}$ ,  $h^+_{\text{VB}}$ ) pairs reducing activity. Aluminium has not been widely reported as a dopant in the literature previously, despite the fact that it may be expected to produce interesting effects in the  $\text{TiO}_2$  system since the ionic radii of  $\text{Ti}^{\text{IV}}$  and  $\text{Al}^{3+}$  are reasonably close (0.75 Å and 0.68 Å) respectively<sup>(108)</sup> and the charges are obviously different. The use of these co-doped samples of titania in photocatalytic polymerization has not been reported widely in the literature, to the best of the author's knowledge. The consideration/ concerns relating to the source used in this work as outlined in Chapter 2, also apply here. Future work should be directed towards elucidating the photocatalytic polymerization activity of these novel doped and co-doped systems using more well defined light sources. This can be achieved by using a source of light, which emits radiation in either UV, and or visible region of the spectrum.

### 3-11 References

1. C. Damm, *J. Photochem. Photobiol. A: Chem.*, 2006, **181**, 279.
2. C. Damm, D.Voltzke, G. Israel, *J. Photochem. Photobiol. A: Chem.*, 2005, **174**, 171.
3. C. Paulus, K. Wilke, H. Breuer, *J. Inf. Rec.*, 1998, **24**, 299.
4. M.Grätzel, A. Hagfeldt, *Chem. Rev.*, 1995, **95**, 49.
5. M. Kruggel, G. Israel, *J. Inf. Rec.*, 1996, **23**, 47.
6. K. Karakitson, X.Verykios, *J. Phys. Chem.*, 1993, **97**,1184.
7. A. Paola, G. Marci, L. Palmisano, M. Schiavello, K. Uosaki, S. Ikeda, B. Ohtani, *J. Phys. Chem. B*, 2002, **106**, 637.
8. V. Bondzie, S. Parker, C. Campbell, *Catal. Lett.*, 1999, **63**,143.
9. N. Nakajima, H. Kato, T. Okazaki, Y. Sakisaka, *Surf. Sci.*, 2004, **93**, 561.
10. U. Diebold, J. Pan, T. Madey, *Surf. Sci.*, 1993, 896, 287.
11. J. Pan, U. Diebold, L. Zhang, T. Madey, *Surf. Sci.*, 1993, **295**, 411.
12. U. Diebold, H. Tao, N. Shinn, *Phys. Rev. B*, 1994, **19**,14474.
13. Y. Shao, W. Chen, E.Wold, J. Panl, *Langmuir*, 1994, **10**, 178.
14. T. Ranjit, I.Willner, S. Bossmann, *Environ. Sci. Technol.*, 2001, **35**, 1544.
15. Y. Lin, Y. Tseng, J. Huang, C. Cheng, *Environ. Sci. Technol.*, 2006, **40**, 1616.
16. X. Wang, J.Yu, C. Chen, F.Wu, *Environ. Sci. Technol.*, 2006, **40**, 2369.
17. B. Narayanan, Z. Yaakob, S. Chandralayyam, F. Saidu, V. Malayattil, *Eur. J. Sci. Res.*, 2009, **28**, 566.
18. F.Tom, G. Bertrand, S. Begin, C. Meunier, O. Barres, D. Klein, *Appl. Catal. B: Environ.*, 2006, **68**, 74.
19. J. Zhao, Y.Yang, *Build. Environ.*, 2003, **38**, 645.
20. T. Salama, I. Ali, M. Mohamed, *J. Mol. Catal. A: Chem.*, 2007, **273**, 198.
21. N. Venkatachalam, M. Palanichamy, B. Arabindoo, V. Murugesan, *Catal. Commun.*, 2007, **8**, 1088.
22. M. Anpo, *Catal. Surv. Jpn.*, 1997, **1**, 169.
23. A. Sakata, T. Kawai, Hashimot, *Chem. Phys. Lett.*, 1982, **88**, 131.
24. H. Harada, T. Veda, *Chem. Phys. Lett.*, 1984, **106**, 229.
25. B. Ohtani, J. Handa, S. Nishimoto, T. Kagira, *Chem. Phys. Lett.*, 1985, **120**, 292.
26. A. Sclafani, L. Palmisano, M. Schiavello, *J. Phys. Chem.*, 1990, **94**, 829.
27. V. Henrich, P. Cox, *The Surface Science of Metal Oxides*, Cambridge University Press, 1994, p. 103.
28. K. Smith, V. Hernich, *Phys. Rev. B*, 1985, **32**, 5384
29. K. Kolasinski, *Surface Science: Foundations of Catalysis and Nanoscience* , John Wiley and Sons Ltd., 2004, p. 13.

30. S. Sato, J. White, *J. Am. Chem. Soc.*, 1980, **102**, 7206.
31. H. Courbon, J. Herman, P. Pichat, *J. Catal.*, 1981, **72**, 129.
32. A. Takeuchi, J. Katzer, *J. Phys. Chem.*, 1981, **85**, 937.
33. B. Kraeutler, A. Bard, *J. Am. Chem. Soc.*, 1978, **100**, 4317.
34. W. Dunn, A. Bard, *Nouv. J. De Chim.*, 1981, **5**, 651.
35. D. Dounghong, E. Borgarello, M. Grätzel, *J. Am. Chem. Soc.*, 1981, **103**, 4685.
36. E. Borgarello, J. Kiwi, E. Pelizzetti, M.Visa, M. Grätzel, *J. Am. Chem. Soc.*, 1981, **103**, 367.
37. A. Mills, *J. Chem. Soc. Chem. Commun.*, 1982, 367.
38. J. Conesa, J. Soria, *J. Phys. Chem.*, 1982, **86**, 1392.
39. T. Apple, P. Gajard, C. Dybowski, *J. Catal.*, 1981, **13**, 92.
40. J. Kiwi, M. Grätzel, *J. Phys. Chem.*, 1984, **88**, 1302.
41. M. Anpo, *Pure Appl. Chem.*, 2000, **72**, 1787.
42. H. Yamashita, M. Harada, J. Misaka, M. Takenchi, M. Anpo, *J. Photochem. Photobiol. A*, 2002, **148**, 257.
43. J. Zhu, W. Zheng, B. He, J. Zhang, M. Anpo, *J. Mol. Catal. A*, 2004, **216**, 35.
44. J. Wu, C. Chen, *J. Photochem. Photobiol. A*, 2004, **163**, 509.
45. M. Anpo, M. Takeuchi, *J. Catal.*, 2003, **216**, 505.
46. H. Yamashita, M. Harada, J. Misaka, M. Takeuchi, B. Neppolian, M. Anpo, *Catal. Today*, 2003, **84**, 191.
47. A. Zaleska, *Recent Patents on Engineering*, 2008, **2**, 157.
48. W. Hung, S. Fu, H. Chu, T. Ko, *Chemosphere*, 2007, **66**, 2142.
49. S. Nahar, K. Hasegawa, S. Kagaya, *Chemosphere*, 2006, **65**, 1976.
50. P. Bouras, E. Stathatos, P. Lianos, *Appl. Catal. B: Environ.*, 2007, **73**, 51.
51. A. Ambrus, N. Balaz, T. Alapi, G. Wittmann, P. Sipos, A. Dombi, K. Mogyoros, *Appl. Catal. B: Environ.*, 2008, **81**, 27.
52. H. Li, G. Zhao, G. Han, B. Song, *Environ. Sci. Technol.*, 2007, **201**, 7615.
53. D. Masih, H. Yoshitake, Y. Izumi, *Appl. Catal. A: Gen.*, 2007, **325**, 276.
54. X. Fan, X. Chen, S. Zhu, Z. Li, Yu, J. Ye, *J. Mol. Catal. A: Chem.*, 2008, **284**, 155.
55. D. Hufschmidt, D. Bahnemonna, J. Testa, C. Emilio, M. Litter, *Photochem. Photobiol. A: Chem.*, 2002, **148**, 223.
56. T. Egerton, J. Mattinson, *Photochem. Photobiol. A: Chem.*, 2008, **194**, 283.
57. S. Kim, S. Hwang, W. Choi, *J. Phys. Chem. B*, 2005, 109, 24260.
58. Y. Zhao, C. Li, X. Liu, F. Gu, H. Du, L. Shi, *Appl. Catal. B: Environ.*, 2008, **79**, 208.

59. M. Serry, R. George, P. Florise, S. Pillai, *J. Photochem. Photobiol. A: Chem.*, 2007, **189**, 258.
60. M. Saif, M. Abdel- Mottaleb, *Inorg. Chim. Acta.*, 2007, **360**, 2863.
61. A. Fijushima, T. Rao, D. Tryk, *J. Photochem. Photobiol. C, Photochem. Rev.*, 2000, **1**, 1.
62. A. Fijushima, T. Rao, D. Tryk, *J. Photochem. Photobiol. C. Photochem. Rev.*, 2000, **1**, 1.
63. E. Kowalska, O. Omar, P. Mahaney, R. Abe, B. Ohtani, *Phys. Chem. Chem. Phys.*, 2010, **12**, 2344.
64. S. Sakthivel, M. Janczarek, H. Kisch, *J. Phys. Chem. B*, 2004, **108**, 19384.
65. Y. Jg, Q. Xiang, M. Zhou, *Appl. Catal.*, 2009, **B90**, 595.
66. X. Zhou, F. Peng, H. Wang, H. Yu, J. Yang, *J. Solid State Chem.*, 2011, **184**, 134.
67. A. Tesvis, N. Spanos, P. Koutsoukos, A.Linde, J. Lyklem, *J. Chem. Soc. Faraday Trans. I*, 1998, **24**, 295.
68. S. Shen, J. Chen, X.Wang, L. Zhao, L. Guo, *J. Power Sources*, 2011, **196**, 10112.
69. M. Litter, J. Navio, *J. Photochem. Photobiol. A: Chem.*, 1996, **98**, 171.
70. M. Nagaveni, S. Hedge, G. Mardas, *J. Phys. Chem.*, 2004, **108**, 20204.
71. T. Lopez, J. Moreno, R. Gomez, X. Bokhimi, A. Wang, H. Mdeira, G. Pecchi, P. Reyes, *J. Mater. Chem.*, 2002, **12**, 714.
72. J. Noh, J. Schwarz, *J. Colloid Interface Sci.*, 1989, **130**, 157.
73. D. Huang, S. Liao, W. Zhau, S. Quan, Z. He, J.Wan, *J. Phys. Chem. Solid*, 2009, **70**, 853.
74. D. Chen, Z. Jiang, J.Geng, J. Zhu, D.Yong, *J. Nanopart. Res.*, 2009, **11**, 303.
75. J. Deng, Y. Zhao, W. Liu, F. Chen, *Mater. Chem. Phys.*, 2009, **117**, 522.
76. X. Shen, J. Guo, Z. Liu, S. Xie, *Appl. Surf. Sci.*, 2008, **54**, 4726.
77. N. Serpone, D. Lawless, R. Khairudinov, *J. Phys. Chem.*, 1995, **99**, 16655.
78. V. Lliev, D. Tomova, L. Bilyarska, A. Eliyas, L. Petrov, *Appl. Catal.*, 2006, **63**, 266.
79. D. Hufschmidt, D. Bahnemann, J. Testa, C.Emilio, M. Litter, *J. Photochem. Photobiol. A: Chem.*, 2002, **148**, 223.
80. M. Hoffmann, S. Martin, W. Choi, D. Bahnemann, *Chem. Rev.*, 1995, **95**, 69.
81. G. Ciston, Z. Saponjic, L. Chen, N. Dimitrijevic, T. Rajh, K. Gary, *J. Catal.*, 2008, **25**, 105.
82. P. Tewari, A. Campbell, *J. Colloid Interface Sci.*, 1982, **55**, 531.
83. E. Kowalska, O. Mahaney, R. Abe, B. Ohtani, *Phys. Chem. Chem. Phys.*, 2010, **12**, 2344.

84. A. Balamurugan, S. Kannan, U. Selvarai, S. Rajeswari, *Artif. Organs.*, 2004, **18**, 41.
85. R. Hong, J. Qian, J. Cao, *Powder Technology*, 2006, **163**, 160.
86. X. Wang, S. Meng, X. Zhang, H. Wang, W. Zhong, Q. Du, *Chem. Phys. Lett.*, 2007, **444**, 292.
87. R. Ojah, S. Dolui, *Sol. Energy Mater. Sol. Cells*, 2006, **90**, 1615.
88. R. Warner, B. Grung, *Transistors Fundamentals for Integrated-Circuit Engineer*, John Wiley and Sons, New York, 1983, p.626.
89. K. Rosche, C. Decker, G. Israel, J. Fouassier, *Eur. Polym. J.*, 1997, **33**, 849.
90. R. Asahi, T. Morikawa, T. Ohwaki, K. Aoki, Y. Taga, *Science*, 2001, **293**, 269.
91. M. Miyauchi, A. Ikezawa, H. Tobimatsu, H. Irie, K. Hashimoto, *Phys. Chem. Chem. Phys.*, 2004, **6**, 865.
92. F. Li, X. Li, F. Hou, K. Cheah, W. Choy, *Appl. Catal. A*, 2005, **285**, 181.
93. S. Yuan, Q. Sheng, J. Zhang, F. Chen, M. Anpo, Q. Zhang, *Micropor. Mesopr. Mater.*, 2005, **79**, 93.
94. C. Wei, X. Tang, J. Liang, S. Tan, *J. Environ. Sci.*, 2007, **19**, 90.
95. T. Umabayashi, T. Yamaki, S. Yamamoto, A. Miyashita, S. Tanaka, T. Sumita, K. Asai, *J. Appl. Phys.*, 2003, **93**, 5156.
96. Y. Wang, G. Zhou, T. Li, W. Qiao, J. Li, *Catal. Commun.*, 2009, **10**, 412.
97. P. Tewari, A. Cambell, *J. Colloid Interface Sci.*, 1982, **55**, 531.
98. C. Liu, X. Tang, C. MO, Z. Qiang, *J. Solid State Chem.*, 2008, **181**, 913.
99. W. Choi, A. Termin, M. Hoffmann, *J. Phys. Chem.*, 1994, **98**, 13669.
100. Y. Cong, J. Zhang, F. Chen, M. Anpo, D. He, *J. Phys. Chem. C*, 2007, **111**, 10618.
101. C. Xie, Q. Yang, Z. Xu, X. Liu, Y. Du, *J. Phys. Chem.*, 2006, **110**, 8587.
102. J. Lukac, M. Klementova, P. Bezdica, S. Bakardjieva, J. Subrt, L. Szatmary, Z. Bastl, J. Jirkovsky, *Appl. Catal B: Environ.*, 2007, **74**, 83.
103. C. Wonyong, T. Anderas, R. Michael, *J. Phys. Chem.*, 1994, **98**, 13669.
104. F. Li, X. Li, *Chemosphere*, 2002, **48**, 1103.
105. H. Hao, J. Zhang, *Microporous Mesoporous Mater.*, 2009, **121**, 52.
106. Y. Coug, J. Zhang, F. Chen, M. Anpo, *J. Phys. Chem. C*, 2007, **111**, 10618.
107. M. Xing, J. Zhang, F. Chen, *J. Phys. Chem.*, 2009, **113**, 12848.
108. F. Cotton, G. Wilkenson, *Advanced Inorganic Chemistry*, 5<sup>th</sup> Edition, Wiley Interscience, 1988, Appendix 4.

## Chapter- four: Towards synthesis of novel viologen acceptors for photovoltaic devices

### 4- 1 Introduction

Viologen based compounds are formed by *N*-alkylation reactions of bipyridal systems to form 1,1'- disubstituted- 4,4' - bipyridinium salts. The general structure of bipyridinium salts is shown in the following figure:

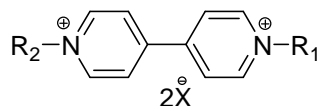


**Figure 4-1:** General structure of viologen compounds.

In this thesis the term "viologen" will be used to mean all compounds with a 4,4' - bipyridine or a 1,10-phenanthrazoline core. The chemical and physical properties of these compounds are to some extent affected by the presence of the counter anion (X<sup>-</sup>)<sup>(1)</sup>. The common name "viologen" was firstly derived by Michaelis<sup>(2,3)</sup>, who reported a violet colour for a solution that formed when 1,1'- dimethyl- 4,4' - bipyridinium (Bipm) was reduced by a one electron reduction to form a dication radical (as a dimer) with a violet colour. Initially, the term viologen was applied to biological systems, whereas in other cases it was used to refer only to the bipyridinium radical cation species. Currently, the name viologen is used to refer to all diquaternized 4,4'-bipyridine cores without the constituents. For this class of the compounds there are three redox forms as shown in the following figure:

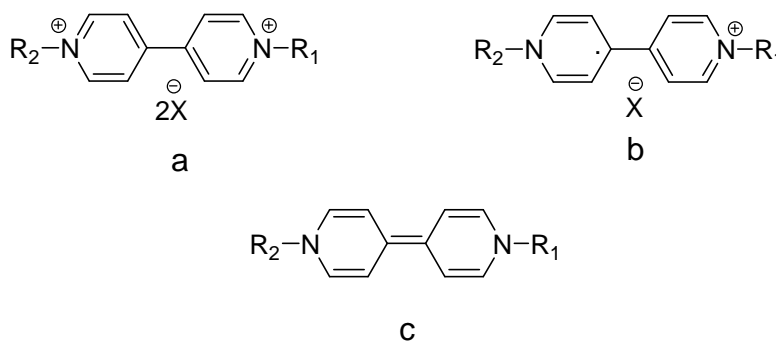


**Figure 4-2:** Redox forms of viologen compounds: (a) Bipyridinium dication, (b) Bipyridinium radical cation and (c) Fully reduced bipyridinium.

#### 4-1-1 Bipyridinium dication ( $\text{Bipm}^{2+}$ )

This redox form of viologen compound is the most stable of the three-redox states. It was reported that the positive charges on the bipyridinium core are mainly located on the nitrogen atoms and to some extent the charge is separated over the entire molecule<sup>(4)</sup>. The ionic character imparted to the salts is due to the presence of these two positive charges, viologen dications are usually found as solid powders or crystals. In some cases, they can be found as liquid crystals especially for viologens with long chain constituents. The pure state was found to be a colourless if there isn't charge transfer with the counter ion<sup>(4,5)</sup>. When  $\text{Bipm}^{2+}$  is hydrogenated, this causes the addition of dihydrogen across (C=C and C=N) bonds of the pyridine rings. This leads to a loss of aromaticity, after that another hydrogen molecule can react directly and the normal product is a mixture of 4,4'-bipyridine and pyridine- piperidine compounds. In view of this process, viologen can be used to catalyse hydrogenation reactions that are performed over the surfaces of noble metals such as Pt with the presence of hydrogen ions. Adsorption of viologens on the surface is a key step in this type of reaction<sup>(6)</sup>. Also the methyl viologen dication can be destroyed by the presence of strong bases in solution with methanol, due to the strong basicity of hydroxide in comparison with 4,4'-bipyridine and it can react as shown in Figure 4-3<sup>(7)</sup>.

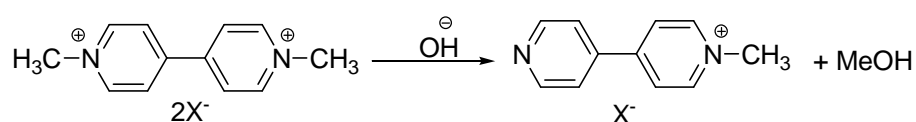


**Figure 4-3:** Bipyridinium dication reacting with a base<sup>(7)</sup>.

Generally, viologen dications possess a relatively low thermal stability, for example if  $\text{Bipm}^{2+} 2\text{Cl}^-$  is heated at over 180 °C it will reduce by two possible routes. The first route results in  $\text{Bipm}^{2+}$  being reduced into  $\text{Bipm}^+$ , and the source of electrons is the oxidation of chloride counter anions yielding  $1/2\text{Cl}_2$ <sup>(8)</sup>. The second route is demethylation to yield a mixture of 4,4' - bipyridine and methyl chloride<sup>(8)</sup>.

#### 4-1-2 Bipyridinium radical cation ( $\text{Bipm}^+$ )

The second redox state for viologen compounds is the radical cation. This is formed by one electron reduction of the respective dication, (Equation 4-1):

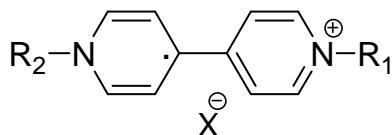


**Figure 4-4:** Structure of bipyridinium radical cation.



It may also be formed by one electron oxidation of the respective  $\text{Bipm}^{\circ}$ . Reduction can be performed by using different sources for the reducing species such as electrodes, in electrochemical reduction, or by using chemical reduction with zinc<sup>(9)</sup>. The radical cations have high stability, which is uncommon in comparison to other classes of chemical radicals that are normally unstable under ambient conditions. The stability of  $\text{Bipm}^{+\cdot}$  is due to high delocalization of the radical cations through the  $\pi$ -framework of the bipyridyl nucleus with the  $N,N'$  substituents which bear some of the charge<sup>(9)</sup>.

#### 4-1-3 Fully reduced dipyridinium compounds ( $\text{Bipm}^{\circ}$ )

This form redox state of viologen is not common<sup>(10)</sup>. It is formed by one electron reduction of the respective radical cation as shown in the following figure:

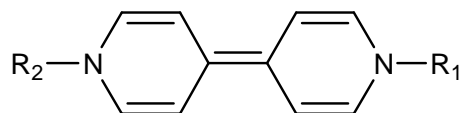


**Figure 4-5:** Structure of the fully reduced compound.

Formation of fully reduced  $\text{Bipm}^{\circ}$  can be represented in the following equations:



This redox form sometimes called the bi-radical and due to its reactivity, it is considered a powerful reducing agent and is found as coloured compounds<sup>(11)</sup>. The solubility of these redox forms of viologen compounds plays an important role in their redox behaviour and in their some potential applications. Generally, the solubility of viologen compounds depends on the solvent, the counter anion, the redox state, and the substituent groups. Radical cations that have relatively large counter anions such as  $\text{NO}_3^{-}$ ,  $\text{BF}_4^{-}$ ,  $\text{ClO}_4^{-}$  and  $\text{PF}_6^{-}$  are soluble in common organic solvents such as MeOH, MeCN and DMF. If the counter anion is small such as  $\text{Cl}^{-}$ ,  $\text{F}^{-}$ ,  $\text{Br}^{-}$ ,  $\text{I}^{-}$ ,  $\text{PO}_4^{3-}$  and  $\text{SO}_4^{2-}$ , the radical cation containing

compounds will not be soluble in organic solvents and they dissolved in aqueous solvents. The presence of nitrate as a counter anion in viologen salts can impart high solubility in aqueous and non- aqueous solvents <sup>(12)</sup>.

#### **4-2 Adsorption of viologen compounds**

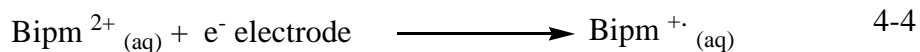
Adsorption of viologen compounds in all three redox states plays an important role in their application in different types of reaction. For example, methyl viologen can be used in the production of hydrogen gas. This reaction is catalyzed by noble metals and the viologen molecules are adsorbed on the surface of the catalyst. Different spectroscopic methods have been used to study this adsorption including cyclic voltammetry and UV- visible spectroscopy. These methods have been used to study the adsorption of different viologen compounds on platinum, gold or their mixtures <sup>(13- 15)</sup>. Obeng and Bard <sup>(16)</sup> studied the process of adsorption of viologen compounds that have surfactant substituents and they reported the formation of a Langmuir adsorption isotherm as determined using cyclic voltammetry. This arises from chemical or physical adsorption of these compounds on the surface of the electrode forming monolayer. These redox active species can result in a broadening of the voltammetric waves. By repetition of the scan several times, the values of rate constant (k) and  $\Delta E_p$  can be calculated for each monolayer thickness (d). A plot of  $\ln(k)$  against (d) gives a linear relationship.

Kobayashi and co-workers <sup>(17)</sup> have studied the adsorption of methyl viologen on mercury, and they reported strong adsorption of bulk  $\text{Bipm}^{2+}$  and  $\text{Bipm}^{+}$  on the surface. It has been found that the methyl viologen dication can be adsorbed more strongly on the surface of the electrode at positive potential than at the point of zero charge. On the other, hand  $\text{Bipm}^{+}$  adsorbed in a vertical orientation on the surface of the electrode under a more negative potential than that of normal redox potential of the  $\text{Bipm}^{2+/+}$  redox couples <sup>(17)</sup>. It has been reported that adsorption of methyl viologen dications and other bipyridinium dications on electrodes having positive charged surfaces occurs due to  $\pi$  - electron interaction between the adsorbed viologen dications and the electrode double layer<sup>(18)</sup>.

#### **4-3 - Electron transfer reaction in viologens**

Reduction of the viologen dication is a common electrochemical reaction that can be performed on inert electrodes. In this process, the electrode used acts as an electron source<sup>(19)</sup>. If both reduced viologen dications and the product radical cation are soluble in the system, then the process of reduction will be reversible according to the Nernst equation. However, there would be some irreversibility in a redox system if either reactant or the product of reduction is not soluble to some extent. In general, for viologens that have

aryl or long chains of alkyl substituent, the expected radical cation that is produced via reduction is insoluble in water, and it can form as a thin film of coloured radical cation salt on the outer surface of the working electrode. In this case, the reaction is expected to occur in two processes (Equations 4-4, and 4-5) <sup>(19)</sup>:

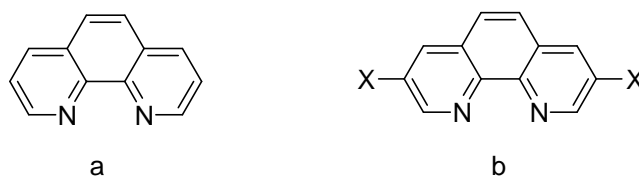


This reaction was suggested by some researchers to take place on the electrode, followed by film growth in three dimensions <sup>(20)</sup>. The value of the formal redox potential for the first electron reduction of bipyridinium dication was found to be dependent upon the substituent alkyl groups in the aqueous solution. For this case, the respective radical cations in general have the same colour whereas, for the cases in which the substituents are aryl groups, the formal redox potentials are more variable and may be positive with respect to the standard hydrogen electrode (SHE). For example,  $E^\circ$  for aqueous cyanophenyl viologen is + 0.10 V for the chloride salt, while it was - 0.69 V for the alkyl substituent for the same salt <sup>(21)</sup>. The value of  $E^\circ$  for these systems is associated with the counter anion. The effect of counter anion is related to the solubility of the viologens in aqueous solution. The solubility of bipyridinium dication salts and radical cations and their redox potential are also dependent on the counter anion type <sup>(22)</sup>.

#### 4-4 Organic conducting polymers

In the recent decades, conjugated polymers have played a significant role in the generation of new materials that can be used in many potential applications such as electronic and optical devices <sup>(23)</sup>. Among the different types of polymer, polythiophenes are an important type of conjugated polymer due to their good solubility in common organic solvents, their thermal stability and low pollution effects. These materials can be applied in electrical conductors, polymer light-emitting diodes (PLEDs) <sup>(24)</sup>, transistors <sup>(25)</sup>, anti-static coatings, sensors <sup>(26)</sup>, batteries, electromagnetic shielding materials, new types of memory devices, nanoswitches, optical modulators and valves, imaging materials <sup>(27)</sup>, polymer electronic interconnectors, and nanoelectronic and optical devices <sup>(28)</sup>. Among the different organic compounds 1,10-phenanthroline derivatives are one of the most important organic functional intermediates due to their physical and chemical properties and they have found widespread application in many areas such as coordination chemistry, materials chemistry analytical chemistry, as well as in redox materials. That is due to their strong chelating ability and conjugated  $\pi$  systems <sup>(29-31)</sup>. Modification of 1,10-phenanthroline can be

performed by introducing halogen substitution at different positions in the first synthetic step when modifying the 1,10-phenanthroline ring. In the last few decades, there have been several reports on the synthesis of 3-bromo or 3,8-dibromo-1,10-phenanthroline<sup>(32)</sup>. After introducing halogen into the framework of phenanthroline, the conjugated  $\pi$  system of 1,10-phenanthroline can be extended by introducing different organic functional groups, so that the energy levels of the resulting molecules can be tuned according to the introduced group. The most important structural change of the 1,10-phenanthroline core occurs with the 3 and 8 position, so that increasing conjugation along this axis can enhance physical and chemical properties. After formation of 3,8-dihalogenated phenanthroline, the  $\pi$  conjugated system can be extended by introducing different functional groups into the framework. For example, thiophene groups can be introduced at the 3- and 8-positions of 1,10-phenanthroline by a carbon-carbon cross-coupling reaction starting from 3,8-dibromo-1,10-phenanthroline<sup>(33)</sup>. The  $\pi$  conjugated systems of poly(arylenes) have been investigated by many workers<sup>(34)</sup>. In addition, the chemistry of  $\pi$  chelating ligands such as 2,2'-bipyridine and 1,10-phenanthroline and their metal complexes have been studied by many researchers for different potential applications such as photovoltaic and optical devices<sup>(35-37)</sup>.



**Scheme 4-6:** 1,10-phenanthroline (a), and 1,10-phenanthroline substituted at positions 3 and 8.

#### 4-4-1 Conjugated polymer for organic solar cells

In the last few years, as a result of concerns over global warming, it has become apparent that classical fuel based energy will need to be replaced by new energy systems using novel technologies. In addition, the classical fuels such as oil, coal and natural gas will be consumed in the near future as well as the detrimental effects of these fuels on the environment. All these reasons have led to a focus on renewable energy sources<sup>(38)</sup>. Solar photovoltaic cells may be good candidates to play a role in the generation of energy in the future. Recently, much attention has been focused on the study and development of this system and by using solar cells, it is possible to convert sunlight into electrical power<sup>(38)</sup>. The research in this field has been dominated over recent decades by technologies that mainly depend on the solid-state p-n junction devices. Controlled conversion of solar

energy can play a key role as one of the technologies that can replace classical fuels in the generation of energy that is suitable for mass usage<sup>(38)</sup>.

Solar photovoltaic cells are capable of generating electrical power from sunlight, and these devices have some advantages in comparison with current inorganic materials. They are relatively cheap in production and purification, and they can be used on flexible substrates and can be shaped to suit architectural applications<sup>(38)</sup>. The most important and effective components of the solar cell are organic polymers. Organic polymers having delocalized  $\pi$  electrons can absorb sunlight with a high efficiency. The bandgap and energy levels of the HOMO and LUMO of these polymers influence the performance of the photovoltaic devices. Extending the conjugated system in these polymers can be performed by blending an electron donor and an acceptor in the main chain of the polymer, within the long conjugation system resulting a low bandgap polymer<sup>(39)</sup>. The polymer that used in solar cells, the polymers should absorb light with a high efficiency at a wavelength in the infrared region. Donor units that are used in the blend should show high ionization potential, whereas the acceptor units should have a high electron affinity. In addition, the blend should also show high charge carrier characteristics to increase photocurrent, good solubility and low cost processing<sup>(39)</sup>. In this context, configuration of polymer photovoltaic cells falls into two types: bilayers and heterojunction devices. The most commonly used is bulk heterojunction (BHJ) devices. In this type, the active layer is composed of a blend of both electrons donating conjugated polymer with an electron acceptor<sup>(39)</sup>, while in bilayer devices electron donating materials and accepting materials are existing in two separated layers. Bilayers and heterojunction devices are shown in the following figure:

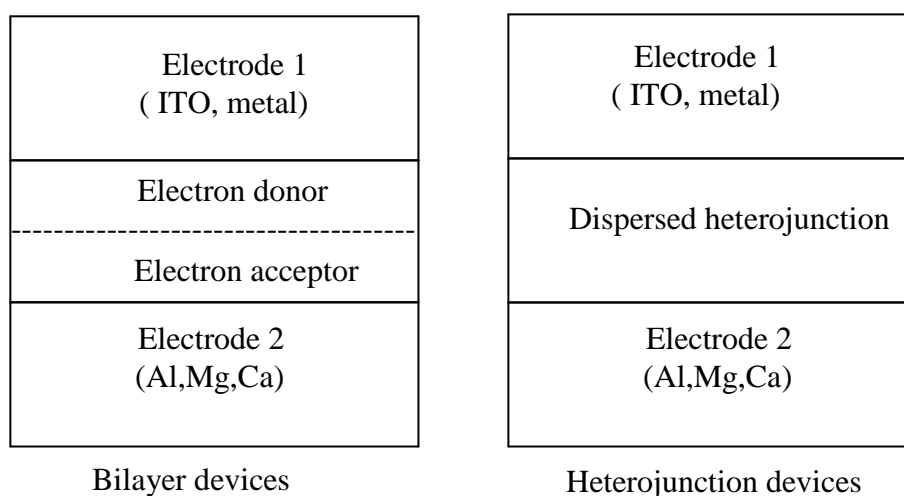
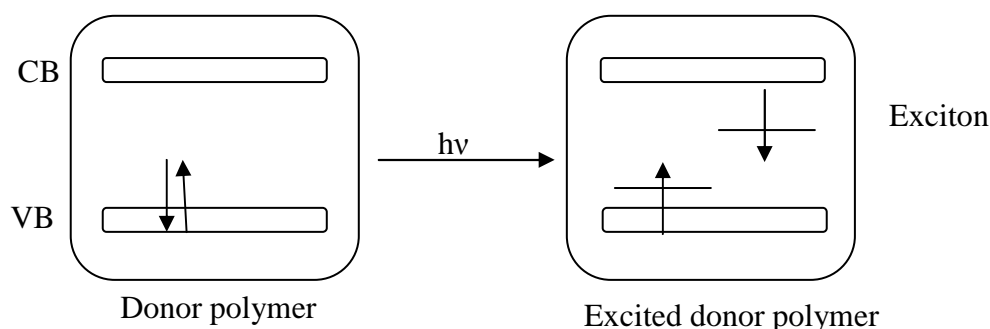


**Figure 4-7:** Bilayer and heterojunction used in photovoltaic devices<sup>(39)</sup>.

When molecular semiconductors absorb light with a suitable energy, the semiconductor produces excitons or electron-hole pairs. Photoinduced electron transfer between donor (D) and acceptor (A) molecules with significantly different HOMO/LUMO energy levels can be used effectively providing a general pathway to more efficient organic photovoltaic cells<sup>(40)</sup>. Many studies have been undertaken on polymer-based photovoltaic cells, and some of these studies have focused on blends or nanocomposites of donor polymer with acceptor materials such as fullerenes, CdSe, TiO<sub>2</sub> nanoparticles, carbon nanotubes, acceptor polymers and small acceptor molecules<sup>(40)</sup>. Photovoltaic cells that are made from polymer fullerene blends showed power conversion efficiencies of about 2-3% using light from the solar spectrum<sup>(41)</sup>. Composites of poly(3-hexylthiophene) and CdSe nanorods have been used to demonstrate photovoltaic power conversion efficiencies as high as 1.7% under illumination with sunlight at intensity of 1000 mW/cm<sup>2</sup><sup>(42)</sup>. The main problem with these systems is the reduction of charge carrier mobility of polymer blends in comparison to the component materials<sup>(42)</sup>. A good alternative approach to avoid this problem can be achieved by using polymeric semiconductors for organic photovoltaic solar cell showed an efficiency around 8%<sup>(43)</sup>. However, there are many reported carrier mobility in conjugated polymers being used in solar cells. This rises from high sensitivity of the morphology of the polymer film. Higher charge carrier mobility of the polymer can increase the efficiency length of electrons and holes that are produced through photovoltaic process. So that improving the charge transfer efficiency from the donor polymer to the acceptor normally phenyl-C61-butyric acid methyl ester (PCBM), can improve the efficiency of solar cell. In terms of the donor polymer for PV solar cell, a block of conjugated copolymer assemblies with covalently tethered or physically sequestered fullerenes and homopolymers with tethered fullerenes and alternating donor-acceptor copolymers can be applied<sup>(42)</sup>. These systems can be used as an alternative approach to avoid some of these problems. It has been found that a layered donor/acceptor heterojunction is an attractive system to achieve efficient polymer solar cells. By using a suitable donor and acceptor polymer, semiconductors having complementary electronic and optical properties can be developed<sup>(42)</sup>. Under these conditions, both the electrons and holes are confined to the acceptor and donor sides of the interface respectively. That can facilitate transport to the collecting electrodes and at the same time minimize charge recombination reaction between electron-hole pairs. Recently, Yang and co-workers<sup>(44)</sup> reported a BHJ solar cell using poly(3,4-ethylenedioxythiophene) with Ag nanowires as an anode. This system showed low bandgap energy of the polymer (1.7 eV) and exhibited power conversion efficiency of 2.5-2.8% under sunlight intensity at 1.5 AM. For efficient contact at the polymer/metal interfaces, the HOMO level of the donor polymer must match the anode

energy level, such as that for indium tin oxide (ITO) which is 4.8 eV and the LUMO level of the acceptor polymer must match the cathode energy level such as aluminium (Al) which is 4.3 eV. There have been few studies on the photovoltaic properties of polymer/polymer donor/acceptor heterojunctions, which is probably due to the lack of acceptor-conjugated polymers that have high electron affinities<sup>(44)</sup>. The general mechanism for the conversion of light into electricity by photovoltaic cell can be demonstrated in the following figure:

- 1- Absorption of light: electron donor or an electron acceptor absorbs photon from the light and forms excited state as follows:



- 2- Charge separation: exciton diffusion at the interface between the electron donor (D), and the electron acceptor (A) as follows:

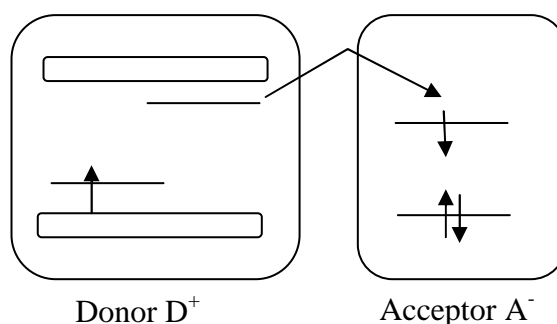


**Figure 4-8:** Mechanism for the conversion of light into electricity with a photovoltaic cell.

A typical conjugated polymer with bandgap around (2.0 eV) can absorb photons of wavelength up to 600 nm which about 25% of total solar energy. Increasing the length of conjugation of the polymer can shift absorption towards higher wavelengths up to 1000 nm for a polymer of lower bandgap (1.2 eV). This can cover about 70-80% of total solar energy, this can result in high efficiency in the efficiency of the solar cell<sup>(44)</sup>.

#### 4-4-2 Conducting polymers comprising viologen

Conducting polymers that contain viologen units have recently received much attention regarding their preparation and the study of their physical and chemical properties. This type of polymer can be used in many modern applications. Polymers containing viologen groups within their structure are attractive owing to their good catalytic properties, as well as their electrochromic properties. This probably results from their redox states which involve  $\text{Bipm}^{2+}/\text{Bipm}^{+\cdot}$  and  $\text{Bipm}^{+\cdot}/\text{Bipm}^{\circ}$ . Various types of viologen polymer can be synthesized<sup>(45,46)</sup>. Generally, polymers featuring the viologen moieties are attractive research area due to their catalytic and electrochromic properties. This arises from their respective redox states from the  $\text{Bipm}^{2+}/\text{Bipm}^{+\cdot}$  and  $\text{Bipm}^{+\cdot}/\text{Bipm}^{\circ}$  redox reactions. Therefore developing electroactive polymers with viologen redox centres becomes more interesting as these materials can be formed on the electrode surface as thin films<sup>(47-49)</sup>. Kelaidopoulou and co-workers<sup>(50)</sup> reported the synthesis and electropolymerization of the indol viologen. They found that this type of viologen compound can give an electroactive thin films of poly(indol) with pendant methyl viologen groups. Structure of this compound is shown in the following figure:

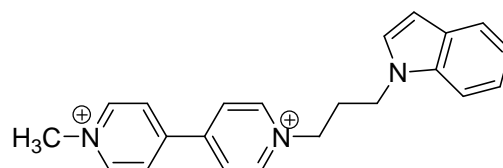


**Figure 4-9:** Indol viologen synthesised by Kelaidopoulou and co-workers<sup>(50)</sup>.

Nambu and co-workers<sup>(51)</sup> synthesised some of viologen polymers with the viologen structure in the main chain or as a pendant group. They used photochromic films modified electrode, it was reported one electron reduced cation radicals  $\text{Bipm}^{+\cdot}$  existing in a dimer - monomer equilibrium. Structures of these polymers are shown in the following figure:

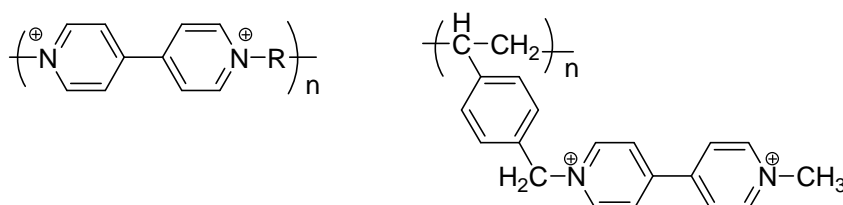


**Figure 4-10:** Polymers featuring viologen units<sup>(51)</sup>.

Nambu and co-workers used photochromic film modified electrodes, and it was reported one electron reduced cation radicals  $\text{Bipm}^{+\cdot}$  existed in a dimer-monomer equilibrium.

Saika and co-workers<sup>(52)</sup> reported the synthesis and electropolymerization of viologen monomers. These compounds formed polyviologen films on electrodes by cathodic electrolysis of bis(4-cyano-1-pyridine) derivatives under weak acid conditions. This process is shown in Figure 4-11.

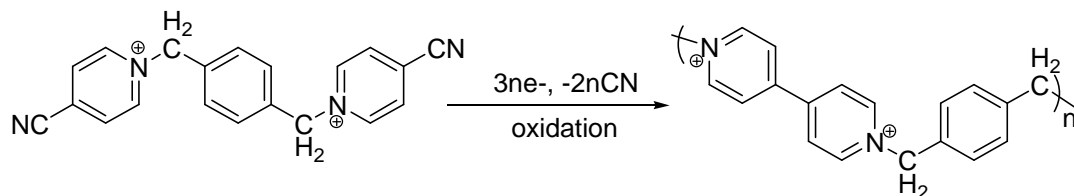
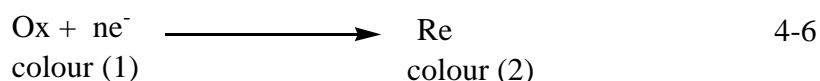


**Figure 4- 11:** Polymer with viologen unit synthesised by Saika and co-workers<sup>(52)</sup>.

Generally, developing different types of polymer that contain electroactive viologen centres is very important as it can give rise to various types of viologen polymers as electroactive polymer films on electrode surfaces. There are many potential applications for viologen polymer modified electrodes such as sensors, electron transfer, phase transfer catalysis, and many photoelectrochemical devices<sup>(53)</sup>. Among these applications, electrochromic devices are probably the most important. Electrochromic materials normally exhibit redox states with different electronic UV-visible absorption spectra upon switching the redox states, generating a new visible region bands. The change in colour between two redox states, oxidized form (Ox) with colour (1) and reduced form (Re) with colour (2) is the basic principle for this device and this process is shown in (Equation 4-6)<sup>(54)</sup>.

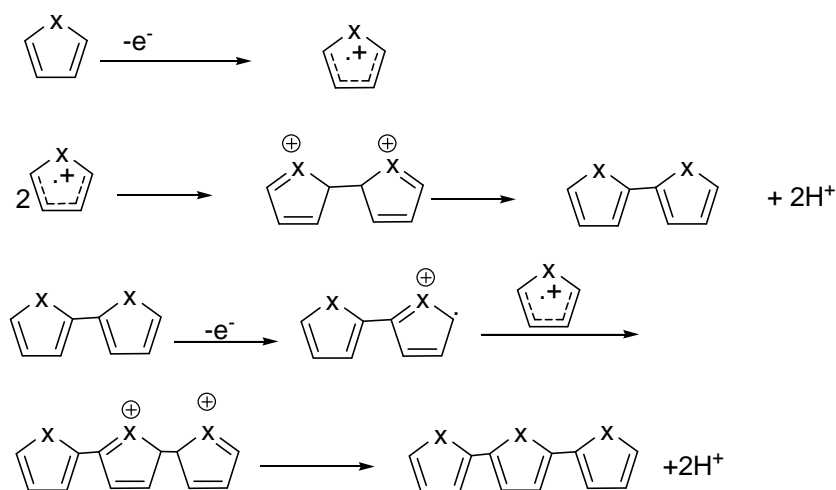


Most viologen compounds are considered as being electrochromic as they have two redox states with different electronic spectra<sup>(54)</sup>. Platt was the first to report the term electrochromism when he investigated a change in the colour of the electrode when studying redox reactions of some viologen compounds<sup>(55)</sup>. Generally, electrochromic devices can be classified into two main groups: displays and shutters. Display devices normally work in the reflective mode and shutters work in the transmission mode. The electrodes in the electrochromic display devices becomes coloured as a result of current flow, the intensity of the colour depending on the amount of species that are formed electrochemically. On the other hand, these colours can be bleached by applying a potential with opposite polarity<sup>(54)</sup>. Generally, preparation of thin films from this type of polymer can be performed in two steps. The first step involves synthesis of the polymer by

electrochemical polymerization followed by coating the electrode with the film of the polymer<sup>(56)</sup>.

#### 4-5 Electrochemical polymerization

Polymerization reactions can be performed either by chemical or electrochemical methods. Electrochemical polymerization can be achieved in two ways, the cathodic route and the anodic route<sup>(57)</sup>. The polymer that is formed by electrochemical routes in its neutral form leads to a reduction of electrical conductivity which prevents the electrode from causing a reduction of further molecules of the monomer in the solution, so that the polymer will form only thin films on the electrode which can't be handled easily<sup>(57)</sup>. Oxidative electropolymerization is more common, this can be performed without using a catalyst and the polymer can be produced as thick films on the electrode, and it is possible to control the thickness of the film using appropriate reaction conditions such as scan rate and concentration of the used monomer<sup>(57)</sup>. Most studies in this respect have been carried out with polypyrroles and have assumed the same mechanism as for other heterocycles<sup>(57)</sup>. The proposed mechanism is similar to that which occurs with aromatic coupling and according to this mechanism, the heterocycle is oxidized to form a radical cation. The radical cation then reacts with another to form a dimer by losing two protons. The heterocycle then regains aromaticity, which is a driving force to lose a proton, and this process continues and the polymer eventually forms on the electrode<sup>(57)</sup>. This mechanism can be represented in the following scheme:



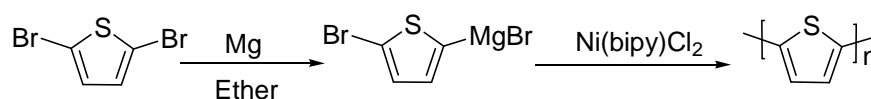
**Scheme 4-12:** Proposed mechanism for electropolymerization<sup>(57)</sup>. Oxidation of monomer molecule produces radical cation, this then coupled with other radical cation to generate dication which then loss two protons to yield a dimer. This process continues until formation of insoluble thin film of the polymer on the electrode.

However, according to this mechanism, the rate determining step is not clear and it is proposed that the coupling of the radical cation is the rate determining step<sup>(57)</sup>. There is it

mechanism proceeds by radical cations reacting directly with the neutral monomer molecules<sup>(58)</sup>. It has been assumed that if the applied potential is not high enough to oxidize monomer molecule and is just sufficient to oxidize only the polymer, so that polymerization doesn't occur, as the produced polymer would dissolve upon cycling of scan rate<sup>(57,58)</sup>. There is an alternative suggestion relating to the role of the oligomers in this mechanism and it was proposed that thiophene is absorbed on the surface of the electrode, indicating the occurrence of the polymerization on the electrode surface. This implies that the oligomer formed in the solution would be unlikely to react with the other oligomer<sup>(58)</sup>. However, this idea was not completely true, as when polymerization was performed under same conditions between chemically synthesized oligomer and thiophene monomer, the formed polymer has different properties. There is other evidence reported from actual material properties and it was found that the mono thiophene polymer was formed as a film on the electrode that can be easily removed from the surface. For another polymer, which was prepared from bis- and tris- thiophene, a very thin polymer was formed and it was covered with a thick and brittle powder. From these observations, it is concluded that formation of the oligomers is not necessary for the formation and growth of a good quality conducting polymers<sup>(58)</sup>.

#### 4-5-1 Doping and bandgap

Many of the physical properties of the polymer can be modified by doping with electron donors or acceptors. The electrical properties of the polymer such as conductivity can be modified. For example, polythiophene has different electrical properties according to whether it is doped or not<sup>(59)</sup>. The conductivity for the undoped polythiophene is  $10^{-11}$  -  $10^{-10}$  S cm<sup>-1</sup>, whereas for the system doped with iodinate the conductivity is much greater than 0.1 S cm<sup>-1</sup>. A general scheme for the synthesis of undoped polythiophene is shown in the following scheme:



**Scheme 4-13:** Chemical synthesis of undoped polythiophenes<sup>(59)</sup>.

The doping process can be used intentionally to create some impurities or defect sites within the polymer structure to improve or tune some of its electrical properties. This process can be undertaken either chemically or electrochemically. In general, there are two types of doping, p-type and n-type. The first type of doping withdraws electrons, while the

secondly pushes the electrons toward the doped system<sup>(59)</sup>. Important examples of p-type dopants are I<sub>2</sub>, AsF<sub>5</sub> and H<sub>2</sub>SO<sub>4</sub>, and electrochemical oxidation on the anode can be undertaken. The n-type dopants can be alkali metals, or cathodic reduction for electrochemical method<sup>(60)</sup>. Doping by the electrochemical method is preferred rather than the chemical method as the doping process can be performed and controlled more easily<sup>(61)</sup>. Polyacetylene is a good example of a simple conjugated polymer and its electrical conductivity has been widely studied with particular regard to bond alternation<sup>(62, 63)</sup>. Generally, polyacetylene (PA) can be produced in two forms *trans* and *cis*. Structure of polyacetylene is shown in the following figure:

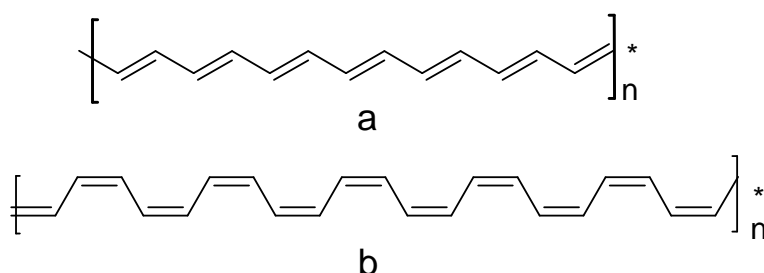


**Figure 4-14:** Structure of polyacetylene (a) *trans* and (b) *cis*.

In a study, Ito and co-workers<sup>(64)</sup> have reported the synthesis of flexible conjugated polyPA. This polymer can be doped with electron donors such as Na or with electron acceptors such as bromine and iodine to give n-type or p-type conductive materials. It was found that the bond alternation model is more stable than the regular model for both isomers. Bond alternation in the *trans* isomer is related to the energy gap between the HOMO and the LUMO, the value of the bandgap depending on the order of bond alternation<sup>(65)</sup>. Doping PA can give rise to a significant increase in conductivity and Raman spectra for PA doped with bromine or iodine indicated the presence of some X<sub>3</sub><sup>-</sup> in the structure of the crystalline polymer. The source of the electron that is attached to X<sub>3</sub><sup>-</sup> seems to be from the polymer as a result of charge transfer. In this case, polymer chains are acting as polycations with the presence of X<sub>3</sub><sup>-</sup> species. Generally, in the doped materials the electrons transfer from the top of the valence band into the acceptor species. Doping with iodine brings the unoccupied part of the HOMO into contact with the Fermi level and this effect imparts metallic properties to the doped materials. Doping PA with electron donors such as Na transfers electrons from the donor into the LUMO band state of PA with PA acting as a polyanion, and Na<sup>+</sup> species are formed. In this case, the Fermi level rises into the LUMO band generating n-type semiconducting materials<sup>(66)</sup>. Introducing defects into the polymer produces radical cations called polarons, when two of these radical cations are combined together they produce a bipolaron<sup>(67)</sup> as shown in Figure 4-15:

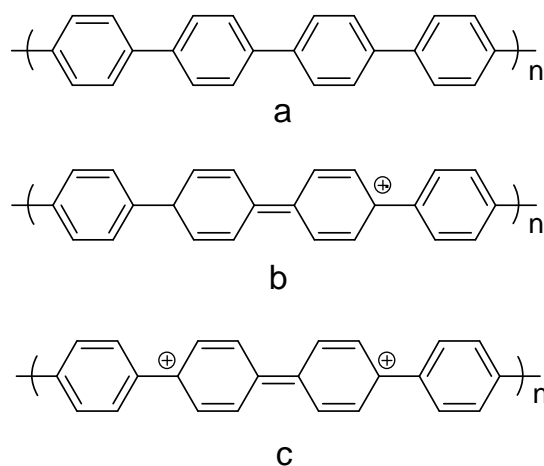


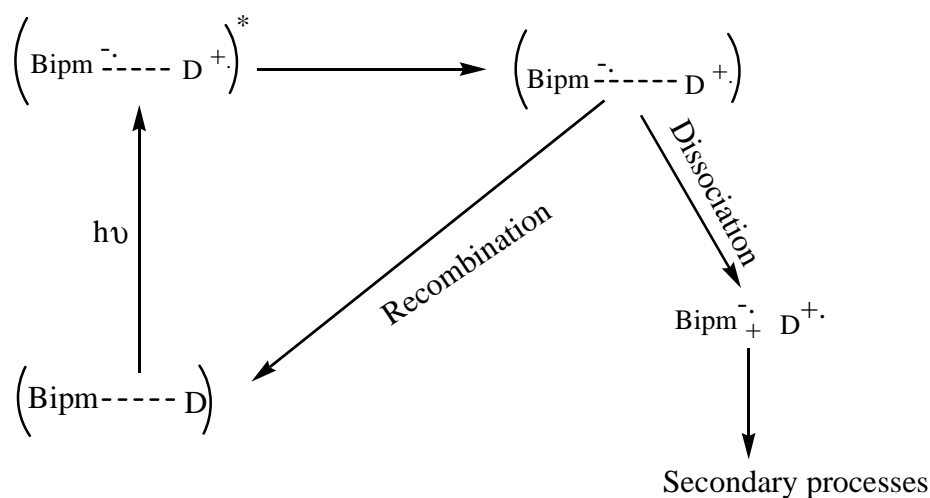
**Figure 4-15:** Doping polymer: (a) neutral polymer, (b) polaron and (c) bipolaron.

For conducting polymers,  $\pi$  orbitals overlap to generate the valence band, while  $\pi-\pi^*$  overlap to form the conduction band. In this system, conduction occurs by electron transfer after getting a sufficient energy in the form of photons or heat<sup>(68)</sup>. For the doped polymer, p-type polarons can be formed via distortion in the structure of the local band, introducing two states in the bandgap that are bonding and anti-bonding formed by removing an electron. Bipolarons can be formed by removing electrons from the previously formed polarons. In terms of energy consideration, one bipolaron is more stable than two polarons. The energy level of bipolaron is always higher the valence band, leading to a reduction in the bandgap and as a result facilitating the transfer of electrons. For example, with doped polyparaphenylene the bonding state is 0.20 eV for the polaron and 0.56 eV for the bipolaron and for the bipolaron the bonding state is empty and so it carries no spin. The concentration of the bipolarons would increase directly with the amount of dopants and interaction between bipolarons can lead to band formation. Due to fact that the bipolaron doesn't have any spin, application of an electrical field can lead to movement which would produce conductivity along the structure of the polymer<sup>(68)</sup>.

#### 4-5-2 Viologen and solar energy conversion

The photochemistry of viologen compounds was first investigated by Ebbesen and Ferraud<sup>(69)</sup> who studied the photochemistry of  $\text{Bipm}^{2+}$  in methanol and water. They reported that photochemistry occurred only by charge transfer between ground state  $\text{Bipm}^{2+}$  and the counter ion. The photoexcited state can follow one of two routes, either charge recombination within the ion pair or the ions can be dissociated from the solvent cage.

In the case of water, the radical pair  $\text{Bipm}^{\cdot+} \text{Cl}_2^{\cdot-}$  was formed with a quantum yield of 0.2, and rate constant about  $10^8 \text{ s}^{-1}$ . These processes are represented in the following scheme:

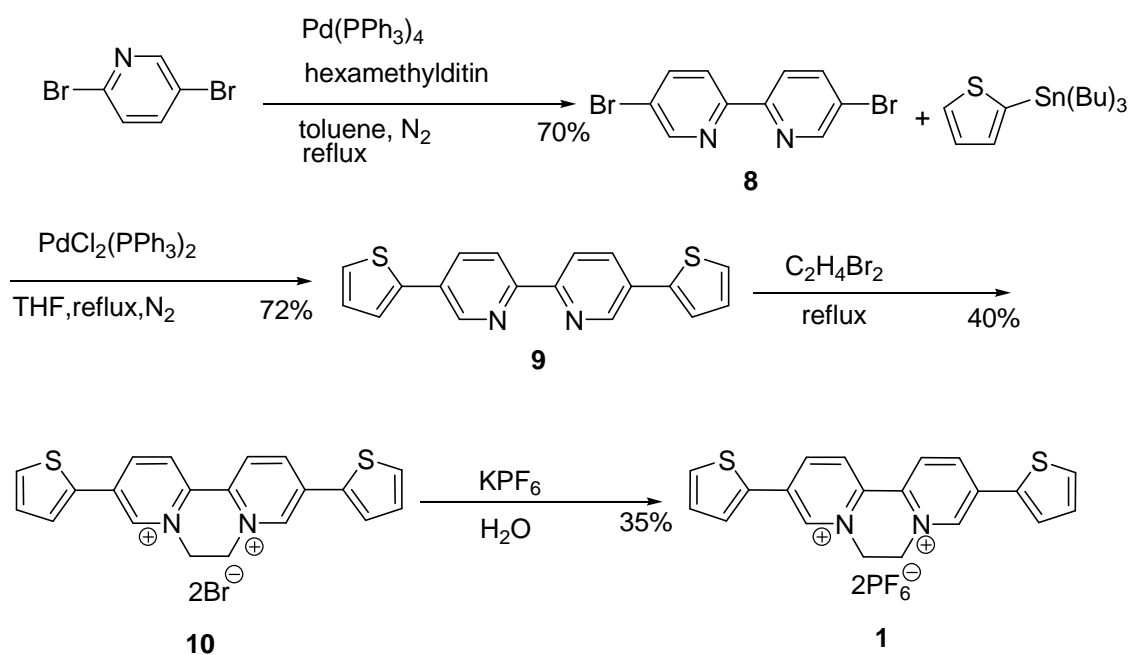


**Scheme 4-16:** Reaction of photoexcited charge transfer complexes, Bipm is a viologen acceptor and D is an electron donor. Secondary processes involve reaction with the solvent molecules, and ionization.

The kinetics of both formation and decay of the radical species are dependent on the pH. If this process was carried out in methanol, there are different radical species. The product of photochemistry was found to be  $\text{Bipm}^{\cdot+} \text{Cl}^{\cdot-}$  with a radical pair of  $\text{Bipm}^{\cdot+} \text{Cl}^{\cdot-}$ . These species are an intermediate in the formation of  $\text{CH}_3\text{O}^{\cdot}$  from  $\text{MeOH}$  <sup>(69)</sup>. Viologen compounds have been used in the construction of molecular architectures on metal, and on semiconductor surfaces. This gives an efficient technique for the design of a new class of nanomaterials <sup>(70)</sup>. Formation of an acceptor- photosensitizer-donor complex can be used with photoactive materials. These types of systems can be used in different applications such as photosynthesis. However, this system is composed mainly of two parts of the acceptor and donor systems. It has been found that through interaction between the photoactive system and the surface, a new field of photonic molecular and photovoltaic device would emerge <sup>(71)</sup>. Formation of self-assembled monolayers (SAMs) <sup>(72)</sup> of organic and organometallic compounds on the surfaces of metal and the semiconductors is a very effective technology for constructing densely packed and well-ordered materials on conducting and semiconducting surfaces. The formation of viologen molecule layers on the surface of tin-doped indium oxide (ITO) by using the acceptor photosensitizer system were successfully achieved on the surface of the ITO <sup>(72)</sup>. This system was further applied to a molecular photovoltaic system with a good quantum yield. However, the performance of SAMs as molecular devices is dependent to some extent on the degree of SAM formation and their properties <sup>(73)</sup>.



yl) pyridine by Stille coupling. This compound was then alkylated with 1,2- dibromoethane to give a viologen salt with bromide as a counter anion. Then the ion exchange reaction using an aqueous solution of  $\text{KPF}_6$  could be performed to convert the  $\text{Br}^-$  compound into a viologen with hexafluorophosphate as a counter anion instead of bromide. It was through that this would improve the solubility of the viologen compound **1** in organic solvent. The synthesis steps are presented in the following scheme:



**Scheme 4-18:** Proposed synthetic route of target compound **1**.

Synthesis of compound **8** was performed from commercially available 2,5-dibromopyridine. This was achieved by reacting the latter in toluene using commercially available hexamethylditin and  $\text{Pd}(\text{PPh}_3)_4$ . The product which was purified by column chromatography affording the final product in 70% yield<sup>(74)</sup>. Compound **9** was synthesized applying the Stille coupling reaction using 2.5 eq of 2-tributylstannylthiophene. The crude product was further purified by column chromatography to afford **9** as a yellow/orange powder in 72% yield<sup>(75)</sup>. Compound **10** was synthesized via an alkylation<sup>(76)</sup> reaction to yield the viologen ( $\text{Br}^-$ ) and this was converted into viologen hexafluorophosphate salt to enhance the solubility<sup>(77)</sup>.

#### 4-6-1-1 Analysis of compound 1

The UV- visible spectrum of compound **1** was recorded in acetonitrile. This compound shows two peaks at 346 nm, and 434 nm. The optically determined bandgap was calculated from the onset of UV-visible spectrum to be 2.52 eV. This compound absorbs strongly in the UV region of the spectrum (346nm) which is related to the  $\pi$ -  $\pi^*$  transitions. The high intensity of this peak is probably due to conjugation between the thiophene and the pyridinium rings. The other peak in the visible region (434 nm) is related to an intramolecular charge transfer complex (CT)<sup>(78)</sup>. This transfer could occur between counter anion and phenanthroline core. The UV- visible spectrum is shown in the following figure:

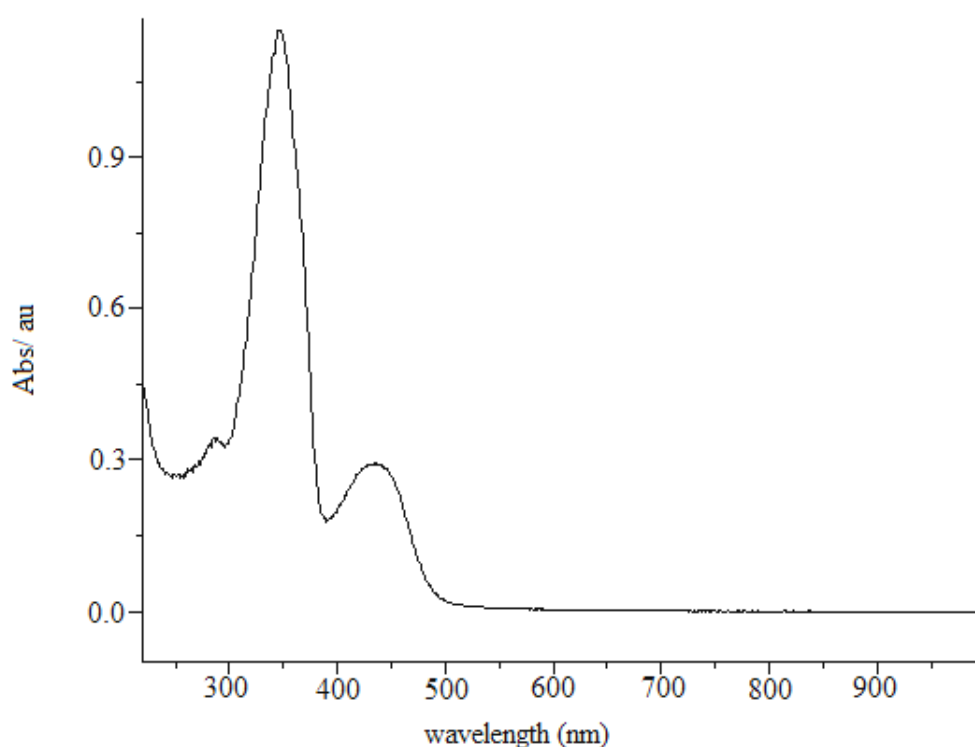


**Figure 4-19:** UV-visible spectrum for compound **1**. Recorded in acetonitrile ( $1 \times 10^{-4}$  M).

#### 4-6-1-2 The voltammogram of compound 1

The voltammogram of compound **1** was recorded in MeCN. Monomer oxidation of this compound shows two peaks, one irreversible at 1.13 V and the other quasi reversible at 1.55 V (Figure 4-20). A dynamic electrochemical run was performed between the two values applying a variable potential with scan rate of  $100 \text{ mV s}^{-1}$ . The estimated HOMO level energy of compound **1** was calculated to be -5.93 eV based on the onset of the

oxidation peak of the ferrocene (0.24 V) and its published value of (4.80 eV)<sup>(79,80)</sup>. The voltammogram for the oxidation of compound **1** is shown in the following figure:

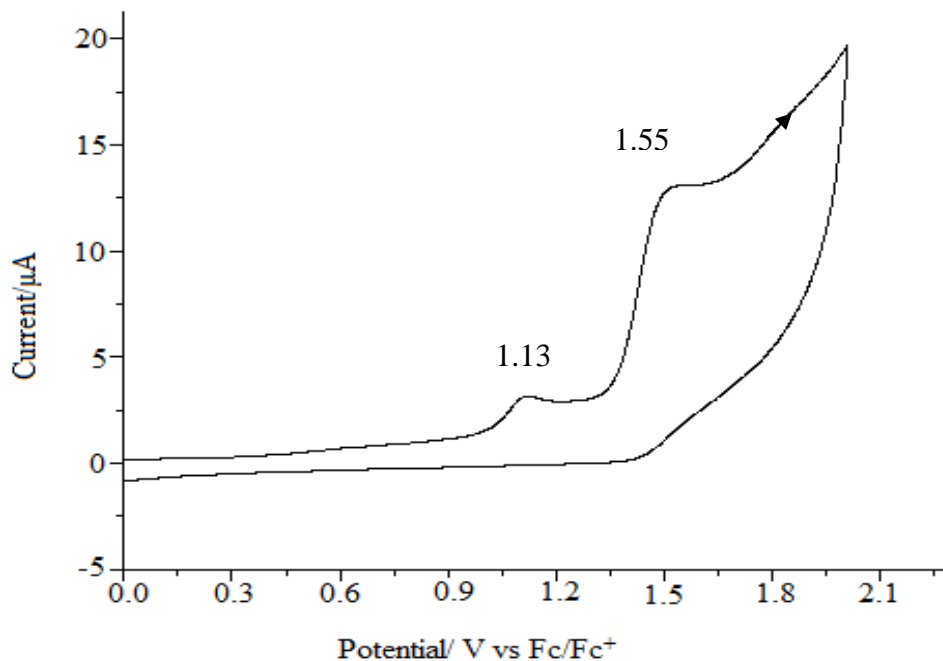


**Figure 4-20:** The voltammogram for oxidation of compound **1** recorded using a glassy working electrode, an Ag wire as a reference electrode and a Pt wire as a counter electrode. Recorded at a concentration of  $1 \times 10^{-4}$  M in MeCN with TBAPF<sub>6</sub> (0.1M) as a supporting electrolyte. Scan rate  $100 \text{ mV s}^{-1}$ .

The reduction of compound **1** showed two reversible peaks at - 0.65 V and at -1.08 V (Figure 4-21). LUMO level of compound **1** was found to be - 4.30 eV based on the onset of the oxidation peak of the ferrocene (0.24 V) and its published value of (4.80 eV)<sup>(79,80)</sup>. The electrochemically determined bandgap for this compound is 1.63 eV. The first reduction peak is probably correlated with conversion of  $\text{Bipm}^{2+}$  to  $\text{Bipm}^{+\cdot}$ . The second reduction peak can be assigned to the further reduction (from  $\text{Bipm}^{+\cdot}$  to  $\text{Bipm}^0$ ). However, the difference in this value from than that estimated from optically determined probably arises from the contribution of air and humidity as well as experimental conditions. Generally, reduction of viologen dications can be performed by two mechanisms as mentioned earlier in equations 4- 4 and 4-5<sup>(81)</sup>. The voltammogram for the reduction of compound **1** is summarised in Figure 4-21.

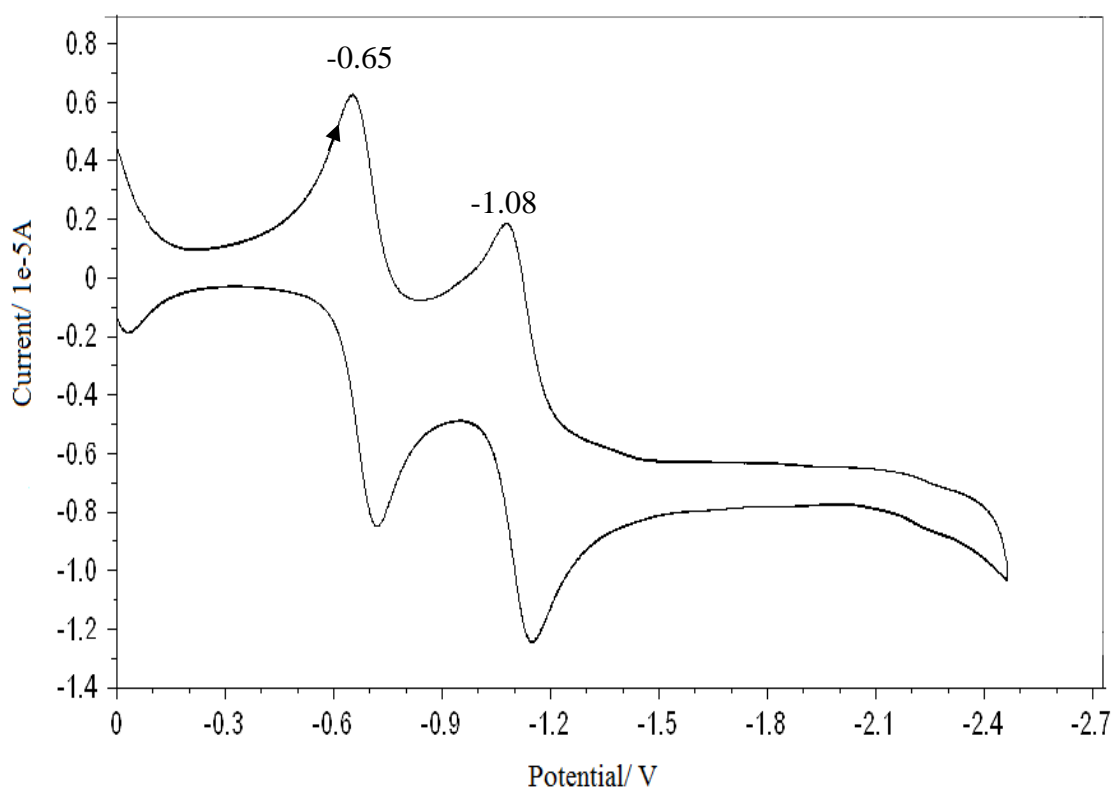


**Figure 4-21:** The voltammogram for reduction of compound **1** recorded using a glassy carbon working electrode, an Ag wire as a reference electrode and a Pt wire as a counter electrode. Recorded at a concentration of  $1 \times 10^{-4}$  M in MeCN with TBAPF<sub>6</sub> (0.1M) as a supporting electrolyte. Scan rate  $100 \text{ mV s}^{-1}$ .

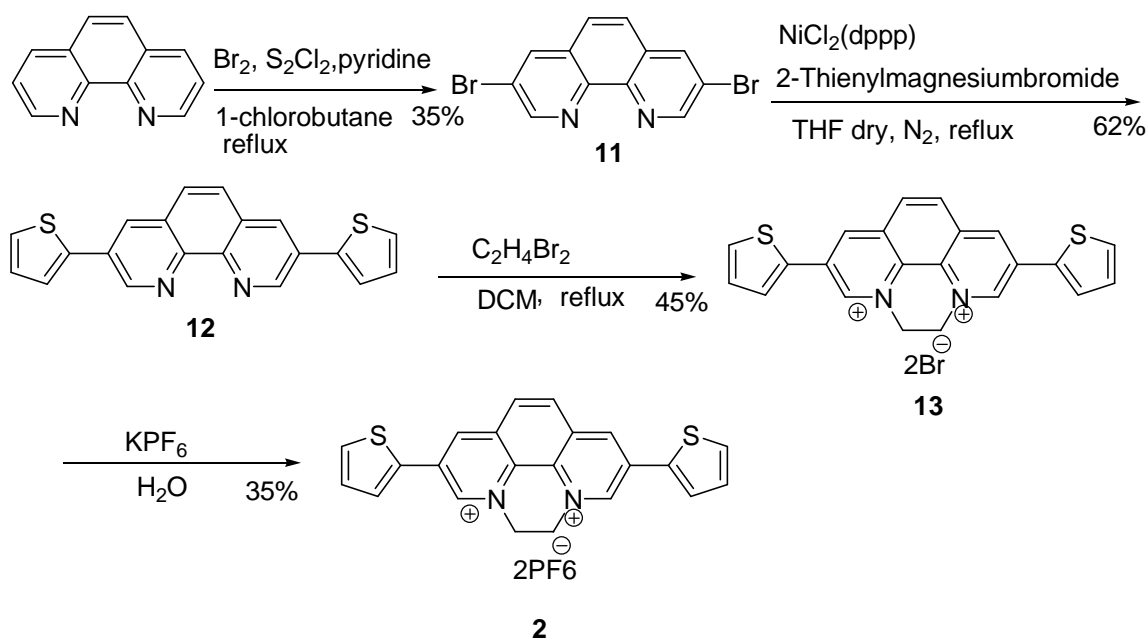
#### 4-6-1-3 Polymerization of compound **1**

Many attempts were made to polymerize this monomer in solution by electrochemical method using different parameters. Successive oxidation, and reduction sweeps were performed. However, no evidence for polymerization was displayed. It is believed that the presence of the positive centres in the core of viologen monomer probably prevents chain growth and polymer formation (see compound **2**). Therefore, we decided to synthesise compound **2** in the hope that this molecule might produce polymer.

#### 4-6-2 Syntheses of targeted compound **2**

The scheme for synthesis of compound **2** starts with 1,10- phenanthroline. This was converted to 3,8- dibromo-1,10- phenanthroline by reaction with a mixture of bromine, sulphur monochloride, and pyridine using 1-chlorbutane as a solvent and and heating under reflux. This compound was then converted to 3,8-di(thiophen-2-yl)-1,10-phenanthroline by Stille coupling. The last compound was alkylated with 1,2- dibromoethane to give viologen salt with bromide as a counter anion. The bromide ion was replaced by hexafluorophosphate by ion exchange reaction using excess aqueous KPF<sub>6</sub>. This reaction

introduces  $\text{PF}_6^-$  as a counter anion instead of  $\text{Br}^-$  to improve the solubility of the viologen compound **2**. The synthetic steps are presented in the following scheme:



**Scheme 4-22:** The synthetic route of target compound **2**.

The starting material 1,10-phenanthroline is a typical  $\pi$  electron deficient aromatic compound, so this compound can be brominated. It has been shown that bromination of phenanthroline with  $\text{Br}_2$  in chloroform without other additives resulted in a yellow precipitate of phenanthroline dibromide intermediate, and when this was heated at  $190\text{ }^\circ\text{C}$  and  $260\text{ }^\circ\text{C}$  there was not any sign of carbon bromination. If thermolysis was performed with an excess of  $\text{Br}_2$ , it afforded a mixture of both 3-bromo-1,10-phenanthroline, and 3,8-dibromo-1,10-phenanthroline in poor yields of about 15 and 5% respectively<sup>(82)</sup>. Direct bromination was not shown to be efficient to achieve a good yield for this reaction. It has been found that the yield can be increased significantly when used with pyridine and sulphur chloride with reaction mixture<sup>(83)</sup>. The reaction was shown to proceed smoothly in a chlorinated solvent such as 1-chlorobutane. The compound 3,8-dibromo-1,10-phenanthroline is an important compound as it is a starting material for liquid crystalline compounds and  $\pi$  conjugated polymers<sup>(83, 84)</sup>.

Compound **12** was synthesized by an Ni-catalyzed cross-coupling reaction of 3,8-dibromo-1,10-phenanthroline with a Grignard reagent. This reaction was effective and a good yield of 62% was achieved<sup>(85)</sup>. Compound **13** was synthesised by the *N*-alkylation reaction with 1,2-dibromoethane. It was then converted to compound **2** by an ion exchange reaction with an aqueous solution of  $\text{KPF}_6$  to give compound **2**<sup>(77)</sup>. This compound was obtained as a yellow/orange powder in 35% yield.

#### 4-6-2-1 Analysis of target compound 2

The UV- visible spectrum of compound **2** was recorded in acetonitrile. Compound **2** shows four peaks at 269 nm, 321 nm, 369 nm and 452 nm. The optically determined HOMO-LUMO bandgap was calculated to be 2.44 eV. This compound absorbs strongly in the UV-vis region of the spectrum and this absorption is related to the  $\pi$ -  $\pi^*$  transitions. The high intensity of this peak is probably due to conjugation between the thiophene and the pyridinium rings. There is another that peak occurs in the visible region (452 nm) which is related to intramolecular charge transfer complexes<sup>(78)</sup>. The UV-visible spectrum is shown in the following figure:

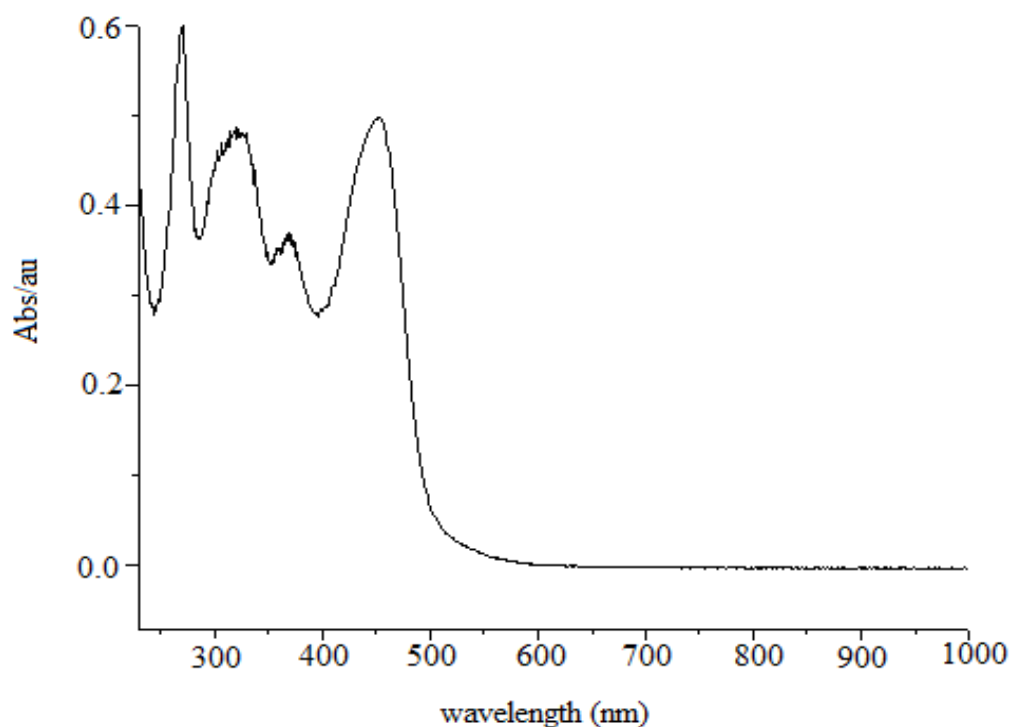


**Figure 4-23:** UV- visible spectrum for compound **2**. Recorded in MeCN ( $1 \times 10^{-4}$  M).

#### 4-6-2-2 The voltammogram of compound 2

To investigate electropolymerization of the compound **2**, cyclic voltammetry was performed in acetonitrile. Monomer oxidation of compound **2** shows two irreversible peaks at at 1.79 V and 1.33 V. A dynamic electrochemical run was performed between the two values by applied potential with a scan rate of  $100 \text{ mV s}^{-1}$ . The estimated HOMO level for this compound was determined to be - 6.13 eV based on the onset of the oxidation peak of the ferrocene (0.24 V) and its published value of (4.80 eV)<sup>(79,80)</sup>. The voltammogram for the oxidation of compound **2** is shown in the following figure:

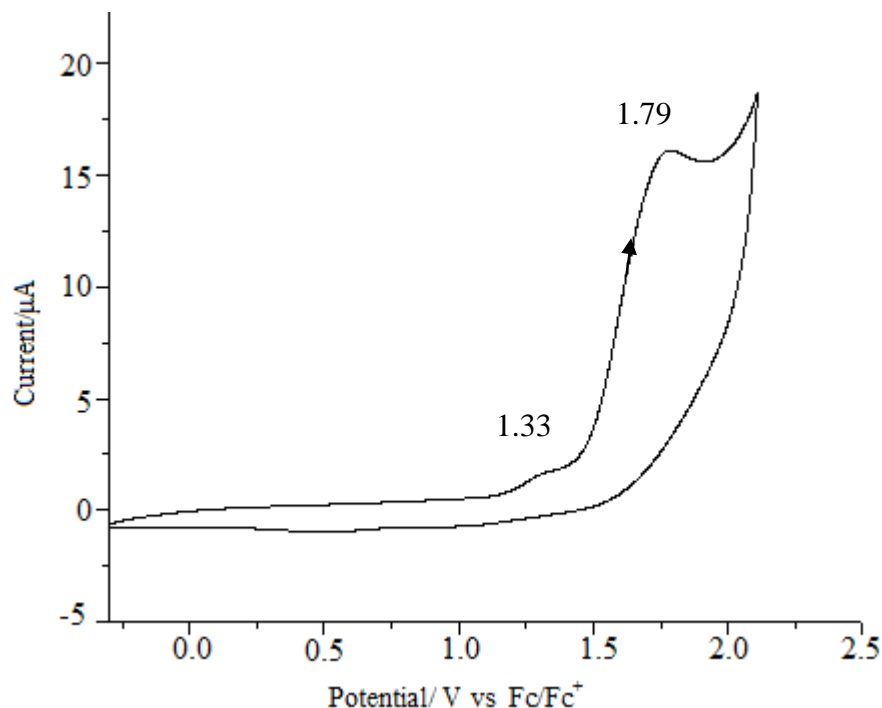


**Figure 4-24:** The voltammogram for oxidation of compound **2** recorded using a glassy carbon working electrode, an Ag wire as a reference electrode and a Pt wire as a counter electrode. Recorded at a concentration of  $1 \times 10^{-4}$  M in MeCN with TBAPF<sub>6</sub> (0.1M) as a supporting electrolyte. Scan rate  $100 \text{ mV s}^{-1}$ .

Reduction of compound **2** showed two peaks; the first peak at  $-0.67 \text{ V}$  and  $-1.30 \text{ V}$ . The first peak is probably related to the conversion of  $\text{Bipm}^{2+}$  to  $\text{Bipm}^{+}$ , while the second peak may be assigned to reduce  $\text{Bipm}^{+}$  to  $\text{Bipm}^0$ . The estimated LUMO level of this compound was  $-4.23 \text{ eV}$  based on the onset of the oxidation of ferrocene ( $0.24 \text{ V}$ ) and its published HOMO value of  $4.80 \text{ eV}$  <sup>(79,80)</sup>. The electrochemically determined bandgap was estimated to be  $1.90 \text{ eV}$ . The voltammogram for reduction of compound **2** is shown in the following figure:

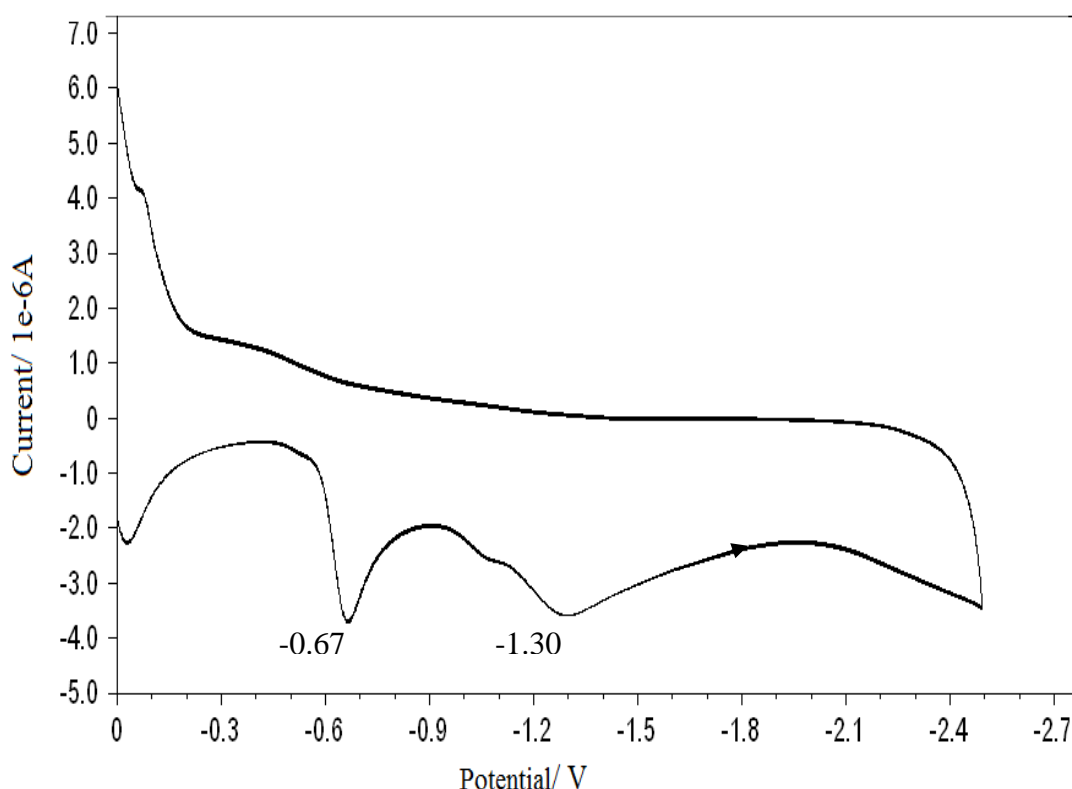


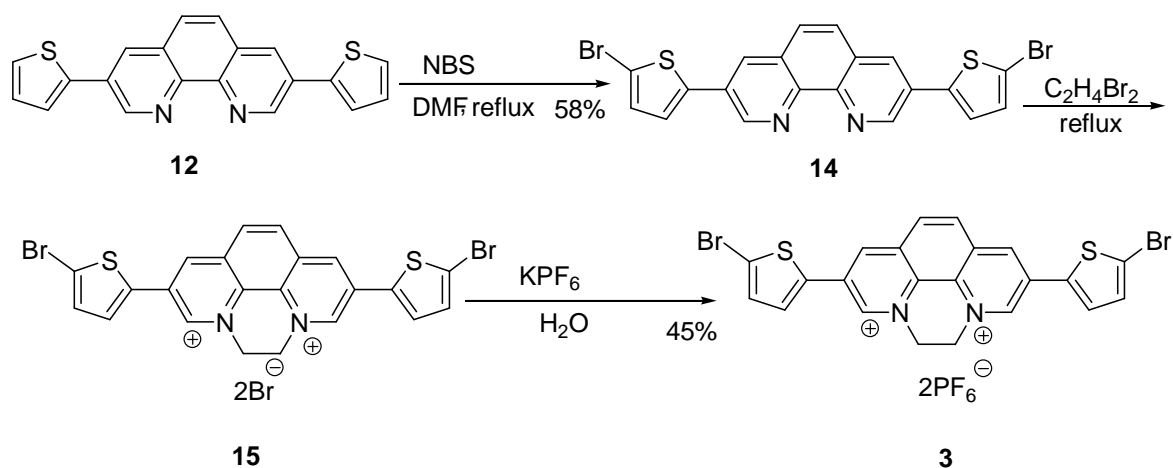
**Figure 4-25:** The voltammogram for reduction of compound **2** recorded using a glassy carbon working electrode, an Ag wire as a reference electrode and a Pt wire as a counter electrode. Recorded at a concentration of  $1 \times 10^{-4}$  M in MeCN with TBAPF<sub>6</sub> (0.1M) as a supporting electrolyte. Scan rate  $100 \text{ mV s}^{-1}$ .

#### 4-6-2-3 Polymerization of compound **2**

Many attempts were made to polymerize the above viologen monomer using different polymerization parameters and conditions. Successive oxidation and reduction sweeps were performed many times. However, polymerization did not occur, probably due to the same reasons that were mentioned previously in case of monomer **1**. Therefore, it was decided to synthesize compound **3** to investigate whether this molecule produces polymer upon electropolymerization.

#### 4-6-3 Synthesis of target compound **3**

The synthesis of compound **3** started with 3,8-dibromo-1,10-phenanthroline<sup>(86,87)</sup>. This was converted to compound **14** by the reaction with *N*-bromosuccinamide (NBS). The resulting compound was alkylated with 1,2- dibromoethane to yield the viologen (bromide) salt. Using an ion exchange reaction with an aqueous solution of KPF<sub>6</sub>, this compound was converted into hexafluorophosphate salt to improve the solubility of the viologen compound **3**. The synthetic steps are presented in the following scheme:



**Scheme 4-26:** The synthetic route of target compound **3**.

Compound **14** was synthesized from **12** by reaction with NBS in a one-pot reaction. This reaction proceeded smoothly under reflux in DMF in the dark to give **14** in a yield of 58%<sup>(87)</sup>. This was then converted into compound **15** by an *N*-alkylation reaction with 1,2-dibromoethane to afford viologen compound **15** which was then converted into viologen hexafluorophosphate salt by reacting with an aqueous solution of  $\text{KPF}_6$  to give the target compound **3**<sup>(77)</sup>. This compound was obtained as an orange powder in 45% yield.

#### 4-6-3-1 Analysis of compound **3**

The UV- visible spectrum of compound **3** was recorded in acetonitrile. This compound shows four peaks at 276 nm, 308 nm, 331 nm and 465 nm. The optically determined bandgap was calculated to be 2.25 eV. The first peak at 276 nm, and the two weak peaks at 308 and 331 nm are related to the  $\pi$ -  $\pi^*$  transitions. The broad peak in the visible region at 465 nm is related to intramolecular charge transfer complexes (CT)<sup>(78)</sup>. The UV-visible spectrum is shown in the following figure:

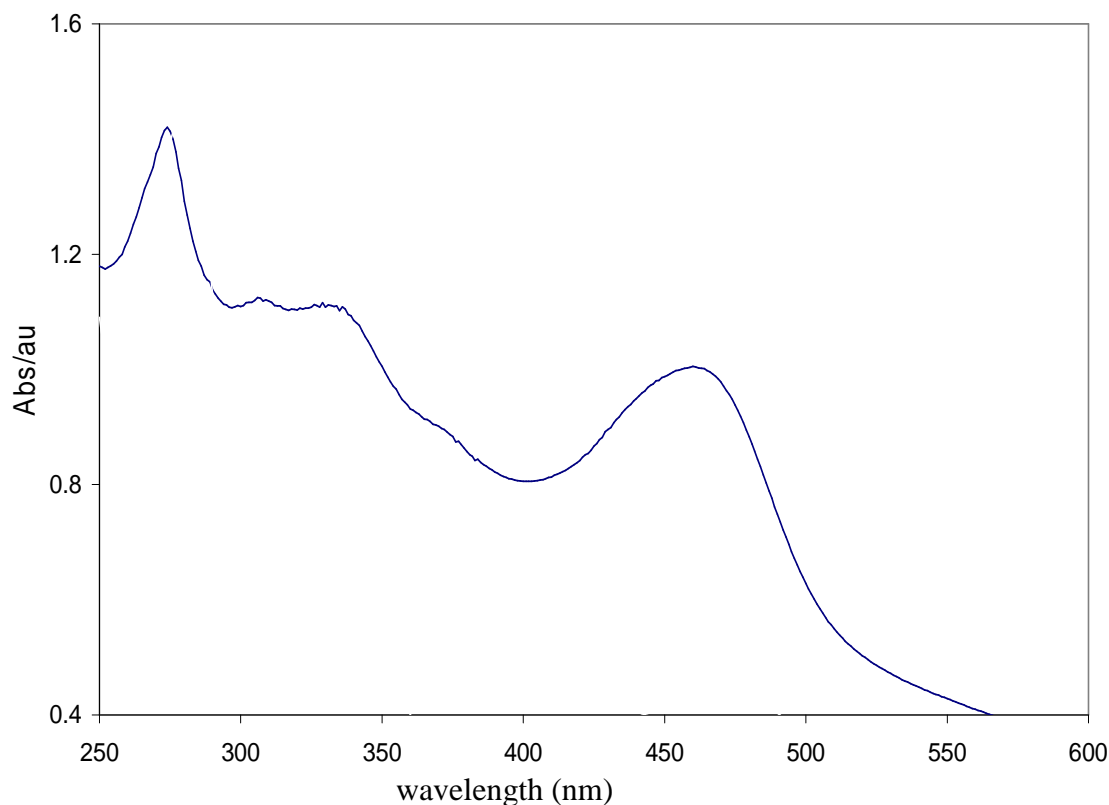


**Figure 4-27:** UV-visible spectrum for compound **3**. Recorded in MeCN ( $1 \times 10^{-4}$  M).

#### 4-6-3-2 The voltammogram of compound **3**

The voltammogram of **3** was studied in acetonitrile. This compound showed one irreversible reduction peak at - 0.61 V. The estimated LUMO level of this compound was - 4.19 eV based on the onset of the oxidation of ferrocene (0.24 V) and its published value of 4.8 eV<sup>(79, 80)</sup>. The presence of one reduction peak for this compound is probably due to reduction of the viologen in a single step ( $\text{Bipm}^{2+}$  to  $\text{Bipm}^0$ )<sup>(81)</sup>. It also shows an oxidation peak (negative current) at +1.21 V, the HOMO level for this compound was - 6.01 eV and the corresponding HOMO to LUMO bandgap was 1.71 eV. For this compound, there is one reduction peak, which is probably due to the one step two electron reduction of the viologen monomer<sup>(81)</sup>. The voltammogram for this compound is shown in the following figure:

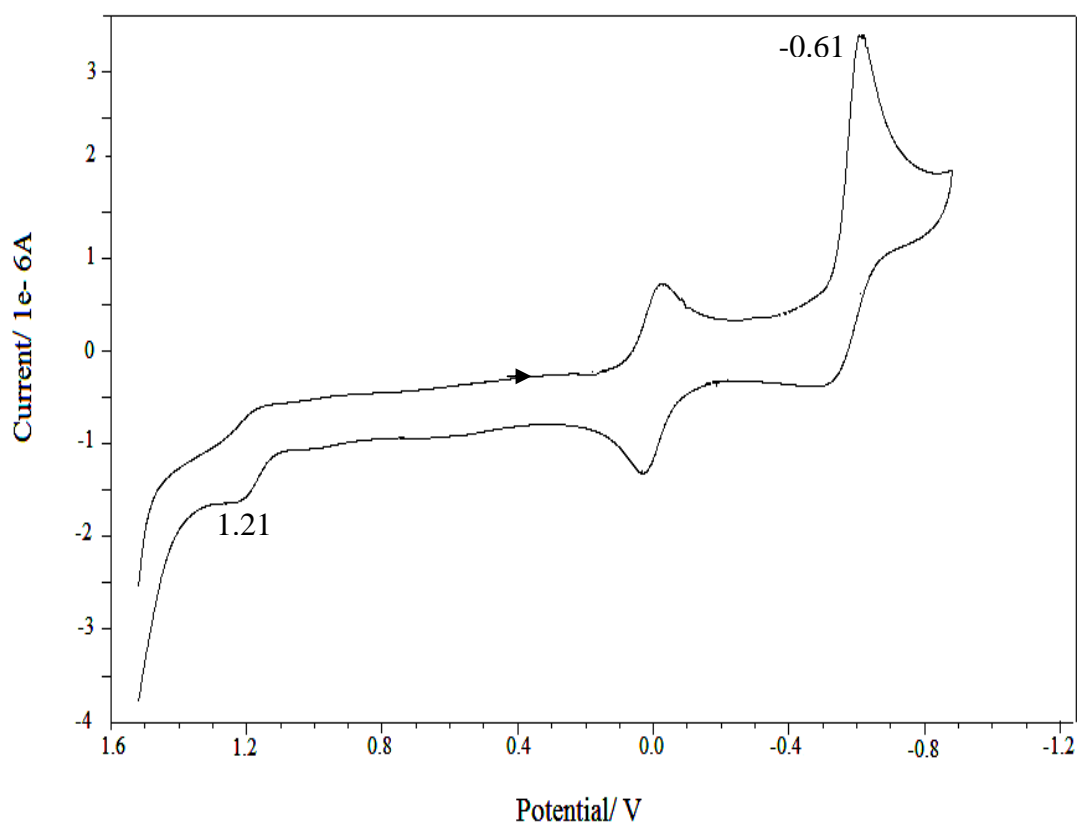
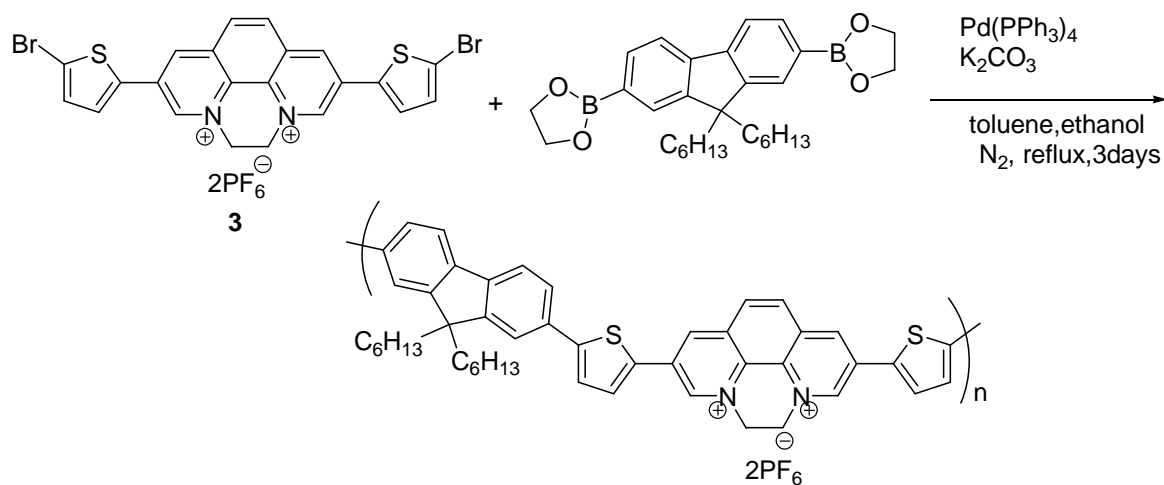


**Figure 4-28:** The voltammogram of compound **3** recorded using a glassy carbon working electrode, an Ag wire as a reference electrode and a Pt wire as a counter electrode. Recorded at a concentration of  $1 \times 10^{-4}$  M in MeCN with TBAPF<sub>6</sub> (0.1M) as a supporting electrolyte. Scan rate  $100 \text{ mV s}^{-1}$ .

#### 4-6-3-3 Polymerization of compound **3**

The chemical polymerization of viologen monomer **3** was performed as shown in the following scheme:



**Scheme 4-29:** Schematic polymerization of compound **3**.

Compound **3** and dioctylfluorene-2,7-diboric acid were dissolved and degassed in ethanol: toluene 1:1 mixture. To this mixture tetra-kis triphenylphosphine Pd(PPh<sub>3</sub>)<sub>4</sub> and

$K_2CO_3$  were added. The whole mixture was then degassed and heated under reflux at 85 °C in the dark for three days<sup>(88)</sup>, with a nitrogen flush and continuous stirring for three days. The obtained solid was dissolved in chloroform, filtered off and the orange solid polymer was dried overnight.

The  $^1H$  NMR spectrum for the viologen polymer showed interesting broad peaks for the polymer. However, characterization of the polymer by GPC didn't give a sufficiently high molecular weight, probably due to the presence of a polar positive viologen centre in the structure of the polymer. The presence of this centre probably retards the elution polymer molecules from the column of the GPC, so that, results a signal in the region of low molecular weight ( $M_n = 3796$ ,  $M_w = 3893$ ,  $PDI = 1.03$ ).

The UV- visible spectrum of the poly(**3**) was recorded in  $CHCl_3$ . The electronic spectrum of the polymer shows three peaks at 282 nm, 310 nm and a broad peak at 473 nm. The optical HOMO to LUMO bandgap was calculated to be 2.19 eV. The last peak in the polymer is shifted to higher wavelength in comparison with the monomer, probably as a result of more delocalization of electrons in the polymer. The UV-visible spectrum is shown in the following figure:

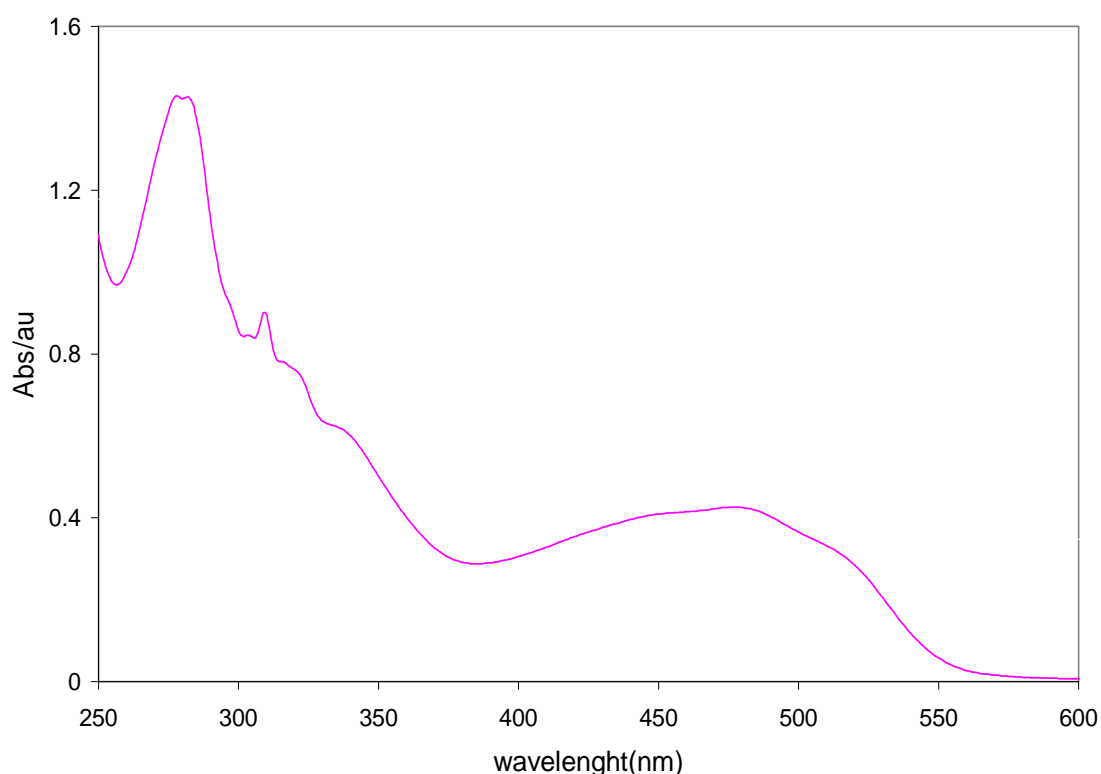


**Figure 4-30:** UV-visible spectrum of viologen polymer. Recorded in  $CHCl_3$  ( $1 \times 10^{-4}$  M).

The emission spectrum of the polymer was measured in chloroform. The emission spectrum for the polymer showed features in the visible region as shown in the following figure:

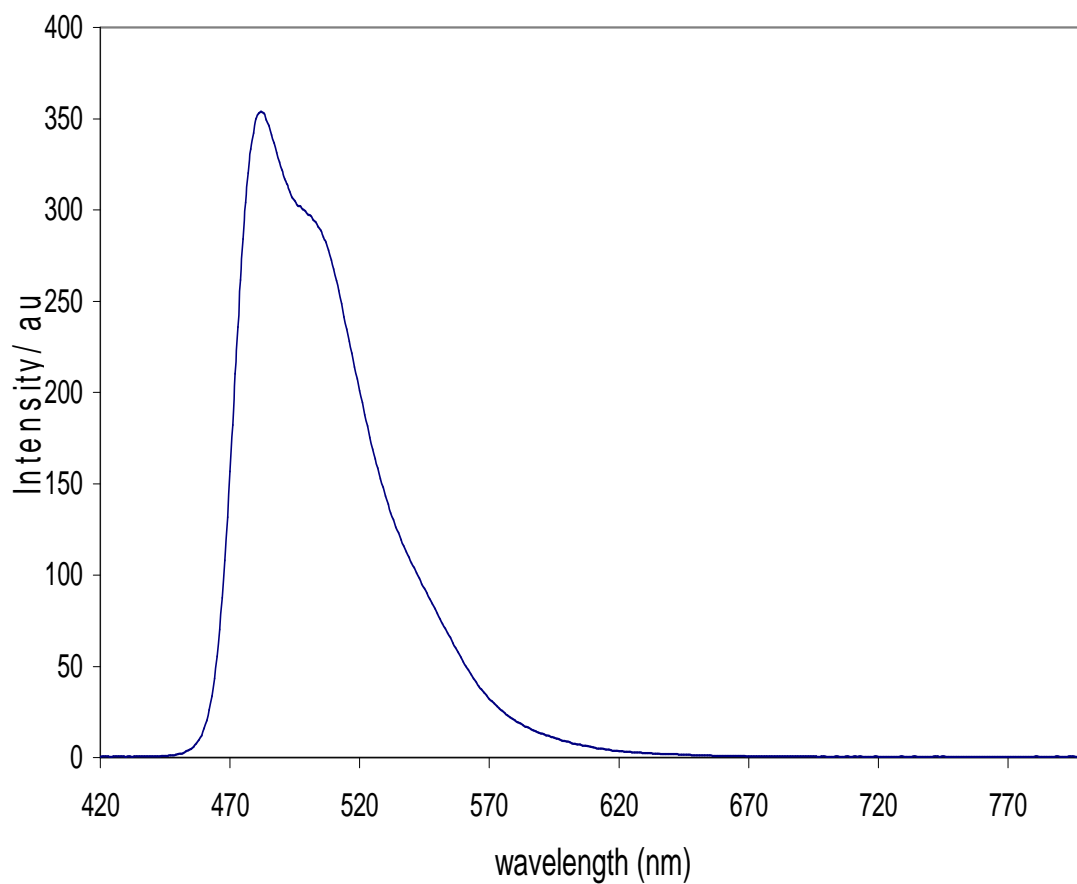


**Figure 4-31:** Emission spectrum of the poly(**3**), excitation wavelength 450 nm. Recorded in  $\text{CHCl}_3$  ( $1 \times 10^{-5}$  M).

The voltammogram of the polymer was recorded in chloroform by using cyclic voltammetry. Polymer redox reaction showed an oxidation peak at 0.82 V, and the estimated HOMO level with respect to the published value for oxidation of ferrocene was -5.62 eV. The voltammogram of poly(**3**) is shown in Figure 4-32.

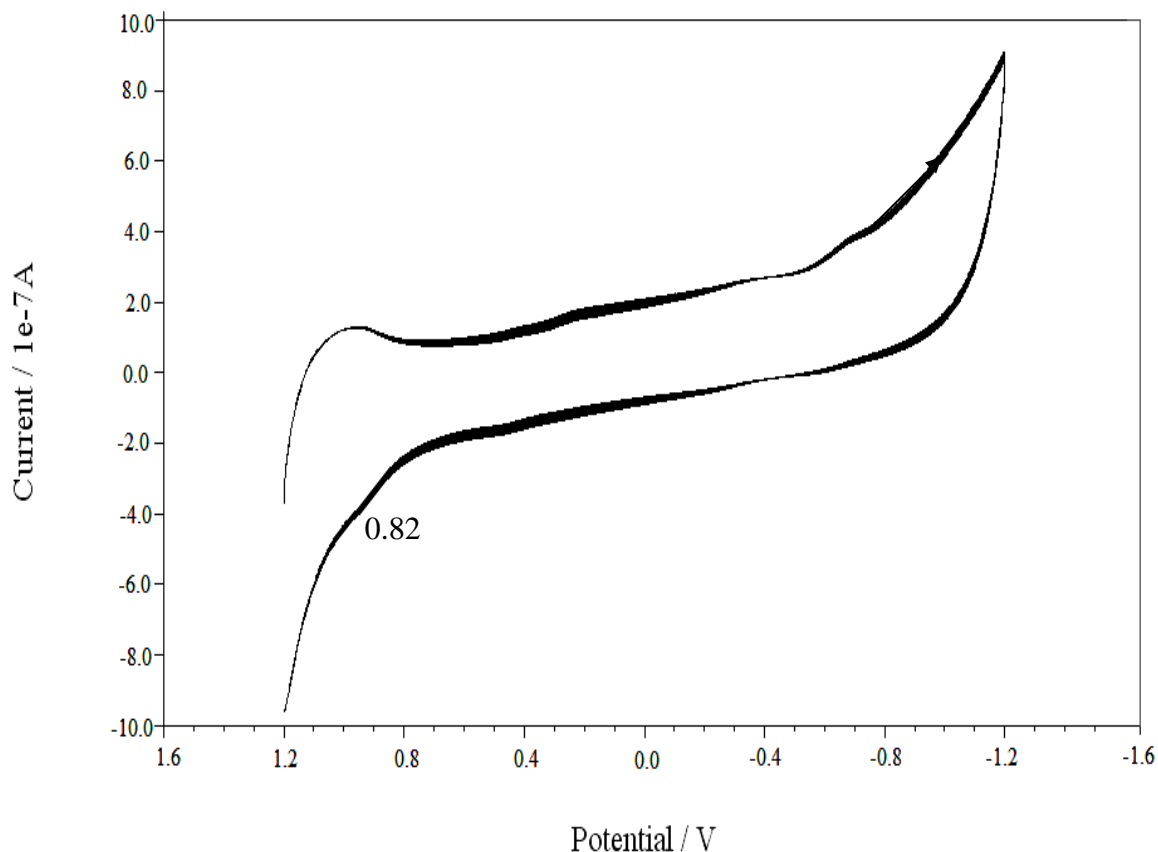
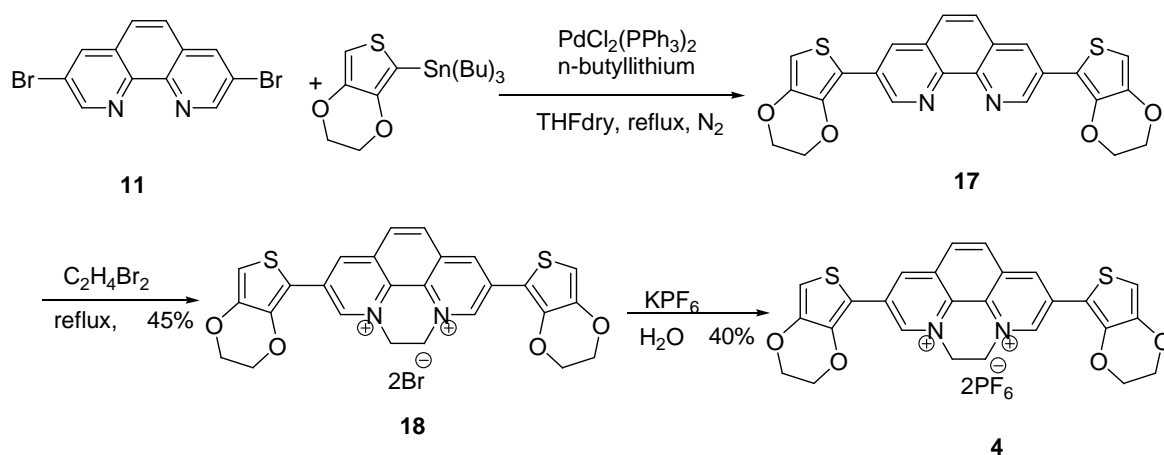


**Figure 4-32:** The voltammogram for poly(**3**) recorded using a glassy carbon working electrode, an Ag wire as a reference electrode and a Pt wire as a counter electrode. Recorded at a concentration of  $1 \times 10^{-4}$  M in  $\text{CH}_3\text{Cl}$  with  $\text{TBAPF}_6$  (0.1M) as a supporting electrolyte. Scan rate  $100 \text{ mV s}^{-1}$ .

#### 4-6-4 Synthesis of target compound **4**

Viologen monomers **1** and **2** did not polymerize by electrochemical route. This probably arises from the presence of positive charges in the core of viologen compound with the presence of thiophene ring in conjugation with phenanthroline core. So that it was aimed to replace thiophene ring with EDOT ring as it more rich electrons. For this reason, we decide to synthesize compound **4**. The proposed route for the synthesis of target compound **4** is shown in the following scheme:



**Scheme 4-33:** Proposed synthetic route of target compound **4**.

The target compounds **1** and **2** didn't polymerize which may be due to poor electron density in the central core for both of these compounds. It was decided to replace the thiophene ring in these compounds by 3,4-ethylenedioxythiophene (EDOT) as it is more electron rich in comparison with the thiophene ring. It was aimed to synthesise target compound **4** as a viologen monomer for electropolymerization. The starting material for this monomer was compound **17**, which was synthesized by the Stille coupling in a yield of 60%<sup>(89)</sup>. This compound was heated under reflux with 1,2- dibromoethane to give compound **18**. This compound was then converted to **4** by ion exchange reaction with potassium hexafluorophosphate to give compound **4** as an orange powder in 40% yield.

#### 4-6-4-1 Analysis of compound **17**

The UV-visible spectrum of compound **17** was recorded in DCM. The absorption spectrum of this compound showed four peaks at 225 nm, 291nm, 362 nm and 381 nm. These absorption peaks are related to the  $\pi$ -  $\pi^*$  transitions. The red shift in the absorption of compound **17** is probably due to conjugation between EDOT ring and phenanthroline core. This indicates the presence of charge transfer character in the electronic absorption for this compound. The optically determined bandgap was calculated to be 3.06 eV. The UV-visible spectrum is shown in the following figure:

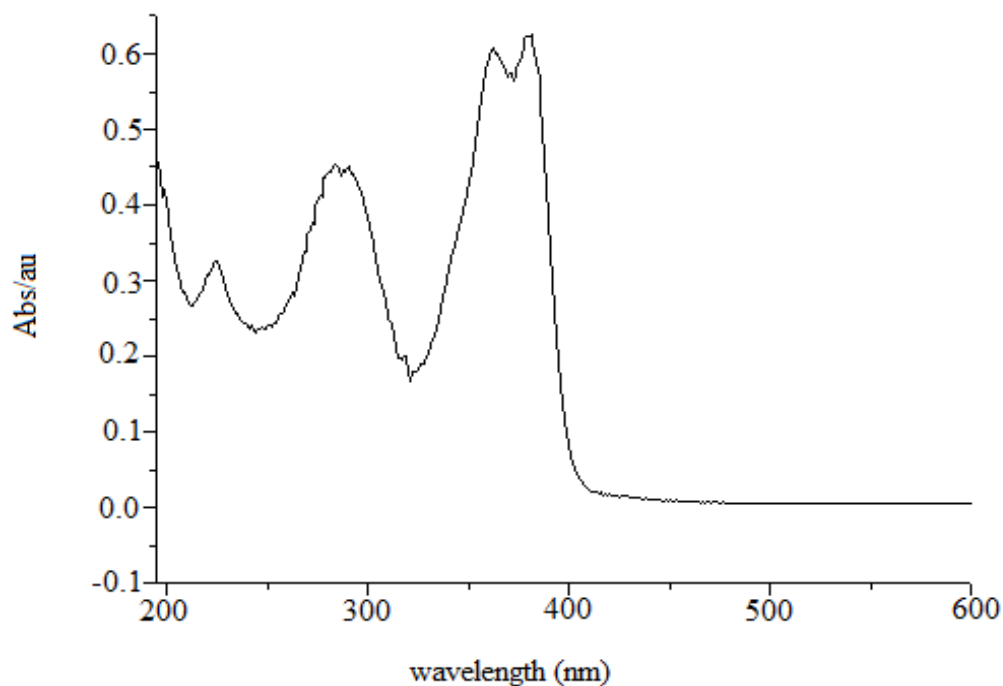


**Figure 4-34:** UV- visible spectrum of compound **17**. Recorded in DCM ( $1 \times 10^{-4}$  M).

The voltammogram for this compound was recorded in DCM. The voltammogram of compound **17** shows an irreversible oxidation wave at +1.02 V. This peak probably related to oxidation of EDOT ring in this compound. The voltammogram for oxidation this compound is shown in the following figure:

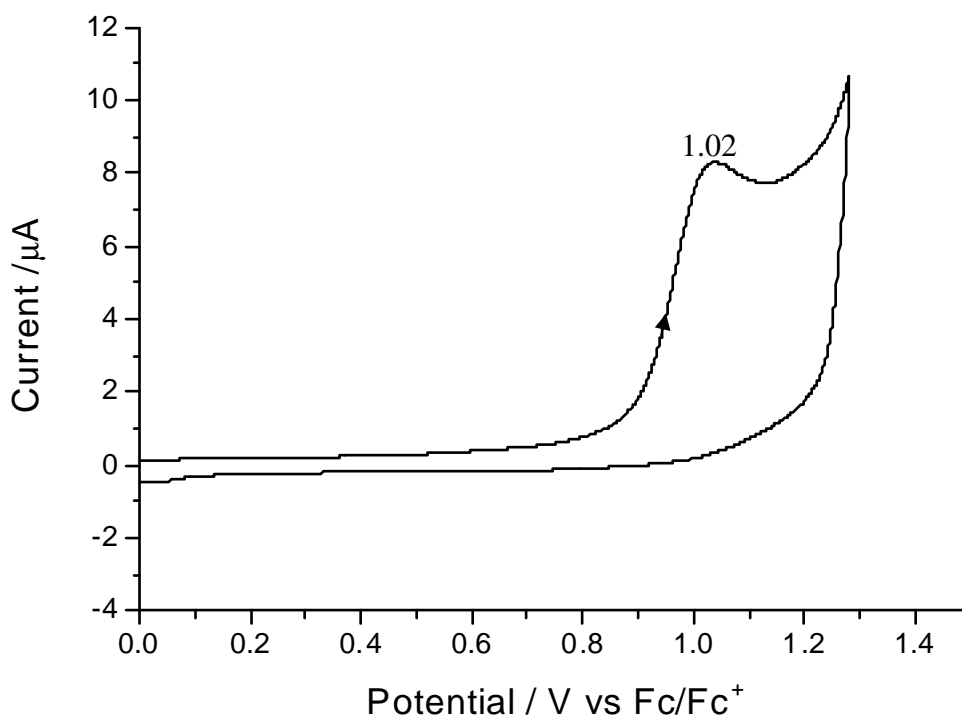


**Figure 4-35:** The voltammogram for oxidation of compound **17** recorded using a glassy carbon working electrode, an Ag wire as a reference electrode and a Pt wire as a counter electrode. Recorded at a concentration of  $1 \times 10^{-4}$  M in DCM with TBAPF<sub>6</sub> (0.1 M) as a supporting electrolyte. Scan rate  $100 \text{ mV s}^{-1}$ .

The voltammogram for reduction compound **17** shows an irreversible peak at -2.15 V. This peak probably related to the reduction of phenanthroline core. This voltammogram is shown in Figure 4-36.

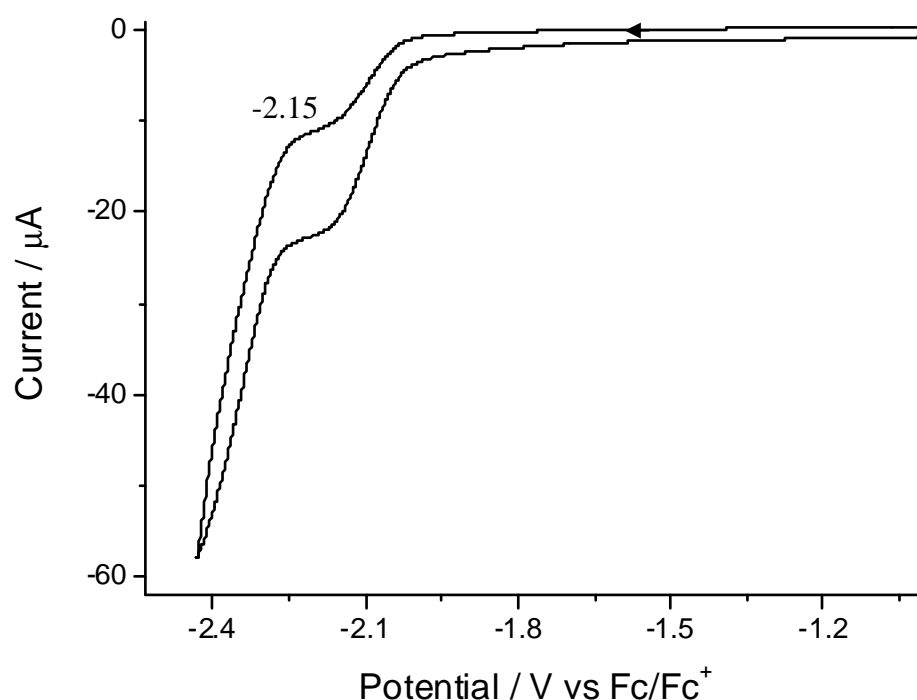


**Figure 4-36:** The voltammogram for reduction of compound **17** on a glassy carbon working electrode, an Ag wire as a reference electrode and a Pt wire as a counter electrode. Recorded at a concentration of  $1 \times 10^{-4}$  M in DCM with TBAPF<sub>6</sub> (0.1 M) as supporting electrolyte. Scan rate of  $100 \text{ mV s}^{-1}$ .

The electrochemically determined HOMO-LUMO bandgap of compound **17** was calculated from the difference in the onset of the first oxidation and reduction processes and the data are shown in the following table:

**Table 4-1:** Electrochemical data for compound **17**.

Onset of oxidation / V	HOMO / eV	Onset of reduction / V	LUMO / eV	HOMO-LUMO bandgap / eV
+ 0.90	-5.70	-2.03	-2.77	2.93

The difference between the HOMO and LUMO values gave an electrochemical HOMO-LUMO bandgap of 2.93 eV, which is slightly lower than the calculated optically determined HOMO-LUMO bandgap that was 3.06 eV.

#### 4-6-4-2 Electrochemical growth of poly(**17**)

The electrochemical growth of poly(**17**) was undertaken from 0 to 1.14 V under 300 segments with using a high concentration  $1 \times 10^{-2}$  M. The following figures showed polymer growth of poly(**17**) under repeated cycling. Repeated cycles for this monomer showed growth in current (also growth of the shoulder) at potential lower than the first oxidation of the monomer can lead to the formation an electroactive film of the polymer<sup>(90)</sup>. The growth of poly(**17**) is shown in the following figures:

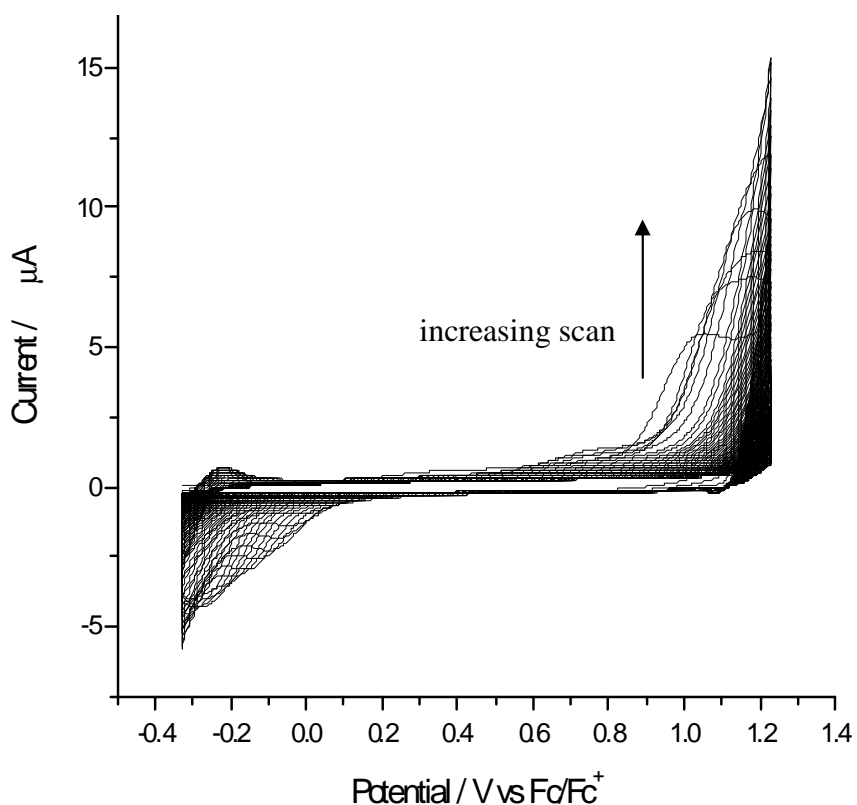


**Figure 4-37:** The voltammogram of growth of poly(**17**) recorded using a glassy carbon working electrode, an Ag wire as a reference electrode and a Pt wire as a counter electrode. Recorded at a concentration of  $1 \times 10^{-4}$  M in DCM with TBAPF<sub>6</sub> (0.1 M) as a supporting electrolyte. Scan rate  $100 \text{ mV s}^{-1}$  over 300 segments. This figure shows polymer growth on the electrode increasingly with repeating cycling.

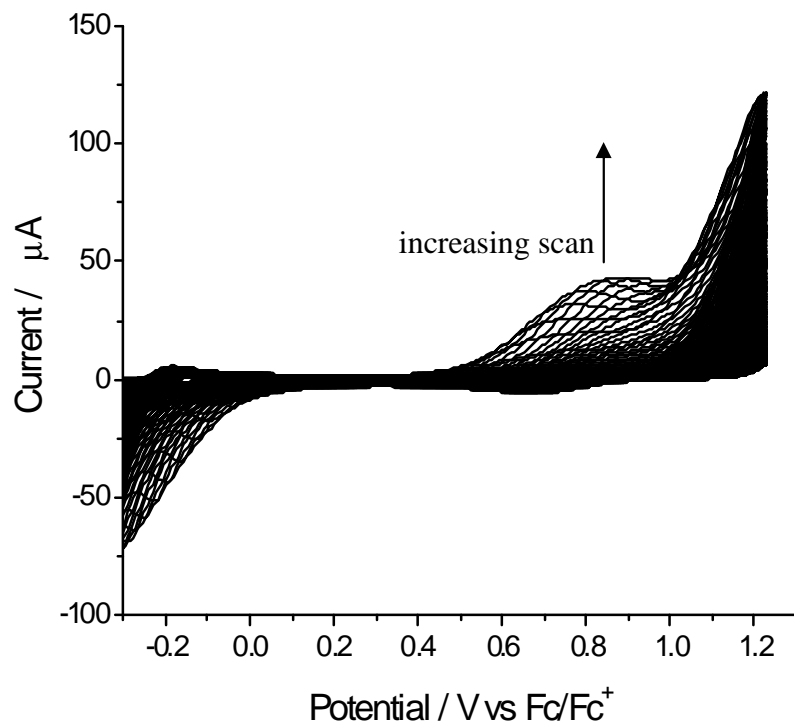


**Figure 4-38:** The voltammogram of growth of poly(**17**) recorded using an ITO as a working electrode, an Ag wire as a reference electrode and a Pt wire as a counter electrode. Recorded at a concentration of ca.  $1 \times 10^{-4}$  M in  $\text{CH}_2\text{Cl}_2$  with  $\text{TBAPF}_6$  (0.1 M) as a supporting electrolyte. Scan rate  $100 \text{ mV s}^{-1}$  over 300 segments. ITO used in this process was transparent and conductive.

#### 4-6-4-3 The voltammogram of poly(**17**)

The voltammogram of poly(**17**) showed an irreversible oxidation peak at + 0.75 V. This peak may be attributed to the oxidation of the polaron and the bipolaron states. The reduction process shows an irreversible peak at -1.75 V. The voltammogram of poly(**17**) is shown in the following figure:

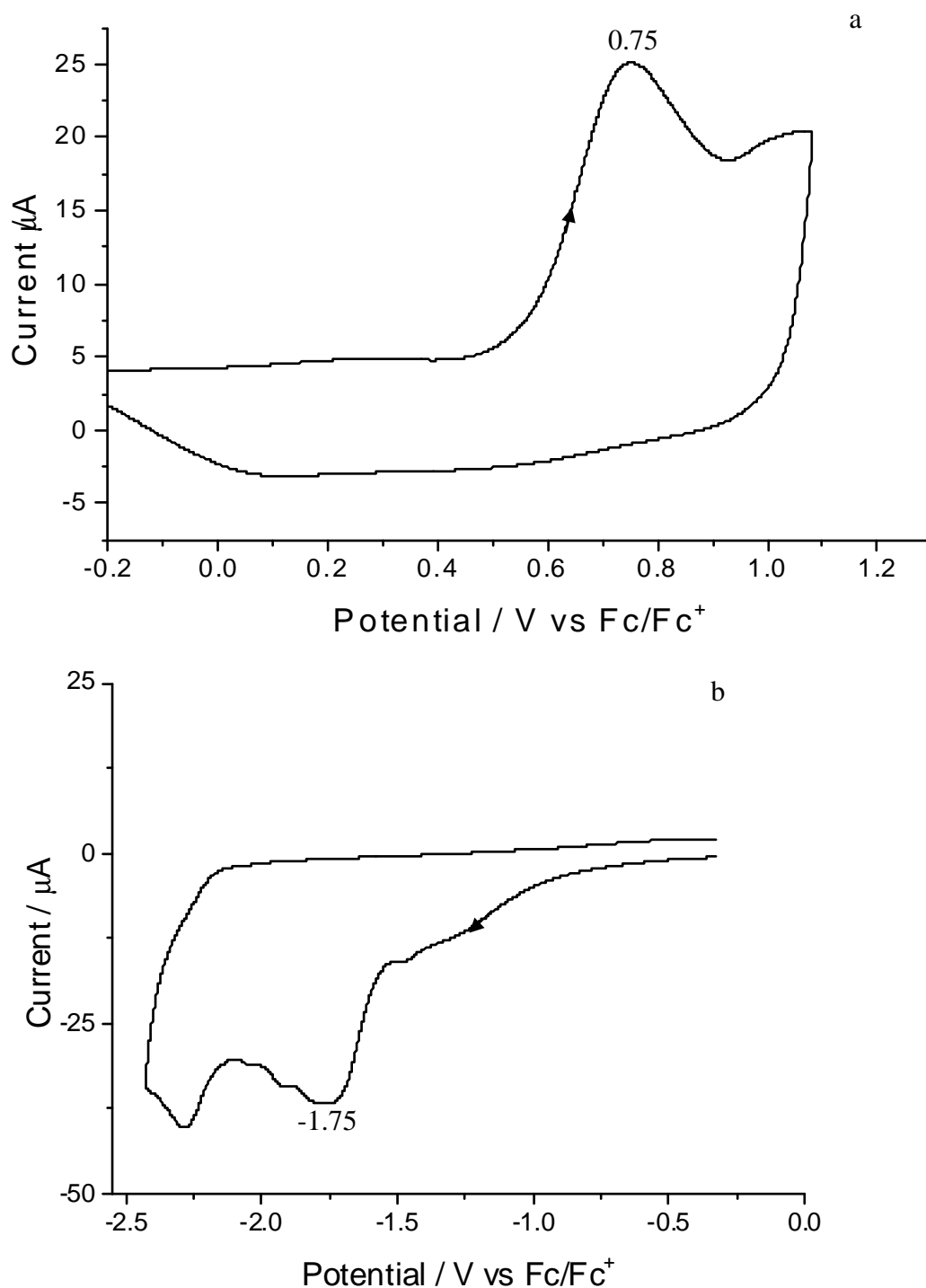


**Figure 4-39:** The voltammogram of oxidation (a) and reduction (b) of poly(**17**) recorded using a glassy carbon working electrode, an Ag wire as a reference electrode and a Pt wire as a counter electrode. Recorded in monomer-free DCM with TBAPF<sub>6</sub> (0.1 M) as a supporting electrolyte. Scan rate of 100 mV s<sup>-1</sup>.

The electrochemically determined bandgap for the polymer was calculated to be 2.07 eV and the electrochemical data for poly(**17**) is summarized in the following table:

**Table 4-2:** Electrochemical data for poly compound (17).

Onset of oxidation / V	HOMO / eV	Onset of reduction / V	LUMO /eV	HOMO-LUMO bandgap /eV
+ 0.56	-5.36	-1.51	-3.29	2.07

The UV-visible spectrum of poly(17) was investigated as a thin film on ITO glass. The optical bandgap of the polymer was calculated by growing the polymer onto a piece of ITO coated glass slide. The polymer was grown by cycling between 0 and 1300 mV vs Fc/Fc<sup>+</sup> then de-doped between (-700 and -500 mV). The absorption spectrum for this polymer is shown in the Figure below. The spectrum shows a  $\lambda_{\text{max}}$  peak of 382 nm for the polymer, so the  $\pi$ - $\pi^*$  transition has a bathochromic shift compared to the monomer. The natural form of poly(17) showed an interband transition at 500 nm which is related to the red of poly(EDOT). This red shift arises from the alternating donor/ acceptor structure. The optical bandgap for the polymer grown on ITO was 2.01 eV is much lower than the band gap determined for the monomer. This probably arises from highly conjugation in the polymer backbone. The UV- visible spectrum for poly(17) is shown in the following figure:

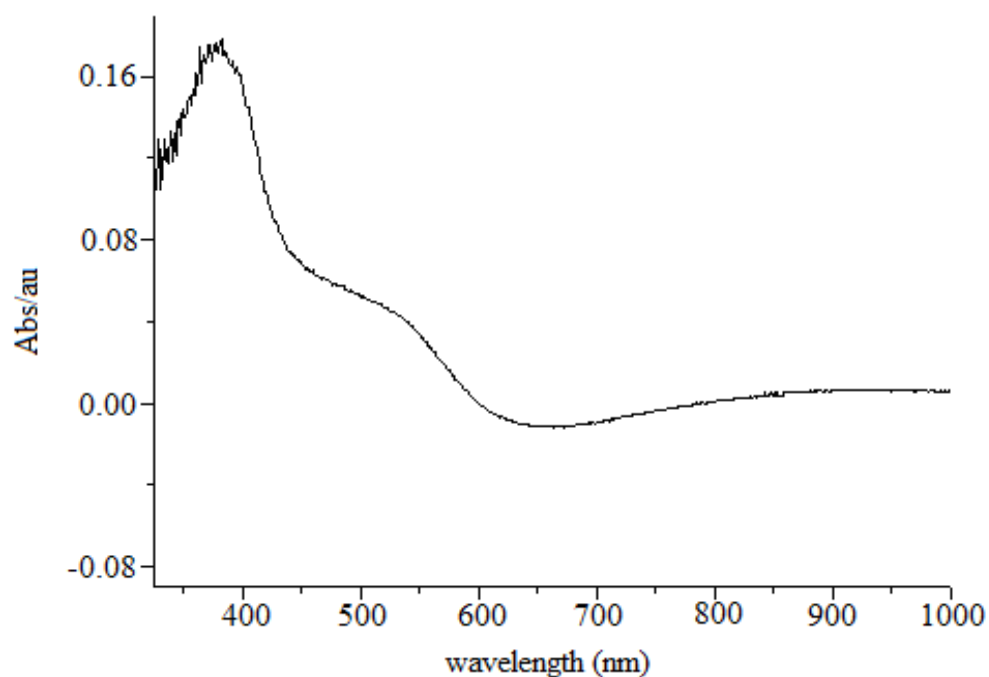


**Figure 4-40:** Absorption spectrum of poly(17) as a thin film on ITO glass.

#### 4-6-4-4 Analysis of compound 4

The UV- visible spectrum of the compound **4** was recorded in acetonitrile. The spectrum of this compound shows three peaks at 281 nm, 341 nm and 566 nm and a shoulder at 525 nm. The optically determined HOMO-LUMO bandgap was calculated to be 1.97 eV. This value is lower than the optical HOMO-LUMO bandgap in compound **17** (3.06 eV). The first and second absorption peaks relate to the  $\pi$ - $\pi^*$  transitions. The third broad absorption peak in the visible region of the spectrum is related to the charge transfer complexes that commonly occur with viologen compounds resulting in broad bands<sup>(78)</sup>. The UV- visible spectrum of this compound is shown in the following figure:

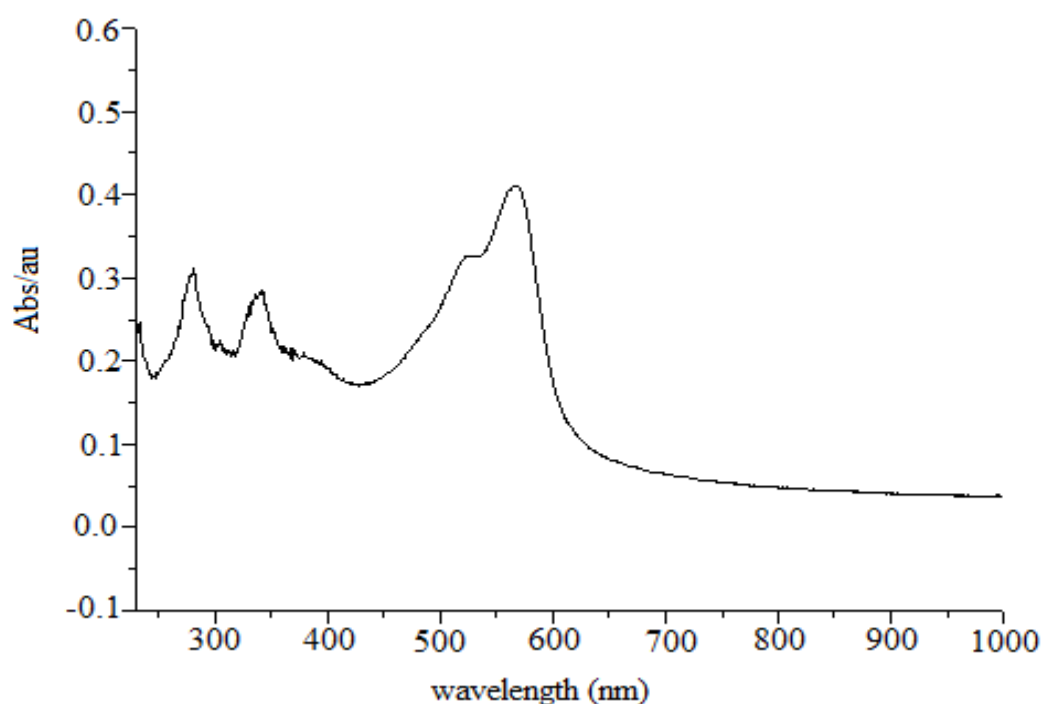


**Figure 4-41:** UV- visible spectrum of compound **4**. Recorded in MeCN ( $1 \times 10^{-4}$  M).

The voltammogram of compound **4** was undertaken in acetonitrile. The voltammogram of compound **4** shows an irreversible peak at + 0.61 V. The reduction process shows an irreversible peak at -1.84 V. The electrochemically determined HOMO-LUMO bandgap of compound **4** was calculated from the difference in the onset of the first oxidation and the reduction and it was calculated to be 2.24 eV. The presence of one reduction peak for this viologen monomer suggests that the reduction of viologen occurred fully in one step<sup>(81)</sup> (from  $\text{Bipm}^{2+}$  to  $\text{Bipm}^0$ ). The voltammogram of this compound is shown in the following figures:

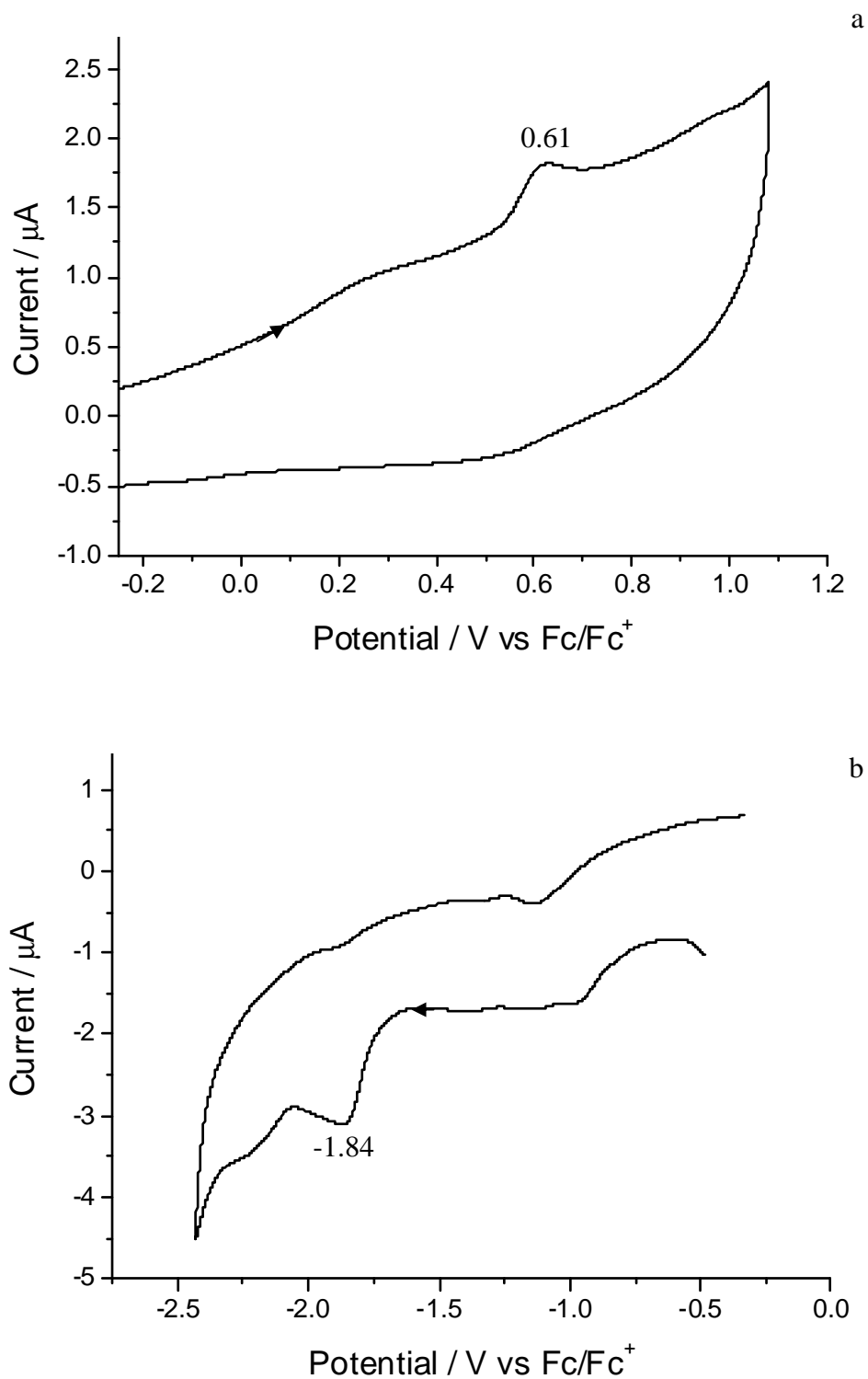


**Figure 4-42:** The voltammogram of oxidation (a) and reduction (b) of compound **4** recorded using a glassy carbon working electrode on ITO slide working electrode, an Ag wire as a reference electrode and a Pt wire as a counter electrode. Recorded at a concentration of ca.  $1 \times 10^{-4}$  M in MeCN with TBAPF<sub>6</sub> (0.1 M) as a supporting electrolyte. Scan rate of  $100 \text{ mV s}^{-1}$ .

The electrochemical data for this compound are summarised in the following table:

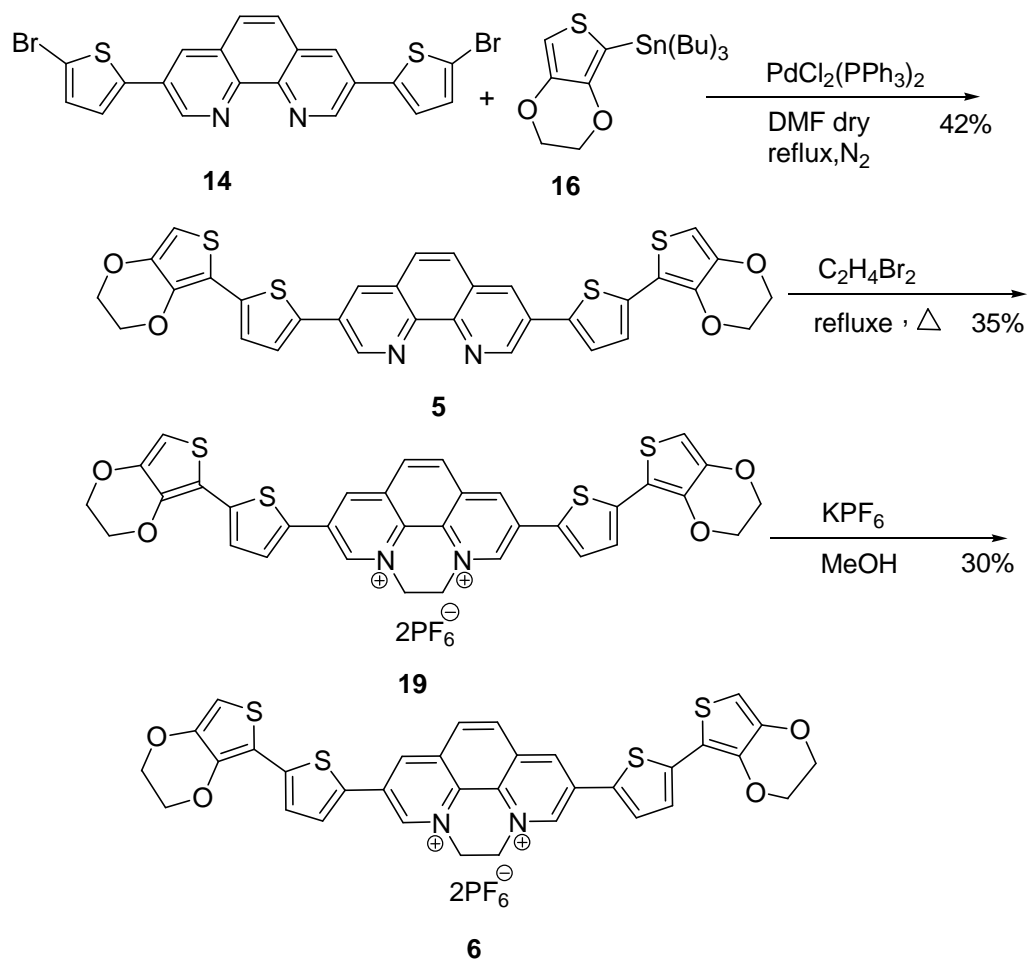
**Table 4-3:** Electrochemical data for compound **4**.

Onset of oxidation / V	HOMO / eV	Onset of reduction / V	LUMO /eV	HOMO-LUMO bandgap /eV
+ 0.52	-5.32	-1.72	-3.08	2.24

The difference between the HOMO and LUMO values gave an electrochemical determined HOMO-LUMO bandgap of 2.24 eV, which is higher than the optically determined HOMO-LUMO bandgap (1.97 eV). Compound **4** was subjected to many attempts at electropolymerization by using several solvents such as dichloromethane and acetonitrile. Also changing the experimental conditions, including using different potentials, substrate concentrations and number of cycles didn't result in growth of the polymer.

#### **4-6-5 Synthesis of target compounds 5 and 6**

The lack of evidence for polymerization of compound **4** spurred us to develop compound **5** and **6**. The proposed route for the synthesis of target compounds **5** and **6** is shown in the following scheme:



**Scheme 4-43:** The synthetic route of compounds **5** and **6**.

Compound **5** was designed to incorporate bifunctionalized phenanthroline featuring thiophene and EDOT rings. It was hoped this compound could be used as a monomer for polymerization, and as a chelating compound, so that it can be used effectively in synthesis of conducting polymers and in the formation of different chelating complexes with some active metals<sup>(88)</sup>. Synthesis of compound **5** was undertaken by Stille coupling of compound **14** with compound **16** to give compound **5** in 42% yield<sup>(89)</sup>. This compound has a high electron rich density due to the presence of the thiophene, and the EDOT rings. This probably facilitates its ability toward electrochemical polymerization, producing a good polymeric film over the working electrode. Compound **19** was synthesized from compound **5** by an *N*- alkylation reaction with 1,2-dibromoethane. The target compound **6** was synthesized from compound **19** by an ion exchange reaction with potassium hexafluorophosphate in MeOH to give compound **6** as a black/ blue powder in 18% yield.

#### 4-6-5-1 Analysis of compound 5

The UV-visible spectrum and voltammogram of compound **5** were recorded in DCM. The absorption spectrum of this compound shows three peaks at 263, 314, and 415 nm, which are related to a  $\pi$ - $\pi^*$  transition, with a high intensity red shifted peak probably arising from the highly conjugated system due to thiophene / EDOT rings. This feature can cause a high conjugation in this compound<sup>(90-92)</sup>. The optically determined HOMO-LUMO bandgap at a higher wavelength of 465 nm was 2.66 eV. This low value of optical bandgap arises from conjugation between donor (EDOT/ thiophene) rings and the acceptor. The UV- visible for this compound is shown in the following figure:

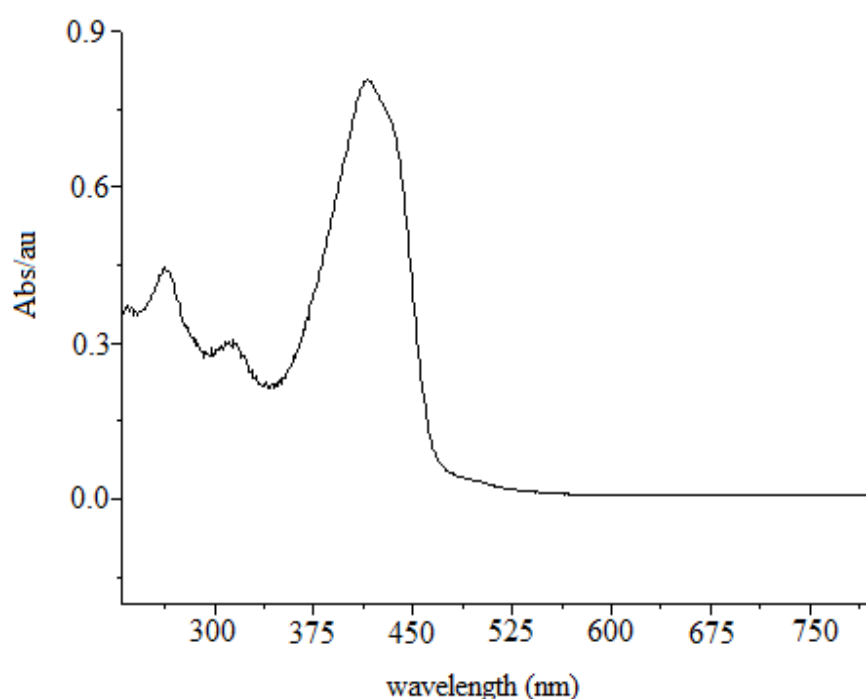


**Figure 4-44:** UV- visible spectrum of compound **5**. Recorded in DCM ( $1 \times 10^{-4}$  M).

#### 4-6-5-2 The voltammogram of compound 5

The voltammogram for this compound shows an irreversible an oxidation waves at + 0.60 and + 0.75 V, a reduction process shows an irreversible peak at -1.98 V. The voltammogram is shown in the following figure:

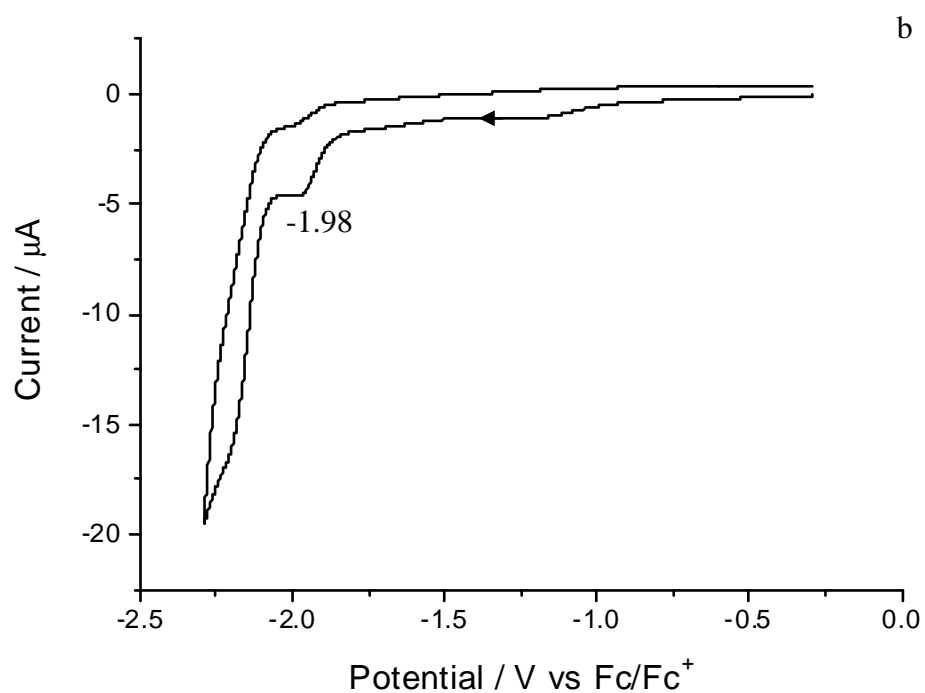
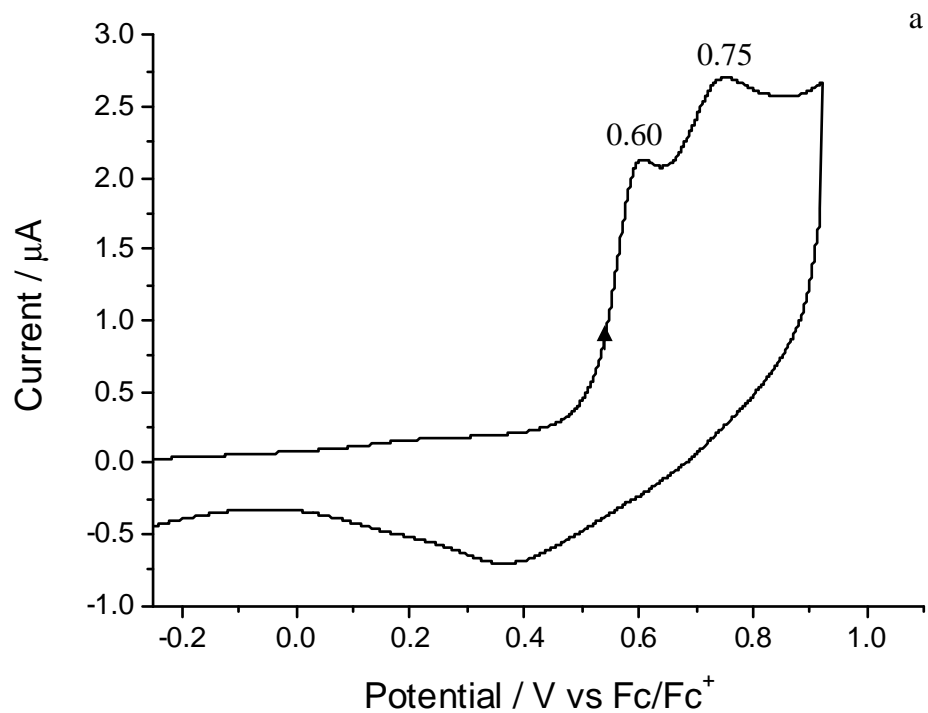


**Figure 4-45:** The voltammogram of oxidation (a) and reduction (b) of compound **5** recorded using a glassy carbon working electrode, an Ag wire as a reference electrode and a Pt wire as a counter electrode. Recorded at a concentration monomer of  $1 \times 10^{-4}$  M in DCM with TBAPF<sub>6</sub> (0.1 M) as a supporting electrolyte. Scan rate of  $100 \text{ mV s}^{-1}$ .

The electrochemically determined HOMO-LUMO bandgap of compound **5** was calculated from the difference in the onset of the first oxidation and reduction and the data is summarised in Table 4-4.

**Table 4-4:** Electrochemical data for compound **5**.

Onset of oxidation / V	HOMO / eV	Onset of reduction / V	LUMO /eV	HOMO-LUMO bandgap /eV
+ 0.53	-5.33	-1.88	-2.92	2.34

The difference between the HOMO and LUMO values gave an electrochemically determined HOMO-LUMO bandgap of 2.34 eV, which is slightly lower than the calculated optical HOMO-LUMO bandgap (2.66 eV). However, this difference probably arises from contribution of air and humidity in the UV- Visible spectrum.

#### **4-6-5-3 Polymer growth of poly(5)**

The electrochemical growth of poly (**5**) was obtained by the electrolytic oxidation of the monomer under use of successive scans. Repeating cycling over this peak results in typical polymer growth. The polymer growth as a thin film deposited on glassy carbon electrode is shown in the following figure:

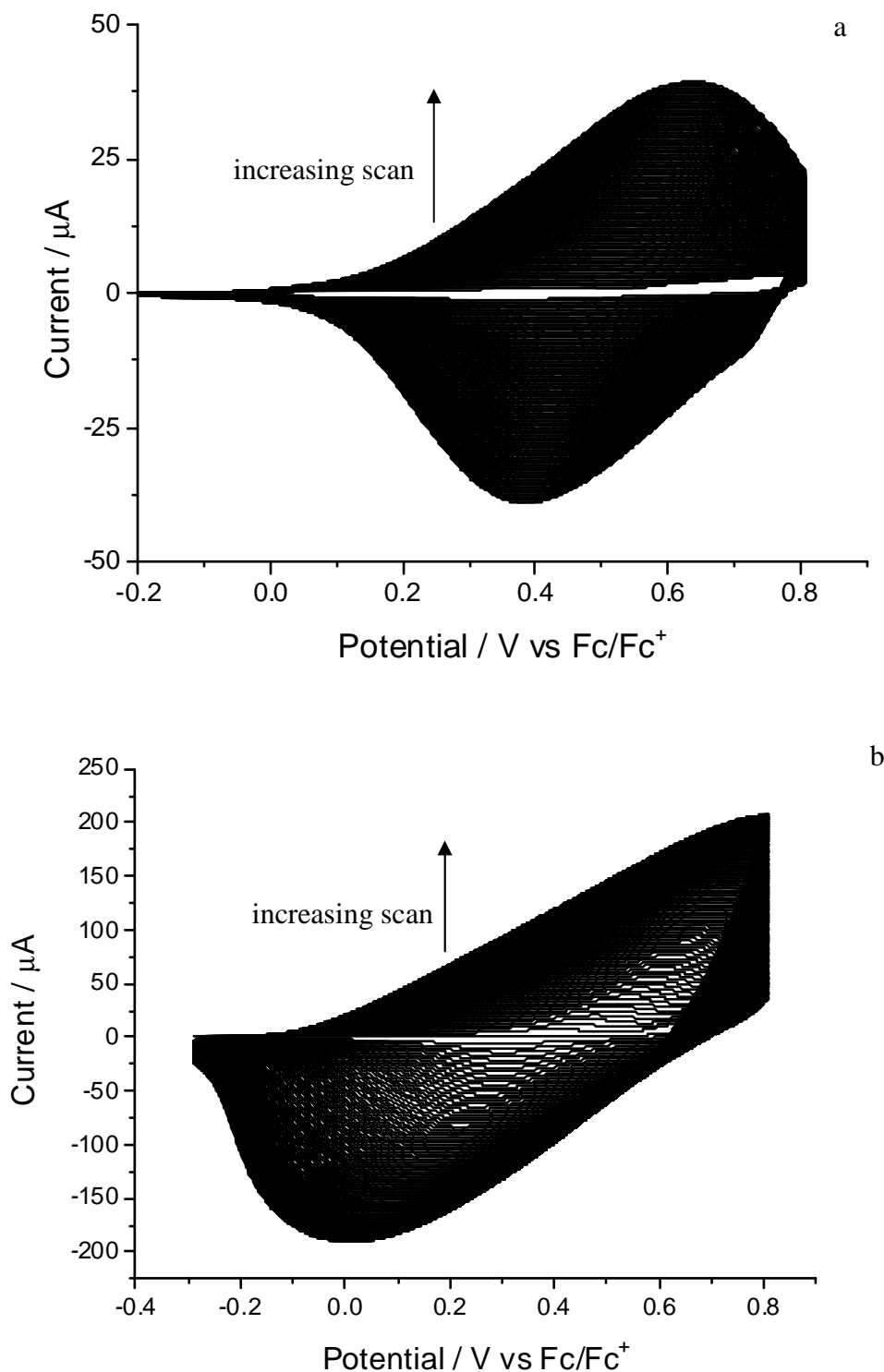


**Figure 4-46:** The voltammogram of growth of poly (**5**) recorded using a glassy carbon (a) and ITO slide (b) on ITO as working electrode, an Ag wire as a reference electrode and a Pt wire as a counter electrode. Recorded at a concentration of monomer-free  $1 \times 10^{-4}$  M in DCM with TBAPF<sub>6</sub> (0.1 M) as a supporting electrolyte. Scan rate  $100 \text{ mV s}^{-1}$  over 300 segments. Polymer growth increasingly developed on the electrode with repeating cycling.

The voltammogram of poly(**5**) was recorded in monomer -free electrolyte. The voltammogram of poly(**5**) showed a broad reversible peak almost at  $+0.64/ +0.63 \text{ V}$ . This peak may be related to the oxidation of the polaron and/ or bipolaron states. The polymer

reduction shows two peaks the first small reversible peak at -1.89/-1.78 V and the second at -2.13 V. The voltammogram of poly(**5**) is shown in the following figure:

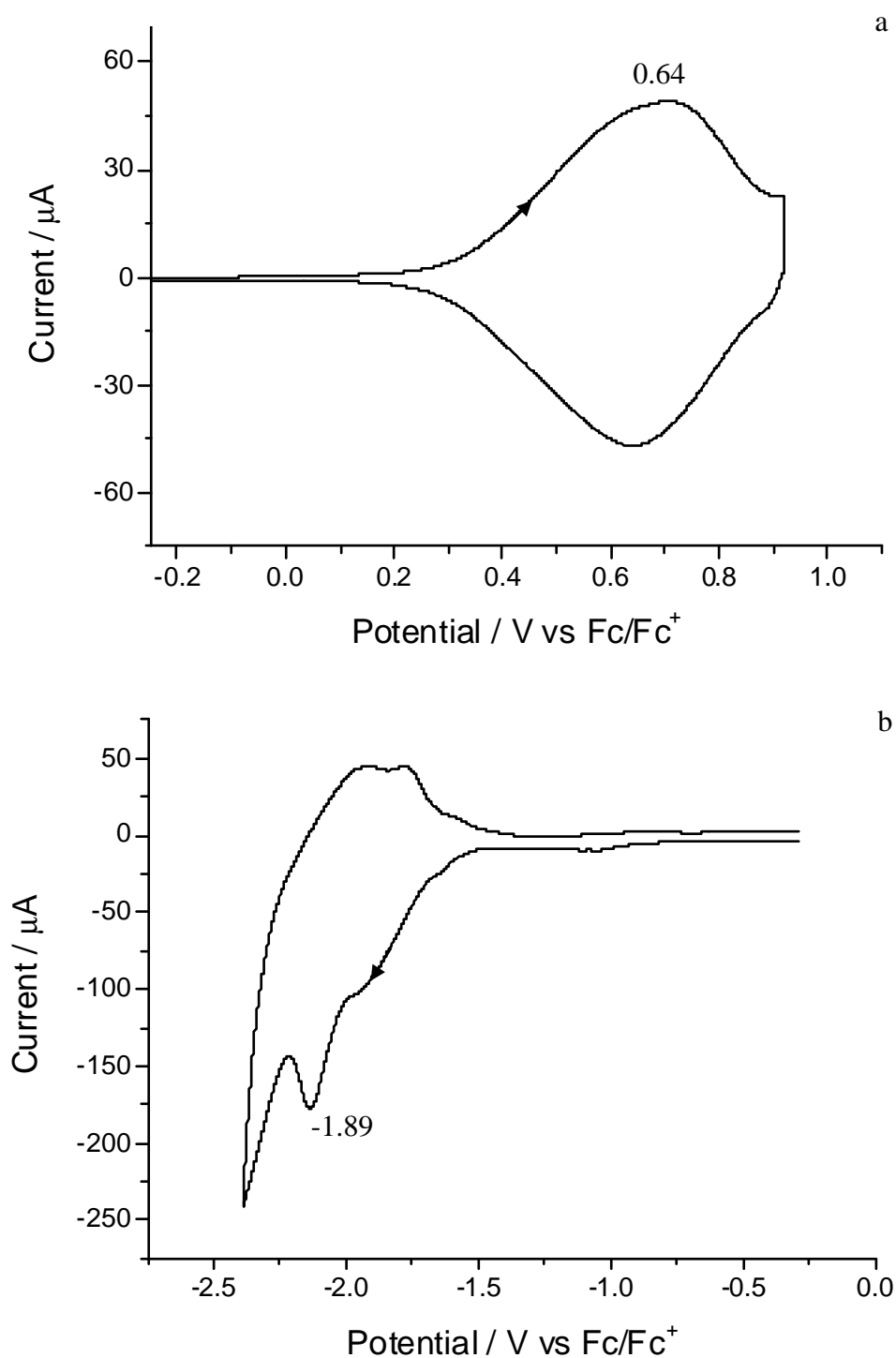


**Figure 4-47:** The voltammogram of oxidation (a) and reduction (b) of poly(**5**) recorded as a thin film on a glassy carbon working electrode, an Ag wire as a reference electrode and a Pt wire as a counter electrode. Recorded at a concentration in monomer-free of  $1 \times 10^{-4}$  M in DCM with  $\text{TBAPF}_6$  (0.1 M) as a supporting electrolyte. Scan rate  $100 \text{ mV s}^{-1}$ .

The electrochemical HOMO-LUMO bandgap of the poly(**5**) are summarised in Table 4-5.

**Table 4-5:** Electrochemical data for poly(**5**).

Onset of oxidation / V	HOMO / eV	Onset of reduction / V	LUMO / eV	HOMO-LUMO bandgap / eV
+ 0.30	-5.10	-1.64	-3.16	1.94

The difference between the HOMO and LUMO values gave an electrochemical HOMO-LUMO bandgap of 1.94 eV, which is lower than the calculated electrochemical HOMO-LUMO bandgap of the monomer (2.34 eV). However, this difference probably arises from contribution of air and humidity in the UV- Visible spectrum.

The oxidation stability of poly(**5**) under oxidation was investigated by repeating cycling over the first redox active peak as shown in the following figure:

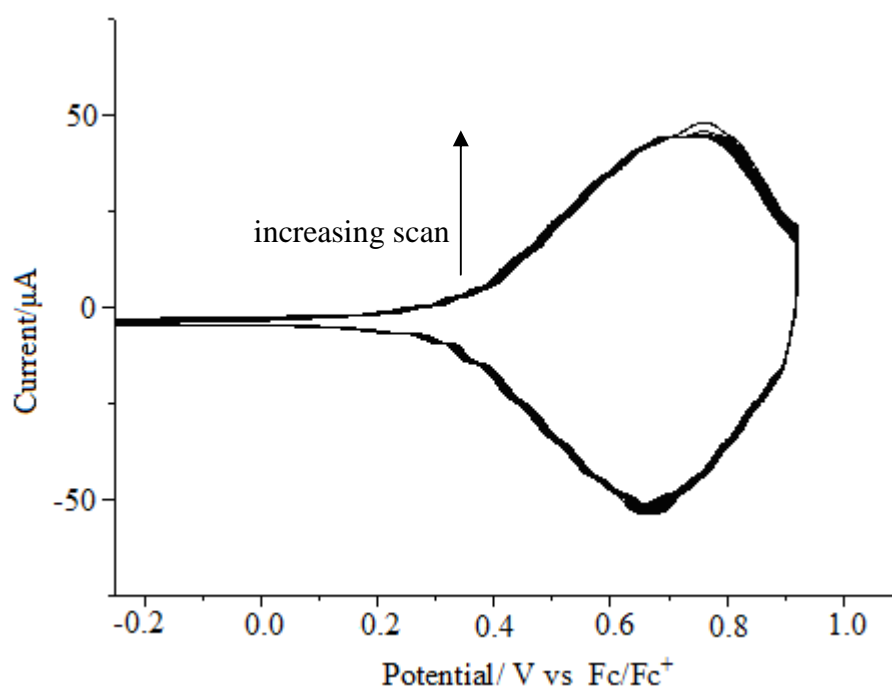


**Figure 4-48:** The voltammogram of oxidation stability of poly(**5**) recorded using a glassy carbon working electrode, an Ag wire as a reference electrode and a Pt wire as a counter electrode. Recorded at a concentration in monomer free of  $1 \times 10^{-4}$  M in MeCN with TBAPF<sub>6</sub> (0.1 M) as a supporting electrolyte. Scan rate  $100 \text{ mVs}^{-1}$  over 100 segments.

The voltammogram of poly(**5**) showed a slight decrease in the amount of exchanged charge. This means that this polymer has a good stability upon cycling. Redox stability is

an important factor for essentially all potential applications of this type of materials such as optoelectronic and electrochromic devices.

The peak currents of the thin film of poly(**5**) deposited on the electrode were recorded in a free electrolyte solution. This showed that current varies linearly with change of the electrochemical scan rate increased from  $25 \text{ mVs}^{-1}$  to  $500 \text{ mVs}^{-1}$ . This behaviour is due to the strongly adsorbed electroactive species of poly(**5**). The scan rate graph of poly(**5**) in monomer free MeCN at different scan rates is shown below:

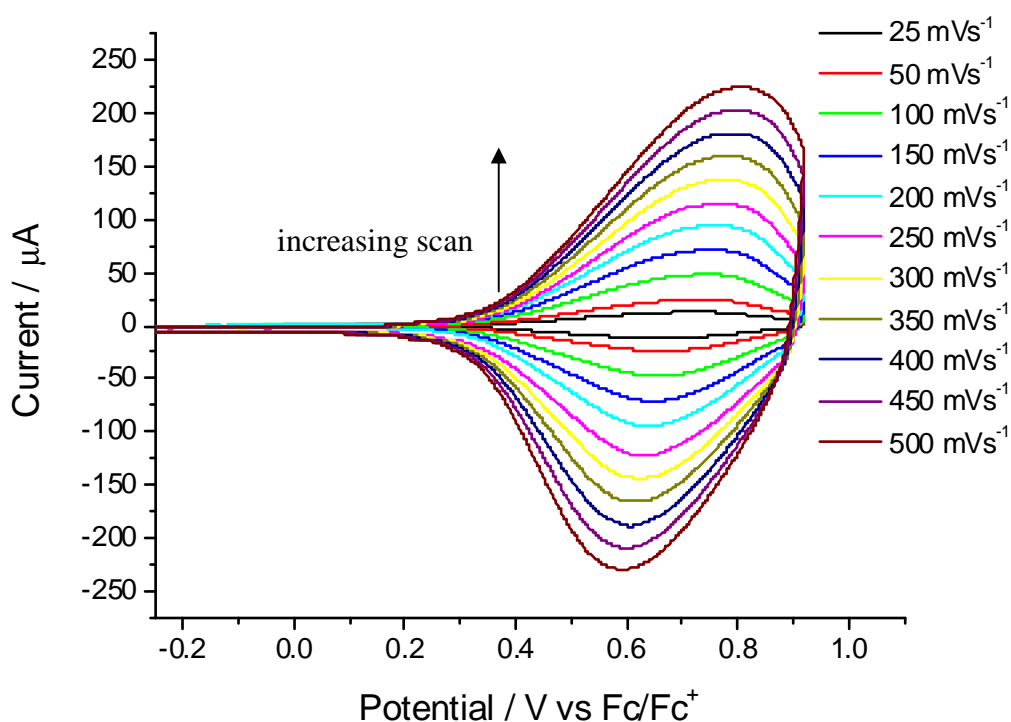


**Figure 4-49:** Scan rate graph of poly(**5**) in monomer free MeCN at varying scan rates:  $25\text{-}500 \text{ mV s}^{-1}$ .

A plot of peak currents versus scan rate provides a straight line confirming a linear relationship between peak current and scan rate and stability of the polymer at the electrode /electrolyte interface. The scan rate against peak current maxima for poly(**5**) showed a good linearity as shown in the following figure:

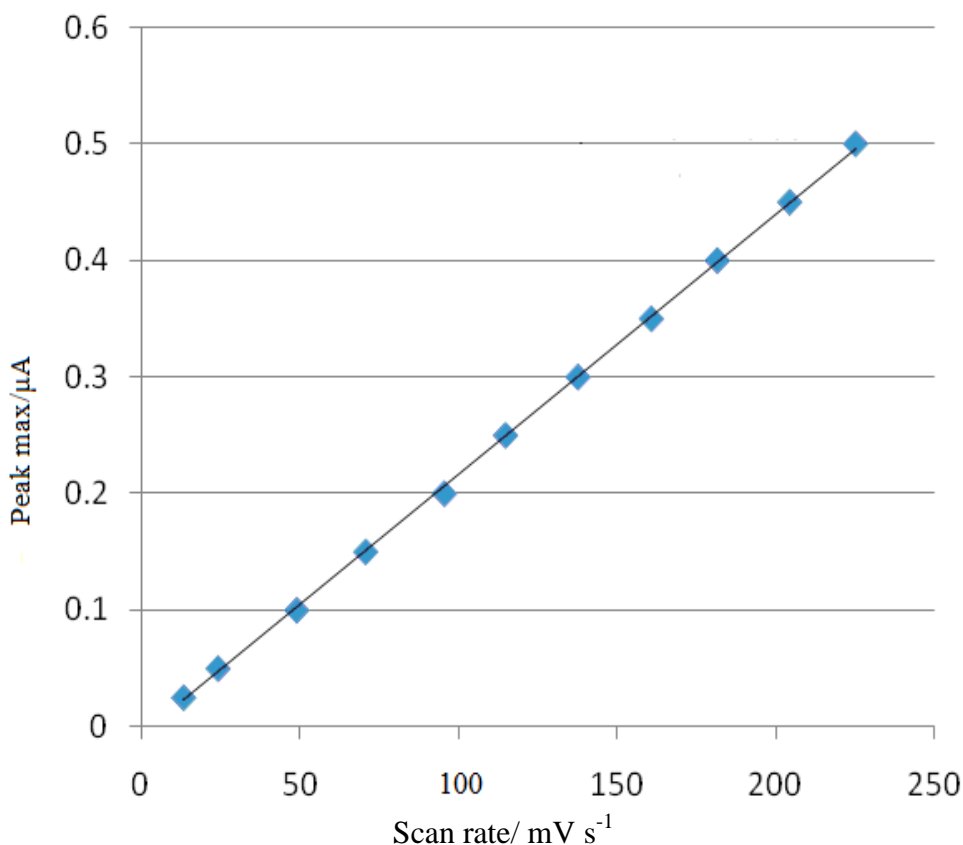


**Figure 4-50:** The scan rate versus peak current plot for poly(**5**).

The UV-visible spectrum of doped and de-doped poly(**5**) as a thin film was performed on the ITO glass as it highly conductive and transparent electrode. The optical bandgap of the polymer was calculated by growing the polymer onto a piece of ITO coated glass slide. The polymer was grown by cycling between 0 and 1100 mV vs Fc/Fc<sup>+</sup> then de-doped between -500 and -300 mV. The absorption spectrum for this polymer is shown in Figure below. The spectrum shows a  $\lambda_{\text{max}}$  peak of 530 nm therefore the polymer, has a 115 nm red shift compared to the monomer. Another small peak is apparent at 436 nm. The optically determined bandgap was calculated to be 1.85 eV. That is a little lower than the electrochemically determined bandgap 1.94 eV.

After doping, the intensity of this interband transition decreases with the appearance of two new absorption peaks at higher wavelengths. In the case of high level of doping the spectra exhibited peaks at higher wavelength near to the IR region of the spectrum<sup>(93)</sup>. The reason for this is probably due to the alternation between donor (EDOT/ thiophene) and the acceptor in the polymer chain. In addition to that, change in the optical absorption confirms protonation of the deposited polymer upon oxidative polymerization. Protonation of the deposited polymer may result due to the production protons upon electrochemical polymerization. The UV- visible spectra are shown in the following figure:

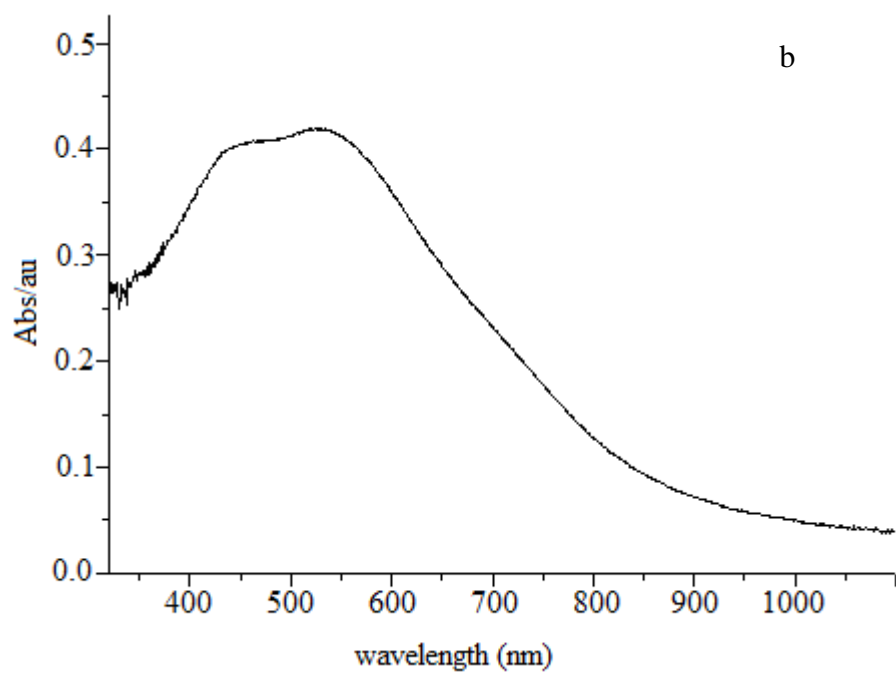
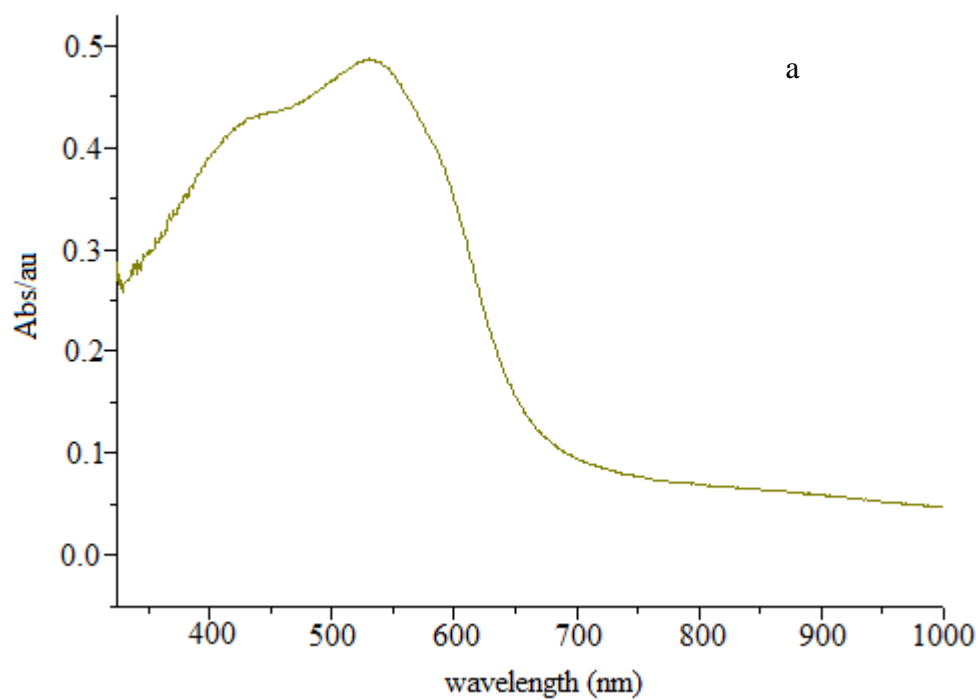


**Figure 4-51:** Absorption spectrum of de-doped (a) and doped (b) of poly(5) as a thin film on ITO glass.

#### 4-6-5-4 Spectroelectrochemistry of poly(5)

The spectroelectrochemistry of poly(5) was recorded on ITO electrode as a thin film is shown in the following figure:

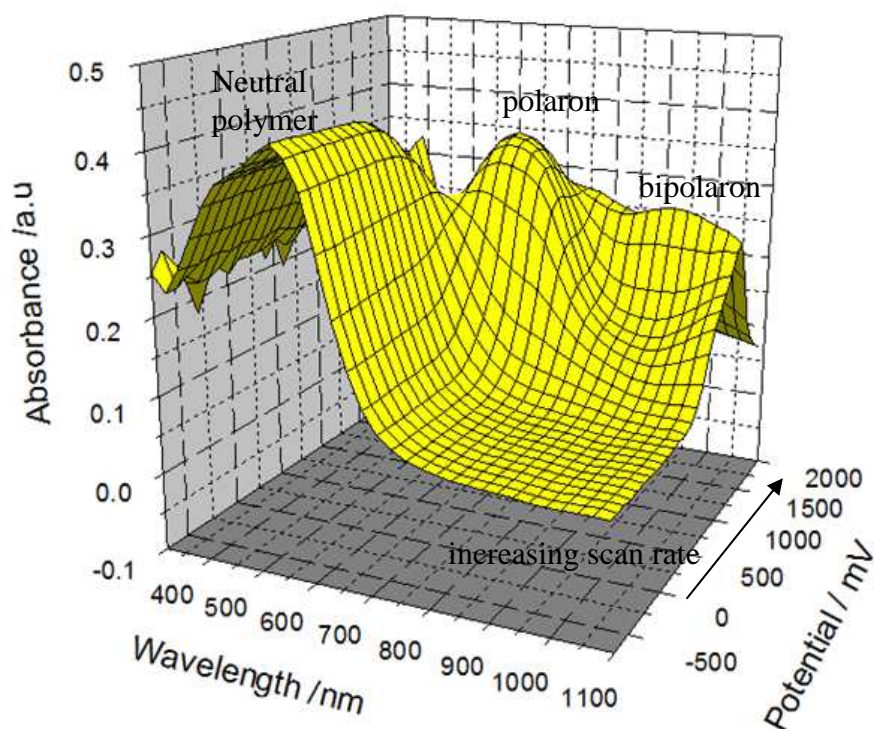


**Figure 4-52:** The spectroelectrochemical plot of p-doped poly(5) deposited on ITO glass using an Ag wire as a reference electrode and a Pt wire as a counter electrode. Experiments were run in monomer-free MeCN solution and in the presence of  $\text{Bu}_4\text{NPF}_6$  (0.1 M).

The spectroelectrochemistry of poly(5) is shown in the above figure. A spectral series of poly(5) at various applied potential ranging from the neutral polymer to the fully oxidized states of the polymer. The neutral polymer shows absorption band at around 500 nm, which is due to donating ability (EDOT)<sup>(94,95)</sup>. This would give lower energy charge transfer absorption with the initial oxidation of the polymer. Upon increasing applied potential, the peak disappeared at about 1.5 V. Beyond this value it was absent and a new sharp peak at 550 nm that may be related to the polaron states appeared. Further increase in the applied potential into 2.0 V leads to the appearance of a new absorption tail at around 950 nm with low intensity. This absorption may be related to the bipolaron states.

The change in optical absorbance at 750 nm for poly(5) was studied on ITO glass as a function of switching rate between - 0.70 and +1.35 V, at varying times: 10.00, 5.00, 2.50, 1.25, 0.50 and 0.25 seconds. The results are shown in the following figure:

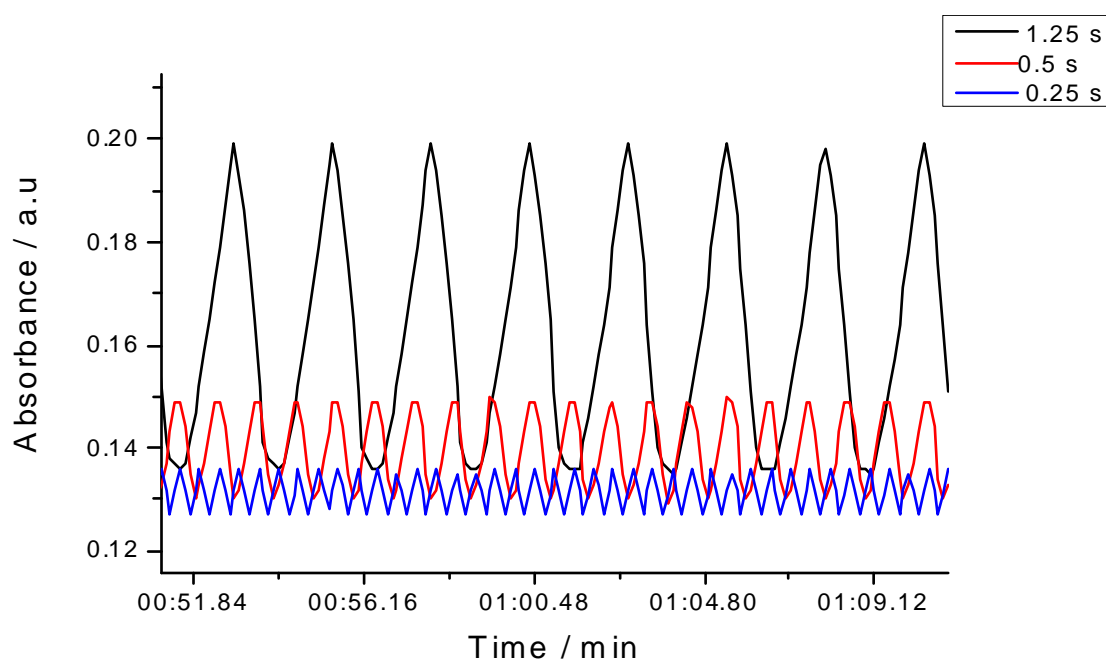
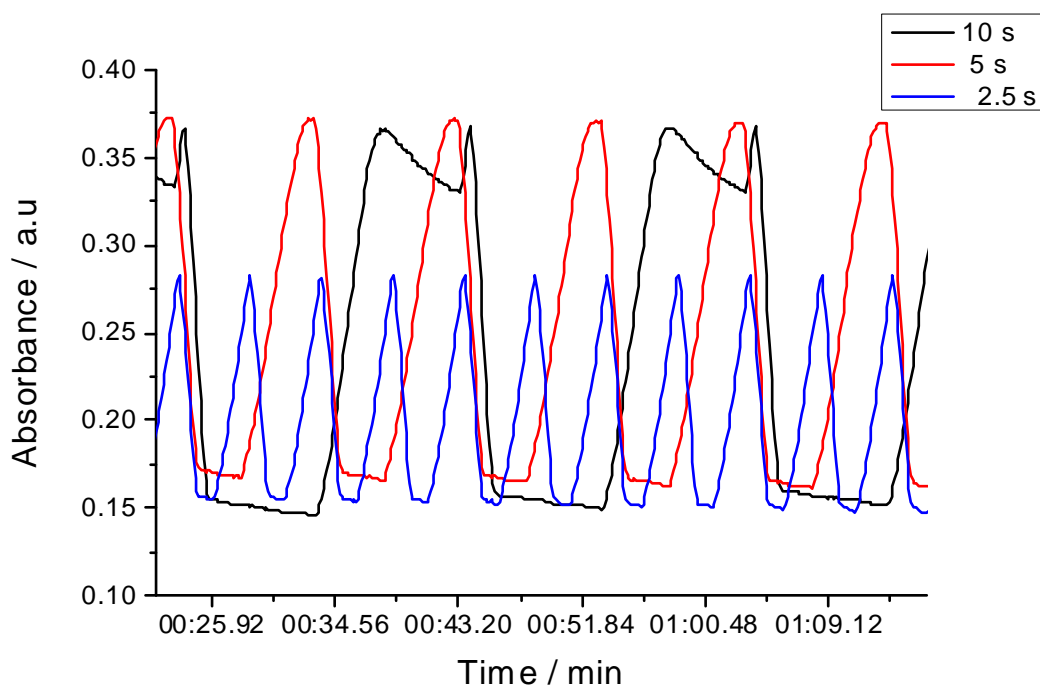


**Figure 4-53:** Change in optical absorbance at 750 nm for poly (**5**) on ITO glass as a function of switching rate between - 0.70 and +1.35 V at varying times.

The ability of the polymer to switch between colour states was tested by measuring the absorbance at 750 nm and switching the potential between - 0.70 V and +1.35 V at different rates, as shown in the above figure. The switching times used for these measurements were 10.00, 5.00, 2.50, 1.25, 0.50 and 0.25 seconds. The percentage change in absorbance for each experiment is shown in Table 4-6.

**Table 4-6:** Switching times and % change in absorbance for poly(5).

Switching time( s)	(% ) Change
10.00	59.28
5.00	55.94
2.50	45.35
1.25	31.81
0.50	12.75
0.25	5.92

#### 4-6-6 Analysis of compound 6

##### 4-6-6-1 UV-visible spectrum and CV of compound 6

The UV-visible spectrum of compound **6** was recorded in MeCN. The spectrum of this compound shows that there are three absorption peaks at 290 nm (weak peak), 426 nm (broad peak) and at 560 nm (broad peak). The first two peaks are related to the  $\pi$ - $\pi^*$  transitions. The broad peak at 426 nm in the visible region is probably a consequence of the highly conjugated nature of the system. The last peak at 560 nm appears to be related to the charge transfer complexes, which commonly occur with viologen compounds<sup>(78)</sup>. The optically determined HOMO to LUMO bandgap for this compound was 1.90 eV. The UV-visible spectrum for this compound is shown in the following figure:

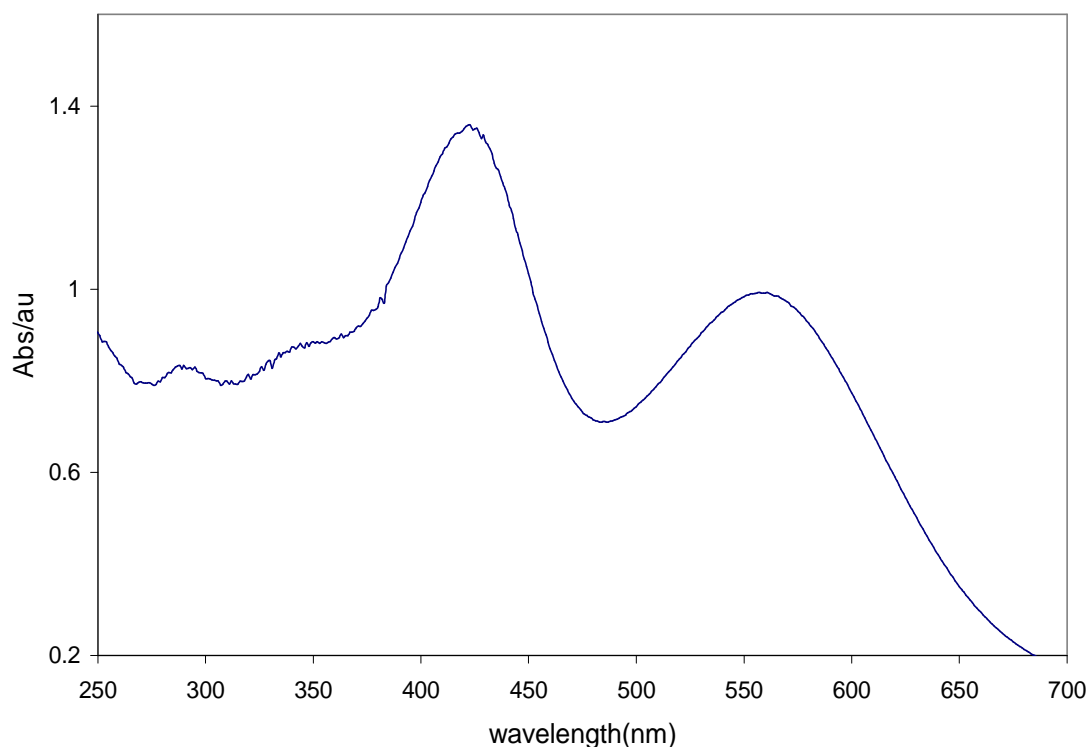


**Figure 4-54:** UV- visible spectrum of compound **6**. Recorded in MeCN ( $1 \times 10^{-4}$  M).

#### 4-6-6-2 The voltammogram of compound 6

The electrochemistry of this compound was recorded in acetonitrile. The voltammogram of compound 6 shows two reversible oxidation waves at + 0.57/ + 0.53 V and + 0.99/ + 0.91 V and the reduction process shows an irreversible peak at -1.87 V. The peak at -1.12 V is possibly from traces oxygen<sup>(93)</sup>. The presence of one reduction peak suggests that full reduction of the viologen (from  $\text{Bipm}^{2+}$  to  $\text{Bipm}^0$ ) occurred in a single step. The voltammogram for this compound is shown in the following figure:

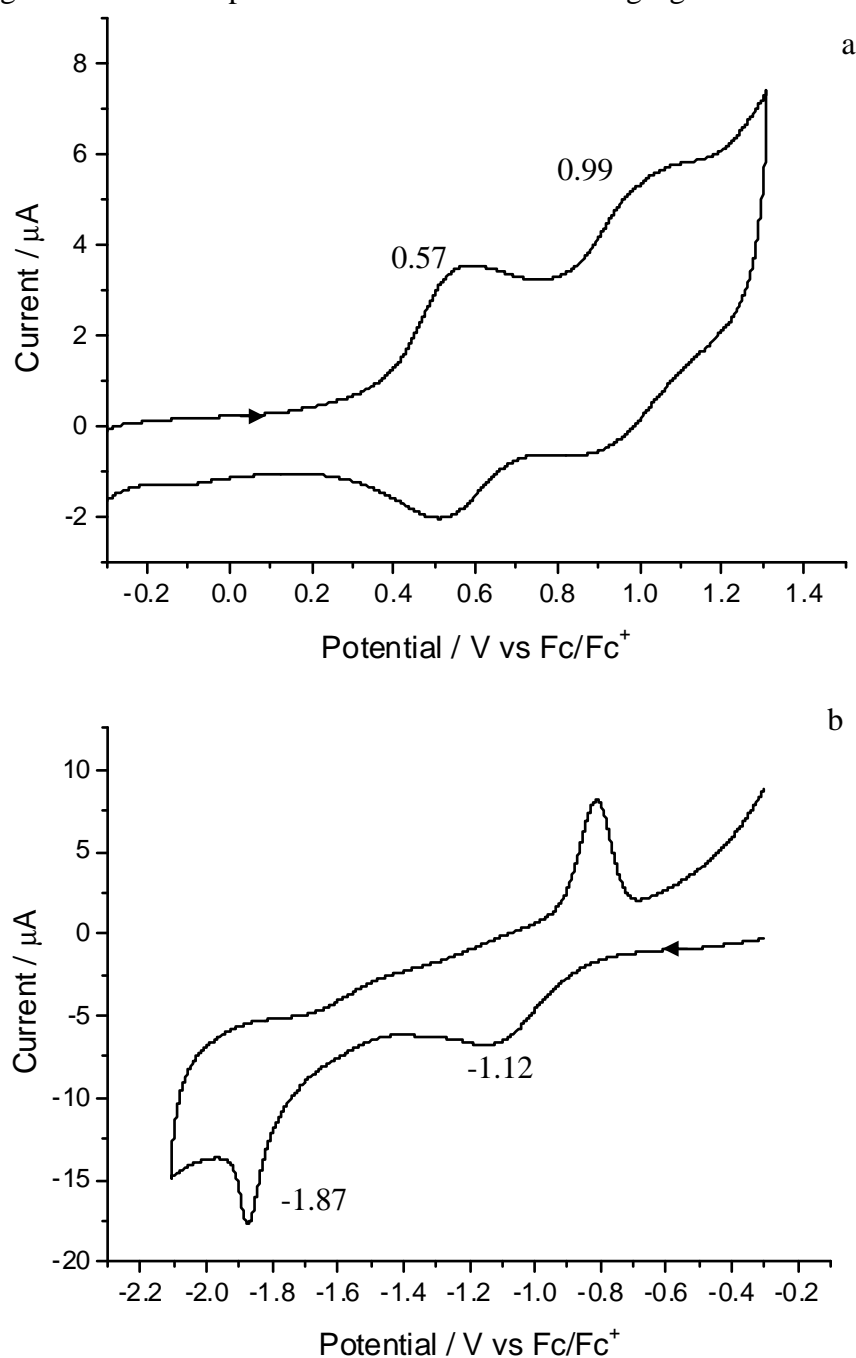


**Figure 4-55:** The voltammogram of oxidation (a) and reduction (b) of compound 6 recorded using a glassy carbon working electrode, an Ag wire as a reference electrode and a Pt wire as a counter electrode. Recorded at a concentration of  $1 \times 10^{-4}$  M in MeCN with  $\text{TBAPF}_6$  (0.1 M) as a supporting electrolyte. Scan rate of  $100 \text{ mV s}^{-1}$ .

The electrochemical data of compound **6** is summarised in Table 4-7

**Table 4-7:** Electrochemical data for compound **6**.

Onset of oxidation / V	HOMO / eV	Onset of reduction / V	LUMO / eV	HOMO-LUMO bandgap / eV
+ 0.39	-5.19	-1.78	-3.02	2.17

From these results, bandgap energy of compound **6** is relatively low this probably arises from conjugated system in this compound due to the presence of thiophene and EDOT rings in conjugation with phenanthroline core.

#### 4-6-6-3 Electrochemical polymerization of compound **6**

The electrochemical growth of poly(**6**) was achieved by the electrolytic oxidation of the monomer under use successive scans in the range - 0.20 to + 1.20 V. The voltammogram of the monomer showed that it was oxidized reversibly at around + 0.55 V in MeCN. The polymer growth by cycling over this peak that result in the growth of the polymer as a thin film deposited on the glassy electrode. The polymer growth is shown in the following figure:

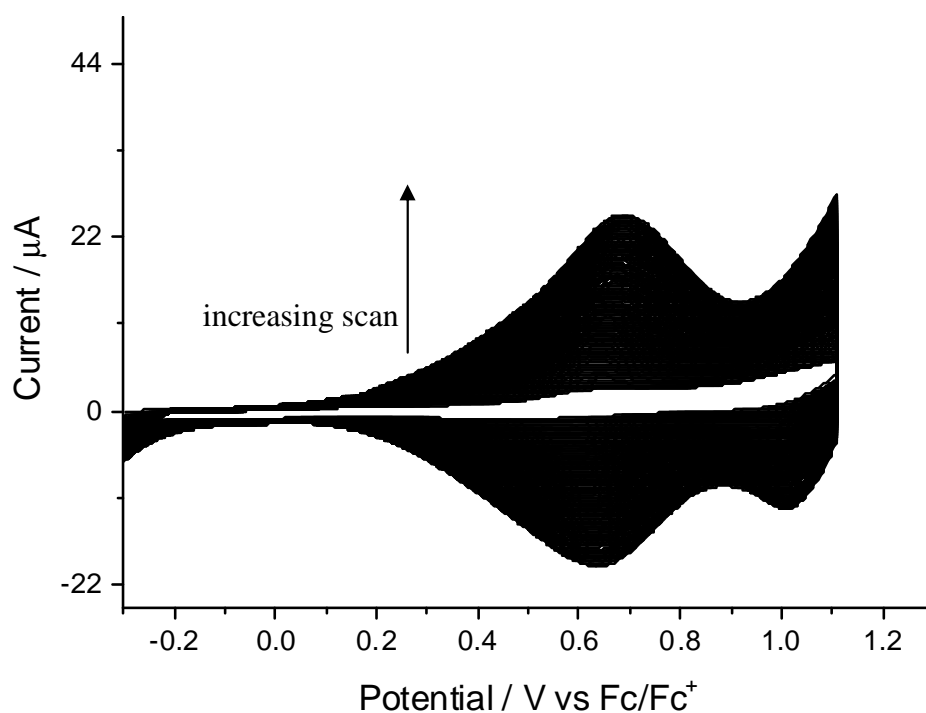


**Figure 4-56:** The voltammogram of growth of poly(**6**) recorded using a glassy carbon as working electrode, an Ag wire as a reference electrode and a Pt wire as a counter electrode. Recorded at a concentration of ca.  $1 \times 10^{-4}$  M in MeCN with TBAPF<sub>6</sub> (0.1 M) as a supporting electrolyte. Scan rate  $100 \text{ mV s}^{-1}$  over 300 segments.

The oxidation and the reduction of poly(**6**) on ITO electrode, shows a reversible broad oxidation peak at + 0.42/ + 0.39 V. This peak may be attributed to the oxidation of the polaron and/ or bipolaron states. Reduction of poly(**6**) shows an irreversible peak at -2.12 V. The voltammogram of poly(**6**) is shown in the following figure:

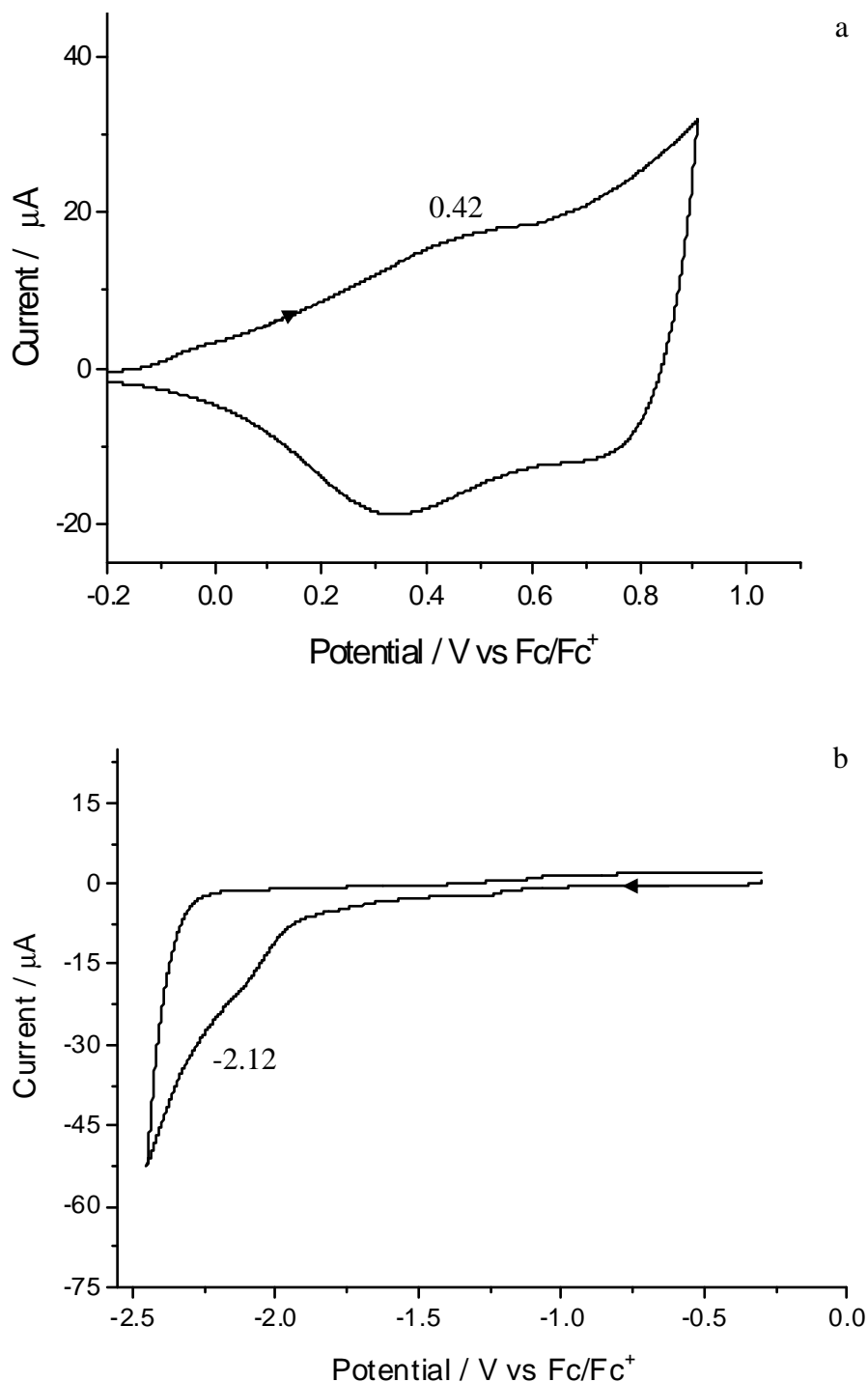


**Figure 4-57:** The voltammogram of oxidation (a) and reduction (b) of poly (**6**) as a thin film recorded using a glassy carbon working electrode, an Ag wire as a reference electrode and a Pt wire as a counter electrode. Recorded in monomer-free DCM with TBAPF<sub>6</sub> (0.1 M) as a supporting electrolyte. Scan rate of 100 mV s<sup>-1</sup>.

The electrochemical data of poly(**6**) is summarised in the following table:

**Table 4-8:** Electrochemical data for poly(**6**).

Onset of oxidation / V	HOMO / eV	Onset of reduction / V	LUMO / eV	HOMO-LUMO bandgap / eV
+ 0.13	- 4.93	-1.85	-2.95	1.98

Oxidation stability of poly(**6**) in monomer- free DCM at a scan rate of  $100 \text{ mVs}^{-1}$  over 100 segments is shown in the following figure:

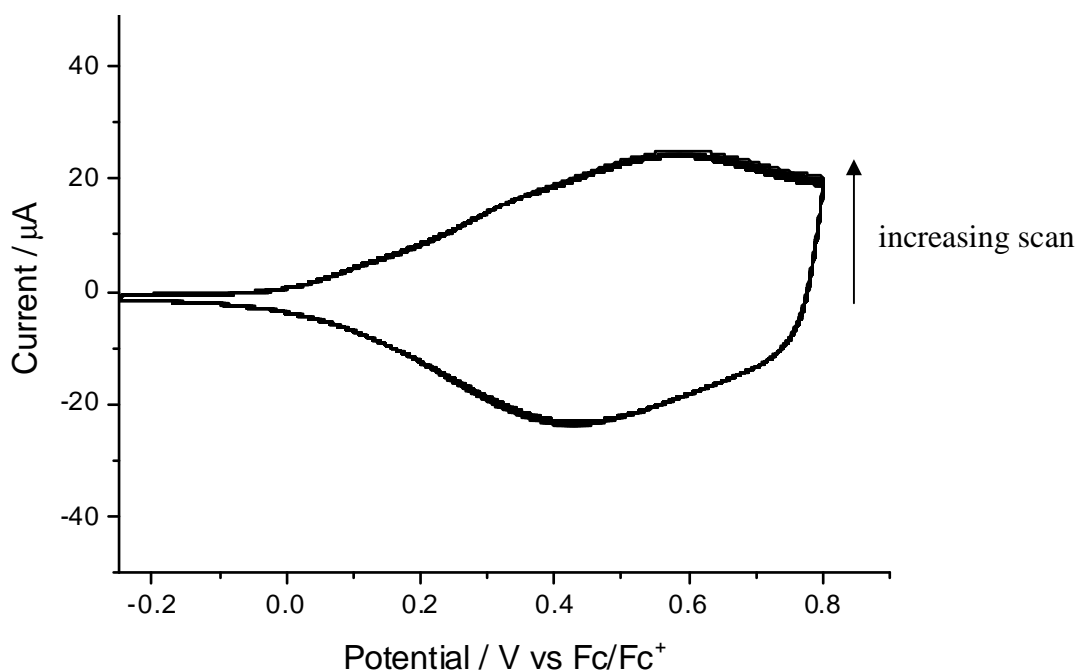


**Figure 4-58:** The voltammogram for oxidation stability of poly(**6**) recorded using a glassy carbon working electrode, an Ag wire as a reference electrode and a Pt wire as a counter electrode. Recorded in monomer- free DCM with  $\text{TBAPF}_6$  (0.1 M) as a supporting electrolyte. Scan rate  $100 \text{ mV s}^{-1}$  over 100 segments.

Repetitive cycling over the first redox active peak tested the stability of the polymer towards oxidation. The polymer is highly stable to anodic conditions, with only a 5.3% decrease in the current response over 100 segments. The influences of scan rate of poly(**6**) in monomer free DCM at varying scan rates:  $25\text{-}500 \text{ mVs}^{-1}$  is shown in the following figure:

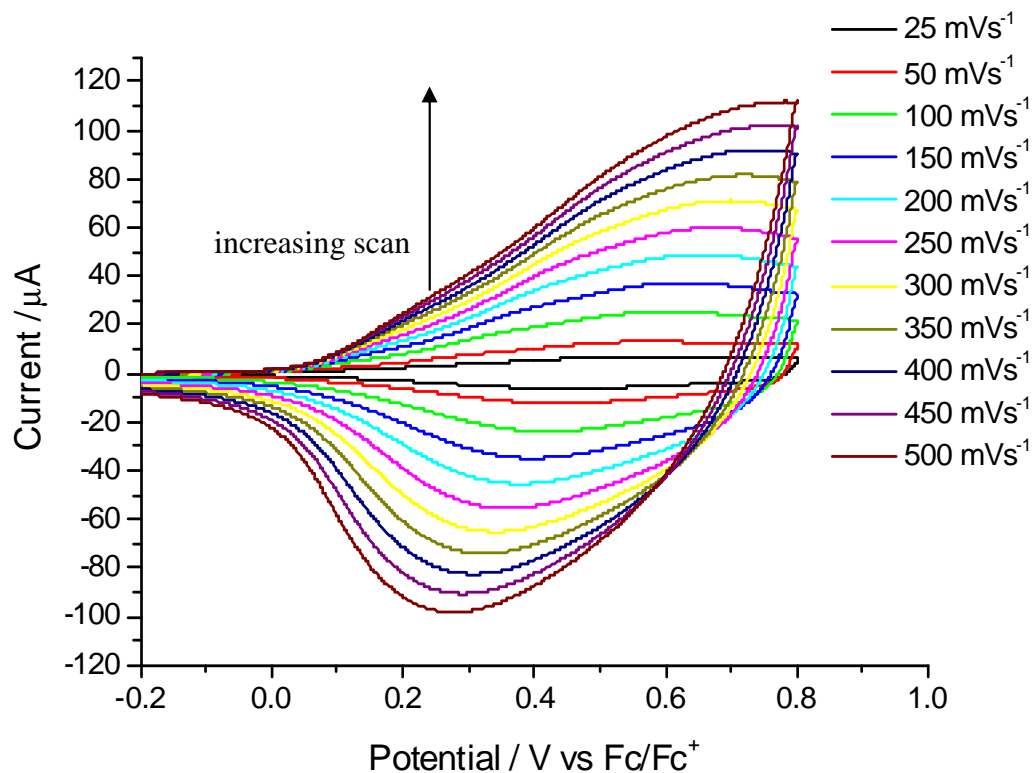


**Figure 4-59:** Scan rate graph of poly(6) in monomer- free DCM at varying scan rates: 25- 500  $\text{mV s}^{-1}$ .

A plot of scan rate against peak current maxima for poly(6) showed a good linearity as shown in the following figure:

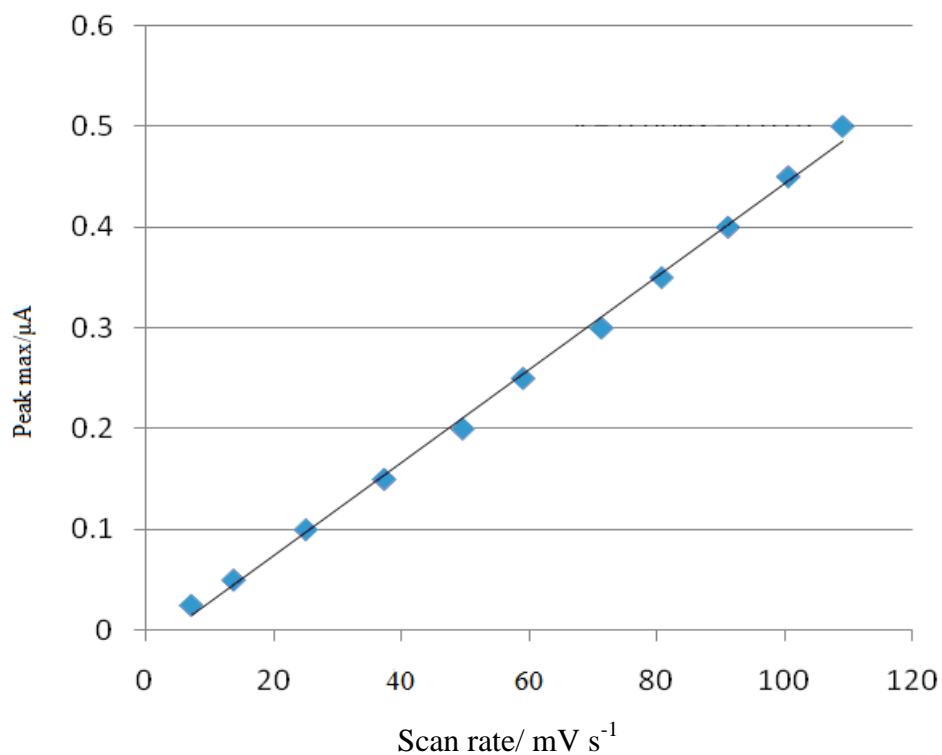


**Figure 4-60:** The scan rate versus peak current plot for poly(6).

The above results show a linear relationship between the peak currents and the scan rate, and confirm that the electroactive species were confined on the surface.

The growth of poly(**6**) on ITO coated glass slide was performed by cycling between 0.0 and 1.3 V vs. Fc/Fc<sup>+</sup>. The polymer growth is shown in the following figure:

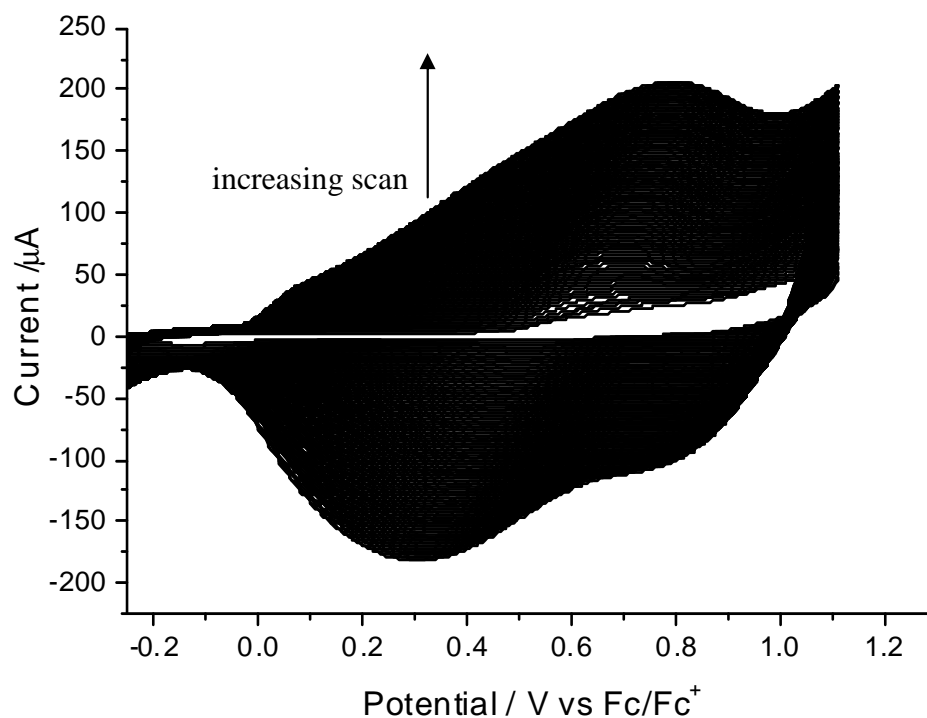


**Figure 4-61:** The voltammogram of growth of poly(**6**) recorded using ITO slide as a working electrode, an Ag wire as a reference electrode and a Pt wire as a counter electrode. Recorded at a concentration of ca  $1 \times 10^{-4}$  M in MeCN with TBAPF<sub>6</sub> (0.1 M) as a supporting electrolyte. Scan rate  $100 \text{ mV s}^{-1}$  over 300 segments.

The absorption spectrum of de-doped and doped thin films of poly(**6**) was investigated on ITO glass. The spectrum shows a  $\lambda_{\text{max}}$  peak of 430 nm. The optically determined bandgap of 1.44 eV is lower than the electrochemically determined bandgap of 1.98 eV. The absorption spectra are shown in the following figure:

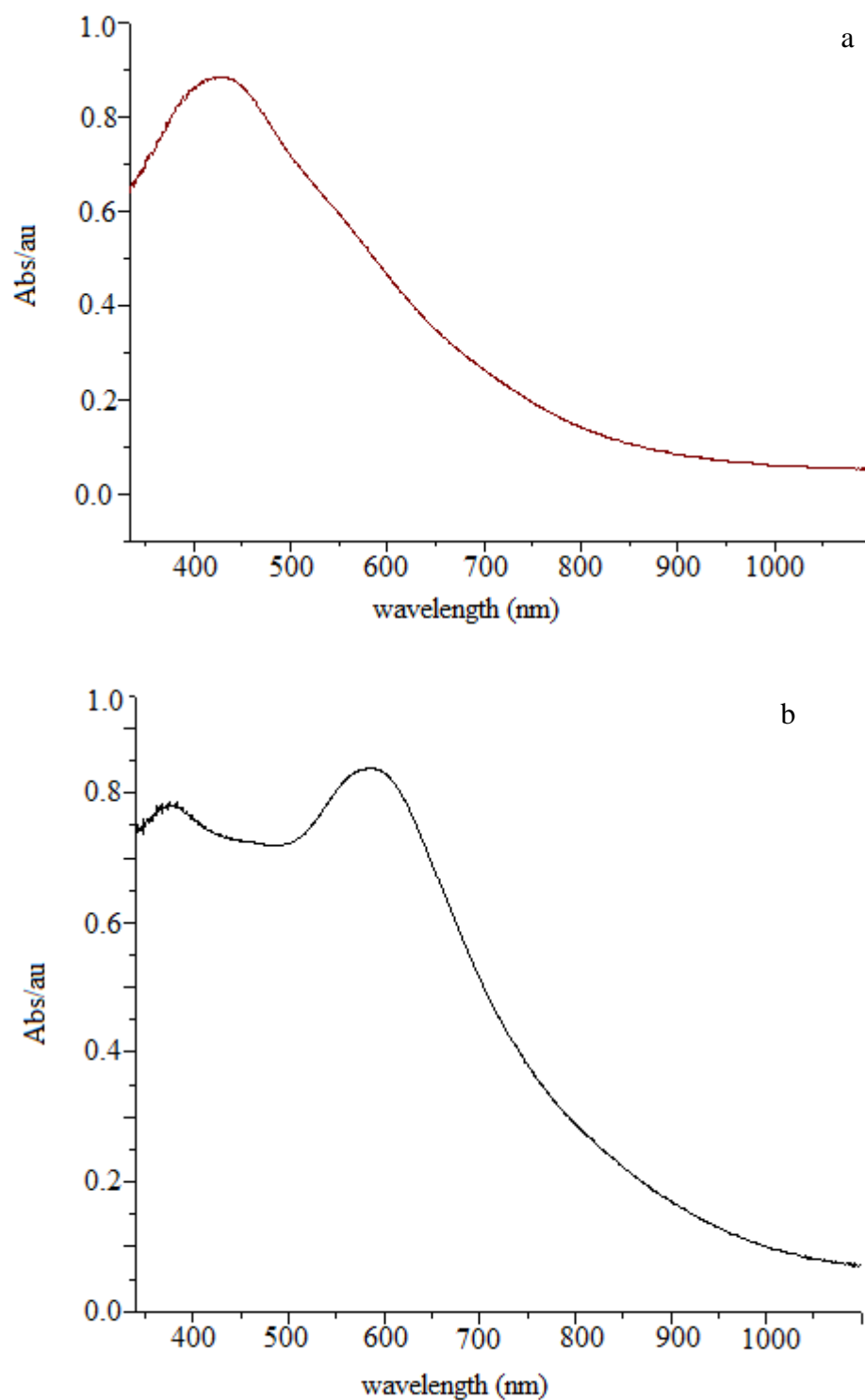


**Figure4-62:** Absorption spectrum of de-doped (a) and doped (b) of poly(6) as a thin film on ITO glass.

The optical bandgap of the polymer was calculated by growing the polymer onto an ITO coated glass slide. The polymer was grown by cycling between 0 and 1300 mV (vs Fc/Fc<sup>+</sup>) electrolyte free monomer then de-doped between -500 and -300 mV in monomer free-DCM.

#### 4-6-6-4 Spectroelectrochemistry of poly(6)

The spectroelectrochemistry of a thin film of poly(6) was investigated at various applied potentials ranging from neutral polymer to fully oxidized polymer. The spectrum shows an absorption band at around 430 nm for the neutral state. Upon oxidation of poly(6) this peak disappears gradually until the applied potential reaches 1.7 V. Beyond this, peak was absent and new two peaks at 600 and 875 nm appear with a lower intensity. These two peaks may be related to the oxidation of polaron and/or bipolaron species<sup>(94,95)</sup>. The spectroelectrochemistry of poly(6) is shown in the following figure:

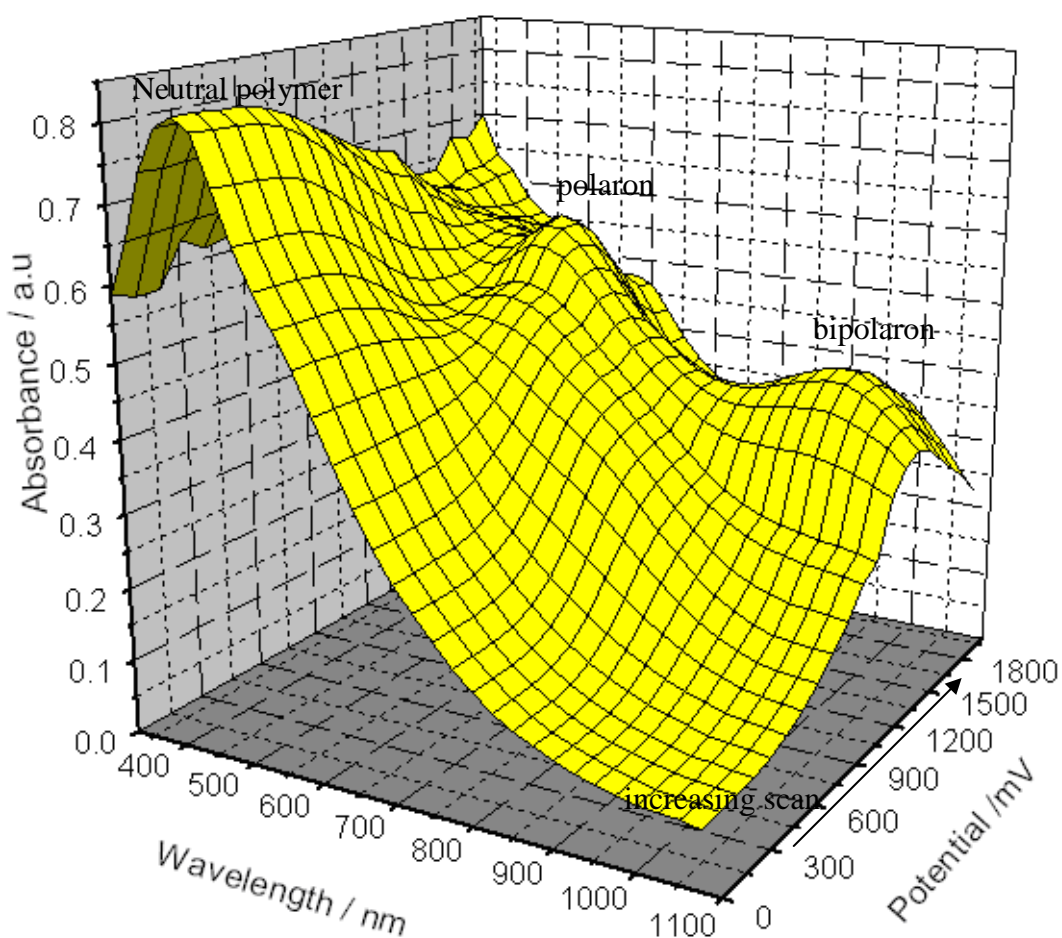


**Figure 4-63:** The spectroelectrochemical plot of p-doped poly(6) deposited on ITO glass using an Ag wire as a reference electrode and a Pt wire as a counter electrode. Experiments were performed in monomer-free DCM solution and in the presence of  $\text{Bu}_4\text{NPF}_6$  (0.1 M).

#### **4-7 Conclusions**

This chapter describes the synthesis of novel viologen species **1- 6, 10, 13, 15, 18** and **19** and the synthesis of bifunctionalized phenanthroline compound **5**. The main building block for these compounds is 1,10- phenanthroline. Generally, the above compounds were targeted for synthesis as they may have potential applications as materials for producing electrochromic devices, catalysts, and photovoltaic devices. Many attempts were made to polymerize viologen monomers **1** and **2**, however, all attempts were unsuccessful. The possible reason for this is the presence of the positive centres in the viologen core, which may prevent growth of the polymer. In monomer **4**, an EDOT ring replaced the thiophene ring, as it is more electron rich than thiophene that could facilitate the polymerization. Many attempts were made to polymerize this monomer, however, none was successful. Gratifyingly the chemical polymerization of compound **3** was achieved together with the electropolymerization of compounds **5** and **6**. From these results, it was found the presence of electron rich moieties in conjugation with phenanthroline core is necessary for polymerization to occur successfully.

#### **4-8 Acknowledgements**

I would like to acknowledge the contribution to this work from the research group of Professor Peter Skabara from the University of Strathclyde, Scotland for their assistance in doing the CV studies. In addition, I would like to record particular gratitude to Saadeldin Elmasly, a PhD Student from Skabara group, for his contribution in undertaking the CV and electrochemical polymerization.

#### 4-9 References:

1. H. Kamgawa, T. Suzuki, *J. Chem. Soc., Chem. Commun.*, 1985, 525.
2. L. Michaelis, E. Hill, *J. Gen. Physiol.*, 1933, **16**, 859.
3. L. Michaelis, *Chem. Rev.*, 1935, **16**, 243.
4. I. Smith, W. Schnieder, *Can. J. Chem.*, 1961, **39**, 1158.
5. R. Cimiraglia, H. Hofmann, J. Tomasi, *J. Molec. Struct.*, 1986, **169**, 213.
6. J. Farrington, A. Ledwith, M. Stam, *J. Chem. Soc., Chem. Commun.*, 1969, 259.
7. J. Joule, K. Mills, G. Smith, *Heterocyclic Chemistry (3<sup>rd</sup> Edn)*, Chapman and Hall, London, 1995.
8. O. Pozat, C. Sourisseau, J. Corset, *J. Molec. Struct.*, 1986, **143**, 203.
9. R. Van der Leest, *J. Electroanal. Chem.*, 1973, **43**, 257.
10. K. Belinko, *Appl. Phys. Lett.*, 1976, **29**, 263.
11. R. Pearson, *Sur. Prog. Chem.*, 1965, **5**, 1.
12. H. Van Dam, J. Ponjee, *J. Electrochem. Soc.*, 1974, **121**, 1555.
13. O. Enea, *Nouv. J. Chem.*, 1982, **6**, 423.
14. O. Enea, *Electrochem. Acta.*, 1985, **30**, 13.
15. O. Enea, *Electrochem. Acta.*, 1986, **31**, 789.
16. Y. Obeng, A. Bard, *New. J. Chem.*, 1992, **16**, 121.
17. K. Kobayashi, F. Fujisaki, T. Yoshimina, K. Nik, *Bull. Chem. Soc. Jpn.*, 1986, **59**, 3715.
18. A. Frumkin, B. Damaskin, *Pure Appl. Chem.*, 1967, **15**, 263.
19. M. Furue, S. Nazakura, *Bull. Chem. Soc. Jpn.*, 1982, **55**, 513.
20. S. Fletcher, L. Duff, R. Barradas, *J. Electroanal. Chem.*, 1979, **100**, 759.
21. D. Rosseinsky, P. Mouk, R. Hann, *Electrochem. Acta.*, 1990, **35**, 1113.
22. C. Cabrera, A. Bard, *J. Electroanal. Chem.*, 1983, **273**, 147.
23. J. Lin, T. Tanaka, K. Sivula, A. Alivisatos, J. Frechet, *J. Am. Chem. Soc.*, 2004, **126**, 6550.
24. Y. Ohmori, M. Uchida, K. Mounk, K. Yoshino, *Jpn. J. Appl. Phys.*, 1991, **30**, 1941.
25. M. Marsella, T. Swager, *J. Am. Chem. Soc.*, 1993, **115**, 12214.
26. M. Marsella, P. Carroll, T. Swager, *J. Am. Chem. Soc.*, 1994, **116**, 9347.
27. T. Skotheim, J. Reynolds, R. Elsenbamer, *Handbook of Conducting Polymers, 2<sup>nd</sup> Edition*, Marcel Dekker, Inc., New York, USA, 1998.
28. F. Li, J. Wiley, *Dalton. Trans.*, 2008, 3977-3980.

29. A. Schilt, *Applications of 1,10-phenanthroline and Related Compounds*, Pergamon, London, 1969.
30. P. Tamasik, Z. Ratajewicz, *Pyridine Metal Complexes*, John Wiley and Sons, New York, 1985.
31. G. Chelacci, R. Thummel, *Chem. Rev.*, 2002, **102**, 3129.
32. C. Boldron, M. Pitie, B. Meunier, *Synlett.*, 2001, **10**, 1629.
33. W. Huang, H. Tanaka, T. Ogawa, *J. Phys. Chem. C*, 2008, **112**, 11513.
34. M. Kim, J. Kang, J. Lee, *Polym. J.*, 2003, **44**, 4189.
35. Y. Yamamoto, T. Maruyama, Z. Zhou, T. Fukuda, S. Sasaki, F. Begum, Y. Yoneda, A. Fukuda, *J. Am. Chem. Soc.*, 1994, **116**, 4832.
36. N. Baek, H. Kim, Y. Lee, J. Kang, T. Kim, G. Hwang, B. Kim, *Thin solid Films*, 2002, **417**, 111.
37. T. Tsutsui, N. Tadaka, S. Saito, E. Ogino, *Appl. Phys. Lett.*, 1994, **65**, 1868.
38. M. Liu, N. Pschirer, N. Baumgarten, K. Mullen, *Chem. Rev.*, 2010, **110**, 11.
39. X. Cai, Y. Gong, Y. Cao, *Sol. Energy Mater. Sol. Cells*, 2010, **94**, 114.
40. W. Huynh, J. Dittmer, A. Alivisatos, *Science*, 2002, **295**, 2425.
41. M. Alam, C. Tonzola, S. Jenekhe, *Macromolecules*, 2003, **36**, 6577.
42. S. Jenekhe, L. Lu, M. Alam, *Macromolecules*, 2001, **34**, 7315.
43. A. Facchetti, *Chem. Mater.*, 2011, **23**, 733.
44. L. Yang, T. Zhang, H. Zhau, S. Price, B. Wiley, W. You, *ACS. Appl. Mater. Interfaces*, 2011, **3**, 4075.
45. A. Kelaidopoulou, G. Kokkinidis, E. Argyropoulou, *Electrochim. Acta.*, 1998, **43**, 987.
46. M. Lieder, C. Schlafer, *J. Electroanal. Chem.*, 1990, **1371**, 2151.
47. E. Dalton, R. Murray, *J. Phys. Chem.*, 1991, **95**, 6383.
48. C. Kim, S. Lee, L. Tinker, S. Bernhard, Y. Loo, *Chem. Mater.*, 2009, **21**, 4583.
49. M. Lapkowski, G. Bidan, *J. Electroanal. Chem.*, 1993, **362**, 249.
50. A. Kelaidopoulou, G. Kokkinidis, E. Coutouli, *Electrochimica. Acta.*, 1998, **43**, 987.
51. Y. Nambu, K. Yamamoto, T. Endo, *J. Chem. Soc, Chem. Commun.*, 1986, **41**, 574.
52. T. Saika, T. Iyodo, T. Shimidzu, *Chem. Lett.*, 1993, 2025.
53. M. Lieder, C. Schlafer, *J. Electroanal. Chem.*, 1996, **411**, 87.
54. P. Mounk, R. Mortimer, D. Rosseinsky, *Electrochromism: Fundamentals and Applications*, VCH, Weinheim, 1995.
55. J. Platt, *J. Chem. Phys.*, 1961, **34**, 862.
56. A. Factor, G. Heinsohn, *Polym. Lett.*, 1971, **9**, 289.
57. J. Roncali, *Chem. Rev.*, 1992, **97**, 711.

58. S. Asavpiriyant, G. Chandler, G. Gunawardena, D. Pletcher, *Electroanal. Chem.*, 1984, **177**, 229.
59. J. Lin, L. Dudek, *J. Polym. Sci., Polym. Chem. Ed.*, 1980, **18**, 2869.
60. A. Kuchison, M. Wolf, B. Patrick, *Inorg. Chem.*, 2010, **49**, 8802.
61. M. Mastragostino, L. Soddu, *Electrochem. Acta.*, 1990, **35**, 463.
62. J. Ander, G. Kapsomenos, G. Leroy, *Chem. Phys. Lett.*, 1971, **8**, 195.
63. J. Ander, G. Leroy, *Int. J. Quantum Chem.*, 1971, **5**, 557.
64. T. Ito, S. Ikeda, H. Shirakawa, *J. Polym.*, 1973, **4**, 460.
65. H. Shirakawa, T. Sakaki, S. Ikeda, *Chem. Lett.*, 1978, **6**, 1113.
66. C. Chiang, M. Druy, S. Gau, A. Heeger, Y. Park, H. Shirakawa, E. Louis, *J. Am. Chem. Soc.*, 1978, **100**, 1013.
67. J. Bredas, R. Chance, R. Silbey, *Phys. Rev. B*, 1982, **26**, 5843.
68. P. Chandrasekha, *Conducting Polymers, Fundamentals and Applications: A Practical Approach*, 1999.
69. T. Ebbesen, G. Ferraud, *J. Phys. Chem.*, 1983, **87**, 3717.
70. Y. Cho, T. Ahn, H. Song, K. Kim, C. Lee, W. Seo, K. Lee, D. Kim, J. Park, *J. Am. Chem. Soc.*, 2005, **127**, 2380.
71. I. Banerjee, L. Yu, H. Matsui, *J. Am. Chem. Soc.*, 2003, **125**, 9542.
72. C. Mirkin, *Inorg. Chem.*, 2000, **39**, 2258.
73. K. Hyung, D. Kim, S. Han, *New J. Chem.*, 2005, **29**, 1022.
74. I. James, J. Chamborn, J. Piere, *J. Chem. Soc. Perkin. Trans.*, 2002, **1**, 1226.
75. S. Zhu, T. Swager, *J. Am. Chem. Soc.*, 1997, **119**, 12568.
76. W. Dehaen, A. Hassner, *J. Org. Chem.*, 1991, **56**, 896.
77. B. Odell, M. Reddington, A. Slawin, N. Spencer, J. Stoddart, D. Williams, *Angew. Chem. Int. Ed. Engl.*, 1988, **27**, 1547.
78. D. Rosseinsky, P. Mounk, *J. Chem. Soc. Faraday Trans. I*, 1993, **89**, 219.
79. J. Prommerhne, H. Vestweber, W. Guss, R. Mahrt, H. Bassler, M. Porsech, *J. Adv. Mater.*, 1995, **7**, 551.
80. Y. He, W. Wu, G. Zhao, Y. Liu, *Macromolecules*, 2008, **41**, 9760.
81. P. Mounk, *The Viologens: Physicochemical Properties, Synthesis and Applications of Solid 4,4'-Bipyridine*, Wiley, New York, 1998.
82. J. Eisch, *J. Org. Chem.*, 1962, **27**, 1318.
83. K. Jackson, J. Ridd, M. Tobe, *J. Chem. Soc. Perkin Trans.*, 1979, **2**, 607.
84. E. Garcia, V. Greco, I. Hunsberger, *J. Am. Chem. Soc.*, 1960, **82**, 4430.
85. K. Araki, H. Endo, G. Masuda, T. Ogawa, *Chem. Eur. J.*, 2004, **10**, 3331.

86. B. Hu, S. Fu, F. Xu, T. Tao, H. Zhu, K. Cao, W. Huang, X. You, *J. Org. Chem.*, 2011, **76**, 4444.
87. W. Mammo, S. Admassie, A. Gadisa, F. Zhang, O. Ingans, *Sol. Energy Mater. Sol. Cells*, 2007, **91**, 1010.
88. M. Sun, Q. Niu, R. Yong, B. Du, W. Yang, J. Peng, Y. Cao, *Eur. Poly. J.*, 2007, **43**, 1916.
89. X. Chen, X. Yang, B. Holliday, *J. Am. Chem. Soc.*, 2008, **130**, 1546.
90. C. Too, G. Wallane, A. Burrell, G. Collis, E. Boge, S. Brodle, E. Evans, *J. Synth. Met.*, 2001, **123**, 53.
91. S. Zhu, T. Swager, *Adv. Mater.*, 1996, **8**, 497.
92. P. Kittlesen, S. White, S. Wrighton, *J. Am. Chem. Soc.*, 1984, **106**, 7389.
93. X. Chen, O. Inganas, *J. Phys. Chem.*, 1996, **100**, 15202.
94. A. Patil, A. Heeger, F. Wudl, *Chem. Rev.*, 1988, **88**, 183.
95. N. Hergue, P. Leriche, M. Allain, P. Blanchard, N. Gallego, P. Frere, J. Roncali, *New. J. Chem.*, 2008, **32**, 932.

## Chapter- five: Towards the synthesis of some novel push-pull systems for potential applications as nonlinear optical materials

### 5-1 Introduction

In the last few decades, there has been much interest in dipolar chromophores of the form (D-  $\pi$ - A), where D is a strong electron donor and A is a strong electron acceptor with a  $\pi$  conjugated bridge linking with both moieties<sup>(1,2)</sup>. These compounds are interesting due to many potential applications in electro- optical devices associated with large second and third-order nonlinear optical effects<sup>(3)</sup>. Thus, highly efficient molecular materials can be produced by appropriate choice of both donor and acceptor units to create sensitizer for dye sensitized solar cells (DSSCs), light-energy conversion, optical devices and sensors<sup>(4)</sup>. In addition, these types of material with (D-A) substituted conjugated molecules are highly polarized and can be considered as intermolecular charge transfer compounds. This property can be used in the construction of low dimensional organic nanostructures. They can also be used in the fabrication of well-defined nanostructures with desired controlled morphology. Low dimensional supra-molecular micro and/or nanostructures can be synthesized from low molecular weight (D-A) substituted with intermolecular charge transfer compounds and this type of design depends mainly on the (D-A) dipole-dipole interaction<sup>(5-7)</sup>. For this type of push-pull material, it has been found that molecules possessing large molecular second order nonlinearity, the hyperpolarizability ( $\beta$ ) can be increased directly by increasing donor and acceptor strengths and increasing the  $\pi$ -conjugation of the spacer unit<sup>(8)</sup>. In order to optimize the  $\beta$  value for these compounds, many conjugated units can be used. Polyenes are often commonly used as  $\pi$  conjugated spacers. This can provide a high efficiency for charge delocalization between donor and acceptor units, as the neutral and charge-separated states consist of similar  $\pi$  systems of alternating single and double bonds<sup>(9)</sup>. However, much effort has been focused upon the development of the synthesis of effective nonlinear optics (NLO) chromophores, which contain conjugated triene segments, for example ethylenic bonds incorporated into a 6-membered ring system. This can enhance thermal stability of the resulting system in comparison with simple triene analogues<sup>(10)</sup>. Some chromophores containing conjugated triene segments are presented in Figure 5-1.

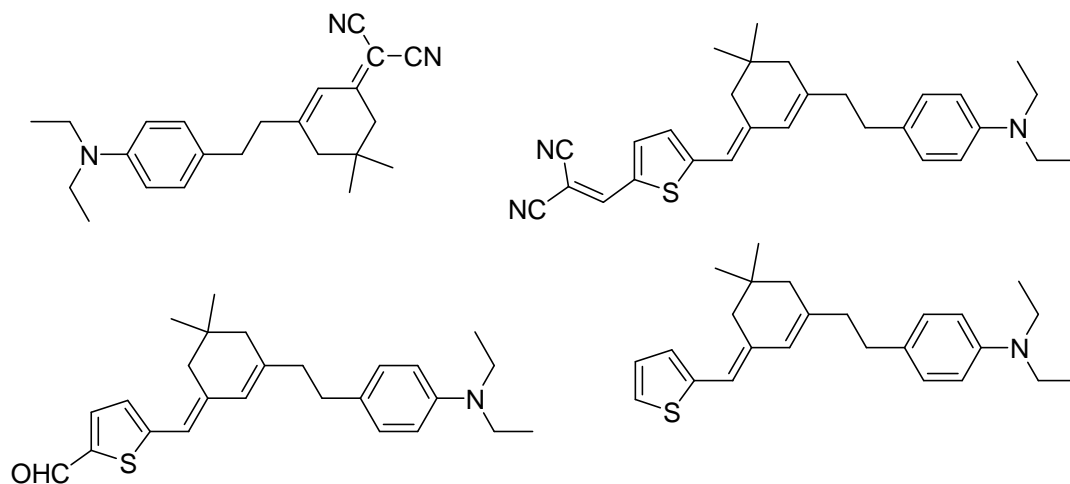


**Figure 5-1:** The structure of some chromophores containing show the conjugated triene segments<sup>(10)</sup>.

In previous work particular attention has been focused on optimizing the second-order nonlinear optical response of the ground-state polarization of molecules by using different systems of electron donors (D) and electron acceptors (A) with  $\pi$ -conjugated spacers<sup>(11,12)</sup>. In this context, Alain and co-workers<sup>(13)</sup> reported the synthesis of some heterobimetallic complexes, which contained ferrocenyl donors with a metal carbonyl moiety as acceptors that were connected by a  $\pi$ -conjugated system. They measured the NLO response for these complexes using the Hyper Rayleigh Scattering (HRS) technique and they found that all the prepared complexes have high second order nonlinearity. It has been found that among these complexes, the chromium carbonyl containing ferrocenyl ligand  $\text{Fc}-(\text{CH}=\text{CH})_2-\text{C}_6\text{H}_5-\{\text{Cr}(\text{CO})_3\}$  showed a higher  $\beta$  value. This probably arises from strong electronic communication between donor/ acceptor moieties in this system<sup>(13)</sup>.

In another study, Das and co-workers<sup>(14)</sup> reported the synthesis of some organic acceptors of anthraquinone linked to ferrocene donors by Schiff base linkages. They investigated the synthesis of symmetrical and asymmetrical substituted donor- acceptor. They measured the microscopic second order nonlinearity in the solution using the HRS technique<sup>(14)</sup>. The structures of some of these compounds are shown in the following figure:

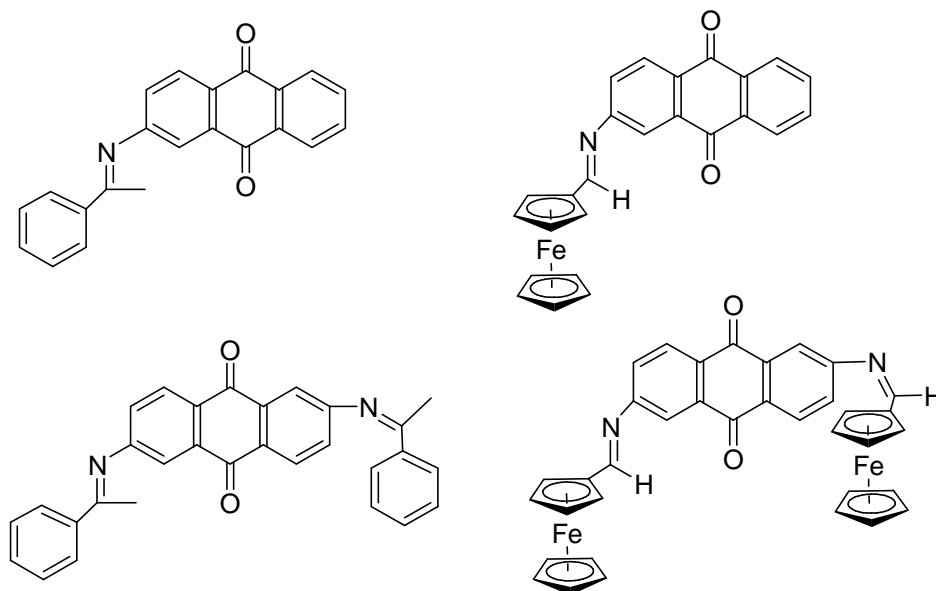


**Figure 5-2:** Structure of anthraquinone acceptors in conjugation with Schiff base and ferrocene moieties<sup>(14)</sup>.

Generally, using systems with delocalized five-membered heteroaromatic rings, such as thiophene, furan and thiazole instead of benzene ring results in an enhanced molecular nonlinear response as quantified through the first molecular  $\beta$ <sup>(15, 16)</sup>. Although a large variety of donors, acceptors and spacer groups have been used for the design of NLO chromophores, the use of pyrrole as a conjugated bridge and/or as a strong donor moiety has rarely been reported in the NLO literature<sup>(17, 18)</sup> which is probably due to the difficulty of their synthesis. The first hyperpolarizabilities of pyrrole-containing NLO chromophores with potential application as nonlinear optical materials have been reported<sup>(19, 20)</sup>.

Lastly, some methods have been used to enhance the properties of these push-pull systems and use them as NLO materials. These systems involve using a series of 1-(4-(thiophene-2-yl)phenyl)-1*H*-pyrroles as efficient push-pull systems bearing pyrrole as a donor group and dicyanovinyl, rhodamine, thiobarbituric acid and indanonedicyanovinyl as acceptor moieties linked through an arylthiophene spacer. These systems have high efficiencies with relatively higher hyperpolarizability values<sup>(20)</sup>. In our work, we are aimed to synthesize of push-pull chromophores with highly conjugation by using different donor/ acceptors moieties in conjugation with phenanthroline spacer. Due to high conjugation in these chromophores it hopes to give good NLO response.

## 5-2 Push-pull systems and nonlinear optics

The NLO responses induced with various types of molecules, either in solution or in the solid state are of great interest in many fields of research<sup>(21)</sup>. Generally, NLO behaviour occurs if the optical properties of the molecules of interest change in the presence of strong external electrical fields such as high-energy laser beams. Many attempts have been made to incorporate organic molecules into various devices that can be used for different purposes, such as optical communication, computing and data storage and image processing<sup>(22)</sup>. As mentioned earlier, among different types of material which can be used as NLO materials, organometallic complexes are an important class as they complexes can exhibit a good NLO response with easily fabricated integration into composite materials. To investigate these compounds in terms of their photonics applications, their accurate molecular  $\beta$  must be measured. Normally HRS is used for this process<sup>(23-25)</sup> as it can be used in evaluating the molecular  $\beta$  in solution. According to this technique, light is scattered at the second harmonic wavelength because of fluctuations in the molecular dipoles, which is monitored as a function for the concentration of the interested chromophore. Generally, this technique is suitable to investigate the quadratic polarizability of different types of molecules<sup>(26)</sup>. Most HRS studies have used an interference filter in order to detect second harmonic light coming from background scattering. At the same time, fluorescence at the same wavelength of the second harmonic light can't be removed completely. Hence, the measured  $\beta$  will be higher than the real value<sup>(25)</sup>. Flipse and co-workers<sup>(26)</sup> reported two-photon fluorescence (TPF). This then was followed by fluorescence in a series of donor / acceptor  $\pi$  spacer conjugation systems such as 4- dimethylamino-4'-nitrostilbene and 4-methoxy-4'-nitrostilbene at a wavelength of 1064 nm. This wavelength was then used as incident light for the study of second harmonic generation (SHG). They suggested that the HRS at 1064 nm was not used in the measurement of the first hyper- polarizability for the above compounds which showed TPF at this wavelength. The structure of some of these compounds is shown in the following figure<sup>(26)</sup>:

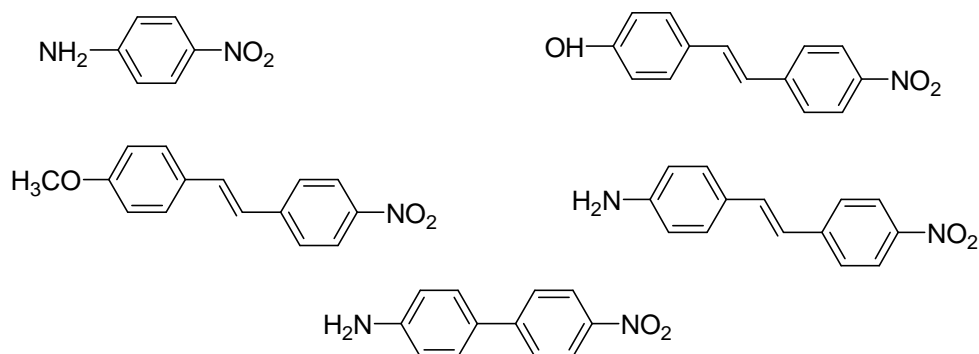


**Figure 5-3:** Structure of some compounds which show two photon absorption<sup>(26)</sup>.

These compounds have a good TPF, this probably arises from strong electronic communication between donor/ acceptor moieties with a  $\pi$  conjugated space unit. Blanchard and co-workers<sup>(27)</sup> reported a large quadratic hyper-polarizability of compounds with ferrocene as an electron donor and the dicyanovinyl group as an acceptor at the two ends of a polyene chain. The structures of some of these compounds are shown in the following figure:

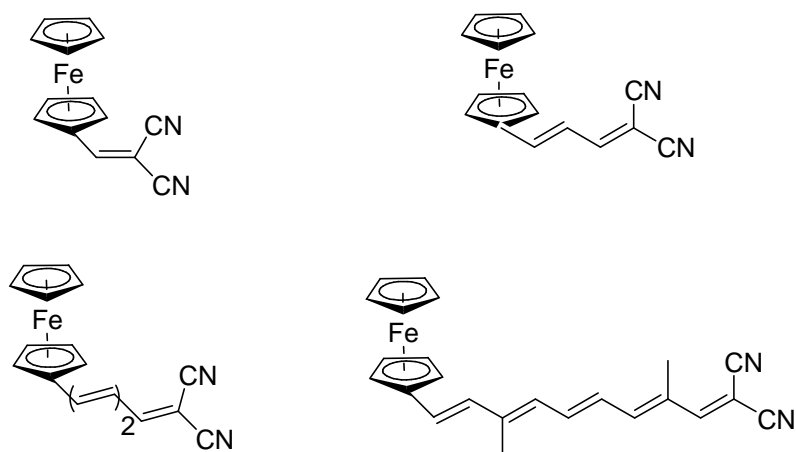


**Figure 5-4:** Compounds with ferrocene as an electron donor and the dicyanovinyl group as an acceptor at the two ends of a polyene chain<sup>(27)</sup>.

In another study, Barlow and co-workers<sup>(28)</sup> reported a large  $\beta$ , which was related to metallocene-  $\pi$  bridge acceptor complexes. They suggested a simple model of orbitals to explain the observed nonlinear behaviour. Other donor- acceptor complexes have been synthesized and their optical properties were studied either in the solution or in the solid state<sup>(13)</sup>. Generally, symmetrical types such as (D-A-D) and (D-A-D-A) are more important than asymmetrically substituted D-A type. This probably due to the nature of the charge distribution from the terminal point in the conjugated system to the middle point in the system. Therefore, this type would be expected to have a large two photon absorption cross-section and then a substantial TPF quantum yield<sup>(29)</sup>.

### 5-3 TCNE and TCNQ incorporating push- pull system

Generally, there are different types of push- pull moieties, among these, the electroactive group tetracyanoethylene (TCNE) is used in many applications in this field as a strong electron acceptor and 7,7,8,8- tetracyanoquinodimethane (TCNQ) is commonly used as a strong electron acceptor. These units are commonly used in the fabrication of optical devices, electrical recording devices, sensors and electrochromic, energy, data storage and magnetic devices<sup>(30)</sup>. These two compounds and their derivatives form good complexes and salts with charge transfer properties. In addition, some of these compounds were found to give good electronic conductivity and possess good magnetic properties<sup>(31)</sup>. Both of TCNE and TCNQ react with electron-rich alkynes affording [2+2] cycloaddition with good yield<sup>(12)</sup>. Generally, these strong electron acceptors can be combined with many electron donor groups such as N,N-dimethylaniline and benzothiadiazole or nitro groups which function as the acceptor. Hence, linking TCNE and/or TCNQ with these donor units with good conjugated  $\pi$ - spacer units can produce materials with good optical and electrical properties<sup>(32)</sup>. It has been reported that the reaction of TCNE and TCNQ with alkynes was dependent on the relative energies of both the HOMO and the LUMO and also on the frontier molecular orbital coefficient at the  $\beta$  position when para-anilino-substituted alkynes linking with an electron withdrawing group such as CN are applied. This would lower the energies of the HOMO and the new HOMO energy being further in its energy from the LUMO of both TCNE and TCNQ leading to reduced interaction between donor-acceptor moieties<sup>(33)</sup>. When TCNE and TCNQ are linked in a conjugation with strong donors, the resulting push-pull chromophores would have good intermolecular charge transfer (CT) interactions with high third-order optical nonlinear behaviour<sup>(8)</sup>. For these materials, electrochemical studies by cyclic voltammetry and rotating disc voltammetry showed that their electron-accepting power was dependent on the effect of TCNE or TCNQ on the electrical properties of these materials<sup>(34)</sup>. Structures of TCNE and TCNQ are shown in the following figure:

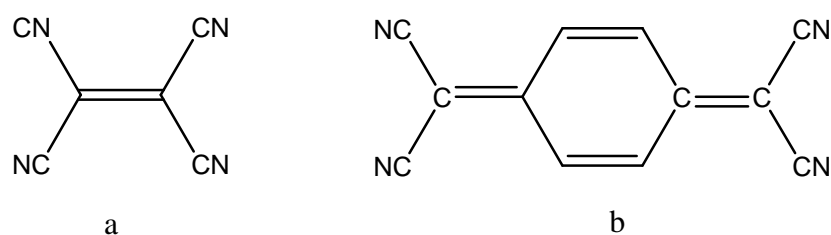


**Figure 5-5:** Structure of strong electron acceptors: (a) TCNE, and (b) TCNQ.

In our study, these two compounds will be incorporated in conjugation with both anilino groups as a good donating group and phenanthroline core. It hopes these dipolar

chromophores to yield a significant absorption in visible region and even up to near IR. In addition to that, it is expected to show good NLO response due to strong electronic communication between donor/ acceptor moieties in these compounds.

### **5-3-1 Symmetrical push-pull system with phenanthroline core**

For the push-pull systems, there are two main groups: symmetric and asymmetric depending on the arrangement of the donor- acceptor groups in the dipolar molecules. It has been reported that symmetrically substituted donor-acceptor-donor systems e.g. (D-A-D) or (D-A-A-D) exhibit a better nonlinear optical response in comparison with unsymmetrical substituted donor-acceptor-donor (D-A-D) systems<sup>(29)</sup>. The first type of system is expected to show large two photons absorption with a good TPF quantum yield<sup>(29)</sup>. This is probably due to the symmetric nature of the charge distribution from the terminal position into the middle of the conjugated systems. As mentioned earlier, TCNE is a strong electron acceptor, which can be effectively used in the fabrication of optical and electrical devices, so that, incorporation of TCNE with a symmetric conjugated framework may give a good approach to achieve a good optical response with a reasonable stability for this system. Among different types of conjugated framework, 1,10-phenanthroline seems to be a good candidate. Due to the rigid framework and its ability to coordinate to different metals and cations, 1,10-phenanthroline can provide an attractive framework for the development of dipolar systems. The charge-separated excited state of 1,10-phenanthroline is polarized along the 3-8 axis of the phenanthroline core<sup>(35)</sup>. It is believed that increasing the conjugation along this axis would stabilize the charge-separated excited state in the visible region.

### **5-4 General aim**

The general aim of this chapter is the synthesis of some novel push-pull materials containing a phenanthroline core as a good  $\pi$ - conjugated spacer. A stable electron acceptor such as TCNE and TCNQ has been linked with an anilino donor resulting in push-pull chromophores. These chromophores possess an efficient intermolecular charge transfer interaction that gives high NLO response. Generally, these materials may be used in some potential applications in nonlinear optics and photovoltaic devices.

## 5-5 Results and Discussion

The compounds **20**, **21**, **22**, **23**, **24** and **25** have been targeted for synthesis as these compounds and/or their derivatives can be potentially used as materials for nonlinear optics and photovoltaic devices. Generally, the main building unit of these compounds is the phenanthroline core. Structures of these compounds are shown in the following figure:

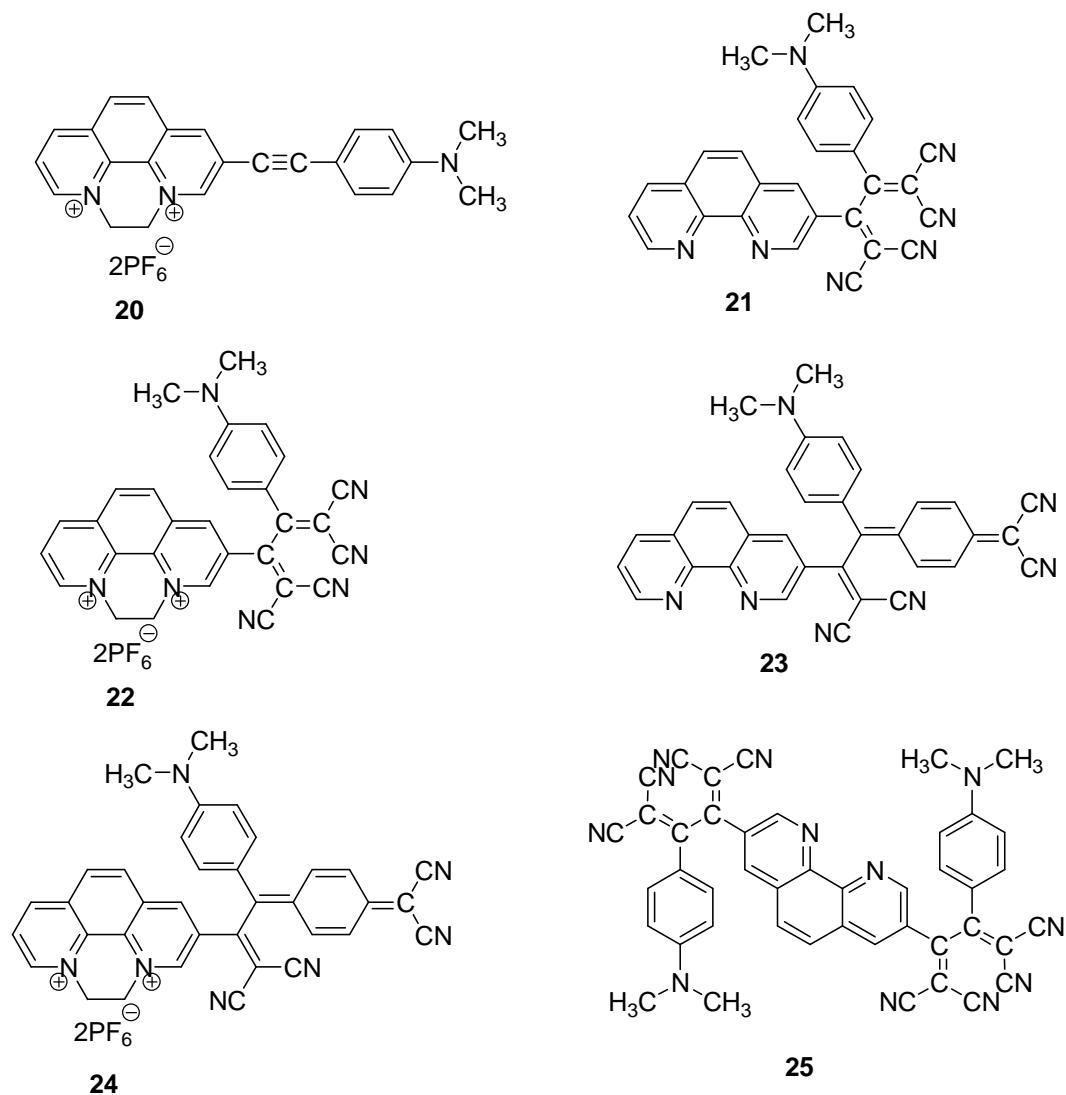
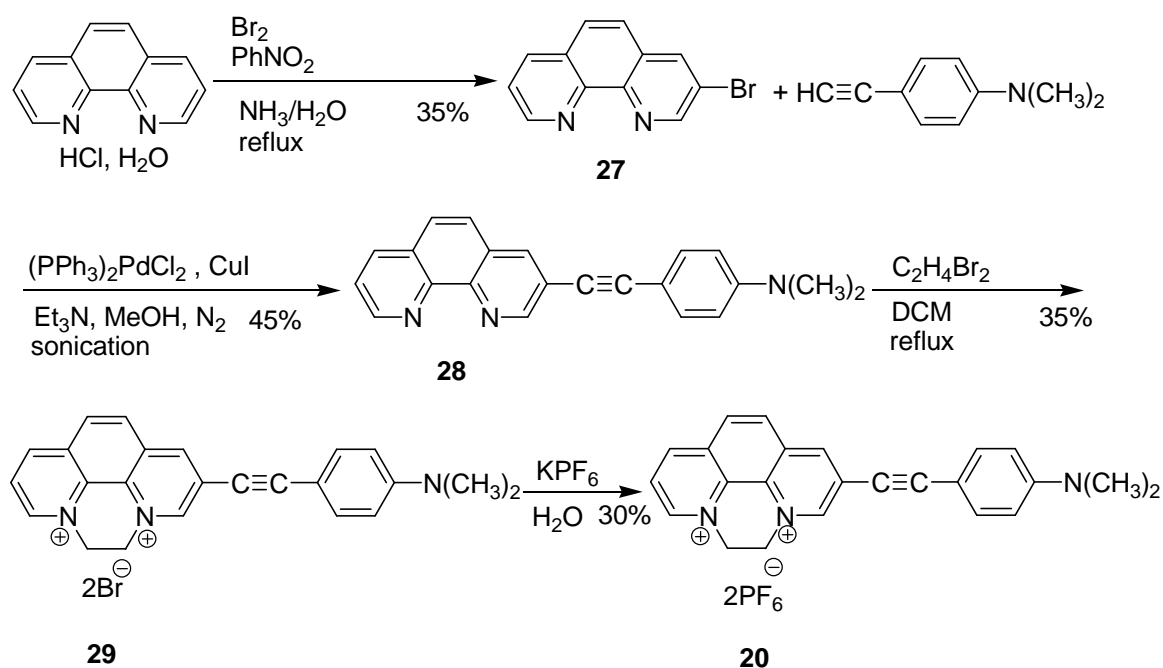


Figure 5-6: Structures of the target compounds.

### 5-5-1 Synthesis of target compound 20

The synthesis of compound **20** starts with commercially available 1,10-phenanthroline hydrochloride monohydrate which was converted to 3-bromo-1,10-phenanthroline. This then was reacted with 4-ethynyl- N,N- dimethylbenzenamine. The last compound was then alkylated with 1,2- dibromoethane to give viologen bromide **29** and by using an ion exchange reaction with an excess of an aqueous solution of  $KPF_6$  afforded compound **20**. The last compound was converted into viologen with hexafluorophosphate as a counter

anion instead of bromide to improve the solubility in common organic solvents. The synthesis steps are presented in the following scheme:



**Scheme 5-7:** Synthetic route of target compound **20**.

The synthesis of compound **27** was achieved from a mixture of 1,10-phenanthroline monohydrochloride monohydrate with bromine and nitrobenzene under reflux. Then the mixture was cooled to room temperature, treated with  $\text{NH}_3/\text{H}_2\text{O}$ , and then extracted with DCM to afford a final product as a yellow powder in 35% yield<sup>(36)</sup>. Compound **28** was synthesized from a mixture of 3-bromo-1,10-phenanthroline with CuI and a bis (triphenylphosphine) palladium dichloride. Another mixture of 4-ethynyl- N,N-dimethylbenzenamine in ( $\text{Et}_3\text{N}/\text{MeOH}$ , 2:1) was mixed together under a  $\text{N}_2$  atmosphere flush and sonication at room temperature for four hours to yield (**28**) as a yellow/orange powder with 45% yield<sup>(37)</sup>. Compound **29** was synthesized by an alkylation reaction between compound **28** and 1,2- dibromoethane. For compound **29** as the counter anion (bromide) is relatively small rendering the compound rarely soluble in common organic solvents. To improve solubility the bromide anion is replaced by hexafluorophosphate by adding an excess of an aqueous solution of  $\text{KPF}_6$  to yield a viologen with hexafluorophosphate counter ion in a good solubility in common organic solvent in a yield of 30%.

### 5-5-2 Analysis of compound **20**

The UV-visible spectra of compounds **20** and **28** were recorded in MeCN and DCM respectively. The spectrum of compound **28** shows two peaks at 280 nm and 380 nm.

These peaks are related to the  $\pi\text{-}\pi^*$  transitions. The optically determined HOMO to LUMO bandgap for this compound was 2.75 eV. Compound **20** shows three peaks at 294 nm, 345 nm and a broad peak at 560 nm. The first two peaks are related to the  $\pi\text{-}\pi^*$  transitions. The last broad peak at 560 nm is related to the intramolecular charge transfer complex<sup>(38)</sup>. Viologen compounds form charge transfer complexes as a result of electronic transitions between the counter anion ( $\text{PF}_6^-$ ) and the positive viologen centre<sup>(39)</sup>. This appears as a broad band in the visible region of the spectrum. The optically determined HOMO-LUMO bandgap for this compound was 1.68 eV. This compound absorbs strongly in the UV region of the spectrum (294 nm and 345 nm). This is related to the  $\pi\text{-}\pi^*$  transitions. The high intensity of these peaks probably due to the conjugation between the phenyl and the pyridinium ring systems. The UV-visible spectra for these compounds are shown in the following figure:

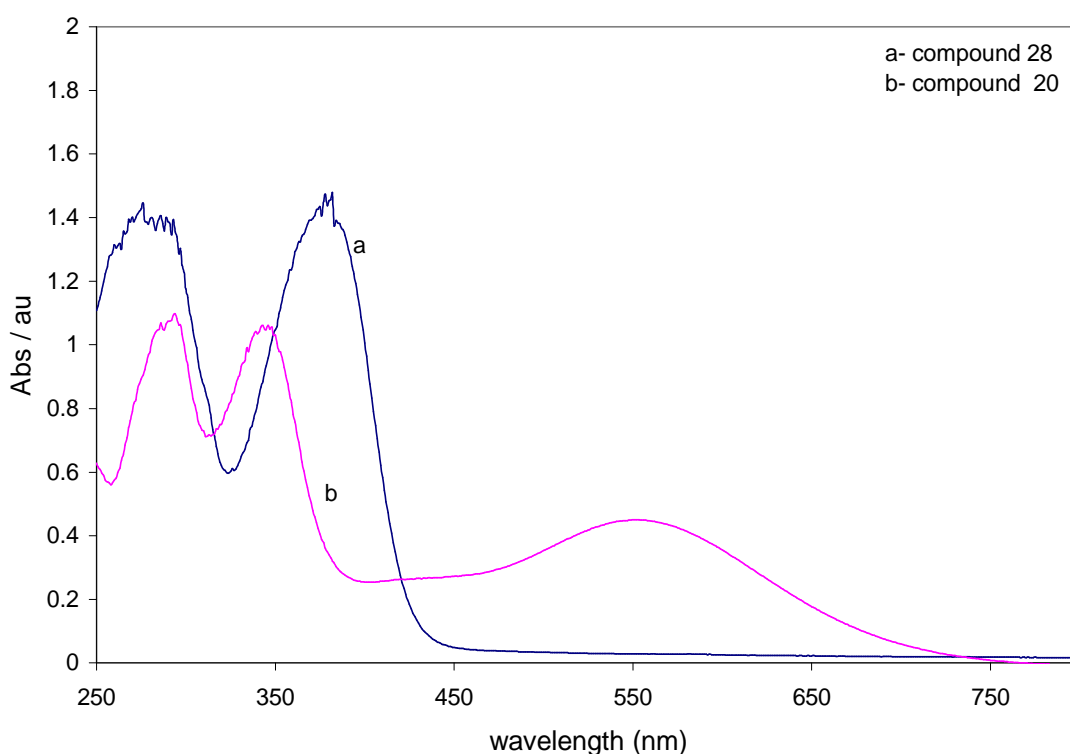


**Figure 5-8:** UV- visible spectra for compounds **20** and **28**. Recorded in MeCN and DCM respectively ( $1 \times 10^{-4}\text{M}$ ).

The voltammogram of compound **20** was recorded in MeCN. The voltammogram of this compound shows two quasi reversible reduction peaks at -0.61 V and the other irreversible at -1.28 V and one oxidation peak at + 0.59 V. The first reduction peak at - 0.61 V is probably related to the first electron reduction of the viologen from  $\text{Bipm}^{2+}$  to  $\text{Bipm}^+$ . The second reduction peak may be assigned to the further reduction of the viologen (from  $\text{Bipm}^+$  to  $\text{Bipm}^0$ ). The LUMO energy for compound **20** was estimated to be - 4.25 eV. The estimated HOMO energy for this compound was -5.30 eV and the

electrochemically determined bandgap was 1.05 eV. The voltammogram of this compound is shown in the following figure:

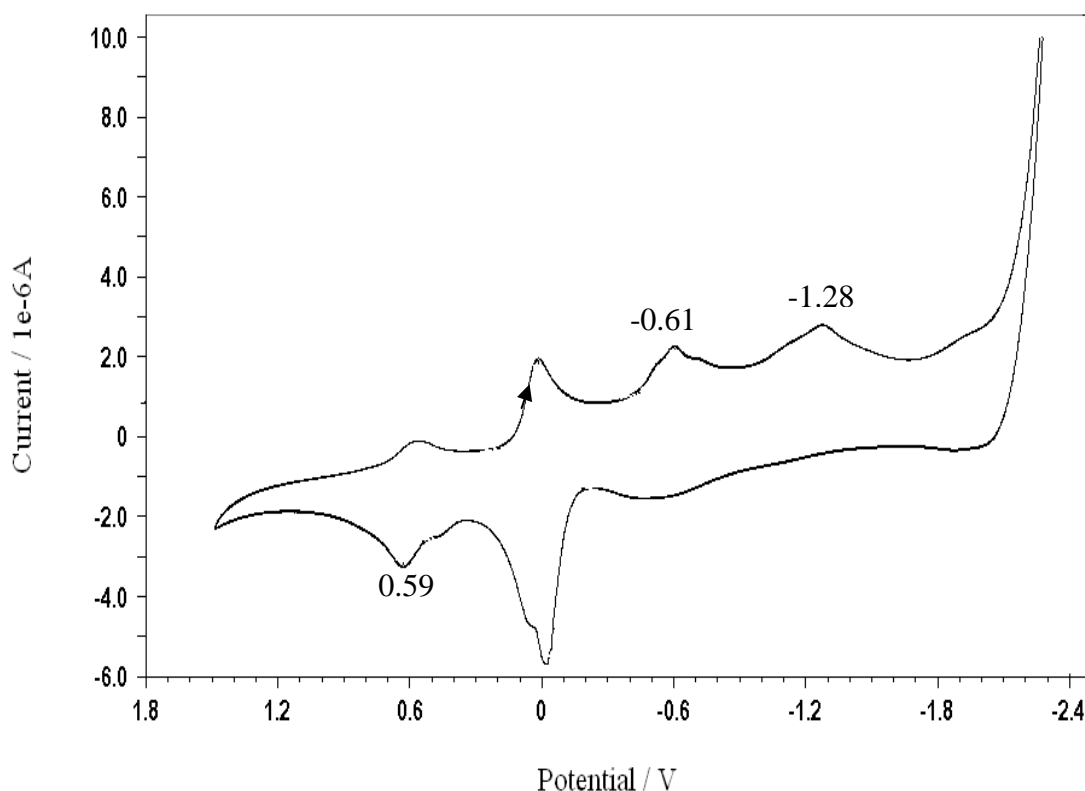
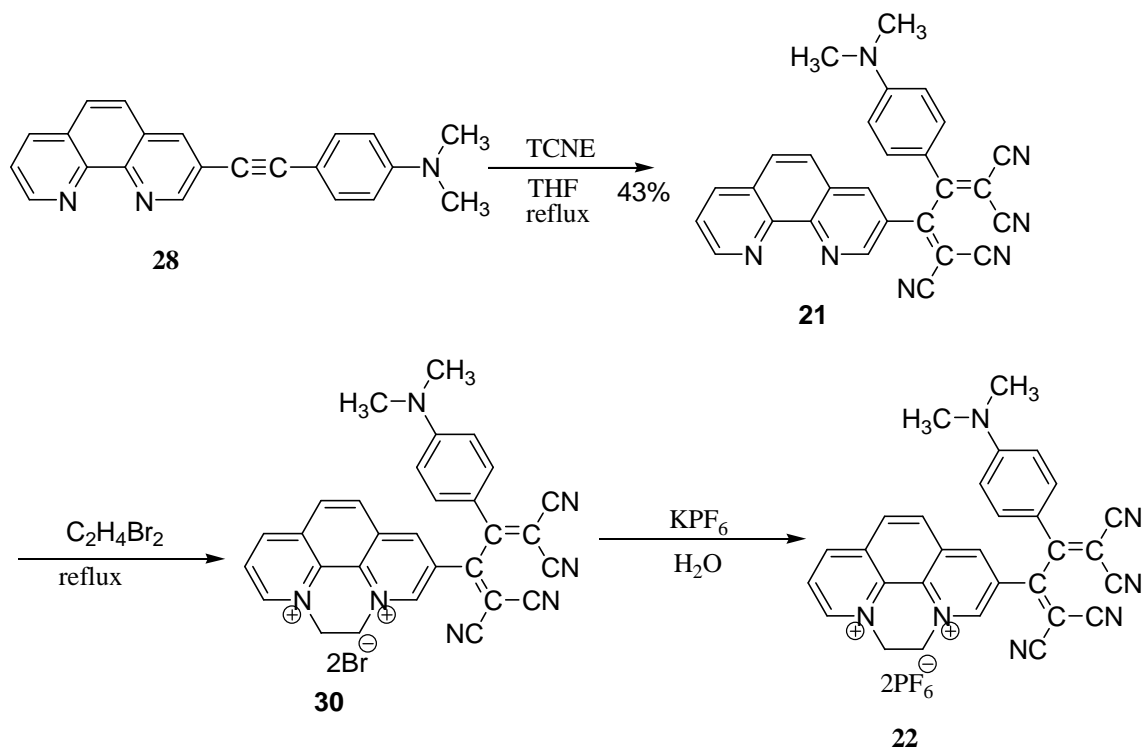


**Figure 5-9:** The voltammogram of compound **20** recorded using a glassy carbon working electrode, an Ag wire as a reference electrode and a Pt wire as a counter electrode. Recorded at a concentration of  $1 \times 10^{-4}$  M in MeCN with TBAPF<sub>6</sub> (0.1M) as a supporting electrolyte. Scan rate of  $100 \text{ mV s}^{-1}$ .

### 5-6 Synthesis of target compounds **21** and **22**

The synthesis of compounds **21** and **22** started with compound **28**. Then this compound was converted into **21** by [2+2] cycloaddition with TCNE. This reaction was presumed to occur by initial bond formation between the alkyne C-atom in the  $\beta$  position to the aniline donor, and the  $\beta$ -C atom of the  $\text{C}=\text{C}(\text{CN})_2$  moieties of each TCNE. This compound then was converted into **22** via a  $\text{S}_{\text{N}}2$  alkylation reaction. The synthetic steps are presented in the following scheme:



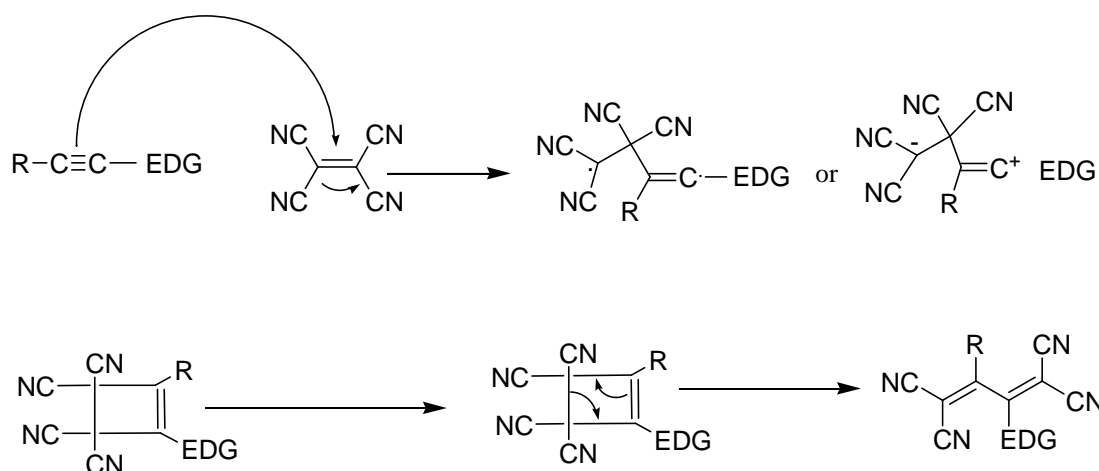
**Scheme 5-10:** Synthetic route of target compounds **21** and **22**.

Compound **21** was synthesized from compound **28** by reaction with 1.5 equivalents of TCNE. The mixture was dissolved in THF, and then it was heated under reflux in the dark with continuous stirring. The crude product was purified by column chromatography to afford a final product as a black/ brown powder with 43% yield<sup>(40,41)</sup>. Synthesis of compound **30** started from **21** by reacting with 1,2-dibromoethane. This then was converted into **22** by ion exchange reaction with potassium hexafluorophosphate to give compound **22**. However, the last compound was characterized by mass spectrometry, which confirmed formation of this compound. Many attempts were made to purify it such as washing, recrystallization and column chromatography using silica gel with (MeOH/  $H_2O$ /  $NH_4Cl$  in 6:3:1), but unfortunately high purity of **22** could not be obtained. This probably arises from decomposition of this compound in the column.

### 5-6-1 Proposed mechanism for [2+2] cycloaddition

Reaction of TCNE and TCNQ with alkyne substituted electron-donating groups (EDG) can proceed by [2+2] cycloaddition. It has been reported that an anilino donor can react with TCNE and TCNQ at room temperature in THF<sup>(41)</sup>. This reaction was presumed to occur by initial bond formation between the alkyne C-atom in the  $\beta$  position to the aniline donor, and the  $\beta$ -C atom of the  $C=C(CN)_2$  moieties of each TCNE and TCNQ. This interaction would give a resonance that is stabilized by zwitterionic or diradical intermediate. These

transformations would involve the HOMO of the cyanoalkynes and the LUMO of the acceptors, Recombination of the charges or unpaired electrons would occur to give the cyclobutane. This would undergo electrocyclic ring opening, this process leads to the final butadiene<sup>(41)</sup>. The general steps of this mechanism are shown in the following scheme:



**Scheme 5-11:** Proposed [2+2] cycloaddition mechanism for the addition of TCNE and TCNQ. EDG is any electron donating group such as amino group.

### 5-6-2 Analysis of compound **21**

The UV-visible spectrum of compound **21** was recorded in DCM and two absorption peaks at 353 nm, and 460 nm are evident. From this spectrum, it is clear that there is a remarkable red shift in the absorption of compound **21** in comparison with **28** as shown in Figure 5-7. This is probably due to the presence of the highly conjugated system for the compound after incorporation of TCNE within the molecule<sup>(42)</sup>. The CT peak at 460 nm reflects the (D-A) strong interaction in this compound, that can result in high delocalization for the electrons and result in a red shift in the electronic spectrum of the molecule.

The optically determined HOMO to LUMO bandgap for **21** was 1.98 eV, which was reduced significantly in comparison with that of **28** probably due to the strong effect of the CT interaction that becomes more efficient after introducing cyano groups and increasing the strength of the acceptor moieties in this compound. The UV- visible spectrum is shown in the following figure:

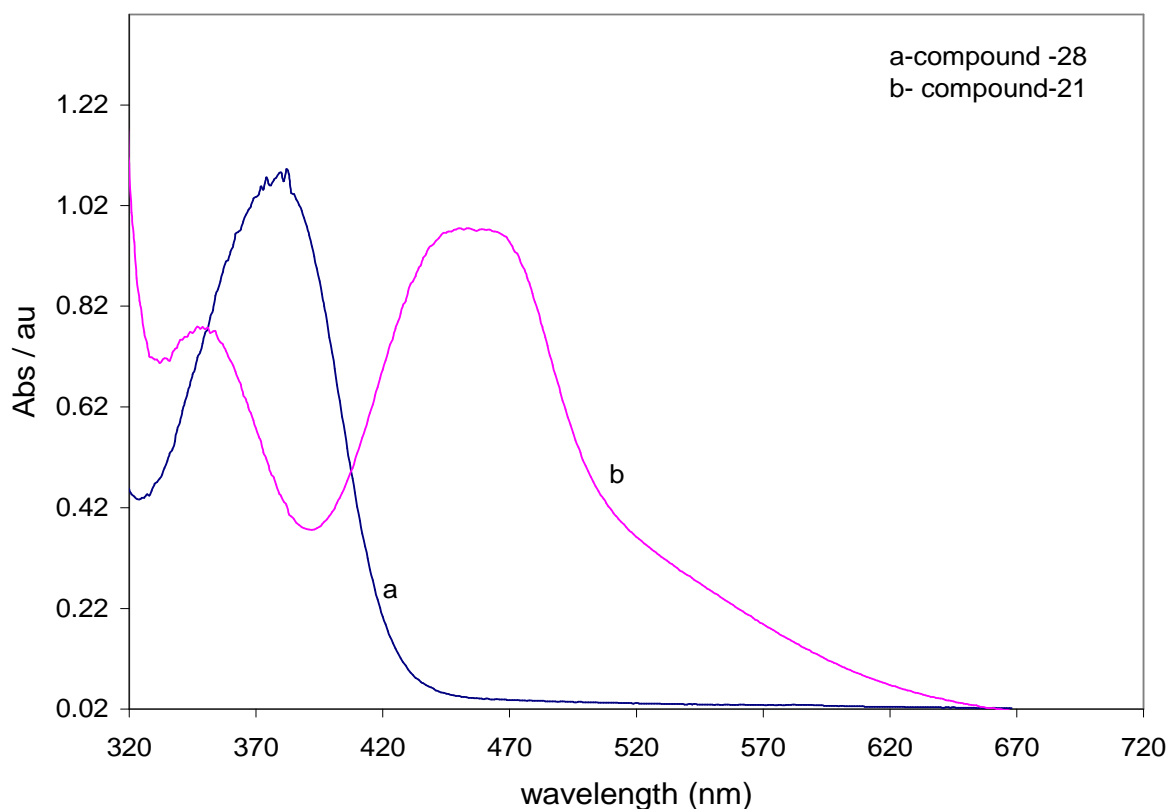


**Figure 5-12:** UV-visible spectrum of compound **21** and **28**. Recorded in DCM ( $1 \times 10^{-4}$ M).

The voltammogram of compound **21** was measured in DCM. The voltammogram of this compound shows two reversible reduction peaks at - 0.84 V and at -1.17 V with respect to ferrocene redox . This compound shows one reversible oxidation peak at + 0.88 V. The reduction of this compound showed two one-electron reduction steps with respect to ferrocene redox. The first reduction occurs at -0.84 V and the second at -1.17 V, the electron capture occurs on the acceptor moieties. The observed one electron oxidation step at + 0.88 V occurs probably due to oxidation of the aniline donor moiety. The LUMO energy of compound **21** is estimated to be - 4.05 eV. The estimated HOMO for this compound was -5.25 eV and the electrochemically determined bandgap was 1.20 eV. However, this value of bandgap was different from that was obtained from UV-visible spectrum (1.98 eV). This probably arises from contribution of air and humidity when run the spectrum. The presence of cyano groups has a dramatic effect on the redox properties of this compound. In this case, CT interaction becomes more efficient due to the increasing strength of the acceptor. The voltammogram of this compound without ferrocene is shown in the following figure:

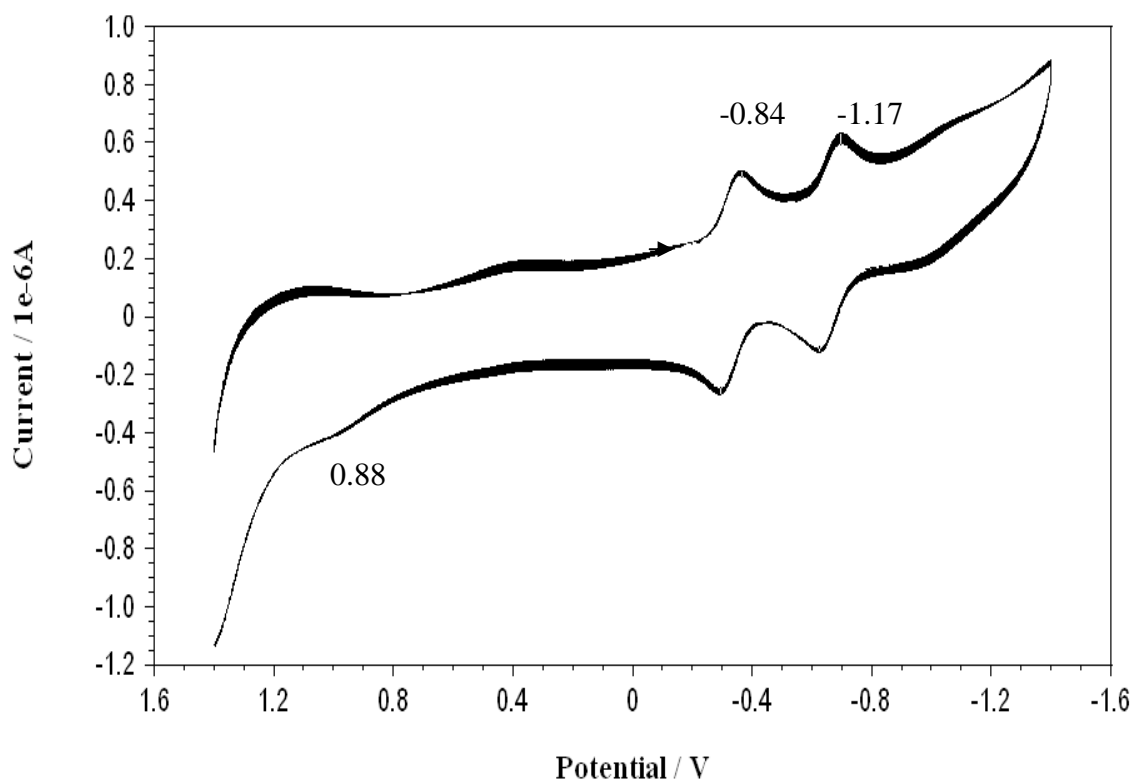
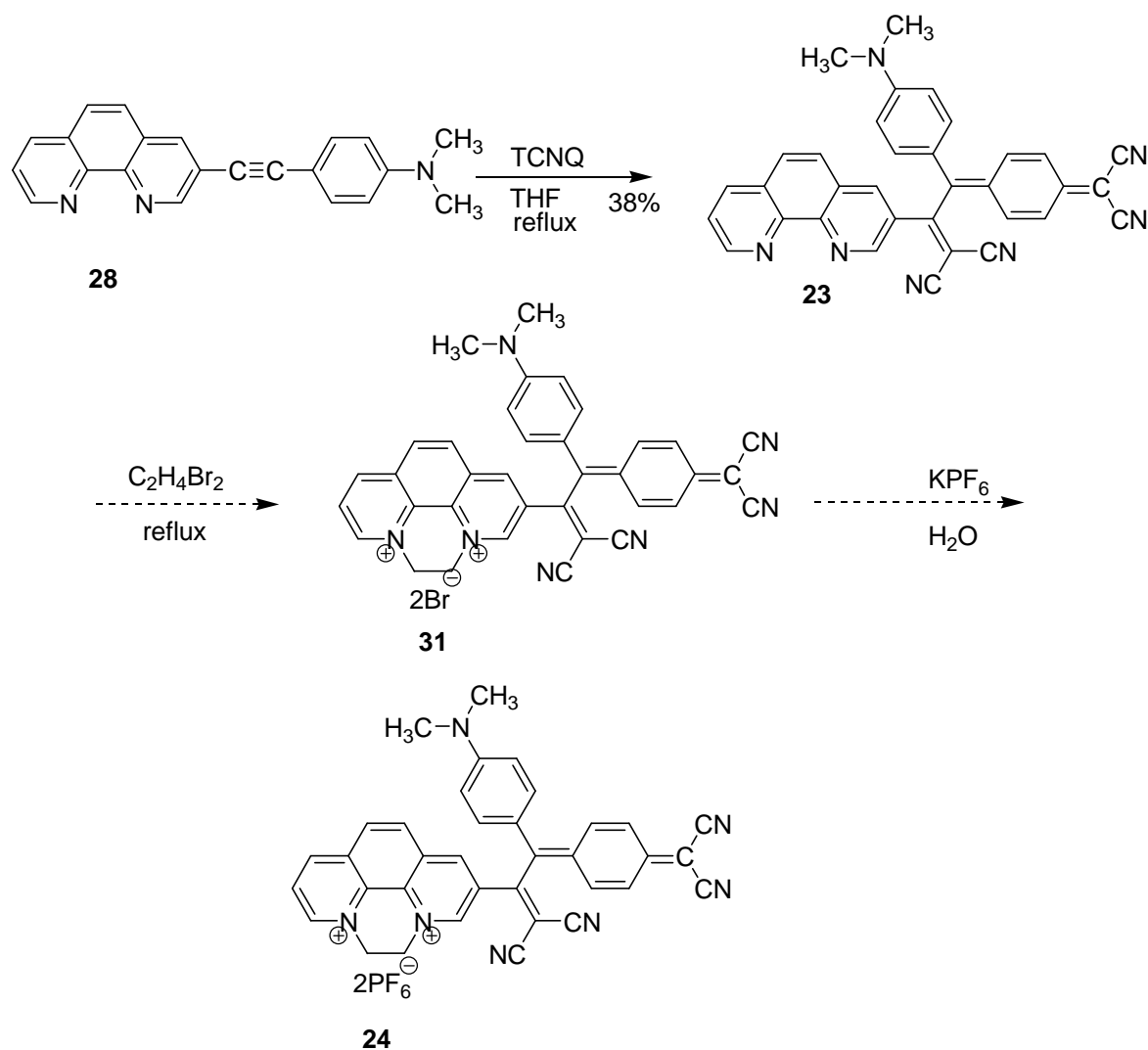


**Figure 5-13:** The voltammogram of compound **21** recorded using a glassy carbon as a working electrode, an Ag wire as a reference electrode and a Pt wire as a counter electrode. Recorded at a concentration of  $1 \times 10^{-4}$  M in DCM with TBAPF<sub>6</sub> (0.1M) as a supporting electrolyte. Scan rate of  $100 \text{ mV s}^{-1}$ .

### 5-7 Synthesis of target compounds **23** and **24**

The synthesis of compound **23** starts with **28** by reacting with TCNQ using THF as a solvent. The mixture was heated under reflux overnight. At the end of reaction, the mixture was purified by column chromatography to yield compound **23**. Then this compound could be alkylated with 1,2 -dibromoethane to give viologen bromide **31** and by using an ion exchange reaction afforded the PF<sub>6</sub><sup>-</sup> salt **24**. The last compound was characterized by mass spectrometry, which confirms formation of this compound. Despite many efforts made to purify it such as washing, recrystallization, and column chromatography using silica gel with (MeOH/ H<sub>2</sub>O/ NH<sub>4</sub>Cl in 6:3:1), it could not be obtained in a pure form. This probably arises from decomposition of this compound in the column. The synthetic steps for these compounds are presented in the following scheme:



**Scheme 5-14:** Schematic synthesis of compounds **23** and **24**.

Compound **23** was synthesized from compound **28** and using 1.5 equivalents of TCNQ in the dark. The mixture was dissolved in THF and then it was heated under reflux in the dark with continuous stirring. The crude product was purified by column chromatography to yield the final product as a black/ green powder with 38% yield<sup>(40)</sup>. Synthesis of compound **31** started from **23** by reacting with 1,2-dibromoethane. This then converted to **24** by an ion exchange reaction with an excess of an aqueous solution of potassium hexafluorophosphate. Then the mixture was filtered of and the precipitate washed with water many times to remove any remaining starting materials. The resulted powder then dried in vacuum overnight.

### 5-7-1 UV-visible spectrum of compound **23**

The UV- visible spectra of compounds **23** and **28** were recorded in DCM. The spectrum of compound **23** shows four absorption peaks at 280 nm, 350 nm, 490 nm and 705 nm. It was found that there was a significant red shift in the absorption of **23** in comparison with **28**

probably due to the highly conjugated nature of this compound after incorporation of TCNQ<sup>(42)</sup>. The spectrum of this compound showed a significant red shift in comparison with compound **21** (Figure 5-12). This probably arises from highly conjugated system in this compound due to incorporate TCNQ moiety in this compound rather than TCNE in compound **21**

The CT peak at 705 nm tails far into near infrared region and the end absorption was observed close to 972 nm. However, this long wavelength absorption reflects strong D-A interaction in this compound that can give a high delocalization for the electrons and make a red shift in the electronic spectrum of the molecule. The optically determined HOMO to LUMO bandgap for **23** was 1.32 eV. The optical bandgap for **23** was reduced significantly in comparison with that of **28**. This probably arises from the strong effect of the CT interaction that becomes more efficient after introducing cyano groups and increasing the strength of the acceptor moieties in this compound. The UV-visible spectra for these compounds are summarized in the following figure:

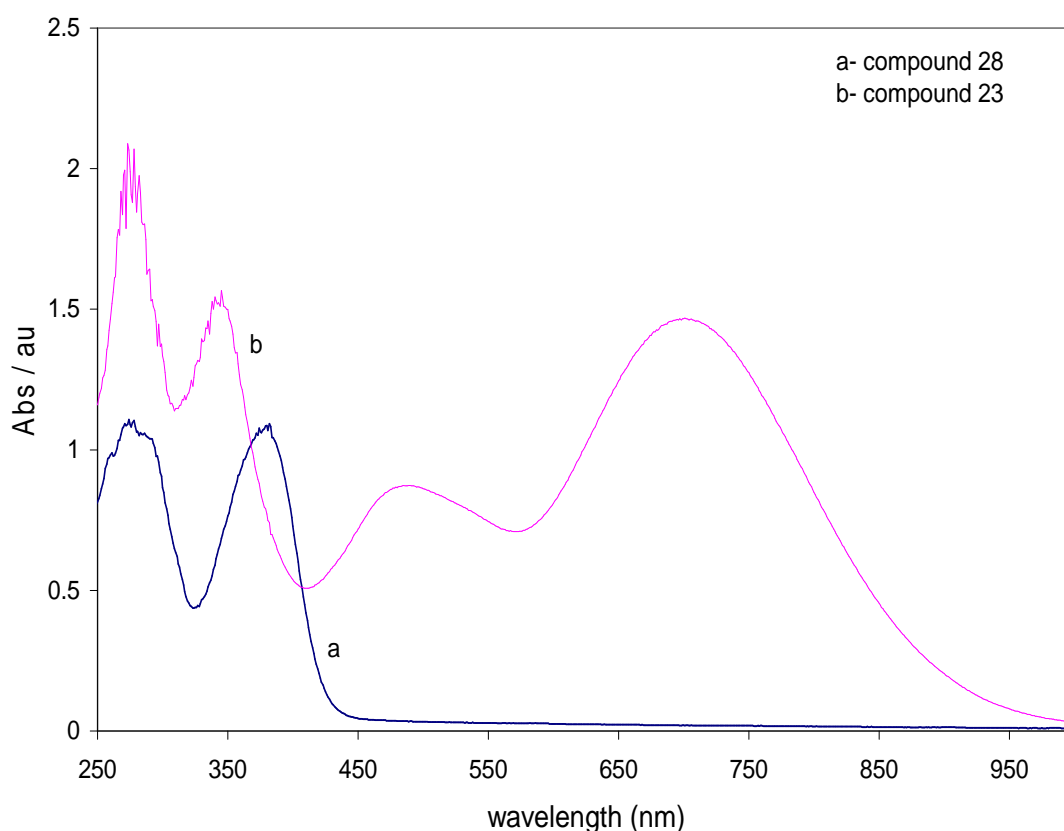


**Figure 5-15:** UV-visible spectra for compounds **23** and **28**. Recorded in DCM ( $1 \times 10^{-4}$  M).

### 5-7-2 The voltammogram of compound **23**

The voltammogram of compound **23** was performed in DCM. The voltammogram of this compound shows two reversible reduction peaks at - 0.65 V and - 0.77 V and one

oxidation peak at + 0.39 V with respect to ferrocene redox . The two one-electron reduction steps at - 0.65 V and - 0.77 V with respect to ferrocene redox. The observed one electron oxidation step at + 0.39 V is presumably oxidation of the aniline group. The estimated LUMO energy of compound **23** was calculated to be - 4.15 eV. The estimated HOMO energy for this compound was -5.19 eV and the electrochemically determined bandgap was 1.04 eV. The presence of cyano groups has a dramatic effect on the redox properties of this compound. In this case, CT interaction becomes more efficient due to the increasing strength of the acceptor; which also affects the oxidation potential. The voltammogram of this compound without ferrocene is shown in the following figure:

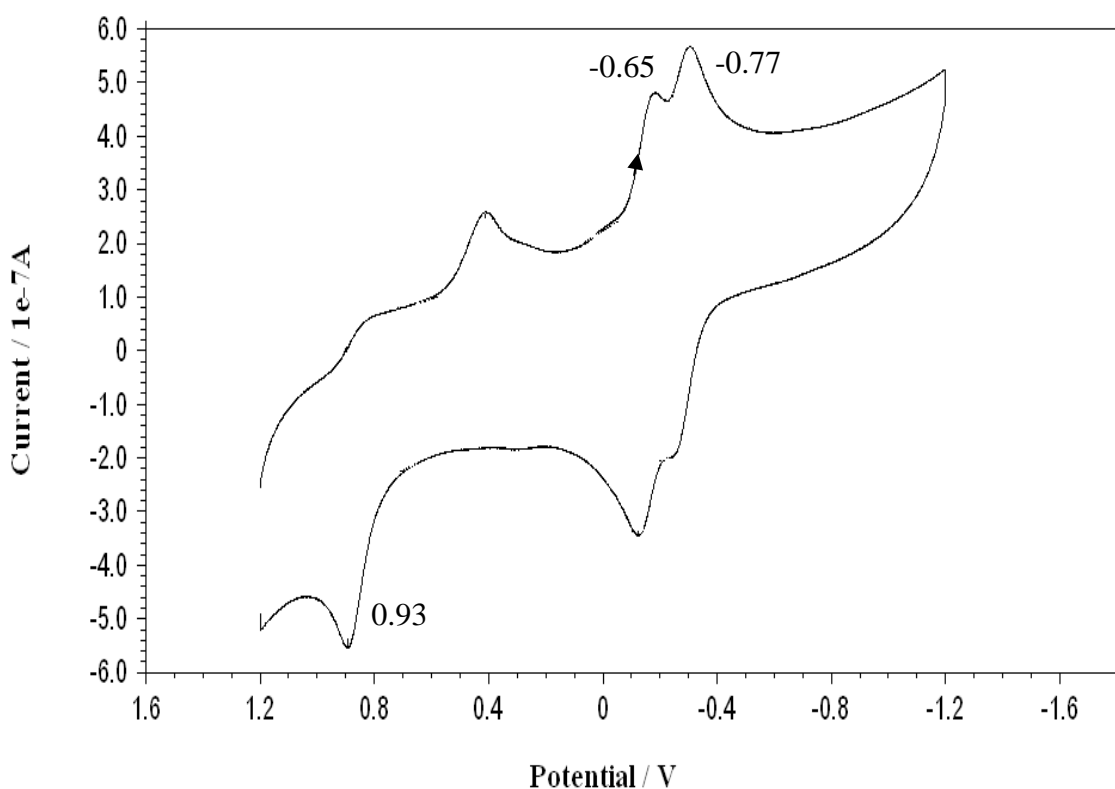
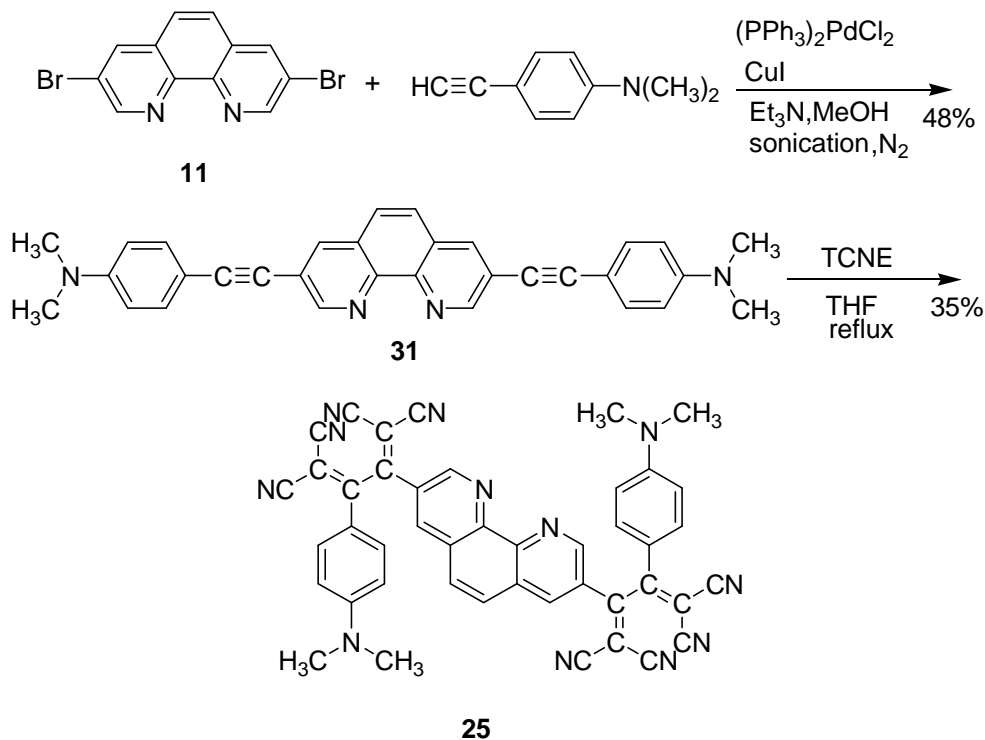


**Figure 5-16:** The voltammogram of compound **23** recorded using a glassy carbon working electrode, an Ag wire as a reference electrode and a Pt wire as a counter electrode. Recorded at a concentration of  $1 \times 10^{-4}$  M in DCM with TBAPF<sub>6</sub> (0.1M) as a supporting electrolyte. Scan rate of  $100 \text{ mV s}^{-1}$ .

In the previous part, we investigated synthesis of some asymmetrical chromophores containing donor/acceptor moieties in conjugation with phenanthroline core. Both optical and redox properties for these compounds have been studied. In the next part, we aimed to synthesize of a symmetrical chromophore based TCNE and anilino groups from two-side addition in conjugation with phenanthroline core.

## 5-8 Synthesis of target compound 25

The synthesis of the target compound **25** was started from 3,8-dibromo-1,10-phenanthroline. This was then converted to compound **31** by reaction with 4-ethynyl-N,N-dimethylbenzenamine. Compound **31** reacted with TCNE to give the target compound **25**. The synthetic steps for compound are summarised in the following scheme:



**Scheme 5-17:** The synthetic route of compound **25**.

The synthesis of compound **31** was achieved by reacting a mixture of compound **11**,  $(\text{PPh}_3)_2\text{PdCl}_2$  and  $\text{CuI}$ . This mixture added to another mixture of 4-ethynyl- N,N-dimethylaniline (2.5 equivalents of compound **11**) and  $\text{Et}_3\text{N}/\text{MeOH}$  (2:1). The final mixture degassed and sonicated at room temperature. The crude product was purified by column chromatography to afford **31** as an orange powder in 48% yield<sup>(36)</sup>.

Compound **25** was synthesized from compound **31** using 2.5 equivalents of TCNE in the dark. The crude product was purified by column chromatography to afford **25** as a brown powder with 35% yield<sup>(40)</sup>.

### 5-8-1 Analysis of compound 25

The UV-visible spectra of compounds **25** and **31** were recorded in DCM. The UV-vis spectrum of compound **31** shows three peaks at 248 nm, 293 nm and 400 nm. These peaks are related to the  $\pi$ - $\pi^*$  electronic transitions for this compound. The optically determined HOMO to LUMO bandgap for compound **31** was calculated to be 2.75 eV. The UV-

visible spectrum for compound **25** shows three absorption bands at 283 nm, 360 nm and 460 nm. From this spectrum, it can be seen that there is a significant shift in the absorption for **25** in comparison with **31** towards visible region of the spectrum. This is probably due to the highly conjugated nature for this compound due to the incorporation of TCNE within the molecule<sup>(42)</sup>. The CT peak at 458 nm indicates there to be a strong interaction between (D-A-A-D) in this compound. This can result in a high delocalization for the electrons and provide a red shift in the electronic spectrum of the molecule. The optically determined HOMO to LUMO bandgap for **25** was calculated to be 1.96 eV. The optically determined bandgap for **25** was reduced significantly in comparison with that of compound **31**. This is probably due to the strong effect of CT interaction, which becomes more efficient after introducing cyano groups and thus increasing the strength of the acceptor moieties in this compound. The UV-visible spectra for these compounds are shown in the following figure:

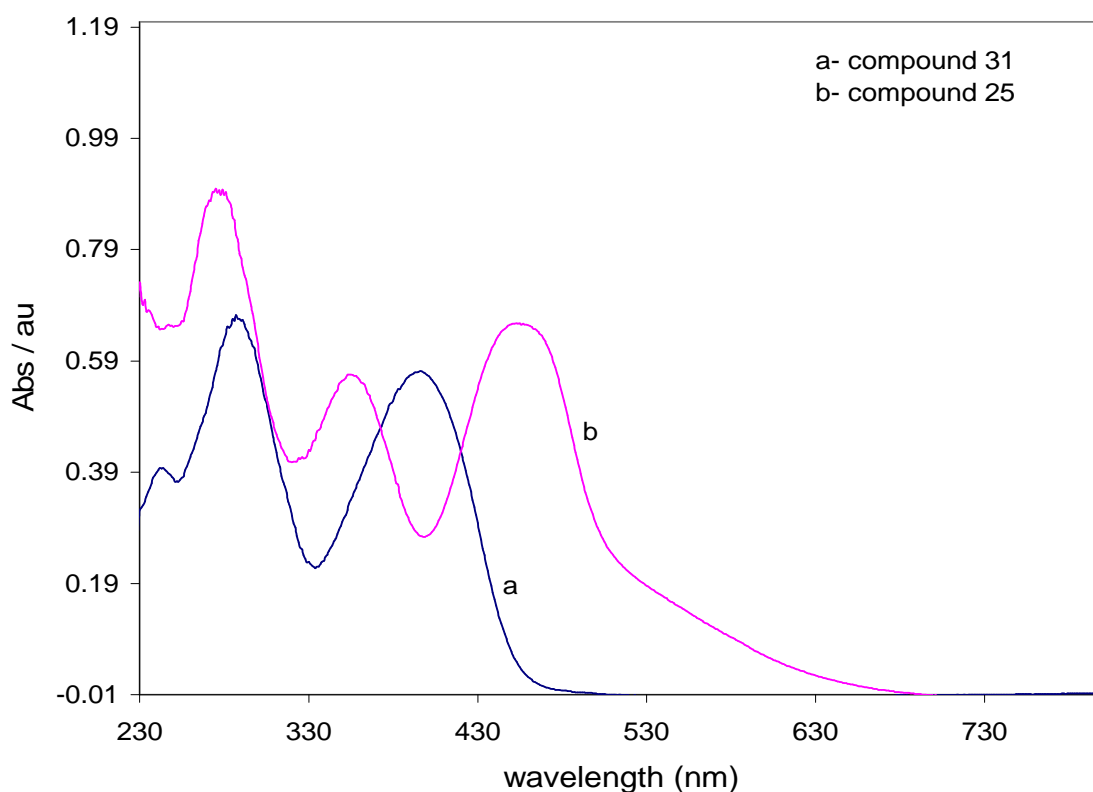


**Figure 5-18:** UV-visible spectra of compounds **25** and **31**. Recorded in DCM ( $1 \times 10^{-4}$  M).

### 5-8-2 The voltammogram of compound **25**

The voltammogram of compound **25** was recorded in DCM. The voltammogram of this compound shows two reversible reduction peaks at -0.82 V and at -1.16 V and one oxidation peak at +0.85 V with respect to ferrocene redox. The two one-electron reduction steps in reduction wave are due to reduction TCNE moieties. The observed one electron oxidation step at +0.85 V occurs on the anilino donor moiety with respect to ferrocene

redox. The estimated LUMO energy of compound **25** was found to be -3.98 eV. The estimated HOMO for this compound was found to be -5.65 eV and the electrochemically determined bandgap was 1.67 eV. However, the difference in value of bandgap that calculated from electrochemistry than that from UV-visible spectrum for compound **25** (1.96 eV) is probably arises from experimental conditions, the presence of cyano groups has a dramatic effect on the redox properties of this compound. In this case, CT interaction becomes more efficient due to the increasing strength of the acceptor. This also can affect the oxidation potential. The voltammogram of this compound without ferrocene is shown in the following figure:

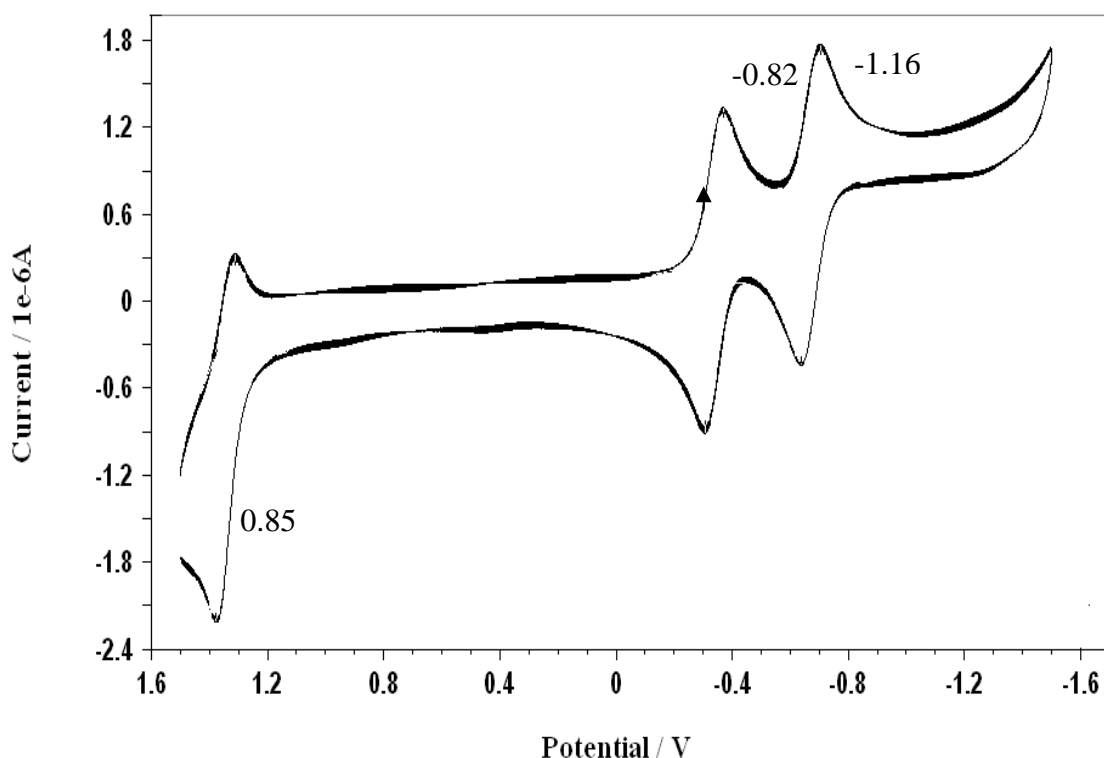


**Figure 5-19:** The voltammogram of compound **25** recorded using a glassy carbon working electrode, an Ag wire as a reference electrode and a Pt wire as a counter electrode. Recorded at a concentration of  $1 \times 10^{-4}$  M in DCM with TBAPF<sub>6</sub> (0.1M) as a supporting electrolyte. Scan rate of  $100 \text{ mV s}^{-1}$ .

## 5-9 Conclusions

This chapter describes the synthesis of some novel dipolar compounds **20-25**, and **30**. These compounds were targeted for synthesis as they may be used in applications such as nonlinear optics and photovoltaic devices. Both TCNE and TCNQ were incorporated within structure of some of these compounds as they are considered as strong acceptors and may therefore significantly increase the push-pull nature of these systems. An asymmetric dipolar system was also synthesized by a one-side addition for TCNE and TCNQ to afford compounds **21** and **23**. A symmetric push-pull system was synthesized by symmetrical addition of TCNE in compound **25**. These compounds showed significant absorption towards the near-IR region, which presumably arises from increased electronic communication between donor/ acceptor moieties in these compounds.

## 5- 10 References

1. L. Dalton, A. Haper, R. Ghosn, M. Ziari, R. Mustacich, *Chem. Mater.*, 1995, **7**, 1060.
2. S. Marder, D. Bertan, L. Cheng, *Science*, 1991, **252**, 103.
3. C. Shu, W. Tsai, *Tetrahedron Lett.*, 1996, **37**, 7055.
4. J. Xu, X. Liu, J. Lv, M. Zhu, C. Huang, W. Zhou, X. Yim, H. Liu, Y. Li, J. Ye, *Langmuir*, 2008, **24**, 4231.
5. X. Zhang, K. Zou, C. Lee, S. Lee, *J. Am. Chem. Soc.*, 2007, **12**, 3527.
6. X. Zhang, W. Shi, X. Meng, C. Lee, S. Lee, *Angew. Chem., Int. Ed.*, 2007, **11**, 1547.
7. C. Zhang, X. Zhang, X. Fan, J. Jie, J. Chang, C. Lee, W. Zhang, S. Lee, *Adv. Mater.*, 2008, **20**, 1716.
8. L. Cheng, W. Tam, S. Marder, A. Stiegman, G. Rikken, C. Spangler, *J. Phys. Chem.*, 1991, **95**, 10643.
9. S. Marder, L. Cheng, B. Tiemann, A. Friedli, J. Perry, *Science*, 1994, **263**, 511.
10. C. Moylan, R. Twieg, V. Lee, S. Sawanson, K. Bettertan, R. Miller, *J. Am. Chem. Soc.*, 1993, **115**, 12599.
11. G. He, L. Tan, Q. Zheng, P. Prasad, *Chem. Rev.*, 2008, **108**, 1245.
12. Y. Shi, Y. Zhang, H. Zhang, J. Bechtel, L. Dalton, B. Robinson, W. Steier, *Science*, 2000, **288**, 119.
13. V. Alain, M. Blanchard-Desce, C. Chen, S. Marder, A. Fort, M. Barzoukas, *Synth. Metals*, 1996, **81**, 133.
14. P. Das, A. Krishnan, S. Pal, P. Nadakumar, A. Samuelson, *Chem. Phys.*, 2001, **265**, 313.
15. R. Miller, V. Lee, C. Moylan, *Chem. Mater.*, 1994, **69**, 1023.
16. E. Breitung, C. Shu, R. McMahon, *J. Am. Chem. Soc.*, 2000, **122**, 1154.
17. A. Facchetti, L. Beverina, M. Van der Boom, E. Dutta, A. Pagani, T. Marks, *J. Am. Chem. Soc.*, 2006, **128**, 2142.
18. J. Davies, A. Elangovan, P. Sullivan, B. Olbricht, D. Bale, T. Ewy, C. Isborn, *J. Am. Chem. Soc.*, 2008, **130**, 10565.
19. M. Raposo, A. Sousa, A. Fonesca, G. Kirsch, *Tetrahedron*, 2005, **61**, 8249.
20. M. Raposo, A. Sousa, G. Kirsch, F. Ferreira, M. Belsley, M. Gomes, A. Fonesca, *Tetrahedron*, 2005, **61**, 11991.

21. P. Prasad, D. Williams, *Introduction to Nonlinear Optical Effects in Molecules and Polymer*, Wiley, New York, 1991.
22. S. Shi, *Contemp. Phys.*, 1994, **35**, 21.
23. B. Beck, U. Grummt, *J. Phys. Chem. B*, 1998, **102**, 664.
24. D. Chemla, J. Zyss, *Nonlinear Optical properties of Organic molecules and Crystals, Vol. I and II*, Academic Press, Orlando, FL, 1987.
25. K. Clays, A. Persoons, L. DeMaeyer, *Adv. Chem. Phys.*, 1994, **85**, 455.
26. M. Flipse, R. De Jonge, R. Woudenberg, A. Marsman, C. Van Warlee, L. Jenneskens, *Chem. Phys. Lett.*, 1995, **245**, 297.
27. M. Blanchard-Desce, C. Runser, A. Fort, M. Barzaukas, J. Lehn, V. Alain, *Chem. Phys.*, 1995, **199**, 253.
28. S. Barlow, H. Bunting, C. Ringham, J. Green, G. Bublitz, S. Boxer, J. Perry, S. Marder, *J. Am. Chem. Soc.*, 1998, **121**, 3715.
29. M. Albota, D. Beljonne, J. Ehrlich, J. Fu, A. Heikal, S. Hess, M. Levin, W. Webb, C. Xu, *Science*, 1998, **281**, 1653.
30. K. Walzer, B. Maennig, M. Pfeiffer, K. Leo, *Chem. Rev.*, 2007, **107**, 1233.
31. J. May, I. Biaggio, F. Bures, F. Diederich, *Appl. Phys. Lett.*, 2007, **90**, 1.
32. M. Kivala, C. Boudon, P. Gisselbrecht, P. Seiler, M. Gross, F. Diederich, *Angew. Chem. Int. Ed. Engl.*, 2007, **46**, 6357.
33. D. Ess, G. Jones, K. Houk, *Adv. Synth. Catal.*, 2006, **348**, 2337.
34. J. Xu, H. Zheng, H. Lin, C. Zhou, Y. Zhao, Y. Li, *J. Phys. Chem. C*, 2010, **114**, 2925.
35. A. Bandyopadhyay, B. Harriman, *J. Chem. Soc. Faraday Trans. I*, 1977, **73**, 663.
36. D. Tzalis, Y. Tor, S. Failla, J. Siegel, *Tetrahedron Lett.*, 1995, **36**, 3489.
37. D. Tzalis, Y. Tor, *Tetrahedron Lett.*, 1995, **36**, 6017.
38. D. Rosseinsky, P. Mounk, *J. Chem. Soc. Faraday Trans.*, 1993, **89**, 219.
39. Y. He, W. Wu, G. Zhao, Y. Lin, *Macromolecules*, 2008, **41**, 9760.
40. P. Reutenauer, M. Kivala, D. Jarowski, C. Boudon, J. Gisselbrecht, M. Gross, F. Diederich, *Chem. Commun.*, 2007, 4898-4900.
41. T. Michinobu, C. Boudon, J. Gisselbrecht, B. Frank, N. Moonen, M. Gross, F. Diederich, *Chem. Eur. J.*, 2006, **12**, 1889.
42. S. Alqaradawi, A. Mustafa, H. Bazzi, *J. Mol. Struct.*, 2012, **1011**, 172.

## **Chapter- six: Synthesis of some novel ruthenium (II) complexes as luminescence materials and for use in dye sensitized solar cells.**

### **6-1 Introduction**

During last few decades, much effort has been focused towards the development of materials that can be used as light-emitting materials for solid-state lighting applications<sup>(1)</sup>. Polymer light-emitting diodes (PLEDs) have been studied extensively since 1990 when the first fabrication of a functioning diode using a conjugated polymer as an electroluminescence device material was reported<sup>(2-4)</sup>. This has some attractive properties such as mechanical strength, processibility, flexibility and relatively low cost<sup>(5)</sup>. In spite of the good progress that has been achieved in this field, there are still some problems with this system. These include low quantum yield, limited lifetime and poor colour purity. It is not easy to produce a high colour purity from organic polymer materials as a result of broad emission peaks<sup>(6)</sup>. Consequently, and as a result of all these drawbacks, efforts have been focused toward use some lanthanide ions to act as the emissive moieties with conjugated polymers when applied as PLEDs. In this case, the energy of the excited states can be harvested into excited orbital states of the lanthanide ions, causing high emission. Additionally, lanthanide metal ions give sharp emission bands as a result of the shielding of the 4f orbitals by the 5s and 5p shells<sup>(6)</sup>. The covalent coupling between lanthanide complexes and the backbone of the polymer can give more effective compositions, possessing a higher efficiency for energy transfer because covalently bound systems are more efficient as a result of the close proximity of the two components. However, conducting polymers with lanthanide complexes can be used in many potential applications such as electrical conductors, batteries, sensors and memory devices<sup>(7)</sup>. Generally, development of molecular devices requires synthesis of functional materials and 1,10-phenanthroline derivatives are an important type of organic building block. These derivatives can be used with many potential applications in coordination chemistry, materials chemistry, analytical chemistry and as probes of redox processes as a result of their strong chelating ability and highly conjugated  $\pi$  systems<sup>(8)</sup>. In this type of derivative, halogen substitution at different positions is the first synthetic step in the modification of the 1,10-phenanthroline ring. The most important substituents in the modification, are the synthesis of 3-bromo and 3,8-dibromo-1,10-phenanthroline by different routes and with various yields<sup>(9)</sup>. After introducing bromide in the framework of 1,10-phenanthroline, the resultant conjugated  $\pi$  system can be extended by introducing different functional groups. Hence, the energy levels of the resulting molecules can be modified accordingly. For example, oligothiophenes can be introduced at the 3 and 8 positions of phenanthroline ring

via carbon- carbon cross-coupling reactions starting with 3,8- dibromo-1,10-phenanthroline<sup>(10)</sup>. In addition, the  $\alpha$ - H atom of the thiophene ring is active for the further coupling, polymerization, and substitution reactions<sup>(10)</sup>. Structures of some phenanthroline derivatives are shown in the following figure:

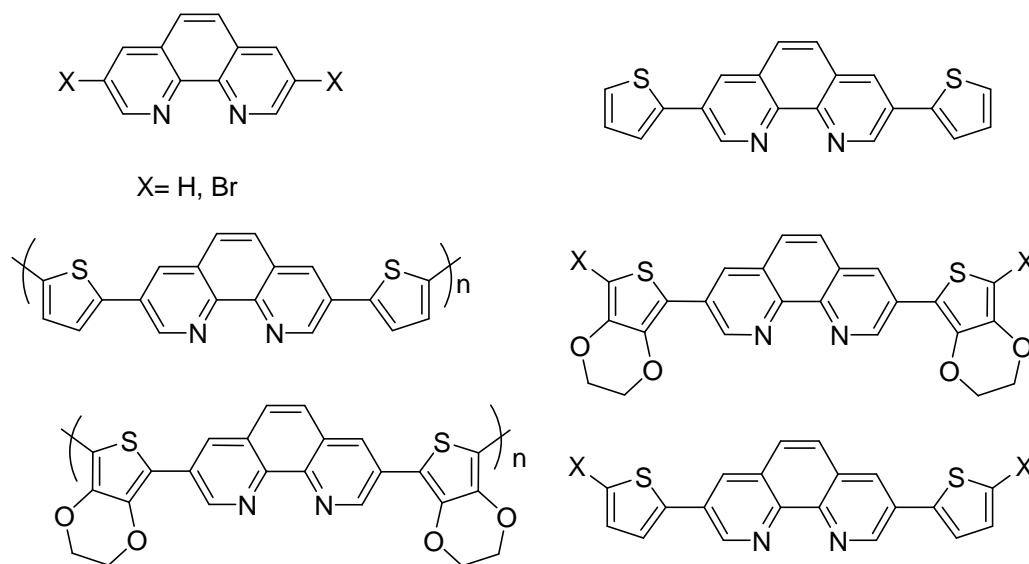


**Figure 6-1:** Structures of some of phenanthroline derivatives.

## 6-2 Ruthenium chelating compounds

The need for redox active chromophoric materials has become a subject of research arising from the ability of these materials to achieve photoinduced charge separation<sup>(11)</sup>. When some metal ion complexes are linked with organic redox chromophores, the resultant compositions would be expected to possess new modified electrochemical and photochemical properties arising from the ability to tune charge separation between both ligand and metal centres<sup>(11)</sup>. In the last ten years, polynuclear bipyridyl Ru(II) complexes linked with some redox-active bridging spacers have been reported to show some interesting photophysical and electrochemical behaviour making them excellent candidates for potential applications as new electronic and photoactive devices. The structures of some of these complexes are shown below<sup>(12)</sup>:

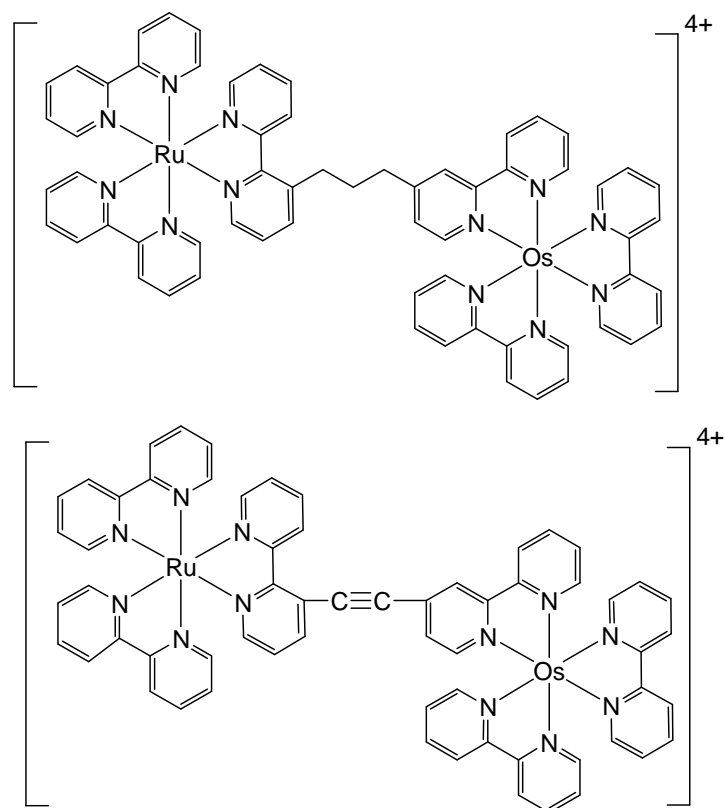


**Figure 6-2:** Structures of some bipyridal Ru(II) complexes<sup>(12)</sup>.

As a result of their good electrochemical and photochemical properties, ruthenium (II) polypyridal complexes have been used effectively in the development of photoactive molecular systems. In this context, many derivatives of ruthenium complexes with bipyridines and 1,10-phenanthroline have been prepared<sup>(13)</sup>. It has been reported that conjugated 1,10-phenanthrolines which are substituted with arylenes at the position 3 and 8 have excellent properties for luminescence and in materials chemistry<sup>(14)</sup>. These derivatives exhibited good photophysical properties due to high electronic delocalization<sup>(14,15)</sup>. In another study, many ruthenium (II) polypyridal complexes have been synthesized and excellent photophysical and electrochemical properties have been reported<sup>(13)</sup>. Suzuki and co-workers<sup>(16)</sup> synthesized some derivatives of ruthenium (II) complexes with 1,10-phenanthroline ligand derivatives and these complexes showed excellent electrochemical and photophysical properties. The 3,8- disubstituted-1,10-phenanthroline derivatives were synthesised by the Pd catalyzed C-N coupling reaction between 3,8-dibromo-1,10-phenanthroline and diphenylamine or with heteroatomic compounds with an N-H bond. The redox properties of these compounds can be modified by coordination with Ru(II) generating multi- redox systems. These electrochemical responsive chelating ligands can play a main role in the development of new sensors and they can also be used in many potential applications as photoactive devices<sup>(16)</sup>. Due to good electrochemical properties of

ruthenium complexes in their monomer forms, therefore research was directed towards polymerization of Ru(II) complexes using both chemical and electrochemical routes.

### 6-3 Conducting polymer of Ru(II) complexes

Metal containing polymers have emerged as a new and interesting class of composite materials that combine some of the redox properties of both conducting polymers and the metal ions<sup>(17)</sup>. Many of these polymers showed unusual optical and electrochemical properties<sup>(18)</sup>. Generally, metal-containing conducting polymers can be classified into three types<sup>(17)</sup>: In the first type, the polymers have the metal group tethered to the conjugated backbone with a linker group e.g. alkyl group. In this case, the polymer acts as a conductive electrolyte, while the metal ions act as tethered groups present within the polymer matrix, in this type the interaction between metal groups and polymer backbone occurs through the linking groups, (ii) In the second type, the metal is directly coupled to the polymer matrix or is coupled to the backbone via a conjugated linker group, and (iii) In the third type, the metal group is directly incorporated with the conjugated backbone. For this type of conducting polymer, the main properties of the polymer depend mainly on the metal group<sup>(17)</sup>. These three types of metal containing conducting polymer are shown in the following figure:

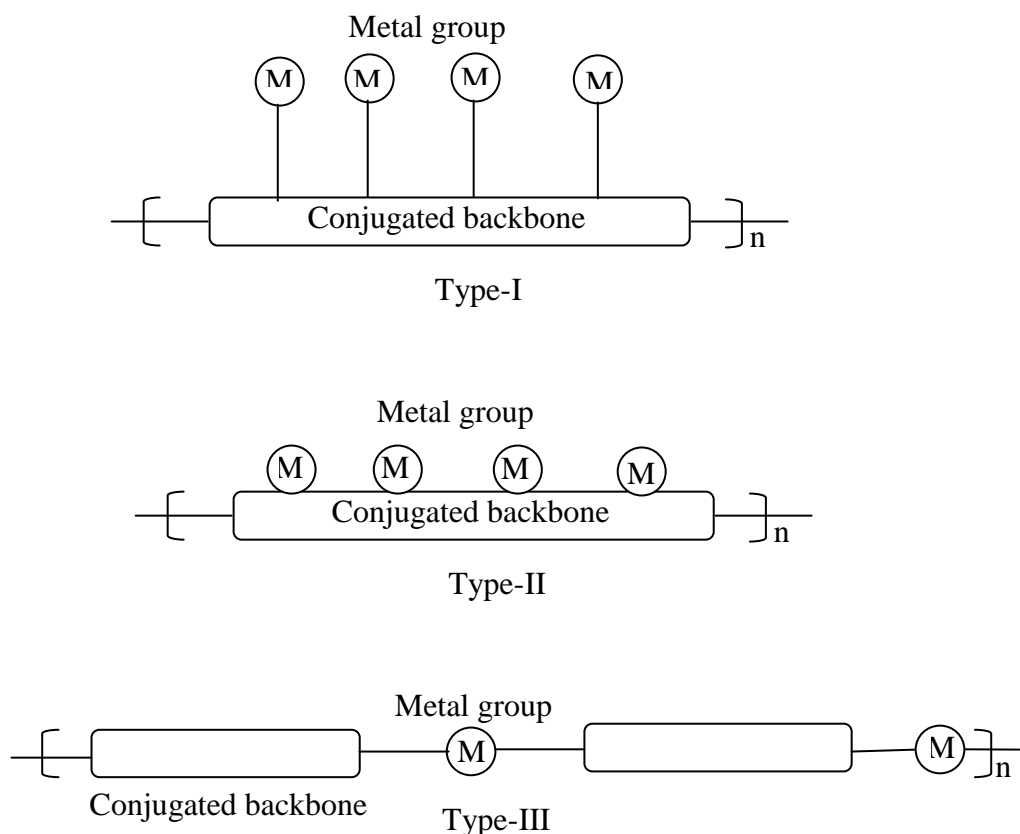


**Figure 6-3:** Metal containing conducting polymer types, in the above figures M is a metal group.

These types of conducting polymer can be synthesized by different methods such as condensation and electropolymerization. The second route is more common method that can be used in the synthesis of type I and II polymers and it normally yields an insoluble thin film of the polymer<sup>(17)</sup>. The advantages of electropolymerization are that the thin film can be produced easily with tuneable thickness and, to some extent, controlled morphology via adjustment of the conditions such as current, voltage and deposition time<sup>(18)</sup>. Additionally, the electrochemical properties of the resulting polymer can be investigated *in-situ*. This enables the polymer to switch between different states e.g. from the conducting state into the insulating state. This type of polymer is a candidate to be used in a number of applications such as for sensors and catalysts<sup>(19)</sup>. Generally, modified electrodes have become of great interest as a result of potential applications in electrolysis processes. The use of polymers as supports for confining some metals at the electrode-solution interface is widespread<sup>(20)</sup>. The conjugated backbone would give electron transfer between metal complex and the electrode. The conjugated linkages in many conjugated polymers can participate in electron transfer between the metal centres and electrodes<sup>(20-23)</sup>. Zotti and co-workers reported that the rate of electron transfer between metal centres that incorporated in substituted polythiophenes containing pendant ferrocene groups was improved when using conjugated linkages as shown in the following figure<sup>(24)</sup>:

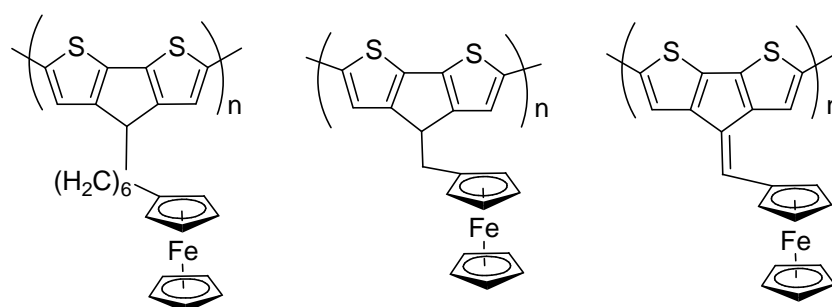
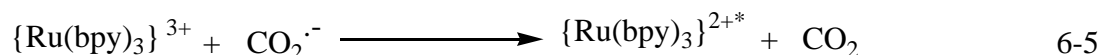
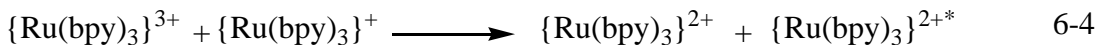
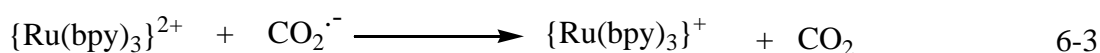


**Figure 6-4:** Structures of substituted polythiophenes containing pendant ferrocene groups<sup>(24)</sup>.

In another study, Cameron and Pickup<sup>(22, 23)</sup> investigated of some ruthenium complexes with conjugated polybenzimidazole. They reported a rapid electron transfer between the metal centres and the conjugated moieties. They found that although there was rapid electron transfer, there was no increase in the luminescence of the Ru(II) moiety. This is probably due to the energy-electron transfer pathways from the excited state of Ru(II) complex to the conjugated groups in the polymer<sup>(22- 24)</sup>. In another study, good luminescence was reported for  $\{\text{Ru}(\text{bipy})_2\}^{2+}$  moieties when covalently bound with a

poly(4-vinyl-pyridine) backbone with a separation distance of order about 50 Å was reported<sup>(25)</sup>. Metallopolymers with  $\{\text{Ru}(\text{bpy})_3\}^{2+}$  increase the rate of charge transport between metal centre and ligands due to physical diffusion as well as the conducting properties of the matrix of the composite in this case. These properties can be used in the development of diagnostic devices requiring luminescent properties of the analyzed materials such as proteins and nucleic acids<sup>(26)</sup>. Oxidation of guanine bases in DNA by  $\{\text{Ru}(\text{bpy})_2(\text{PVP})_{10}\}^{2+}$  produced electrochemically as a thin film generates the photoexcited state of  $\{\text{Ru}(\text{bpy})_2\}^{2+*}$ . This excited state can then relax to the ground state which can be used in the detection of the damage in DNA that caused by styrene oxide<sup>(27)</sup>. Hogan and co-workers<sup>(25,28)</sup> reported the production of light as a result of the reaction of Ru(II) metal centres with oxalate. The authors reported that  $\{\text{Ru}(\text{bpy})_3\}^{2+}$  would oxidize in the presence of a solution of the oxalate as shown in the following equations<sup>(29,30)</sup>:



**Scheme 6-5:** Oxidation of ruthenium complex in a solution containing oxalate producing electrochemiluminescence.

The above processes occur for metallopolymer films that were deposited on the metallic electrodes in the presence of pendant  $\{\text{Ru}(\text{bpy})_2\}^{2+}$  centres<sup>(25)</sup>.

#### 6-4 Dye sensitized solar cells

In the last few decades, there has been great interest in the development of new sources of energy because classical fuels such as oil may be consumed in the next few years.

Furthermore, use of such classical fuels also causes high levels of the pollution. The conversion of solar energy into electrical power could play a major role as one of the most important technologies that can replace fossil fuel. The currently used inorganic solar cells

made from traditional inorganic semiconductors are not suitable for mass usage due to high cost<sup>(31)</sup>. Generally, photovoltaic devices are based on charge separation at the interface formed between two different materials with different conduction mechanisms. This concept can be applied to the generation of electrical power using photovoltaic devices. Dye sensitized solar cells (DSSCs) seem to be good candidate types of organic photovoltaic cell arising from their high efficiency, processibility and relatively low cost in comparison with inorganic silicon panel cells<sup>(32)</sup>. The properties of the photosensitizer used with DSSCs plays an important role in their efficiency. Some poly pyridine Ru(II) complexes have been used as efficient photosensitizers as these complexes showed intense metal to ligand charge transfer ( MLCT) transitions in the visible region of the electromagnetic spectrum. In addition, these complexes are relatively stable in both oxidized and reduced states. Also, their spectral photophysical and electrochemical properties can be tuned easily by the introduction of appropriate ligands<sup>(33)</sup>. Initially, the best reported efficiency for DSSCs was for the cell developed by Grätzel and co-workers<sup>(34)</sup>. They used cis-dithiocyanatobis(4,4'- dicarboxy-2,2'-bipyridine) ruthenium(II) (coded N3) which showed a broad absorption band in the visible region. This system gave a maximum reported efficiency in conversion of the solar energy into electrical power of 11% using a nanostructured titania electrode with iodine solution as a redox electrolyte<sup>(34)</sup>. In DSSCs there are two types of ligand that are linked with Ru(II), these are termed anchor ligands and the ancillary ligands. The anchor ligand is responsible for grafting the dye onto the surface of semiconductor titania and provides electronic coupling between the excited state of the dye and the conduction band of titania. The ancillary ligand is responsible for the spectral properties of the complex<sup>(35)</sup>. For rapid and efficient electron transfer between the excited state of the dye and the conduction band of titania, the LUMO of the dye must be higher than conduction band of titania. In order to regenerate the ground state of the dye, the HOMO must be lower than the oxidation potential of the redox mediator. So that, modification of the dye is a key point to improve the performance of DSSCs<sup>(35)</sup>. One way to find new metal complex sensitizer with high conversion efficiency was performed via the introduction of a  $\pi$ -conjugated moiety into the ancillary ligand of the dye.

#### **6-4-1 Operation principle of the Grätzel dye sensitized nanocrystalline solar cell**

Dye sensitized solar cells are composed of a dye photosensitizer which is bound to the surface of TiO<sub>2</sub> via anchor ligands. The dye should adsorb effectively on the surface to provide good electronic communication between excited state of the photosensitized dye (S\*) and the conduction band of titania. In addition, the dye should absorb light in the

visible region of the solar spectrum to harvest sunlight effectively. The surface of titania should be penetrated by the redox solution electrolyte which is normally iodine solution. The general design for DSSC is shown in the following figure<sup>(36)</sup>:

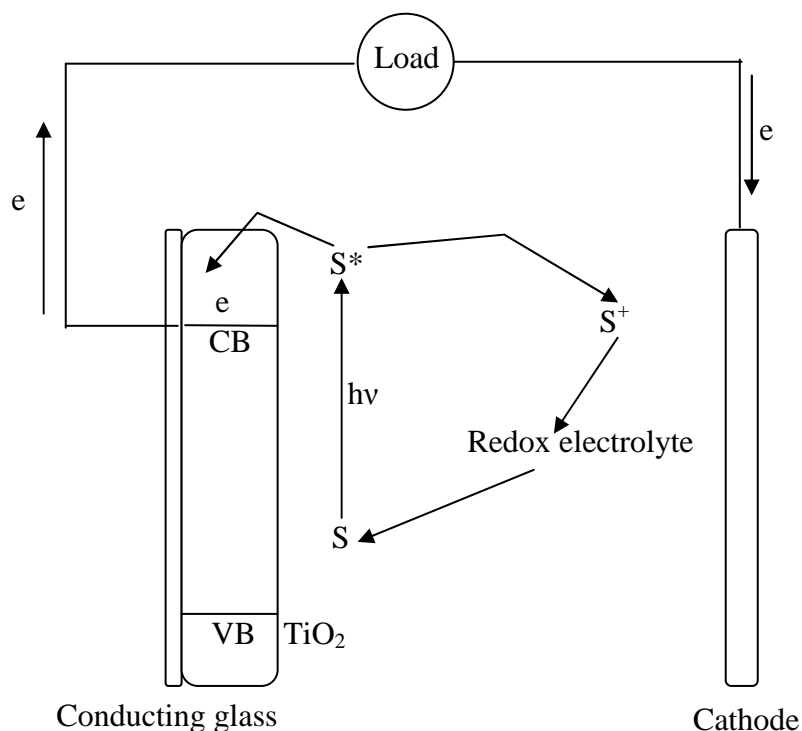


**Figure 6-6:** Principle of operation of the proposed DSSC.

When the dye absorbs light it converts into an excited state (singlet or triplet), which then injects electrons into the conduction band of titania, and then regeneration of the ground state of the dye via reduction with redox electrolyte ( $I/I_3^-$ ) to provide the required charge separation. After the excitation process, charge injection would occur and electrons are transferred and collected at the transparent conducting electrode, while holes are collected at the Pt electrode<sup>(37)</sup>. The first researchers in this field of photovoltaic application were Grätzel and Regan<sup>(38)</sup> who further developed this system extensively by optimization of the design the cell, the redox electrolyte are dye, and the inorganic semiconductor. The efficiency of this device was around 11% for the system using iodine as a redox electrolyte. However, this system has some drawbacks such as long- term stability and complexity in manufacture<sup>(39)</sup>. Production of this system for commercial mass usage is not possible due to several reasons. For example, the presence of the volatile  $I_2$  and volatile solvent require suitable sealing and the redox electrolyte ( $I/I_3^-$ ) is corrosive for the cell electrodes. For these reasons, alternative cells employing different redox systems have been investigated. These redox systems involve  $I/I_3^-$  in the solid or gel phase<sup>(39-41)</sup>, ionic liquids<sup>(42)</sup>, plastic crystals<sup>(43)</sup> and small organic molecules<sup>(44)</sup>. However, the efficiency for the cell when using this redox system was lower than 11%. This is probably as a result of

the reduction of hole mobility, low rates of electron transfer and weak communication between the dye and redox system. Recently, Grätzel and co-workers<sup>(45)</sup> developed an alternative DSSC by replacing the ruthenium-iodide system with two metal containing porphyrin dyes as co-sensitizers with the use of  $\text{Co}^{\text{II/III}}$  tris(bipyridal) as a redox electrolyte instead of  $(\text{I}/\text{I}_3^-)$  in conjugation with a co-sensitizer of two porphyrin dyes with zinc. This system can improve absorption of high portion of sunlight and increase electron exchange that results in improvement efficiency of the conversion of sunlight into power to 12.3%. This power conversion was achieved under irradiation with solar light intensity of  $1000 \text{ W/m}^2$  at 298K.

#### **6-4-2 General design of dyes for DSSCs**

Much effort has been focused on improving the efficiency of DSSCs by optimization of the dye photosensitizer used to harvest the light. Development of the dye has involved modification of the metal and the ligands as well as other subsistent groups used in the photosensitizer complex<sup>(46-48)</sup>. This has involved both mononuclear<sup>(49)</sup> and polynuclear dyes with different metals e.g. Ru(II), Os(II), Pt(II), Re(I), Cu(I) and Fe(II)<sup>(50, 51-56)</sup>. In addition to metal-complex dyes, some organic photosensitizer dyes such as coumarin, squaraine, indoline, and other molecules of conjugated donor/ acceptor organic dyes have been investigated<sup>(57-61)</sup>. Generally, the dye and the photosensitizer used in DSSCs must have some essential design properties as mentioned earlier to achieve high efficiency for harvesting light and conversion of this light into electrical power<sup>(62)</sup>. Common complexes include  $\{(4,4' \text{-CO}_2\text{H})_2\text{bipy}\}_2\text{Ru}(\text{NCS})_2$ , coded as (N3) and the doubly deprotonated analogue which is coded (N719). Ru complex with terpyridal ligands produced an anionic Ru-terpyridine complex system that is called black dye, which provides good efficiency of the incident monochromatic photon- to- current conversion efficiency (IPCE) in the range of 400- 700 nm with cell efficiency more than 10%. This dye is used as a reference dye in this system and the efficiencies of other dyes are normally referenced to it<sup>(63, 64)</sup>.

#### **6-4-3 Methods of attaching dye to semiconductor in DSSCs**

Acidic groups, mainly carboxylic acid groups, or sometimes phosphonic acid linkers attach most of the dyes to the surface of inorganic semiconductor<sup>(65)</sup>. There are other types of moieties can be used in the linkage between the dye and titania, but these types are not commonly used in DSSCs<sup>(65, 66)</sup>. Carboxylic acid groups form ester bonding with the titania surface generating strong contact between dye and the surface and as a result of this good electronic communication between dye and the surface is achieved. Although high

efficiency DSSCs uses this type of linker between these two parts in the cell, the main disadvantage of this relates to the stability of the cell. Dye attached to titania by carboxylic acid groups may be desorbed from the surface in the presence of traces of water, which consequently impact seriously on the long term stability of the cell. However, this effect can be reduced by the introduction of hydrophobic groups in the dye which can enhance stability of the dye towards desorption induced by the presence of traces of water in the liquid or gel redox electrolyte. It was reported that used a polymer gel  $I^-/I_3^-$  electrolyte instead of aqueous redox electrolyte and the system showed a good stability towards both prolonged thermal treatment and light soaking similar to expected outdoor conditions for solar cells<sup>(67)</sup>. A significant loss mechanism that involves recombination of electrons from the conduction band of titania with the redox electrolyte, called the dark current, can also be inhibited by using dyes with hydrophobic groups attached. These dyes would form a hydrophobic network preventing the interaction between the surface of titania and  $I_3^-$ , effectively this loss<sup>(67)</sup>. In another study, DSSC with phosphonic acid linkers showed efficiency greater than 8% for a non-carboxylic acid linker. However, this type showed some characteristic changes in comparison with the first type, such as blue shift in the absorption region, enhanced stability and a relatively slower rate of charge recombination<sup>(64)</sup>.

## 6-5 Ruthenium complexes for dye sensitized solar cells

DSSCs in comparison with traditional silicon-based solar cells have received much attention as promising candidates for new technology to produce renewable energy from sunlight. This arises from their relatively low manufacture cost, and impressive photovoltaic performance. Photosensitizers are fall into two categories: Ru-base photosensitizer complexes and metal free organic photosensitizers<sup>(68, 69)</sup>. Ru(II) complexes used widely as photosensitizes for solar cells. These complexes have been used effectively due to their intense transition in visible light with high molar extinction coefficient for metal to ligand charge transfer (MLCT). In addition, ruthenium photosensitizer solar cells showed relative stability in both reduced and oxidized states and their absorption spectrum can be tuned easily via incorporation an appropriate ligand<sup>(70-73)</sup>. Introducing  $\pi$ -conjugated groups with ancillary ligands and substituting one of the H atoms of the carboxylic group in the bipyridal moiety of the anchor ligand with a highly conjugated group can result in an increase of the extinction coefficient to higher values. This would result in an increase in the photocurrent density of the DSSCs<sup>(74-76)</sup>. Nguyen and co-workers<sup>(77)</sup> reported the synthesis of some heteroleptic Ru(II) complexes with conjugated bipyridine ligands. Maximum power conversion efficiency 14% was obtained in reference

to dye N3 under the same cell fabrication and measurement procedure. It is believed that this higher efficiency was related to the enhancement of the molar extinction coefficient that can facilitate charge generation cascade and at the same time reduce charge recombination. Structures of these dyes are shown in the following figure<sup>(77)</sup>:

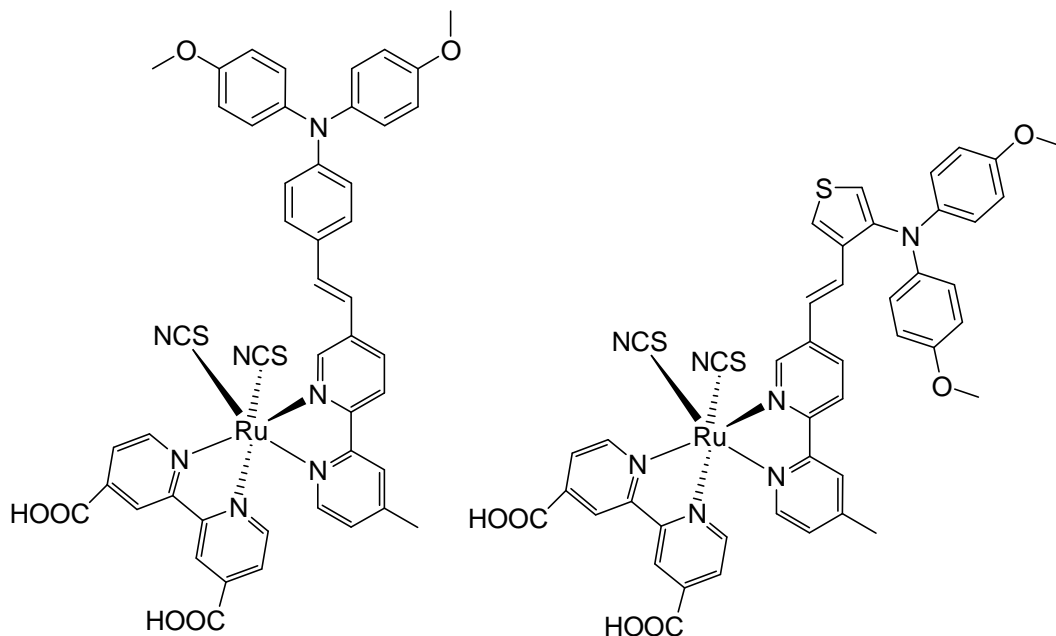


**Figure 6-7:** DSSCs of Ru(II) complexes containing conjugated bipyridine ligands<sup>(77)</sup>.

### 6-6 The general aim

The aim of the work described in this chapter is the synthesis of some Ru (II) complexes with a phenanthroline core due to their excellent chelating properties. These types of compounds and their polymeric derivatives can be used in many potential applications such as luminescence and materials chemistry as well as dye sensitized solar cells.

### 6-7 Results and Discussion

The compounds **32- 36** have been targeted for synthesis as these compounds and/ or their polymeric or other derivatives are potentially useful for application as photoactive and electroactive molecular systems, luminescence devices, photovoltaic materials, and in coordination chemistry. The structures of these compounds are shown in the following figure:

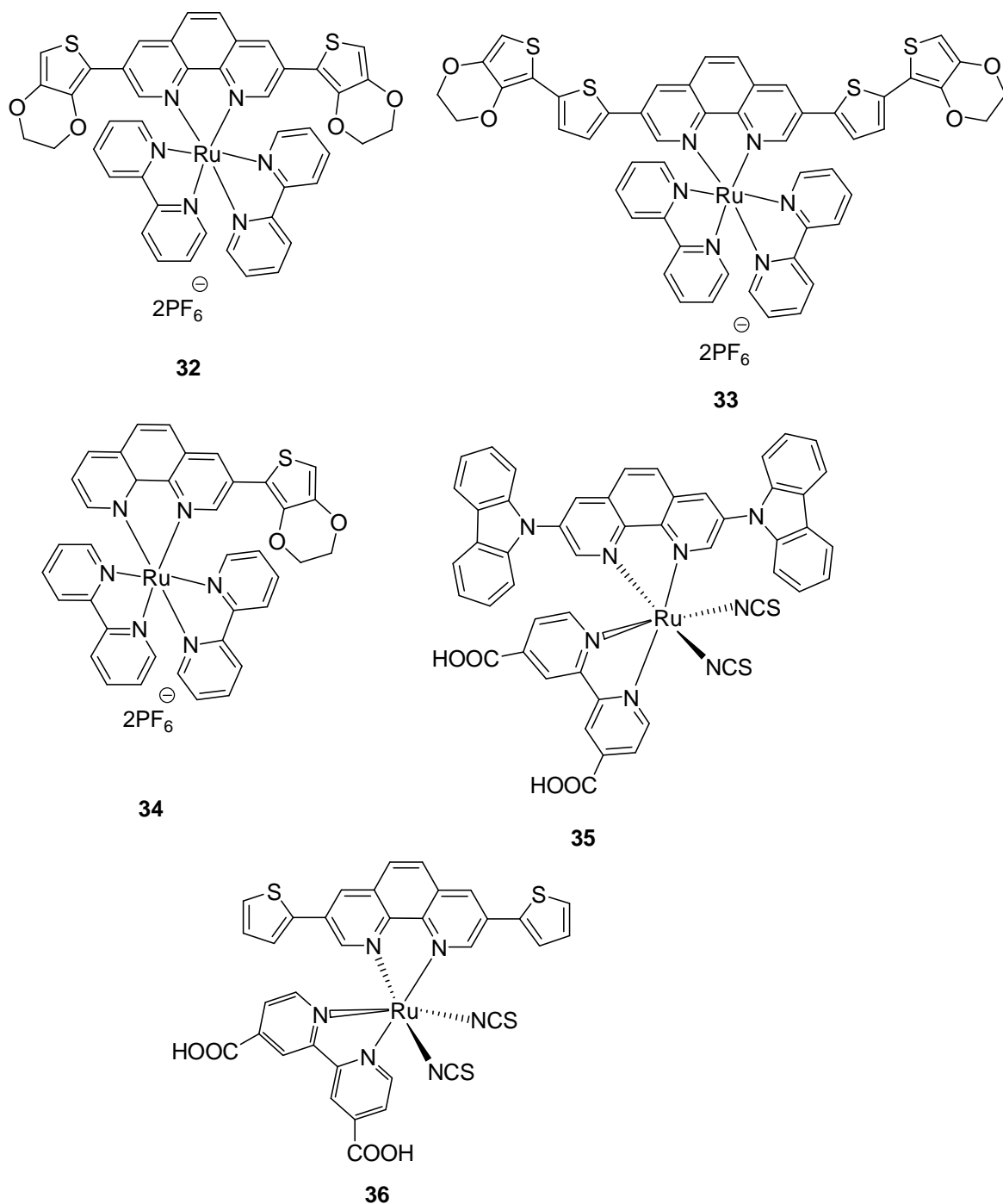
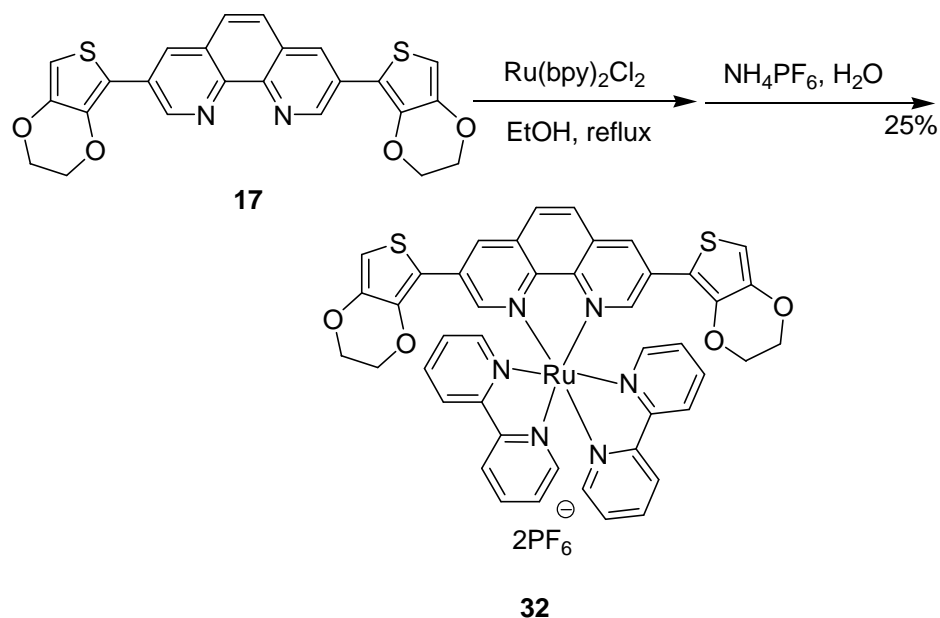


**Figure 6-8:** Structures of the targeted compounds.

### 6-7-1 Synthesis of compound 32

The proposed synthesis of compound **32** starts with compound **17**. This would react with dichloro-bis(2,2'-bipyridyl) ruthenium(II) ( $\text{Ru}(\text{bipy})_2\text{Cl}_2$ ). The synthesis is shown in the following scheme:



**Scheme 6-9:** The synthetic route of compound **32**.

Stoichiometric reaction of compound **17** with Ru(II) complex followed by the addition of  $\text{NH}_4\text{PF}_6$  afforded compound **32** as an orange powder.

#### 6-7-1-2 Analysis of compound **32**

Crystals suitable for X-ray crystallography were obtained by slow evaporation of a 1:1 mixture of acetonitrile/ diethyl ether<sup>(78)</sup>. The molecular structure of compound **32** was confirmed by X-ray crystallography. The complex **32** ( $\text{C}_{44}\text{H}_{32}\text{F}_{12}\text{N}_6\text{O}_4\text{P}_2\text{F}_{12}\text{S}_2\text{Ru}$ ,  $M=1163.40$ ), has a monoclinic space group  $C2/c$ , the unit cell dimensions of which are  $a=12.1077(7)$  Å,  $b=27.6852(18)$  Å,  $c=29.0080(2)$  Å,  $\alpha=90^\circ$ ,  $\beta=101.665(6)^\circ$ ,  $\gamma=90^\circ$ . The crystal volume was  $9522.6(11)$  Å<sup>3</sup>. The complex has distorted octahedral geometry and Ru-N bond lengths [ $1.570(6)$  Å] of bpy and [ $2.057(6)$  Å]. The X-ray structure of complex **32** as determined by X-ray crystallography is shown in the following figure:

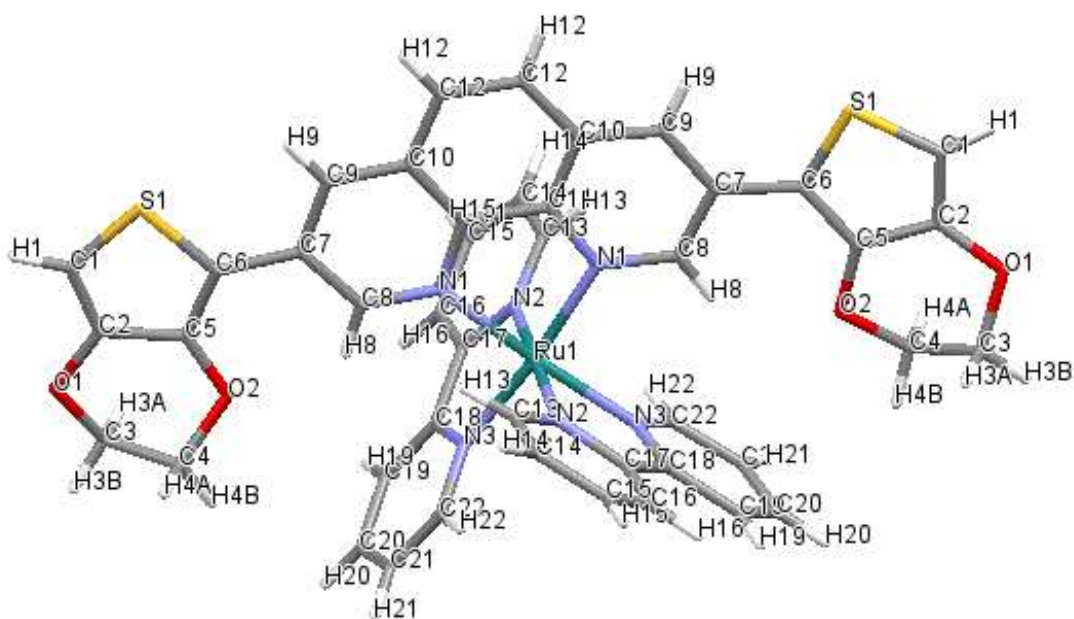


**Figure 6-10:** X-ray crystal structure of compound **32**, hydrogen atoms,  $\text{PF}_6^-$  anion and solvated MeCN and diethyl ether are omitted for clarity.

### 6-7-1-3 UV-visible spectrum of compound **32**

The UV-vis spectrum of compound **32** was measured in MeCN. The absorption spectrum of this compound exhibits three absorption peaks at 287 nm, 390 nm and 414 nm and a shoulder at 468 nm. The optically determined HOMO-LUMO bandgap at higher wavelength is 2.36 eV. The first peak is due to the  $\pi$ - $\pi^*$  transitions between donating moiety such as EDOT group and the accepting moieties such as phenanthroline and bpy ligands. The peak at 390 nm is related to the charge transfer transition between electron donating group (EDOT) to the electron- accepting group (1,10-phenanthroline). The band at 390 nm is related to the charge transfer transitions between the electron donating group (EDOT) and electron accepting group (1,10-phenanthroline)<sup>(79,80)</sup>. However, the complex **32** shows ruthenium complex bands at 287 and 414 nm respectively, assigned to the characteristic  $\text{bpy}(\pi$ - $\pi^*)$  transitions, and  $\text{Ru}^{\text{II}}(\text{d}\pi)$  to the  $\text{bpy}(\text{p}\pi^*)$  and to the phen( $\text{p}\pi^*$ ) charge transfer transition. The broad peak at 414 nm is related to the metal- ligand charge transfer transitions. This transfer normally occurs in the range of 400- 500 nm. Generally, presence of a red shift in the absorption spectrum of the complex is related to the effect of Ru(II) complex coordination on the conjugated  $\pi$  system<sup>(81)</sup>. In addition, there is a weak band at 350 nm which could be assigned to a d-d transitions and which may be hidden in the case of more intense  $\pi$ - $\pi^*$  bands nearby<sup>(82)</sup>. The UV-visible spectrum for this compound is shown in the following figure:

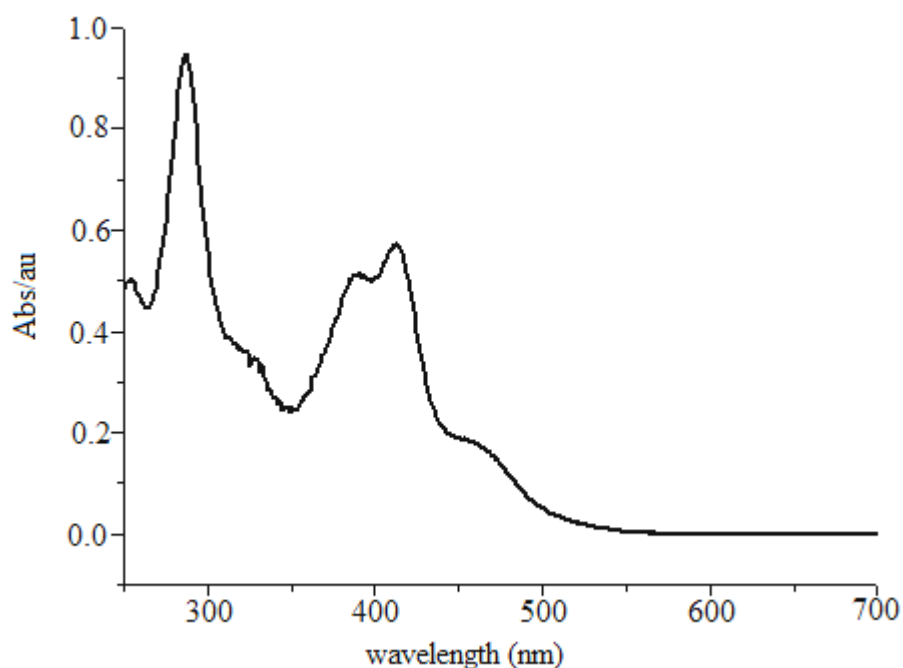


**Figure 6-11:** UV- visible spectrum of compound **32**. Recorded in MeCN ( $1 \times 10^{-4}$  M).

#### **6-7-1-4 The voltammogram of compound 32**

The voltammogram of this compound was recorded in MeCN. In the oxidation region, Ru(II) complex showed two characteristic oxidation couples at 0.25 V and 0.75 V which can be assigned to  $\text{Ru}^{\text{III}}/\text{Ru}^{\text{II}}$  <sup>(83)</sup>. This complex showed three reversible redox couples at -1.40 V, -1.65 V and -1.88 V. These peaks are related to the reduction of the chelating ligands in the complex. The assignment of the reduction peaks is not trivial, and the reduction process at -1.40 V is believed to be associated with the monoelectronic reduction of the phenanthroline ligand. The other peaks at -1.65 and -1.88 V can be assigned to the successive monoelectronic reductions of each bpy ligand <sup>(84)</sup>. The voltammogram of compound **32** is shown in the following figure:

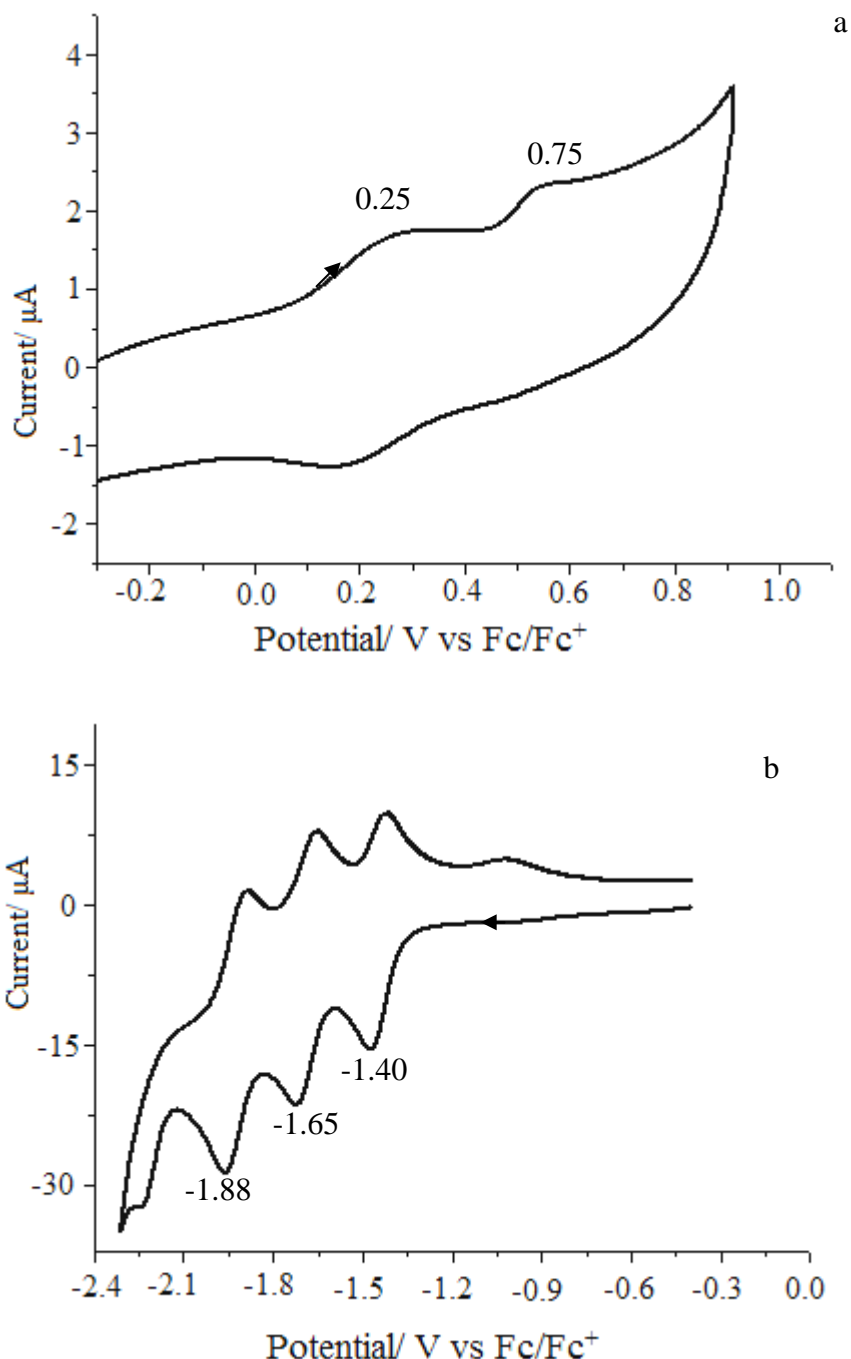


**Figure 6-12:** The voltammogram of compound **32**, oxidation (a) and reduction (b) recorded using a glassy carbon working electrode, an Ag wire as a pseudo reference electrode and a Pt wire as a counter electrode. Recorded at a concentration of  $1 \times 10^{-4}$  M in MeCN with TBAPF<sub>6</sub> (0.1 M) as a supporting electrolyte. Scan rate of  $100 \text{ mV s}^{-1}$ .

The electrochemical data of this compound are summarised in the following table:

**Table 6- 1:** Electrochemical data for monomer complex **32**.

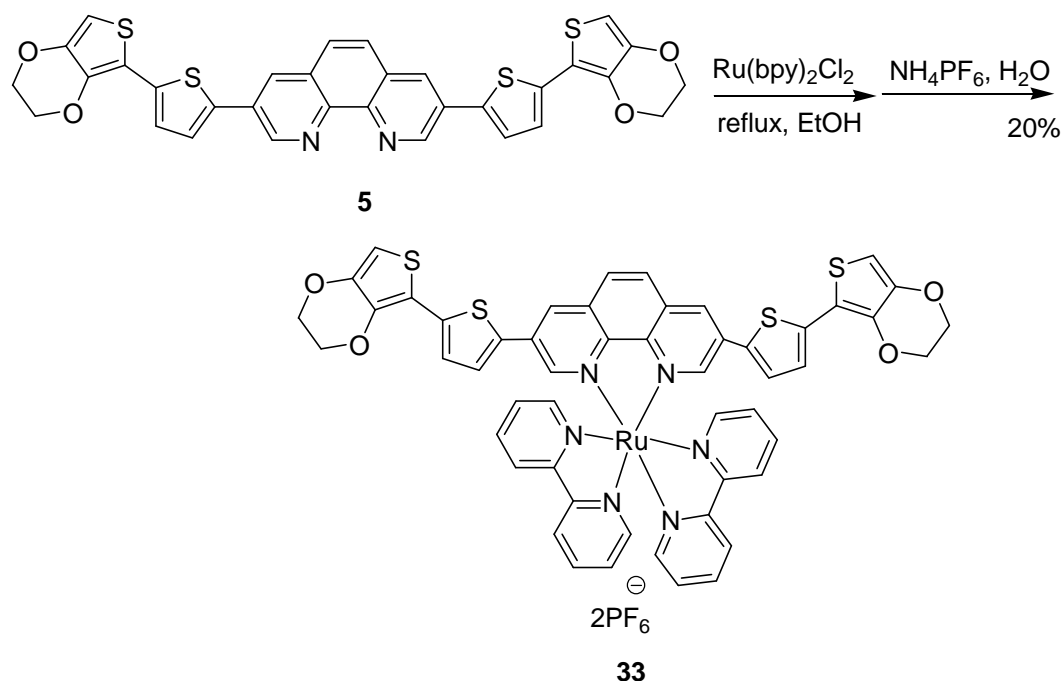
Onset of oxidation / V	HOMO / eV	Onset of reduction / V	LUMO /eV	HOMO-LUMO bandgap /eV
+ 0. 71	- 4.87	-1.35	-3.45	1.42

### 6-7-1-5 Electrochemical polymerisation of compound 32

Many attempts were made to electropolymerize compound **32** by varying experimental conditions. However, successive oxidation/ reduction sweeps were undertaken. For polymerization to proceed new peaks should be observed at roughly 0.2 V. The magnitude of the increment that would be expected to increase with the number of scans<sup>(85)</sup>. However, polymerization didn't occur, in spite of some new oxidation waves which developed under repeated cycling. However, these waves did not increase in intensity upon repeated redox cycling. This suggests that the molecule being produced is not sufficiently larger than the initial monomer molecule or at most is a dimer.

### 6-7-2 Synthesis of target compound 33

To provide a candidate that was more likely to undergo electropolymerization we decided to synthesize compound **33**. The proposed synthesis of **33** was to start with compound **5** which would be reacted with the dichloro-bis(2,2'-bipyridyl) ruthenium(II) complex. The reaction scheme is shown below:



**Scheme 6-13:** The synthesis of compound **33**.

Compound **5** and the ruthenium (II) complex were mixed and dissolved in  $\text{EtOH}$ , the mixture was heated under reflux in air. Then this mixture was treated with  $\text{NH}_4\text{PF}_6$  to afford compound **33** as an orange/ red powder<sup>(80)</sup>.

### 6-7-2-1 Analysis of compound 33

The UV- visible spectrum and the voltammogram of this compound were measured in acetonitrile. The absorption spectrum of this compound exhibits three peaks at 241 nm, 286 nm and 450 nm. Coordination of {Ru(bpy)<sub>2</sub>} with the phenanthroline core should affect the electronic properties of the phenanthroline ring which may affect the degree of the conjugation between EDOT/ thiophene and phenanthroline ring. This compound showed ruthenium complex bands at 286 and 450 nm, which would be related to the characteristic bpy ( $\pi$ -  $\pi^*$ ) transitions and Ru<sup>II</sup>(d $\pi$ ) to the bpy (p $\pi^*$ ) and to the phen (p $\pi^*$ ) charge transfer transition<sup>(78,79)</sup>. The band at 241 nm may be related to the EDOT  $\pi$ -  $\pi^*$  transition. Additionally, the broad peak at 450 nm also can be related to MLCT transition. This transfer normally occurs in the range of 400- 500 nm<sup>(85,86)</sup>. Generally, presence of red shift in the absorption of the complex is related to the effect of Ru(II) complex coordination on the conjugated  $\pi$  system<sup>(81)</sup>. The optically determined HOMO-LUMO bandgap is 2.32 eV. The UV- visible spectrum is shown in the following figure:

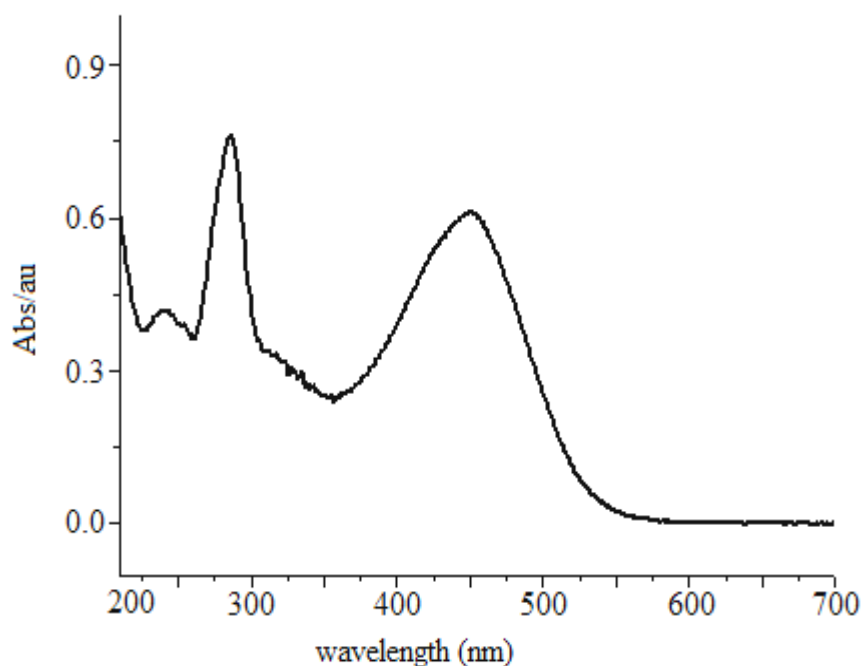


**Figure 6-14:** UV-visible spectrum of compound **33**. Recorded in MeCN ( $1 \times 10^{-4}$  M).

The voltammogram of compound **33** was recorded in MeCN. In the oxidation region, the Ru(II) complex showed two characteristic oxidation couples at 0.82, and 1.16 V. It has been reported that these are assigned to the Ru<sup>III</sup>/ Ru<sup>II</sup> processes<sup>(83)</sup>. In the reduction region, this complex showed reversible reduction couples at -1.30 V, -1.60 V, -1.80 V and -1.90 V. These reduction couples are related to the reduction of the chelating ligands in the complex. The reduction process at -1.30 V is believed to be associated to the

monoelectronic reduction of the phenanthroline ligand. The other peaks at -1.60 V, -1.80 V and -1.90 V could be assigned to the successive monoelectronic reductions of each bpy ligands<sup>(86)</sup>. The voltammogram of this complex is shown in the following figure:

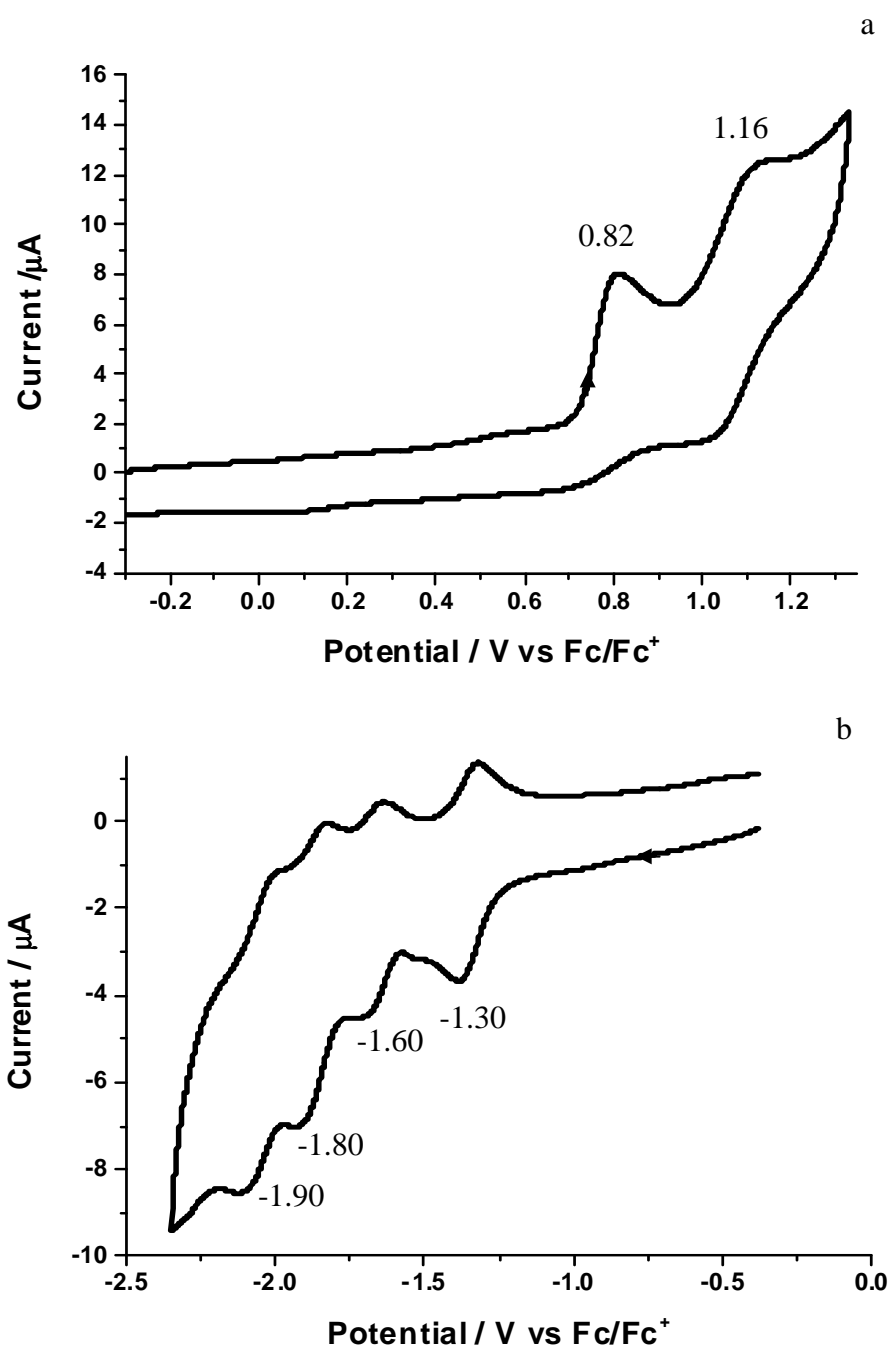


**Figure 6-15:** The voltammogram of compound **33**, oxidation (a) and reduction (b) recorded using a glassy carbon working electrode, an Ag wire as a pseudo reference electrode and a Pt wire as a counter electrode. Recorded at a concentration of  $1 \times 10^{-4}$  M in MeCN with TBAPF<sub>6</sub> (0.1 M) as a supporting electrolyte. Scan rate of  $100 \text{ mV s}^{-1}$ .

Electrochemical data of monomer concentration  $1 \times 10^{-4}$  M of compound **33** are summarised in the following table:

**Table 6-2:** Electrochemical data for monomer complex **33**.

Onset of oxidation / V	HOMO / eV	Onset of reduction / V	LUMO / eV	HOMO-LUMO bangap / eV
+ 0.75	-5.55	-1.34	-3.46	2.09

### 6-7-2-2 Electropolymerization of compound **33**

The electropolymerization of compound **33** was performed in CH<sub>3</sub>CN to form poly(**33**) as shown below. The CV of compound **33** in the scan range of 0.10 to 1.20 V (vs Fc/ Fc<sup>+</sup>) showed evidence of polymer growth. Repeat scan cycles in this range results in polymer growth as a thin film on the working electrode. Evidence for polymer growth of poly(**33**) on the electrode is shown in the following figure:

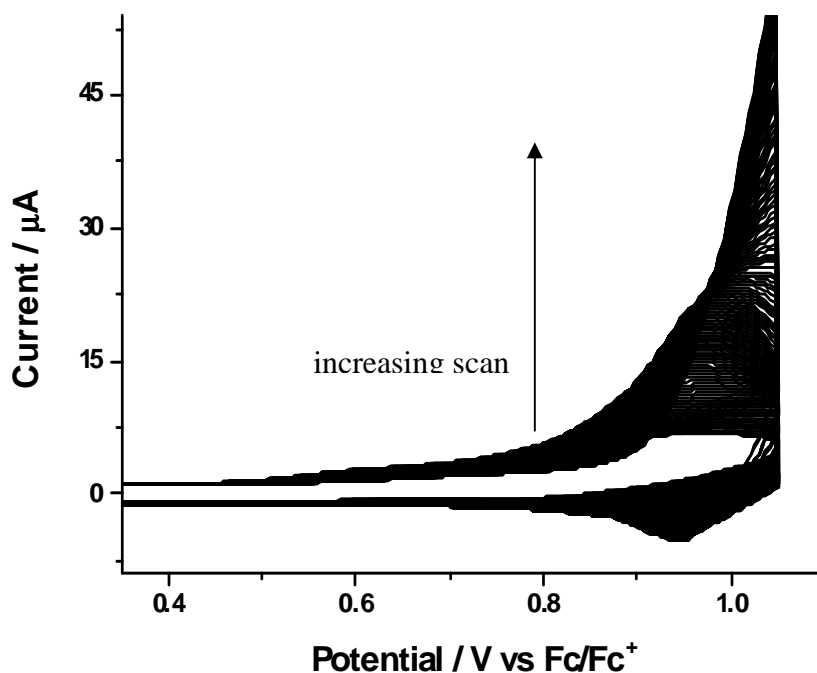


**Figure 6-16:** The voltammogram of growth poly(**33**) recorded using a glassy carbon working electrode, an Ag wire as a reference electrode and a Pt wire as a counter electrode. Recorded at a concentration of  $1 \times 10^{-4}$  M in MeCN with TBAPF<sub>6</sub> (0.1 M) as a supporting electrolyte. Scan rate of  $100 \text{ mV s}^{-1}$  over 300 segments.

The voltammogram of poly(**33**) as a thin film was performed on a glassy carbon electrode. The CV exhibited two reversible processes in the range (0.0- 1.0 V) at 0.40 V and 0.75 V. These peaks may be related to the oxidation of the ligand and to the Ru<sup>III</sup>/ Ru<sup>II</sup> processes respectively. On the reverse scan the reduction peak may be related to the reduction of the

oxidized electrochemically generated species of poly(**33**). The bandgap for poly(**33**) was determined by using cyclic voltammetry to find the HOMO and LUMO levels. This can be done by undertaken by subtracting the oxidation onset and reduction onset from the HOMO and LUMO levels of ferrocene. The calculated bandgap for the polymer was 1.78 eV. The voltammogram of poly(**33**) is shown in the following figure:

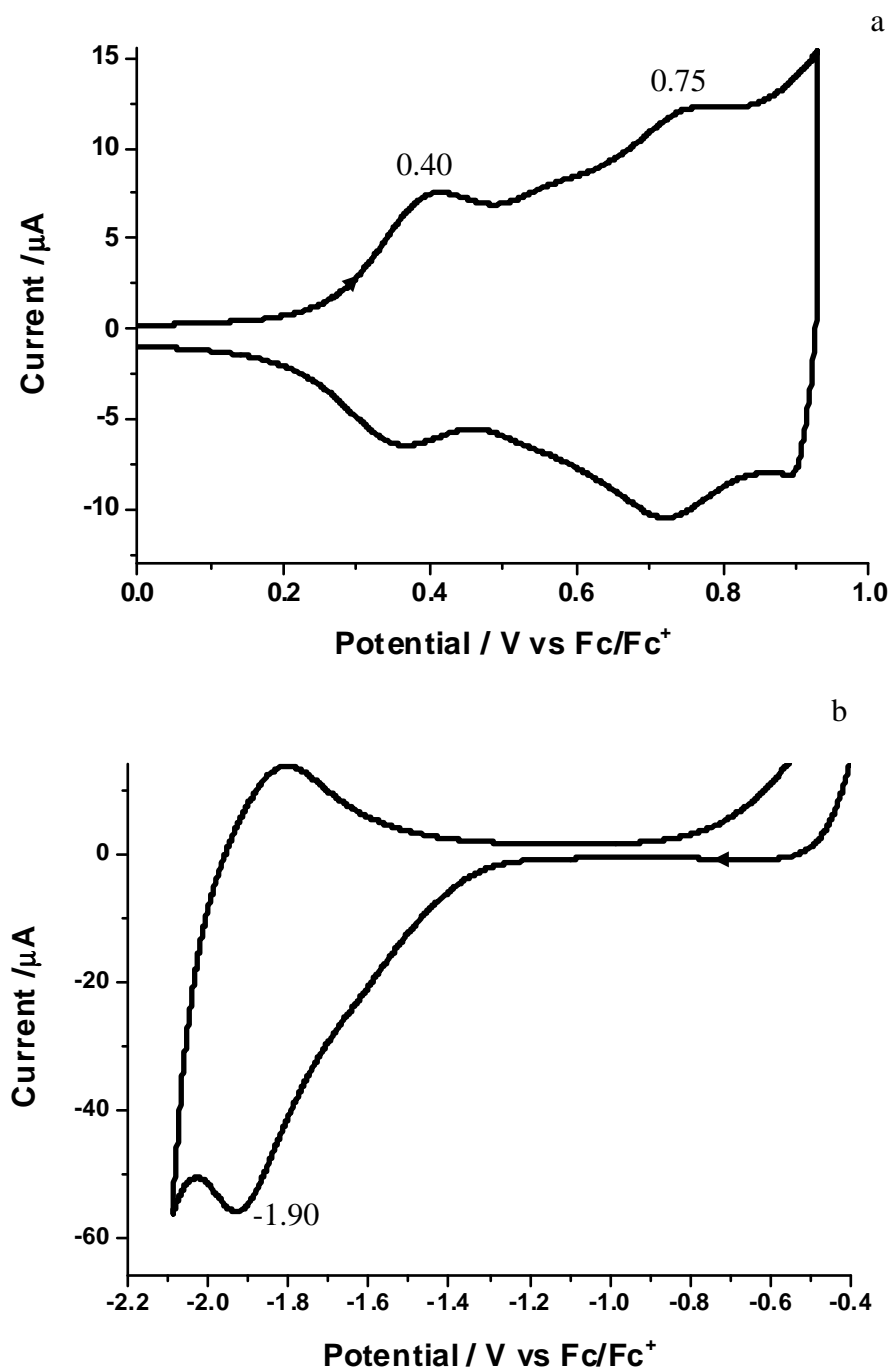


**Figure 6-17:** The voltammogram of oxidation (a) and reduction (b) of poly(**33**) as a thin film recorded using a glassy carbon working electrode, an Ag wire as a reference electrode and a Pt wire as a counter electrode. Recorded in monomer-free DCM with  $\text{TBAPF}_6$  (0.1 M) as a supporting electrolyte. Scan rate of  $100 \text{ mV s}^{-1}$ .

The electrochemical data for poly(**33**) is shown in the following table:

**Table 6-3:** Electrochemical data for poly(**33**).

Onset of oxidation / V	HOMO / eV	Onset of reduction / V	LUMO / eV	HOMO-LUMO bangap / eV
+ 0.27	-5.07	-1.51	-3.29	1.78

The peak currents of the thin film of poly(**33**) deposited on the electrode was recorded in electrolyte- free solution. This showed that current varies linearly with change of the rate of electrochemical scan ranged from  $25 \text{ mV s}^{-1}$  to  $500 \text{ mV s}^{-1}$ . This behaviour is related to the strongly adsorbed electroactive species in the thin film on the electrode. The scan rate graph of poly(**33**) in monomer-free DCM at varying scan rates is shown in Figure 6-18. A graph of peak current versus scan rate of poly(**33**) in monomer- free DCM is shown in Figure 6-19.

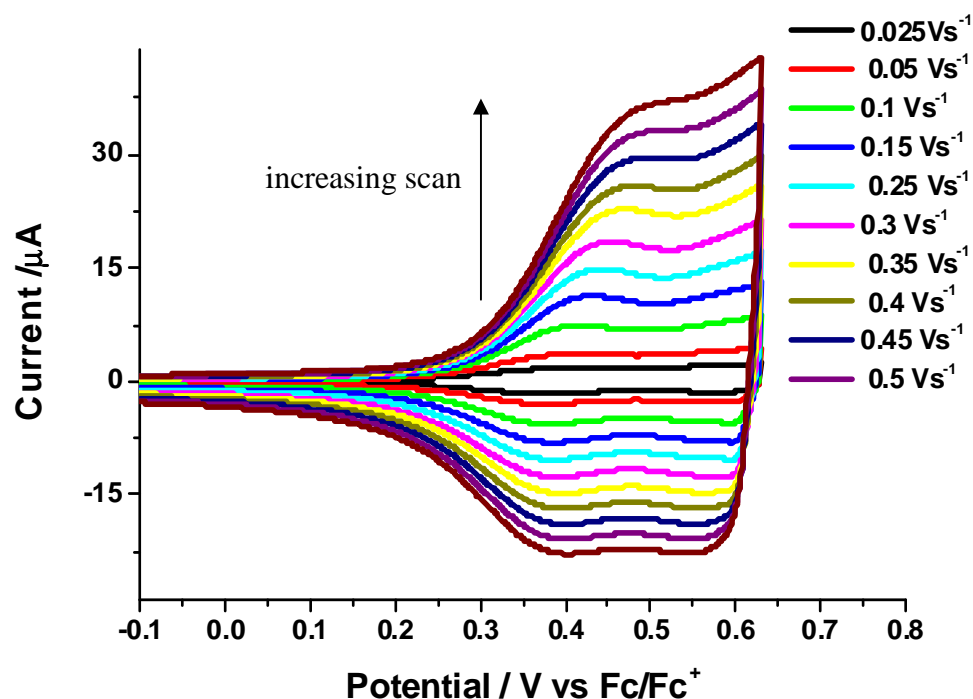


**Figure 6-18:** Scan rate graph of poly(**33**) in monomer free dichloromethane at varying scan rates:  $25\text{-}500 \text{ mVs}^{-1}$ .

A plot scan rate against peak maxima for poly(**33**) is shown in the following figure:

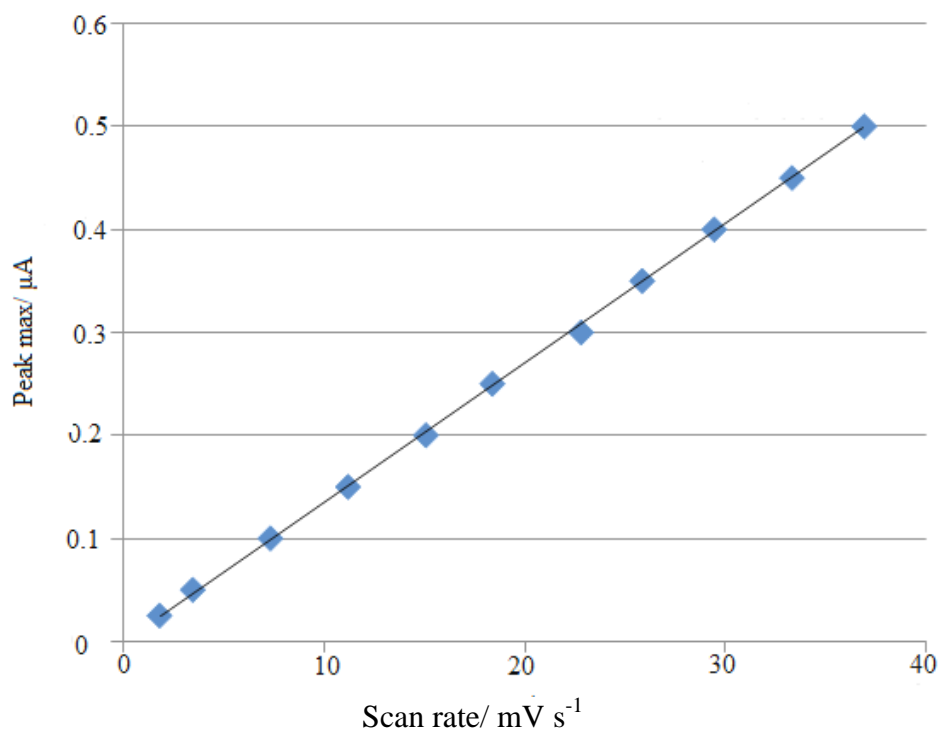


**Figure 6-19:** The scan rate versus peak current maxima of poly(**33**).

From this figure, it can be seen that, there is a linear relationship between the peak currents, and the scan rate indicating the electroactive species is confined on the surface of electrode. The oxidation stability of poly(**33**) in monomer- free dichloromethane at a scan rate of  $100 \text{ mV s}^{-1}$  over 100 segments is shown in the following figure:

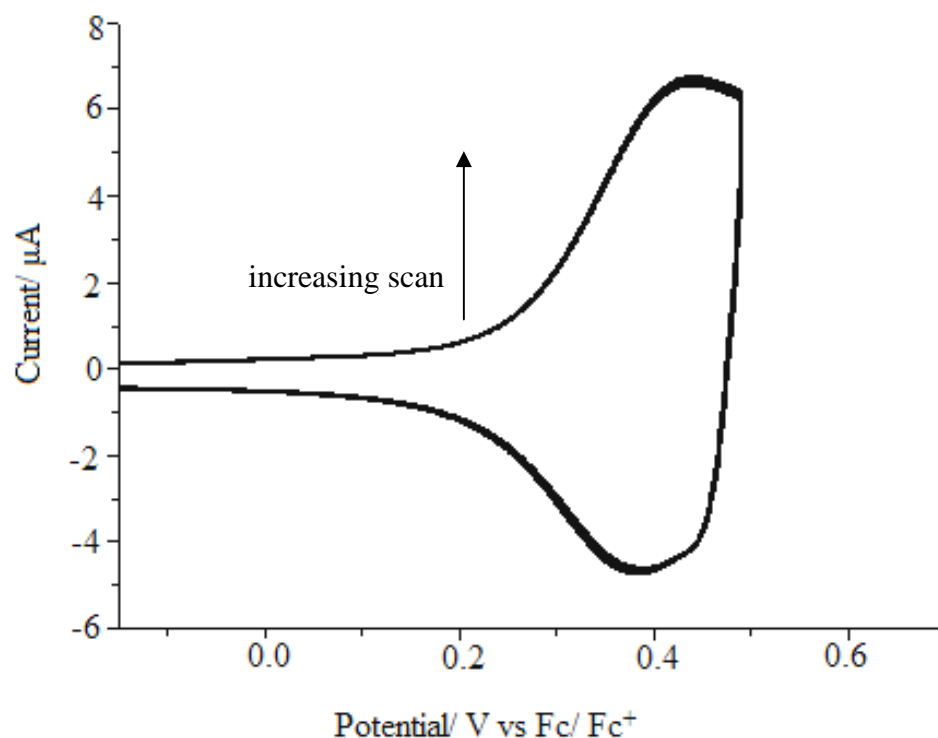


**Figure 6-20:** The voltammogram for oxidation stability of poly(**33**) recorded using a glassy carbon working electrode, an Ag wire as a reference electrode and a Pt wire as a counter electrode. Recorded in monomer- free DCM with TBAPF<sub>6</sub> (0.1M) as a supporting electrolyte. Scan rate of 100 mV s<sup>-1</sup> over 100 segments.

The UV-visible spectrum of doped and de-doped of poly(**33**) as a thin film was performed on ITO glass. The UV- visible spectrum of poly(**33**) showed a  $\lambda_{\text{max}}$  peak at 434 nm. The optically determined bandgap of 1.90 eV is slightly higher than the electrochemically determined bandgap in the polymer (1.78 eV). However, the film showed absorption bands in the visible region at 585 and 493 nm. These bands can be assigned to Ru<sup>II</sup> to the polypyridine and thiophene/ EDOT  $\pi$ -  $\pi^*$  transitions. The UV- visible spectrum of the film is shown in the following figure:

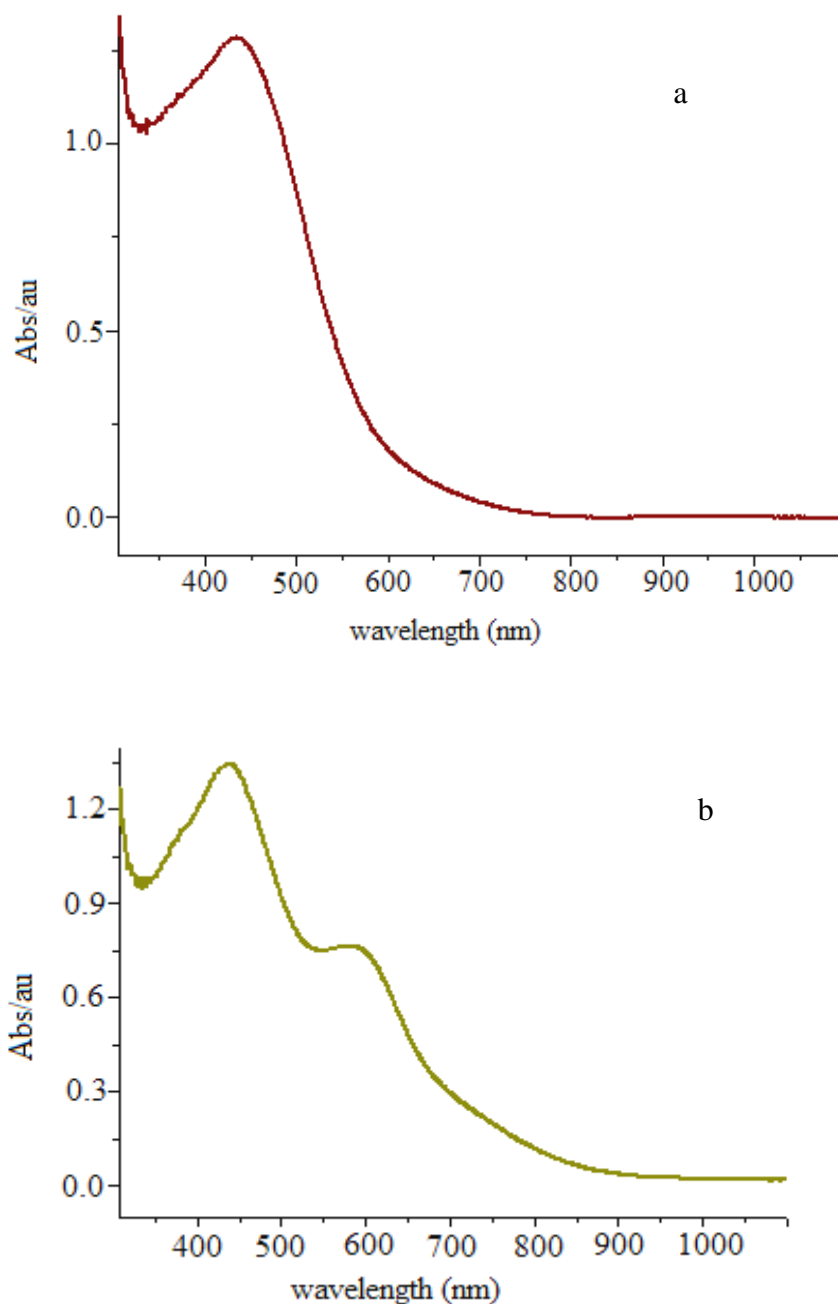


**Figure 6-21:** Absorption spectra of de-doped light brown (a) and doped dark yellow (b) of poly(33) as a thin film on ITO glass.

### 6-7-2-3 Spectroelectrochemistry of poly(33)

The spectroelectrochemistry of poly(33) is shown in Figure 6-22. The spectrum of poly(33) recorded at different applied potentials (from the neutral polymer to the fully oxidized states of the polymer). The neutral polymer shows absorption band at around 400 nm, this is due to the  $\pi$ - $\pi^*$  transitions of poly (EDOT)<sup>(87)</sup>. This may result in lower energy charge transfer absorption with the initial oxidation of the polymer. By increasing applied potential this peak continued until applied potential reaches 1.20 V, then it decreased at higher potential. Beyond this value there is a weak absorption peak at potential of 1.5 V,

this peak appears at higher wavelengths with an absorption tail at around 950 nm. This absorption peak may be related to the bipolaron states. The spectroelectrochemistry of poly(**33**) is shown in the following figure:

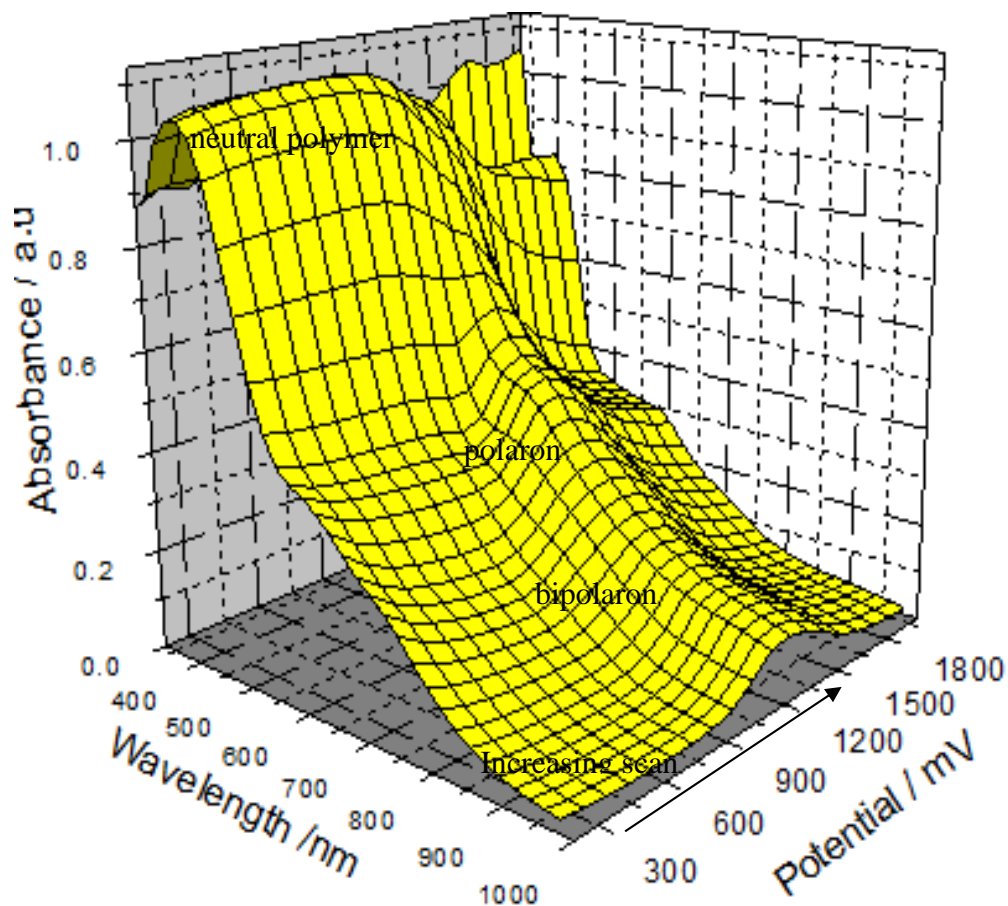
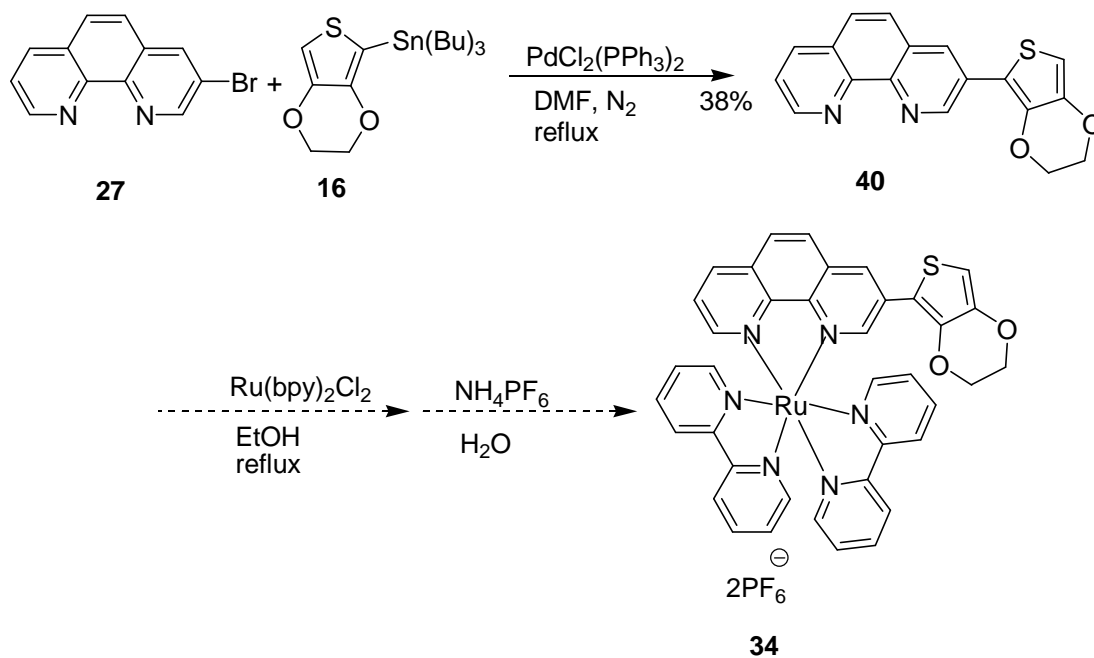


**Figure 6-22.** Spectroelectrochemical plot of p-doping poly(**33**) performed as a thin film deposited on ITO glass recorded, using an Ag wire as a reference electrode and a Pt wire as a counter electrode. Experiments were run in monomer-free DCM solution and in the presence of Bu<sub>4</sub>NPF.

### 6-7-3 Synthesis of target compounds **34** and **40**

The proposed synthesis of compound **34** starting from compound **27** as shown in the following scheme:



**Scheme 6-23:** Synthesis of compound **34**.

The synthesis of compound **40** was achieved from compound **27** and compound **16**. Then this compound was reacted with ruthenium (II) (bpy)<sub>2</sub>Cl<sub>2</sub>, the resulting mixture was treated with an aqueous solution of NH<sub>4</sub>PF<sub>6</sub> to afford **34** as the 2PF<sub>6</sub><sup>-</sup> salt<sup>(78)</sup>.

#### 6-7-3-1 Analysis of compound **40**

The UV- visible spectrum of compound **40** was recorded in DCM. This spectrum shows three bands at 234 nm, 283 nm and 340 nm. The first two peaks are related to the π-π\* transitions. The last peak at 340 nm is related to the π-π\* transitions between the EDOT ring and the phenanthroline core. The optically determined bandgap was found to be 3.10 eV. The UV-visible spectrum is shown in the following figure:

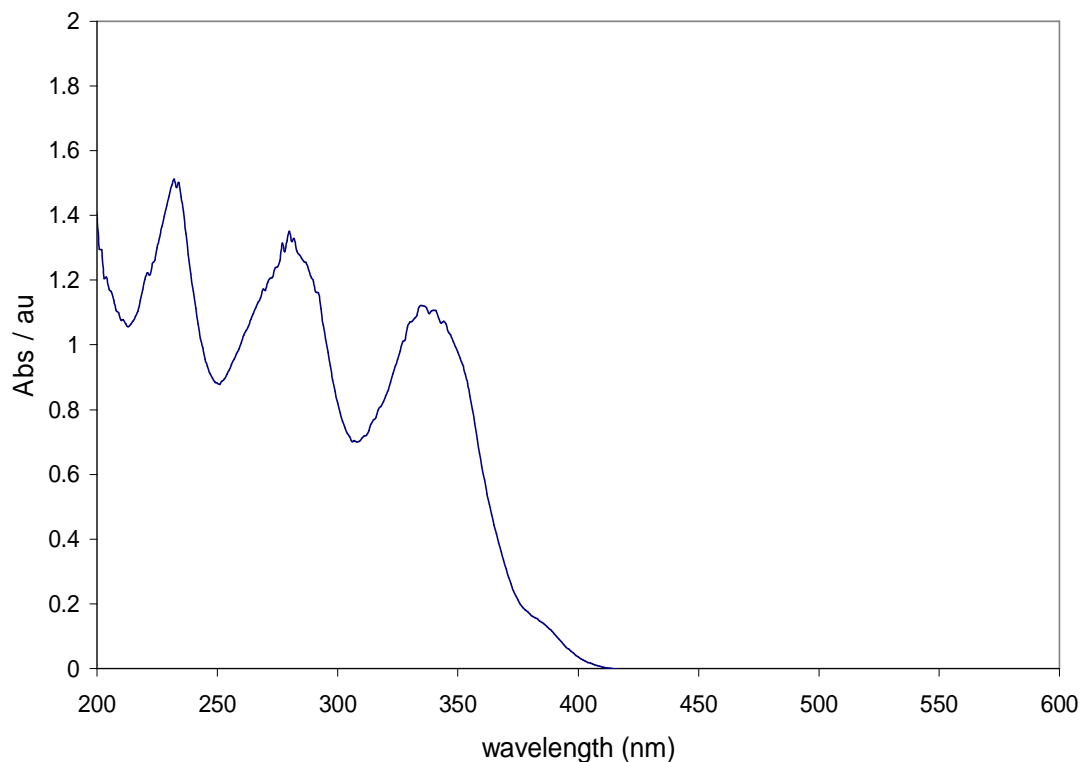


**Figure 6-24:** UV- visible spectrum for compound **40**. Recorded in DCM ( $1 \times 10^{-4}$  M).

#### 6-7-3-2 The voltammogram of compound **40**

The voltammogram of this compound was undertaken in DCM. The voltammogram of this compound shows two reduction peaks at -2.02 V and -2.37 V. In addition, it shows an oxidation peak at +1.07 V. The estimated HOMO energy level for this compound was -5.87 eV, and the estimated LUMO energy was -2.78 eV. The electrochemically determined bandgap was found to be 3.09 eV. The voltammogram of this compound is shown in the following figure:

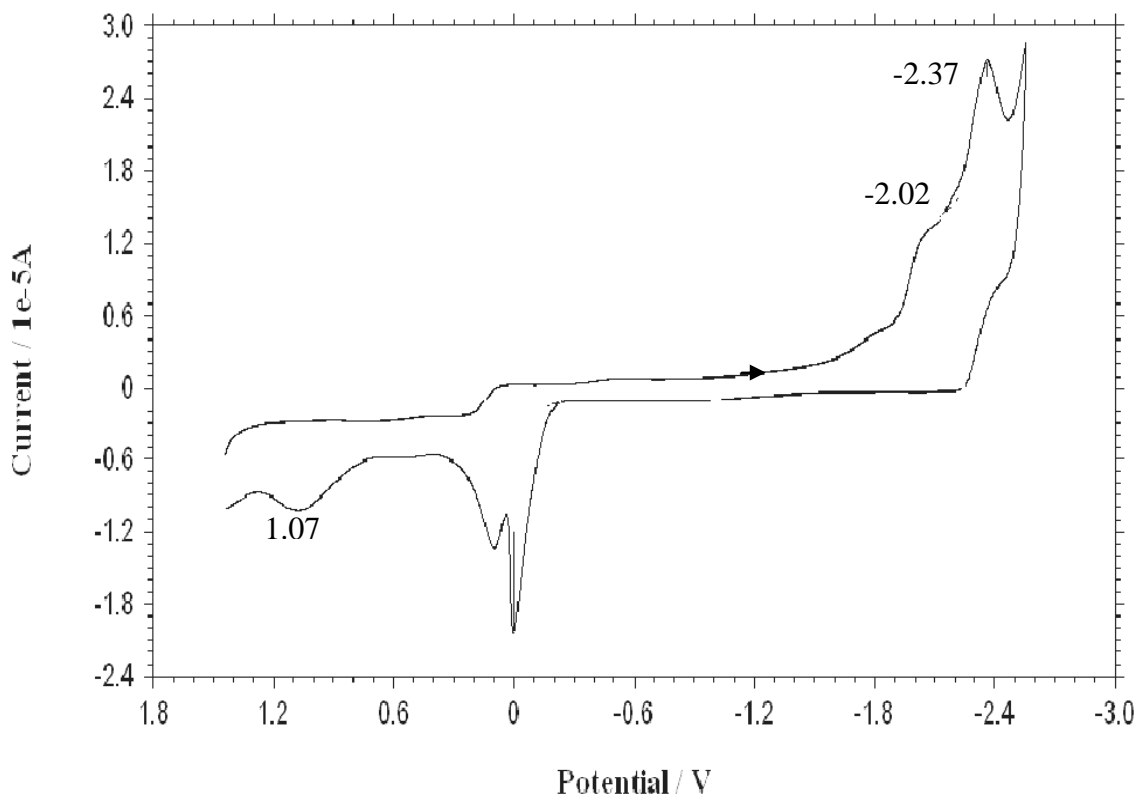


**Figure 6-25:** The voltammogram of compound **40** recorded using a glassy carbon working electrode, an Ag wire as a reference electrode and a Pt wire as a counter electrode. Recorded at a concentration of  $1 \times 10^{-4}$  M in DCM with TBAPF<sub>6</sub> (0.1 M) as a supporting electrolyte. Scan rate of  $100 \text{ mV s}^{-1}$ .

#### 6-7-4 Analysis of compound **34**

Many efforts were made to purify compound **34** such as washing, and recrystallization. In addition column chromatography using an eluent mixture of MeOH, H<sub>2</sub>O and NH<sub>4</sub>Cl (6:3:1) was applied. However, the product could not be obtained in high purity.

#### 6-8 Synthesis of dye sensitized solar cells (DSSCs)

The materials **35** and **36** were targeted for synthesis for application in DSSCs. Both of these dyes were synthesized in one reaction pot. The synthetic route for dye **35** is shown in the following scheme:

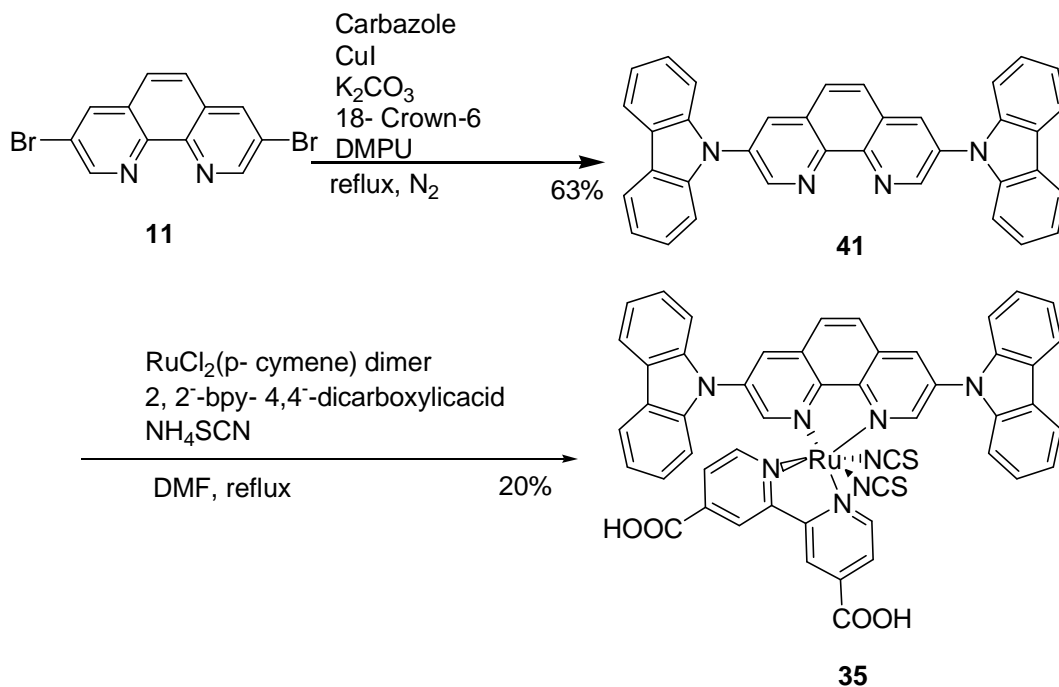


**Figure 6-26:** Synthesis of compound **35**.

The synthesis of compound **35** started from compound **11**. Compound **41** was synthesized by reacting of compound **11** with a mixture of 9*H*-carbazole, CuI, K<sub>2</sub>CO<sub>3</sub>, 18-crown-6 and DMPU. This mixture was heated under reflux in a N<sub>2</sub> atmosphere, and after purification with column chromatography yielded compound **41** as a yellow powder<sup>(88)</sup>. This compound was then used as a starting material in the synthesis of compound **35** by reaction with a mixture RuCl<sub>2</sub>(p-cymemne) dimer, 2,2'- bipy-4,4'-dicarboxylic acid and an excess of NH<sub>4</sub>SCN. The resultant crude was purified using Sephadex column to afford compound **35** as a brown/ red powder in a yield of 20%<sup>(89)</sup>. The synthetic route of compound **36** is shown in the following scheme:

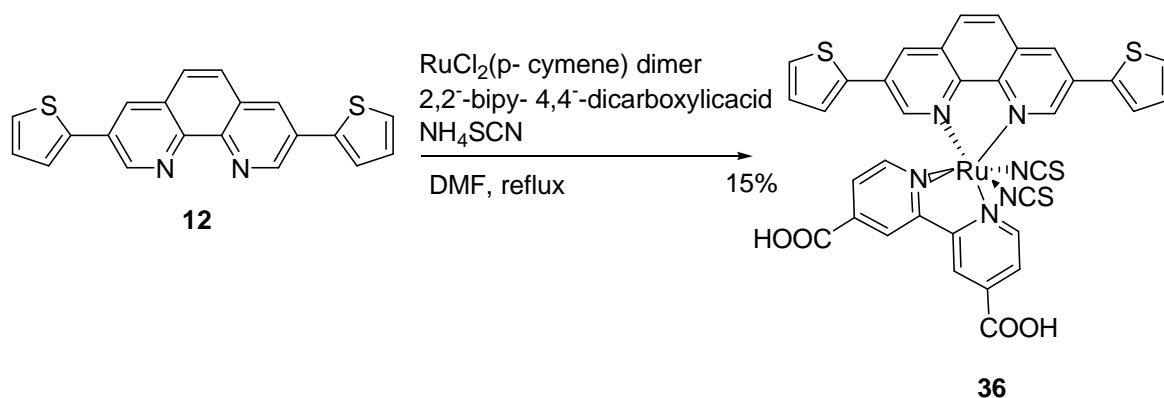


**Figure 6-27:** Synthesis of compound **36**.

Compound **36** was synthesized from compound **12** using RuCl<sub>2</sub>(p-cymemne) dimer, 2,2'- bipy- 4,4'-dicarboxylic acid and an excess of NH<sub>4</sub>SCN. The crude product was purified using sephadex column to afford compound **36** as a brown powder in a yield of 15%<sup>(89)</sup>.

### 6-8-1 Analysis of compound 35

The UV-visible spectrum of compound **35** was recorded in DMF and that of compound **41** was recorded in DCM. The electronic spectrum of compound **41** shows three peaks at 288 nm, 340 nm and 365 nm. The spectrum of compound **35** shows four peaks at 312 nm, 335 nm (very weak), 400 nm and 525 nm. For compound **41**, the peaks at 288 nm, 340 nm, and 365 nm are assigned to the  $\pi$ - $\pi^*$  transitions between carbazole and phenanthroline core. The optically determined bandgap for compound **41** was 3.02 eV. For compound **35**, the three bands at 312 nm, 335 nm and 400 nm are related to the intraligand  $\pi$ - $\pi^*$  transitions of dicarboxylic-bipyridal and phenanthroline- carbazole ligand. The band at 525 nm may be related to the metal to ligand charge transfer transitions of the Ru<sup>II</sup> complexes<sup>(89)</sup>. The absorption peak at 525 nm is a characteristic of the MLCT transitions, and it is an important factor for the determination efficiency of the dye to be used as a photosensitizer. The optically determined bandgap for this compound was calculated to be 2.07 eV. The UV-visible spectrum is shown in the following figure:

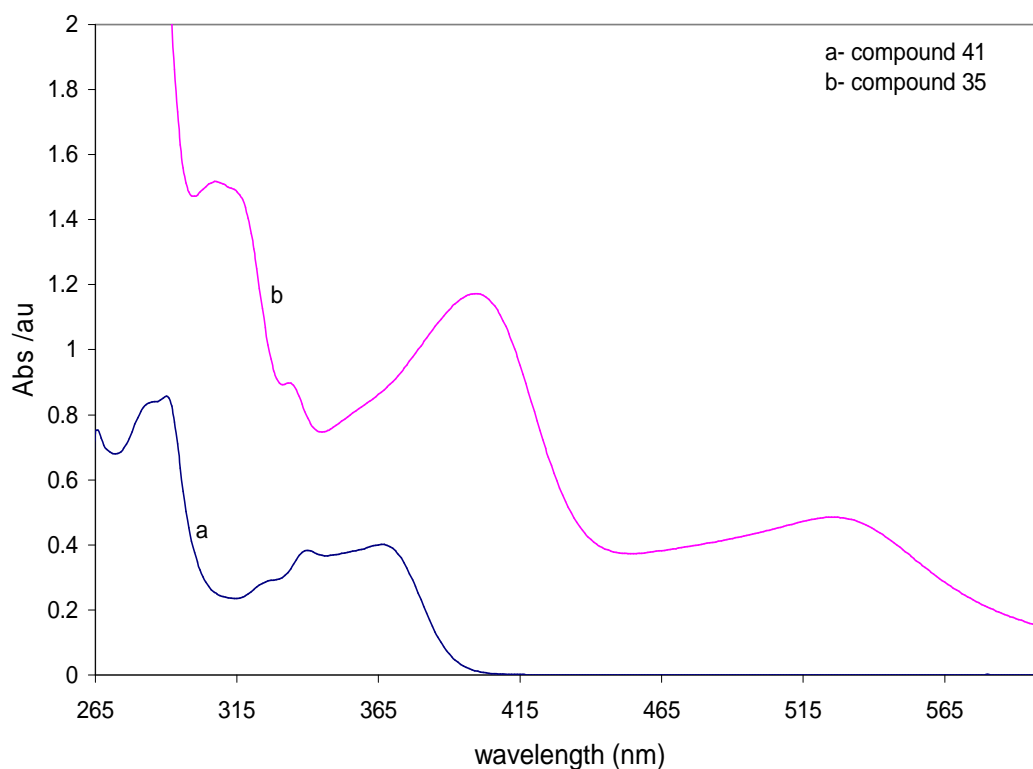


**Figure 6-28:** UV- visible spectra for compounds **35**. Recorded in DMF ( $1 \times 10^{-4}$  M) and compound **41**. Recorded in DCM ( $1 \times 10^{-5}$  M).

### 6-8-2 The voltammogram of compound 35

The voltammogram of compound **35** was recorded in DMF and showed one irreversible oxidation peaks at + 0.77 V. The first peak is related to the oxidation of the metal centre and the second may be related to the oxidation of the ligand. The oxidation peaks are irreversible as the oxidation potential of the thiocyanate is close to that of  $\text{Ru}^{2+}$  (<sup>90</sup>). The HOMO energy was estimated to be 5.57 eV. The reduction peak for this compound is similar to that of water, which is a possible consequence of the ambient atmosphere experimental conditions. However, the voltammogram shows two reduction peaks at -1.28 V and -1.65 V. The estimated LUMO energy level was -3.52 eV. The electrochemically determined bandgap for this compound was calculated to be 2.05 eV. The voltammogram is shown in the following figure:

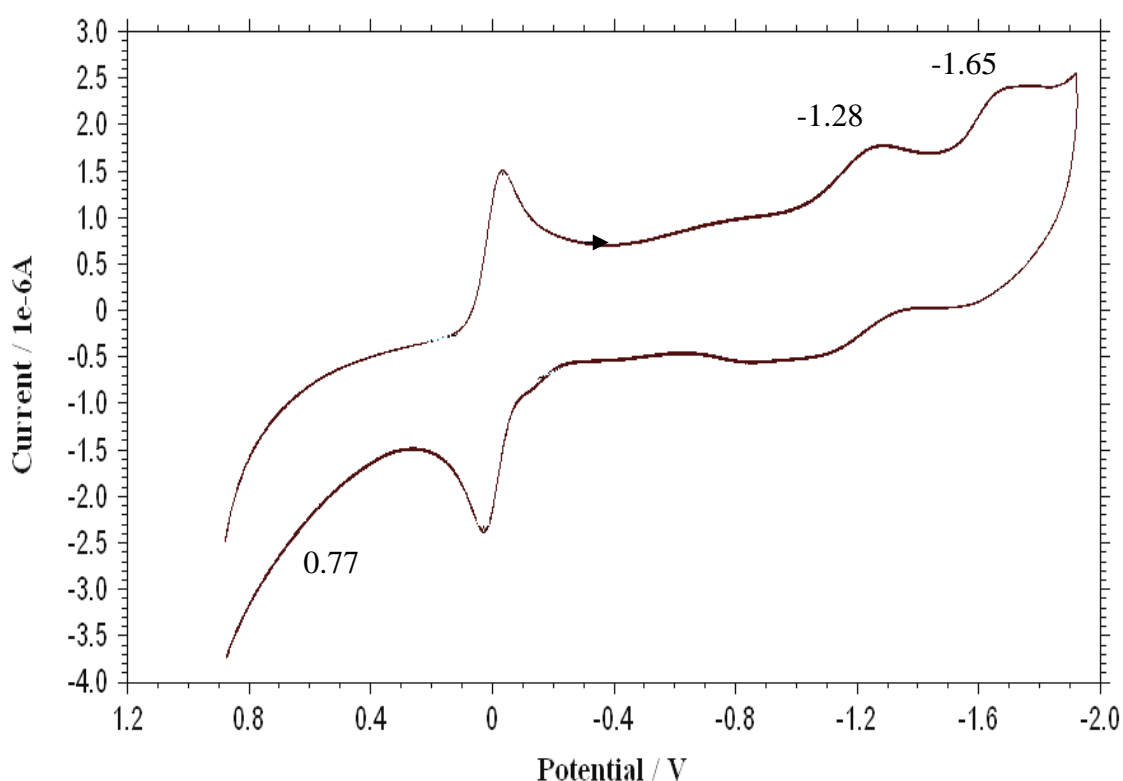


**Figure 6-29:** The voltammogram of compound **35** recorded using a glassy carbon working electrode, an Ag wire as a reference electrode and a Pt wire as a counter electrode. Recorded at a concentration of  $1 \times 10^{-4}$  M in DMF with  $\text{TBAPF}_6$  (0.1 M) as a supporting electrolyte. Scan rate of  $100 \text{ mV s}^{-1}$ .

### 6-8-3 Analysis of compound 36

The UV- visible spectrum of compound **36** was recorded in DMF and that of compound **12** was recorded in DCM. The spectrum of compound **12** shows two absorption bands at 285 nm and 360 nm. These bands are related to the  $\pi$ - $\pi^*$  transitions between the thiophene ring

and the phenanthroline core. The optically determined bandgap for this compound was 3.10 eV. Compound **36** shows three main absorption bands at 304 nm, 376 nm and 530 nm. The bands at 304 nm and 376 nm are related to the intraligand  $\pi$ - $\pi^*$  transition of dicarboxylbipyridal and phenanthroline-thiophene ligand. The absorption band in the visible region (530 nm) may be due to the metal- ligand charge transfer complex<sup>(89)</sup>. This is a characteristic peak of the MLCT transitions is considered as an important factor in the efficiency of the dye to be used as a photosensitizer. The optically determined bandgap for this compound was calculated to be 2.07 eV. The UV-visible spectra are shown in the following figure:

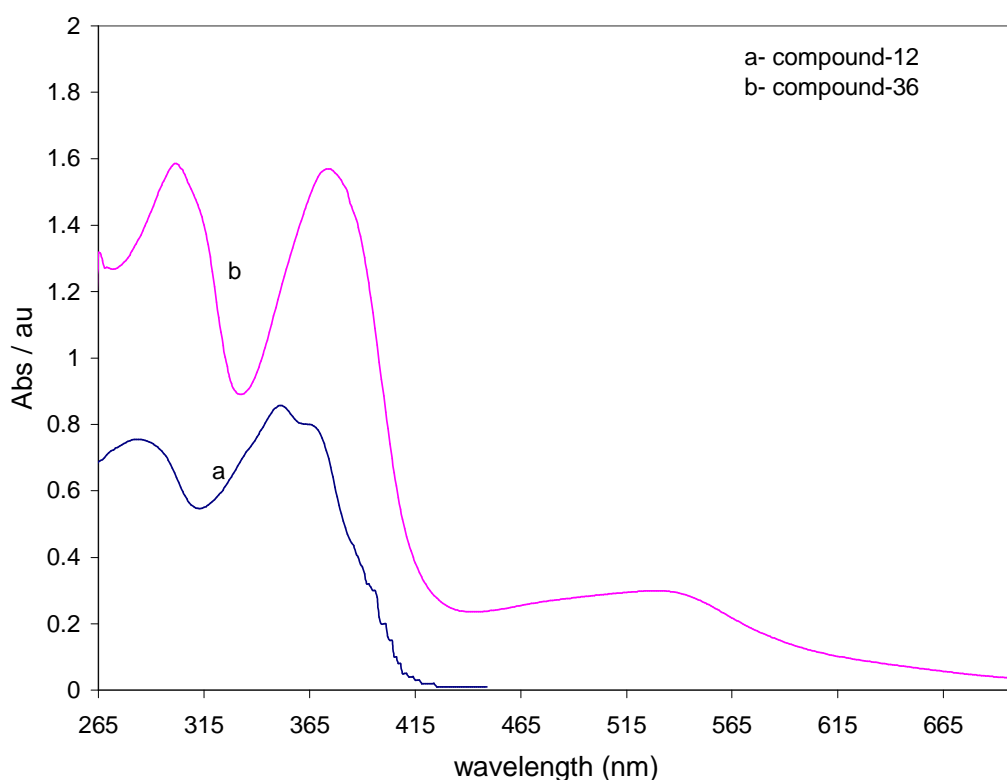


**Figure 6-30:** UV- visible of compounds **36**. Recorded in DMF ( $1 \times 10^{-4}$  M) and compound **12**. Recorded in DCM ( $1 \times 10^{-5}$  M).

#### 6-8-4 The voltammogram of compound **36**

The voltammogram of compound **36** was recorded in DMF. The CV of this compound shows an oxidation wave at + 0.46 V. This peak is related to the oxidation of the metal centre. The HOMO energy was estimated to be -5.26 eV. The reduction of this compound shows to reduction peaks at - 1.60 V, and -1.80 V. The estimated LUMO energy was -3.20 eV. The electrochemically determined bandgap for this compound was found to be 2.06 eV. The voltammogram is shown in the following figure:

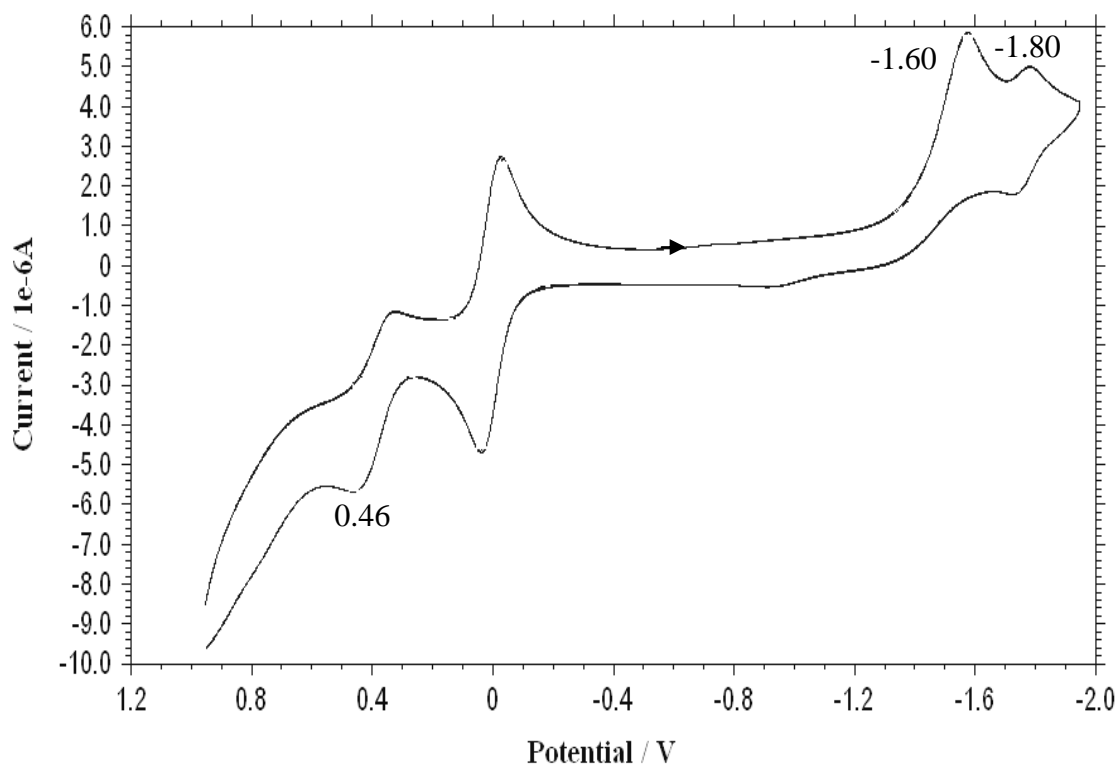


**Figure 6- 31:** The voltammogram of compound **36** recorded using a glassy carbon working electrode, an Ag wire as a reference electrode and a Pt wire as a counter electrode. Recorded at a concentration of  $1 \times 10^{-4}$  M in DMF with TBAPF<sub>6</sub> (0.1 M) as a supporting electrolyte. Scan rate of  $100 \text{ mV s}^{-1}$ .

### 6-9 Dye sensitization over TiO<sub>2</sub>

The UV- visible spectra for the adsorbed dyes **35** and **36** on a TiO<sub>2</sub> film were investigated in comparison with the reference dye **719** (Figure 6-32). The adsorption process was achieved by immersion TiO<sub>2</sub> films in solution of the dye (0.5 mM) for 24 hours. This process gives an indication about the amount of the dye, which adsorbed effectively on the titania film. Before adsorption, electronic spectra of dyes **35** and **36** showed three main bands around 304 nm, 376 nm, and 530 nm. When these dyes adsorbed on titania they show a main feature band in the range of 380- 590 nm. This band is related to the MLCT transition between metal centre and the ligand in these dyes. The UV- visible spectra for these dyes and the reference dye are shown in Figure 6-33.

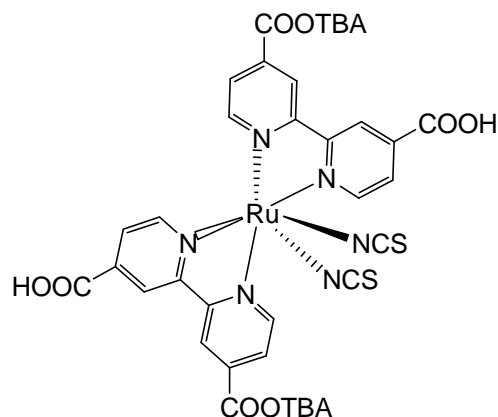


**Figure 6-32:** The structure of reference dye **719**<sup>(34)</sup>.

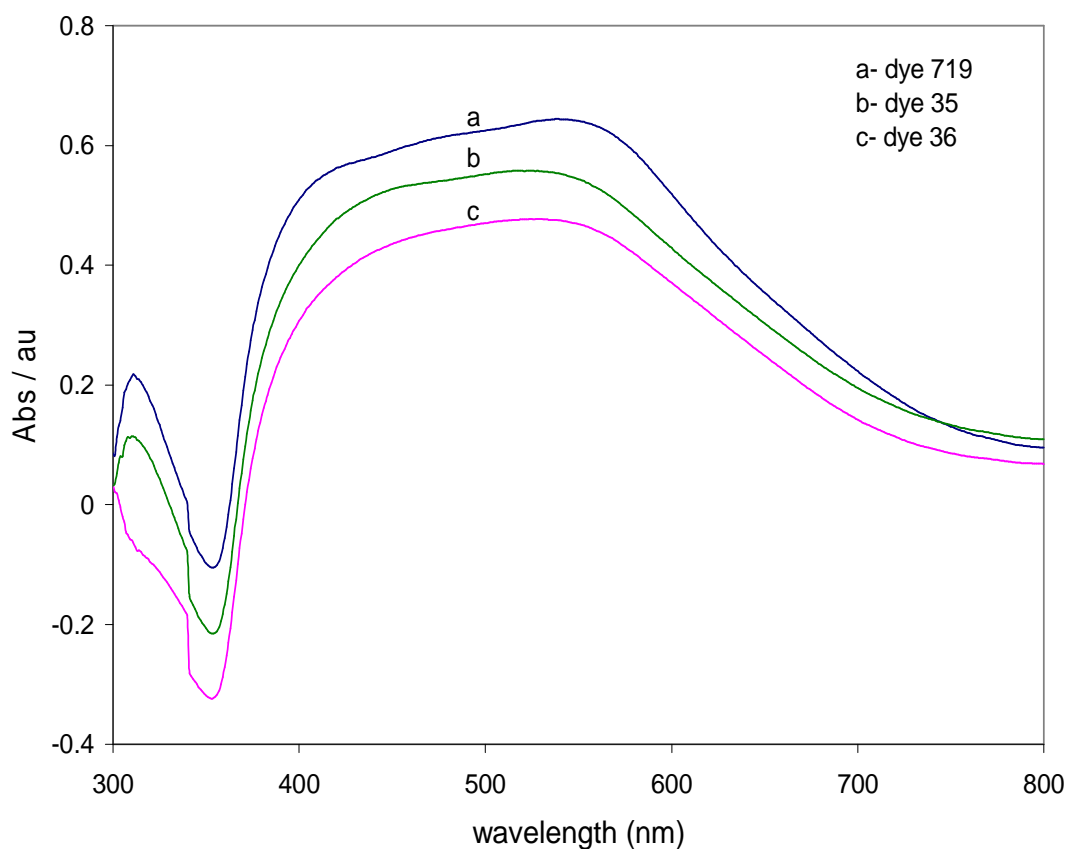


**Figure 6-33:** UV- visible spectra for adsorbed dyes **35**, **36** and the reference dye **719** on a TiO<sub>2</sub> film.

### 6-10 Current-voltages for photovoltaic devices

The following figure shows the photocurrent density-voltage characteristic curves of reference dye **719**, dyes **35** and **36**. The detailed devices parameters are summarized in Table 6-1. Under illumination density of 1.5 AM, the DSSC of **35** showed a photocurrent density ( $J_{sc}$ ) of 1.36 mA/cm<sup>2</sup>, and an open circuit potential ( $V_{oc}$ ) of 0.490 V with a fill factor (FF) of 0.45 which yielded a power efficiency of 0.26%. The DSSC of **36** showed a  $J_{sc}$  of 1.22 mA/cm<sup>2</sup>,  $V_{oc}$  of 0.429 V and FF of 0.41 which yielded a power conversion

efficiency of 0.19%. The low efficiency of these two dyes is probably due to the very low photocurrent density, which is related with the ability of the dye to harvest light. The short circuit current densities of the device with dye **35** and dye **36** were 1.36 mA/cm<sup>2</sup> and 1.22 mA/cm<sup>2</sup> respectively. However, these values are lower than that for the device with dye **719** (reference dye). This is probably associated with the molar extinction coefficient of MLCT in solution, which was higher for dye **719** in comparison with these dyes. In addition, the open circuit voltage for devices with dyes **35** and **36** were lower than that of the reference dye. It has been reported that the open circuit photovoltage of DSSCs is dependent on the Fermi level (FL) of TiO<sub>2</sub><sup>(91)</sup>. The Fermi level in this device is affected by the concentration of protons on the surface of titania. However, high concentration of H<sup>+</sup> on the TiO<sub>2</sub> surface reduces the FL, and the low concentration of H<sup>+</sup> gives a high titania FL. So that difference in number of protons in dyes **35** and **36** in comparison with reference dye can affect on their efficiency in conversion of solar radiation into electrical power<sup>(92)</sup>. These results are shown in Table 6-4 and Figure 6-34.

**Table 6-4:** Photocurrent density ( $J_{sc}$ ), open- circuit voltage ( $V_{oc}$ ) for dyes **35** and **36** with reference dye **719**.

Dye	$J_{sc}$ mA/ Cm <sup>2</sup>	$V_{oc}$ / V	FF	Efficiency%
Dye 719	1.93	0.551	0.64	1.77
Dye 35	1.36	0.490	0.45	0.78
Dye 36	1.22	0.429	0.41	0.56

However, these results are low in comparison with reference dye, in addition to that the efficiency of dye **719** is low in comparison with the efficiency of this dye in other reported studies. This dye showed efficiency around 10% under AM 1.5 solar radiation of 1000 W/m<sup>2</sup><sup>(34)</sup>. We believe the reason for that probably related to the solar radiation system that was used in testing of these dyes

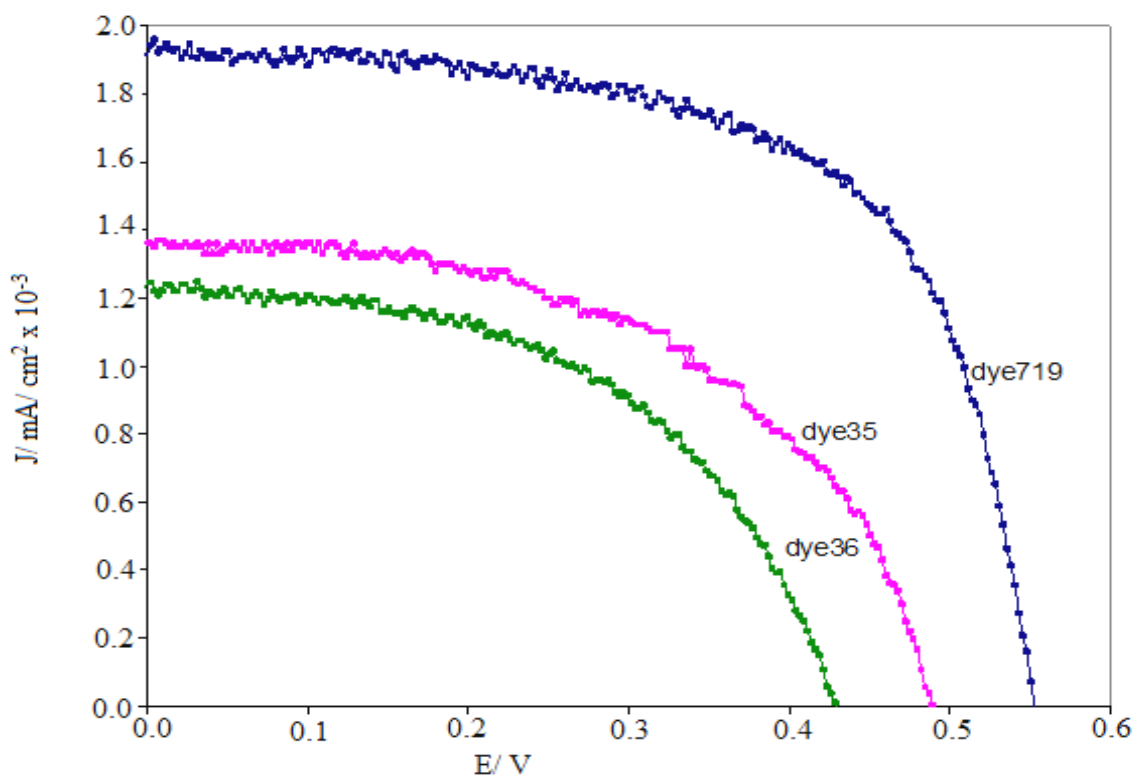


**Figure 6-34:** Current density-voltage of photovoltaic devices **35** and **36** with respect to the reference dye **719** under irradiation of 1.5 AM simulated sunlight of  $1000 \text{ W / m}^2$ . Concentration of all dyes solution 0.5 mM.

### 6-11 Conclusions

This chapter describes the synthesis of novel ruthenium complexes **32-36**. These compounds and/ or their polymeric analogues may possibly be used for many potential applications spanning photo-and materials chemistry. Many attempts were made to polymerize compound **32** by electrochemical polymerization applying different parameters but unfortunately, it did not polymerize. Complex **33** electropolymerized easily and showed good polymer growth on an electrode surface yielding a thin layer of poly(**33**). Compounds **35** and **36** are new ruthenium complexes that were synthesized via incorporating carbazole and thiophene moiety into a 1,10-phenanthroline core. The synthesised dyes **35** and **36** were used in the fabrication of solar cells. The activity of these dyes as DSSCs was tested in comparison with the reference dye **719** as a reference dye. However, these dyes showed lower PV characteristics in comparison with the reference dye. This probably arises from poor stability of dyes under illumination conditions. This can affect negatively on their ability to harvest light and poor electronic communication between the adsorbed dye and titania surface.

## **6-12 Acknowledgements**

I gratefully acknowledge the contribution to this work from the research group of Professor Peter Skabara from the University of Strathclyde, Scotland for their assistance with the CV studies. In addition, I would like to give a special acknowledgement to Saadeldin Elmasly a PhD Student from Skabara group for his contribution in the CV and electrochemical polymerization. I would like also to thank the research group of Dr. Neil Robertson from the University of Edinburgh and especially a PhD Student, Nina Chadwick, for her assistance in undertaking fabrication and the test for DSSC application.

## 6-13 References

1. T. Ogawa, H. Ozawa, M. Kawao, H. Tanaka, *J. Mater. Sci: Mater. Electron.*, 2007, **18**, 939.
2. H. Ozawa, M. Kawoo, H. Tanaka, *Langmuir*, 2007, **23**, 6365.
3. Y. Saitoh, T. Koizumi, K. Osakada, T. Yamamoto, *Can. J. Chem.*, 1997, **75**, 1336.
4. S. Zhu, S. Swager, *J. Am. Chem. Soc.*, 1997, **119**, 12568.
5. R. Charles, A. Perroto, *J. Inorg. Nucl. Chem.*, 1964, **26**, 373.
6. A. Altomare, M. Burla, M. Canialli, G. Cascarano, G. Giacovazzo, A. Polidori, *J. Appl. Cryst.*, 1999, **32**, 115.
7. R. Angelici, *Coord. Chem. Rev.*, 1990, **105**, 61.
8. G. Chelucci, R. Thummel, *Chem. Rev.*, 2002, **102**, 3129.
9. C. Boldron, M. Pitie, B. Meunier, *Synth. Lett.*, 2001, **10**, 1629.
10. W. Huang, H. Tanaka, T. Ogawa, *J. Phys. Chem.*, 2008, **112**, 11513.
11. F. Barigelletti, L. Flamigni, *Chem. Soc. Rev.*, 2000, **29**, 1.
12. X. Shen, T. Moriuchi, T. Hirao, *Tetrahedron Lett.*, 2003, **44**, 7711.
13. A. Mishra, M. Fischer, P. Bäuerle, *Angew. Chem. Int. Ed.*, 2009, **28**, 2474.
14. H. Joshi, R. Jamshidi, *Angew. Chem. Int. Ed. Engl.*, 1999, **38**, 2722.
15. E. Birchner, U. Grummt, A. Goller, T. Pautzsch, D. Egbe, M. Al-Higari, *J. Phys. Chem.*, 2001, **105**, 10307.
16. H. Suzuki, T. Kanbara, T. Yamamoto, *Inorg. Chim. Acta.*, 2004, **357**, 4335.
17. M. Wolf, *Adv. Mater.*, 2001, **13**, 8.
18. R. Kingsborough, T. Swager, *Prog. Inorg. Chem.*, 1999, **48**, 123.
19. A. Deronizer, J. Moutet, *Coord. Chem. Rev.*, 1996, **147**, 339.
20. P. Pickup, *J. Mater. Chem.*, 1999, **9**, 1641.
21. J. Ochmanska, P. Pickup, *J. Electroanal. Chem.*, 1989, **271**, 83.
22. C. Cameron, P. Pickup, *Chem. Commun.*, 1997, **3**, 303.
23. C. Cameron, P. Pickup, *J. Am. Chem. Soc.*, 1999, **121**, 7710.
24. G. Zotti, G. Schiavon, S. Zecchein, A. Berlin, G. Pagzani, A. Canavesi, *Synth. Metals*, 1996, **76**, 255.
25. L. Dennany, C. Hogan, T. Keyes, R. Forster, *Anal. Chem.*, 2006, **78**, 1412.
26. J. Velasca, *Electrolumin. Electroanal.*, 1991, **3**, 261.
27. L. Dennany, R. Forster, J. Rusling, *J. Am. Chem. Soc.*, 2003, **125**, 5213.
28. C. Hogan, R. Forster, *Anal. Chem. Acta.*, 1999, **396**, 13.
29. X. Zhang, A. Bard, *J. Phys. Chem.*, 1988, **92**, 5566.
30. I. Rubinstein, A. Bard, *J. Am. Chem. Soc.*, 1981, **103**, 5007.

31. M. Grätzel, *Nature*, 2001, **414**, 338.
32. P. Liska, S. Ito, B. Takeru, M. Grätzel, *J. Am. Chem. Soc.*, 2005, **127**, 16835.
33. S. Paek, H. Choi, C. Lee, M. Kang, K. Song, M. Nazeeruddin, J. Ko, *J. Phys. Chem. C*, 2010, **114**, 14646.
34. C. Klein, K. Nazeeruddin, D. Censo, P. Liska, M. Grätzel, *Inorg. Chem.*, 2004, **43**, 4216.
35. W. Zeng, Y. Cao, Y. Bai, Y. Wang, Y. Shi, M. Zhang, F. Wang, Y. Pan, P. Wang, *Chem. Mater.*, 2010, **22**, 1915.
36. N. Robertson, *Angew. Chem. Int. Ed. Engl.*, 2006, **45**, 2338.
37. M. Grätzel, *J. Photochem. Photobiol. C*, 2003, **4**, 145.
38. O. Regan, M. Grätzel, *Nature*, 1991, **353**, 737.
39. P. Wang, S. Zakeeruddin, J. Moser, M. Nazeeruddin, T. Sekiguchi, M. Grätzel, *Nature*, 2003, **2**, 402.
40. M. Kang, J. Kim, Y. Kim, J. Won, N. Park, Y. Kang, *Chem. Commun.*, 2005, 889.
41. M. Kang, Y. Kim, J. Won, Y. Kang, *Chem. Commun.*, 2005, 2686.
42. P. Wang, S. Zakeeruddin, J. Moser, R. Humphrey, M. Grätzel, *J. Am. Chem. Soc.*, 2004, **126**, 7164.
43. P. Wang, G. Dai, S. Zakeeruddin, M. Forsyth, D. MacFarlane, M. Grätzel, *J. Am. Chem. Soc.*, 2004, **126**, 13590.
44. J. Kruger, R. Plass, L. Cevey, M. Piccirelli, M. Grätzel, U. Bach, *Appl. Phys. Lett.*, 2001, **7**, 2085.
45. A. Yella, H. Lee, H. Tsao, C. Yi, A. Chandiran, M. Nazeeruddin, E. Diau, C. Yeh, S. Zakeeruddin, M. Grätzel, *Science*, 2011, **334**, 629.
46. L. Spiccia, G. Deacan, C. Kepert, *Coord. Chem. Rev.*, 2004, **248**, 1329.
47. R. Argazzi, N. Iha, H. Zabri, F. Odobel, C. bignozzi, *Coord. Chem. Rev.*, 2004, **248**, 1299.
48. A. Polo, M. Itokazu, N. Iha, *Coord. Chem.*, 2004, **248**, 1343.
49. C. Bignozzi, R. Argazzi, C. Kleverlan, *Chem. Soc. Rev.*, 2000, **29**, 87.
50. M. Nazeeruddin, A. Kay, I. Rodicio, R. Humphry, E. Muller, P. Liska, N. Vlachopolous, M. Grätzel, *J. Am. Chem. Soc.*, 1993, **115**, 6382.
51. R. Argazzi, G. Iarramona, C. Contado, C. Bignozzi, *J. Photochem. Photobiol. A*, 2004, **164**, 15.
52. A. Islam, H. Sugihara, K. Hara, Li Singh, R. Katoh, M. Yanagida, Y. Takahashi, S. Murata, H. Arakawa, *Inorg. Chem.*, 2001, **40**, 5371.
53. E. Geary, L. Yellow, L. Jack, S. Parsons, N. Hirata, J. Durrant, N. Robertson, *Inorg. Chem.*, 2005, **44**, 242.

54. G. Hasselmann, G. Meyer, *J. Phys. Chem.*, 1999, **212**, 39.
55. N. Alonso- Vante, J. Nierengarten, J. Sauvage, *J. Chem. Soc. Dalton Trans.*, 1994, 1649.
56. P. Jayaweera, S. Palayangoda, T. Tennakone, *J. Photochem. Photobiol. A*, 2001, **140**, 173.
57. K. Hara, Z. Wang, T. Sato, A. Furube, R. Katoh, H. Sugihara, Y. Dan, C. Kasada, A. Shinpo, S. Suga, *J. Phys. Chem. B*, 2005, **109**, 15476.
58. S. Alex, U. Santhosh, S. Das, *J. Photochem. Photobiol. A*, 2005, **172**, 63.
59. T. Horiuchi, H. Miura, K. Sumioka, S. Uchida, *J. Am. Chem. Soc.*, 2004, **126**, 12218.
60. Y. Chen, C. Li, Z. Zeng, W. Wang, X. Wang, B. Zhang, *J. Mater. Chem.*, 2005, **15**, 1654.
61. K. Hara, T. Sato, R. Katoh, A. Furube, T. Yoshihara, M. Murai, M. Kurashige, S. Ito, A. Shinpo, S. Suga, H. Arakawa, *Adv. Funct. Mater.*, 2005, **15**, 146.
62. A. Haque, E. Palomares, B. Cho, A. Green, N. Hirata, D. Klug, J. Durrant, *J. Am. Chem. Soc.*, 2005, **127**, 3456.
63. M. Nazeeruddin, P. Pechy, M. Grätzel, *Chem. Commun.*, 1997, 1705.
64. M. Nazeeruddin, S. Zakeeruddin, R. Humphery- Baker, M. Jirousek, P. Liska, N. Vlachopoulos, V. Shklover, M. Grätzel, *Inorg. Chem.*, 1999, **38**, 6298.
65. P. Wang, C. Klein, J. Moser, R. Charret, P. Comte, S. Zakeeruddin, M. Grätzel, *J. Phys. Chem. B*, 2004, **108**, 17553.
66. S. Altobello, C. Bignozzi, S. Caramori, G. Larramona, S. Quici, G. Marzanni, L. Lakhmiri, *J. Photochem. Photobiol. A*, 2004, **166**, 91.
67. P. Wang, S. Zakeeruddin, J. Moser, M. Nazeeruddin, T. Sekiguchi, M. Grätzel, *Nat. Mater.*, 2003, **2**, 402.
68. A. Hagfeldt, G. Boschloo, L. Sun, L. Kloo, H. Petterson, *Chem. Rev.*, 2010, **110**, 6595.
69. T. Kwon, V. Armel, A. Nattestad, U. Bach, S. Lind, K. Gordon, W. Tang, D. Jones, A. Holmes, *J. Org. Chem.*, 2011, **76**, 4088.
70. J. Jang, N. Masaki, J. Xia, S. Noda, S. Yanagids, *Chem. Commun.*, 2006, **23**, 2460.
71. P. Wang, S. Zakeeruddin, J. Moser, P. Comte, V. Aranoys, A. Hagfeldt, M. Nazeeruddin, M. Grätzel, *Adv. Mater.*, 2004, **16**, 1806.
72. Y. Xu, S. Sun, J. Fan, X. Peng, *J. Photochem. Photobiol. A: Chem.*, 2007, **188**, 317.
73. J. Faiz, A. Philippopoulos, A. Kontos, P. Felaras, Z. Pikramen, *Adv. Funct. Mater.*, 2007, **17**, 54.

74. H. Sugihara, L. Singh, K. Sayama, H. Arakawa, M. Nazeeruddin, M. Grätzel, *Chem. Lett.*, 1998, **10**, 1005.
75. R. Renourad, R. Fallahpour, M. Nazeeruddin, S. Gorelsky, A. Lever, M. Grätzel, *Inorg. Chem.*, 2002, **41**, 367.
76. P. Wang, C. Klein, R. Humphry, S. Zakeeruddin, M. Grätzel, *J. Am. Chem. Soc.*, 2005, **127**, 808.
77. H. Nguyen, D. Nguyen, N. Kim, *Adv. Nat. Sci.*, 2010, **1**, 25001.
78. M. Shiotsuka, Y. Inui, M. Ito, S. Onaka, T. Ozeki, H. Chiba, *Acta. Cryst.*, 2006, **62**, 980.
79. D. McClenaghan, R. Passalacqua, F. Loiseau, S. Campagan, B. Verheyde, A. Hameurlaine, W. Dehaen, *J. Am. Chem. Soc.*, 2003, **125**, 5356.
80. M. Bryce, *Adv. Mater.*, 1999, **11**, 11.
81. K. Araki, H. Endo, G. Masuda, T. Ogawa, *Chem. Eur. J.*, 2004, **10**, 3331.
82. T. Yamamoto, Z. Zhou, T. Maruyama, T. Kanbara, *Synth. Met.*, 1993, **55**, 1209.
83. T. Pappenfus, K. Mann, *Inorg. Chem.*, 2001, **40**, 6301.
84. K. Walters, L. Trouillet, S. Guillereze, *Inorg. Chem.*, 2000, **39**, 5496.
85. J. Roncali, *Chem. Rev.*, 1992, **92**, 711.
86. A. Juris, V. Balzani, F. Barigelletti, S. Campagna, P. Belser, A. Vonzelewsky, *Coord. Chem. Rev.*, 1988, **84**, 85.
87. X. Cheng, O. Ingans, *J. Phys. Chem.*, 1996, **100**, 15202.
88. Q. Zhang, J. Chen, Y. Cheng, L. Wang, D. Ma, X. Jing, F. Wang, *J. Mater. Chem.*, 2004, **14**, 895.
89. C. Chen, H. Lu, C. Wu, J. Chen, K. Chuan, *Adv. Funct. Mater.*, 2007, **17**, 29.
90. M. Yanagida, L. Singh, K. Nazeeruddin, M. Grätzel, K. Sayama, K. Hara, R. Katoh, A. Islam, H. Arakawa, M. Nazeeruddin, *J. Chem. Soc., Dalton Trans.*, 2000, 2817.
91. J. Bisquert, D. Cahen, G. Hodes, S. Rühle, A. Zaban, *J. Phys. Chem. B*, 2004, **108**, 8106.
92. S. Yan, J. Hupp, *J. Phys. Chem.*, 1996, **100**, 6867.

## **Chapter- seven: Suggestions and further work**

### **Chapter: two**

In terms of modification of titania surface by doping nitrogen, it was found that doping titania samples with nitrogen at 400 and 500 °C showed improvement in the photoactivity of doped samples in comparison with neat samples. While doped titania with nitrogen at 600 °C gave negative activity. In addition, the PZC point for neat and doped samples was measured, and it was found that, PZC value was increased with increase of doping temperature for these samples. Further research could include doping titania with various non-metal species and investigate which of them can show better activity in photocatalytic reactions. The most important point here is to test these systems under visible light or even under normal solar radiation, as this would be more desirable from an economical point of view. Additionally, these materials could be applied to the treatment of industrial wastewater.

### **Chapter: three**

In this chapter, modification of titania samples was performed by doping some metal ions. In addition, for selected samples of titania co-doped with nitrogen at three temperatures 400, 500 and 600° were investigated. Generally, samples that were doped with metal ions and that were co-doped at 400 and 500 °C showed higher photoactivity in comparison with neat titania samples. Samples that were co-doped at 600° exhibited lower activity with respect to the neat samples. However, in all doped and co-doped cases, doping did not alter crystalline structure of titania samples. The metal doped and co-doped titania seems to provide efficient catalysts that can be used in heterogeneous photocatalytic processes. Important further work would be to irradiate this system using visible light and other higher wavelength regions of the solar spectrum, as stated above. Furthermore, the study of the activity of these materials as a function of the amount of doped metal within the titania would be beneficial.

#### **Chapter: four**

This chapter represented synthesis of some novel viologen monomers in conjugation with 1,10-phenanthroline core. These compounds can be applied in some potential applications especially as electroactive and catalysis materials. Both of chemical and electrochemical polymerization routes were applied in the polymerization of these monomers. However, unfortunately, some of them did not polymerize, this probably arises from lack of long conjugation system. So that, increasing the extent of conjugation by introducing different moieties at the 3- and 8-positions of the 1,10-phenanthroline core before quaternization reaction could increase ability of polymerization and increase absorption within the near-IR region; a property which is thought to be important in developing high efficiency photovoltaic materials. In addition, it should be possible to incorporate more electron rich moieties (such as thiophene) to the phenanthroline core as this may facilitate electropolymerization of these systems. The resulting polymers could show interesting electron accepting properties and may find applications in PV devices.

#### **Chapter: five**

This chapter described synthesis of some novel push-pull chromophores featuring 1,10-phenanthroline core. Some of these compounds were incorporated with TCNE and TCNQ as electron acceptors and with anilino group as an electron donor. These compounds are expected to be used in some potential applications such as NLO materials and telecommunication materials. These compounds showed a significant absorption shift towards near-IR region of the spectrum. This probably arises from strong electronic communication between donor/ acceptor moieties in these compounds. Further work could involve the synthesis of symmetrical push-pull chromophores featuring a phenanthroline core. The opposing nature of the dipole moments of these materials could provide systems with interesting optical and NLO properties.

#### **Chapter: six**

This chapter described synthesis of some novel Ru(II) complexes that featuring phenanthroline core. Some of these compounds were polymerized by electrochemical polymerization. These complexes can be used in some potential applications such as coordination chemistry and PV devices. In addition, these compounds and/ or their

polymeric forms can be used as electroactive materials. Further research focusing on the synthesis of the next generation of ruthenium complexes featuring increased absorption in the near-IR by increasing conjugation within the molecule and adjusting the electronic characteristics of the dye so it overlaps better with that of the titania and the electrolyte within the DSSCs are clearly important further goals. A more detailed investigation of the physical properties of the electropolymerized ruthenium complexes could well lead to this material finding applications as a donor system for the fabrication of BHJ photovoltaic devices.

## Chapter- eight: Experimental

### 8-1 Doping of titanium dioxide with nitrogen

#### 8-2 Doping reactor

The ammonolysis reactor was used for doping titanium dioxide with nitrogen. The gases used in the doping in this unit were ammonia (BOC grade N3.8), and nitrogen (BOC oxygen free, 99.998%). These gases were passed through a vertical quartz glass reactor with a sintered disc at the half distance along the tube. The flow of the gas through the tube was controlled by a series of Brooks 5850 TR mass flow controllers. The effluent gas of the unit was passed through a sulfuric acid flask in order to neutralize any remaining  $\text{NH}_3$ . The whole unit was placed in controlled ventilated fume cupboard. Heating was achieved utilizing a Carbolite furnace fitted with a Eurotherm temperature controller. In each experiment about 0.8 g of the material was held in a vertical quartz glass reactor and subjected to a flow of  $\text{NH}_3$  ( $92 \text{ mL} \cdot \text{min}^{-1}$ ). The ammonolysis reactor is shown in the following photograph:



**Figure 8-1:** A photograph of ammonolysis reactor unit used for doping samples with nitrogen.

### **8-3 Doping TiO<sub>2</sub> with Nitrogen**

Doping nitrogen was performed by using 0.8 -1.0 g of anatase titanium (IV) oxide nanopowder, purity from supplier 99.7% anatase supplied by the Aldrich Company, titanium (IV) oxide nanopowder 99.5% rutile supplied by the Aldrich company, and P25 titania hydrophilic fumed metal oxide supplied by Lawrence Industries. The reaction was carried out by flowing ammonia under heating, the temperature ramp rate was 25°C / min, and the ammonia flow rate employed was 92 mL /min. The reaction was run at the final temperature for three hours. Doping was undertaken at three different temperatures 400, 500 and 600 °C. After three hours, the NH<sub>3</sub> flow was stopped, and then samples were cooled to ambient temperature under a N<sub>2</sub> flow. The resultant modified materials (TiO<sub>2-x</sub>N<sub>x</sub>) were characterised with different spectroscopic and analytical methods such as UV-visible spectroscopy, XRD, BET analysis and microelemental analysis. This general procedure was also employed for other modified TiO<sub>2</sub> samples.

#### **8-3-1 Samples characterization**

##### **8-3-1-1 Elemental analysis**

Micro elemental analysis (CHN) was employed to quantify nitrogen species in the doped samples by using CHN elemental analysis (EAI Extra Analytical CE-440 Elemental Analysis).

##### **8-3-1-2 BET Surface area measurements**

The surface areas of the samples were determined from the adsorption of nitrogen at -196 °C according to the BET method. Surface areas of the samples were calculated from the linear part of the BET plots (in the range  $p/p_0 = 0 - 0.3$ ). The measurements were undertaken by using a Micrometrics Gemini III 2375 Surface Area Analyser.

##### **8-3-1-3 UV-visible Spectra for nitrogen doped titania**

The UV- Visible spectra for parent and modified samples were measured using a Cary 500, UV-Vis-NIR Spectrophotometer. The powders were pressed in the sample compartment to obtain a uniform surface.

##### **8-3-1-4 Powder X- ray diffraction (PXRD) for the samples**

X-ray powder diffraction was measured with a Siemens D5000 Diffractometer at room temperature using Cu-K $\alpha$  radiation with wavelength of 1.5148 Å, (40 kV, 40 mA). The patterns were collected using a step scan of 0.02° 2 $\theta$  over a range of 5° to 85° 2 $\theta$  with a counting time per step of 0.08 seconds. Typical powder (PXRD) experiments were undertaken by irradiation the samples from a moving source and a moving detector which

measures measured the intensity of the diffracted X- rays. All measurements were carried out in the Bragg- Brentano geometry using a flat plate sample. The Scherrer equation was applied to selected reflections to obtain crystallite size<sup>(1)</sup>.

#### **8-3-1-5 Evaluation of PZC for titania doped with nitrogen**

The PZC for catalysts was measured by potentiometric titration. In this method, ionic strength was maintained using a solution of  $\text{KNO}_3$  (0.03 M, 100 mL ) to which NaOH (1M, 1.0 mL) was added. The resultant solution was then titrated with  $\text{HNO}_3$  (0.10M) and the pH curve recorded. Following this a mixture of 100 mL of  $\text{KNO}_3$  with 0.20 g of titania was stirred for 24 hours, then 1.0 mL of NaOH was added and titrated with  $\text{HNO}_3$  and the resultant pH curve recorded as for the blank solution. The same procedure was followed with all the other samples of titania. Results of the titration are plotted as a volume of the added acid against pH of the mixture and the PZC was taken as the point of intersection with the blank pH curve<sup>(2)</sup>.

#### **8-4 Photochemical reactor**

The reaction unit was supplied by Photochemical Reactors Ltd (Quartz Immersion Well Reactor RQ400). It comprised a cylindrical flask reaction vessel with a flattened bottom for stirring and heating. This was fabricated from borosilicate glass. The irradiation lamp was effectively surrounded by the reaction mixture. The lamp was held within a double walled immersion well, which was made of quartz, allowing the passage of water during reaction for cooling. In addition, this unit had a system for changing gases and withdrawal of samples during the reaction. The unit was provided with a 125-Watt power supply (Model 3110). The whole unit was surrounded by a wooden box to prevent any interaction with stray light from the laboratory environment and to contain the UV light generated by the lamp. The lamp was a medium pressure lamp (125 Watt, model 3010), immersion type. This lamp produces radiation which predominantly in the 365-366 nm wavelength region. Additionally, it produces a significant amount of radiation in the visible region of the solar spectrum at 405-408 nm, 436 nm and 546 nm, and at 577-579 nm. The whole reaction unit is shown in the following photograph:

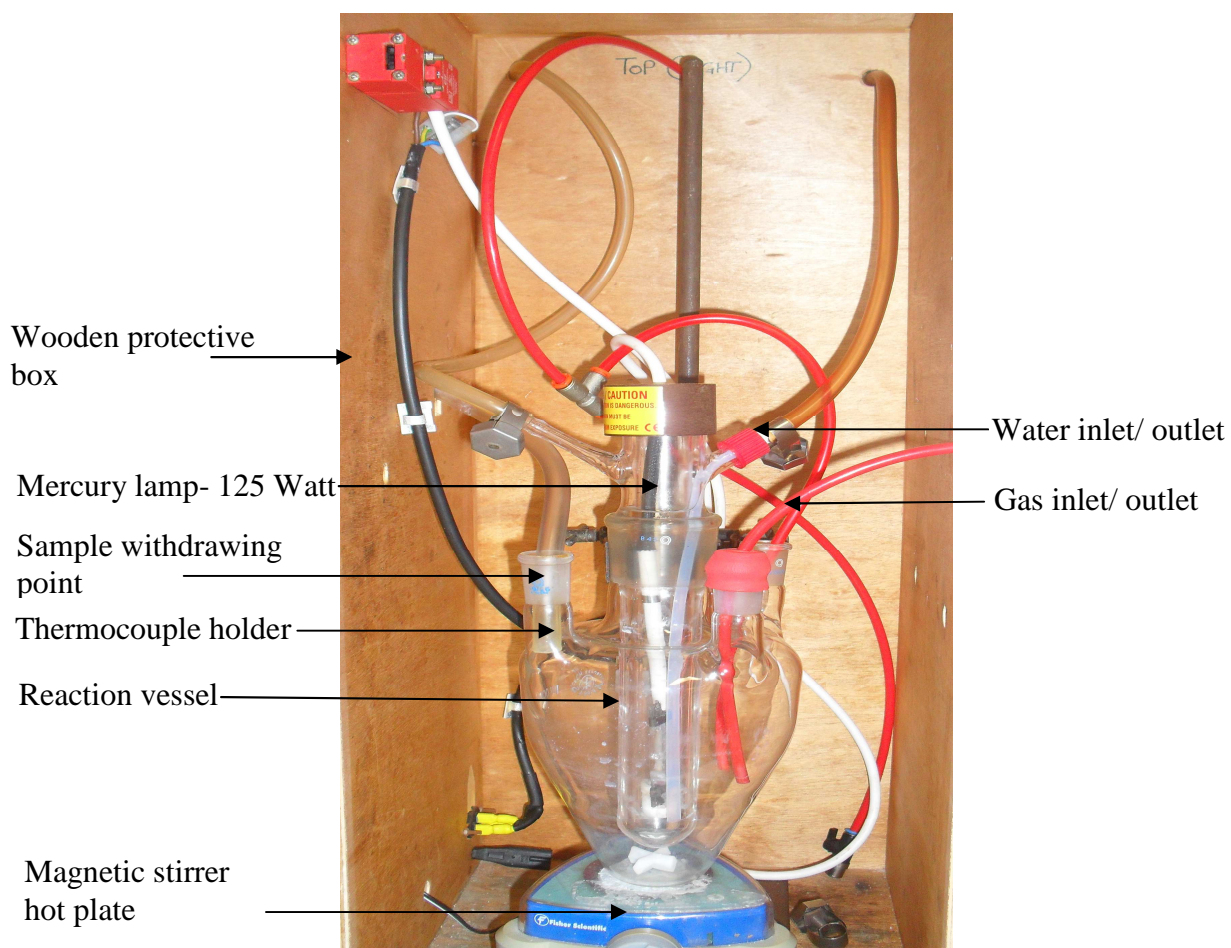


**Figure 8-2:** A Photograph of reactor configuration diagram of the photoreaction unit.

## 8-5 Photocatalytic activity for nitrogen doped titania

### 8-5-1 Photocatalytic decomposition of MB over parent and nitrogen doped TiO<sub>2</sub>

Photocatalytic activity was investigated for photocatalytic decomposition of methylene blue, by measuring the loss of absorbance of a  $2.5 \times 10^{-5} \text{ mol dm}^{-3}$  solution of methylene blue. Reactions were performed by stirring a suspension of 0.01 g of material in 100 mL of methylene blue solution at 20 °C in air. In order to account for the effects of adsorption of the dye, TiO<sub>2</sub> samples were stirred in the dye solution for 10 minutes prior to an aliquot being withdrawn and analysed (the dark reaction). Subsequently, the reaction vessel was illuminated and periodic sampling was performed to determine the degradation measured as the change in absorbance at 655 nm.

## **8-5-2 Photocatalytic polymerization**

### **8-5-2-1 Preliminary experiments**

To investigate photocatalytic polymerization over titania a series of experiments were undertaken using purified methyl methacrylate (MMA) over titania (anatase) under irradiation with UV light at room temperature as follows:

1- In this experiment, 2.0 g of MMA (99.95%) and 0.2 g of neat anatase were suspended with 25 ml of distilled water using a normal conical flask (Pyrex glass) under irradiation with UV light and stirring at room temperature for three hours. Then the solid was separated by centrifugation, washed with water to remove free monomer, and then dried overnight. The solid was washed thoroughly with THF to dissolve free chains of the polymer if it was formed (extracted polymer). The remaining polymer on the catalyst is the bound polymer. The extracted polymer was analyzed by GPC and  $^1\text{H}$  NMR. The bound polymer was investigated by thermal gravimetric analysis (TGA) and FTIR spectroscopy. The  $^1\text{H}$  NMR spectrum exhibited some peaks of the polymer for this case.

2- This experiment was similar to the first one except using nitrogen doped anatase instead of neat anatase. The same procedure as above was followed in this part, and it gave a polymer as in the above step.

3- This experiment was similar to that in part one but without light, and no polymer was formed in this case.

4- This experiment was similar to the procedure in step one but without the presence of titania, and there was no evidence for polymer formation in this case.

### **8-5-2-2 Photocatalytic polymerization over anatase**

Photocatalytic polymerization over anatase was carried out as follows: 0.15 g titanium dioxide (anatase, 99.7%) was suspended in 100 mL of distilled water and to this, a required amount of the monomer was added. The mixture then was stirred for ten minutes under normal atmosphere prior to irradiation with UV light from the middle pressure mercury lamp. The product then was separated by centrifugation, the solid then washed with water to remove unreacted monomer, dried in a vacuum. The crude product then dissolved in THF with vigorous stirring. Then the mixture was separated by centrifugation. The extracted polymer was precipitated by adding an excess of methanol with stirring to give the final solid polymer that is the extracted polymer. The results of photocatalytic polymerization were represented as a conversion ratio against irradiation time and the conversion ratio was calculated according to the following relation:

$$\text{Conversion\%} = 1 - \frac{w_o - w_t}{w_o} \times 100\%$$

$w_o$  is the weight of the used monomer

$w_t$  is the weight of the produced polymer

### **8-5-3 Polymer Characterization**

#### **8-5-3-1 FTIR spectroscopy**

The FTIR spectra for MMA, PMMA extracted and PMMA grafted anatase were recorded in a Fourier Transform Infrared Spectrometer (FTIR -8400S, Shimadzu). Infrared spectra were obtained using a silver gate apparatus in air atmosphere.

This gate was provided with a position to hold both solid and liquid samples. FTIR spectra were performed by measuring percentage of transmittance against wavenumber in the range of 600- 4000  $\text{cm}^{-1}$ . No of scans; 20- 30 and resolution 2  $\text{cm}^{-1}$ .

#### **8-5-3-2 $^1\text{H}$ NMR spectroscopy**

Further investigation for the extracted polymer was conducted using  $^1\text{H}$  NMR spectroscopy for MMA and extracted PMMA using Bruker DPX 400 spectrometer with chemical shift values in ppm relative to residual chloroform ( $\delta_{\text{H}} = 7.26$ ) as standard for  $^1\text{H}$  NMR.

#### **8-5-3-3 Scanning electron microscopy (SEM)**

Morphological studies for each of neat anatase and grafted with PMMA and extracted PMMA have been undertaken using Scanning Electron Microscopy (SEM), (Philips XL30E Scanning Electron Microscope). An acceleration voltage of 25 kV was used. A double sided adhesive carbon tape supplier mounted on a 0.5 aluminium SEM stub was used for loading of samples. The samples were coated using a Polaron SC7640 Auto/ Manual High resolution Sputter Coater with a gold/ platinum target. All the samples were coated with gold or platinum prior to run SEM to improve the bulk conductivity of the sample.

#### **8-5-3-4 Thermal gravimetric analysis (TGA)**

The polymer was further investigated by thermal gravimetric analysis (TGA) were performed under both air and nitrogen atmospheres using a TGAQ500 Instrument. The average weight of the samples was 4-5 mg using Pt pan were used to hold the samples. The flow of air and  $\text{N}_2$  at a rate of 50 mL/ min and heating rate of 10  $^{\circ}\text{C}$ / min were used.

#### **8-5-4 Photocatalytic decomposition of MB over PMMA grafted anatase**

The photocatalytic activity of the parent and PMMA grafted anatase was investigated for the photocatalytic decomposition of methylene blue. Photocatalytic activity was determined by measuring the loss of absorbance of a  $2.5 \times 10^{-5}$  mol. dm<sup>-3</sup> aqueous solution. Reactions were performed by stirring a suspension of 0.01 g of material in 100 mL of MB solution. Samples were stirred in the dye solution at 20 °C for 10 minutes prior to start irradiation. Then reaction mixture was illuminated with radiation from middle pressure mercury lamp and periodic sampling was performed to determine the conversion of methylene blue (measured as the change in absorbance at 655 nm). The results were recorded as loss absorbance against irradiation time.

#### **8-5-5 Photocatalytic polymerization of MMA over nitrogen doped anatase**

Photocatalytic polymerization was conducted over anatase doped with nitrogen at 400 °C, 500 °C and 600 °C. In each experiment, 150 mg of material was suspended in 100 mL of distilled water and to this 2 mL of MMA was added. The mixture then was stirred for ten minutes under a normal atmosphere prior to irradiation with UV light from a middle pressure mercury lamp with continuous stirring at 20 °C for two hours. The product then was separated by centrifugation, the solid then washed with water to remove unreacted monomer and then dried in a vacuum overnight. The crude product was then dissolved in THF with vigorous stirring and the resulted mixture was separated by centrifugation. The solid obtained was found to contain bound polymer and the liquid to contain extracted polymer. Characterization of polymer was performed by using same methods that were used in case of polymerization over neat anatase.

#### **8-5-6 Effect of temperature on the polymerization over nitrogen doped anatase**

The effect of temperature on photocatalytic polymerization over nitrogen doped anatase was investigated by following the conversion of MMA into PMMA at different temperatures with the other parameters of the reaction being fixed. In each experiment, 2 mL of MMA and 0.15 g of material were suspended in 100 mL of distilled water. The reaction was conducted by stirring the mixture in dark for ten minutes prior to start irradiation with UV light from a middle pressure mercury lamp and continuous stirring under air atmosphere for two hours at different reaction temperatures. The results were recorded as conversion % of the used monomer to the corresponding polymer. The conversion percentage was calculated from difference in the weight of the resulted polymer

and its corresponding polymer. Then this value was recorded as a function of the reaction temperature.

## **8-6 Photopolymerization**

### **8-6-1 Photopolymerization under UV irradiation**

A required amount of purified monomer was degassed to exclude oxygen, and to this a required quantity of 2,2'- azo-bis(isobutyronitrile) (AIBN), (99% Sigma Aldrich) was added. The initiator was weighed and kept in the dark to avoid any interaction with stray light in the lab. The reaction materials were mixed together with the solvent, the mixture then was purged with nitrogen gas for about five minutes prior to the start of irradiation to provide a nitrogen rich environment. The reaction was started by irradiation with UV light from the medium pressure mercury lamp. Photopolymerization of styrene (99.95%, Sigma Aldrich) and MMA (99.95% Sigma Aldrich) were carried out by using AIBN as an initiator under inert atmosphere. Reaction was carried out at 20 °C for two hours under irradiation with UV light. To determine the effect of irradiation time on photopolymerization a series of experiments were undertaken at 20 °C in which 2 mL of the used monomer was mixed with 0.02 g of AIBN as an initiator with 100 mL of toluene. The mixture was flushed with N<sub>2</sub> for 5 minutes prior to the irradiation with UV light from the middle pressure mercury lamp to exclude the oxygen from the solution. Then the reaction was started by irradiation the mixture with continuous stirring and nitrogen flushing. At the end of reaction, the produced polymer was precipitated by adding methanol with vigorous stirring and the resulted polymer was dried overnight.

#### **8-6-2-1 Kinetics of polymerization**

To study the effect of irradiation time on photopolymerization, a series of experiments were undertaken at different times (from 30 to 120 minute). In each experiment, 2 mL of MMA(99.5%) and ST(99.5%) was mixed with 0.02 g of AIBN and suspended in 100 mL of toluene at 20 °C. The mixture was flushed with nitrogen for 5 minutes prior to irradiation with middle pressure lamp to exclude the oxygen from the solution. The reaction then was initiated by irradiation of the mixture with continuous stirring under nitrogen flushing for two hours. At the end of reaction, the produced polymer was precipitated by adding methanol with vigorous stirring and the resultant polymer was dried for overnight. The yield of polymerization was reported as the percentage of conversion against irradiation time.

### **8-6-2-2 The effect of the amount of the used monomer**

To study the effect of using different amounts of monomer under the same reaction conditions on the conversion of monomer to the corresponding polymer. A series of experiments were undertaken in which a required amount of the used monomer was mixed with 0.02 g of AIBN and the resulting mixture was suspended in 100 mL of toluene at 20 °C. The mixture was stirred in dark for ten minutes prior to irradiation with UV light. The reaction was initiated by illumination from the middle pressure mercury lamp for two hours with continuous stirring in a N<sub>2</sub> flush. The results are presented as percentage of conversion for both MMA and ST against irradiation time.

### **8-6-2-3 Effect of inert atmosphere on the rate of reaction**

In order to investigate the effect of the atmosphere on photopolymerization, a series of experiments were performed under flowing nitrogen. In each experiment, 2 mL of MMA (99.5%) and ST (99.5%) was mixed with 0.02 g of AIBN. This mixture then was suspended in 100 mL of toluene with initiation under a nitrogen atmosphere at 20 °C. Reaction was initiated by irradiation and was continuous stirred for two hours. The same procedure was followed in conducting experiments according to above conditions under normal atmosphere.

### **8-6-2-4 Effect of the reaction temperature on the photopolymerization**

In order to investigate the effect of temperature on photopolymerization a series of experiments was performed. In each experiment, 2 mL of MMA (99.5%) and ST (99.5%) was mixed with 0.02 g of AIBN. The mixture was suspended in 100 mL of toluene with nitrogen flush over reaction mixture. Reaction was initiated by irradiation and continuous stirring for two hours at different reaction temperatures was undertaken.

### **8-6-2-5 Thermal polymerization of ST and MMA**

To make a comparison between thermal and photoinitiation of polymerization a series of experiments were undertaken. In each experiment, a mixture of 2 mL of MMA (99.5%), ST (99.5%) and 0.02 g of AIBN was suspended in 100 mL of toluene under flowing nitrogen for two hours. These experiments were conducted at different temperatures by controlled heating a reaction mixture and the results are represented as a conversion percentage as a function of the reaction temperature.

## **8-7 Modification titania by doping metals**

Doping titanium dioxide (anatase, rutile and P25) with aluminium, copper and cobalt was performed by the impregnation method. According to this method a required amount (3%) (of the used titania) of nitrate salts of each metal  $\text{Al}(\text{NO}_3)_3$  (89%),  $\text{Cu}(\text{NO}_3)_2$  (99%) and  $\text{Co}(\text{NO}_3)_2$  (98%) was mixed with 100 mL of an aqueous suspension of titania. The mixture was stirred at 70 ° C for five hours, and then was cooled to room temperature and dried at 110 ° C, washed with distilled water and dried overnight. The resulting powder was then calcined at 300 ° C for 12 hours. These samples were characterized using UV-visible spectroscopy and XRD patterns. The weight percentage of these metals in the doped samples of titania was determined using atomic absorption technique.

### **8-7-1 Atomic absorption**

The weight percentage of aluminium, copper and cobalt dopants introduced was determined using atomic absorption spectroscopy (Perkin Elmer Analyst 400). Titania samples were digested under heating in concentrated sulphuric acid. In each experiment, 0.135 g of metal-doped titania sample was dissolved in 20 mL of concentrated sulphuric acid under heating at 60 ° C for two hours. Then 1 mL of each sample was diluted to 20 mL with distilled water. Standard solutions of each metal ( $\text{Al}^{3+}$ ,  $\text{Co}^{2+}$  and  $\text{Cu}^{2+}$ ) were used to find a calibration curve for each element. For each element, absorption was performed by using a desired lamp that fits with the element. Then the concentration of each element in the doped samples was determined using calibration method with standard solutions of each metal.

### **8-7-2 Photocatalytic polymerization over metals doped anatase**

Photocatalytic polymerization over metal-doped anatase was carried out as follows: 0.15 g of material was suspended in 100 mL of distilled water and to this 2 mL of the monomer was added. The mixture then was stirred for ten minutes under normal atmosphere prior to starting irradiation with UV light from a middle pressure mercury lamp. The product was then separated by centrifugation, and then washed with water to remove unreacted monomer and dried in a vacuum for overnight. The crude product was then dissolved in THF with vigorous stirring and the mixture was separated by centrifugation. The solid was found to contain bound polymer and the liquid contains extracted polymer. The extracted polymer was precipitated by adding an excess of methanol with vigorous stirring.

## 8-8 Experimental of organic materials

### 8-8-1 General notes

In this work, all the reactions were carried out under a nitrogen atmosphere unless otherwise noted. In addition, the reagents and starting materials were obtained from commercial sources and were used as received unless stated. Solvents were obtained from commercial sources and used as received, and dried solvents were obtained from the solvent purifier system (SPS). Reactions that are sensitive towards air or moisture were performed in the oven dried glassware. Purification of crude materials was performed by flash column chromatography using Fisher Matrix silica 60. Macherey-Nagel aluminium backed plates pre-coated with silica gel 60(UV254), were used for thin layer chromatography (TLC) and visualized using ultra violet light (UV). Purification of the dyes (35) and (36) that were synthesized to be used in dye sensitized solar cells (DSSCs) was carried out by flash column chromatography using Sephadex (Sigma Aldrich).  $^1\text{H}$  NMR and  $^{13}\text{C}$  NMR spectra were recorded using a Bruker DPX 400 spectrometer with chemical shift values in ppm with reference to the tetramethylsilane (TMS). The residual chemical shifts for the standard solvents applied were as follows: for chloroform ( $\delta_{\text{H}}=7.26$ ,  $\delta_{\text{C}}=77.20$ ), acetonitrile ( $\delta_{\text{H}}=1.94$ ,  $\delta_{\text{C}}=1.32$  and  $118.26$ ), dimethyl sulfoxide ( $\delta_{\text{H}}=2.52$ ,  $\delta_{\text{C}}=39.47$ ), acetone ( $\delta_{\text{H}}=2.05$ ,  $\delta_{\text{C}}=29.85$ ,  $206.26$ ) and  $\text{D}_2\text{O}$  ( $\delta_{\text{H}}=4.80$ ). For  $^1\text{H}$  NMR,  $J$  values were recorded in Hertz.  $^1\text{H}$  NMR signals in the NMR spectra were recorded as singlets (s), doublets (d), triplets (t), quartets (q), multiplets (m).

Mass spectra were recorded using a JMS-700 instrument. Micro elemental analysis was employed to quantify of N, C and H in the doped samples using CHN elemental analysis (EAI Extra Analytical. CE-440 Elemental Analysis).

For the electrochemical studies, the electrochemically determined bandgap was calculated from the relation between HOMO and LUMO energy levels for the corresponding compound as follows<sup>(3)</sup>:

$$E_{\text{g}} = \text{LUMO} - \text{HOMO}$$

$$\text{LUMO} = -4.8 - E_{\text{reduction}}$$

$$\text{HOMO} = -4.8 - E_{\text{oxidation}}$$

The optically determined bandgap was calculated from UV-vis spectroscopy and the onset wavelength of the spectrum by applying Planck- Einstein relationship as follows<sup>(3)</sup>:

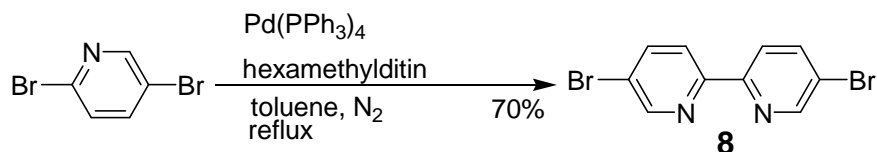
$$E = h\nu = hc/\lambda$$

$$E_{\text{g}}(\text{eV}) = 1240/\lambda_{\text{nm}}$$

Where,  $h$  is a Planck constant,  $c$  is light velocity,  $\lambda$  is the wavelength onset at a higher absorption, and  $E_{\text{g}}$  is the optical bandgap energy for the corresponding compound.

## 8-8-2 Synthetic experimental

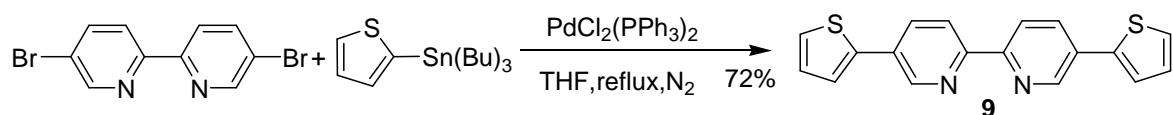
### 5,5'-Dibromo-2,2'-bipyridine (**8**)<sup>(4)</sup>



A mixture of a commercially available 2,5-dibromopyridine (supplied by Sigma Aldrich) (0.80 g, 3.38 mmol), tetra-kis(triphenylphosphino) palladium (0.08 g, 0.07 mmol) and hexamethylditin (0.55 g, 1.69 mmol) were dissolved in toluene (50 mL). This mixture was degassed and heated under reflux for three days in a  $\text{N}_2$  atmosphere. The mixture then was cooled to room temperature and mixed with 20 mL of diethyl ether. It was then filtered to give the crude product. The crude product was further purified using column chromatography silica gel using chloroform/ methanol (99.9: 0.1) as an eluent solution. The final product was then concentrated and dried under vacuum overnight to yield a white powder (0.74 g, 70%).

Mp: 222- 224 °C (Lit 225-226 °C)<sup>(4)</sup>;  $^1\text{H NMR}$  ( $\text{CDCl}_3$ , 400 MHz),  $\delta$ = 8.71 (2H, d,  $J$  = 2.3), 8.30 (2H, dd,  $J$  = 2.2,  $J$  = 8.5), 7.94 (2H, dd  $J$  = 2.3,  $J$  = 8.5). MS (FAB)  $\text{C}_{10}\text{H}_6\text{Br}_2\text{N}_2^+$ , 314.12.

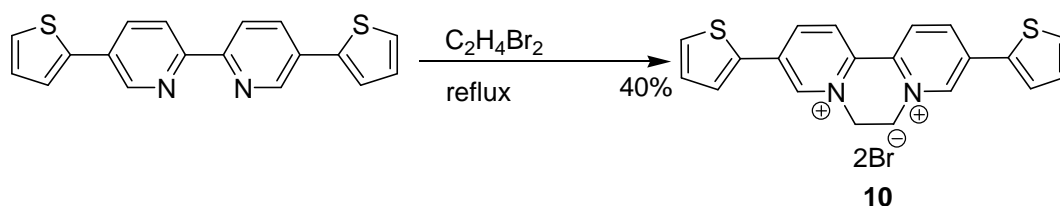
### 5,5'-Bis(thiophene-2-yl)-2,2'-bipyridine (**9**)<sup>(5)</sup>



5,5'-Dibromo-2,2'-bipyridine (0.30 g, 0.96 mmol), 2-tributylstannylthiophene (0.89 g, 2.50 mmol) and  $\text{PdCl}_2(\text{PPh}_3)_2$  (0.03 g, 0.07 mmol) were dissolved in dry DMF (40 mL). This mixture was degassed with  $\text{N}_2$  and then heated under reflux under a  $\text{N}_2$  atmosphere for 36 hours with continuous stirring. The mixture was then cooled to room temperature and the solvent was evaporated under vacuum to yield the crude product. This then was further purified by silica gel column chromatography, using an eluent mixture of DCM: PET (8:2) to afford (**9**) as a yellow powder (0.21 g, 70%).

$^1\text{H NMR}$  ( $\text{CDCl}_3$ , 400 MHz)  $\delta$ = 8.95 (m, 2H), 8.43 (d,  $J$  = 8.3, 2H), 8.0 (dd,  $J$  = 8.4,  $J$  = 2.4, 2H), 7.40 (m, 4H), 7.16 (m, 2H). MS (FAB)  $\text{C}_{18}\text{H}_{12}\text{N}_2\text{S}_2^+$ , 320.20. Anal. Calc. for  $\text{C}_{18}\text{H}_{12}\text{N}_2\text{S}_2$ , Calcd: C, 67.46; H, 3.75; N, 8.75. Found: C, 67.35; H, 3.82; N, 8.66.

### 5,5'-Bis(thiophene-2-yl)-2,2'-bipyridinium-2,2'-dibromide (**10**)

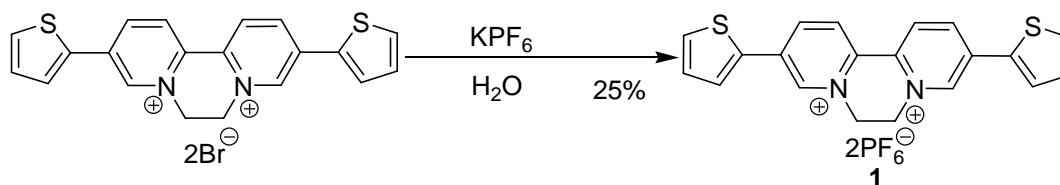


5,5' - Bis(thiophene-2-yl)-2,2' - bipyridine (0.20 g, 0.63 mmol) was dissolved DCM (20 mL) and to this a mixture of 1,2-dibromoethane (5 mL) was added. This mixture was heated under reflux in air with continuous stirring for two days. The mixture was then cooled to room temperature and the product was filtered. The solid was washed with DCM (5 x50) to remove unreacted starting material. The final product was then dried under vacuum overnight yielding compound **10** as a red/ yellow powder (0.10 g, 30%).

MP: 218- 220 °C; <sup>1</sup>H NMR (D<sub>2</sub>O, 400 MHz) δ= 9.82 (s, 2H), 9.14 (d, *J*= 4.8, 4H), 8.19 (d, *J*= 4.8, 2H), 8.08 (d, *J*= 4.8, 2H), 7.44 (t, *J*= 8.5, *J*= 4.6, 2H), 5.35 (s, 4H);

<sup>13</sup> C NMR (100 MHz, D<sub>2</sub>O) δ= 52.5, 127.7, 129.9, 130.1, 132.4, 134.5, 136.4, 137.1, 142.0, 143.14; MS (FAB) C<sub>20</sub>H<sub>16</sub>N<sub>2</sub>S<sub>2</sub><sup>2+</sup>, 348.25; Anal. Calc. for C<sub>20</sub>H<sub>16</sub>N<sub>2</sub>S<sub>2</sub>Br<sub>2</sub>, Calcd: C, 47.21; H, 3.15; N, 5.51. Found: C, 46.98; H, 3.28; N, 5.37.

### 5,5' - Bis(thiophene-2-yl)-2,2'-bipyridinium-2,2'-bis hexafluorophosphate (**1**)

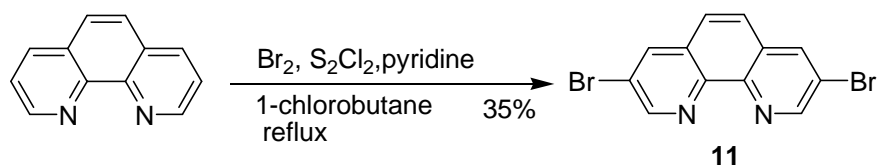


Compound **10** (0.20 g, 0.40 mmol) was dissolved in distilled water (40 mL). This solution was added dropwise to 40 mL of an aqueous solution of KPF<sub>6</sub> (0.30 g, 1.63 mmol). The resulting mixture was then left for three hours to ensure complete precipitation. The solid formed was filtered and washed with distilled water (5 x 50 mL). The product was dried under vacuum overnight to yield compound **1** as a red powder (0.07 g, 25%).

MP: 185 °C dec; <sup>1</sup>H NMR (400 MHz, CD<sub>3</sub>CN) δ=9.25 (s, 2H), 8.94(d, *J*= 8.4, 4H), 8.73 (d, *J*= 8.4, 2H), 7.95 (dd, *J*= 9.4, *J*= 3.30, 2H), 7.41 (t, *J*= 9.4, *J*= 3.3, 2H), 5.17 (s, 4H);

<sup>13</sup> C NMR (100 MHz, CD<sub>3</sub>CN) δ= 52.2, 117.8, 127.2, 129.8, 132.2, 134.2, 136.7.136.5, 141.9, 142.9; MS (FAB) C<sub>20</sub>H<sub>16</sub>N<sub>2</sub>S<sub>2</sub><sup>2+</sup>, 348.25; Anal. Calc. for C<sub>20</sub>H<sub>16</sub>N<sub>2</sub>S<sub>2</sub>P<sub>2</sub>F<sub>12</sub>, Calcd: C, 37.59; H, 2.51; N, 4.39. Found: C, 37.45; H, 2.62; N, 4.50.

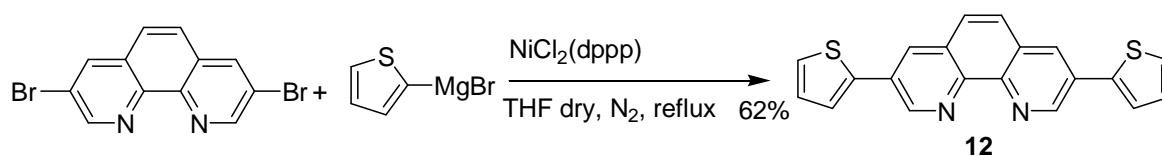
### 3,8-Dibromo-1,10-phenanthroline (**11**)<sup>(6)</sup>



1,10-Phenanthroline (5.0 g, 27.8 mmol) was dissolved in 1-chlorobutane (200 mL). A mixture of bromine (14.0 g, 88.0 mmol), pyridine (7.1 g, 90.0 mmol) and sulfur monochloride (12.3 g, 91.0 mmol) were added to the first mixture. The resulting mixture was heated under reflux in air for 18 hours and then cooled to room temperature. The solid formed was separated and subsequently treated with a mixture of NaOH (1M, 20 mL) and chloroform (20 mL), stirring for 30 minutes. The crude product then extracted and passed through a short column of silica gel using chloroform as an eluent and the solvent was evaporated under vacuum to give the crude product. The crude product was further purified by recrystallization from 1,1,2,2-tetrachloroethane to afford compound **11** as a white powder (3.10 g, 33%).

MP: 223-225 °C. (Lit 221-222 °C);  $^1\text{H NMR}$  ( $\text{CDCl}_3$ , 400 MHz)  $\delta$  = 7.73 (s, 2H), 8.39 (d,  $J$  = 2.2, 2H), 9.17 (d,  $J$  = 2.2, 2H). MS (FAB)  $\text{C}_{12}\text{H}_6\text{N}_2\text{S}_2^+$  = 338.15. Anal. Calc. for  $\text{C}_{12}\text{H}_6\text{N}_2\text{Br}_2$ , Calcd: C, 42.58; H, 1.77; N, 8.28. Found: C, 42.48; H, 1.87; N, 8.34.

### 3,8-Di(thiophene-2-yl)-1,10-phenanthroline (**12**)<sup>(7)</sup>

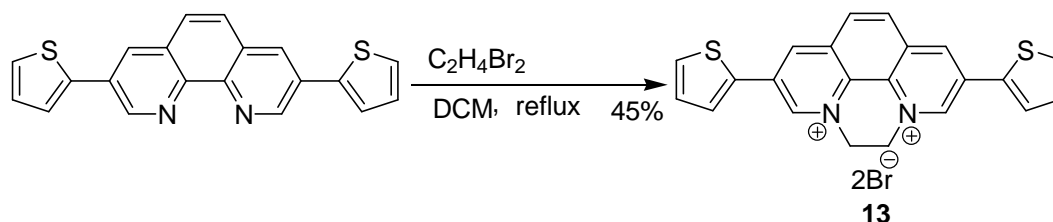


A solution of 3,8-dibromo-1,10-phenanthroline (0.50 g, 1.48 mmol) and  $[\text{NiCl}_2(\text{dppp})]$  (0.02 g, 0.04 mmol) dissolved in dry THF (10 mL) under a  $\text{N}_2$  atmosphere at 0 °C. Then 2-thienylmagnesium bromide reagent (0.77 mL) was added carefully at this temperature. Then reaction mixture was warmed up to room temperature and held for two hours before being heated under reflux in  $\text{N}_2$  overnight. Then reaction was cooled to room temperature and quenched with a saturated solution of  $\text{NH}_4\text{Cl}$  (20 mL), extracted with chloroform (4 x 100), and washed with aqueous NaCl (3 x 50 mL). The crude product was purified by column chromatography, silica gel using an eluent mixture of DCM: PET (8:2) yielding **12** as a yellow powder (0.32 g, 62%).

$^1\text{H NMR}$  ( $\text{CDCl}_3$ , 400 MHz)  $\delta$  = 9.45 (d,  $J$  = 2.3, 2H), 8.36 (d,  $J$  = 2.3, 2H), 7.84 (s, 2H), 7.60 (dd,  $J$  = 3.6,  $J$  = 1.7, 2H), 7.45 (dd,  $J$  = 5.1,  $J$  = 1.2, 2H), 7.21 (t,  $J$  = 8.7,  $J$  = 3.7, 2H).

MS (FAB)  $C_{20}H_{12}N_2S_2^+$ , 344.15. Anal. Calc. for  $C_{20}H_{12}N_2S_2$ , Calcd: C, 69.73; H, 3.49; N, 8.14. Found: C, 69.62; H, 3.58; N, 8.20.

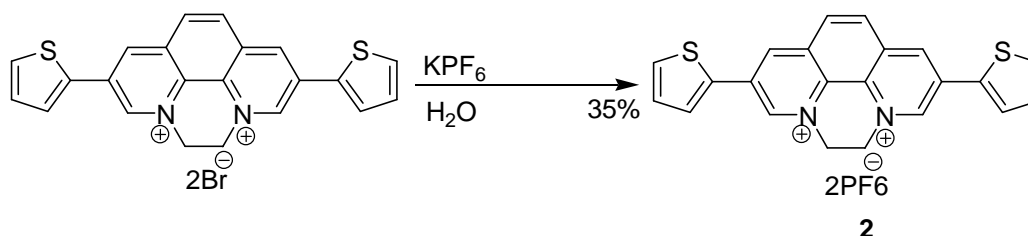
### 3,8-Di(thiophene-2-yl)-1,10-phenanthroline-1,10-bipyridiniumbromide (**13**)



3,8- Di(thiophen-2-yl)-1,10- phenanthroline (0.30 g, 0.87 mmol) was dissolved in DCM (30 mL) and to this mixture 1,2-dibromoethane (5 mL) was added. The mixture then was heated under reflux in air for two days. Following this, the mixture was cooled to room temperature and left for five hours before being filtered. The precipitate formed was separated and washed with DCM (5 x 50 mL) to remove unreacted starting material. The final product was then dried under vacuum to yield compound **13** as a red/ orange powder (0.21 g, 45%).

Mp: 290 °C dec;  $^1H$  NMR(400 MHz,  $D_2O$ )  $\delta$ = 9.85 (d,  $J$ = 1.9, 2H), 9.42 (d,  $J$ = 1.9, 2H), 8.50 (s, 2H), 7.94 (dd,  $J$ = 5.9,  $J$ = 0.9, 2H), 7.80 (dd,  $J$ = 5.9,  $J$ = 0.9, 2H), 7.25 (t,  $J$ = 5.6,  $J$ = 0.9, 2H), 5.64 (s, 4H);  $^{13}C$  NMR (100 MHz,  $D_2O$ )  $\delta$ = 52.2, 126.9, 129.5, 129.8, 129.9, 131.6, 131.7, 134.3, 134.9, 140.5, 145.7; MS (FAB)  $C_{22}H_{16}N_2S_2^{2+}$ , 372.20; Anal. Calc. for  $C_{22}H_{16}N_2S_2Br_2$ , Calcd: C, 49.60; H, 3.00; N, 5.26. Found: C, 49.55; H, 2.96; N, 5.18.

### 3,8-Di(thiophene-2-yl)-1,10-phenanthroline, 1,10-bipyridinium - bis(hexafluorophosphate) (**2**)

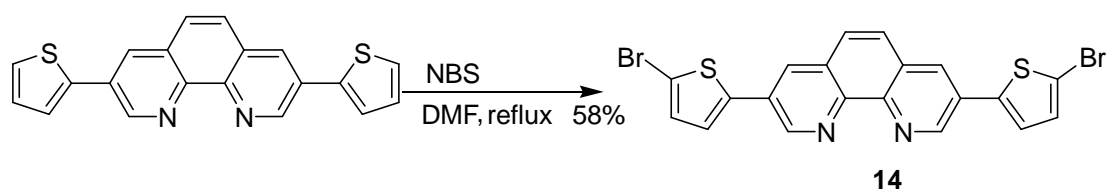


Compound **13** (0.20 g, 0.38 mmol) was dissolved carefully in distilled water (20 mL). This solution was added dropwise to an aqueous solution of potassium hexafluorophosphate (0.20 g, 1.09 mmol) in air. The resulting mixture was kept in air for three hours and then it was filtered. The solid was washed with water (5x 50 mL) to

remove any remaining starting materials, and was dried under vacuum overnight yielding compound **2** as a red powder (0.10 g, 39%).

Mp: 210°C dec;  $^1\text{H}$  NMR (400 MHz,  $\text{CD}_3\text{CN}$ )  $\delta$  = 9.68 (d,  $J$  = 2.11, 2H), 9.48 (d,  $J$  = 2.11, 2H), 8.57 (s, 2H), 8.10 (dd, 5.9,  $J$  = 0.9, 2H), 7.94 (dd,  $J$  = 5.9,  $J$  = 0.9, 2H), 7.44 (t,  $J$  = 5.8,  $J$  = 0.9, 2H), 5.50 (s, 4H);  $^{13}\text{C}$  NMR (100 MHz,  $\text{CD}_3\text{CN}$ )  $\delta$  = 51.9, 117.0, 126.7, 129.5, 129.7, 131.3, 131.9, 133.7, 134.8, 140.2, 145.6; MS (FAB)  $\text{C}_{22}\text{H}_{16}\text{N}_2\text{S}_2^{2+}$ , 372.20; Anal. Calc. for  $\text{C}_{22}\text{H}_{16}\text{N}_2\text{S}_2\text{P}_2\text{F}_{12}$ , Calcd: C, 39.86; H, 2.42; N, 4.23. Found: C, 39.74; H, 2.54; N, 4.10.

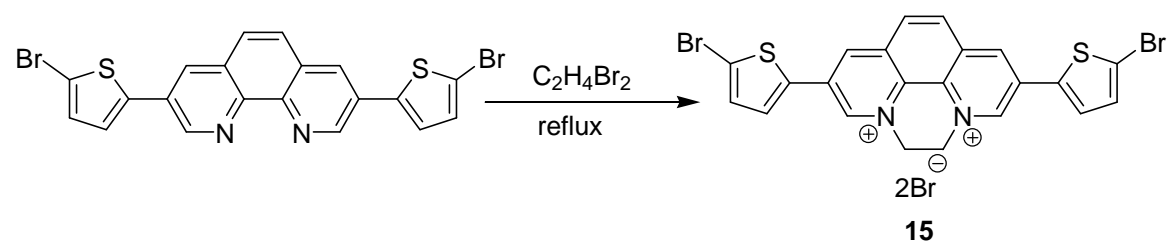
### 3,8-Bis(5-bromothiophen-2-yl)-1,10-phenanthroline (**14**)<sup>(8)</sup>



3,8-Di(thiophen-2-yl)-1,10-phenanthroline (0.50 g, 1.45 mmol) was dissolved in DMF (30 mL) and to this mixture N-bromosuccinimide (0.55 g, 3.00 mmol) was added. The mixture was heated under reflux in air overnight. Then it was cooled to room temperature and the mixture was filtered and the resulting solid was washed with methanol (6 x 50 mL). The solid then was dried under vacuum overnight to afford compound **14** as a yellow powder (0.38 g, 52%).

Mp: 253-255 °C. (Lit 251- 253 °C)<sup>(9)</sup>;  $^1\text{H}$  NMR (400 MHz, d-DMSO)  $\delta$  = 9.42 (d,  $J$  = 2.4, 2H), 8.71 (d,  $J$  = 2.4, 2H), 8.07 (s, 2H), 7.77 (d,  $J$  = 3.4, 2H), 7.44 (d,  $J$  = 3.4, 2H). MS (FAB)  $\text{C}_{20}\text{H}_{10}\text{Br}_2\text{N}_2\text{S}_2^+$ , 501.74.

### 3,8-Bis(5-bromothiophen-2-yl)-1,10-phenanthroline-1,10-bipyridiniumbromide (**15**)

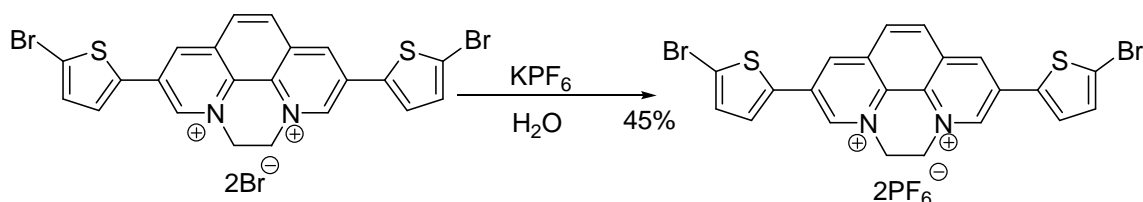


Compound **14** (0.20g, 0.30 mmol) was mixed with 1,2-dibromoethane (10 mL). The mixture was heated under reflux in air overnight. The reaction was cooled to room temperature and kept in air at room temperature for three hours. The mixture was then

filtered, and the obtained solid washed with DCM (5 x50 mL) to remove unreacted starting material and then dried under vacuum overnight to yield compound **15** as a red/ yellow solid (0.10 g, 48%).

Mp: 292 °C dec; <sup>1</sup>H NMR (400 MHz, d- DMSO) δ =10.26 (s, 2H), 9.71 (s, 2H), 8.63 (s, 2H), 8.10 (d, *J*= 4.2, 2H), 7.63 (d, *J*= 4.2, 2H), 5.57 (s, 4H); MS (FAB) C<sub>22</sub>H<sub>14</sub>Br<sub>2</sub>N<sub>2</sub>S<sub>2</sub><sup>2+</sup>, 530.10; Anal. Calc. for C<sub>22</sub>H<sub>14</sub>N<sub>2</sub>S<sub>2</sub>Br<sub>4</sub>, Calcd: C, 38.26; H, 2.03; N, 4.06. Found: C, 38.10; H, 2.21; N, 4.22. For compound **15**, it was impossible to obtain <sup>13</sup>C due to poor solubility of this compound. However, Carbone skeleton for this compound was confirmed by <sup>13</sup>C of it respective compound (**3**) as it has same Carbone skeleton and just differ in the counter anion.

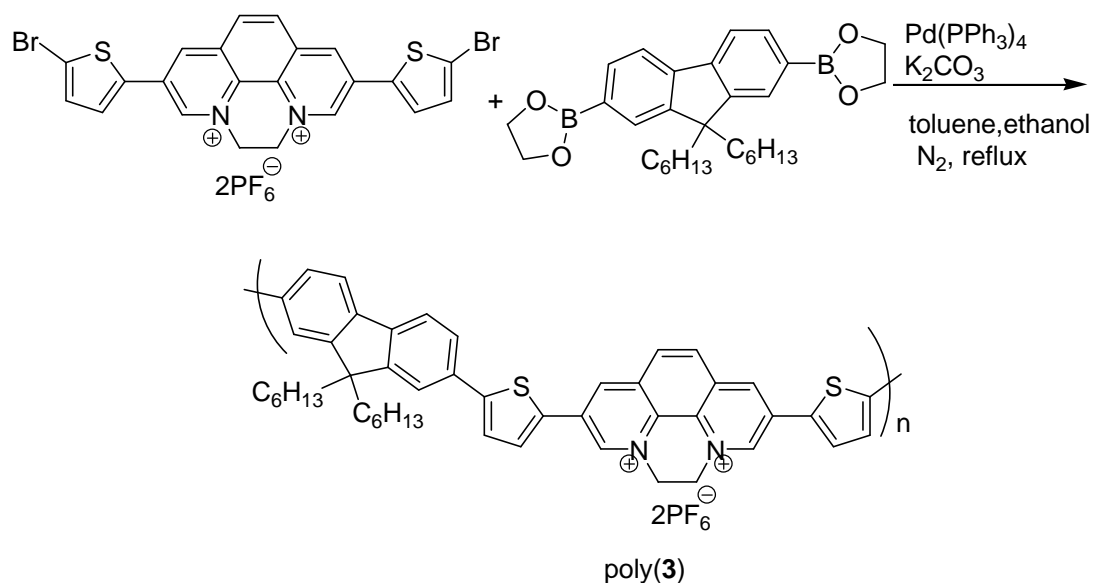
**3,8-Bis(5-bromothiophen-2-yl)-1,10-phenanthroline-1,10-bipridinium-bis(hexafluorophosphate) (3)**



Compound **15** (0.20 g, 0.29 mmol) was dissolved carefully in distilled water (20 mL). This solution was added dropwise in air to 20 mL of an aqueous solution of KPF<sub>6</sub> (0.16 g, 0.88 mmol). The mixture was then filtered and the resulting solid washed with water (5x 50 mL), and then dried overnight to yield compound **3** as an orange powder (0.12 g, 45%).

Mp: 240 °C dec; <sup>1</sup>H NMR (400 MHz, d- acetone) δ =10.34 (d, *J*= 1.9, 2H), 9.81 (d, *J*=1.9, 2H), 8.85 (s, 2H), 8.01 (d, *J*= 4.1, 2H), 7.55 (d, *J*=4.1, 2H), 6.08 (s, 4H); <sup>13</sup>C NMR (100 MHz, CD<sub>3</sub>CN) δ= 52.0, 117.0, 118.3, 129.9, 130.2, 131.4, 132.6, 133.0, 136.3, 140.40, 145.5; MS (FAB) C<sub>22</sub>H<sub>14</sub>Br<sub>2</sub>N<sub>2</sub>S<sub>2</sub><sup>2+</sup>, 530.10; Anal. Calc. for C<sub>22</sub>H<sub>14</sub>Br<sub>2</sub>N<sub>2</sub>S<sub>2</sub>P<sub>2</sub>F<sub>12</sub>, Calcd: C, 32.20; H, 1.71; N, 3.41. Found: C, 32.05; H, 1.82; N, 3.53.

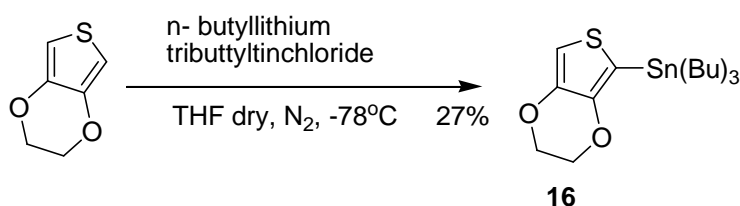
### Chemical polymerization of compound (3)



Viologen monomer **3** (0.400 g, 0.488 mmol) and 9,9- dioctylfluorene-2,7-diboronic acid ( 0.700g, 1. 460 mmol) were dissolved and degassed with 30 mL of ethanol: toluene (1:1 mixture). To this mixture tetra-kis triphenylphosphine (0.030 g, 0.025 mmol) and K<sub>2</sub>CO<sub>3</sub> (10 mL, 2M) were added in darkness. The whole mixture was then degassed and heated under reflux at 85 °C in the dark with nitrogen flush and continuous stirring for three days<sup>(10)</sup>. The reaction was cooled to room temperature, the solvent left to evaporate, and the obtained solid was then dried under vacuum. Then this solid was dissolved in THF (50 mL) with continuous stirring and then an excess of MeOH (300 mL) was added to the mixture with vigorous stirring. No precipitate was formed upon adding methanol. Water (100 mL) was then added to that mixture with stirring to obtain a precipitate. The precipitate was then filtered and then dried under vacuum overnight to yield an orange solid (0.13 g, 19%).

Mp: 185 °C dec; GPC, M<sub>n</sub> = 3796, M<sub>w</sub> = 3893, PDI= 1.035; <sup>1</sup>H NMR (400 MHz, CDCl<sub>3</sub>) δ = 8.28- 8.10 (m), 8.05 (s), 7.92- 7.88 (m), 7.80- 7.72(m), 7.75- 7.60 (m), 7.39- 7.28 (m), 6.92- 6.78 (m), 2.95 (s), 2.10-1.85 (m), 120- 0.95 (m), 0.72-0.50 (m).

### 2-(Tributylstannyl)- 3,4-(ethylenedioxythiophene)<sup>(11)</sup> (**16**)

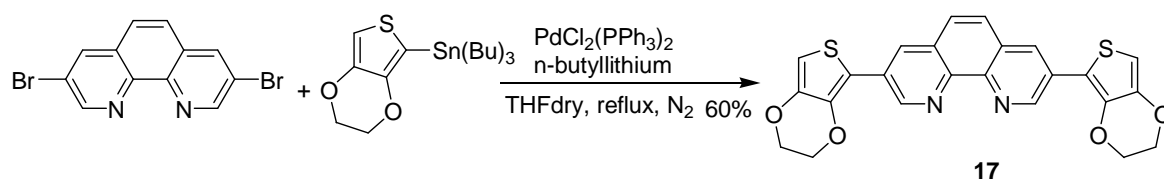


Commercially available 3,4-(ethylenedioxythiophene) (2.00 g, 14.01 mmol) was dissolved in dry THF (60 mL). This mixture was cooled to -78 °C using a mixture of (dry ice/

acetone), then *n*-butyllithium 1.6 M (10 mL, 16.20 mmol) was added dropwise at this temperature under a N<sub>2</sub> atmosphere. The resulting mixture was stirred for one hour at -78 °C, and then tributyltin chloride (5.95 g, 18.80 mmol) was added dropwise under a N<sub>2</sub> atmosphere with continuous stirring for another hour. Then the resulting mixture was allowed to warm to room temperature overnight. The mixture was then diluted with diethyl ether (100 mL), extracted with diethyl ether (5 x 100 mL), washed with NaHCO<sub>3</sub> (3 x 100 mL), and then washed with water (3 x 100 mL). The organic layer was dried with MgSO<sub>4</sub>. The mixture then filtered and the solvent was then removed under reduced pressure to afford compound **16** as a yellow oily liquid (1.60 g, 27%).

<sup>1</sup>H NMR (CDCl<sub>3</sub>, 400 MHz): δ= 6.54 (s, 1H), 4.12 (s, 4H), 1.60- 1.48 (m, 6H), 1.38- 1.32 (m, 6H), 1.10 (t, 9H), 0.90 (q, 6H).

### 3,8- Bis(3,4-(ethylenedioxy) thien-2-yl)-1,10-phenanthroline (**17**)<sup>(12)</sup>

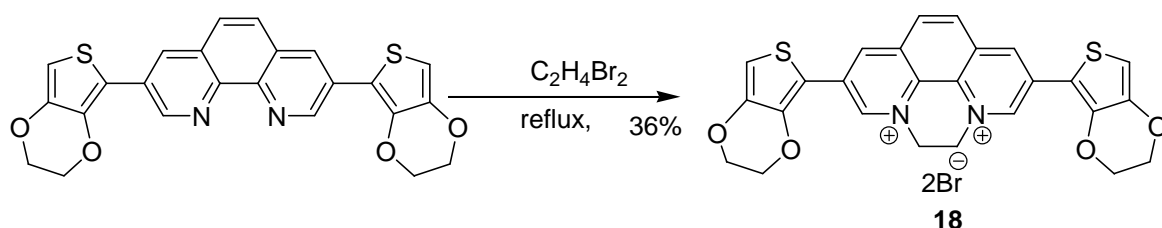


A solution of PdCl<sub>2</sub>(PPh<sub>3</sub>)<sub>2</sub> (0.04 g, 0.06 mmol) in dry THF (5 mL) was cooled to -78 °C using a mixture of dry ice/ acetone. To this mixture *n*-BuLi (1.6 M, 0.5 mL) was added carefully. Then mixture was stirred at -78 °C under a N<sub>2</sub> atmosphere for 20 minutes, and then warmed up to room temperature for about hour until this mixture was turned into a dark blue solution. Then this solution was added to a solution of 3,8- dibromo-1,10-phenanthroline (0.40 g, 1.18 mmol) and 2-(tributylstannyl)-3,4-(ethylenedioxythiophene) (1.30 g, 3.02 mmol) in dry DMF (40 mL). The resulting mixture then heated under reflux in N<sub>2</sub> overnight. The reaction then was cooled to room temperature and DCM (100 mL) was added. Washing with saturated NH<sub>4</sub>Cl (3 x 50 mL) and then with an aqueous solution Na<sub>2</sub>(EDTA) (3 x50 mL) and finally H<sub>2</sub>O (4x 50 mL) was undertaken. The organic layer was separated and collected and the solvent left to evaporate. The crude product then dissolved in ethyl acetate (100 mL) and the solid formed was separated by filtration. This solid was washed with diethyl ether (3 x 50 mL) and then further purified by silica gel column chromatography, using a DCM/ PET mixture (7:3) as an eluent. The fractions were collected and the solvent was evaporated and the solid dried under vacuum overnight to yield compound **17** as a yellow powder (0.32 g, 60%).

MP: + 300 °C; <sup>1</sup>H NMR (CDCl<sub>3</sub>, 400 MHz): δ= 9.46 (d, *J*= 2.4, 2H), 8.48 (d, *J*= 2.4, 2H), 7.77 (s, 2H), 6.45 (s, 2H), 4.42 (m, 4H), 4.31 (m, 4H). MS (FAB) C<sub>24</sub>H<sub>16</sub>N<sub>2</sub>O<sub>4</sub>S<sub>2</sub><sup>+</sup>, 460.26.

Anal. Calc. for  $C_{24}H_{16}N_2O_4S_2$ , Calcd: C, 62.57; H, 3.48; N, 6.08. Found: C, 62.48; H, 3.60; N, 6.15.

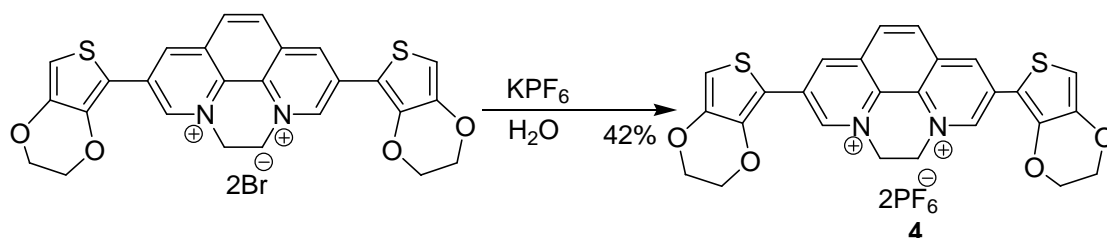
**3,8-Bis(3,4-(ethylenedioxy) thien-2-yl)-1,10-phenanthroline-1,10-bipyridinium bromide (18)**



3,8- Bis(3,4-(ethylenedioxy) thien-2-yl)-1,10- phenanthroline ( 0.30 g, 0.65 mmol) was mixed with 1,2- dibromoethane (10 mL). The mixture was heated under reflux overnight in air. Then the reaction was cooled to room temperature, filtered and the obtained solid washed with DCM (5x 50 mL) to remove unreacted material. The solid was dried under vacuum overnight to afford (18) as a red/ brown solid (0.14 g, 36%).

Mp: 244 °C dec;  $^1H$  NMR (DMSO, 400 MHz):  $\delta$ = 9.92 (s, 2H), 9.53 (s, 2H), 8.68 (s, 2H), 7.22 (s, 2H), 5.70 (s, 4H), 4.56 (s, 4H), 4.40 (s, 4H);  $^{13}C$  NMR (DMSO, 100 MHz)  $\delta$ = 145.0, 143.4, 142.4, 137.8, 131.9, 130.5, 129.4, 126.3, 108.9, 105.5, 65.7, 64.2, 52.3; MS (FAB)  $C_{26}H_{20}N_2O_4S_2^{2+}$ , 488.20; Anal. Calc. for  $C_{26}H_{20}N_2O_4S_2Br_2$ , Calcd: C, 48.13; H, 3.09; N, 4.32. Found: C, 47.96; H, 3.20; N, 4.45.

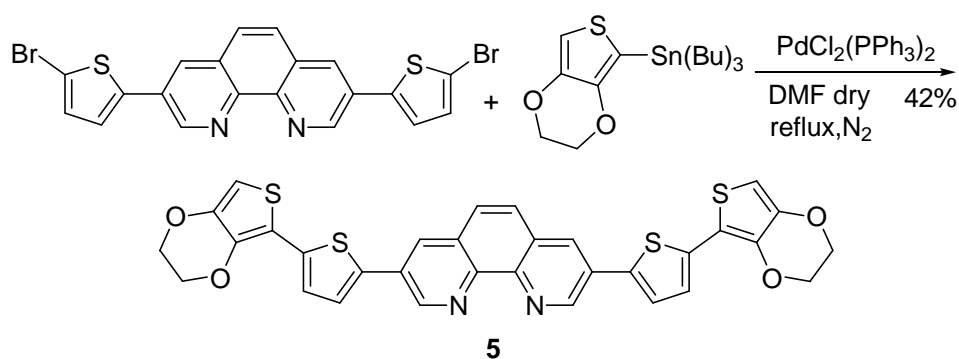
**3,8- Bis(3,4-(ethylenedioxy) thien-2-yl)-1,10-phenanthroline-1,10-bipyridinium-bis(hexafluorophosphate) (4)**



Compound **18** (0.20 g, 0.30 mmol) was dissolved in distilled water (25 mL). The resulting solution was added dropwise to another solution of 25 mL of an aqueous solution of  $NH_4PF_6$  (0.15 g, 0.92 mmol) in air. The mixture was kept in air for three hours and then the solid was formed filtered and then washed with water (5 x 50 mL) and dried in vacuum overnight to afford compound **4** as a red powder (0.10 g, 42%).

Mp: 196 °C dec;  $^1\text{H}$  NMR ( $\text{CD}_3\text{CN}$ , 400 MHz):  $\delta$ = 9.68 (d,  $J$ = 1.8, 2H), 9.35 (d,  $J$ = 1.8, 2H), 8.48 (s, 2H), 6.95 (s, 2H), 5.46 (s, 4H), 4.58 (m, 4H), 4.42 (m, 4H);  $^{13}\text{C}$  NMR (d-  
acetone, 100 MHz)  $\delta$ = 146.2, 145.1, 143.9, 139.2, 134.4, 132.6, 130.8, 129.4, 109.9,  
106.4, 66.8, 65.3, 54.1; MS (FAB)  $\text{C}_{26}\text{H}_{20}\text{N}_2\text{O}_4\text{S}_2^{2+}$ , 488.20; Anal. Calc. for  
 $\text{C}_{26}\text{H}_{20}\text{N}_2\text{O}_4\text{S}_2\text{P}_2\text{F}_{12}$ , Calcd: C, 40.08; H, 2.57; N, 3.60. Found: C, 39.91; H, 2.71; N,  
3.44.

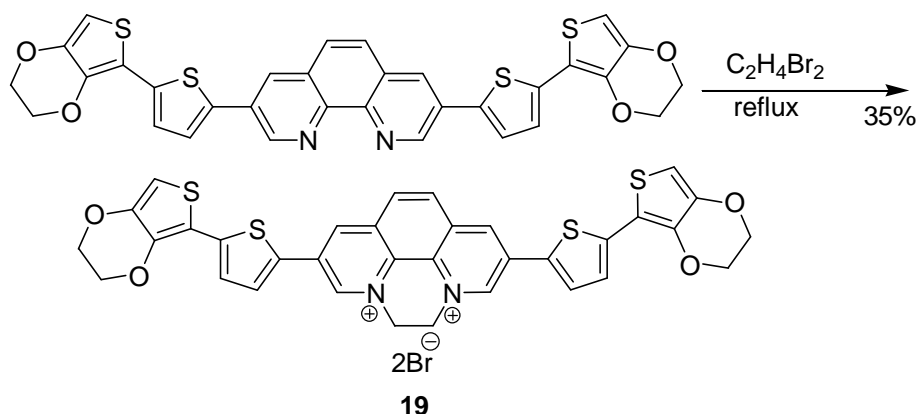
### 3,8-Bis( thiophen- 2- yl)-3,4- bis(ethylenedioxy) thien-2-yl)-1,10-phenanthroline (5)



A mixture of 3,8- bis(5-bromothiophen-2-yl)-1,10- phenanthroline (0.20 g, 0.40 mmol), 2-(tributylstannyl)- 3,4- (ethylenedioxythiophene) (0.510 g, 1.18 mmol), and trans-dichlorobis(triphenylphosphine)palladium(II) (0.03 g, 0.04 mmol) were dissolved in dry THF (30 mL). This mixture was degassed under a  $\text{N}_2$  atmosphere and then heated under reflux in  $\text{N}_2$  for 24 hours. Then it was cooled to room temperature, solvent evaporated to yield a crude product. This then was further purified by silica gel column chromatography, using an eluent mixture of DCM/ PET (8:2) to yield compound **5** as an orange powder (0.11g, 40%).

Mp: 220 °C dec;  $^1\text{H}$  NMR ( $\text{CDCl}_3$ , 400 MHz):  $\delta$ = 9.42 (d,  $J$ = 2.1, 2H), 8.31 (d,  $J$ = 2.1, 2H), 7.79 (s, 2H), 7.51(d,  $J$ = 3.8, 2H), 7.28 (d,  $J$ = 3.8, 2H), 6.30 (s, 2H), 4.42 (m, 4H), 4.30 (m, 4H);  $^{13}\text{C}$  NMR ( $\text{CDCl}_3$ , 100 MHz)  $\delta$ = 147.7, 144.7, 141.9, 138.1, 138.0, 136.3, 130.8, 129.4, 128.4, 127.1, 125.0, 123.9, 111.9, 97.7, 65.2, 64.6; MS (FAB)  $\text{C}_{32}\text{H}_{20}\text{N}_2\text{O}_4\text{S}_4$ , 624.20; Anal. Calc. for  $\text{C}_{32}\text{H}_{20}\text{N}_2\text{O}_4\text{S}_4$ , Calcd: C, 61.52; H, 3.21; N, 4.49. Found: C, 61.45; H, 3.32; N, 4.62.

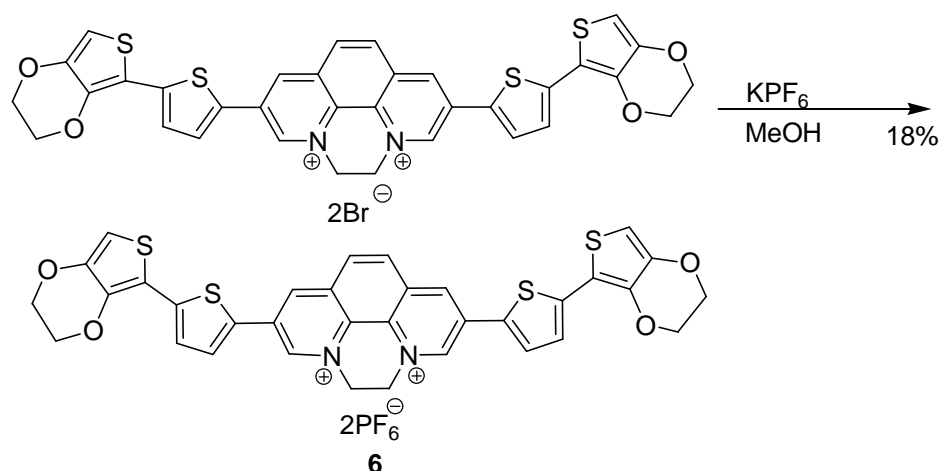
**3,8-Bis( thiophen- 2- yl)- 3,4-bis(ethylenedioxy) thien-2-yl) 1,10-phenanthroline-1,10-bipyridiniumbromide (19)**



A mixture of compound **5** (0.20 g, 0.32 mmol) and 1,2- dibromoethane (10 mL) was heated under reflux with continuous stirring under air for two days. This mixture was then cooled to room temperature and maintained at this temperature for five hours. The mixture was filtered and the obtained solid washed with DCM (5 x 50 mL) and then dried under vacuum overnight to afford compound **19** as a black solid (0.10 g, 35%).

Mp: 295 °C dec; <sup>1</sup>H NMR (d-DMSO, 400 MHz): δ= 10.26 (s, 2H), 9.42 (s, 2H), 8.42 (s, 2H), 7.42 (d, *J*= 3.6, 2H), 7.26 (d, *J*= 3.6, 2H), 6.65 (s, 2H), 5.78 (s, 4H), 4.43 (m, 4H), 4.31 (m, 4H); MS (FAB) C<sub>34</sub>H<sub>24</sub>N<sub>2</sub>O<sub>4</sub>S<sub>4</sub><sup>2+</sup>, 652.10; Anal. Calc. for C<sub>34</sub>H<sub>24</sub>N<sub>2</sub>O<sub>4</sub>S<sub>4</sub>Br<sub>2</sub>, Calcd: C, 50.21; H, 2.95; N, 3.45. Found: C, 50.11; H, 3.08; N, 3.60.

**3,8-Bis( thiophen- 2- yl)- 3,4-bis(ethylenedioxy) thien-2-yl) 1,10-phenanthroline-1,10-bipyridinium-bis(hexafluorophosphate) (6)**

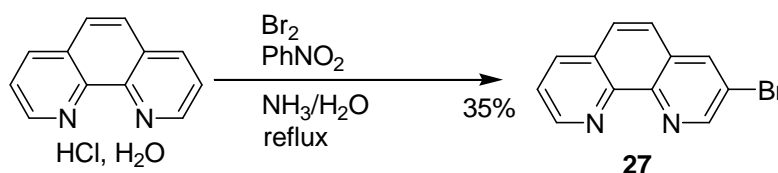


Compound **19** (0.10 g, 0.12 mmol) was dissolved in methanol (30 mL) and the resulting mixture was filtered. The eluent solution was added dropwise in air to a 25 mL of an aqueous solution of KPF<sub>6</sub> in MeOH (0.20 g, 1.09 mmol). The resulting mixture was left in

air for five hours and then it was filtered. The obtained solid washed with methanol (5 x 50 mL) and then was dried under vacuum overnight to yield compound **6** as a black/ green solid (0.03 g, 18%).

Mp: 285 °C dec; <sup>1</sup>H NMR (CD<sub>3</sub>CN, 400 MHz): δ= 9.57 (d, *J*= 1.9, 2H), 9.25 (d, *J*= 1.9, 2H), 8.44 (s, 2H), 7.90 (d, *J*= 4.1, 2H), 7.45 (d, *J*= 4.1, 2H), 6.55 (s, 2H), 5.46 (s, 4H), 4.47 (m, 4H), 4.33 (m, 4H); <sup>13</sup>C NMR (CD<sub>3</sub>CN, 100 MHz) δ= 54.5, 64.5, 65.8, 97.1, 117.2, 122.6, 124.1, 126.9, 128.9, 129.9, 131.2, 136.8, 138.5, 139.1, 141.6, 144.1, 148.2; MS (FAB) C<sub>34</sub>H<sub>24</sub>N<sub>2</sub>O<sub>4</sub>S<sub>4</sub><sup>2+</sup>, 652.10; Anal. Calc. for C<sub>34</sub>H<sub>24</sub>N<sub>2</sub>O<sub>4</sub>S<sub>4</sub>P<sub>2</sub>F<sub>12</sub>, Calcd: C, 43.30; H, 2.55; N, 2.97. Found: C, 43.18; H, 2.66; N, 3.10.

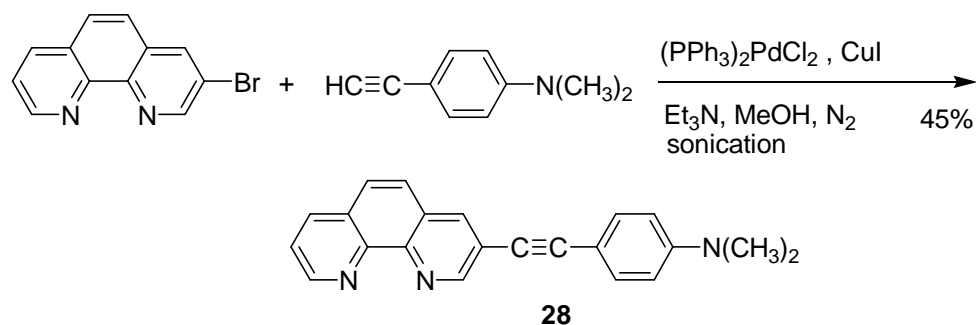
### 3-Bromo-1,10-phenanthroline (**27**)<sup>(13)</sup>



A mixture of commercially available 1,10- phenanthroline hydrochloride monohydrate (5.00 g, 21.50 mmol), and nitrobenzene (20 mL) were mixed together and heated under reflux at 140 °C. To this mixture, a solution of bromine (3.3 mL) and nitrobenzene (9.3 mL) was added dropwise over a period of one hour. The final mixture was maintained under reflux at 140 °C in air for a further four hours. Then it was cooled to room temperature, treated with an aqueous solution of NH<sub>3</sub> (100 mL), extracted with DCM (4 x100 mL) and washed with water (3 x100 mL) and finally dried over MgSO<sub>4</sub>. The solution was filtered and the solvent was evaporated under reduced pressure and the remaining suspension dissolved in DCM (20 ml). The crude product was further purified by silica gel column chromatography, using an eluent mixture of DCM/ MeOH (9.5:0.5). The obtained fractions were collected and the solvent was evaporated and the resultant solid then was dried under vacuum overnight to yield compound **27** as a white/yellow powder (2.20 g, 40%).

Mp: 166- 168 °C (Lit 164- 167 °C); <sup>(10)</sup> <sup>1</sup>H NMR ( CDCl<sub>3</sub>, 400 MHz), δ= 9.20 ( dd, *J*= 4.4, *J*= 1.5, 1H), 9.19 (d, *J*=2.2, 1H), 8.40 (d, *J*=2.2, 1H), 8.26 (dd, *J*= 8.1, *J*= 1.5, 1H), 7.83 (d, *J*= 8.8, 1H), 7.72 (d, *J*= 8.8, 1H), 7.65 (dd, *J*= 8.1, *J*= 4,4, 1H). MS (FAB) C<sub>12</sub>H<sub>7</sub>N<sub>2</sub>Br, 259.21.

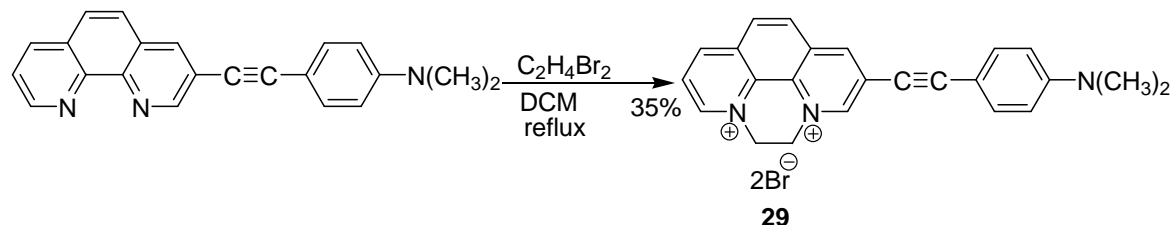
#### 4-(2-(1,10-Phenanthroline-8-yl)ethynyl)-N,N-dimethylbenzenamine (28)



A mixture of 3-bromo-1,10-phenanthroline (0.23 g, 0.90 mmol),  $\text{CuI}$  (0.03 g, 0.16 mmol) and  $\text{PdCl}_2(\text{PPh}_3)_2$  (0.07 g, 0.10 mmol) was degassed under a  $\text{N}_2$  atmosphere. Another mixture of 4-ethynyl-N,N-dimethylbenzenamine (0.20 g, 1.40 mmol) with triethylamine/methanol (24/12) mL was degassed under a  $\text{N}_2$  atmosphere. This mixture was added into the first mixture-using syringe under a  $\text{N}_2$  atmosphere. The resulting mixture was sonicated at room temperature for four hours, after which it was then dissolved in DCM (200 mL) washed with water (4 x 100 mL) and then dried over  $\text{MgSO}_4$ . The mixture was filtered and the solvent was evaporated under vacuum to yield a crude material which was further purified by silica gel column chromatography, using an eluent mixture DCM/ EtOAc (7:3) to yield compound **28** as a yellow/ brown solid (0.12 g, 42%).

Mp: 208-210 °C;  $^1\text{H NMR}$  ( $\text{CDCl}_3$ , 400 MHz):  $\delta$ = 9.25 (d,  $J$ = 2.1, 1H), 9.15 (dd,  $J$ = 6.8,  $J$ = 1.9, 1H), 8.30 (d,  $J$ = 2.0, 1H), 8.22 (dd,  $J$ = 9.2,  $J$ = 2.0, 1H), 7.75 (m, 2H), 7.61 (dd,  $J$ = 9.1,  $J$ = 4.3, 1H), 7.45 (d,  $J$ = 4.3, 2H), 6.69 (d,  $J$ = 4.3, 2H), 3.02 (s, 6H);  $^{13}\text{C NMR}$  ( $\text{CDCl}_3$ , 100 MHz)  $\delta$ = 40.1, 60.4, 84.7, 95.5, 108.9, 111.9, 120.7, 123.0, 126.1, 127.1, 127.9, 128.7, 133.0, 136.0, 136.9, 144.2, 146.1; MS (FAB)  $\text{C}_{22}\text{H}_{17}\text{N}_3$ , 323.10; Anal. Calc. for  $\text{C}_{22}\text{H}_{17}\text{N}_3$ , Calcd: C, 81.68; H, 5.26; N, 13.00. Found: C, 81.53; H, 5.40; N, 13.10.

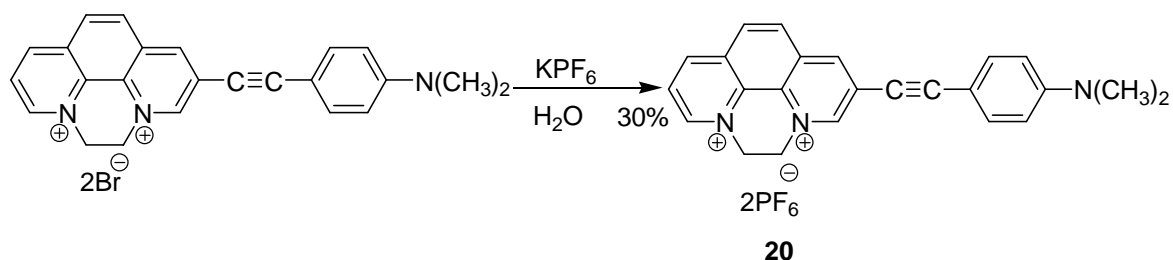
#### 4-(2-(1,10-Phenanthroline-8-yl)ethynyl)-N,N-dimethylbenzenamine-1,10-bipyridinimbromide (29)



Compound **28** (0.20 g, 0.62 mmol) was dissolved in DCM (20 mL) and mixed with 1,2-dibromoethane (10 mL) and the mixture heated under reflux in air overnight. The mixture was then cooled to room temperature and maintained at this temperature for five hours.

The precipitate that formed was filtered and washed with DCM (5 x100 mL) and then was dried under vacuum overnight to yield compound **29** as a dark/ blue powder (0.11 g, 35%). Mp: 290 °C dec; <sup>1</sup>H NMR (D<sub>2</sub>O, 400 MHz): δ= 9.72 (s,1H), 9.53 (d, *J*= 7.2, 1H), 9.45 (d, *J*= 7.2, 1H), 9.32 (s,1H), 8.54 (m, 1H), 7.98 (d, *J*= 7.5, 2H), 6.96 (d, *J*= 7.5, 2H), 6.87 (d, *J*= 7.5, 2H), 5.61 (s, 4H), 3.05 (s, 6H); MS (FAB) C<sub>24</sub>H<sub>21</sub>N<sub>3</sub><sup>2+</sup>, 351.2; Anal. Calc. for C<sub>24</sub>H<sub>21</sub>N<sub>3</sub>Br<sub>2</sub>, Calcd: C, 56.34; H= 4.11; N, 8.22. Found: C, 56.18; H, 4.24; N, 8.38.

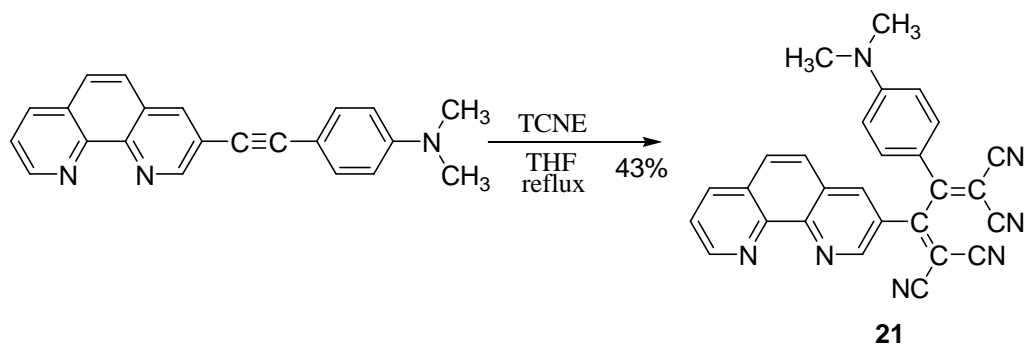
**4-(2-(1,10- Phenanthroline-8-yl)ethynyl)-N,N-dimethylbenzenamine-1,10-bipyridinim-bis(hexafluorophosphate) (20)**



Compound **29** (0.20 g, 0.39 mmol) was dissolved in distilled water (25 mL). This was then added dropwise in air to 25 mL of an aqueous solution of KPF<sub>6</sub> (0.20 g, 1.09 mmol). The resulting mixture was maintained in air for five hours, and then filtered and washed with water (5 x50 mL), and then dried under vacuum overnight to yield compound **20** as a black/ blue solid (0.07 g, 30%).

Mp: 220°C dec; <sup>1</sup>H NMR (CD<sub>3</sub>CN, 400 MHz): δ= 9.46 (s,1H), 9.38 (d, *J*= 8.3, 1H), 9.33 (d, *J*= 8.3, 1H), 9.27 (s,1H), 8.53(m, 1H), 8.05 (d, *J*= 9.1, 2H), 7.61 (d, *J*= 9.1, 2H), 6.80 (d, *J*= 9.2, 2H), 5.50 (s, 4H), 3.10 (s, 6H); <sup>13</sup>C NMR (CD<sub>3</sub>CN, 100 MHz) δ= 39.0, 51.8, 52.0, 52.2, 110.6, 111.7, 117.0, 127.0, 127.1, 129.2, 129.4, 130.0, 130.3, 131.2, 131.52, 133.67, 145.50, 147.68, 147.75, 148.40; MS (FAB) C<sub>24</sub>H<sub>21</sub>N<sub>3</sub><sup>2+</sup>, 351.2; Anal. Calc. for C<sub>24</sub>H<sub>21</sub>N<sub>3</sub>P<sub>2</sub>F<sub>12</sub>, Calcd: C, 44.92; H, 3.28; N, 6.55. Found: C, 44.73; H, 3.44; N,6.72.

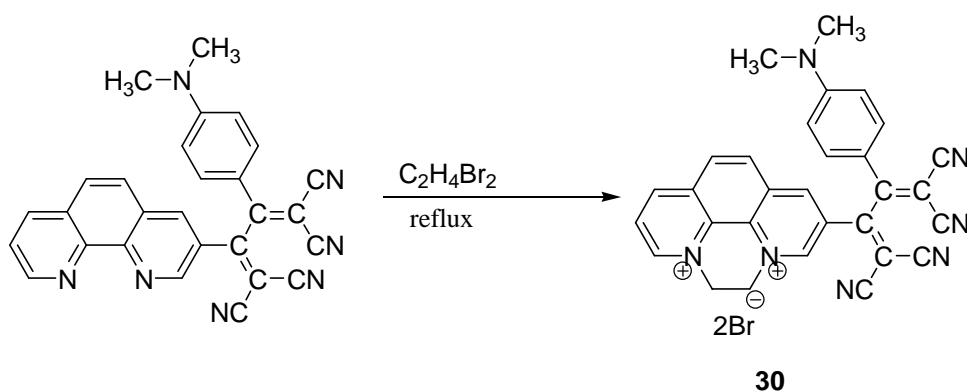
**2-(4-(Dimethylamino)phenyl)-3-(1,10-phenanthroline-8-yl)buta-1,3,4,4-tetracarbonitrile (21)**



A mixture of compound **28** (0.20 g, 0.62 mmol) and TCNE (0.14 g, 1.10 mmol) was dissolved in THF (25 mL). This mixture was heated under reflux in air overnight, after which it was cooled to room temperature and the solvent left to evaporate. The crude product was further purified by silica gel column chromatography, using an eluent mixture of DCM/ PET (7:3) to yield compound **21** as a brown/ dark powder (0.12 g, 43%).

Mp: 174- 176 °C; <sup>1</sup>H NMR (CDCl<sub>3</sub>, 400 MHz): δ= 9.31(d, *J*= 2.4, 2H), 9.20 ( dd, *J*= 5.80, *J*= 1.4, 2H), 8.67 (d, *J*= 1.4, 1H), 8.32 (dd, *J*= 9.5, *J*= 1.6, 1H), 7.93 (d, *J*= 1.6, 1H), 7.85 (dd, *J*= 12.4, *J*= 4.3, 1H), 7.74 (dd, *J*= 12.4, *J*= 4.4, 1H), 6.74 (d, *J*= 4.5, 2H), 3.18 (s, 6H); <sup>13</sup>C NMR (CDCl<sub>3</sub>, 100 MHz) δ= 40.3, 89.4, 110.8, 111.6, 112.5, 113.6, 114.11, 117.4, 124.7, 126.5, 127.1, 127.5, 128.9, 130.4, 132.6, 136.4, 137.4, 145.2, 148.1, 148.3, 151.2, 154.7, 161.8, 169.3; MS (FAB) C<sub>28</sub>H<sub>17</sub>N<sub>7</sub>, 451.19; Anal. Calc. for C<sub>28</sub>H<sub>17</sub>N<sub>3</sub>, Calcd: C, 74.47; H, 3.77; N, 21.72. Found: C, 74.28; H, 3.90; N, 21.86.

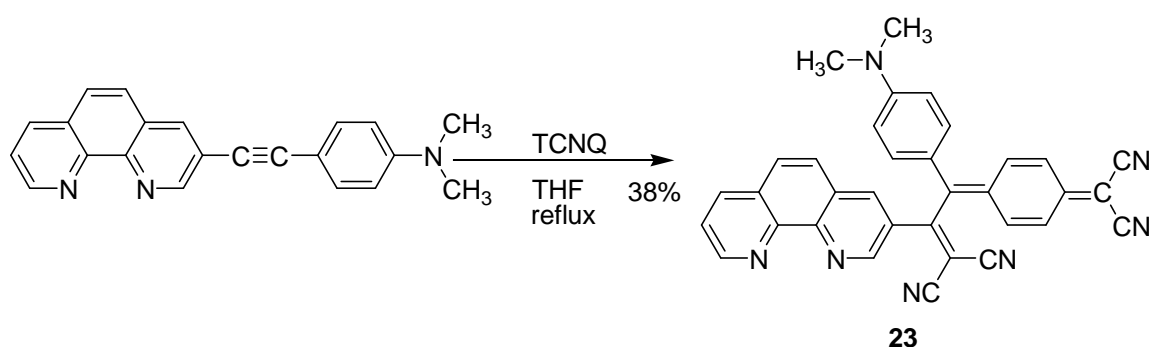
**2-(4-(Dimethylamino)phenyl)-3-(1,10-phenanthroline-8-yl)buta-1,3,4,4-tetracarbonitrile -1,10-bipyridiniumbromide (30)**



Compound **21** (0.20 g, 0.45 mmol) was dissolved in DCM (25 mL) and then it was mixed with 1,2- dibromoethane (5 mL). The reaction mixture was heated under reflux for two days after which it was cooled to room temperature, filtered off and the resulting solid

washed with DCM (5 x100 mL) and then dried under vacuum overnight. The compound was purified by recrystallization and by silica gel column chromatography, using an eluent mixture of MeOH/ H<sub>2</sub>O/ NH<sub>4</sub>Cl<sub>sat</sub> (6:3:1). However, this compound could not be obtained in a pure form. This probably arises from decomposition of this compound in the column. Mass spectrometry showed a signal for this compound in crude material, MS (FAB) C<sub>30</sub>H<sub>21</sub>N<sub>7</sub><sup>2+</sup> = 482.20.

### 3-{7,7,8,8-Tetracyanoquinodimethane}-1,10-phenanthroline (**23**)

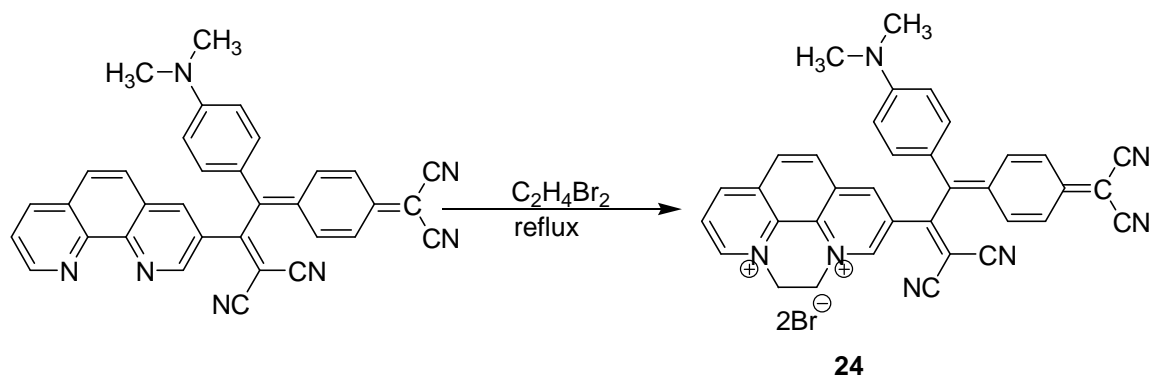


A mixture of compound **28** (0.20 g, 0.62 mmol) and TCNQ (0.18 g, 0.88 mmol) was dissolved in THF (25 mL) and heated under reflux overnight. Then the reaction was cooled to room temperature and the solvent was evaporated to give a crude product, which was further purified by silica gel column chromatography, using an eluent mixture of DCM/ PET (7:3). The fractions were collected and the final product was dried under vacuum to yield compound **23** as a black/ green powder (0.13 g, 38%).

Mp: 220 °C dec; <sup>1</sup>H NMR (CDCl<sub>3</sub>, 400 MHz): δ= 9.18 (dd, *J*= 8.7, *J*= 3.2, 1H), 8.67 (d, *J*= 3.2, 1H), 8.30 (dd, *J*= 8.5, 3.2, 1H), 7.90 (m, 2H), 7.70 (dd, *J*= 11.5, *J*= 4.3, 1H), 7.52 (dd, *J*= 11.5, *J*= 4.3, 1H), 7.29 (m, 4H), 7.18 (dd, *J*= 11.3, *J*= 1.9, 1H), 7.07 (dd, *J*= 11.3, *J*= 1.9, 1H), 6.69 (d, *J*= 2.0, 2H), 3.12 (s, 6H);

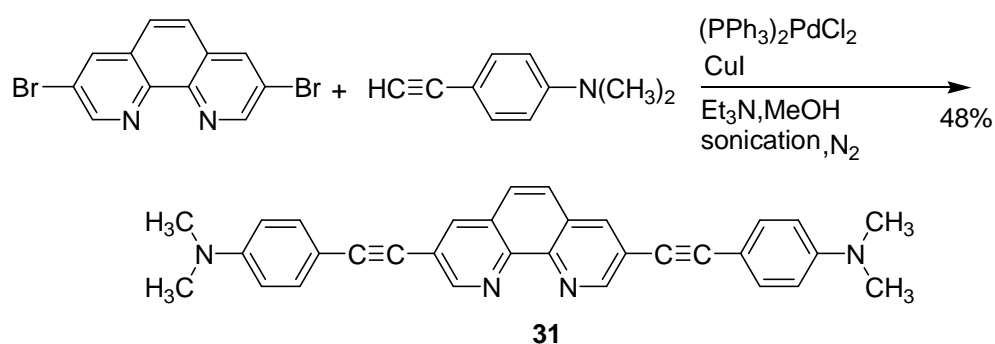
<sup>13</sup>C NMR (CDCl<sub>3</sub>, 100 MHz) δ= 40.2, 89.4, 111.9, 112.7, 114.5, 123.3, 124.5, 125.6, 125.9, 126.3, 127.5, 128.7, 130.3, 132.9, 134.0, 134.5, 135.8, 136.3, 137.0, 149.0, 150.3, 151.2, 153.0, 153.8, 169.4; MS (FAB) C<sub>34</sub>H<sub>21</sub>N<sub>7</sub>, 527.30; Anal. Calc. for C<sub>34</sub>H<sub>21</sub>N<sub>7</sub>, Calcd: C, 77.38; H, 3.98; N, 18.59. Found: C, 77.20; H, 4.13; N, 18.72.

### 3-{7,7,8,8-Tetracyanoquinodimethane}-1,10-phenanthroline-1,10-bipyridiniumbromide (**24**)



Compound **23** (0.20 g, 0.38 mmol) was dissolved in DCM (25 mL) and then 1,2-dibromoethane (5 mL) was added to the mixture. Then the mixture was heated under reflux for two days. The reaction was then cooled to room temperature, filtered and the resulting solid washed with DCM (3 x 100 mL) and then dried under vacuum. The crude product was purified by silica gel column chromatography, using an eluent mixture of MeOH/H<sub>2</sub>O/ NH<sub>4</sub>Cl<sub>sat</sub> (6:3:1). However, this compound couldn't be obtained in pure form. Mass spectrometry showed a signal for this compound in crude material, MS (FAB), C<sub>36</sub>H<sub>25</sub>N<sub>7</sub><sup>2+</sup> = 555.3.

### 3,8-Bis[p-(dimethylamino) phenylethynyl]- 1, 10-phenanthroline (**31**)<sup>(14)</sup>

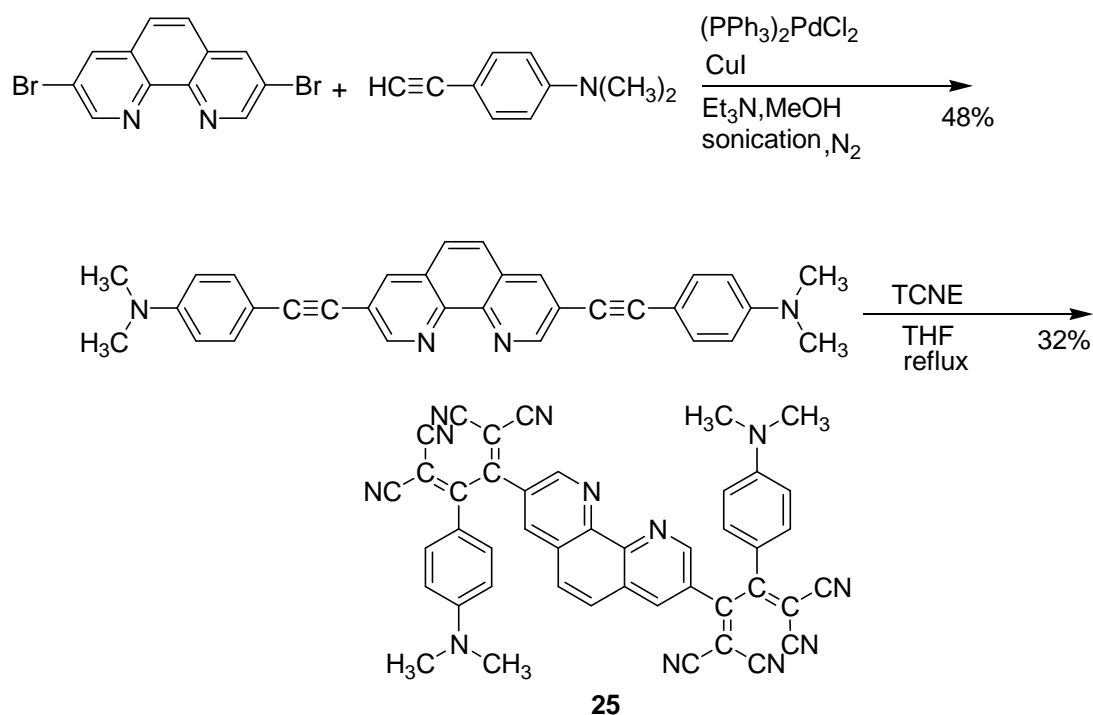


A mixture of 3,8- dibromo-1,10-phenanthroline (0.20 g, 0.60 mmol), PdCl<sub>2</sub>(PPh<sub>3</sub>)<sub>2</sub> (0.04 g, 0.06 mmol) and CuI (0.02 g, 0.10 mmol) was degassed under a N<sub>2</sub> atmosphere. Another mixture of 4- ethynyl-N,N-dimethylaniline) ( 0.26 g, 1.80 mmol) was dissolved in Et<sub>3</sub>N/ MeOH (24: 12) mL. The second mixture was added under N<sub>2</sub> into the first mixture, and the resultant mixture was sonicated at room temperature under N<sub>2</sub> for four hours. Then it was dissolved in DCM (100 mL), washed with water (3 x 100 mL) and then treated with

an aqueous solution of  $\text{Na}_2(\text{EDTA})_{\text{sat}}$  (100 mL) and dried over  $\text{MgSO}_4$ . Then it was filtered and the solvent was evaporated to give a crude product which was further purified by silica gel column chromatography, using an eluent mixture of DCM/ PET (7:3) to yield compound **31** as an orange powder (0.13 g, 46%).

Mp: + 300 °C;  $^1\text{H}$  NMR ( $\text{CDCl}_3$ , 400 MHz):  $\delta$ = 9.24 (d,  $J$ = 2.1, 2H), 8.31 (d,  $J$ = 2.1, 2H), 7.75 (s, 2H), 7.50 (d,  $J$ = 8.9, 4H), 6.70 (d,  $J$ = 8.9, 4H), 3.04 (s, 12H). MS (FAB)  $\text{C}_{32}\text{H}_{26}\text{N}_4^+$ , 466.42. Anal. Calc. for  $\text{C}_{32}\text{H}_{26}\text{N}_4$ , Calcd: C, 82.33; H, 5.57; N, 12.10. Found: C, 82.24; H, 5.66; N, 12.11.

### Bis[3-(4-dimethylamino)buta-1,3-diene-1,1,4,4- tetracarbonitrile]-1,10 - phenanthroline (**25**)

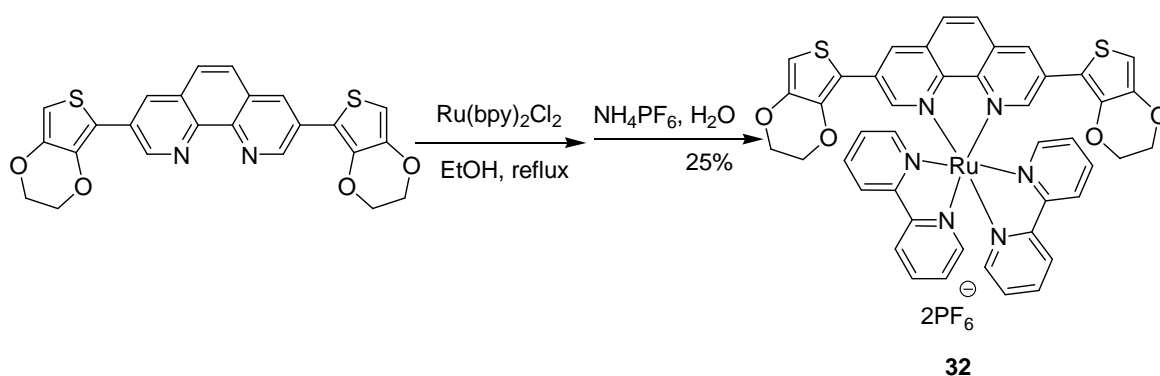


A mixture of compound **31** (0.20 g, 0.43 mmol) and TCNE (0.16 g, 1.25 mmol) was dissolved in THF (30 mL). This mixture was heated under reflux overnight in air. Then the was cooled to room temperature, and the solvent evaporated and the crude product was further purified by silica gel column chromatography, using an eluent mixture of DCM/PET (8:2) to yield compound **25** as a brown powder (0.10 g, 32%).

Mp: 278 °C dec;  $^1\text{H}$  NMR ( $\text{CDCl}_3$ , 400 MHz):  $\delta$ = 9.23 (dd,  $J$ = 8.6,  $J$ = 2.3, 2H), 8.71 (d,  $J$ = 2.3, 2H), 8.47 (d,  $J$ = 2.4, 2H), 7.85 (d,  $J$ = 9.3, 4H), 6.77 (d,  $J$ = 9.3, 4H), 3.20 (s, 12H);  $^{13}\text{C}$  NMR ( $\text{CDCl}_3$ , 100 MHz)  $\delta$ = 40.3, 112.5, 124.6, 126.4, 128.5, 128.6, 128.9, 132.0, 132.0,

132.2, 132.6, 136.3, 137.3, 148.2, 151.3; MS (FAB) C<sub>44</sub>H<sub>26</sub>N<sub>12</sub>, 722.28; Anal. Calc. for C<sub>44</sub>H<sub>26</sub>N<sub>12</sub>, Calcd: C, 73.10; H, 3.60; N, 23.26. Found: C, 72.98; H, 3.72; N, 23.38.

**Bis(2,2'-bipyridine)-3,8-(EDOT)-2',2''-yl)-1,10-phenanthroline) ruthenium (II) [Ru(bpy)<sub>2</sub>(DTEDOT)] (PF<sub>6</sub>)<sub>2</sub> (**32**)**

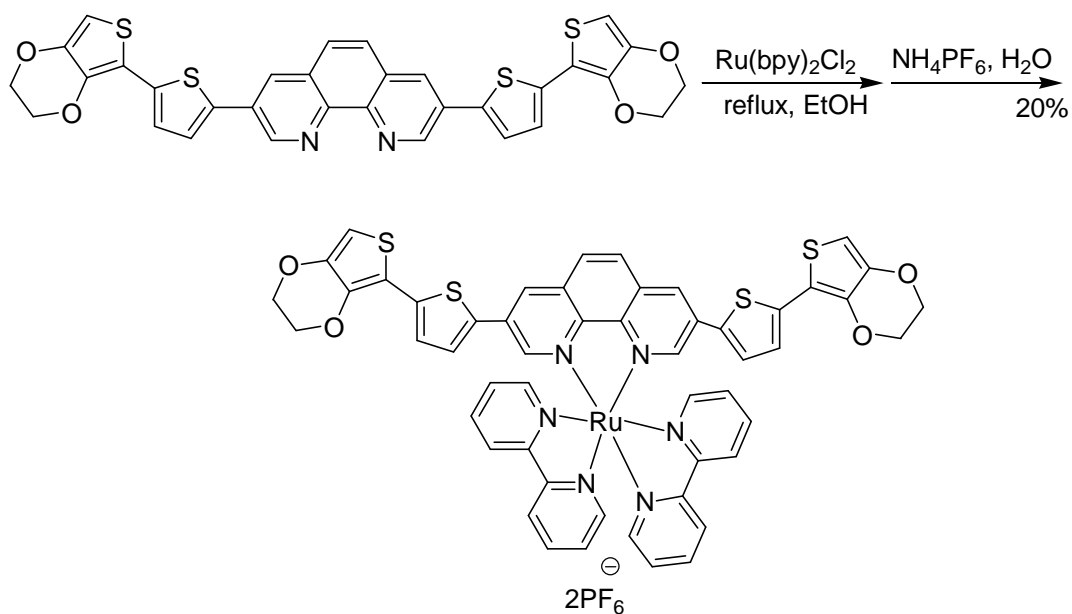


Compound **17** (0.17 g, 0.37 mmol) and Ru(bpy)<sub>2</sub>Cl<sub>2</sub> (0.18 g, 0.37 mmol) were dissolved in ethanol (50 mL). This mixture was heated under reflux in air for five hours and the solution was cooled to room temperature, filtered and the filtrate concentrated under reduced pressure. Then 50 mL of an aqueous solution of NH<sub>4</sub>PF<sub>6</sub> (0.24 g, 1.48 mmol) was added. The precipitate formed was filtered and washed with water (5 x 50 mL) and then washed with diethylether (5 x 50 mL). The solvent was evaporated under vacuum to yield compound **32** as an orange solid (0.11 g, 25%).

Mp: 286 °C dec; <sup>1</sup>H NMR (d-DMSO, 400 MHz): δ= 8.95 (d, *J*=8.2, 2H); 8.86 (d, *J*=8.2, 2H), 8.70 (d, *J*= 1.8, 2H), 8.37 (d, *J*= 1.8, 2H), 8.32 (t, *J*=15.7, 8.0, 4H), 8.13 (t, *J*= 15.7, *J*= 7.9, 2H), 7.98 (*J*= 5.3, 2H), 7.82 (d, *J*= 5.3, 2H), 7.67 (t, *J*= 13.3, *J*= 6.6, 2H), 7.39 (t, *J*= 13.3, *J*= 6.6, 2H), 6.91 (s, 2H), 4.20 (m, 4H), 4.10 (m, 4H).

<sup>13</sup>C NMR (CDCl<sub>3</sub>, 100 MHz) δ= 64.0, 64.9, 101.5, 110.9, 117.0, 123.8, 127.1, 127.2, 128.0, 129.4, 130.3, 131.6, 137.5, 137.6, 141.0, 142.3, 144.7, 148.5, 151.8, 152.0, 156.6, 157.2; MS (FAB) C<sub>44</sub>H<sub>32</sub>N<sub>6</sub>S<sub>2</sub>O<sub>4</sub>Ru<sup>2+</sup>, 873.20; Anal. Calc. for C<sub>44</sub>H<sub>32</sub>N<sub>6</sub>S<sub>2</sub>O<sub>4</sub>RuP<sub>2</sub>F<sub>12</sub>, Calcd: C, 45.38; H, 2.75; N, 7.22. Found: C, 45.25; H, 2.90; N, 7.32.

**3,8-Bis( thiophen- 2- yl)- 3,4- bis (ethylenedioxy) thien-2-yl) 1,10-phenanthroline ruthenium (II)[ Ru(bpy)<sub>2</sub>(DTEDOT)] (PF<sub>6</sub>)<sub>2</sub> (**33**)**

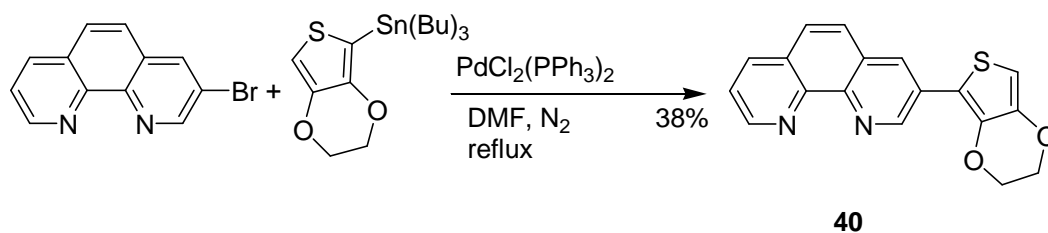


A mixture of compound **5** (0.23 g, 0.37 mmol) and Ru(bpy)<sub>2</sub>Cl<sub>2</sub> ( 0.18 g, 0.37 mmol) were dissolved in ethanol (50 mL). The mixture was heated under reflux in air for five hours and then was cooled to room temperature, filtered and the resulting filtrate was concentrated under vacuum. The last solution was added to 50 mL of an aqueous solution of NH<sub>4</sub>PF<sub>6</sub> (0.24 g, 1.48 mmol). The resulting precipitate then was filtered and washed with water (5 x 50 mL) and then with diethylether (5 x 50 mL), dried under vacuum overnight to yield compound **33** as a red solid (0.10 g, 20%).

Mp: 280 °C dec; <sup>1</sup>H NMR (CD<sub>3</sub>CN, 400 MHz): δ= 8.71 (d, *J*= 6.8, 2H), 8.60 (d, *J*= 8.3, 2H), 8.25 (d, *J*= 8.3, 2H), 8.19 (dd, *J*= 8.3, *J*= 1.10, 2H), 8.18 (s, 2H), 8.07 (d, *J*= 7.7, 2H), 8.04 (t, *J*= 15.8, *J*= 7.7, 2H), 7.96 (d, *J*= 5.5, 2H), 7.80 (d, *J*= 5.5, 2H), 7.55 (t, *J*= 12.2, *J*= 6.6, 2H), 7.34 ( d, *J*= 6.6, 2H), 7.30 (d, *J*= 6.6, 2H), 7.24 (d, *J*= 6.7, 2H), 6.45 (s, 2H), 4.43 (m, 4H), 4.32 (m, 4H); <sup>13</sup>C NMR (CD<sub>3</sub>CN, 100 MHz) δ= 64.3, 65.04, 98.3, 116.1, 117.0, 117.0, 123.6, 124.0, 124.1, 127.0, 127.1, 128.3, 128.4, 130.4, 130.7, 132.2, 135.0, 137.6, 137.9, 142.2, 145.6, 148.6, 152.0, 152.2, 156.7, 157.4; MS (FAB)

C<sub>52</sub>H<sub>36</sub>N<sub>6</sub>S<sub>4</sub>O<sub>4</sub>Ru<sup>2+</sup>, 1037.6; Anal. Calc. for C<sub>52</sub>H<sub>36</sub>N<sub>6</sub>S<sub>4</sub>O<sub>4</sub>RuP<sub>2</sub>F<sub>12</sub>, Calcd: C, 47.01; H, 2.71; N, 6.33. Found: C, 46.86; H, 2.87; N, 6.44.

### 3-(2,3-Dihydrothieno[3,4-b][1,4]dioxin-7yl)-1,10-phenanthroline (40)



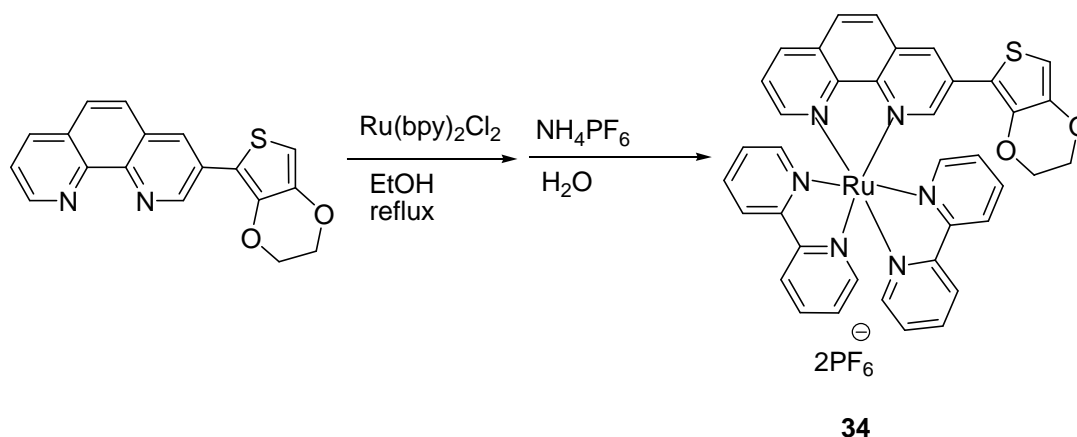
A mixture of 3-bromo-1,10-phenanthroline (0.40 g, 1.54 mmol), 2-(tributylstannyl)-3,4-(ethylenedioxythiophene) (0.82 g, 1.90 mmol) and  $\text{PdCl}_2(\text{PPh}_3)_2$  (0.05 g, 0.08 mmol) was dissolved in dry DMF (50 mL). This mixture was then degassed and heated under reflux in a  $\text{N}_2$  atmosphere overnight. The reaction was cooled to room temperature and the solvent was evaporated to give a crude product. The crude product was then further purified by silica gel column chromatography, using an eluent mixture of DCM/ PET (8:2) to yield compound **40** as an orange/ yellow powder (0.17 g, 38%).

Mp: 163- 165 °C;  $^1\text{H}$  NMR ( $\text{CDCl}_3$ , 400 MHz):  $\delta$ = 9.50 (d,  $J$ = 2.4, 1H), 9.18 (d,  $J$ = 2.7, 1H), 8.53 (d,  $J$ = 2.7, 1H), 8.23 (dd,  $J$ = 9.73,  $J$ = 3.6, 1H), 7.80 (d,  $J$ = 3.6, 2H), 7.61 (dd,  $J$ = 8.3,  $J$ = 3.6, 1H), 6.46 (s, 1H), 4.42 (m, 2H), 4.32 (m, 2H);

$^{13}\text{C}$  NMR ( $\text{CDCl}_3$ , 100 MHz)  $\delta$ = 64.5, 65.0, 99.6, 113.8, 122.7, 126.7, 126.9, 127.0, 128.3, 128.50, 131.2, 135.9, 139.9, 142.4, 144.1, 146.2, 148.1, 150.4;

MS (FAB)  $\text{C}_{18}\text{H}_{12}\text{N}_2\text{SO}_2$ , 320.7; Anal. Calc. for  $\text{C}_{18}\text{H}_{12}\text{N}_2\text{SO}_2$ , Calcd: C, 67.35; H, 3.74; N= 8.73. Found: C, 67.14; H= 3.90; N, 8.83.

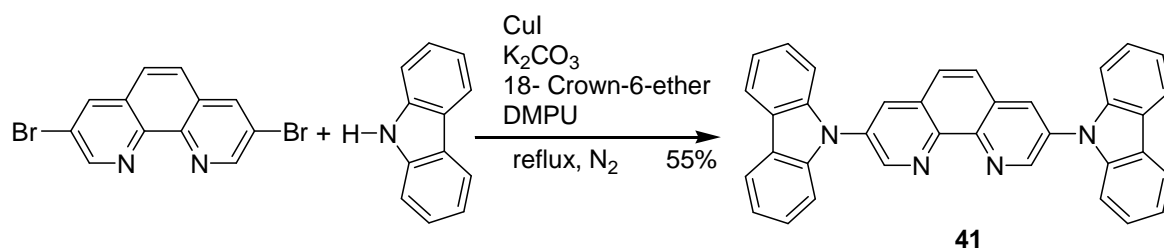
### 3-(2,3-Dihydrothieno[3,4-b][1,4]dioxin-7yl)- 1,10-phenanthroline ruthenium (II)[ Ru(bpy)<sub>2</sub>(DTEDOT)] (PF<sub>6</sub>)<sub>2</sub> (34)



Compound **40** (0.12 g, 0.37 mmol) and  $\text{Ru}(\text{bpy})_2\text{Cl}_2$  (0.18 g, 0.37 mmol) were dissolved in ethanol (50 mL), then was heated under reflux in air for five hours. The mixture was then cooled to room temperature, filtered and the resulting filtrate was concentrated by vacuum. The last solution was added to 50 mL aqueous solution of  $\text{NH}_4\text{PF}_6$  (0.24 g, 1.48 mmol).

The resulting precipitate then was filtered and washed with water (5 x 50 mL) and then with diethylether (5 x 50 mL), dried under vacuum overnight to yield **34**. However, this compound could not obtain in pure form despite use of purification methods such as washing, recrystallization and column chromatography.

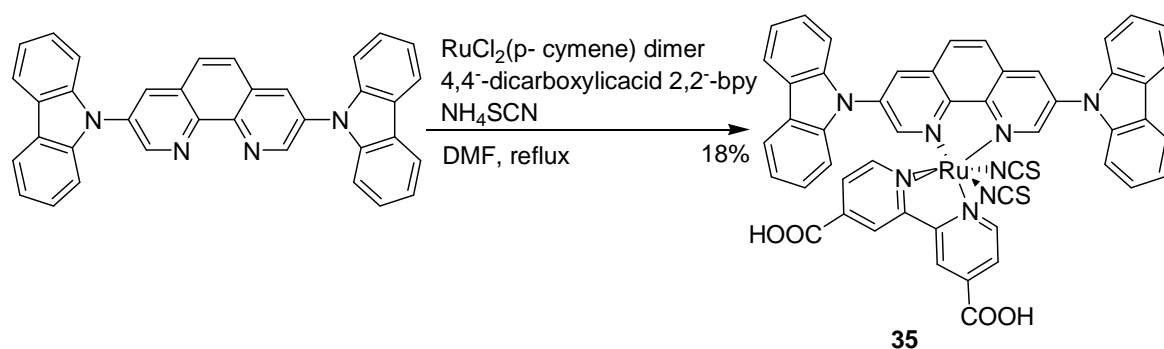
### 3,8-Di(9H-carbazol-9-yl)-1,10-phenanthroline (**41**)<sup>(15)</sup>



A mixture of 3,8- dibromo-1,10-phenanthroline (0.50 g, 1.50 mmol), 9H-carbazole (0.59 g, 3.50 mmol), CuI (0.03 g, 0.15 mmol), 18-crown-6-ether (0.01 g, 0.05 mmol), DMPU (0.11 g, 0.84 mmol) and K<sub>2</sub>CO<sub>3</sub> (0.83 g, 6.00 mmol) were mixed and degassed under a N<sub>2</sub> atmosphere. The mixture was then heated under reflux in a N<sub>2</sub> atmosphere overnight. The reaction was cooled to room temperature and quenched with HCl (1M, 50 mL). The solid was then filtered and washed with an aqueous solution of NH<sub>3</sub> (10%, 100 mL) and then with water (3 x 100 mL). The solvent evaporated and the crude product was purified by silica gel column chromatography, using an eluent mixture of DCM/ PET (8:2) to yield compound **41** as yellow solid (0.42 g, 55%).

<sup>1</sup>H NMR (CDCl<sub>3</sub>, 400 MHz): δ= 9.53 (d, *J*= 2.4, 2H), 8.55 (d, *J*= 2.4, 2H), 8.22 (d, *J*= 7.6, 4H), 8.02 (s, 2H), 7.56 (d, *J*= 7.6, 4H), 7.49 (t, *J*= 7.6, 4H), 7.39 (t, 7.6, 4H). MS (FAB) for C<sub>36</sub>H<sub>22</sub>N<sub>4</sub>, 510.20. Anal. Calc. for C<sub>36</sub>H<sub>22</sub>N<sub>4</sub>, Calcd: C, 84.66; H, 34.31; N, 10.98. Found: C, 48.56; H, 4.43; N, 11.06.

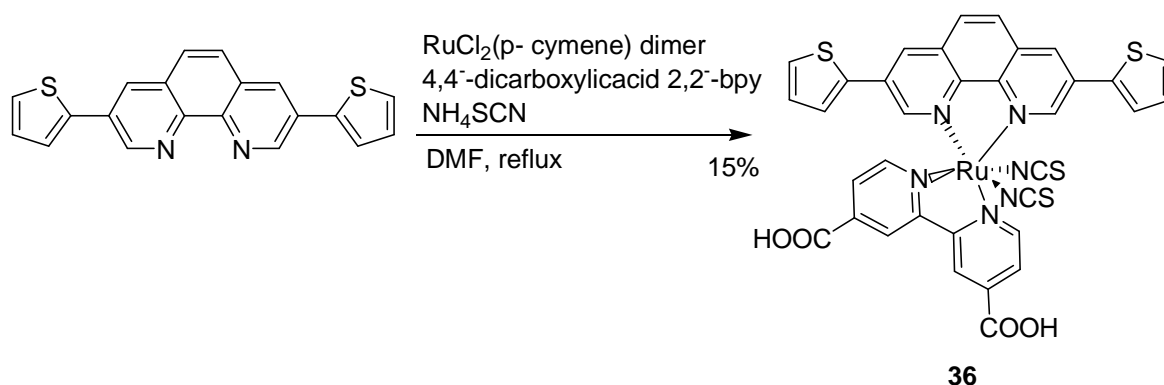
[ Ru(dcbpy)- 3,8- di(9H- carbazol-9-yl)-1,10- phenanthroline(NCS)<sub>2</sub>] (35)



Compound **41** (0.36 g, 0.71 mmol), RuCl<sub>2</sub>( p-cymene) dimer were dissolved dry DMF (50 mL), degassed and then heated under reflux at 80 °C for four hours under a N<sub>2</sub> atmosphere. Then 4,4'- dicarboxylic acid- 2,2'- bipyridine (0.17 g, 0.71 mmol) was added to this mixture and the resultant mixture was heated under reflux at 160 °C for a further four hours. Then an excess of NH<sub>4</sub>SCN (0.40 g, 5.25 mmol) was added to the reacting mixture and also heated under reflux at 130 °C for five hours. Then mixture was cooled to room temperature, the solvent was evaporated and the obtained solid was separated by filtration, washed with water (4 x 100 mL), and then with diethyl ether (4 x 100 mL) and then dried in air. The crude product was then dissolved in a MeOH/ NaOH (20 mL), and passed through a column of Sephadex (methanol as an eluent). The main band then was collected and concentrated under reduced pressure. A few drops of nitric acid (0.01 M) were added to precipitate the product to yield compound **35** as a brown/ red powder (0.11 g, 18%).

Mp: 284°C dec; <sup>(12)</sup> <sup>1</sup>H NMR (DMSO, 400 MHz): δ= 9.90 (s,1H), 9.61(d, J= 5.30, 1H), 9.38 (s, 1H), 9.14 (s, 1H), 9.05 (d, J= 8.80, 2H), 8.57 (d, J= 8.80, 1H), 8.46 (d, J=8.80, 1H), 8.40 (d, J= 8.80, 2H), 8.23 (m, 4H), 7.95 (m, 4H), 7.62 (m, 4H), 7.41 (m, 4H), 7.32 (m,4H); MS (FAB), 972.10; Anal. Calc. for C<sub>50</sub>H<sub>30</sub>N<sub>8</sub>S<sub>2</sub>O<sub>4</sub>Ru, Calcd: C, 61.72; H, 3.09; N, 11.52. Found: C, 61.50; H, 3.26; N, 11.71.

[ (Ru(dcbpy)- 3,8-di(thiophen-2-yl)1,10-phenanthroline(NCS)<sub>2</sub>] (**36**)



A mixture of compound **12** (0.24 g, 0.71 mmol) and RuCl<sub>2</sub>(p-cymene) dimer was dissolved in dry DMF (50 mL). This mixture was then degassed and then heated under reflux at 80 °C for four hours under a N<sub>2</sub> atmosphere. Then 4,4'-dicarboxylic acid-2,2'-bipyridine (0.17 g, 0.71 mmol) was added and the resulting mixture was heated under reflux at 160 °C for a further four hours. Then an excess of NH<sub>4</sub>SCN (0.40 g, 5.25 mmol) was added to the reacting mixture and heated under reflux at 130 °C for five hours. Then the mixture was cooled to room temperature, the solvent was evaporated and obtained solid was then separated by filtration, washed with water (4 x 100 mL), followed by washing with diethyl ether (4 x 100 mL) and finally dried in air. The crude product then dissolved in MeOH/NaOH mixture (20 mL) and passed through a column of Sephadex (using methanol as an eluent). The main band then was collected and concentrated under reduced pressure. A few drops of nitric acid (0.01 M) was added to precipitate the product to yield compound **36** as a dark/brown powder (0.08 g, 15%).

Mp: 262 °C dec; <sup>1</sup>H NMR (DMSO, 400 MHz): δ = 9.88 (d, *J* = 1.5, 1H), 9.34 (d, *J* = 1.6, 1H), 9.10 (s, 1H), 8.85 (s, 1H), 8.74 (s, 1H), 8.63 (s, 1H), 8.34 (d, *J* = 8.9, 1H), 8.23 (d, *J* = 8.9, 1H), 8.04 (d, *J* = 5.2, 2H), 7.95 (d, *J* = 5.3, 2H), 7.86 (d, *J* = 5.3, 2H), 7.70 (d, *J* = 5.2, 1H), 7.59 (d, *J* = 5.3, 1H), 7.43 (m, 2H), 7.18 (m, 2H); MS (FAB), 805.20; Anal. Calc. for C<sub>34</sub>H<sub>20</sub>N<sub>6</sub>S<sub>4</sub>O<sub>4</sub>Ru, Calcd: C, 50.67; H, 2.48; N, 10.43. Found: C, 50.48; H, 2.63; N, 10.56.

### 8-8-3 Fabrication of DSSC device.

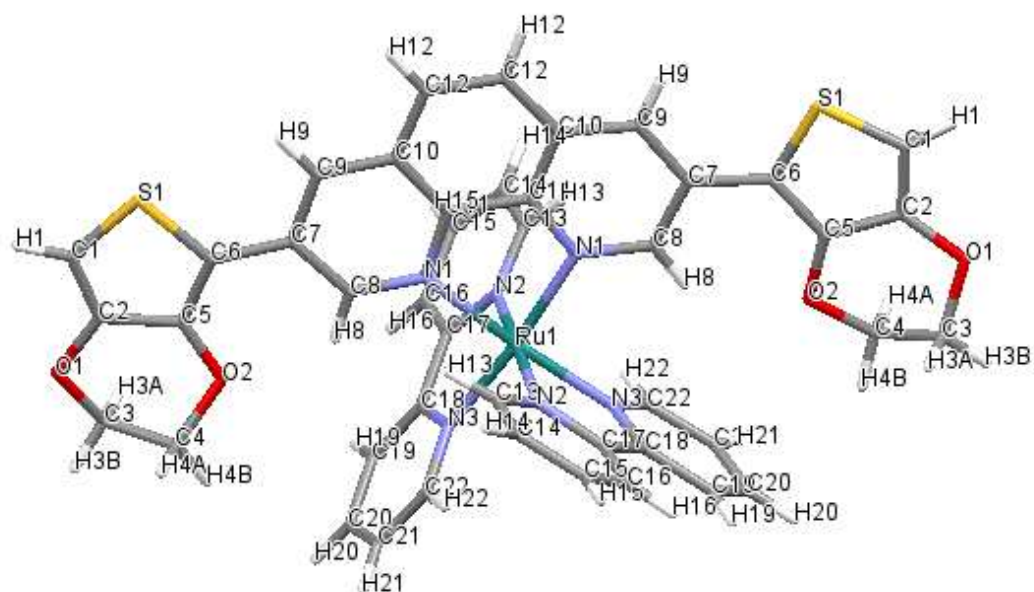
The solar cell devices were fabricated according to the procedure that reported by Grätzel and co-workers<sup>(16)</sup>. The transparent anode made from glass plate of fluoride-doped tin dioxide (F/ SnO<sub>2</sub>). This glass plate washed in water and then with ethanol and dried. The plate then immersed in 40 mM of TiCl<sub>4</sub> to enhance bonding strength between FTO glass substrate and TiO<sub>2</sub> layer. Then the glass washed with water and ethanol and then dried in vacuum. Then, this electrode was coated from conducting side with TiO<sub>2</sub> paste (18NR-T paste from dyesol). Then it was sintered at 450 °C for 30 min, and then sintered electrode treated with TiCl<sub>4</sub> 40 mM in order to improve surface roughness for dye adsorption, which can result in high photocurrent. Then TiO<sub>2</sub> electrode immersed in dye solution, 0.5 mM, 10 mL of dye solution in 1:1 of CH<sub>3</sub>CN/ tert-butylalcohol for 24 hour. Another conducting plate of FTO glass with a sheet resistance of 8- 10 Ω, drill a hole in TCE (15 ohm) 2.2 mm thickness. This plate washed with water and then with 0.1 M HCl in ethanol. Then this electrode cleaned with acetone in ultrasonic for ten minute. Then this electrode was heated in air flow at 400 °C for 30 minute to remove residual organic materials. Then deposited a Pt catalyst one drop by a pipette in the hole and heated at 400 °C for 15 minute. Then sandwich these two plates (electrodes) by hot melt, and the hole covered by Bynel 35 μm with iron soldering. Then pierce a hole in Bynel using a needle, and then drop electrolyte (I/T<sub>3</sub>) in the hole that was pierced by using vacuum and ambient pressure to drop the electrolyte in to the hole. Then this hole was covered by Bynel 1.35 μm and covered glass 0.1 mm and sealed it. The two plates are then joined and sealed together to prevent electrolyte from leaking. The surface area, which was selected from a sintered electrode, was 0.385 cm<sup>2</sup>. Instrument used was a Sciencetech Inc Solar Simulator, Model SF150 with an AM1.5 filter from Muller. The lamp is calibrated to 1000 W/m<sup>2</sup> by a reference silicone diode, which it was calibrated by GBSOL.

## 8-9 References

1. N. Goncalves, J. Garvelho, Z. Lima, J. Sasaki, *Mat. Lett.*, 2012, **72**, 36.
2. J. Vakros, C. Kordulis, A. Lycourghiotis, *Chem. Commun.*, 2002, 1980-1981.
3. G. Collis, A. Burrell, *J. Org. Chem.*, 2003, **68**, 8974.
4. J. Bruce, J. Chambron, P. Kolle, J. Sauvage, *J. Chem. Soc. Perkin Trans.1*, 2002, 1226.
5. S. Zhu, T. Swager, *Adv. Mater.*, 1996, **8**, 497.
6. Y. Saitog, T. Koizumi, K. Osakada, T. Yamamoto, *Can. J. Chem.*, 1997, **75**, 1336.
7. K. Araki, H. Endo, G. Masuda, T. Ogawa, *Chem. Eur. J.*, 2004, **10**, 3331.
8. W. Mammo, S. Admassie, A. Gadisa, F. Zhang, O. Inganas, M. Andersson, *Sol. Energy Mater. Sol. Cells*, 2007, **91**, 1010.
9. B. Hu, S. Fu, F. Xu, T. Tao, H. Zhu, K. Cao, W. Haung, X. You, *J. Org. Chem.*, 2011, **76**, 4444.
10. M. Sun, Q. Niu, R. Yang, B. Du, R. Liu, W. Yang, J. Peng, Y. Cao, *Eur. Polym. J.*, 2007, **43**, 1916.
11. S. Zhu, T. Swager, *J. Am. Chem. Soc.*, 1997, **119**, 12568.
12. X. Chen, X. Yang, B. Holliday, *J. Am. Chem. Soc.*, 2008, **130**, 1546.
13. D. Tzalis, Y. Tor, S. Failla, J. Siegel, *Tetrahedron Lett.*, 1995, **36**, 3489.
14. H. Joshi, R. Jamshid, Y. Tor, *Angew. Chem. Int. Ed.*, 1999, **38**, 2722.
15. H. Suzuki, T. Kanbara, T. Yamamoto, *Inorg. Chim. Acta.*, 2004, **375**, 4335.
16. M. Grätzel, S. Ito, P. Chen, P. Comte, M. Nazeeruddin, P. Liska, P. Peachy, *Prog. Photovol: Res. Appl.*, 2007, **10**, 768.

## 8-10 Appendix

### 8-10-1 X- ray crystallography data of compound 32



### 8-10-2 Crystal structure information

Empirical formula	C <sub>44</sub> H <sub>32</sub> F <sub>12</sub> N <sub>6</sub> O <sub>4</sub> P <sub>2</sub> Ru S <sub>2</sub>
Formula weight	1163.40
Temperature	150(2) K
Wavelength	0.71073 Å
Crystal system, space group	Monoclinic, C2/c

#### Unit cell dimensions

a = 12.1077(7) Å	alpha = 90°
b = 27.6852(18) Å	beta = 101.665(6)°
c = 29.008(2) Å	gamma = 90°

Volume	9522.6(11) Å <sup>3</sup> , Z = 8
Calculated density	1.752 Mg/m <sup>3</sup>
Absorption coefficient	0.591 mm <sup>-1</sup>
F(000)	5088
Crystal size	0.27 x 0.10 x 0.04 mm

Theta range for data collection 2.94 to 24.83 deg.

Limiting indices -14<=h<=14, -32<=k<=31, -34<=l<=32

Reflections collected / unique 35287 / 8137 [R(int) = 0.1193]

Completeness to theta = 24.83 98.9 %

Absorption correction Analytical

Max. and min. transmission 0.9767 and 0.8567

Refinement method Full-matrix least-squares on F<sup>2</sup>

Data / restraints / parameters 8137 / 72 / 744

Goodness-of-fit on F<sup>2</sup> 1.017

Final R indices [I>2sigma(I)] R1 = 0.0704, wR2 = 0.1538

R indices (all data) R1 = 0.1403, wR2 = 0.1998

Extinction coefficient none

Largest diff. peak and hole 0.99 and -0.76 e.A<sup>-3</sup>

**8-10-3 Table 2: Atomic coordinates (x 10<sup>4</sup>) and equivalent isotropic displacement parameters (Å<sup>2</sup> x 10<sup>3</sup>) for compound 32**

U(eq) is defined as one third of the trace of the orthogonalized U<sub>ij</sub> tensor.

	x	y	z	U(eq)
Ru(1)	4807(1)	3955(1)	8763(1)	29(1)
S(1)	1425(2)	5348(1)	10026(1)	45(1)
S(2)	9359(2)	2815(1)	10348(1)	54(1)
O(1)	-140(5)	5955(2)	8876(2)	61(2)
O(2)	1678(5)	5332(2)	8715(2)	46(2)
O(3)	8135(5)	2696(2)	9010(2)	50(2)
O(4)	10157(5)	2123(2)	9298(2)	54(2)
O(5'')	6830(20)	6536(10)	9965(10)	93(8)
O(5')	7440(30)	6982(12)	9813(11)	110(10)
O(5)	6740(20)	6388(8)	9082(8)	108(7)
O(6)	3969(18)	1839(8)	2203(8)	134(7)
N(1)	5686(5)	4562(2)	8636(2)	28(1)

N(2)	3677(5)	4269(2)	8225(2)	30(2)
N(3)	5480(5)	3503(2)	8324(2)	35(2)
N(4)	3872(5)	3334(2)	8791(2)	36(2)
N(5)	5936(5)	3717(2)	9358(2)	28(1)
N(6)	4188(5)	4327(2)	9275(2)	31(2)
C(1)	6762(6)	4668(3)	8829(3)	33(2)
C(2)	7278(7)	5092(3)	8744(3)	41(2)
C(3)	6672(8)	5428(3)	8439(3)	45(2)
C(4)	5572(7)	5319(3)	8226(3)	38(2)
C(5)	5092(7)	4882(3)	8316(3)	35(2)
C(6)	3967(7)	4711(3)	8091(3)	33(2)
C(7)	3251(7)	4974(3)	7744(3)	44(2)
C(8)	2240(8)	4778(3)	7530(3)	50(2)
C(9)	1932(7)	4332(3)	7671(3)	48(2)
C(10)	2668(7)	4096(3)	8015(3)	41(2)
C(11)	6300(7)	3616(3)	8096(3)	41(2)
C(12)	6813(8)	3283(3)	7858(3)	53(2)
C(13)	6452(8)	2809(3)	7852(3)	53(3)
C(14)	5615(8)	2680(3)	8085(3)	51(2)
C(15)	5130(7)	3036(3)	8321(3)	39(2)
C(16)	4188(7)	2948(3)	8558(3)	43(2)
C(17)	3607(8)	2512(3)	8546(4)	57(3)
C(18)	2709(9)	2478(3)	8765(4)	59(3)
C(19)	2374(7)	2865(3)	8997(3)	50(2)
C(20)	2973(7)	3294(3)	9000(3)	40(2)
C(21)	436(7)	5709(3)	9687(3)	53(2)
C(22)	529(7)	5696(3)	9230(3)	46(2)
C(23)	366(8)	5994(3)	8474(3)	58(3)
C(24)	784(8)	5508(3)	8342(3)	57(3)
C(25)	1409(7)	5384(3)	9147(3)	41(2)
C(26)	1979(6)	5171(3)	9550(3)	36(2)
C(27)	3306(6)	4626(3)	9232(3)	34(2)
C(28)	2950(6)	4848(3)	9619(3)	32(2)
C(29)	3550(6)	4738(3)	10065(3)	37(2)
C(30)	4481(6)	4428(3)	10128(3)	34(2)
C(31)	5162(7)	4302(3)	10586(3)	36(2)
C(32)	6055(7)	4011(3)	10619(3)	39(2)
C(33)	4783(6)	4223(2)	9728(3)	30(2)
C(34)	5715(6)	3908(2)	9768(2)	28(2)
C(35)	6361(6)	3794(3)	10212(3)	33(2)
C(36)	7259(6)	3475(3)	10228(3)	35(2)
C(37)	7486(6)	3274(3)	9825(3)	35(2)
C(38)	6800(6)	3413(2)	9385(3)	33(2)
C(39)	8418(6)	2940(3)	9828(3)	38(2)
C(40)	8716(7)	2687(3)	9465(3)	40(2)
C(41')	8380(20)	2294(9)	8720(8)	80(9)
C(41)	8947(17)	2584(6)	8688(7)	44(5)
C(42)	9537(9)	2148(4)	8828(4)	69(3)
C(43)	9706(7)	2400(3)	9607(3)	45(2)
C(44)	10126(8)	2438(3)	10076(3)	56(3)
C(51)	7766(11)	6561(5)	9831(5)	92(4)
C(52)	7668(10)	6293(4)	9366(4)	82(3)
C(61)	4476(11)	2191(5)	2352(5)	26(3)

P(1)	2573(13)	3573(6)	2533(7)	48(4)
F(1)	3261(19)	3087(9)	2671(18)	72(9)
F(2)	3714(14)	3853(8)	2530(9)	58(8)
F(3)	1902(19)	4065(6)	2389(10)	44(6)
F(4)	2470(20)	3449(10)	1995(8)	104(9)
F(5)	2680(20)	3705(12)	3069(7)	86(10)
F(6)	1430(14)	3301(9)	2532(9)	93(8)
P(1')	2658(15)	3599(7)	2620(7)	60(5)
F(1')	3400(20)	3143(11)	2800(20)	108(16)
F(2')	3700(20)	3849(11)	2457(9)	87(10)
F(3')	1910(30)	4064(9)	2460(12)	88(12)
F(4')	2255(19)	3376(10)	2108(8)	127(13)
F(5')	3050(20)	3836(13)	3133(8)	90(9)
F(6')	1600(20)	3365(12)	2782(12)	175(18)
P(2)	9834(4)	4008(2)	8794(2)	35(2)
F(7)	9760(8)	4386(4)	9191(4)	94(4)
F(8)	10269(7)	3577(3)	9138(3)	91(4)
F(9)	11105(8)	4175(4)	8826(4)	94(4)
F(10)	8579(8)	3849(3)	8760(4)	106(4)
F(11)	9840(11)	3666(4)	8361(4)	128(5)
F(12)	9406(8)	4442(4)	8445(4)	103(4)
P(2')	9820(12)	4011(5)	8819(5)	95(9)
F(7')	9526(18)	4564(6)	8911(8)	109(8)
F(8')	8812(12)	3850(5)	9080(6)	62(6)
F(9')	10674(16)	4024(11)	9315(7)	193(15)
F(10')	8896(17)	4043(10)	8342(6)	169(13)
F(11')	10041(18)	3457(6)	8730(9)	119(9)
F(12')	10806(15)	4139(7)	8556(7)	99(8)

---

**8-10-4 Table 3-7: Bond lengths [ $\text{\AA}$ ] and angles [deg] for compound 32**

---

Ru(1)-N(2)	2.050(5)
Ru(1)-N(1)	2.063(6)
Ru(1)-N(6)	2.066(6)
Ru(1)-N(3)	2.067(7)
Ru(1)-N(4)	2.069(6)
Ru(1)-N(5)	2.079(5)
S(1)-C(21)	1.710(9)
S(1)-C(26)	1.723(8)
S(2)-C(44)	1.695(10)
S(2)-C(39)	1.732(8)
O(1)-C(22)	1.374(10)
O(1)-C(23)	1.427(11)
O(2)-C(25)	1.366(10)
O(2)-C(24)	1.452(10)
O(3)-C(40)	1.364(9)
O(3)-C(41)	1.52(2)
O(4)-C(43)	1.376(10)
O(4)-C(42)	1.418(11)

O(5")-C(51)	1.27(3)
O(5")-O(5')	1.55(4)
O(5')-C(51)	1.23(3)
O(5)-C(52)	1.28(2)
O(6)-C(61)	1.18(2)
N(1)-C(1)	1.342(9)
N(1)-C(5)	1.376(9)
N(2)-C(10)	1.338(9)
N(2)-C(6)	1.353(9)
N(3)-C(11)	1.337(10)
N(3)-C(15)	1.360(10)
N(4)-C(20)	1.354(10)
N(4)-C(16)	1.361(10)
N(5)-C(38)	1.333(9)
N(5)-C(34)	1.377(9)
N(6)-C(27)	1.337(9)
N(6)-C(33)	1.396(9)
C(1)-C(2)	1.376(10)
C(2)-C(3)	1.386(11)
C(3)-C(4)	1.383(11)
C(4)-C(5)	1.389(10)
C(5)-C(6)	1.465(11)
C(6)-C(7)	1.393(10)
C(7)-C(8)	1.368(12)
C(8)-C(9)	1.376(12)
C(9)-C(10)	1.363(10)
C(11)-C(12)	1.375(11)
C(12)-C(13)	1.380(12)
C(13)-C(14)	1.375(13)
C(14)-C(15)	1.394(12)
C(15)-C(16)	1.466(12)
C(16)-C(17)	1.394(12)
C(17)-C(18)	1.369(13)
C(18)-C(19)	1.370(13)
C(19)-C(20)	1.389(11)
C(21)-C(22)	1.352(12)
C(22)-C(25)	1.429(11)
C(23)-C(24)	1.516(12)
C(25)-C(26)	1.363(11)
C(26)-C(28)	1.459(10)
C(27)-C(28)	1.423(11)
C(28)-C(29)	1.383(10)
C(29)-C(30)	1.398(11)
C(30)-C(33)	1.405(11)
C(30)-C(31)	1.456(10)
C(31)-C(32)	1.337(11)
C(32)-C(35)	1.439(11)
C(33)-C(34)	1.413(10)
C(34)-C(35)	1.399(10)
C(35)-C(36)	1.393(10)
C(36)-C(37)	1.372(11)
C(37)-C(38)	1.428(10)
C(37)-C(39)	1.459(11)

C(39)-C(40)	1.372(11)
C(40)-C(43)	1.427(11)
C(41)-C(42)	1.42(2)
C(43)-C(44)	1.356(12)
C(51)-C(52)	1.523(16)
C(61)-C(61)#1	1.38(3)
P(1)-F(6)	1.576(15)
P(1)-F(4)	1.577(17)
P(1)-F(5)	1.578(16)
P(1)-F(2)	1.585(13)
P(1)-F(1)	1.592(15)
P(1)-F(3)	1.598(14)
P(1')-F(1')	1.576(17)
P(1')-F(6')	1.586(17)
P(1')-F(3')	1.586(17)
P(1')-F(2')	1.588(17)
P(1')-F(4')	1.591(16)
P(1')-F(5')	1.607(17)
P(2)-F(10)	1.566(10)
P(2)-F(7)	1.570(10)
P(2)-F(11)	1.574(11)
P(2)-F(8)	1.576(10)
P(2)-F(12)	1.590(10)
P(2)-F(9)	1.592(10)
P(2')-F(12')	1.583(16)
P(2')-F(11')	1.587(17)
P(2')-F(9')	1.592(18)
P(2')-F(10')	1.597(18)
P(2')-F(7')	1.605(17)
P(2')-F(8')	1.623(16)
N(2)-Ru(1)-N(1)	78.9(2)
N(2)-Ru(1)-N(6)	93.1(2)
N(1)-Ru(1)-N(6)	89.8(2)
N(2)-Ru(1)-N(3)	94.1(2)
N(1)-Ru(1)-N(3)	95.8(3)
N(6)-Ru(1)-N(3)	171.6(2)
N(2)-Ru(1)-N(4)	95.5(2)
N(1)-Ru(1)-N(4)	172.1(2)
N(6)-Ru(1)-N(4)	96.0(3)
N(3)-Ru(1)-N(4)	78.9(3)
N(2)-Ru(1)-N(5)	172.7(2)
N(1)-Ru(1)-N(5)	97.4(2)
N(6)-Ru(1)-N(5)	80.5(2)
N(3)-Ru(1)-N(5)	92.6(2)
N(4)-Ru(1)-N(5)	88.7(2)
C(21)-S(1)-C(26)	92.6(4)
C(44)-S(2)-C(39)	92.5(4)
C(22)-O(1)-C(23)	111.4(7)
C(25)-O(2)-C(24)	111.7(6)
C(40)-O(3)-C(41)	108.6(9)
C(43)-O(4)-C(42)	113.3(7)
C(51)-O(5'')-O(5')	50.4(16)

C(51)-O(5')-O(5'')	53.1(17)
C(1)-N(1)-C(5)	118.2(6)
C(1)-N(1)-Ru(1)	126.5(5)
C(5)-N(1)-Ru(1)	115.3(5)
C(10)-N(2)-C(6)	117.4(6)
C(10)-N(2)-Ru(1)	127.0(5)
C(6)-N(2)-Ru(1)	115.5(5)
C(11)-N(3)-C(15)	118.8(7)
C(11)-N(3)-Ru(1)	126.0(5)
C(15)-N(3)-Ru(1)	114.7(6)
C(20)-N(4)-C(16)	119.4(7)
C(20)-N(4)-Ru(1)	125.6(5)
C(16)-N(4)-Ru(1)	115.0(6)
C(38)-N(5)-C(34)	118.6(6)
C(38)-N(5)-Ru(1)	128.7(5)
C(34)-N(5)-Ru(1)	112.7(5)
C(27)-N(6)-C(33)	117.7(6)
C(27)-N(6)-Ru(1)	129.8(5)
C(33)-N(6)-Ru(1)	112.5(5)
N(1)-C(1)-C(2)	123.2(7)
C(1)-C(2)-C(3)	119.2(8)
C(4)-C(3)-C(2)	118.4(8)
C(3)-C(4)-C(5)	120.5(7)
N(1)-C(5)-C(4)	120.4(7)
N(1)-C(5)-C(6)	113.9(6)
C(4)-C(5)-C(6)	125.8(7)
N(2)-C(6)-C(7)	121.3(7)
N(2)-C(6)-C(5)	115.9(6)
C(7)-C(6)-C(5)	122.7(7)
C(8)-C(7)-C(6)	119.4(8)
C(7)-C(8)-C(9)	119.5(8)
C(10)-C(9)-C(8)	118.2(8)
N(2)-C(10)-C(9)	124.2(8)
N(3)-C(11)-C(12)	123.2(8)
C(11)-C(12)-C(13)	118.0(9)
C(14)-C(13)-C(12)	120.2(9)
C(13)-C(14)-C(15)	118.9(8)
N(3)-C(15)-C(14)	120.9(8)
N(3)-C(15)-C(16)	115.2(7)
C(14)-C(15)-C(16)	123.8(8)
N(4)-C(16)-C(17)	120.1(9)
N(4)-C(16)-C(15)	115.2(7)
C(17)-C(16)-C(15)	124.7(8)
C(18)-C(17)-C(16)	119.4(9)
C(17)-C(18)-C(19)	121.1(9)
C(18)-C(19)-C(20)	117.8(9)
N(4)-C(20)-C(19)	122.2(9)
C(22)-C(21)-S(1)	111.1(7)
C(21)-C(22)-O(1)	124.3(8)
C(21)-C(22)-C(25)	113.2(8)
O(1)-C(22)-C(25)	122.5(8)
O(1)-C(23)-C(24)	111.1(8)
O(2)-C(24)-C(23)	110.2(7)

C(26)-C(25)-O(2)	124.6(7)
C(26)-C(25)-C(22)	112.5(8)
O(2)-C(25)-C(22)	122.8(7)
C(25)-C(26)-C(28)	129.6(7)
C(25)-C(26)-S(1)	110.6(6)
C(28)-C(26)-S(1)	119.8(6)
N(6)-C(27)-C(28)	123.9(7)
C(29)-C(28)-C(27)	117.2(7)
C(29)-C(28)-C(26)	121.4(7)
C(27)-C(28)-C(26)	121.4(7)
C(28)-C(29)-C(30)	121.1(8)
C(29)-C(30)-C(33)	118.4(7)
C(29)-C(30)-C(31)	124.1(7)
C(33)-C(30)-C(31)	117.5(7)
C(32)-C(31)-C(30)	120.7(7)
C(31)-C(32)-C(35)	122.2(7)
N(6)-C(33)-C(30)	121.7(7)
N(6)-C(33)-C(34)	117.1(7)
C(30)-C(33)-C(34)	121.2(7)
N(5)-C(34)-C(35)	122.5(7)
N(5)-C(34)-C(33)	117.2(6)
C(35)-C(34)-C(33)	120.3(7)
C(36)-C(35)-C(34)	117.5(7)
C(36)-C(35)-C(32)	124.4(7)
C(34)-C(35)-C(32)	118.1(7)
C(37)-C(36)-C(35)	121.1(7)
C(36)-C(37)-C(38)	118.1(7)
C(36)-C(37)-C(39)	122.8(7)
C(38)-C(37)-C(39)	119.1(7)
N(5)-C(38)-C(37)	122.1(7)
C(40)-C(39)-C(37)	130.1(7)
C(40)-C(39)-S(2)	109.7(6)
C(37)-C(39)-S(2)	120.2(6)
O(3)-C(40)-C(39)	124.6(7)
O(3)-C(40)-C(43)	121.9(8)
C(39)-C(40)-C(43)	113.5(7)
C(42)-C(41)-O(3)	110.3(13)
O(4)-C(42)-C(41)	117.1(11)
C(44)-C(43)-O(4)	125.4(8)
C(44)-C(43)-C(40)	111.7(8)
O(4)-C(43)-C(40)	122.9(8)
C(43)-C(44)-S(2)	112.6(7)
O(5')-C(51)-O(5")	77(2)
O(5')-C(51)-C(52)	117.4(19)
O(5")-C(51)-C(52)	109.1(16)
O(5)-C(52)-C(51)	111.8(15)
O(6)-C(61)-C(61)#1	124.7(13)
F(6)-P(1)-F(4)	90.0(8)
F(6)-P(1)-F(5)	90.5(8)
F(4)-P(1)-F(5)	179.2(13)
F(6)-P(1)-F(2)	179.2(15)
F(4)-P(1)-F(2)	89.8(8)
F(5)-P(1)-F(2)	89.6(8)

F(6)-P(1)-F(1)	90.6(9)
F(4)-P(1)-F(1)	90(2)
F(5)-P(1)-F(1)	91(2)
F(2)-P(1)-F(1)	90.1(9)
F(6)-P(1)-F(3)	90.4(14)
F(4)-P(1)-F(3)	89.6(10)
F(5)-P(1)-F(3)	89.8(10)
F(2)-P(1)-F(3)	88.8(13)
F(1)-P(1)-F(3)	178.9(16)
F(1')-P(1')-F(6')	90.9(11)
F(1')-P(1')-F(3')	178(3)
F(6')-P(1')-F(3')	88(2)
F(1')-P(1')-F(2')	90.7(11)
F(6')-P(1')-F(2')	178.3(17)
F(3')-P(1')-F(2')	90(2)
F(1')-P(1')-F(4')	92(2)
F(6')-P(1')-F(4')	90.3(9)
F(3')-P(1')-F(4')	89.7(10)
F(2')-P(1')-F(4')	90.2(9)
F(1')-P(1')-F(5')	89(3)
F(6')-P(1')-F(5')	89.9(9)
F(3')-P(1')-F(5')	89.2(11)
F(2')-P(1')-F(5')	89.5(8)
F(4')-P(1')-F(5')	178.8(16)
F(10)-P(2)-F(7)	92.1(5)
F(10)-P(2)-F(11)	86.6(7)
F(7)-P(2)-F(11)	174.4(7)
F(10)-P(2)-F(8)	91.3(5)
F(7)-P(2)-F(8)	95.8(7)
F(11)-P(2)-F(8)	89.7(6)
F(10)-P(2)-F(12)	89.2(5)
F(7)-P(2)-F(12)	84.5(6)
F(11)-P(2)-F(12)	90.0(6)
F(8)-P(2)-F(12)	179.3(6)
F(10)-P(2)-F(9)	179.4(7)
F(7)-P(2)-F(9)	87.9(6)
F(11)-P(2)-F(9)	93.4(7)
F(8)-P(2)-F(9)	89.3(5)
F(12)-P(2)-F(9)	90.2(5)
F(12')-P(2')-F(11')	88.2(9)
F(12')-P(2')-F(9')	90.9(8)
F(11')-P(2')-F(9')	94.0(16)
F(12')-P(2')-F(10')	91.9(9)
F(11')-P(2')-F(10')	91.3(16)
F(9')-P(2')-F(10')	174.1(15)
F(12')-P(2')-F(7')	94.7(13)
F(11')-P(2')-F(7')	176.8(14)
F(9')-P(2')-F(7')	87.3(10)
F(10')-P(2')-F(7')	87.2(10)
F(12')-P(2')-F(8')	176.9(13)
F(11')-P(2')-F(8')	88.8(9)
F(9')-P(2')-F(8')	89.9(9)
F(10')-P(2')-F(8')	87.6(8)

Symmetry transformations used to generate equivalent atoms:

#1 -x+1,y,-z+1/2

**8-10-5 Table 4-7: Anisotropic displacement parameters ( $\text{\AA}^2 \times 10^3$ ) for compound 32**

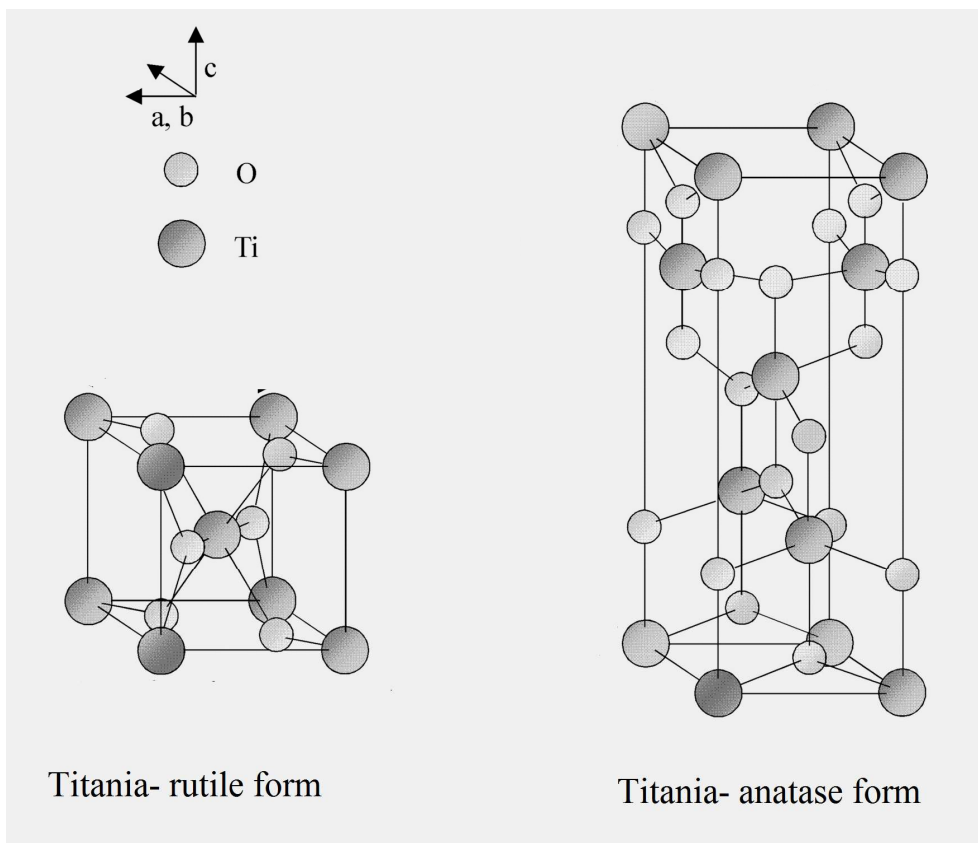
The anisotropic displacement factor exponent takes the form:

$$-2 \pi^2 [ h^2 a^{*2} U_{11} + \dots + 2 h k a^* b^* U_{12} ]$$

	U11	U22	U33	U23	U13	U12
Ru(1)	34(1)	24(1)	25(1)	1(1)	0(1)	1(1)
S(1)	42(1)	53(1)	42(1)	-3(1)	12(1)	4(1)
S(2)	47(1)	56(2)	49(1)	3(1)	-11(1)	11(1)
O(1)	50(4)	80(5)	53(4)	5(4)	8(3)	24(3)
O(2)	43(4)	59(4)	34(3)	2(3)	7(3)	12(3)
O(3)	51(4)	52(4)	42(4)	1(3)	-3(3)	21(3)
O(4)	50(4)	46(4)	61(4)	5(3)	0(3)	16(3)
N(1)	36(4)	24(3)	24(3)	-2(3)	9(3)	0(3)
N(2)	42(4)	25(3)	19(3)	3(3)	1(3)	4(3)
N(3)	42(4)	30(4)	26(3)	2(3)	-5(3)	8(3)
N(4)	33(4)	31(4)	38(4)	4(3)	-10(3)	-3(3)
N(5)	33(4)	26(3)	22(3)	4(3)	-2(3)	-2(3)
N(6)	33(4)	26(3)	31(4)	1(3)	2(3)	-6(3)
C(1)	38(5)	31(4)	32(4)	-6(3)	8(4)	1(4)
C(2)	42(5)	38(5)	45(5)	-6(4)	15(4)	-2(4)
C(3)	64(6)	31(5)	47(5)	4(4)	27(5)	-4(4)
C(4)	56(6)	29(4)	31(4)	7(4)	11(4)	2(4)
C(5)	47(5)	26(4)	34(5)	2(4)	9(4)	11(4)
C(6)	42(5)	31(4)	28(4)	1(4)	9(4)	8(4)
C(7)	61(6)	41(5)	31(5)	6(4)	10(4)	12(4)
C(8)	60(6)	48(6)	33(5)	-2(4)	-9(5)	16(5)
C(9)	45(5)	50(6)	40(5)	1(4)	-15(4)	8(4)
C(10)	48(5)	33(4)	37(5)	3(4)	0(4)	-3(4)
C(11)	55(6)	29(5)	39(5)	4(4)	8(4)	15(4)
C(12)	69(7)	42(5)	51(6)	0(5)	16(5)	18(5)
C(13)	64(7)	49(6)	39(5)	-13(4)	-3(5)	23(5)
C(14)	57(6)	34(5)	56(6)	-9(5)	-2(5)	6(4)
C(15)	45(5)	28(5)	38(5)	-4(4)	-7(4)	6(4)
C(16)	43(5)	33(5)	47(5)	-8(4)	-9(4)	6(4)
C(17)	57(6)	35(5)	68(7)	-5(5)	-12(5)	-5(5)
C(18)	56(6)	35(5)	78(7)	10(5)	-7(5)	-16(5)
C(19)	44(5)	48(6)	53(6)	15(5)	-4(5)	-14(4)
C(20)	42(5)	39(5)	35(5)	14(4)	-7(4)	-2(4)
C(21)	45(5)	65(6)	50(6)	-13(5)	11(4)	10(5)
C(22)	41(5)	47(5)	51(6)	-7(4)	9(4)	11(4)
C(23)	45(6)	74(7)	54(6)	7(5)	7(5)	18(5)
C(24)	51(6)	71(7)	44(6)	2(5)	1(5)	8(5)
C(25)	38(5)	44(5)	36(5)	-7(4)	1(4)	-5(4)

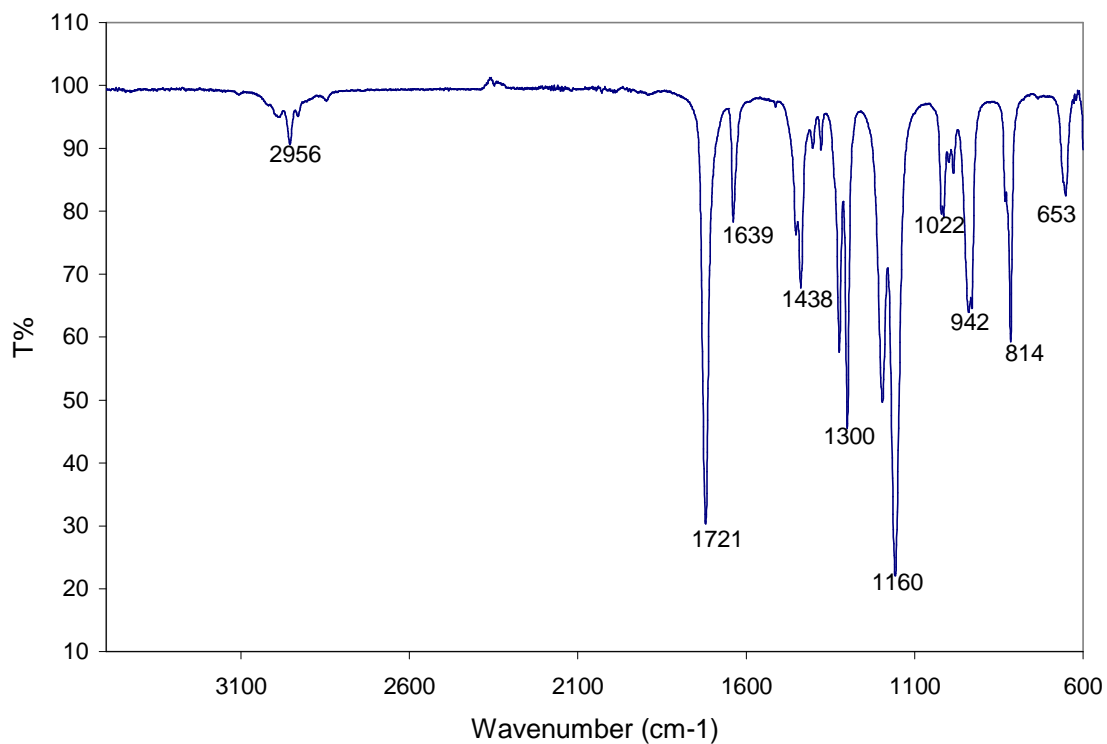
C(26)	30(4)	46(5)	33(5)	-6(4)	12(4)	-7(4)
C(27)	37(5)	30(4)	34(5)	3(4)	8(4)	-3(4)
C(28)	31(4)	32(4)	34(5)	-4(4)	8(4)	-9(3)
C(29)	35(5)	39(5)	39(5)	1(4)	11(4)	-6(4)
C(30)	31(4)	37(5)	35(5)	-5(4)	6(4)	-8(4)
C(31)	49(5)	34(4)	26(4)	-1(4)	8(4)	-1(4)
C(32)	48(5)	40(5)	26(4)	-2(4)	-1(4)	-10(4)
C(33)	35(4)	25(4)	28(4)	0(3)	3(3)	-6(3)
C(34)	35(4)	22(4)	25(4)	-1(3)	3(3)	-4(3)
C(35)	32(4)	31(4)	33(4)	7(4)	1(4)	-7(3)
C(36)	33(5)	37(5)	31(5)	4(4)	1(4)	-5(4)
C(37)	34(5)	32(4)	34(5)	10(4)	-5(4)	-4(3)
C(38)	38(5)	22(4)	36(5)	3(3)	4(4)	-2(3)
C(39)	31(4)	36(5)	42(5)	6(4)	-3(4)	1(4)
C(40)	40(5)	30(4)	42(5)	4(4)	-10(4)	1(4)
C(41')	89(18)	84(17)	54(13)	-45(14)	-17(13)	65(15)
C(41)	57(13)	23(10)	50(11)	-10(9)	5(10)	-7(9)
C(42)	53(7)	85(8)	64(7)	-6(6)	3(5)	5(6)
C(43)	37(5)	32(5)	62(6)	4(4)	-1(5)	5(4)
C(44)	44(6)	55(6)	60(6)	11(5)	-11(5)	6(4)
P(1)	45(6)	35(7)	67(8)	8(5)	16(5)	-11(4)
F(1)	71(12)	30(9)	130(30)	24(10)	45(13)	8(8)
F(2)	32(10)	32(13)	109(18)	2(10)	7(9)	-7(8)
F(3)	38(11)	26(12)	60(11)	0(8)	-9(8)	-9(9)
F(4)	170(20)	52(10)	101(14)	-33(10)	63(14)	-21(11)
F(5)	70(14)	150(30)	38(11)	0(11)	13(10)	40(15)
F(6)	47(9)	46(11)	190(20)	40(13)	20(12)	-6(7)
P(1')	77(9)	27(6)	72(9)	-1(5)	7(6)	-1(5)
F(1')	130(20)	80(20)	120(30)	40(18)	30(14)	27(15)
F(2')	140(20)	80(20)	58(11)	13(11)	40(12)	-14(16)
F(3')	110(20)	70(20)	75(16)	-10(12)	-13(14)	11(15)
F(4')	86(14)	110(20)	150(20)	-96(19)	-60(16)	28(13)
F(5')	120(20)	93(13)	46(10)	8(9)	-5(11)	2(13)
F(6')	170(30)	65(13)	350(50)	0(20)	190(30)	-25(16)
P(2)	25(3)	53(5)	29(3)	-5(3)	9(2)	18(3)
P(2')	85(14)	62(13)	130(18)	-16(12)	3(12)	-5

### 8-10-2 TiO<sub>2</sub> unit cell structure

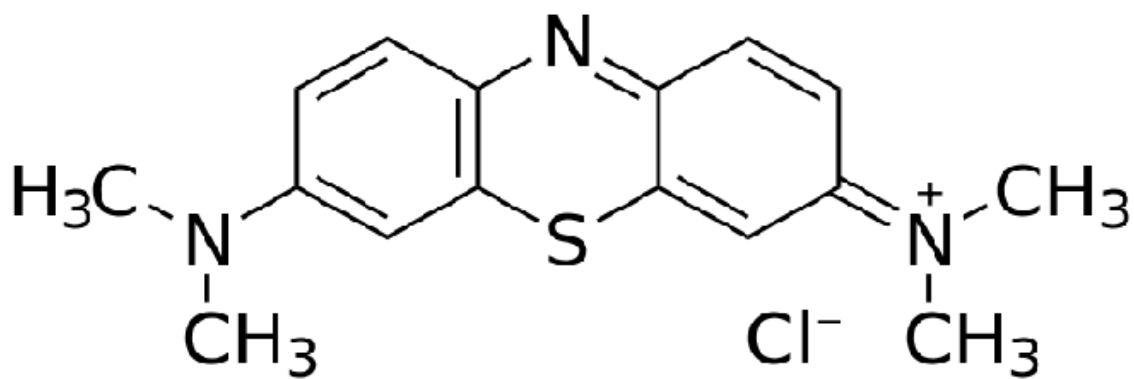
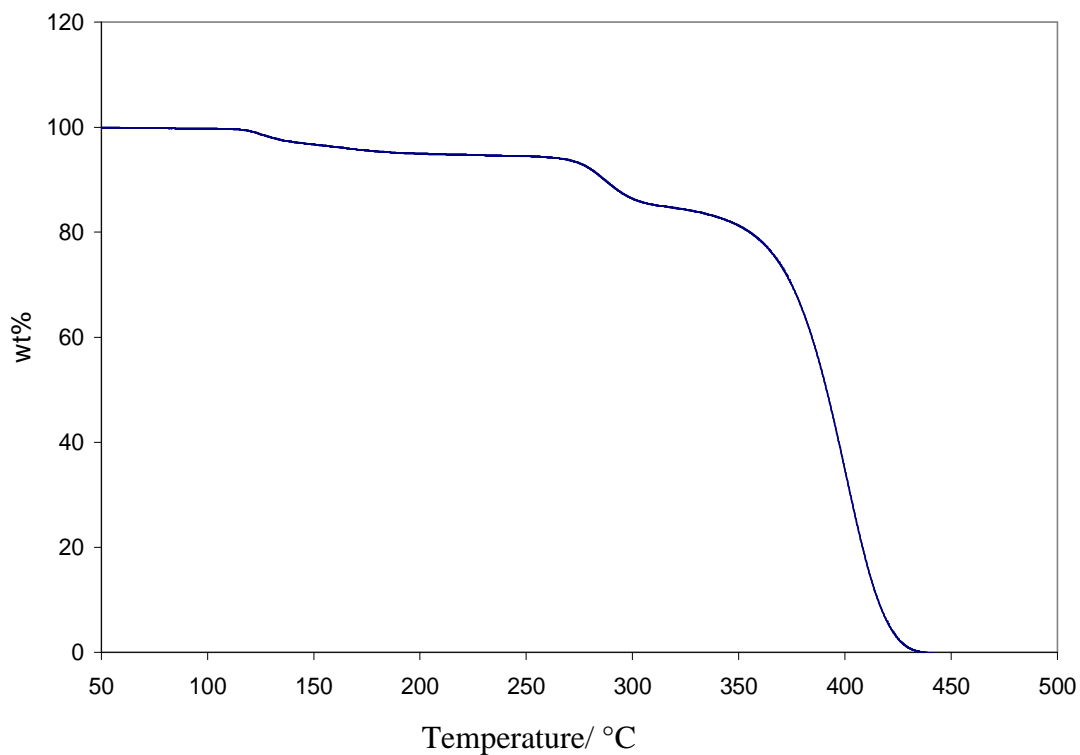


Re- printed from ( A. Fahmi, C. Minot, B. Silvi, M. Causa, *Phys. Rev. B*, 1993, **47**, 11717.)

### 8-10-3 FTIR spectrum of MMA



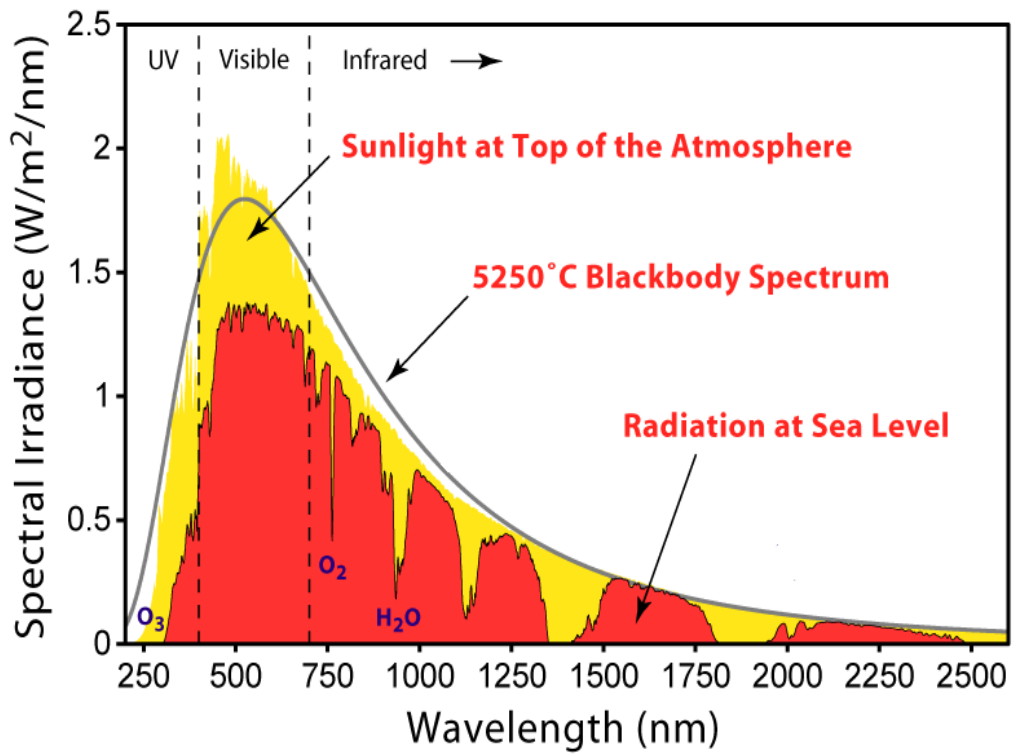
#### 8-10-4 TGA of PMMA that extracted from TiO<sub>2</sub>



**Methylene blue dye**

Re-printed from ( E. Golz, D. Griend, *Anal. Chem.*, 2013, **85**, 1240).

### AM 1.5 solar radiation spectrum



Ref: [http://upload.wikimedia.org/wikipedia/commons/4/4c/solar\\_spectrum.png](http://upload.wikimedia.org/wikipedia/commons/4/4c/solar_spectrum.png).